FLEXURAL MODELLING OF STEEL FIBRE REINFORCED SPRAYED CONCRETE

by

Peter Alwyn Jones

A Doctoral Thesis

Submitted in partial fulfilment of the requirements of the award of

Doctor of Philosophy of Loughborough University

10th August 1998

ABSTRACT

A current limitation on the structural use of steel fibre reinforced sprayed concrete (that equally applies to cast steel fibre reinforced concrete) is a distinct lack of accepted design rationales and codes of practice. The research presented here describes the development of a model, based on conventional principles of mechanics, for predicting the flexure behaviour of a wet process sprayed concrete reinforced with deformed steel fibres. The model uses a stress-block diagram to represent the stresses (and resultant forces) that develop at a cracked section by three discrete stress zones: (a) a compressive zone; (b) an uncracked tensile zone; and (3) a cracked tensile zone. By using this concept it is shown that the stress-block diagram, and hence flexural behaviour, is a function of six principal parameters: the compressive stress-strain relation; the tensile stress-strain relation; fibre pull-out behaviour; the number and distribution of fibres across the crack in terms of their positions, orientations and embedment lengths; and the strain/crack-width profile in relation to the deflection of the beam.

An experimental investigation was undertaken to obtain relationships for these parameters. Five tests were identified and developed as part of this investigation: a single fibre pull-out test; a compression test; a strain analysis test; a fibre distribution analysis test; and a flexural toughness test. The majority of the investigation used cast (as opposed to sprayed) specimens so that the test variables under investigation could be better controlled. Spraying trials were also successfully undertaken to demonstrate the pumpability and sprayability of the adopted mixes and to verify the use of the model for both cast and sprayed specimens.

The results of the modelling analysis showed a reasonable agreement between the model predictions and experimental results in terms of the load-deflection response. However, the accuracy of the model is probably unacceptable for it to be currently used in design. A subsequent analysis highlighted the single fibre pull-out test and the sensitivity of the strain analysis tests as being the main cause of the discrepancies. As a result, recommendations are made for how the model might be improved.

Overall this research has provided a valuable insight into the reinforcing mechanisms, fracture processes and characteristics of failure associated with the flexural behaviour of steel fibre reinforced concrete. It is envisaged that the proposed model could form the basis of a design rationale which requires only the matrix strength, fibre type, fibre content, beam size and loading geometry as design input parameters. Consequently, it could offer a much needed link between flexural toughness performance and structural design, by allowing designers to make informed choices regarding the mix design in order to meet the ultimate and serviceability requirements of a particular application.

Dedicated in loving memory
to my father, Owen Jones.

TABLE OF CONTENTS

Acknowledgements

I wish to thank Loughborough University for funding and supporting this Ph.D. as part of a University Studentship, without which it would not have been possible.

I wish to thank both my Supervisor of Research - Dr. Peter Robins - and my Director of Research - Dr. Simon Austin - for their professional and personal support, guidance and encouragement during the last four years. In particular, I would like to thank them for giving me the opportunity to undertake this Ph.D. and thereby fulfil an ambition.

I wish to thank the other members of the academic, laboratory, administrative and research staff affiliated to the Department of Civil and Building Engineering at Loughborough University who also contributed to this thesis. Special thanks are due to Dr. Jim Chandler for his advice on digital image processing and measurement, particularly in the use of the computer software Visilog and his own least squares image transformation program; Malcolm Gould for his skill and patience in the manufacture of key elements of the experimental apparatus including the steel mould and fibre positioning block used for casting the single fibre pull out test specimens, the aluminium yoke used in the flexural toughness tests, the steel target and stencils used in the strain analysis tests and the LVDT support collars used in the compression and fibre pull-out tests; David Spendlove for his advice on concrete mixing, curing and testing, and for training me in the use of the laboratory equipment; Mark Harrod for his advice on photography; Vince Scotham in the Department of Mechanical Engineering for developing the strain analysis photographs; Terry Smith and Bob Temple in the Department of Production Engineering for producing the X-ray photographs; and Leigh Payton for digitising the X-ray photographs as part of his B.Eng. final year project.

Special thanks are due to Gunform Limited, particularly John and Andy Dunlop and everyone involved in the successful steel fibre reinforced concrete spraying trial at Falmouth in November 1996. I am much indebted for their time and use of their equipment which they contributed free of charge. I also thank Fosroc International

Limited for undertaking the preliminary spraying trial, free of charge, at their facility in Birmingham during August 1995. In particular, I wish to thank Keith Gordan, Les Talbot and Roy Gibson for making this trial a success.

I wish to thank all the material suppliers who contributed specialist advice and materials to the experimental work. In particular the following:

Bekaert Building Products	-	steel fibres;
Castle Cement Limited	-	Portland cement;
Porterway Limited	-	aggregates;
Elkem Microsilica	-	silica fume slurry;
Sika Limited	-	superplasticiser; and
Tecni Measure Limited	-	strain gauges and adhesives.

I wish to thank all my family for their support and encouragement during the preparation of this thesis. Particularly my mother, who has had to put up with me during the last six months of the preparation of this thesis.

Lastly, but by no means least, I wish to thank my partner Lucy for supporting me when I first decided to undertake this Ph.D. and then for her continual encouragement, support and devotion. This thesis is as much her accomplishment as mine.

Notation

a	-	pitch of lines on an undeformed grating
A	-	empirical constant used in equation 6.1
A_c	-	compressive stress block area per unit beam width
A_f	-	fibre cross-sectional area
b	-	beam width
B	-	brittleness ratio
c	-	neutral axis depth
c^t	-	depth over which concrete can transfer stress at the cracked section of a beam
d	-	beam depth
d^*	-	notch size
d_f	-	fibre diameter
E_c	-	static modulus of elasticity in compression
E_t	-	static modulus of elasticity in tension
f_N	-	pull-out force of the N^{th} fibre across a crack
f_c	-	compressive strength
f_t	-	tensile strength
$F_{comp.}$	-	total resultant compressive force
$F_{tensile}$	-	total resultant tensile force
F_n	-	total fibre bridging force transferred by the n^{th} fibre zone across a crack
K_1,K_2		empirical constants used in equations 7.6, 7.7 and 7.8
K^*	-	empirical constant used in equation 7.9
l	-	beam span
l_f	-	fibre embedment length
l_{ch}	-	characteristic length
l_i	-	distance between adjacent grid spots on an undeformed grid
l_p	-	distance between the load points of a third-point loaded beam
Δl_x	-	change in the distance between adjacent grid spots in the x-direction
L	-	total beam length
L^{tot}_{2D}	-	apparent total fibre length in 2D space
L^*_{2D}	-	apparent fibre embedment length in 2D space
L^{tot}_{3D}	-	total fibre length in 3D space
L^*_{3D}	-	fibre embedment length in 3D space
M_e	-	internal moment capacity of a beam in flexure
M_n	-	internal moment generated by the n^{th} fibre zone across a cracked beam in flexure
n	-	fibre geometry constant
N	-	total number of fibres bridging a cracked section of a beam in flexure
N_f	-	fibres density
$(Nf)_n$	-	fibre density in the n^{th} fibre zone of a cracked beam in flexure
p_x	-	distance between Moiré fringes
P	-	flexural load capacity of a beam
P_a	-	applied load

P_n	-	probabilistic single fibre pull-out force
R_w R_e, $R_{30,10}$		toughness quotients as defined in Figure 2.19 (p. 52)
s	-	average fibre spacing
S_g	-	strain gauge factor
U_{pf}	-	projected fibre length
V_f	-	fibre volume fraction
x_c	-	position of the centroid of the compressive stress block relative to the neutral axis
w	-	crack-width
$\overline{w}$	-	average crack-width
w_{max}	-	maximum crack-width
w_c	-	critical crack-width
y_n	-	position of the mid-point of the n^{th} fibre zone relative to the neutral axis
y_N	-	position of the N^{th} fibre relative to the neutral axis
y_c,y_t	-	position of a resultant tensile and compressive force relative to the neutral axis
y_g	-	position of the centreline of a strain gauge relative to the neutral axis
α	-	scale factor
β	-	fibre efficiency factor
δ_m	-	deflection of a beam at mid-span relative to the supports
δ_c	-	deflection of a beam at a crack relative to the supports
δ^*	-	deflection of a third-point loaded beam at mid-span relative to the load points
ε_x,ε_y	-	axial strain in the x and y directions
ε_{max}	-	the strain measured at the extreme compressive face of a beam in flexure
ε_c	-	compressive strain
ε^*_c	-	compressive strain corresponding to f_c
ε_{cr}	-	tensile cracking strain
γ_{xy}	-	shear strain
λ,η	-	empirical constants used in equation 3.3
θ_f	-	fibre orientation
θ_{2D}	-	fibre orientation in 2D space
θ_{3D}	-	fibre orientation in 3D space
σ	-	axial stress
σ_{max}	-	maximum axial stress
σ_c	-	compressive stress
σ_t	-	tensile stress
σ_m	-	matrix tensile stress
σ_{fe}	-	equivalent flexural strength
σ_{fu}	-	flexural strength of a fibre reinforced concrete matrix
σ_o	-	flexural strength of a plain concrete matrix
σ_a	-	aggregate bridging stress
σ_f	-	fibre bridging stress
σ_{ps}	-	fibre pre-stress
dR/R	-	change in electrical resistance
CMOD	-	crack mouth opening displacement

1. INTRODUCTION

1.1 BACKGROUND

Plain, or unreinforced, sprayed concrete like conventionally cast unreinforced concrete is a relatively brittle material with limited capacity to resist tensile stresses and strains without cracking. As a result the material is commonly reinforced with a variety of materials including: steel mesh or bars pre-fixed to the surface on to which the plain sprayed concrete is applied; or discrete short fibres added to the plain concrete during the mixing process to produce fibre reinforced sprayed concrete. A wide range of fibre types are available including steel, polymeric and glass, but steel fibres have by far the largest usage (Robins, 1995).

Although the inclusion of short, randomly distributed fibres has long been recognised as an effective means of improving the physical properties of a brittle matrix (Hannant, 1978; Balaguru and Shah, 1994), the use of steel fibres in sprayed concrete has only been commercially available since the early 1970's. However, since its inception, steel fibre reinforced sprayed concrete has undergone extensive technological advancement and is currently established all over the world as a versatile and cost-effective construction method for a wide range of applications where conventional reinforcement, such as wire mesh, can be difficult and expensive to install. One of the main benefits of the material is its ability to sustain flexural or tensile load at large deformations after the matrix has cracked. This is known as the energy-absorption capacity or toughness of the material. Consequently, its largest application is in the temporary or permanent ground support for tunnelling, mining and slope stabilisation work, where its enhanced post-crack load resistance and ductility under deforming ground is of great importance. However, it is increasingly being used in other applications including thin shell dome structures, canal linings, strengthening of masonry arches, and the repair and rehabilitation of concrete structures (Austin, 1995).

Flexural behaviour, or more specifically flexural toughness, is one of the most important properties of steel fibre reinforced sprayed concrete for many structural applications. This property is commonly characterised by a load-deflection curve obtained from flexural tests on beam specimens under third-point loading. Although there is no question about the contribution of fibres to enhancing flexural toughness, how to evaluate it and express it as a useful parameter for design purposes is still under debate. Furthermore while some attempts have been made at modelling the flexural behaviour of steel fibre reinforced concrete (sprayed and cast), no one model has been able to fully explain what actually happens at the critical cracked section in terms of the fracture processes or fibre-matrix interactions. Consequently, a current limitation on the structural use of the material (that equally applies to cast steel fibre concrete) is a distinct lack of accepted design codes of practice, which has resulted in a general lack of confidence in its use as a permanent structural material.

Recent, and continued, improvements in materials and spraying technology will ensure that steel fibre reinforced sprayed concrete continues to be the preferred construction method for many specialist applications that utilise its flexibility and post-crack structural performance. However, its development as a permanent structural material will only continue if the following research needs can be addressed:

- to develop a better understanding of the fracture processes and reinforcing mechanisms associated with the material under flexural loading;
- to develop methods of quantifying the stresses and forces that occur at the critical cracked section under flexural loading, and to relate these to the load-deflection response; and
- to develop appropriate design rationales and procedures which are universally accepted for the design of the material.

The research described in this thesis primarily concentrates on addressing these needs.

1.2 TERMINOLOGY

A wide range of expressions are currently in use to describe the sprayed concrete material and process (including sprayed concrete, shotcrete and gunite). Consequently, terminology has become confused. Therefore, throughout this thesis the term 'sprayed

concrete' is used to describe all spray applied concrete and mortars, even though some references (generally of Scandinavian or North American origin) may refer to this material as shotcrete or gunite.

1.3 AIMS AND OBJECTIVES OF THIS THESIS

The principal aim of this thesis was to investigate the reinforcing mechanisms and fracture processes associated with steel fibre reinforced sprayed concrete under flexural load, in order to develop a model - based on conventional principles of mechanics - to predict flexural behaviour in the form of a load-deflection response.

The proposed model uses a stress-block diagram approach to represent the stresses (and resultant forces) that develop at the critical section of a steel fibre reinforced concrete beam under flexural loading. A theoretical analysis undertaken by the author on a propagating crack in flexure showed that the stress-block diagram can be represented by three distinct zones: (a) a compression zone; (b) an uncracked tensile zone; and (c) a cracked tensile zone. Furthermore, the cracked tensile zone can be further divided into three sub-zones: an aggregate bridging zone; a fibre bridging zone and a traction free zone. By using this concept it was proposed that the shape and magnitude of the stress-block diagram is related to the following principal parameters: the compressive stress-strain relation; the tensile stress-strain relation; single fibre pull-out behaviour; the number and distribution of fibres across the critical section in terms of their positions, orientations and embedment lengths; and the strain/crack-width profile at the critical section in relation to mid-span deflection. If relationships can be established for these parameters, then the shape and magnitude of the stress-block diagram can be predicted for a given mid-span beam deflection. Hence, providing equilibrium of force in the stress-block diagram is satisfied, the flexural load capacity of a beam can be computed using conventional principals of mechanics. This process can then be repeated for a range of increasing mid-span deflection values in order to determine the complete flexural load-deflection response.

In view of the above aims, the principal objective of this study was to test the following hypothesis:

Given the matrix compressive strength, fibre volume, fibre type, cross-section dimensions and loading geometry of a steel fibre reinforced sprayed concrete beam, the flexural load-deflection curve can be predicted using a stress-block diagram approach, if the following principal parameter relationships are known:

- *the uniaxial compressive stress-strain relationship;*
- *the uniaxial tensile stress-strain relationship;*
- *the single fibre pull-out load versus crack-width relationship;*
- *the number, distribution, embedment lengths and orientation of the fibres bridging the cracked section of the beam; and*
- *the strain profile and the crack-width profile in relation to mid-span beam deflection.*

It was envisaged that if the model could be shown to predict the load-deflection response, then it could provide a valuable insight into the fracture processes and reinforcing mechanisms associated with flexural behaviour of both cast and sprayed steel fibre reinforced concrete. Consequently, it could form the basis of a design rationale for predicting flexural behaviour, and thereby provide a link between structural design and flexural toughness performance.

1.4 OVERVIEW OF WORK CARRIED OUT

The work carried out centred on modelling the flexural behaviour of a typical wet process sprayed concrete, reinforced with 30mm long and 0.5mm diameter hooked-ended steel fibres in a range of quantities between 0-120kg/m^3 (that is between approximately 0-1.5% by volume). This particular fibre was chosen as being typical of the fibres used in a large proportion of wet process steel fibre reinforced sprayed concrete applications. The overall programme of work was divided into five stages as follows.

1. A literature review of current knowledge to identify the main research needs relating to (i) the future development of steel fibre reinforced sprayed concrete, and (ii) the flexural modelling of steel fibre reinforced concrete.

2. Formulation of the proposed model theory and concepts including the principal parameters and data requirements.
3. Experimental investigation and data collection to obtain the principal parameter relationships for use in the model.
4. Model implementation, testing and results.
5. Conclusions and recommendations for further study.

The experimental investigation used three base concrete mixes, designated Matrix A, B and C, to which steel fibres were added in quantities of 40, 80 and 120kg/m^3. The design of the mixes only differed in the proportion of the silica fume they contained. This enabled the influence of silica fume on the properties of the mixes to also be investigated. The principal mix was Matrix C which contained a silica fume content of 10% by weight of cement. Matrix B was a secondary mix containing a silica fume content of 5% by weight of cement, and Matrix A was a control mix containing no silica fume.

The majority of the experimental investigation used cast (as opposed to sprayed) specimens so that the test variables and material parameters under investigation could be better controlled. However, spraying trials were also undertaken to demonstrate the pumpability and sprayability of the three mixes and to verify the use of the model for predicting the behaviour of both cast and sprayed specimens.

Five different tests were identified and developed as part of the investigation.

1. **Single fibre pull-out tests** - to determine the fibre pull-out load versus crack-width relationship. The results were used to model the forces transferred by the fibres bridging the cracked section of a beam.
2. **Compression tests** - to determine the compressive stress-strain relationship, and associated elastic modulus values. The results were used to model the compressive stress-block. Elastic modulus values determined from the test data were also used to model the uncracked tensile stress-block.
3. **Flexural toughness tests** - to determine typical load-deflection responses for a range of beam sizes under four point loading. The results were used to compare with, and verify, the model predictions.
4. **Strain analysis tests** - to determine the strain and crack-width profiles occurring at the critical section of a beam under four point loading. The results

were used to model the strain and crack-width profiles occurring at the critical section in relation to the mid-span beam deflection.

5. **Fibre distribution analysis** - to determine data relating to the number and distribution of fibres bridging a cracked section of a beam under four point loading, in terms of the fibre densities and the statistical distributions associated with fibre orientation and embedment length. These results were used in combination with the single fibre pull-out test results to model the forces transferred by the fibres bridging the cracked tensile zone of the stress-block diagram.

The testing of the model centred around the prediction of the flexural load-deflection response for the principal matrix (Matrix C) using two modelling approaches.

i. Modelling the load deflection responses associated with the strain analysis test beams, and then comparing the results with the measured responses.
ii. Modelling the generalised load-deflection responses associated with the different fibre contents, beam sizes and beam types investigated, and then comparing the results with the average responses obtained from the flexural toughness tests.

In each case, flexural loads were predicted at mid-span deflections of 0.05, 0.1, 0.2, 0.5, 1.0, 2.0 and 4.0mm.

The results of the modelling analysis showed that the model is capable of predicting the general shape of the load-deflection response associated with a sprayed or cast steel fibre reinforced concrete. However the accuracy of the model is probably unacceptable for it to be currently used as a design tool. A subsequent analysis highlighted the single fibre pull-out tests and the accuracy of the strain analysis tests as being the main causes of the discrepancies between the predicted and measured loads. As a result, recommendations were made for how the model might be improved.

Overall this study provides a valuable insight into the reinforcing mechanisms, fracture processes and kinematics of failure associated with steel fibre reinforced concrete in flexure. It also provides the basis of a design rationale for steel fibre reinforced concrete which requires only the matrix strength, fibre type, fibre volume, beam size and loading geometry as design input parameters. Consequently, it could

offer a much needed link between flexural toughness performance and structural design.

1.5 THESIS STRUCTURE

The contents of this thesis are organised as follows.

Chapter 2 provides a state-of-the-art review of steel fibre reinforced sprayed concrete. It introduces the different processes of application together with a review of specification, constituent materials, mix design, fresh and hardened properties (particularly flexural toughness) and current design methods. The main aim of this chapter is to identify the main research needs hindering the future development of this material.

Chapter 3 deals with the flexural behaviour of steel fibre reinforced concrete. It is presented as three sections: (1) a review of the reinforcing mechanisms and fracture processes which influence the shape and characteristics of the flexural load-deflection curve; (2) a review of the principal parameters associated with flexural behaviour, together with the methods available for measuring and predicting these parameters; and (3) a review of the models currently available for predicting flexural behaviour. The main aim of this chapter is to review past work and current thinking, and thereby identify the main research needs associated with the modelling of flexural behaviour.

Chapter 4 describes the research methodology on which the aims and objectives of this thesis are based. It introduces the concepts of the proposed model, together with its assumptions, principal parameters and data requirements. An outline of the experimental investigation undertaken to obtain the principal parameter relationships for use in the model is also given.

Chapter 5 describes the development, production and quality control of the sprayed and cast concrete mixes used in the experimental investigation, together with the spraying trials undertaken to demonstrate their pumpability and sprayability.

Chapter 6 describes the experimental investigation undertaken. It presents the overall testing programme, and then describes each of the five tests adopted in detail including: test development, test procedure, data analysis, and presentation and discussion of results.

Chapter 7 presents the implementation and testing of the model. It describes how the experimental data was used in the model, and then how the model was implemented to obtain predictions of flexural behaviour. The model predictions are then compared with experimental results to assess the accuracy and validity of the model.

Chapter 8 brings together the conclusions drawn from the study in terms of the experimental investigation (Chapter 6) and the model development and analysis (Chapter 7). Recommendations for future development of the model are discussed, together with areas of further study.

2. STEEL FIBRE REINFORCED SPRAYED CONCRETE: A REVIEW

2.1 INTRODUCTION

In this chapter the state-of-the-art of steel fibre reinforced sprayed concrete technology will be reviewed in the context of this thesis. It will introduce the different processes of application, together with a review of specification, constituent materials, mix design methodology, fresh and hardened properties - particularly flexural toughness - and current structural design rationales and procedures. The main research needs hindering the future development of the material in applications involving flexural loads will also be highlighted, particularly in terms of material behaviour and design methodology.

Although this chapter relates specifically to steel fibre reinforced sprayed concrete, the majority of what follows - particularly the spraying processes, specification, constituent materials and mix design methodology - applies equally to plain (non-fibre reinforced) sprayed concrete.

2.2 SPRAYING PROCESSES

2.2.1 Overview

Steel fibre reinforced sprayed concrete can be applied by either of two methods: the dry process and the wet process. Although both methods are capable of producing equally high quality concrete, there are essential differences between them which influence the choice of method for different applications (Maidl and Sommavilla,1995).

2.2.2 Dry Process

General

In the dry process, a dry - or slightly damp - mixture of cement, aggregate, fibres, and powdered admixtures (if required) are batched and thoroughly mixed. This mixture is

then added to the delivery equipment (a mechanical feeder or `gun`), where it is metered into a delivery hose and conveyed by compressed air to a nozzle. Water is injected at or close to the nozzle, and the wet concrete mixture projected onto the surface to be sprayed at velocities ranging typically between 30-60m/s (Austin, 1995a). The process is therefore self-compacting. Variations in the basic method of production include adding liquid admixtures or steel fibres, or both, via separate hoses at the nozzle. The whole process is illustrated in Figure 2.1.

Plant and equipment

The two most common types of dry process spraying machines are the rotating barrel gun (Figures 2.2a) and the rotating feed bowl gun (Figure 2.2b), which provide typical outputs of between 0.5 to 10m^3 per hour (Zangerle, 1996; Austin, 1995a; ACI 506R, 1990). The advantages of these machines are their simple operation and relatively small size. They can also be driven by diesel, electric or compressed air motors.

The spray nozzle design forms an essential part of dry process, as it initiates the mixing of the dry material with the water (ACI 506R, 1990). The rate of water addition is controlled by a valve which the nozzle operator continually adjusts in response to the consistence of the in-situ material. Consequently, accurate water control is essential to the success of dry process sprayed concrete.

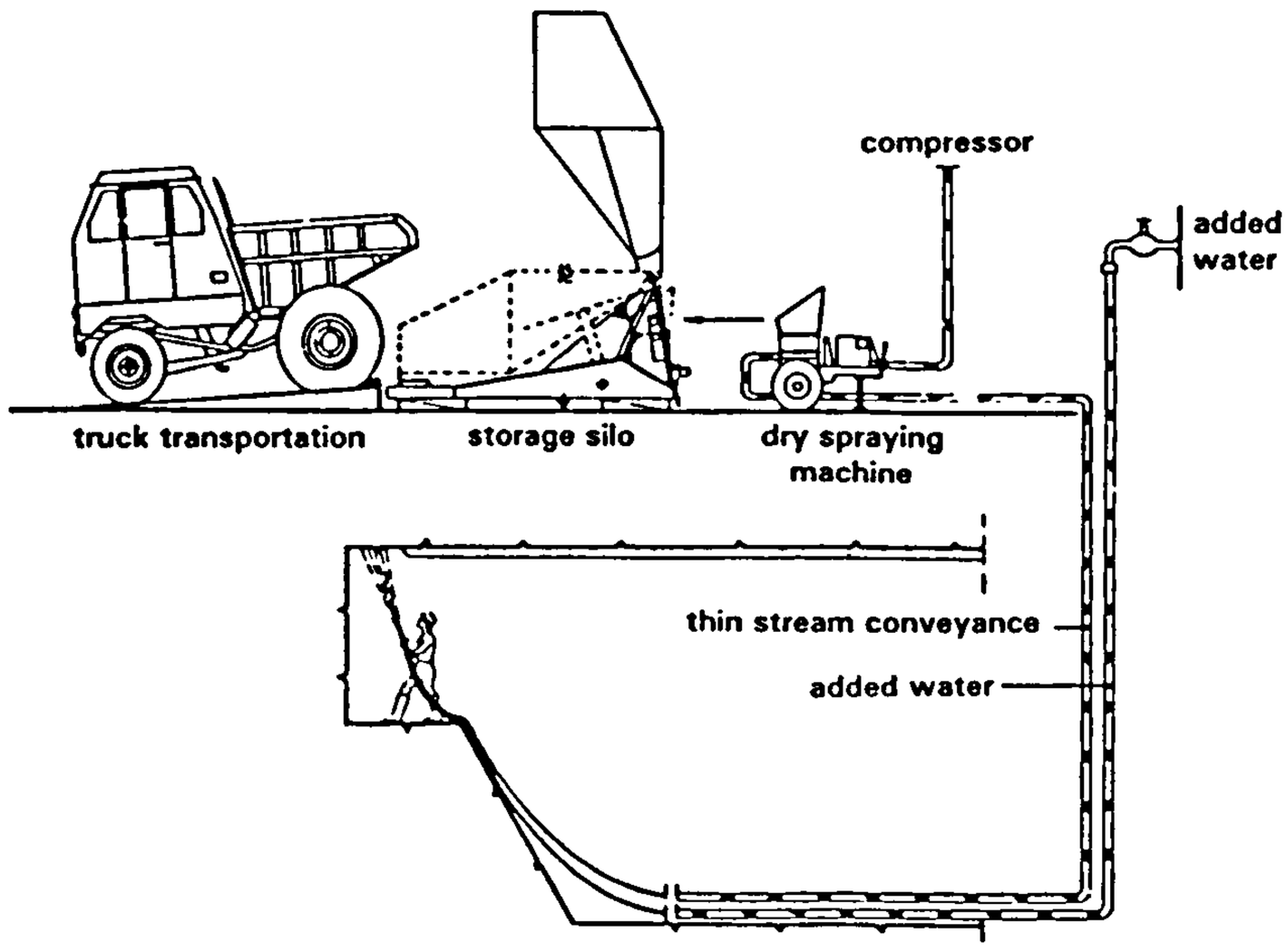

Figure 2.1 The dry process spraying method (Maidl and Sommavilla, 1995).

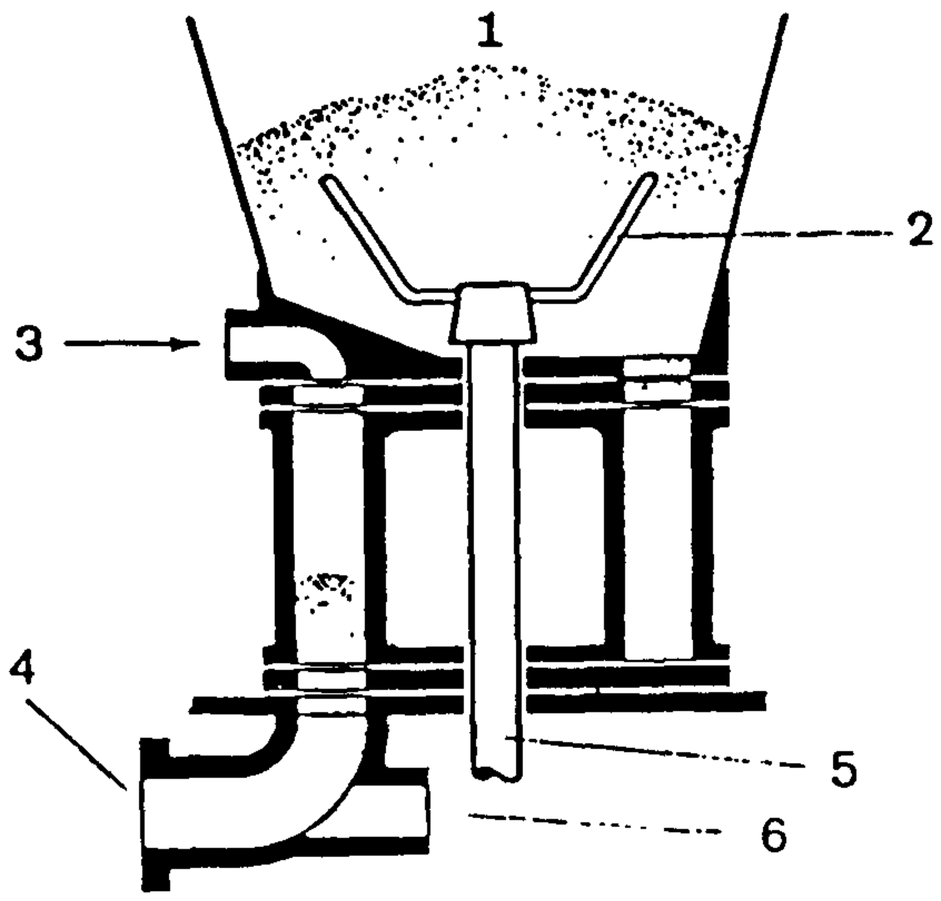

(1) Material feeding/inlet
(2) Agitator
(3) Compressed air
(4) Material exit
(5) Drive shaft
(6) Compressed air

Figure 2.2(a) A Schematic of a rotating barrel gun (Aliva).

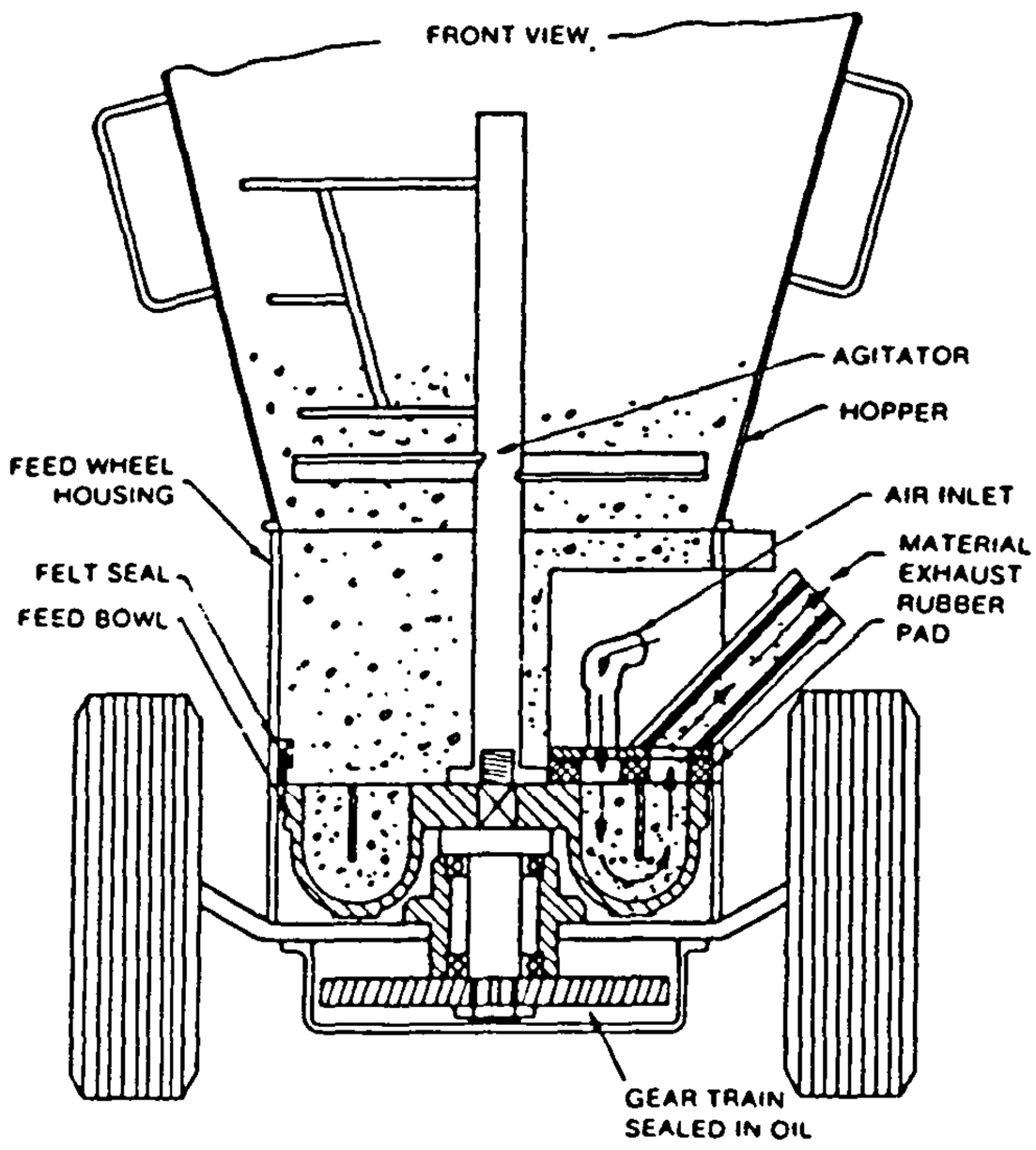

Figure 2.2(b) A Schematic of a rotating feed bowl gun (Reed Gunform).

Batching and mixing

Mixes are combined by either manual site batching, automatic site batching or using pre-bagged material (Austin, 1995a). The actual method used will depend upon economical and practical considerations. Pre-damping or pre-moisturising the dry materials before they enter the gun is recognised as an effective method of reducing dust formation and material rebound, and is also thought to improve the hydration of cement in the mix (Morgan, 1995).

2.2.3 Wet Process

General

In the wet process, all the ingredients including the mixing water but excluding any accelerators are batched and thoroughly mixed. The wet mixture is then metered into a delivery hose where it is conveyed by displacement to a nozzle. Compressed air is injected into the nozzle to atomise the concrete mix and project it on to the surface to be sprayed at velocities ranging typically between 10-30m/s (Austin, 1995a). Fibres can either be added as additional aggregate in the batching process, or directly into the ready mixed concrete mass. Liquid accelerators, if required, can also be injected at the nozzle. The whole process is illustrated in Figure 2.3.

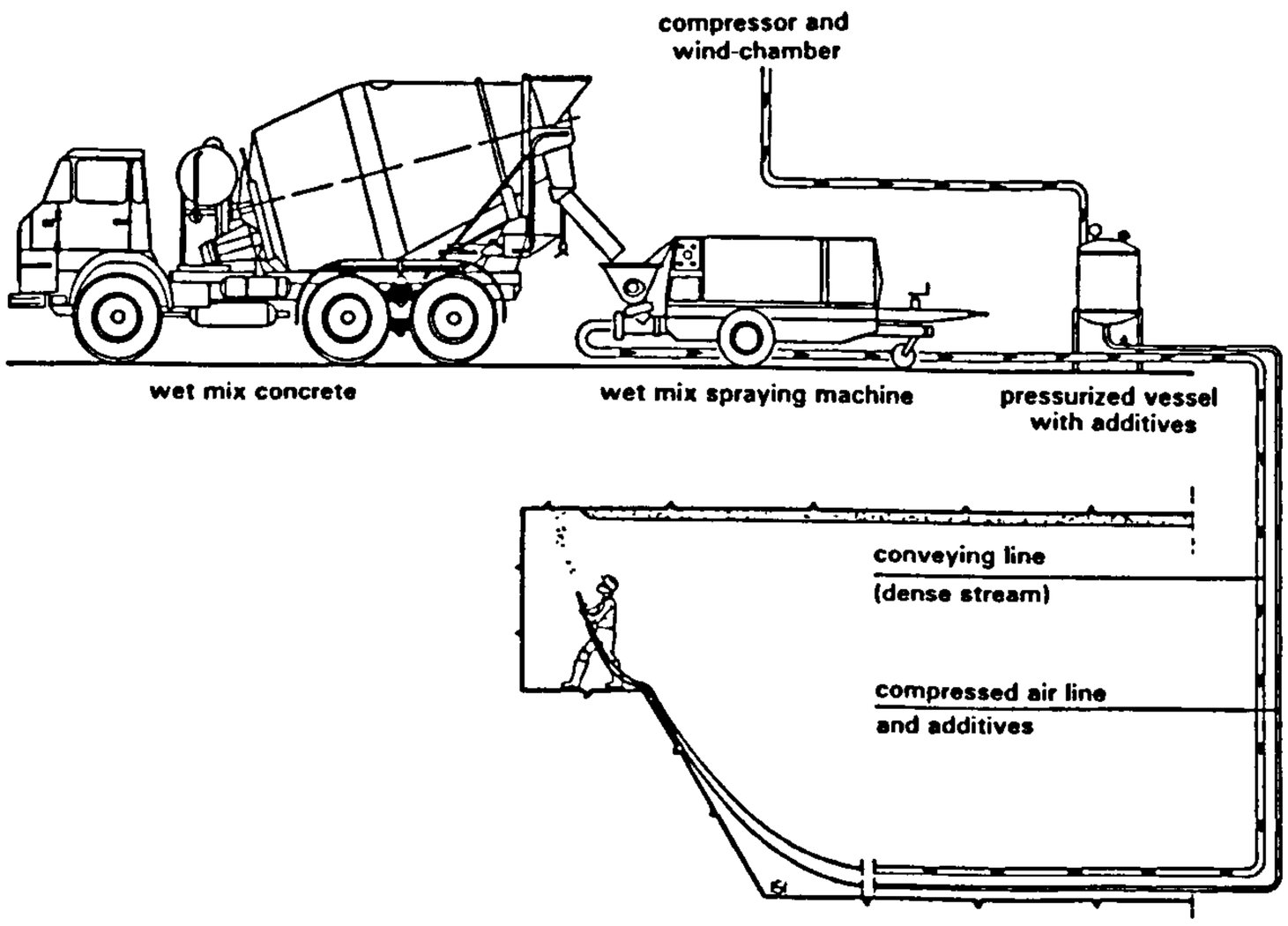

Figure 2.3 The wet process spraying method.

Plant and equipment

The following types of concrete pump are most commonly used for conveying the concrete mix to the nozzle:

- the double-piston pump (Figure 2.4) - medium to high output (5-20 m^3/hour); and
- the worm or screw pump (Figure 2.5) - low output (up to 5 m^3/hour).

Note, however, that due to the relatively small size of worm pumps there is a restriction on the particle size that can be conveyed with this type of pump. Consequently, piston pumps are used almost exclusively for conveying steel fibre reinforced sprayed concrete.

There are a variety of nozzle designs available (ACI 506R, 1990), but essentially they only differ in the way the compressed air is injected: either transversely into the concrete stream or at the circumference of the nozzle through a ring of jets (Maidl and Sommavilla, 1995). Hose sizes are dictated by fibre lengths and the capacity of the pump; typically they are 50 to 100mm in diameter (ACI 506.1R, 1984).

The use of robots and automatic nozzle operation equipment has greatly improved the working environment and quality of wet process spraying over recent years, and they are increasingly being used in tunnelling and other large underground work (Okada, 1995; Anderson and Dalseg, 1993; Maidl 1991). Further details can be found in Maidl and Sommavilla (1995).

Mixing and batching

For low volume applications (up to 5m^3), materials are usually batched on site in a conventional drum mixer or more commonly in a mixer that is integrated with the pump (Austin, 1995a). For medium and large volume applications (above 5m^3/hour), the mix can be batched off-site by a ready-mixed concrete supplier and then transported to site via a transit mixer where it is fed into the pump. However where very large volumes are required, it is becoming more common to batch the mix on site in purpose built batching plants where the quality of the mix can be better controlled by the spraying contractor (Lewis, 1997).

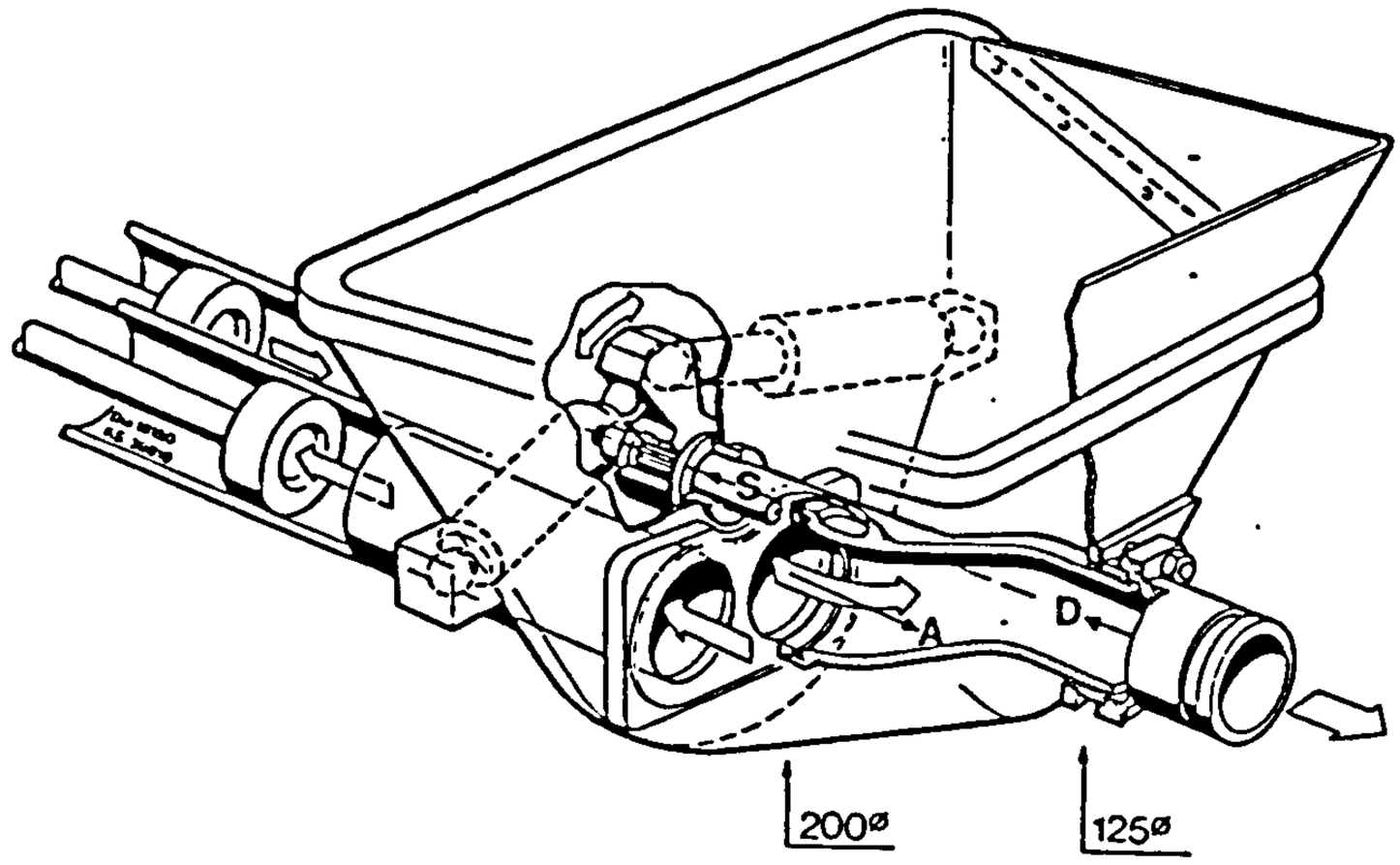

Figure 2.4 A double piston pump (Vandewalle, 1990).

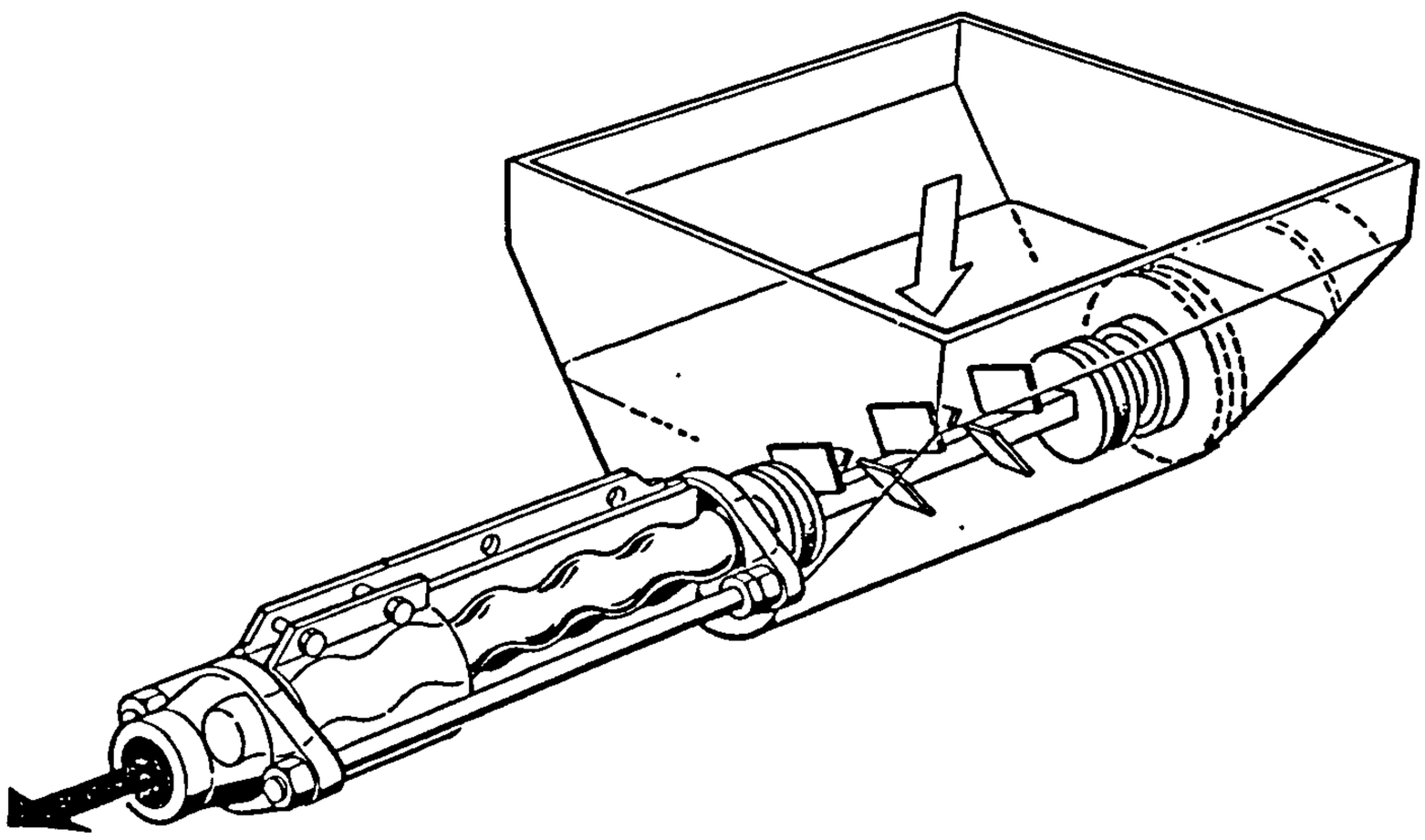

Figure 2.5 A worm pump (Vandewalle, 1990).

2.2.4 Sprayed Concrete Placement

Spraying technique

The quality of the in-place sprayed concrete primarily depends on the skills and experience of the spraying gang, and in particular the nozzle operator. The most important factors include: the control of mixing water (dry process) and accelerator (wet process), maintaining a steady and continuous supply of material to the nozzle, optimising the nozzle velocity, and adopting correct spraying technique. Comprehensive guidance on good practice and spraying technique is given in ACI 506R - *Guide to Shotcrete* (1990).

Rebound and overspray

During the spraying process losses in sprayed material, especially fibres, can arise from three main sources:

- overspray - material that misses the sprayed surface;
- cutback - excess material that adheres and is subsequently removed; and
- rebound - material that does not adhere but ricochets off the sprayed surface.

Rebound losses are typically in the order of 20-50% in the dry process and 5-15% in the wet process, and generally contain high proportions of fibres (15-70%) and coarse aggregates, with some fine aggregates and small amounts of cement (Austin, 1995a; Banthia *et al.*, 1994; Vandewalle, 1990). Not only do these losses increase the cost of application, but rebound losses also change the in-situ mix proportions from those batched. Recent developments to reduce material and fibre rebound include optimising the mix design in terms of particle kinematics (Armelin *et al.*, 1996), and using silica fume as a cement replacement (Wolsiefer and Morgan, 1993; Vandewalle, 1990; Overlie and Rippentropp, 1987).

Further information relating to rebound and other spraying losses can be found in Austin (1995a).

Finishing and curing

A natural sprayed finish is considered to be the preferred finish because the surface is not disturbed, and therefore the concrete quality in terms of bond to substrate, fibre encasement, strength and durability is unaffected (Maidl and Sommavilla, 1995; ACI

506R, 1990). Other types of finish, including finishing coats, are discussed in ACI 506R (1990).

Curing is best achieved by keeping the sprayed concrete continuously moist by covering with wet hessian (Austin, 1995a). However, wet curing is not always practical. In such cases, spray or brush applied curing membranes can provide an alternative method of curing, providing no additional sprayed concrete is to be applied. Natural curing may also be used if the relative humidity is at least 85% (ACI 506R, 1990). A recent and innovative development involves the use of internal curing admixtures which are added to the wet process sprayed concrete during mixing (Melbye, 1995).

2.2.5 Health and Safety

The application of sprayed concrete can be hazardous, not least when it is used as underground support for tunnelling and mining. In these situations working conditions can be very unpleasant due to the following:

- high cementitious dust emissions (particularly in the dry process);
- material rebound containing steel fibres, coarse aggregate and toxic/corrosive admixtures;
- handling of hazardous materials, including alkali-accelerators and hydrating cement; and
- heavy physical exertion (particularly by the nozzle operator in the wet process).

As a consequence, much research effort has been aimed at improving the working environment. Current developments include: (a) reducing dust emissions (Ono, 1996; Tazawa, 1995) and rebound (Morgan, 1991;Vandewalle, 1990; Armelin *et al.*, 1996); (b) increasing the use of robotic spraying equipment (Okada, 1995; Maidl, 1991); and (c) the development of alkali-free accelerators (Garshold and Melbye, 1996; Mai and Burge, 1996).

Further details relating to health and safety can be found in Miller (1995) and the Institution of Civil Engineers guideline on NATM in soft ground tunnelling (1996).

2.2.6 Quality Control

The main factors which determine the quality of the sprayed concrete include the specification, design, materials, spraying technique and craftsmanship (ACI 506R, 1990). Material testing either insitu, or on prepared test specimens, is commonly used to assess quality (Malmberg, 1993; EFNARC, 1996; ACI 506.2, 1995). Further information and documentation relating to material selection, specification, quality control and test procedures can be found in a recent review by Austin (1995b).

The use of steel fibres in structural applications normally requires two additional, but important quality control procedures. Assessments should be made of both the in-situ fibre content and flexural toughness performance, to help in the evaluation of the specified in-situ material performance requirements.

In-situ fibre content can be determined from either fresh samples, or hardened samples cut from the in-situ sprayed material or a test panel (EFNARC, 1996). These tests are essential for evaluating the performance of in-situ fibre reinforced sprayed concrete in structural applications, but can also be commonly used to evaluate fibre rebound (Armelin and Helene, 1995).

2.2.7 Choice of spraying process

A comparison between the wet and dry spraying processes is illustrated in Table 2.1. Further reviews comparing technical and economical aspects are given by Maidl and Sommavilla (1995) and Maidl and Feyerabend (1995). These comparisons show that there can be no fundamental preference for one of the two methods, as both methods offer unique advantages for a range of applications. For example, the dry method is more suited to low volume applications where an intermittent supply of relatively small quantities of concrete is required (i.e. bridge repairs). Whereas the wet process is more suited to high volume applications where cost-effectiveness and high placement rates are demanded (i.e. mining and tunnel construction). However, in the future, the wet process is expected to become more popular due to some significant advantages over the dry process including: a better working environment with less dust emissions, more consistent material quality and reduced material rebound.

Factor	Dry mix	Wet mix
1. Equipment	Lower total investment Maintenance relatively simple and infrequent	Less equipment at the jobsite Less wear rate in pump, hoses and nozzle Up to 60% less air consumption
2. Mixing	At the jobsite or at mixing/batching plant Premixed, dry ingredients can be used but cannot be left open in humid or wet environments Performance impaired by wet sand	Accurate mixing at mixing/batching plant Can use bulk ready mix Wet sand acceptable
3. Output	Rarely exceeds 5 m³/h in place Can be conveyed over longer distances than wet mixes	Higher than similar dry mix machines 2-10 m³/h with hand-held nozzle up to 20 m³/h with manipulator
4. Rebound	Can be 15-40 % from vertical walls 20-50 % from overhead Forms rebound pockets Loss of aggregates makes compliance with mix specification difficult, and excess cement is usually added	Low rebound with correct mix, can be less than 10%. Rebound pockets do not occur Little loss of aggregate
5. Quality	Higher strength, due to lower W/C-ratio Less homogeneous quality as the water addition is regulated by the operator and discontinuous material supply.	More difficult to obtain high strength, due to higher W/C-ratio More homogeneous quality
6. Impact velocity	Higher: - better adhesion - easier to use overhead	General adequate for tunnel/mining work
7. Additives	Powders added in mixer or before hopper Liquids at the nozzle	Generally as liquid
8. Dust	High dust production can be reduced by prewetting with 5-15% moisture (semi-wet method) or by moving the water ring back from the nozzle.	Very little dust formed Better visibility No danger of lamination by dust
9. Versatility	can be used for: sand-blasting guniting refractory materials re-surfacing	Can be used as concrete pump for pouring in place

Table 2.1 Comparison between the wet and dry processes (Vandewalle, 1990).

2.3 SPECIFICATION

In the past, specifications for sprayed concrete have often been weak, partly because of the designer's lack of familiarity and understanding of the production process and the purpose of the material (Austin, 1995b). In recent years there has been major worldwide developments in both specifications and guideline documentation, reflecting both the increasing use of the material and the needs of clients, designers and contractors for more detailed specifications and guidance. A brief overview of the main documentation currently available is given below.

In the United States, ACI Committee 506 has produced a series of documentation covering all aspects of sprayed concrete. General guidance is given in ACI 506R (1990) *Guide to Shotcrete* - re-approved 1995 - and ACI 506.1R (1984) *State-of-the-Art report on Fiber Reinforced Shotcrete* - re-approved 1989 - which gives recommendations on the applicability of both wet and dry process sprayed concrete to different types of construction, together with equipment and material requirements, and application procedures. More specific guidance is given in: ACI 506.2 (1995) *Specification for Shotcrete*; ACI 506.3R (1991) *Guide for the certification of Shotcrete Nozzleman*; and ACI 506.4R (1994) *Guide for the Evaluation of Shotcrete*.

In Japan, the Japanese Society of Civil Engineers (JSCE) has produced a *Guideline for Construction of Steel Fibre Reinforced Shotcrete* (1984). This gives advice on constituent materials, mix design, equipment, placing and quality control for both the wet and dry processes.

In Europe, there are a number of national standards and specifications for sprayed concrete including: DIN 18 551 (1991) *Sprayed Concrete; Production and Quality Control*; AFTES (1992) *Recommendations on Sprayed Concrete: Technology and Practice*; and the Norwegian Concrete Association NB No.7 (1993) *Sprayed Concrete for Rock Support - Technical Specification and Guidelines*. The European Federation of National Associations of Specialist Contractors and Material Suppliers for the Construction Industry (EFNARC) Technical Committee for Sprayed Concrete - which includes members from eleven countries - has published a *European Specification for Sprayed Concrete* (1996). This document provides recommendations for all aspects of sprayed concrete including: materials; mix design; execution of

spraying; durability; test methods; and quality control. More recently, the Technical Committee TC 104 of CEN has set-up a working group to produce a European Normative (EN) standard for sprayed concrete (Franzen and Malmberg, 1996). However, this document has currently only been published in draft form (CEN, 1997).

The International Tunnelling Association (ITA) has also produced a *Status Report on Shotcrete in Tunnelling* (1991), *Shotcrete for Underground Support: a State-of-the-Art Report with Focus on Steel Fibre Reinforcement* (Franzen, 1992), and *Shotcrete for Rock Support: a Summary Report on the State-of-the-Art in 15 Countries* (Malmberg, 1993). The latter of these is a detailed review of sprayed concrete, which includes substantial reference to the documentation described in this section.

Finally, there is a substantial amount of additional documentation which relates to the specification and design of steel fibre reinforced concrete in general (both sprayed and cast). This includes: ACI 544.4R (1988) *Design Considerations for Steel Fibre Reinforced Concrete*; ASTM C1116 (1991) *Standard Specification for Fiber-Reinforced Concrete and Shotcrete*; and JSCE (1984a) *Standard Test Methods.*

Further details relating to the specification of sprayed concrete can be found in Austin (1995b).

2.4 MATERIALS

2.4.1 Cement

Before the 1980`s most sprayed concrete was made with Ordinary Portland cement (OPC) as the only cementing material (Robins, 1995). Since that time a variety of special blended cements have been developed, containing a mixture of cements differing in chemical composition and physical properties, in order to produce cements with specific properties (Neville, 1995). Some of these cements can achieve rapid setting and/or high early strength (Schmidt, 1995; Morgan, 1991a) similar to the effects of accelerating admixtures, but supposedly without the associated adverse side effects (for example on shrinkage, long-term strength and durability). OPC is however likely to remain the most widely used cement type but increasingly in combination with cementitious additives, particularly silica fume and fly ash.

Property	Portland cement (OPC)	Fly ash (pfa)	Blast furnace slag (ggbfs)	Silica fume
Surface area (m^2/kg)	350-500	300-600	300-500	15000-20000
Bulk density (kg/m^3)	1300-1400	1000	1000-1200	200-300
Specific gravity	3.12	2.30	2.90	2.20
SiO_2 (%)	20	50	38	92

Table 2.2 Comparative properties of some cementitious materials (Lewis, 1996).

2.4.2 Cementitious Additives

Silica fume

Silica fume is a highly pozzolanic mineral admixture which can be added to sprayed concrete as an additive, or as a cement replacement, to improve the spraying and hardened properties of a concrete mix (Wolsiefer and Morgan, 1993; Morgan, 1992; Parker, 1985 & 1986; Lewis, 1996). The unique properties of silica fume, compared with other cementitious materials, are due to its much smaller particle size (approximately 100 times finer than cement) and its significantly higher reactive silica content (SiO_2) as shown in Table 2.2. These properties ensure that it combines with and distributes the products of hydration more effectively, thus improving the homogeneity and density of the concrete (Neville, 1995).

Silica fume is used as a cement replacement in both the wet and dry processes, usually at between 3 and 15% by weight of cement (Malmberg, 1993). When used in the wet process, a water-reducer or superplasticiser is also required to maintain workability. Improvements in steel fibre reinforced sprayed concrete properties, performance and production techniques, through the addition of silica fume, have been reported for both the wet process (Wolsiefer and Morgan, 1993; Overlie and Rippentropp, 1987) and the dry process (Morgan,1988). The main benefits include:

- more cohesive consistency resulting in improved adhesion to sprayed surface and increased one-pass application thickness;
- improved pumpability (by preventing bleeding and segregation);
- improved bond to various substrates, and between cement matrix and fibres;
- reduced rebound and dust emissions;

- increased compressive and flexural strengths; and
- enhanced durability, particularly with respect to density, chemical attack, freeze-thaw, and permeability.

Silica fume can be added in a undensified or condensed powdered form (Parker, 1985; Wolsiefer and Morgan, 1993) or as an aqueous slurry (Parker, 1985). Due to its extremely small particle size, the powdered forms have been found to be difficult to handle, transport and mix effectively. Silica fume slurry, consisting of a 50/50 aqueous suspension of silica fume powder, has been developed to overcome these drawbacks and is now widely used in wet process applications (Lewis, 1996).

Fly ash

Fly ash can also be added as a cement replacement (Neville, 1995; Morgan, 1995; Morgan, 1992), but its benefits and pozzalonic effect is more limited than silica fume as shown in Table 2.2. The main benefits include:

- reduced water demand and improved workability and pumpability of wet process sprayed concrete, due to the spherical shape of the fly ash particles;
- reduced heat of hydration and potential thermal cracking;
- improved chemical resistance;
- cheaper alternative to silica fume; and
- provides additional fines where high cement contents are to be avoided.

Fly ash has been used in both wet and dry processes (typically at between 10-40% by weight of cement), but compared with silica fume its use has so far been limited. However, it was recently used in the mix design for two major tunnelling projects in the UK (Annett and Varley, 1996; Earnshaw, 1997).

2.4.3 Aggregates

The aggregate quality and grading is of major importance in both wet and dry process sprayed concrete. The particle size distribution must be well graded, and only show small variations, to provide a pumpable and sprayable mix with minimal segregation, minimum rebound, and a high degree of compaction (Neville, 1995). A range of recommended aggregate grading curves are available for both the wet and dry process (ACI 506R, 1990; Vandewalle, 1990; Malmberg, 1993; EFNARC, 1996; Norwegian Concrete Association, 1993).

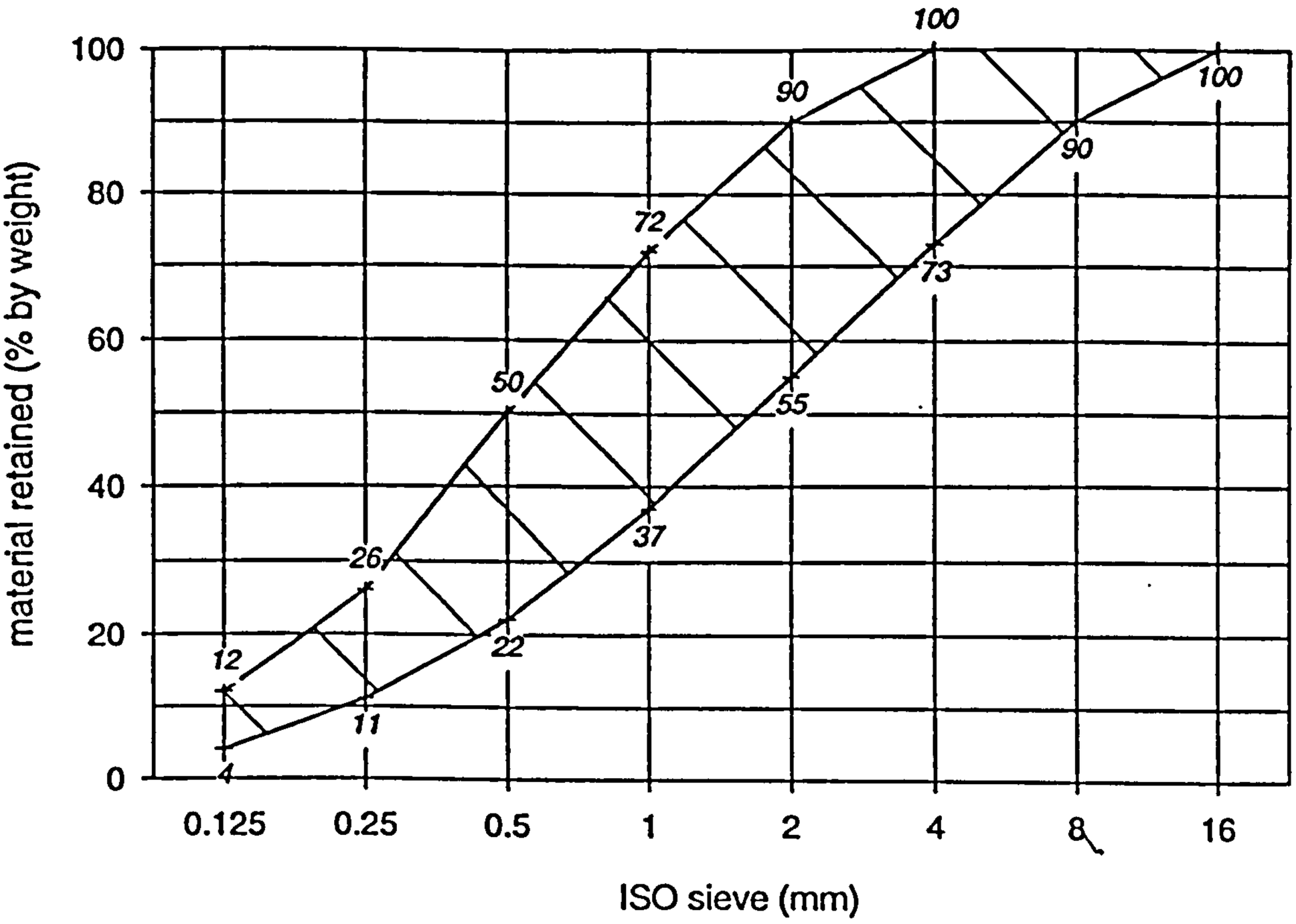

Figure 2.6 Recommended aggregate grading curve (EFNARC, 1996).

Of particular importance in the wet process, is the amount and distribution of fines (particles less than 0.125mm). Too little fine material causes segregation and the risk of clogging in the hose, although this can be overcome by the addition of more cement or silica fume. In contrast, a high fines content can result in stickiness and difficult handling characteristics, which can be overcome by increasing the addition of water reducing admixtures or superplasticisers (Neville, 1995). Establishing a suitable balance of fines is therefore essential during the mix design stage.

According to Melbye (1994), when selecting aggregates for the wet process the following criteria should apply:

- the particle size distribution curve should fall within the shaded area of Figure 2.6;
- the quantity of particles greater than 8mm should not exceed 10% of the total, and no particles should be greater than 16mm; and
- no fraction should constitute more than 30% of the total.

Further discussions relating to the aggregate requirements for both the wet and dry process can be found in Malmberg (1993).

2.4.4 Admixtures

The use of concrete admixtures is now regarded as a necessity to obtain specific properties in fresh and hardened steel fibre reinforced sprayed concrete. Types of admixtures commonly used include:

- superplasticisers/ water-reducers;
- accelerators;
- air-entrainers; and
- hydration control systems.

However of these, only accelerators can be used in the dry process. Whereas, a wet process mix can include one, some, or all of them depending on the particular requirements of the application.

Superplasticisers/water reducers

Superplasticisers (high performance water-reducers) can significantly improve the workability and cohesiveness of wet process sprayed concrete by more effectively dispersing the 'fines'. Chemically, they are either sulphonated melamine formaldehyde condensates (which form a lubricating film on the particle surfaces), or sulphonated napthalene formaldeyde condensates (which electrically charge the cement particles so that they repel each other). Further details can be found in Neville (1995).

When superplasticisers are well dispersed, the cement particles flow around each other more easily and coat the aggregate particles more effectively. They are therefore used to either increase workability for a given water/cement ratio, or to significantly reduce the water/cement ratio for a given workability (Neville, 1995). In sprayed concrete applications they are mainly used to improve the pumpability of mixes with relatively low water/cement ratios, without causing excessive bleeding or segregation, but they are increasingly being used to produce high strength concrete. They are particularly advantageous in mixes containing silica fume.

The effect of superplasticisers only lasts for a short duration (approximately 20 minutes) after which the workability returns to normal. For this reason they should be added to the mix immediately prior to placing (Neville, 1995). Generally, they do not affect the setting of concrete and can be used at high dosages - typically between 4-

10kg/m^3 depending on the individual mix specification, water/cement ratio, required workability, and the cement and aggregate types (Melbye, 1994). Furthermore they do not appear to have long-term detrimental effects on the hardened properties of the mix as no retrogression of strength seems to have been reported (Neville, 1995).

Accelerators

Steel fibre reinforced sprayed concrete often requires the addition of set accelerators to rapidly reduce workability at the point of spraying, and to cause rapid setting and increased early strength development. This allows sprayed concrete to be used as an immediate support in many underground tunnelling applications. The most common types include alkali aluminates (sodium or potassium) and sodium silicates (water glass).

Alkali alluminate accelerators increase the rate of cement hydration and, thereby, produce high early strengths. For example, the initial set can occur in less than 60 seconds, with associated compressive strengths greater than 0.4MPa after 20-30 minutes (Melbye, 1994). However, the disadvantages of these type of accelerators include:

- a reduction in long term strength compared to non-accelerated concrete (Morgan, 1995);
- impaired durability (Beaupre *et al.*, 1994);
- sensitive to different cement types (i.e. they do not work with every type of cement); and
- a health hazard due to their high alkalinity (pH greater than 12.5), making them aggressive to skin and eyes.

In contrast, sodium silicates do not take part in the hydration process, but only have a momentary gluing effect (lasting less than 10 seconds), which causes a sharp reduction in workability. As a result they do not contribute to early age strength development (Melbye, 1994). However, they are less aggressive than alkali aluminates (pH less than 12.5) and are thought to cause a smaller reduction in long-term strength.

Accelerators can either be added as a liquid (wet and dry process) or as a powder (dry process only). Dosage rates vary depending upon the type of accelerator used but generally range between 4-8% (Melbye, 1994). Higher dosages tend to increase setting

times and early strength development, but reduce long-term strength as shown in Figure 2.7 and Figure 2.8 respectively.

Alkali-free accelerators (pH between 3-6) have recently been developed for use in the wet process (Garshol and Melbye, 1996; Prat and Frouin, 1996). These products can improve working conditions (by their reduced alkalinity) and reduce the environmental effects arising from their disposal. However, their long term durability requires further validation, before they can completely replace the traditional accelerators types.

Air entrainers

Air entraining admixtures can be used in wet process mixes to improve freeze-thaw durability in specific applications (Beaupre *et al.*, 1994). Further information relating to their use is given in Malmberg (1993).

Hydration control systems

The performance, flexibility and economic viability of wet process steel fibre reinforced sprayed concrete has recently been improved with the development of hydration control systems. These systems typically consist of a two component admixture that allows complete control over the rate of cement hydration (Melbye, 1993; Coverdale *et al.*, 1996):

- a *stabilising component*, which is added during batching to improve workability and pumpability of the concrete, and to restrict cement hydration by up to 72 hours; and
- an *activating component*, which is added at the nozzle and consists of a 'slump killer' and modified accelerator to reverse the effect of the stabiliser.

These systems have been shown to provide a long open time, reduced accelerator dosage, and flexibility for intermittent applications (Garshol, 1995).

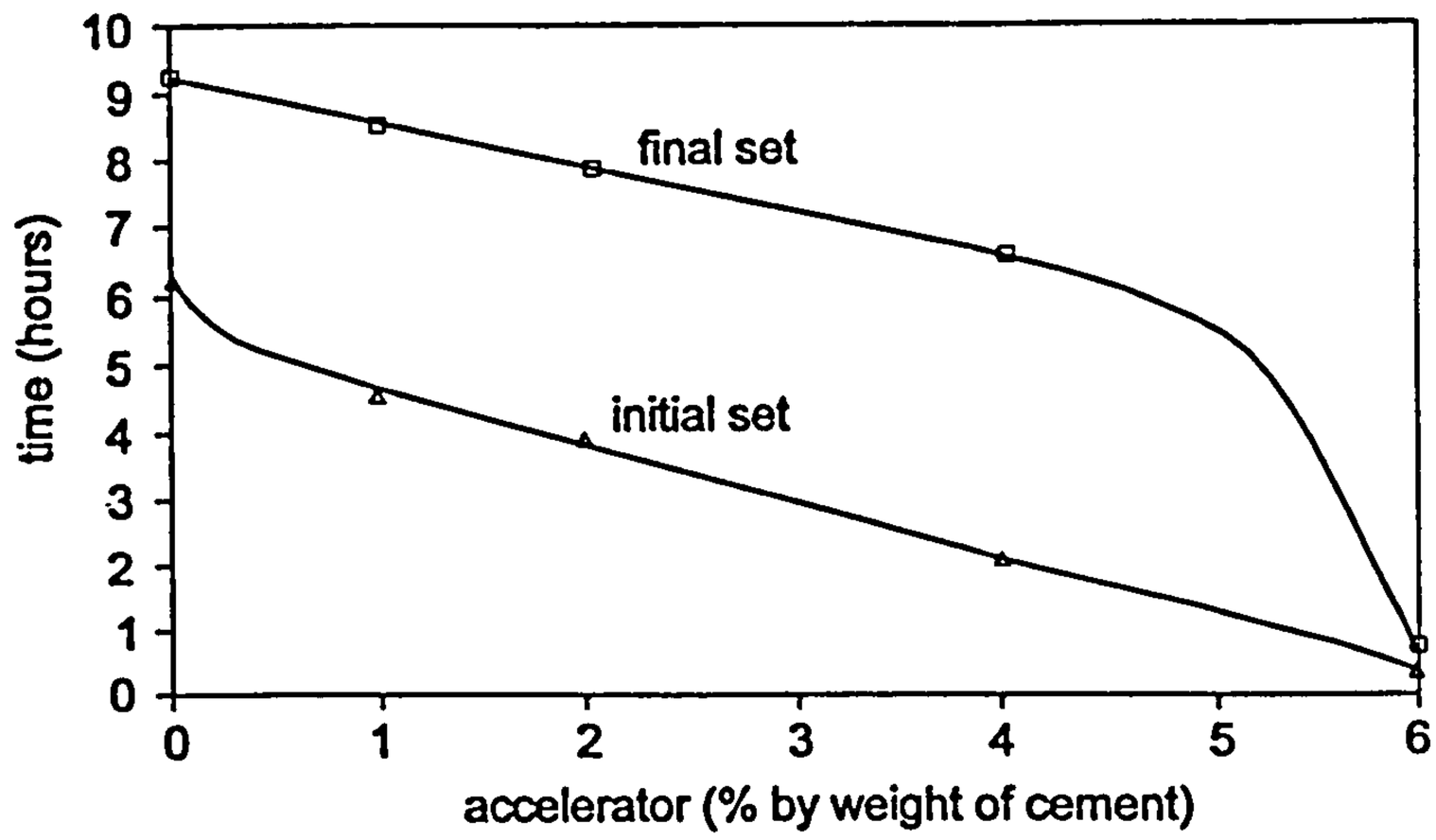

Figure 2.7 **Influence of an accelerator on setting time (Morgan, 1995).**

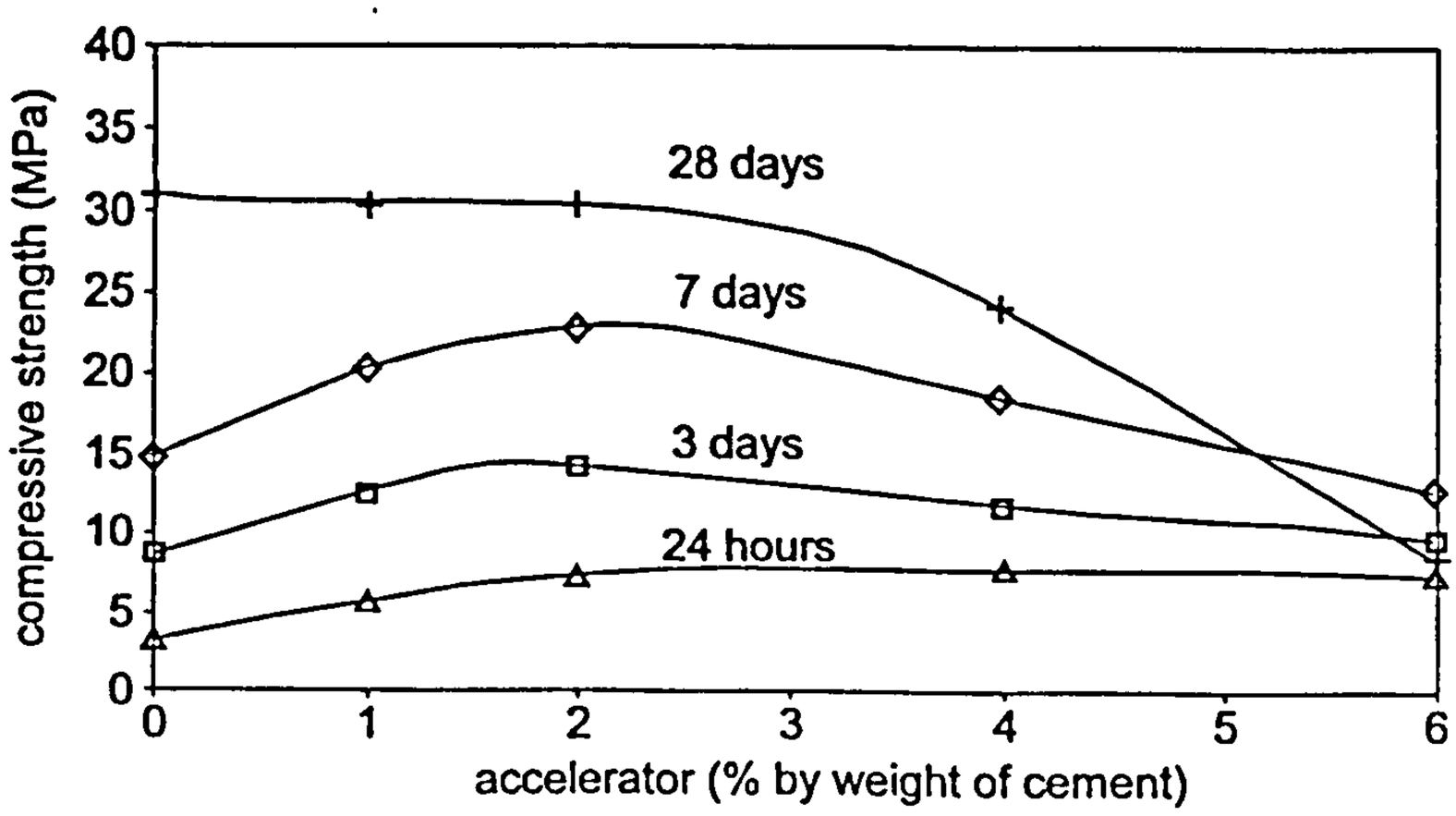

Figure 2.8 **Influence of an accelerator on strength development (Morgan, 1995).**

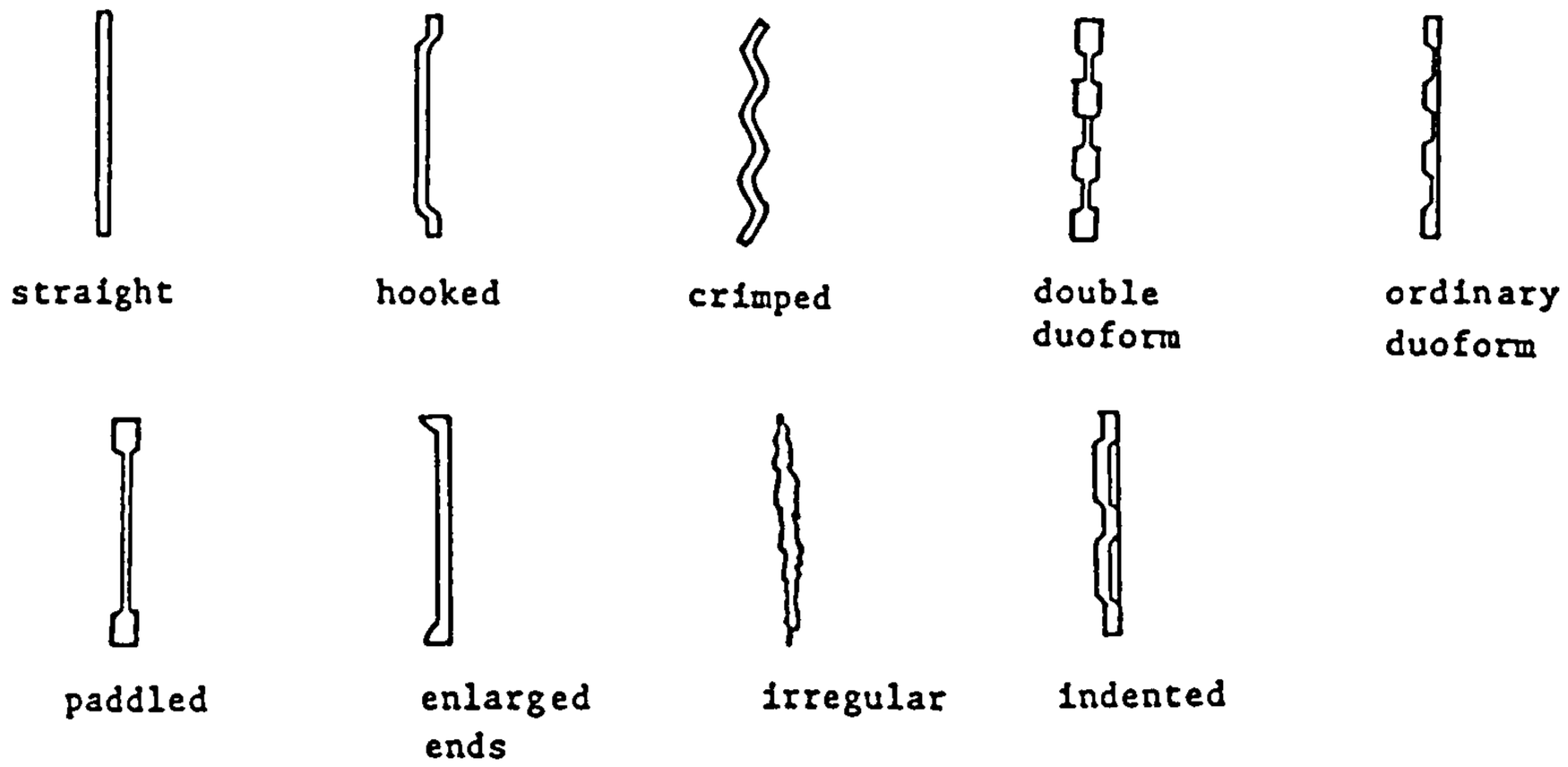

(a) Steel fiber shapes

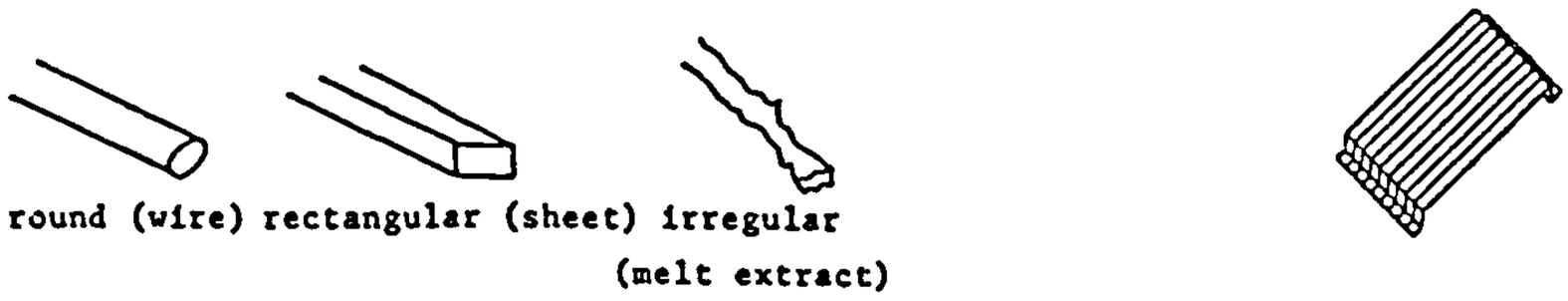

(b) Steel fiber cross sections

(c) Fibers glued together into a bundle

Figure 2.9 Different types of steel fibre in current use (Soroushin and Bayasi, 1995).

2.4.5 Steel Fibres

General

Steel fibres have been used in the majority of fibre reinforced sprayed concrete applications because they can better enhance crack resistance, toughness performance and impact properties compared with other fibre types (Morgan, 1995; Vandewalle, 1990). There is a wide range available, in a variety of shapes, sizes and steel types (Banthia *et al.*, 1994; Chang *et al.*, 1993; Balaguru and Shah, 1992). The most common types are deformed in one way or another and have typical fibre lengths ranging between about 25-40mm and aspect ratios (defined as length/diameter) of between 50-100. Figure 2.9 shows some of the proprietary fibre types in current use.

The higher the fibre aspect ratio and volume concentration, the higher the performance of the sprayed concrete, but also the more difficult it becomes to mix, convey and spray. Collated (glued) fibres, which disperse as the glue dissolves, have a reduced tendency to ball due to their lower aspect ratio, and therefore have superior

mixing characteristics compared with single fibres (Vandewalle, 1990; Balaguru and Shah, 1992).

Fibre v mesh reinforcement

The comparative performance of fibre and mesh reinforcement has been investigated by a number of researchers and extensively documented (Vandewalle, 1990; Austin, 1995b; Kirsten, 1992 & 1993; Kirsten and Labrum, 1990). In the majority of these studies, the results show that fibre reinforcement produces similar flexural strengths, and superior post-cracking toughness performance.

Additional advantages of fibres compared with mesh include the following (Vervaeke and Moyson, 1996; Vandewalle, 1990):

- saving in time and cost, because the fixing of reinforcement is not required;
- elimination of potential voids behind mesh reinforcement;
- the exact contours of the spraying surface can be followed allowing a uniform application thickness; and
- a homogenous reinforcing effect over the whole cross-section, compared with a mesh reinforcement which is difficult to locate accurately.

2.5 MIX DESIGN

2.5.1 General

The mix design of sprayed concrete is basically governed by the same principles which apply to conventional cast concrete. The main factors controlling strength and durability are the water-cement ratio, air void content and degree of compaction. But more specifically, the mix design must take account of the method of application - either the wet or dry process. General recommendations can be found in a recent state-of-the-art report by Malmberg (1993).

2.5.2 Wet process

A wet process mix is designed for strength and workability in a similar way to conventionally pumped concrete. Typically, the mix needs to comply with the following criteria:

- be sufficiently fluid so that it can be pumped through the delivery hose without segregating;
- be sprayed without sloughing and provide sufficient build thickness;
- be able to achieve specified early and long term strength requirements;
- allow for the effect of material rebound - particularly fibre rebound; and
- provide low drying shrinkage and long term durability.

In the past sprayed concrete technology was not sufficiently advanced to meet these criteria, and as a result poor quality wet process sprayed concrete was usually produced. However over the last 5-10 years this situation has changed, mainly because of significant developments in wet process spraying equipment and concrete admixtures (Section 2.2 and 2.4). Consequently, the wet process is gradually becoming the dominant method of application.

Wet process mix designs generally comply with the recommendations given in Table 2.3, which excludes any additional requirements for accelerators or hydration control systems. Further wet process mix designs can be found in Holtman and Opsahl (1996), Garshol (1995), Banthia *et al.* (1994a), Hasen *et al.* (1993), Morgan (1991) and Wood (1990).

material type	quantity (kg/m^3)	material type	quantity
Portland cement	450-550	silica fume	2-8% of c.w.
aggregate, 0-8mm	1450-1500	superplasticiser	0.4-0.6% of c.w.
steel fibres	30-80	water/cementitious ratio	0.38-0.45

Table 2.3 A typical wet process mix design (Melbye *et al.*, 1995).

2.5.3 Dry process

A dry process mix is more difficult to proportion due to the much higher levels of material rebound (especially coarse aggregate and steel fibres) which can significantly effect the insitu proportions (Austin, 1995b). In addition, because the water content is controlled by the nozzle operator the water-cement ratio cannot be specified.

Generally dry process mixes contain well graded aggregate (maximum size between 6 to 10mm), with an aggregate/cementitious ratio in the range 3:1 to 4:1 by weight

(producing insitu ratios in the range 1.8:1 to 3.2:1 - depending upon the amount of rebound), and an estimated water-cement ratio between 0.35 and 0.45 (Austin, 1995b). Further dry process mix designs can be found in Morgan (1991), Chang *et al.* (1993), Wood (1990), and Banthia *et al.* (1992).

2.6 FRESH PROPERTIES

Factors that influence the behaviour of freshly mixed (or placed) steel fibre reinforced sprayed concrete include: mix design; fibre type; fibre geometry; and fibre volume fraction. In general the addition of fibres makes the mix more stiff, although water reducing admixtures can be added to improve workability (Balaguru and Shah, 1992). Hannant (1978) has also shown that a greater volume and size of coarse aggregate results in greater fibre interactions which can also lead to mixing, placing and compaction problems. As a result the maximum aggregate size should be restricted to less than 10mm for common fibre additions (typically between 40-80kg/m^3).

During the placement of fresh steel fibre reinforced sprayed concrete, the main properties to consider are:

- pumpability (wet process only): a measure of the ease of pumping concrete without segregation, bleeding or blocking; and
- sprayability: a measure of the efficiency of the concrete to adhere to the sprayed surface in terms of bond (adhesion), high build-up thickness (cohesion), low rebound and susceptibility to sloughing.

In the wet process it is generally considered that if a mix can be pumped, then it can be sprayed. Pumpability is usually assessed by measuring the workability of the mix using a standard slump test. One approach is to produce a flowable mix (100-150mm slump) that can be easily pumped, and then to add an accelerator at the nozzle to enhance the adhesive properties (sprayability). This method is commonly used for applications requiring long conveyance distances. An alternative approach, which is commonly used for short conveyance distances, is to produce a medium workability mix (50-100mm slump) which has both acceptable pumpability and sprayability properties but is non-accelerated.

Sprayability (in both wet and dry processes) can be assessed by either thickness-to-sloughing tests (Morgan, 1991a) or the measurement of material rebound (Banthia *et al.*, 1994). Morgan (1995) reports single pass build-up thickness and rebound quantities for both the dry and wet process - with and without silica fume. The results show that wet process mixes generally have greater build-up thickness, and lower material rebound values, than dry process mixes.

The fresh properties of sprayed concrete were recently reviewed by Malmberg (1993), and further information relating to the fundamentals of pumpability and sprayability of wet process sprayed concrete can be found in the work of Beaupre and Mindess (1996 & 1993) and Beaupre *et al.* (1993).

2.7 HARDENED PROPERTIES

2.7.1 Introduction

This section reviews the relevant hardened properties of steel fibre reinforced sprayed concrete which influence its flexural behaviour. **Flexural toughness, which is the most important hardened property in the context of this thesis, is discussed separately in Section 2.8.**

2.7.2 Compressive strength

Compressive strength is generally measured by compression testing of cores extracted from either test panels, in-situ sprayed concrete, or from cubes sawn from test panels (ACI 506R, 1990; Malmberg, 1993; EFNARC, 1996). Results of several researchers (Vandewalle, 1990; Banthia *et al.*, 1994; Morgan, 1991; Balaguru and Shah, 1992) show that only small improvements in compressive strength can result from the addition of steel fibres at the rates commonly used in sprayed concrete (40 to 80 kg/m^3).

Typical compressive strengths for dry process mixes are in the range 30-60 MPa at 28 days, for aggregate-cement ratios between 4:1 and 2.5:1 and unspecified water-cement ratios (Robins, 1995a). In contrast, wet process mixes have traditionally produced 28 day compressive strengths ranging between 20-45 MPa for mixes consisting of a water-cement ratios between 0.7-0.45 and no admixtures. However, by using

combinations of silica fume and superplasticisers in the mix design, it is now possible to produce wet process mixes with compressive strengths comparable with (and even higher than) the dry process (Morgan, 1995).

Some researchers (Robins and Austin, 1985; Armelin and Helene, 1995) have investigated the influence of fibre orientation (assumed to be roughly two-dimensional perpendicular to the direction of spraying) on the compressive strength of dry process mixes, and found significant anisotropic behaviour, as illustrated in Figure 2.10.

Banthia *et al.* (1994b) recently compared the compressive strengths of wet process steel fibre reinforced sprayed concrete specimens with cast specimens using similar mixes. They found the compressive strengths of cast specimens (average 40 MPa) were consistently higher than those of sprayed specimens (average 27 MPa), and concluded that this was the result of better compaction in the cast specimens. However, they did not appear to account for the potential weakening of the sprayed specimens, due to surface damage/microcracking, caused by them being cored from sprayed panels.

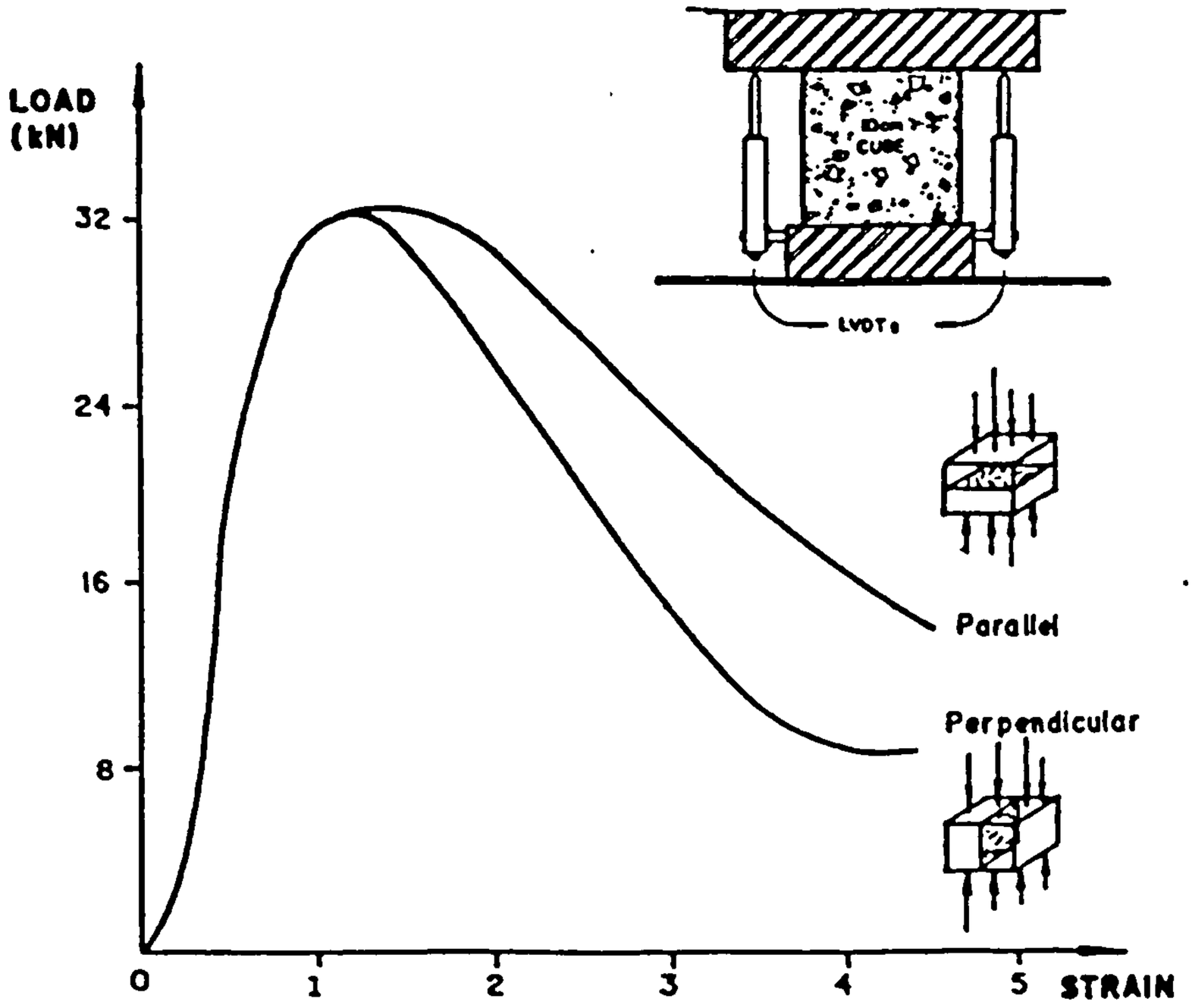

Figure 2.10 The effect of fibre orientation on the compressive behaviour of dry process sprayed concrete (Armelin and Helene, 1995).

2.7.3 Flexural strength

Flexural strength is usually determined by performing standard four-point beam tests on specimens sawn from test panels (e.g. EFNARC, 1996; ASTM C78, 1984; BS1881:Part 118:1983). For steel fibre reinforced sprayed concrete, two values of flexural strength are significant: the 'first-crack' flexural strength, determined as the strength at which the load-deflection curve first deviates from linearity (i.e. the limit of proportionality), and the ultimate flexural strength (or modulus of rupture) corresponding to peak load (Robins, 1995a). The first-crack strength increases with increasing matrix strength and is only marginally influenced by fibre additions, but the ultimate strength increases with increasing matrix strength, fibre aspect ratio, fibre pull-out resistance and volume concentration (Ramakrishnan, 1985). For low fibre volumes these two strengths essentially coincide. However, above a critical fibre volume the ultimate strength can increase significantly (Balaguru and Shah, 1992). By definition, the ultimate flexural strength occurs at peak load and is therefore relatively easy to determine. In contrast, the determination of first-crack strength is more difficult and in some cases may even be subjective. This is discussed in more detail in Section 2.8.

The addition of the steel fibres to a plain sprayed concrete mix, at the addition rates commonly used (40-80 kg/m^3), has been shown to increase flexural strength by around 13-24% for the dry process and 6-24% for the wet process (Banthia *et al.*, 1994). Reported values for both wet and dry process mixes are generally in the range 5-10 MPa (ACI 506.1R, 1984; Vandewalle, 1990; Banthia *et al.*, 1994, 1994a & 1992; Ramakrishnan, 1985; Robins, 1995). However, it has been suggested by Wolsiefer and Morgan (1993) that similar increases in flexural strength can be more economically achieved through the use of silica fume and superplasticisers.

Banthia *et al.* (1994b) recently compared the flexural strength of sprayed and cast beams made from similar steel fibre reinforced wet process mixes. In nearly all cases the sprayed specimens were generally stronger in flexure, even though their compressive strengths were lower (Section 2.7.2). Note that this result appears to contradict the argument presented in the previous paragraphs, which implies that the flexural strength is mainly a matrix property that should increase with increasing matrix strength. In response to this contradiction, the authors suggest that this result

may be due to changes in the matrix structure, or beneficial fibre orientation effects, produced by the spraying process.

2.7.4 Tensile Strength

Although steel fibre reinforced sprayed concrete is not normally designed to resist direct tension, a knowledge of its elastic and post-crack behaviour is of value in structural modelling. However, it can be very difficult to test a specimen in direct tension which is free from eccentricity and secondary stresses (Neville, 1995). Consequently only very limited tensile strength data relating to sprayed concrete has been published (Vandewalle, 1990; Opsahl and Buhre, 1985; Casanova and Rossi, 1995).

2.7.5 Modulus of Elasticity

The secant modulus of elasticity (in compression or tension) is an important property for design, quality control and structural modelling. Test methods vary depending upon the proportion of ultimate strength to which the secant is taken, typically between 33-40% of ultimate strength, and whether the test specimen is loaded in compression or tension (EFNARC, 1996; ASTM C469, 1994; BS 1881:Part 121:1983). Various researchers have found that the addition of steel fibres does not appreciably influence the value of secant modulus (compressive or tensile) of wet or dry process sprayed concrete at the fibre addition rates commonly used (Vandewalle, 1990; Armelin and Helene, 1995; Ramakrishnan *et al.*, 1981). Reported values for the static modulus of elasticity typically range between 17 and 41 GPa depending upon matrix strength (ACI 506R, 1990).

2.7.6 Other Hardened Properties and Characteristics

Other hardened properties - including early age strength, bond to substrate, impact resistance, shrinkage, corrosion, and durability - although important in sprayed concrete applications, are not relevant in the context of this thesis, and therefore are not discussed. However, further information and test data relating to these properties can be found in Morgan (1995), Balaguru and Shah (1992), and Robins (1995).

2.8 FLEXURAL TOUGHNESS

2.8.1 Introduction

The enhanced toughness of steel fibre reinforced sprayed concrete has long been recognised as one of the most important benefits of incorporating steel fibres into plain concrete. However, toughness is not the easiest of properties to define and its measurement has been a source of much debate during the last twenty years. In general terms, the toughness of fibre reinforced concrete can be regarded as the energy required to cause failure by complete separation (ACI 506.1R, 1984), and is commonly characterised by calculating the area under the load-displacement curve obtained experimentally. Many tests have been developed to directly characterise toughness (or energy absorption capacity) in simple loading configurations such as compression, flexure, shear and tension (Barr *et al.*, 1996; Gopalaratnam and Gettu, 1995; RILEM, 1985; Barr and Newman, 1985; Taylor *et al.*, 1996). Flexural tests are the most popular because they are thought to simulate more realistically the loading conditions in many practical situations.

The characterisation of flexural toughness is most widely determined using unnotched beam specimens tested in four-point loading, as shown in Figure 2.11(a) (Gopalaratnam and Gettu, 1995). Lesser used, but perhaps more suitable for the characterisation of fracture toughness parameters, is the three-point bending test on centre-notched beams, as shown in Figure 2.11(b) (Jamet *et al.*, 1995). In addition, EFNARC (1996) has recently recommended the use of a more application specific plate-bending test, as shown in Figure 2.11(c). Although the plate test may facilitate easier practical implementation of toughness results in selected applications (e.g. tunnel linings), it involves complex triaxial stresses and is therefore regarded primarily as a quality control test. In contrast, the flexural beam test produces a predominantly uniaxial stress-state and is therefore more suitable for obtaining a fundamental understanding of the basic mechanics of flexural behaviour. Therefore, this thesis only considers the flexural beam test.

Gopalaratnam and Gettu (1995) recently published a comprehensive review of the wide variety of standard methods and recommended guidelines currently available for determining flexural toughness from the load-deflection response of a test beam. They

categorised the different methods by the basic concepts used in computing toughness values: energy-based dimensionless indices; energy absorption capacity; residual strength measurement; equivalent flexural strength measurement; strength-based dimensionless indices; and deflection-based dimensionless indices. However, the load-deflection curve is influenced by many factors (including fibre type, geometry and volume; matrix composition; specimen size; loading configuration; loading rate; deflection measurement accuracy; and the type of test control), which have raised many concerns about the standard test methods, resulting in considerable debate over how flexural toughness should be characterised and used in design (Barr *et al.*, 1996; Gopalaratnam and Gettu, 1995; Banthia and Trottier, 1995; Morgan *et al.*, 1995). This section outlines the most widely used and recognised test methods and discusses the concerns in more detail. The most recent developments relating to flexural toughness characterisation are also discussed.

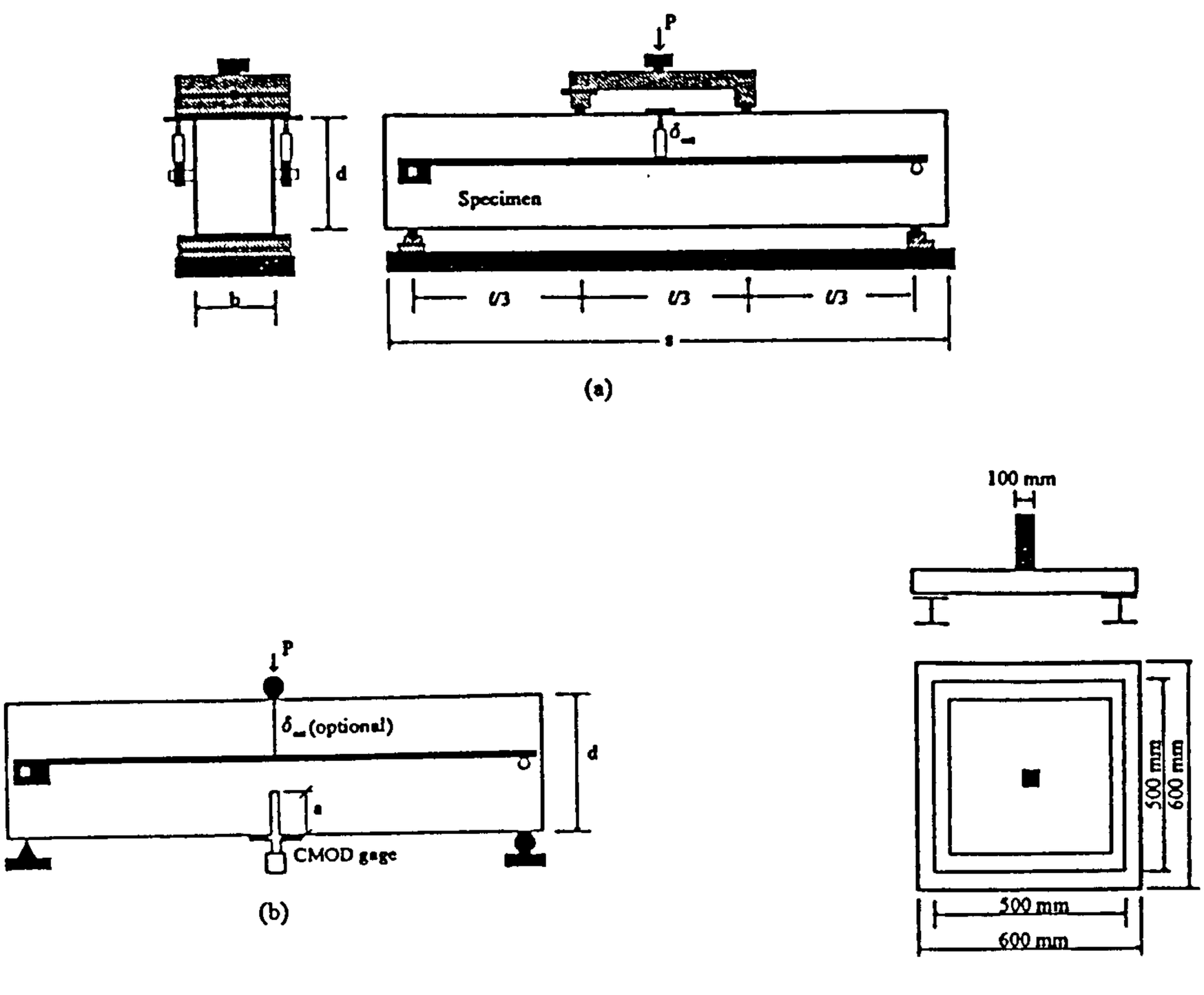

Figure 2.11 General test configuration used for flexural toughness testing: (a) four-point bending; (b) notched-beam test; and (c) plate test (Gopalaratnam and Gettu, 1995).

2.8.2 Standard Test Methods for Flexural Toughness Characterisation

General

The most widely recognised standard test methods are detailed below, which all use unnotched beam specimens tested under a four-point loading configuration (Figure 2.11(a)). Although there are differences in the specimen size, shape, test span and load rate control in these test methods, the greatest differences are in the manner in which toughness is defined and calculated.

ASTM C-1018

The ASTM C-1018 (1994) method involves calculating dimensionless toughness indices (I_5, I_{10}, I_{20},etc.) from the energy required to deflect a test beam to a prescribed deflection as a multiple of the first crack deflection. The first crack is defined as the point on the load-deflection curve at which the form of the curve first becomes non-linear. Residual strength factors are then calculated as $R_{M,N} = C(I_N - I_M)$ where C $= 100/(N-M)$, as shown in Figure 2.12. When using this method it is important to note that all three parameters - first-crack strength, toughness index and residual strength factor - are all needed to fully define toughness behaviour (Gopalaratnam *et al.*, 1991).

JSCE-SF4

In the Japan Society of Civil Engineers JSCE-SF4 (1984b) method, flexural toughness is measured as the area under the load-deflection curve up to a prescribed deflection of $1/150^{th}$ of the span and is expressed in units of absolute energy (Nm). This measure of toughness is used to calculate an equivalent flexural strength (termed flexural toughness factor) up to the prescribed deflection, as shown in Figure 2.12.

Norwegian Concrete Association NBP No.7

In the Norwegian Concrete association (1993) method, flexural toughness is measured as simply the residual strength retained in a standard beam at prescribed mid-span deflections of 1mm and 3mm. Toughness is evaluated by comparing measured residual strengths against specified minimum requirements according to four toughness classes, as shown in Table 2.4.

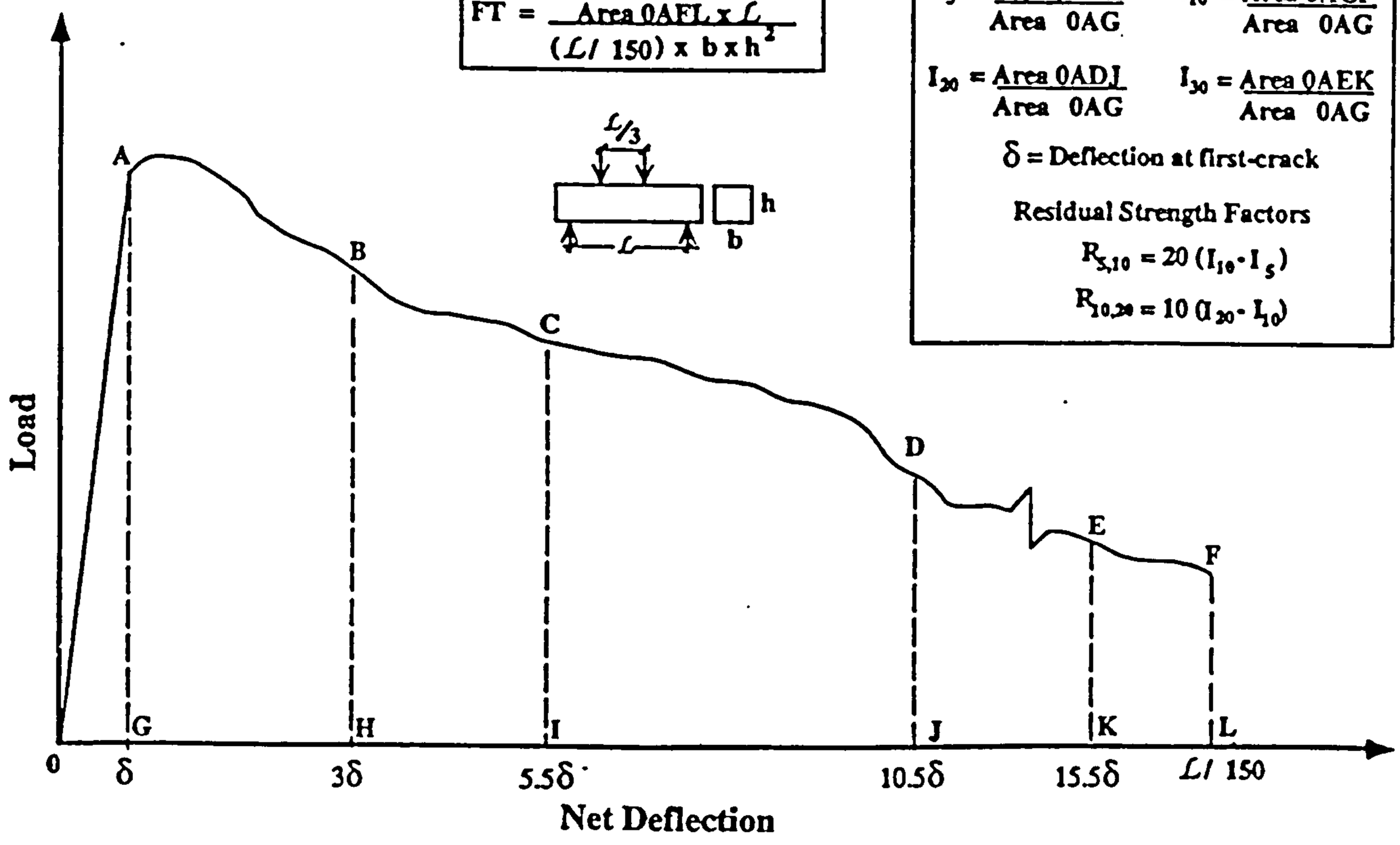

Figure 2.12 **ASTM C1018 and JSCE-SF4 toughness characterisation techniques (Banthia and Trottier, 1995).**

Toughness class	Deflection	
	1 mm	3 mm
0	Non reinforced concrete	
1	Type and amount of fibre specified	
2	2,0 MPa	1,5 MPa
3	3,5 MPa	3,0 MPa

Table 2.4 **Toughness characterisation in accordance with the Norwegian Concrete Association (1993).**

2.8.3 Concerns With the Standard Test Methods and Proposed Improvements

Deflection measurement

Deflection measurement and its influence on toughness characterisation has been discussed in many recent studies (Gopalaratnam and Gettu, 1995; Banthia and Trottier, 1995; Morgan *et al.*, 1995; Gopalaratnam *et al.*, 1991; El-Shakra and Gopalaratnam, 1993; Johnston, 1995; Chen *et al.*, 1995). These have shown that in flexural toughness tests it is imperative that beam net deflections are measured, which exclude any extraneous effects due to local deformations of the beam at the loading points, elastic and inelastic deformations at the supports and specimen rocking effects.

Toughness characterisation methods that rely directly on first-crack deflections (e.g. ASTM C1018) have been shown to be significantly affected by errors in deflection measurement, due to gross overestimation of first crack deflections and therefore first crack energy (Banthia and Trottier, 1995; Gopalaratnam *et al.*, 1991; El-Shakra and Gopalaratnam, 1993; Johnston, 1995). The JSCE-SF4 flexural toughness factor is also affected by errors in deflection measurement, but not as dramatically as in ASTM C1018 (Banthia and Trottier, 1995; El-Shakra and Gopalaratnam, 1993). In addition, changes in the shape of the load-deflection curve due to errors in deflection measurement may also affect residual strength measurements in accordance with NBP No.7 (1993).

Net deflection measurement can be achieved by using a "yoke" (Figure 2.13), which allows measurement of mid-span deflection in relation to the neutral axis of the beam at its supports. Figure 2.14 illustrates the effect on the shape of the load-deflection curve as a result of different deflection measurement methods.

Identification of first-crack

The calculation of toughness indexes in accordance with ASTM C1018 (1994) requires an accurate assessment of the first-crack deflection and hence first-crack energy. Any error in the location of the first-crack point on the load-deflection curve will lead to significant error in the values of the various indices. In practice the location of the first-crack point from the load-deflection curve can be highly subjective, resulting in variations in the measured index values (Gopalaratnam and Gettu, 1995; Banthia and Trottier, 1995; Chen *et al.*, 1995). Morgan *et al.* (1995)

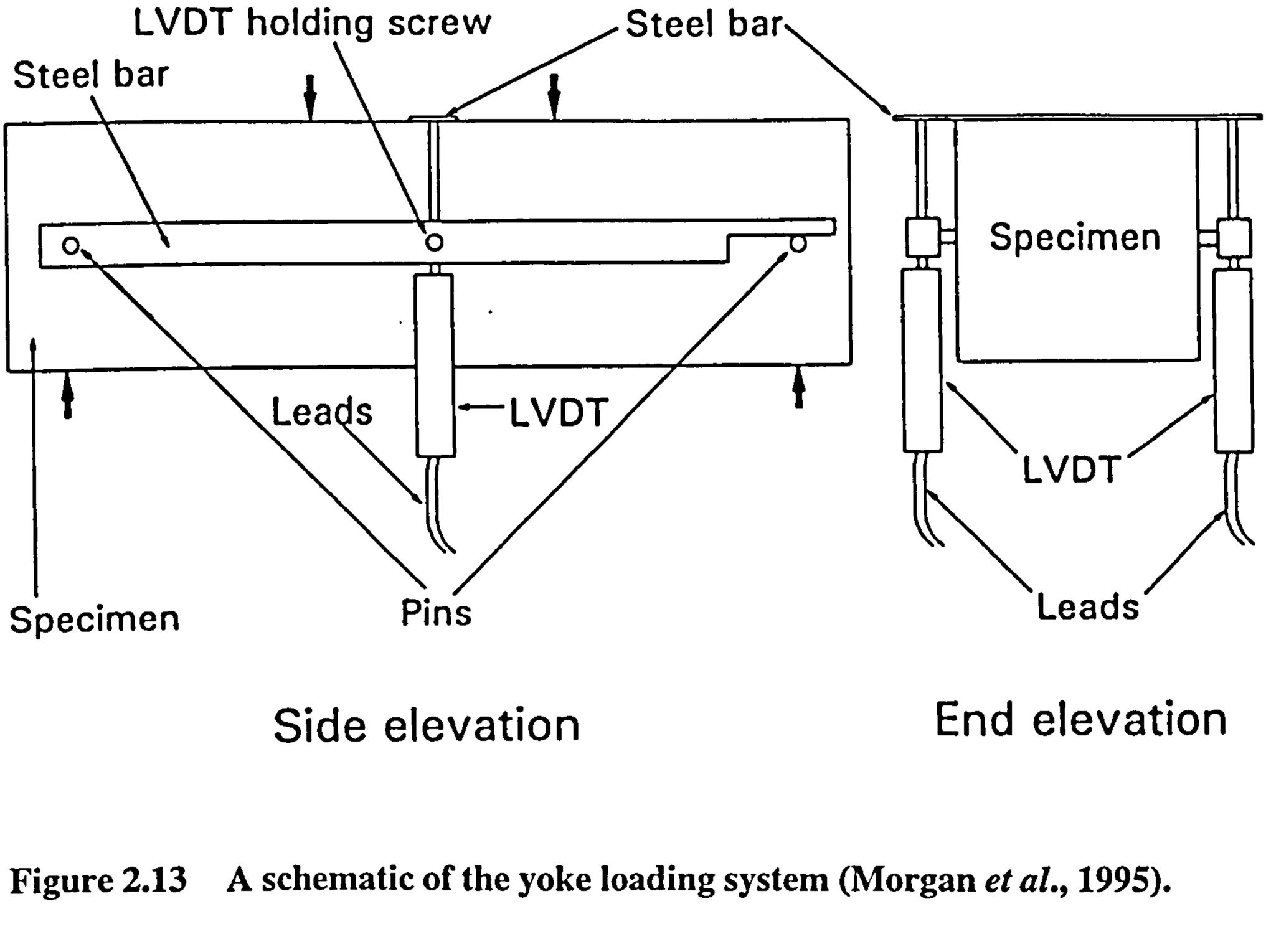

Figure 2.13 A schematic of the yoke loading system (Morgan *et al.*, 1995).

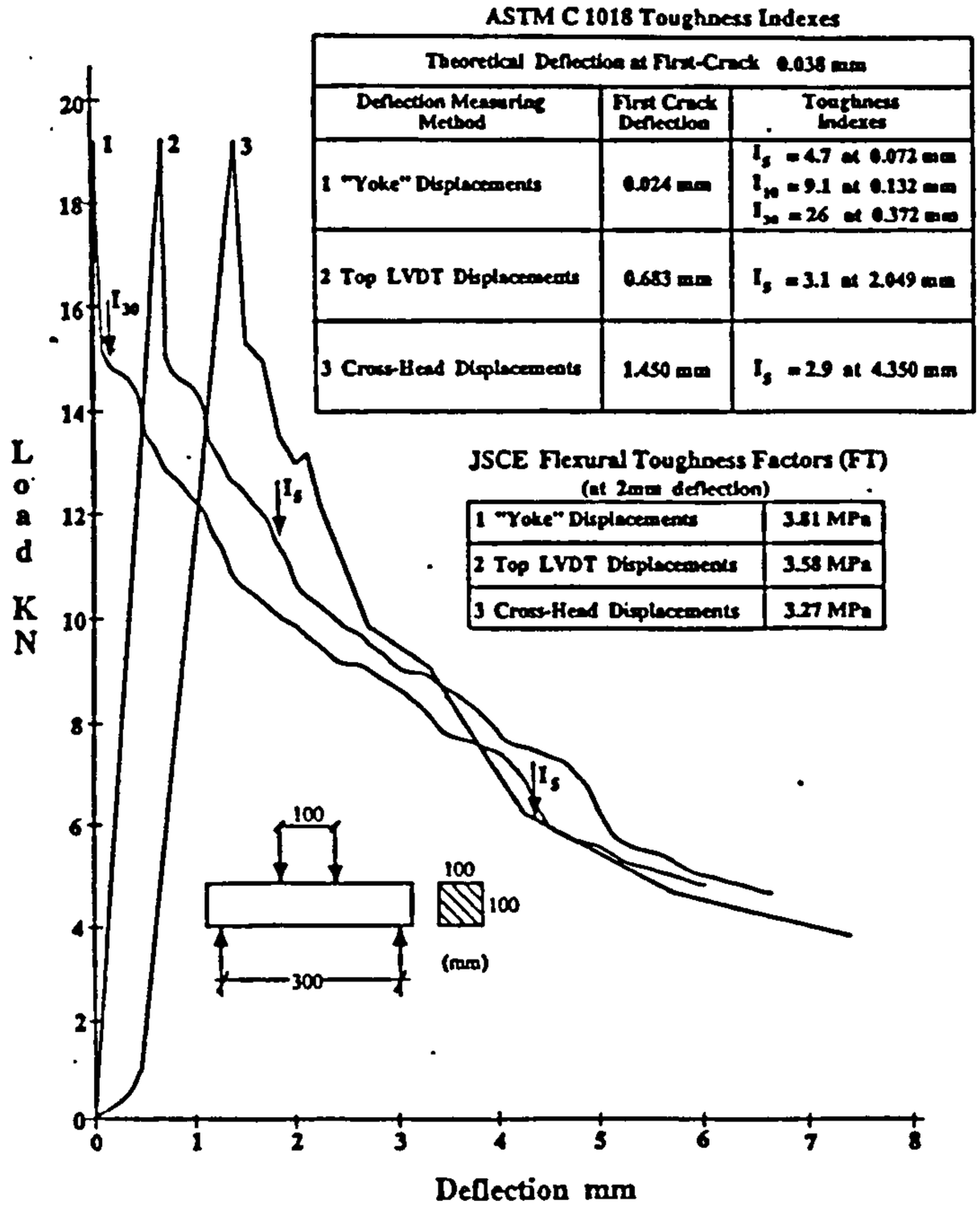

Figure 2.14 Flexural load-deflection curves showing the effect of three different deflection measurement techniques (Banthia and Trottier, 1995).

propose that the difficulty in locating the first-crack is because, in the strictest sense, there is no such thing as a discrete first-crack point in a flexural test. They suggest that progressive microcracking, which occurs as the beam deflects, causes substantial non-linearity in the load-deflection curve prior to peak load. As a result, the first-crack point can be almost impossible to locate accurately. In order to help locate and validate the first-crack point, a formula for estimating the first-crack deflection based on elastic theory has recently been proposed (Johnston, 1995; Chen *et al.*, 1995; ASTM (1994)). However, a much greater improvement could be achieved if an objective method of defining the first-crack point was adopted, as has been done in some European standards (Gopalaratnam and Gettu, 1995).

In contrast, the JSCE-SF4 (1984b) and NBP No.7 (1993) methods are not dependent on first-crack and therefore avoid the inaccuracies associated with its identification.

Instability after the peak-load

It is not uncommon in deflection controlled four-point flexural tests that the peak-load is followed by a temporary loss of stability where the strain energy stored in the machine is released suddenly (Banthia *et al.*, 1994). Consequently, the load-deflection response immediately following peak load cannot be considered to be the actual response of the specimen. This problem of instability is exemplified in the case of a high strength matrix with a low fibre content (Banthia and Trottier, 1995).

Recent studies (Johnston, 1995; Chen *et al.*, 1995; Banthia *et al.*, 1994; Balaguru *et al.*, 1992; Gopalaratnam *et al.*, 1991) have shown that the ASTM C1018 toughness indices I_5 and I_{10}, which normally fall in the region of instability, are not sensitive to either fibre efficiency or fibre volume fraction. It has also been suggested that matrix strength affects the zone of instability (Balaguru *et al.*, 1992). Higher strength concrete exhibits a more brittle post-crack response and as a result the region of instability can extend to include even *I20* (Banthia *et al.*, 1994; Banthia and Trottier, 1995). It is only when the test regains stability that the ASTM C1018 toughness indices begin to show differences in the various fibre types (Banthia and Trottier, 1995a; Banthia *et al.*, 1994; Ramakrishnan *et al.*, 1994; Balaguru *et al.*, 1992; Gopalaratnam *et al.*, 1991). This is further discussed by Nemegeer and Tatnall (1995).

The influence of test instability after peak-load is not as significant in the JSCE-SF4 method. Recent studies have shown this method to be more capable than ASTM C-1018 in distinguishing between various fibre types (Banthia *et al.*, 1994; Ramakrishnan *et al.*, 1994; Gopalaratnam *et al.*, 1991). Similarly, in the NBP No.7 method the specified deflections of 1mm and 3mm are sufficiently large that they are normally outside the zone of instability (Morgan *et al.*, 1995).

Test instability can be minimised by using a closed-loop test control system (Gopalaratnam and Gettu, 1995), which adjusts to changes in the stiffness of the specimen as peak-load is reached in order to maintain a constant rate of mid-span deflection. This is more difficult to perform than cross-head control and requires sophisticated and expensive equipment.

Size effects

Generally, toughness characterisation based on the load-deflection response is dependent on the size and geometry of the test specimen used. First-crack strength, flexural strength and post-peak toughness have been shown to decrease with an increase in the beam depth and 'structural brittleness' (Gopalaratnam and Gettu, 1995; Gopalaratnam *et al.*, 1991; Ward and Li; 1990; Ramakrishnan *et* al., 1994). Recent work by Chen *et al.*(1994) has shown that the ASTM C1018 indices and the JSCE-SF4 toughness factor are dependent on the cross-sectional size and span of the test specimens, unless the specimens are geometrically similar. All the toughness parameters decreased with an increase in the span-to-depth ratio. In addition, where the depth and span were unchanged, toughness also appeared to increase with an increase in the width of the specimens. For these reasons, it is strongly recommended that flexural toughness testing should be conducted using standard size specimens (Morgan *et al.*, 1995).

From the above, it appears that any flexural toughness characterisation method based on a load-deflection response will be influenced by specimen size and geometry. Consequently, Gopalaratnam and Gettu (1995) suggest that full account of these effects should be taken when attempting to extrapolate results from laboratory specimens to full-size structures.

Unsymmetrical cracking effects

Another problem arising from four-point flexural load tests, which affects all three test methods under discussion, is the possible unsymmetrical nature of the main crack in the test. Deflection is generally controlled/measured from the mid-span position, even though the crack can occur anywhere within the middle third of the beam. Therefore, the position of the crack relative to mid-span may influence the deflection measured, and hence the shape of the load-deflection curve. However, none of the standard test methods appear to address this issue.

Shear effects

Gopalaratnam & Gettu (1995) argue that the extremely small shear span-to-depth ratio of 1, which is common to ASTM C1018 and JSCE-SF4, causes unusually high stresses in the shear spans, and may cause changes in the mode of failure. In contrast, the NBP No.7 method adopts a more 'plank-like' beam with a span-to-depth ratio of 6, in which the influence of shear stresses are considered to be less pronounced (Morgan *et al.*, 1995).

Design and specification considerations

The use of absolute or relative toughness parameters (e.g. total energy and toughness indices) as material properties in current design practice is not evident. Design engineers require toughness parameters which have readily understood meaning in terms of commonly used engineering properties (e.g. strength). Furthermore, they require a knowledge of the complete load-deflection behaviour to provide flexibility in the incorporation of different application and serviceability requirements. It therefore appears that a toughness classification approach based on residual strength, or equivalent flexural strength, expressed in terms of deformation capacity offers the most practical method of evaluating flexural toughness for use in design.

Unfortunately, the current methods which measure residual strengths and equivalent flexural strengths maybe too restrictive in the deflection limits at which toughness is measured. For example the JSCE-SF4 method, which is based on a single deflection limit of span/150, has been criticised for being well in excess of the serviceability/deflection limits of most applications, and is therefore unable to characterise toughness behaviour at smaller deflections (Banthia and Trottier, 1995).

In contrast, NBP No.7 does provide deflection limits that are a little more application specific, but residual strengths are only measured at two discrete deflections. Complete flexibility can only be achieved by specifying continuous residual strengths curves. However, even if residual strengths are incorporated into a design rationale, there is still the problem of how the deformation demand of a full-size structure should be related to the deflection of a laboratory test beam. In this respect, a recent proposal by Stille *et al.* (1995) to use angular deformations is a possibility that merits further development.

In addition, current sprayed concrete specifications (as recently reviewed by Austin, 1995b) are predominantly only used for quality control purposes, and appear to bear no relation to the performance of the particular structure. Therefore, the designer is unable to relate (or quantify) the performance of test specimens to the design. This has invariably resulted in the use of very conservative designs in some applications (Lewis, 1997; Green, 1993), which poses a fundamental question: how are the results from a flexural toughness test used, or applied, in structural design?.

Improving flexural toughness characterisation methods

From the above concerns, it appears that there is a critical need to develop better methods for the characterisation of flexural toughness. In particular, improvements should address the following requirements:

- avoid the use of first-crack deflection to define toughness;
- adopt a deflection measuring system that measures net deflection exclusive of any extraneous deflections;
- use shallow beams with span-to-depth ratios greater than 5, and shear-span-to-depth ratios greater than 2, to minimise the effect of excessive shear stresses;
- adopt a standard beam size to counter the effects of specimen size on toughness measurement;
- ensure stability of the test at all times through the use of a very stiff test machine (relative to the stiffness of the test specimen) incorporating a closed-loop deflection control system;
- use residual strength, or equivalent flexural strength, over a continuous range of deflection limits as a measure of toughness;

- use deflection limits (expressed in terms of angular deformation) which are application specific and serviceability related; and
- develop design rationales and methods that relate the flexural toughness performance of laboratory test beams to the behaviour of full-size structures.

2.8.4 Recent Developments

The most recent developments to improve flexural toughness characterisation are detailed below.

EFNARC (1996)

The draft EFNARC specification (published in October 1993) allowed toughness to be characterised by either - or both - residual strength, in accordance with NBP No.7 (1993), or residual strength factor in accordance with ASTM C1018 (1994). However, because these two toughness methods do not give comparable results, this approach to toughness characterisation was subsequently found to be confusing (Nemegeer, 1996). In addition, given the recent doubts and debate concerning the toughness index approach (Section 2.8.3), it was subsequently decided by the EFNARC drafting committee to avoid the use of ASTM C1018 in favour of a residual strength approach.

As a result, the test method specified in the final EFNARC document (published in September 1996) draws on the strengths of the NBP No.7 (1993) method and minimises its weaknesses. Flexural toughness is characterised by relating the load-deflection curve to a set of residual strength curves, in terms of a 'residual strength class', over a continuous deflection range between 0.5mm and 4mm (angular deformations between 1/450 and 1/56), as shown in Figure 2.15. It allows the designer complete flexibility in the choice of deformation performance and toughness capacity to suit a particular application. Flexural strength is considered independently of residual strength, and a method of objectively measuring its value is also specified (Figure 2.16).

Author's note: the test method specified in the final EFNARC document was developed from consultations involving myself, Dirk Nemegeer, Simon Austin, and Peter Robins during the summer of 1996.

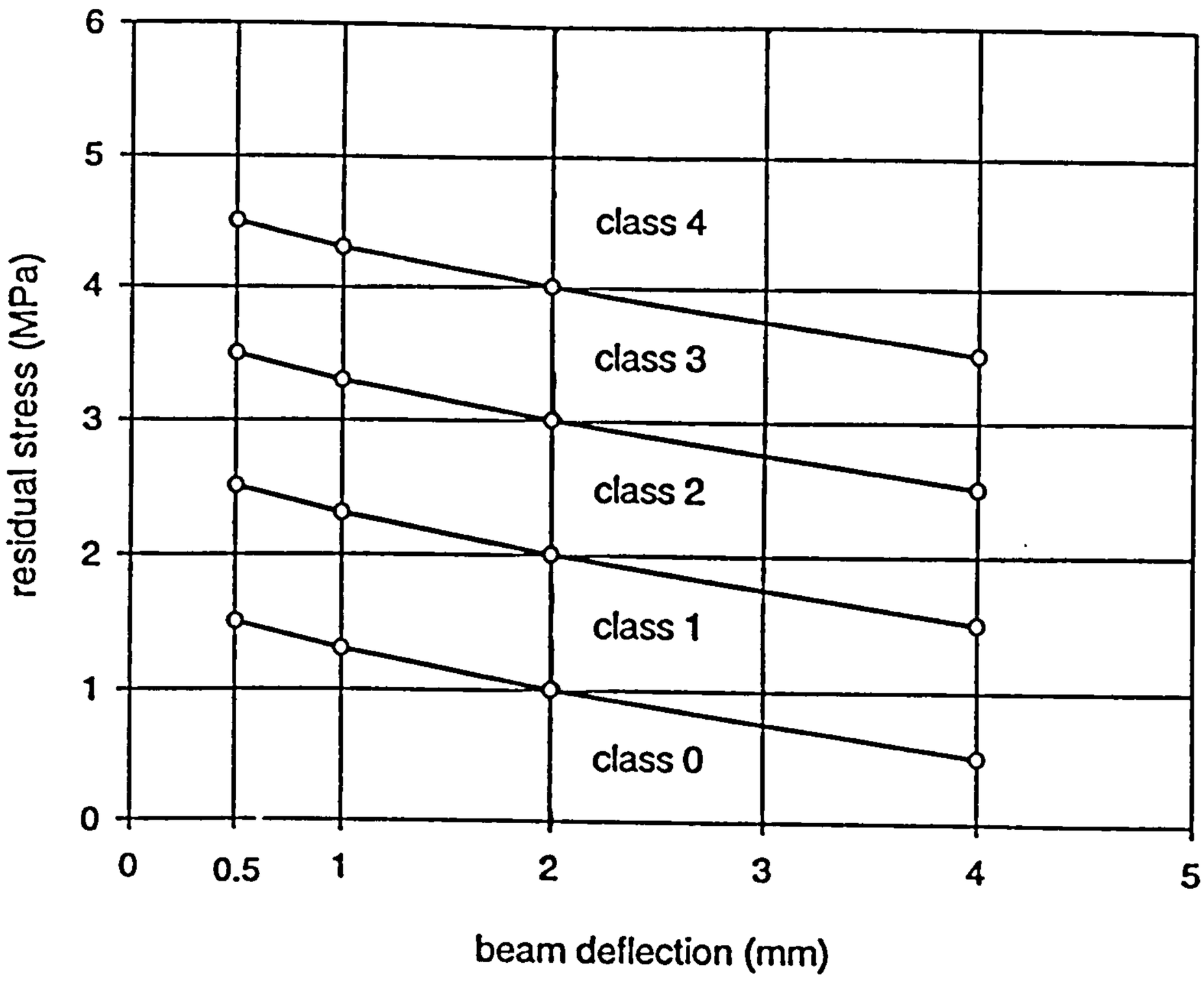

Figure 2.15 EFNARC residual strength classes (EFNARC, 1996).

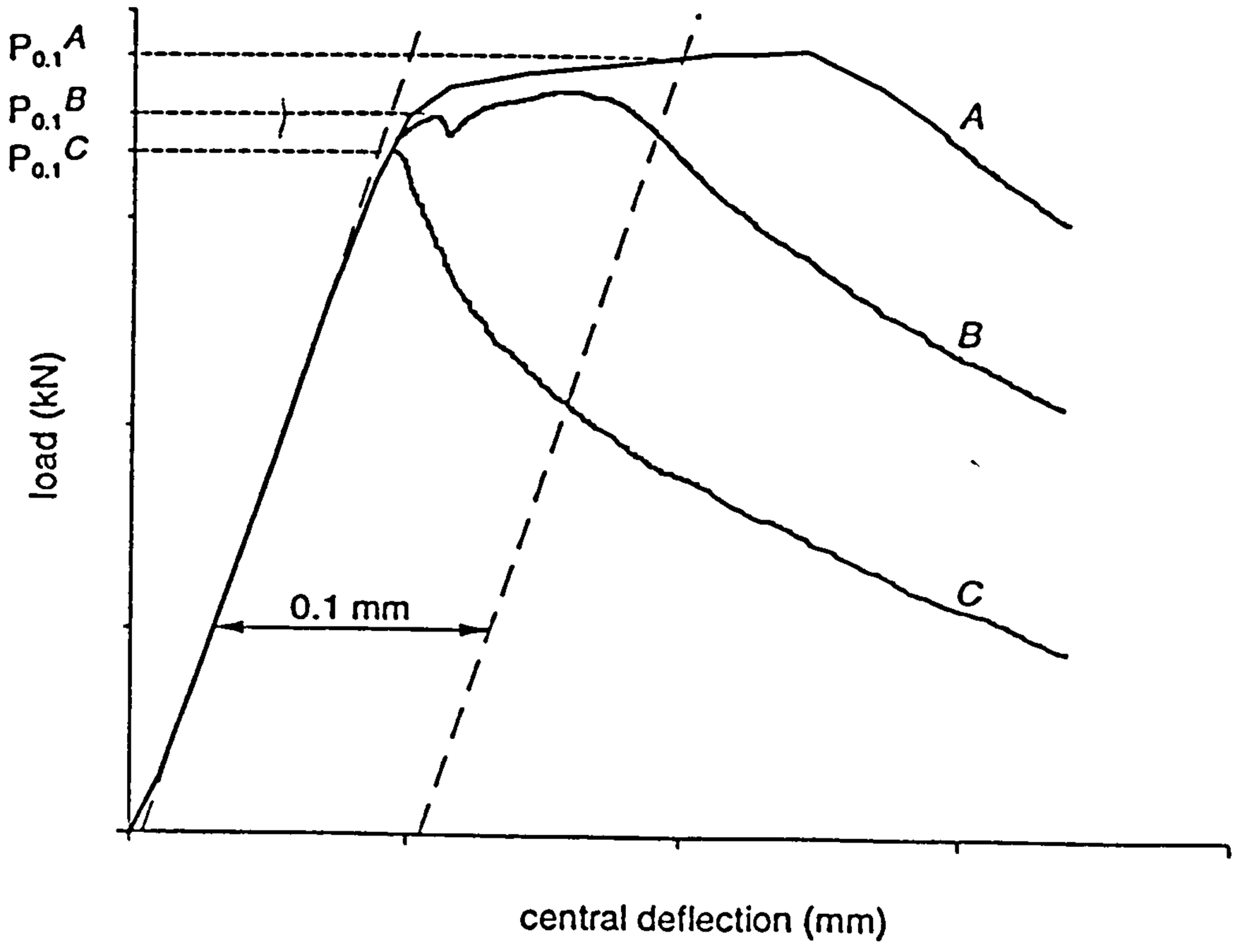

Figure 2.16 Objective measurement of flexural strength (EFNARC, 1996).

Morgan et al. (1995)

This proposal is similar in concept to EFNARC (1996) method but with the following significant differences:

1. The ASTM C1018 (1992) preferred beam is adopted (100mm width x 100mm depth, over a 300mm span), even though it is considered unfavourable due to shear effects (Section 2.8.3).
2. Deflection limits range between 0.5mm (1/600 angular deformation) to 2mm (1/150).
3. Toughness performance (measured as a residual strength) is expressed as a percentage of the design flexural strength.

Banthia and Trottier (1995)

In this proposal, toughness is calculated as a post-crack equivalent flexural strength, similar to the JSCE SF-4 method (1984), but the characterisation is based on a range of deflection limits from span/300 to span/150, which makes this method more general than the JSCE method. However, a more significant departure from the JCSE method is the exclusion of pre-peak energy from the calculation of equivalent flexural strength. It is not clear why this approach is adopted, but the exclusion of pre-peak energy appears inappropriate and misleading. This becomes obvious in a fibre reinforced concrete with high fibre contents which can display relatively large values of pre-peak energy.

Notched beams

As an alternative, and possible improvement, to toughness characterisation, the use of notched beams has been investigated (Barr *et al.*, 1996; Gopalaratnam and Gettu, 1995; Jamet *et al.*, 1995; Taylor *et al.*, 1996, Gopalaratnam *et al.*, 1991). This type of test specimen is controlled by the crack mouth opening displacement (CMOD) in place of the mid-span deflection (Figure 2.11(b)). It has been suggested by some researchers (Barr *et al.*, 1996; Gopalaratnam and Gettu, 1995; Jamet *et al.*, 1995; Balaguru and Shah; 1992; Gopalaratnam *et al.*, 1991) that a load-CMOD approach to toughness characterisation has the following advantages:

- CMOD measurement automatically excludes all extraneous deformations typically associated with deflection measurements, and is therefore less prone to errors;
- CMOD can be readily related to crack-width limits and as a result to application specific levels of serviceability;
- the results can be related to fundamental fracture mechanics and crack propagation behaviour of fibre reinforced concrete; and
- unlike the unnotched specimen, deformation behaviour in the notched specimen is always localised at the centre of the beam (i.e. at the notch).

However, to date only a limited amount of research data has been published, and consequently, although this approach offers a promising alternative to toughness characterisation, further work is needed to: (a) better understand the effect of specimen size and notch depth on the resulting load-CMOD response curve; and (b) the feasibility of its use and its practical implementation.

2.9 DESIGN

2.9.1 Introduction

A current limitation in the structural use of steel fibre reinforced sprayed concrete (which equally applies to cast steel fibre concrete) is the lack of accepted design codes of practice; this has resulted in a general lack of confidence in its use as a permanent structural material. For unloaded applications, or where the design loads are purely compressive, conventional reinforced concrete codes of practice can be used (i.e. BS8110, 1985). However, no recognised standard design codes exist for structural applications involving axial and bending forces (ACI 544.4R, 1988).

The most common design methods are based on empirical or semi-empirical concepts for tunnel lining design, sometimes in combination with numerical methods using finite elements (Barton and Chryssanthakis, 1996; Swoboda and Hafez, 1995; Swoboda and Moussa, 1994), and rarely use flexural toughness properties (ACI 506.1R, 1984). The most well known methods (which include provision for both steel mesh and fibre reinforcement) are detailed in the following sections.

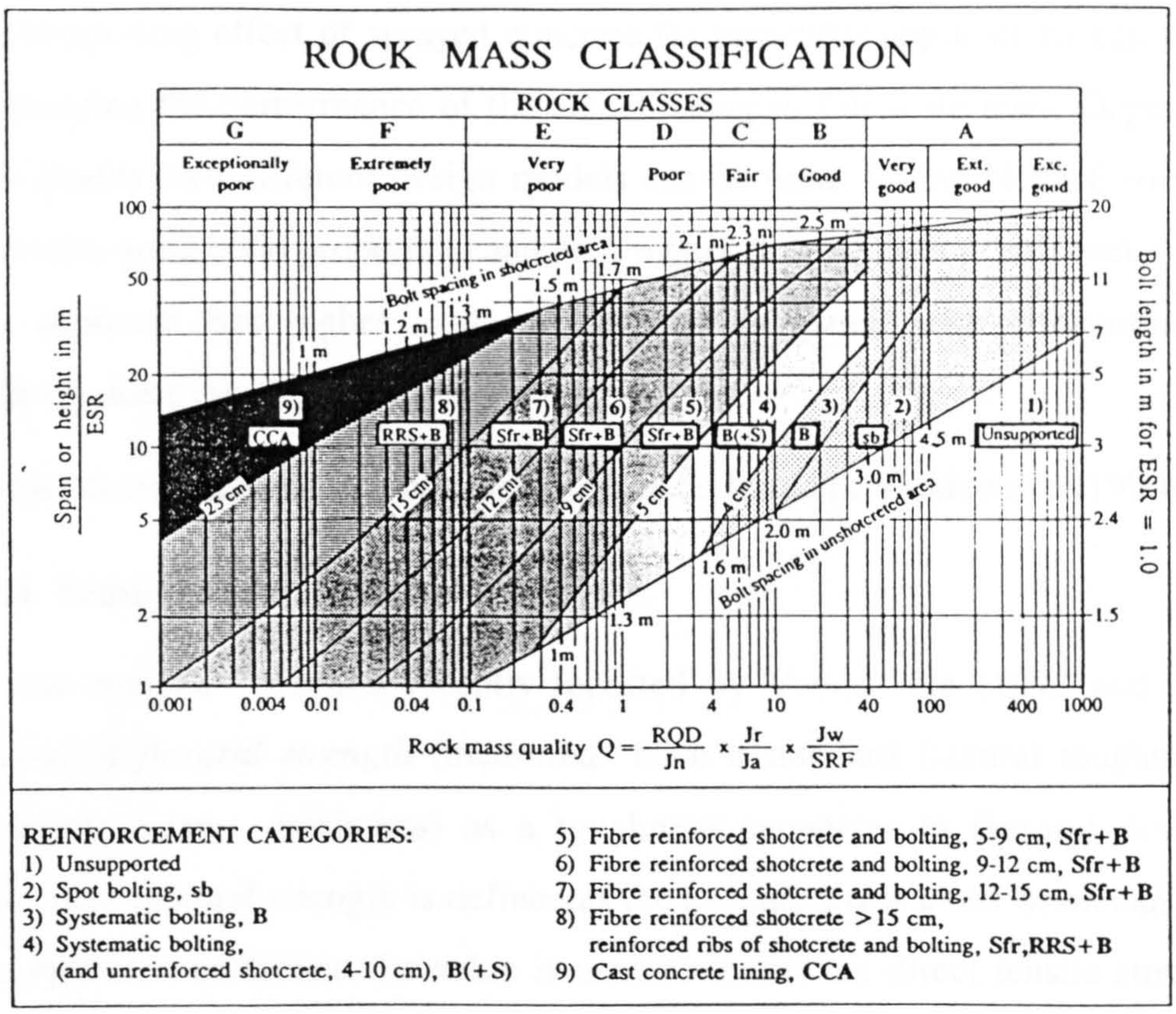

REINFORCEMENT CATEGORIES:

1) Unsupported
2) Spot bolting, sb
3) Systematic bolting, B
4) Systematic bolting, (and unreinforced shotcrete, 4-10 cm), B(+S)
5) Fibre reinforced shotcrete and bolting, 5-9 cm, Sfr+B
6) Fibre reinforced shotcrete and bolting, 9-12 cm, Sfr+B
7) Fibre reinforced shotcrete and bolting, 12-15 cm, Sfr+B
8) Fibre reinforced shotcrete >15 cm, reinforced ribs of shotcrete and bolting, Sfr,RRS+B
9) Cast concrete lining, CCA

Figure 2.17 Q-system of rock mass classification (Barton *et al.*, 1995).

2.9.2 Empirical methods

New Austrian Tunnelling Method (NATM)

NATM (described by Barton *et al.*, 1995) is an observational method initially developed for weak ground tunnelling, but has recently been modified for use in soft ground (ICE, 1996). An initial support design is selected from past experience and its deformation during construction is observed/monitored. Any additional strengthening support is based on an assessment of the monitoring results.

Norwegian Method of Tunnelling (NMT)

This method, based on over 1200 case records, uses the Q-system of rock mass classification (Grimstad and Barton, 1994; Barton *et al.*, 1995), as shown in Figure 2.17, to select an appropriate support design. It is generally considered more suitable for jointed hard rocks which are drilled and blasted.

2.9.3 Semi-empirical methods

The supporting effect of sprayed concrete for particular applications can be obtained by studying the performance of the actual lining in full-scale tests. Depending upon rock quality two different design models can be used: falling block theory (for hard rock with good bond properties) and arch theory (for medium to soft rocks). However, this approach has higher cost implications compared with conventional design methods due to the need for full-size tests.

Further details relating to these methods can be found in Vandewalle (1990).

2.9.4 Semi-analytical methods

A semi-analytical method recently reported by Vandewalle (1993 and 1990) uses *equivalent flexural strength* (measured from a standard flexural toughness test on laboratory beams specimens) as a toughness parameter in flexural design, where equivalent flexural strength is defined as the average stress a test beam can support up to a specified deflection. Its value is used to model the direct tensile stress across a cracked section in the tensile zone. The procedure uses a simplified stress-block (Figure 2.18), in combination with factors of safety. The characteristic flexural strength is used as the tensile stress parameter up to the crack strength, and characteristic equivalent flexural strength is used after crack formation. A given fibre type can be characterised by an *identity chart* of toughness ratings (Moens and Nemegeer, 1991), as shown in Figure 2.19, to determine the flexural strength (σ_{fu}) and equivalent flexural strength (σ_{fe}), for a given concrete strength, as a function of fibre content. Examples of tunnel lining design using this method are given by Vandewalle (1990).

This concept has recently been incorporated in a design guideline (Nemegeer, 1996; Bekaert, 1997), for both sprayed and cast applications, and appears to be the only design method currently available that specifically incorporates flexural toughness parameters. Unfortunately, the parameters are derived from a generalised toughness measurement approach based on arbitrary deflection limits, and therefore the deformation behaviour at small deflections may not be fully utilised. In some cases this drawback may result in a too conservative design due to significant underestimation of post-crack flexural strength. Furthermore, no account is taken of

the size effect when extrapolating equivalent flexural strengths determined from laboratory beam tests to the full-size structure in the design.

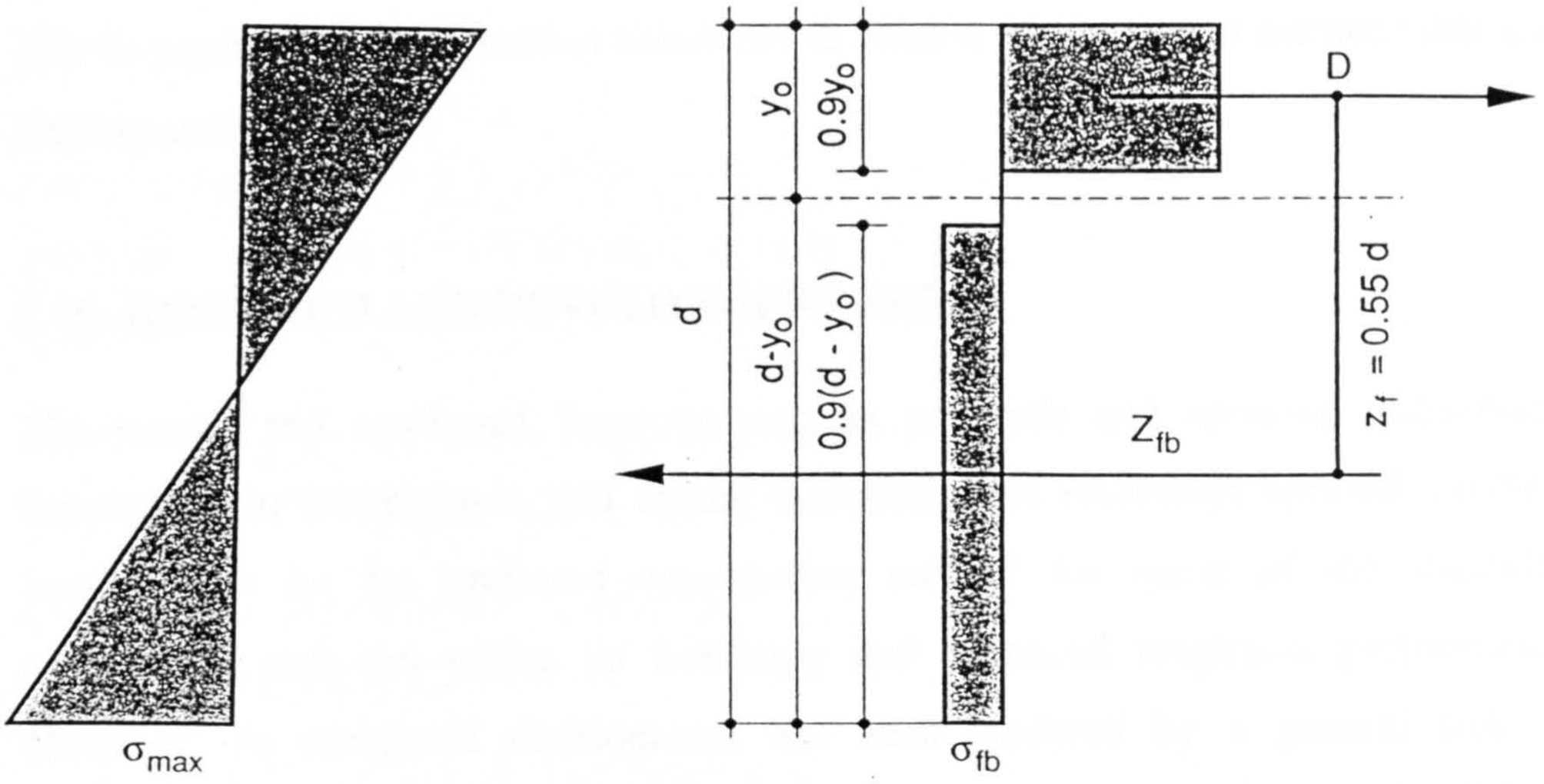

Figure 2.18 Simplified stress block diagram (Vandewalle, 1990).

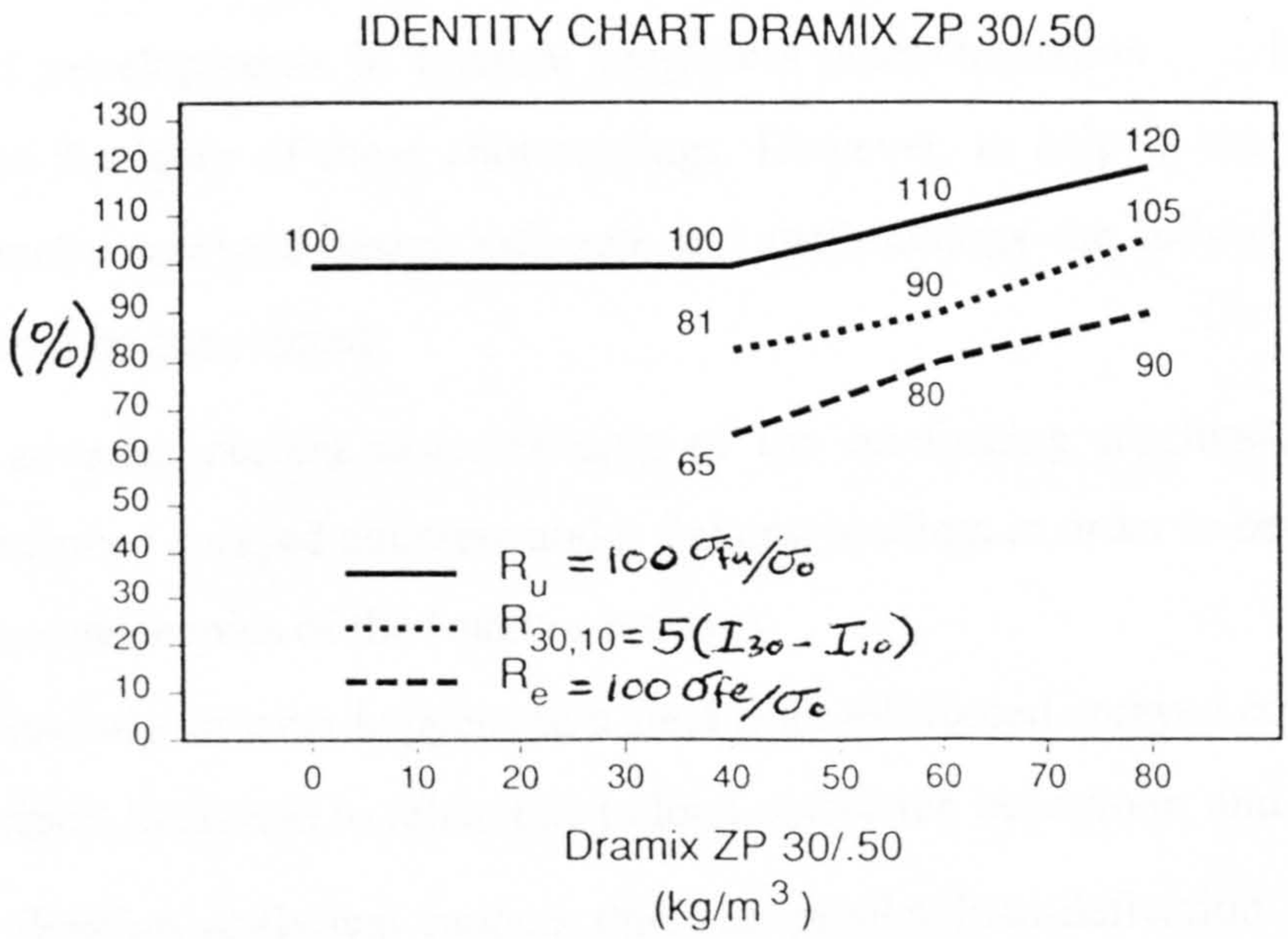

Figure 2.19 A typical identity chart for steel fibre reinforced sprayed concrete (Vandewalle, 1990).

2.9.5 Future needs

To fully utilise the potential of steel fibre reinforced sprayed concrete as a permanent structural material, there is a critical need to develop fully analytical design rationales and procedures, preferably based on conventional principles of mechanics (similar to the stress-block approach used in conventional reinforced concrete design), which are able to predict load-deformation behaviour in flexure for any given member size and loading configuration.

2.10 RESEARCH AND DEVELOPMENT NEEDS

The recent, and continued, improvements in materials and spraying technology, highlighted in this chapter, will ensure that steel fibre reinforced sprayed concrete continues to be the preferred construction method for many of the specialist applications that can utilise its flexibility and enhanced toughness performance. However, its continued development has been hindered by a general lack of confidence in its use, particularly for applications involving flexural loads. This is mainly the result of :

- a lack of appropriate analytical design rationales and methods; and
- a lack of quality control tests which measure flexural toughness parameters that can be quantitatively used in design.

Recent developments in flexural toughness characterisation have attempted to address the latter of these shortcomings. However, to help in the development of a universally accepted design rationale and methodology the following research needs must first be considered:

- to advance current understanding of the reinforcing mechanisms of steel fibre reinforced sprayed concrete under flexural loading, in order to better understand the micromechanics of the fracture process;
- to investigate what happens to a steel fibre reinforced sprayed concrete beam under flexural loads and to relate this to load-deflection behaviour; and
- to develop analytical models that can predict load-deflection behaviour for any given member size and loading configuration.

The remainder of this thesis addresses these specific needs.

3. FLEXURAL BEHAVIOUR OF STEEL FIBRE REINFORCED CONCRETE

3.1 INTRODUCTION

This chapter reviews the current state of knowledge associated with the flexural behaviour of steel fibre reinforced concrete. It is presented in three sections as follows:

Section 3.2 A review of the reinforcing mechanisms and their influence on the shape and characteristics of the load-deflection curve.

Section 3.3 A review of the principal material parameters associated with flexural behaviour.

Section 3.4 A review of the models currently available for predicting flexural behaviour.

The steel fibre reinforced sprayed concrete review presented in Chapter 2 indicated that wet process steel fibre reinforced sprayed concrete may only differ from cast steel fibre reinforced concrete in its method of application and, hence, its fibre distribution and degree of compaction. Therefore, in relating this chapter to the remainder of this thesis it is assumed that the reinforcing mechanisms, and influencing parameters, associated with the structural behaviour of steel fibre reinforced concrete are essentially the same in both sprayed (wet process) and cast mixes.

3.2 THE LOAD DEFLECTION CURVE: REINFORCING MECHANISMS AND INFLUENCING PARAMETERS

3.2.1 Characteristics of the load-deflection curve

A typical load-deflection response, obtained from a flexural toughness test, for a steel fibre reinforced concrete beam compared with a typical load-deflection response for a plain concrete beam is shown in Figure 3.1. The behaviour of the fibre reinforced concrete beam can be characterised by three distinct points as follows:

- Point A: limit of proportionality (often termed the first crack load);
- Point B: peak load or ultimate flexural strength; and
- Point C: beam failure.

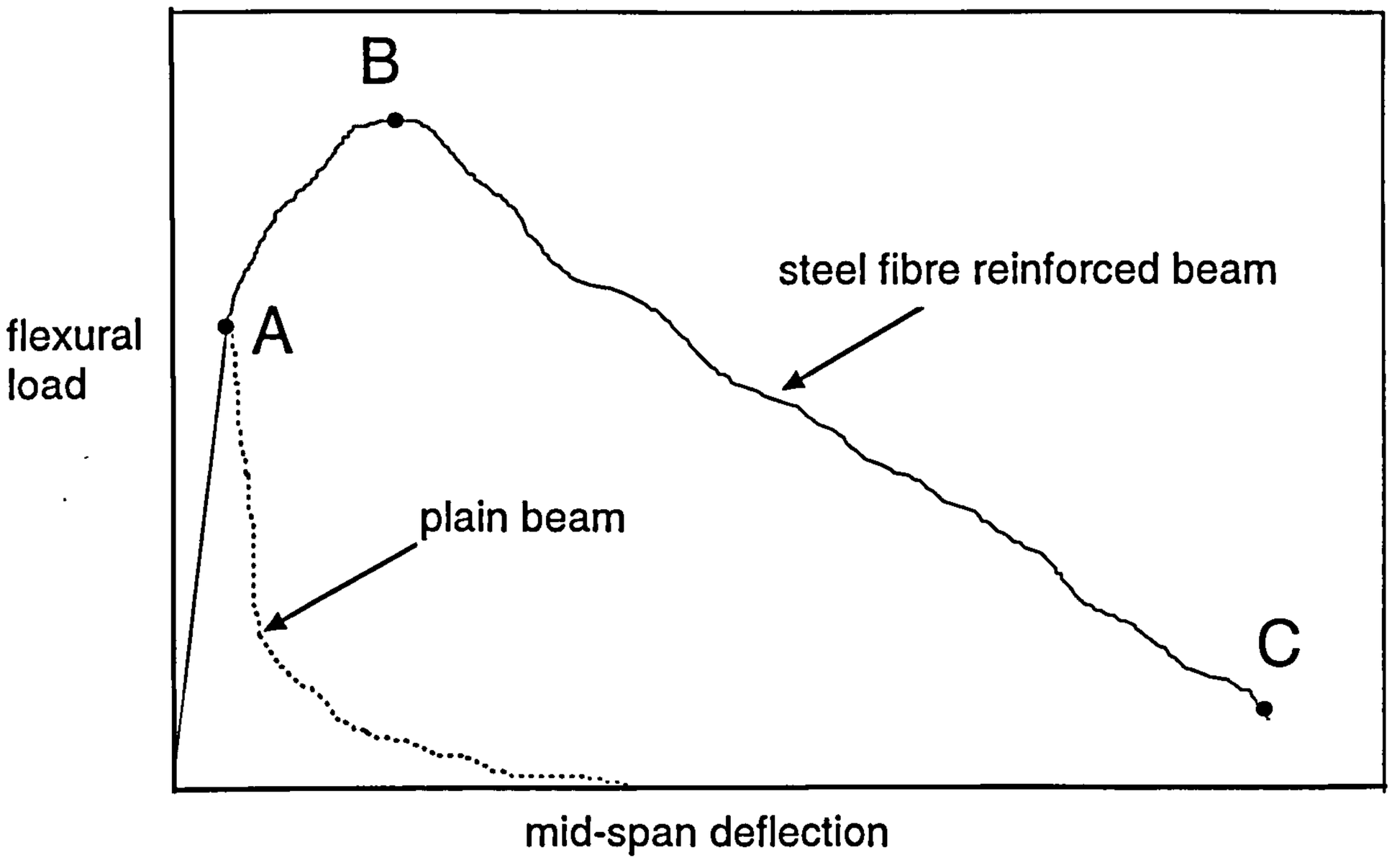

Figure 3.1 Typical load-deflection response of a steel fibre reinforced concrete beam compared with a plain concrete beam.

Up to point A, the beam is uncracked and the curve is approximately linear elastic. At Point A, the matrix tensile strength is reached causing microcracking to develop in the tensile region, resulting in a gradual reduction in the stiffness of the specimen. In the plain beam, microcracking rapidly develops into a macro-crack over the full depth of the beam causing the flexural capacity to quickly drop to zero (Banthia, 1990). But, in the fibre reinforced beam, the presence of fibres stabilises the cracking process by a variety of toughening mechanisms, thereby restricting the development and widening of the microcracks (Li and Maalej, 1996 and 1996a). Thus, a post-crack flexural capacity is sustained by the specimen due to the progressive transfer of concrete stress to the fibres bridging the propagating cracks.

The microcracking process continues until the maximum load is reached (Point B in Figure 3.1), which is thought to coincide with the first macro-crack (Balaguru and Shah, 1992). In addition, at some stage between Points A and B the fibres begin pulling-out from the matrix depending upon the fibre type and volume fraction. After

Point B, further increases in the deflection of the beam cause the macro-crack to widen and propagate over a greater beam depth causing more fibres to pullout. As the beam deflects further, crack widening continues until the fibres begin being completely pulled-out or fracturing (initially at the tensile face), eventually leading to the failure of the beam at Point C.

Generally, failure occurs at a single crack for fibre contents less than 80kg/m^3. However, multiple cracking has been shown to occur at greater fibre contents (Keer and Hannant, 1986; Hannant, 1978). In the case of short fibres (i.e. less than 40mm in length), a variety of failure patterns may develop after Point A depending upon the fibre geometry and volume content (Batson, 1994):

1. Complete fracture of the composite occurs after the matrix cracks.
2. The composite continues to support a decreasing load after the matrix cracks - known as strain softening.
3. The composite continues to support an equal or greater load after the matrix cracks - known as strain hardening.

3.2.2 Stress and strain considerations

Prior to the concrete matrix cracking (Point A in Figure 3.1) the stresses and strains in the composite are both linearly distributed across the depth of the beam. However, with the onset of microcracking and the subsequent macro-crack development the shape of the stress and strain distributions are drastically affected. In particular, cracking causes the neutral axis to move towards the compressive face of the beam, so that the equilibrium of the section below the neutral axis is predominantly maintained by the pull-out resistance of the fibres bridging the cracks (Hannant, 1978; Banthia, 1990). Hence, in the cracked section the compressive stresses (and hence compressive forces) are still related to the composite strains, but the tensile forces are now provided by the fibres pulling out across the widening crack. Thus, there can be no simple relationship between stress and strain in the cracked section.

Although it is generally accepted that the concrete continues to behave elastically in the compressive zone after the matrix has cracked - with maybe a slight non-linear response near the compressive face (Swift and Smith, 1978) - the stress distribution in the tensile zone is not so well understood. As a result, the stress and strain

distributions in the cracked section have been represented by a variety of different shapes (Mangat and Gurusamy, 1987; Hannant, 1978; Nemegeer, 1996; Dwarakanath and Nagaraj, 1991).

3.2.3 Influencing parameters on the shape of the load-deflection curve

From extensive experimental investigations involving concrete beams containing 0-160kg/m^3 of steel fibres (Banthia and Trottier, 1995a; Ramakrishnan *et al.*, 1994; Balaguru and Shah, 1992; Balaguru *et al.*, 1992; Gopalaratnam *et al.*, 1991; Soroushian and Bayasi, 1991; Ward and Li, 1990; Gopalaratnam and Shah, 1985), the main parameters influencing the shape of the load-deflection curve have been shown to include: fibre volume; fibre type and geometry; specimen size; and matrix composition.

The main findings of the investigations listed above are summarised below:

- There is no appreciable difference in the elastic modulus, determined from the load-deflection curve, up to the first-cracking load for fibre volumes between 0-160kg/m^3 (Balaguru and Shah, 1992; Gopalaratnam and Shah, 1985; Banthia and Trottier, 1995a; Gopalaratnam *et al.*, 1991).
- An increase in fibre volume results in an increase in ductility and energy-absorption capacity - improvements between 0-60kg/m^3 are much higher than for further increases in fibre volumes (Balaguru *et al.*, 1992).
- At large fibre volumes (over 90kg/m^3) the peak strength and first-cracking strength are quite distinct, but at lower fibre volumes these two strengths generally coincide (Banthia and Trottier, 1995a).
- As matrix strength increases the composite becomes more brittle, and therefore displays a steeper drop in post-peak load (Balaguru *et al.*, 1992; Banthia and Trottier, 1995a; Ward and Li, 1990). However, for a given matrix strength, the size of the post-peak load drop decreases with an increase in fibre volume (Balaguru *et al.*, 1992).
- Hooked-end steel fibres are generally better at enhancing flexural strength and flexural toughness properties than other deformed and straight fibre types (Balaguru and Shah, 1992; Ramakrishnan *et al.*, 1994; Banthia and Trottier, 1995a; Balaguru *et al.*, 1992; Soroushian and Bayasi, 1991).

- Increasing the loading rate increases the peak load, the deflection at peak load, and the steepness and size of the post-peak load drop (Gopalaratnam and Shah, 1985).
- An increase in beam depth tends to reduce flexural strength, and enhance the brittleness of the post-peak failure response (Karihaloo, 1995; Ward and Li, 1990).

3.3 EVALUATION OF THE PRINCIPAL PARAMETERS ASSOCIATED WITH FLEXURAL BEHAVIOUR

From the foregoing discussion and analysis, the flexural capacity of a steel fibre reinforced concrete beam can be regarded as a function of the following principal parameters: fibre pull-out behaviour; fibre distribution; compressive and tensile stress-strain relationships at the critical section; and the strain distribution and crack-width profile with respect to the mid-span deflection of the beam. This section reviews the current knowledge relating to the experimental and theoretical evaluation of each of these parameters.

3.3.1 Fibre pull-out behaviour

Experimental evaluation

Fibre pull-out tests, which measure the force required to pull out a fibre embedded in a matrix under uniaxial tension, are commonly used to investigate fibre/matrix bond behaviour. The earliest tests were used to determine the average fibre-matrix interfacial bond strength of straight fibres, by dividing the maximum pull-out load by the nominal interfacial fibre surface area (Gray and Johnson, 1978). However, it has since been recognised that the maximum pull-out load is not proportional to the length of a straight fibre, due to non-linear shear stress distributions at the fibre/matrix interface (Bartos, 1981), and in the case of hooked-end fibres (which provide a predominantly mechanical bond) this measure of bond strength may be meaningless (Giaccio and Zerbino, 1992). Therefore, it is now generally held that the pull-out load versus fibre-slip curve provides the most useful means of characterising fibre pull-out behaviour.

A variety of tests have been developed for measuring the fibre pull-out load versus slip response (Bartos, 1981), of which the most common are illustrated in Figure 3.2. However, when choosing a pull-out test for a particular investigation various

researchers (Balaguru and Shah, 1992; Bartos, 1981; Maage, 1978) suggest that the following points should first be considered:

- the test should simulate the fibre located in the composite as closely as possible, and should avoid unrealistic boundary conditions or stress concentrations;
- both the matrix and fibre should be subjected to tension;
- the whole length of the fibre should be embedded in the matrix;
- the test should allow for the accurate variation of fibre orientation and embedded length;
- the test should allow for the accurate measurement of fibre slip; and
- the testing of both single and multiple fibres should be possible.

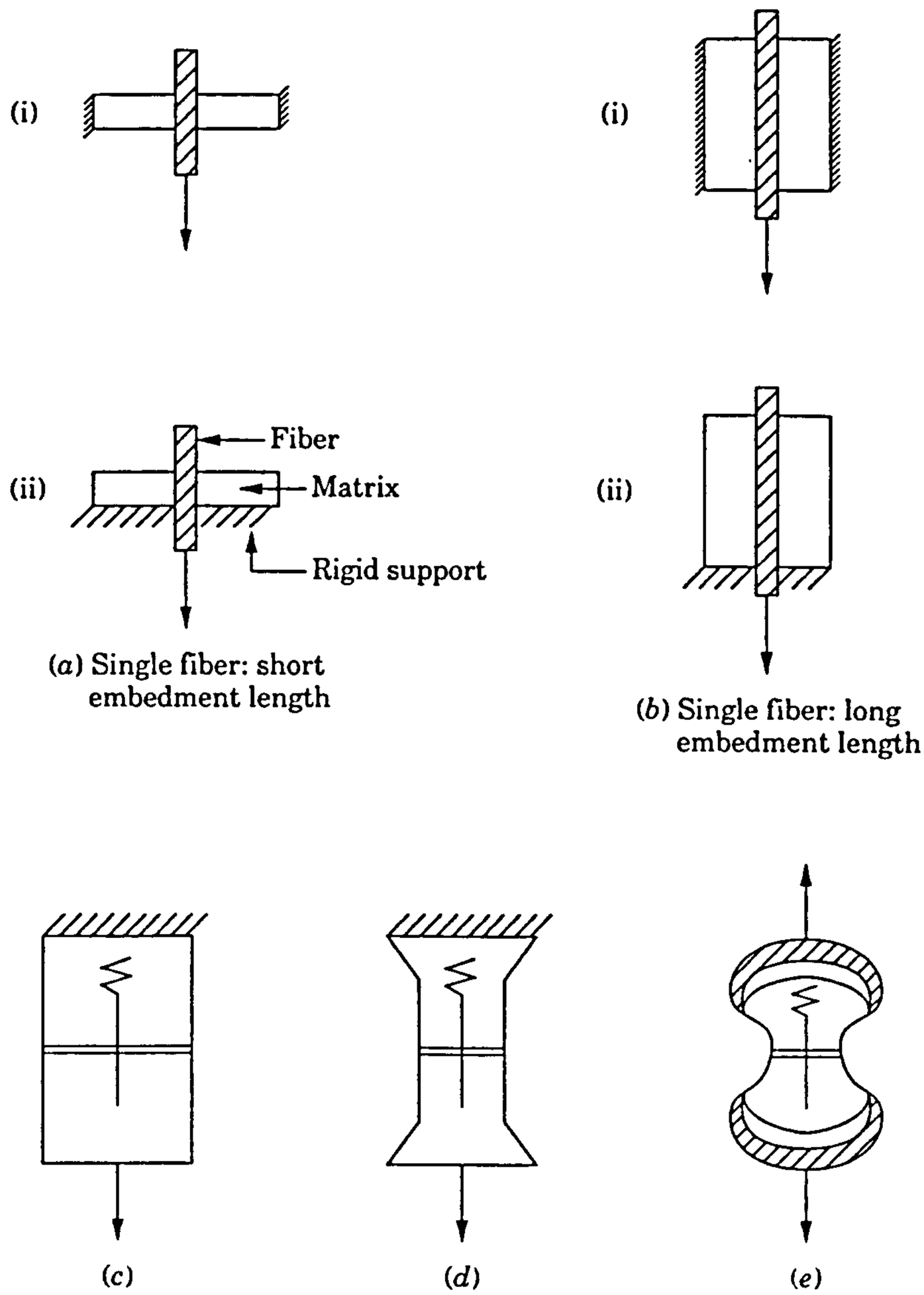

Figure 3.2 Schematic illustrations of typical fibre pull-out test set-ups (Balaguru and Shah, 1992).

It can be seen from Figure 3.2 that the pull-out tests reported to date have generally involved pull-out across an artificially cracked matrix. Consequently, no account has been taken of the pre-crack fibre-matrix interfacial stress distribution or the change in this distribution which occurs at the instant the matrix cracks. In addition, the tests are commonly controlled by cross-head displacement, which may induce a region of instability after peak load (Banthia and Trottier, 1994). Therefore, a more stable closed loop deflection control system should be adopted (Gopalaratnam and Abu-Mathkour, 1987).

Influencing factors

There is a vast amount of published pull-out data relating to straight steel fibres (Mandel *et al*, 1987; Gopalaratnam and Abu-Mathkour, 1987; Wei *et al.*, 1986; Bartos, 1981; Gray and Johnson, 1978; Pinchin and Tabor, 1978; Naaman and Shah, 1976; Naaman and Shah, 1975). However, these fibre types have now been almost entirely replaced with deformed fibres for most applications. Consequently, this discussion will mainly relate to the results of investigations using deformed steel fibres, and in particular to the more common hooked-end types, although where appropriate results from straight fibres will be referred to for comparative purposes.

The shape of the pull-out response curve associated with a deformed fibre have been extensively investigated as a function of several influencing variables, including:

- fibre type and geometry (Banthia and Trottier, 1994; Naaman and Najm, 1991; Banthia, 1990; Maage, 1978; Burakiewicz, 1978; Stroeven *et al.*, 1978; Maage, 1977; Hughes and Fattuhi, 1975);
- fibre orientation with respect to the loading direction (Banthia and Trottier, 1994; Bartos and Duris, 1994; Maage, 1977; Naaman and Shah, 1975;);
- matrix strength (Banthia and Trottier, 1994; Naaman and Najm, 1991; Narayanan and Kareen-Palanjian, 1986);
- matrix composition (Naaman and Najm, 1991; Banthia, 1990; Gray and Johnston, 1984; Gopalaratnam and Abu-Mathkour, 1987; Wei *et al.*, 1986);
- loading rate (Pacios and Shah, 1995; Banthia, 1990;);
- steel properties (Krishnadev *et al.*, 1992; Banthia *et al.*, 1992); and
- surface treatments (Tattersall and Urbanowicz, 1974).

However, very few researchers have investigated the influence of fibre embedment length (Naaman and Najm, 1991) or fibre diameter (Narayanan and Kareen-Palanjian, 1986).

The main findings of these investigations are summarised below:

- Hooked-end and crimped fibres have a higher resistance to pullout than smooth fibres and provide greater composite toughness due to the additional mechanical anchorage (Banthia and Trottier, 1994; Naaman and Najm, 1991). However, excessive fibre deformations can cause undesirable premature fibre fracture resulting in a reduced pull-out toughness measurement. Thus, deformed fibres are only effective at increasing toughness if complete fibre pull-out occurs (Banthia, 1990).
- Increasing the angle of inclination of the fibre with respect to the direction of loading decreases the peak pull-out load and increases the slip at peak load (Banthia and Trottier, 1994; Bartos and Duris, 1994; Maage, 1977). This is thought to be the result of: (1) additional shear and bending stresses imposed on the inclined fibre which lowers its yield strength; and (2) matrix crushing at the point where the fibre enters the matrix, leading to an increase in the measured slip (Banthia and Trottier, 1994).
- In terms of the toughness (measured as the energy absorbed) of a fibre up to a certain slip, with respect to inclination angle, researchers have found conflicting results. The toughness of crimped and enlarged-ended fibres has been shown to decrease as the inclination angle is increased (Banthia and Trottier, 1994), whereas the toughness of hooked-end and straight fibres has been shown to maximise at a non-zero inclination angle - typically between 15-40 degrees (Banthia and Trottier, 1994; Naaman and Shah, 1975).
- Increasing the matrix strength increases both the peak pull-out load and the post-peak performance (Naaman and Najm, 1991; Narayanan and Kareen-Palanjian, 1986), although a higher matrix strength has been shown to make undesirable fibre fracture more likely (Banthia and Trottier, 1994).
- The use of silica fume has been shown to enhance the pull-out behaviour of hooked-end fibres, although in the case of excessively deformed fibres this enhanced bond strength may lead to premature fibre fracture (Banthia, 1990).

- The moderate increase in the pull-out load resulting from an increase in the embedded length from 12mm to 25mm for a hooked-end fibre is shown in Figure 3.3 (Naaman and Najm, 1991). No pull-out curves appear to exist in the literature for hooked-end fibres with embedded lengths less than 10mm.
- Peak fibre pull-out load has been shown to increase with an increase in loading rate (Banthia, 1990).
- The fibre volume of the matrix, from which the fibre is pulled out, does not appear to influence fibre pull-out behaviour for volumes less than 3% - i.e. less than 240kg/m^3 (Naaman and Najm, 1991).

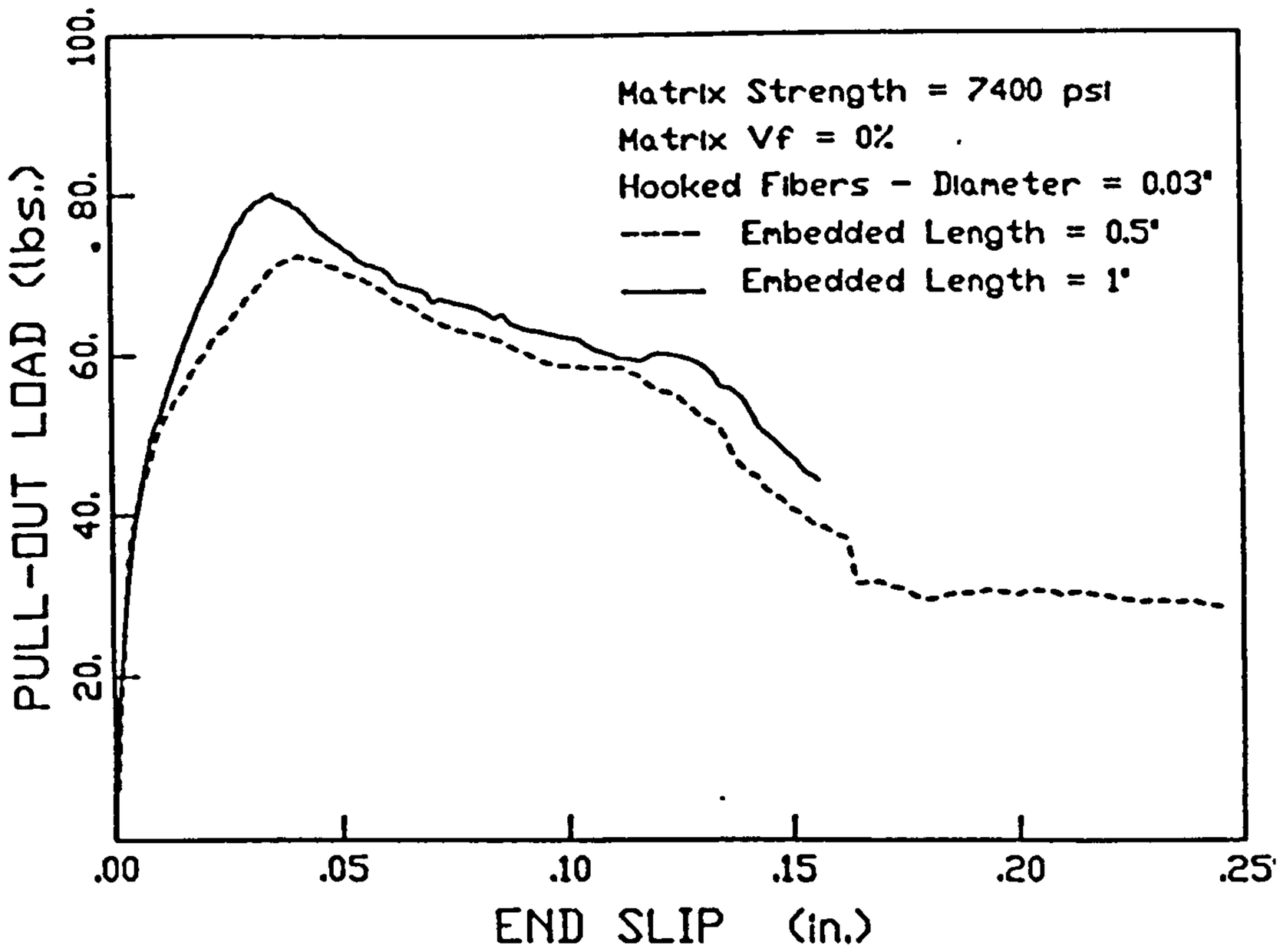

Figure 3.3 Effect of fibre embedment length on the pull-out response of hooked-end fibres (Naaman and Najm, 1991) - 1 lb = 4.448N; 1 in. = 25.4mm.

Multiple fibre pull-out tests have also been used to investigate fibre pull-out behaviour (Hughes and Fattuhi, 1975; Maage, 1977; Naaman and Shah, 1976; Mandel *et al*, 1987). However, the use of these tests to quantitatively measure pull-out behaviour is complicated by the difficulty in achieving a uniform distribution of load to all the fibres (Bartos, 1981). In addition, because the tests are commonly performed with all the fibres aligned at the same angle, it is difficult to relate the results to the pull-out behaviour of a randomly distributed fibre composite. Despite these drawbacks, results from these tests have shown that a reduction in fibre spacing causes an increase in

matrix spalling, which causes a reduction in overall pull-out performance (Hughes and Fattuhi, 1975). This observation is thought to be the result of interactive fibre-matrix stress-concentrations which increase as the fibre spacing is reduced (Maage, 1977).

Bond mechanisms and the theoretical modelling of pull-out behaviour

The pull-out behaviour of a deformed fibre is associated with three main bond mechanisms (Bartos, 1981): (1) adhesion - existing as elastic shear bond at the fibre-matrix interface; (2) friction - existing as a frictional shear bond which permits relative slips along the fibre-matrix interface once the adhesion bond is broken; and, (3) mechanical anchorage - typically existing as crimps or hooks along the length of the fibre, which create localised load transfer points between the fibre and matrix. The bond mechanisms associated with straight fibres are essentially the same except no mechanical anchorage exists.

The mechanisms associated with the pull-out behaviour of straight steel fibres have been well documented (Bartos, 1981; Shah and Ouyang, 1992), and as a result numerous analytical and empirical models have been developed to predict the pull-out response curve (Naaman *et al.*, 1991 and 1991a; ; Nammur and Naaman, 1989; Wang *et al.*, 1988; Gopalaratnam and Shah, 1987; Jenq and Shah, 1986;). At the early stages of loading, stress transfer between the fibres and matrix is dominated by the elastic adhesion bond. As the load is increased, the fibre-matrix interfacial shear strength is eventually exceeded, which breaks the adhesive bond causing progressive debonding to occur along the length of the fibre-matrix interface. The completion of this debonding process is thought to occur close to the peak pull-out load, after which the post-peak response is dominated by the frictional bond which gradually diminishes to zero as the remaining fibre embedded length is pulled-out.

In contrast, the mechanisms associated with the pull-out behaviour of deformed fibres are not so well understood, and as a result very few analytical models have been developed (Chanvillard and Aitcin, 1992; Chanvillard, 1992). In addition, because the pull-out response of a deformed fibre is dominated by the mechanical anchorage bond the models developed for straight fibres are of limited use for deformed fibres (Banthia and Trottier, 1994).

In an attempt to quantify the influence of the mechanical anchorage bond Naaman and Najm (1991) isolated this bond component by greasing the surface of a hooked-end fibre in a pull-out test. The pull-out load-slip curve obtained was then superimposed on that of a smooth fibre of the same length and diameter, and the resulting curve compared with that obtained from a normal hooked-end fibre as shown in Figure 3.4. The result clearly illustrates the dominant influence of the mechanical bond component on the shape and magnitude of the pull-out curve. In the same paper, the authors also suggest that the mechanical bond fails by the fibre deformation straightening and pulling-out along the imprint of its geometry.

The pull-out response of a hooked-end fibre has also been investigated by Pompo *et al* (1996). Using video photography on specially prepared specimens they visually recorded the fibre pull-out process and correlated it with the measured pull-out response curve. Their analysis suggested that the pull-out response of hooked-end fibres can be characterised by four distinct regions:

- Region I: An elastic response followed by debonding along the fibre-matrix interface.
- Region II: Fibre pull-out and corresponding fibre straightening - where the peak load occurs at a displacement corresponding to the length of the fibre deformation (i.e. approximately 4mm for a Dramix® hooked-end fibre), and corresponds to the end of the straightening process.
- Region III: Frictional sliding, and scraping, of the partially bent fibre within the straight matrix duct.
- Region IV: Removal of the fibre from the matrix.

The work of Pompo *et al* (1996), and Naaman & Najm (1991), has shown how the pull-out response of a hooked-end steel fibre is dominated by the mechanical anchorage bond. As a result, the geometry of the hooked end together with the steel properties should be regarded as the main parameters influencing the shape of the pull-out response curve.

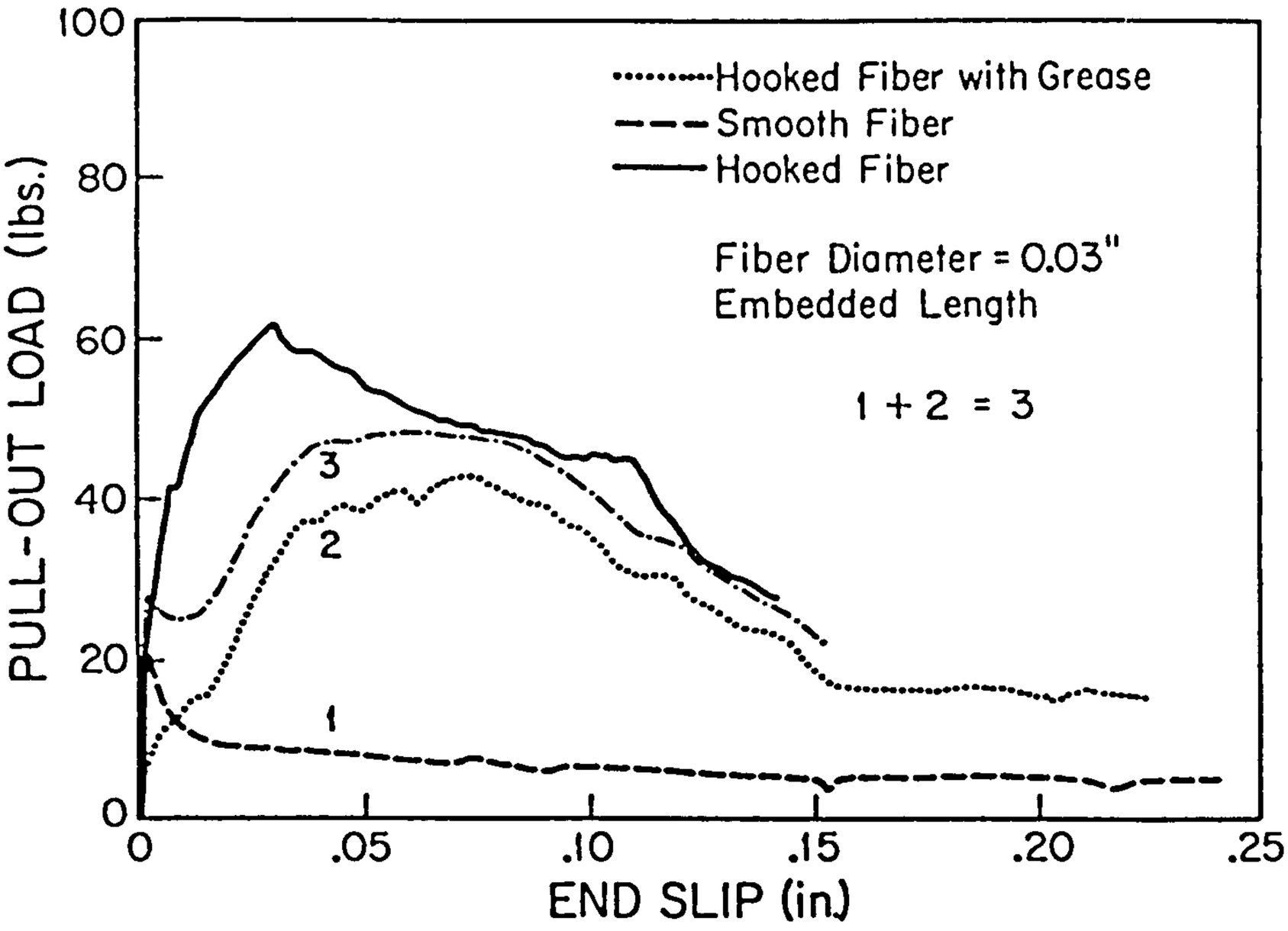

Figure 3.4 **Contribution of end hook on the pull-out of hooked-end fibres (Naaman and Najm, 1991) - 1 lb = 4.448N; 1 in. = 25.4mm.**

3.3.2 Fibre distribution

General

The load transferred across a crack in a fibre reinforced composite can be regarded as a function of the pull-out behaviour of the individual fibres in combination with the fibre distribution properties. These fibre distribution properties include the number of fibres bridging the crack (i.e. fibre density), and the individual fibre orientations and embedment lengths. This section reviews current methods available for the experimental and theoretical evaluation of these properties.

Experimental evaluation

The two main experimental methods available for evaluating fibre distribution properties are the manual method and the X-ray method.

The manual method simply involves counting the number of fibres per unit area intersecting a plane within the composite. The intersecting plane can be either the actual fractured surfaces of a test beam (Soroushian and Lee, 1990) or a pre-determined sawn section (Armelin and Banthia, 1997; Armelin and Helene, 1995). These methods have been used to compare fibre densities and distributions between

different locations in the specimen with respect to the casting direction (Soroushian and Lee, 1990; Edgington and Hannant, 1972) and, in the case of sprayed concrete, the spraying direction (Armelin and Helene, 1995; Austin and Robins, 1993). The main advantages of this method includes its simplicity, low cost, and an ability to obtain distribution data from the actual fractured surfaces. However, the analysis can be time consuming and only localised data can be obtained. Furthermore, it cannot evaluate the orientation of individual fibres.

The X-ray method involves analysing X-ray photographs of specimens sawn from the composite under investigation (Stroeven and Shah, 1978; Kasperkiewicz *et al.*, 1978). Using this method fibre distribution has been evaluated by a variety of technologies: (1) simply using the photographs to observe how fibre distribution is influenced by the casting/placement method (Austin, 1984; Ramakrishnan *et al.*, 1981); (2) counting the number of fibres intersecting the section plane to evaluate fibre density (Stroeven, 1986); (3) counting the number of fibres intersecting a superimposed grid line, from photographs taken on different planes of orientation, and relating the results to average fibre density and degree of orientation using stereological relationships (Stroeven, 1993 & 1996; Stroeven and Stroeven, 1995; Stroeven and Shah, 1978); and (4) determining the mean spacing between fibres, along a superimposed base-line, and theoretically relating its value to fibre volume content (Kasperkiewicz *et al.*, 1978). The main advantages of the X-ray method are that the global fibre distribution can be evaluated and the analysis can be automated by using image processing equipment (Stroeven, 1986). However, the technique can be expensive and can only be performed if clear and readable X-ray images can be obtained. Consequently, there are limitations on the specimen thickness and fibre volume content depending upon the power and quality of the X-ray equipment used (Kasperkiewicz *et al.*, 1978).

Influencing factors

Fibre distribution has been shown to be influenced by many factors including: casting and placement technique; specimen size; fibre size, geometry and volume content; and maximum aggregate size (Hannant, 1978). Stroeven (1986) investigated the influence of fibre content, specimen size, and workability on the fibre distribution of cast specimens which were compacted by external vibration. He found that during vibration there was a tendency for the fibres to segregate under the influence of

gravity causing higher densities at the base of the specimens. The size of the specimen mould was also found to influence fibre alignment. Similar theoretical and experimental studies were undertaken by Soroushian and Lee (1990), who found that: (1) fibre type (hooked-end or straight) does not affect fibre distribution; (2) external vibration tends to orientate the fibres into horizontal planes parallel to the plane of vibration; (3) the combination of vibration effects with the restrictions imposed on fibre orientation by the size of the specimen mould, results in the global fibre distribution moving away from a 3-D 'random' distribution and tending towards a 2-D distribution; and (4) only when the smallest cross-sectional dimension of the mould exceeds two times the fibre length does the fibre distribution tend towards a 3-D distribution.

Theoretical evaluation

A variety of theoretical expressions have been developed for evaluating average fibre distribution parameters (Hannant, 1978; Romualdi and Mandel, 1964; Stroeven, 1993; Soroushian and Lee, 1990). Fibre orientation effects have been related to a fibre efficiency factor (Hannant, 1978) or orientation factor (Soroushian and Lee, 1990). Basically, this factor represents the efficiency with which a given fibre distribution can resist a tensile force in the direction of loading. It is commonly derived as the ratio of the average projected fibre length in the direction of loading, for all possible fibre orientations, to the actual fibre length. Fibre efficiency factors are commonly used to modify rule of mixtures models (Balaguru and Shah, 1992), or to predict the number of fibres per unit cross-sectional area (N_f) from the general equation:

$$N_f = \beta \,.\, (V_f / A_f) \qquad \text{equation 3.1}$$

where β is the fibre efficiency factor, V_f is the volume fraction of steel fibres in the concrete, and A_f is the cross-sectional area of a single fibre (Soroushian and Lee, 1990). The value of the efficiency factor depends on a variety of variables including fibre distribution, boundary effects, specimen size and the method of casting. As a result, a wide range of values have been reported (Romualdi and Mandel, 1964; Hannant, 1978; Soroushian and Lee, 1990; Stroeven, 1993), which show the value of this factor reducing from unity to approximately 0.41-0.20 as the fibre distribution changes from 1D to a random 3-D distribution.

The average fibre spacing can also be used to predict the number of fibres per unit cross-sectional area. However, there has been some controversy regarding the correct method of calculation (Hannant, 1978). Romualdi and Mandel (1964) developed an expression based on the distance between the centroids of individual fibres, though a more logical approach was suggested by Krenchel (1975) who determined the average fibre spacing statistically, on the basis of the number of fibres crossing a unit area of a given plane section assuming a uniform fibre configuration. Using this approach, and assuming a 3-D random orientation of cylindrical fibres in a square array, the average fibre spacing s is given by the following equation:

$$s = \sqrt{\frac{\pi}{2}} \frac{d_f}{\sqrt{V_f}} \approx 1.25 \frac{d_f}{\sqrt{V_f}} \qquad \text{equation 3.2.}$$

where s is the fibre spacing, d_f is the diameter of the fibre and V_f is the fibre volume fraction.

Fibre length efficiency factors have also been derived for use in law of mixture models (Hannant, 1978; Lim *et al.*, 1987). However, when attempting to predict the average fibre pull-out force across a crack the average fibre pull-out length multiplied by the average interfacial bond strength has generally been considered more appropriate (Hannant, 1978; Mangat and Gurusamy, 1987).

3.3.3 Stress-strain behaviour in compression

General

Typical stress-strain curves for fibre reinforced concrete in compression are shown in Figure 3.5. This section reviews the experimental and analytical methods for determining this relationship and discusses the main parameters influencing its shape.

Experimental evaluation

The shape of the compressive stress-strain curve may be affected by many factors associated with the test system adopted, including: the specimen size and geometry; the preparation of specimen end surfaces; the stiffness of the test machine; the rate of applied stress; and the strain measuring technique. A review of these factors has been undertaken by various researchers, the main findings of which are summarised below:

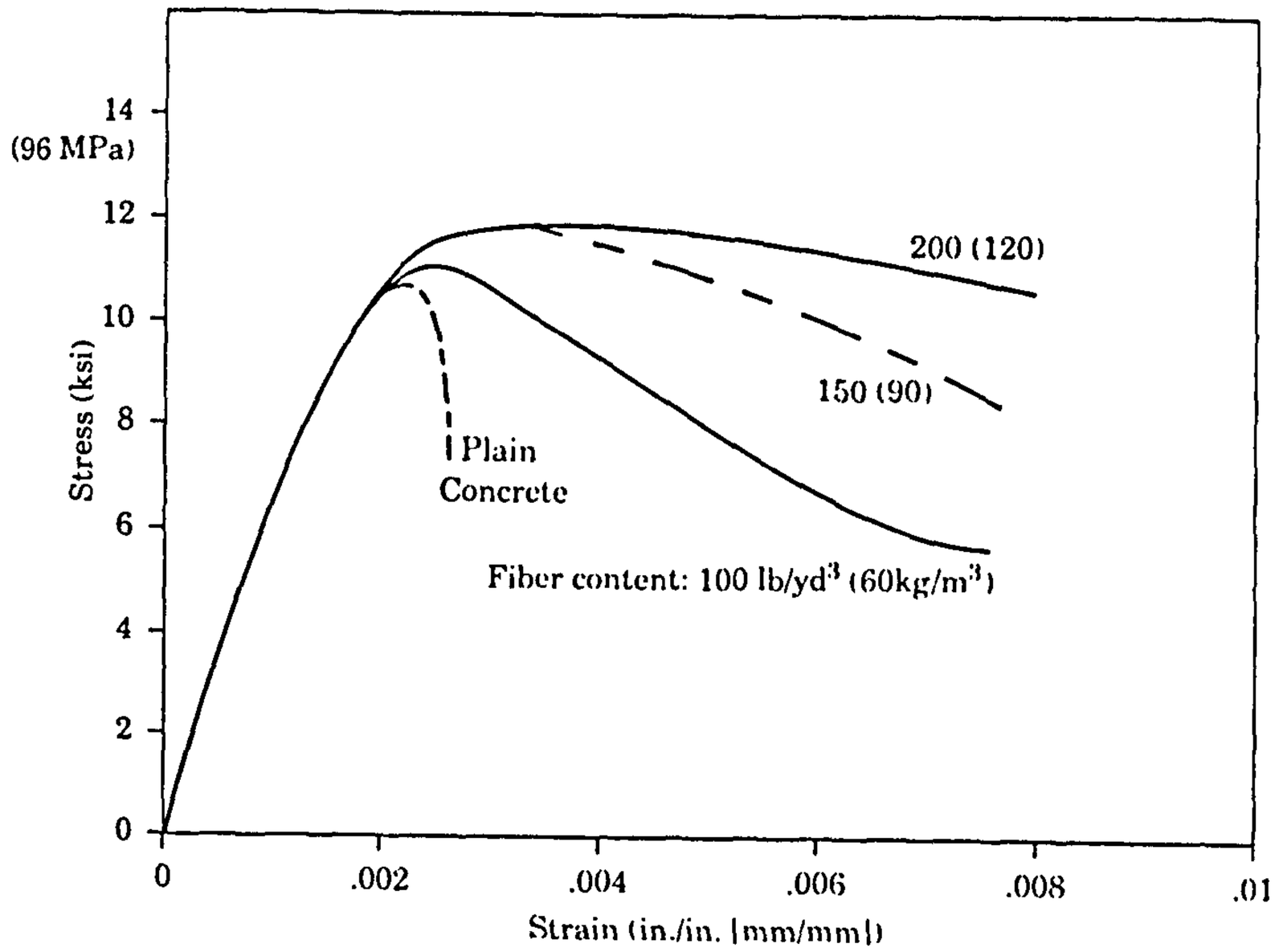

Figure 3.5 Stress-strain behaviour of fibre reinforced concrete in compression (Balaguru and Shah, 1992).

- Figure 3.6 shows the size effect relationship between mean cylinder compressive strength and specimen size - cubes and prisms have been shown to exhibit similar behaviour (Neville, 1995). It can be seen that beyond a certain size (approximately 500mm diameter) the size effect disappears.
- To avoid the wall effect, the minimum dimension of the specimen should be at least 3-4 times the maximum size of aggregate (Neville, 1995).
- Increasing the rate of applied loading, generally reduces the observed strains and increases the stresses. However, within the practical range of loading rates (between 0.07-0.7MPa per second) the effects of these influences can be regarded as negligible (Neville, 1995).
- The influence of the height/least lateral dimension ratio (h/d) on the compressive strength, when compared with the standard h/d ratio of 2, is illustrated in Figure 3.7. For a h/d ratio less than 1.5, strength increases rapidly due to the restraining effect of the test platens. But between a h/d ratio of 1.5 and 4, the influence on strength is negligible. For values of h/d above 5, strength rapidly decreases due to slenderness effects. Hence, a compression test specimen with h/d ratio between 2

and 5 (i.e. a prism or cylinder type specimen) is generally recommended (Neville, 1995).

- Strain should be measured from the actual deformation of the specimen, and should exclude any extraneous deformations from the test machine (Shah *et al.*, 1978; Hughes and Fattuhi, 1978).
- The test should be performed with a rigid test machine that can be controlled by a closed-loop system using the specimen strain as the controlling parameter - as opposed to the cross-head displacement (Hughes and Fattuhi, 1978). Closed-loop testing is thought to avoid the sudden failure of the specimen, immediately following peak load, by controlling the rate at which the strain energy is released by the test machine (Shah *et al.*, 1978; Neville, 1995).

Further recommendations relating to the compression testing of concrete can be found in the various test standards available for determining the static compressive modulus of elasticity.

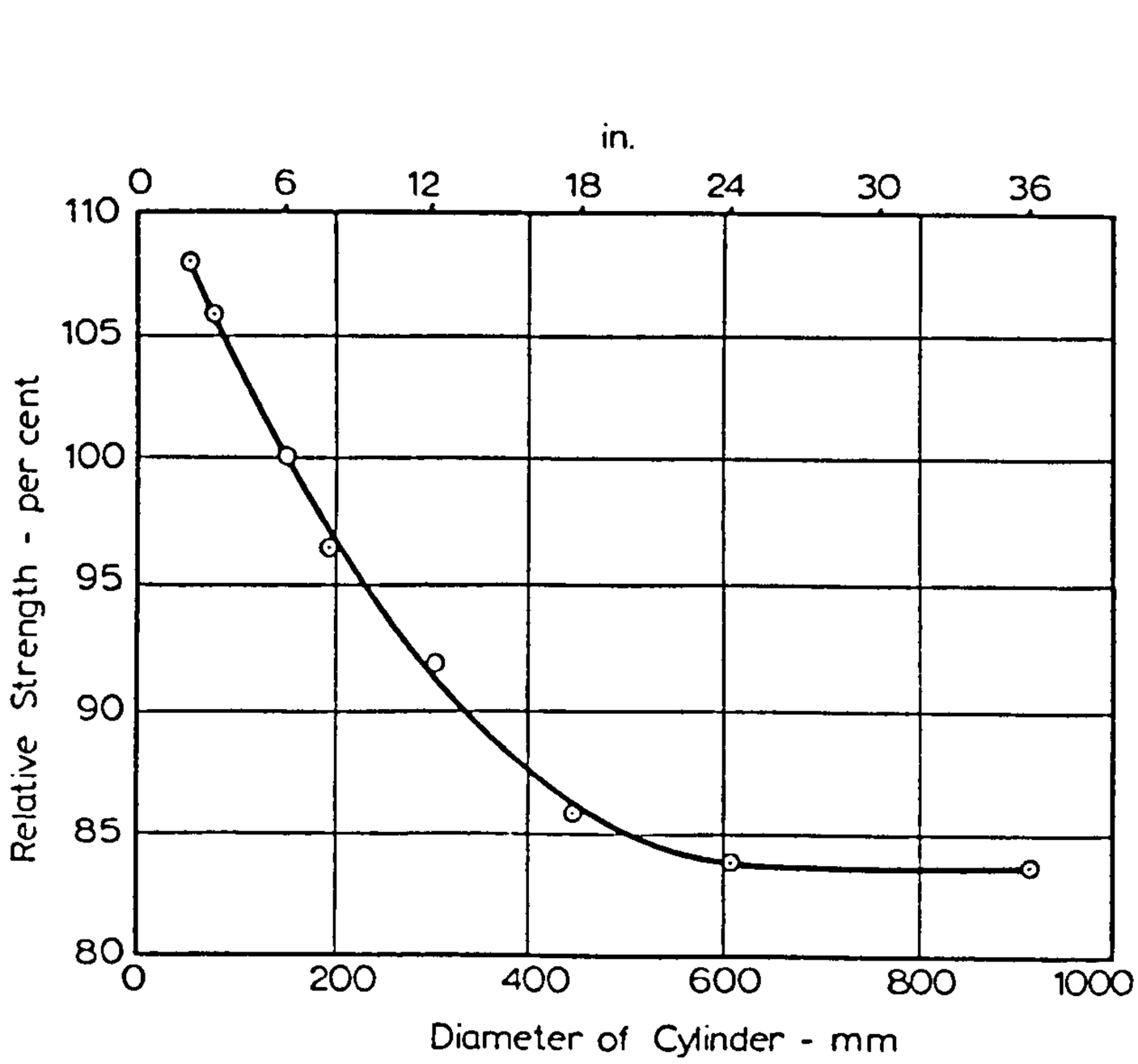

Figure 3.6 Compressive strength of cylinders of different sizes (Blanks and McNamara, 1935).

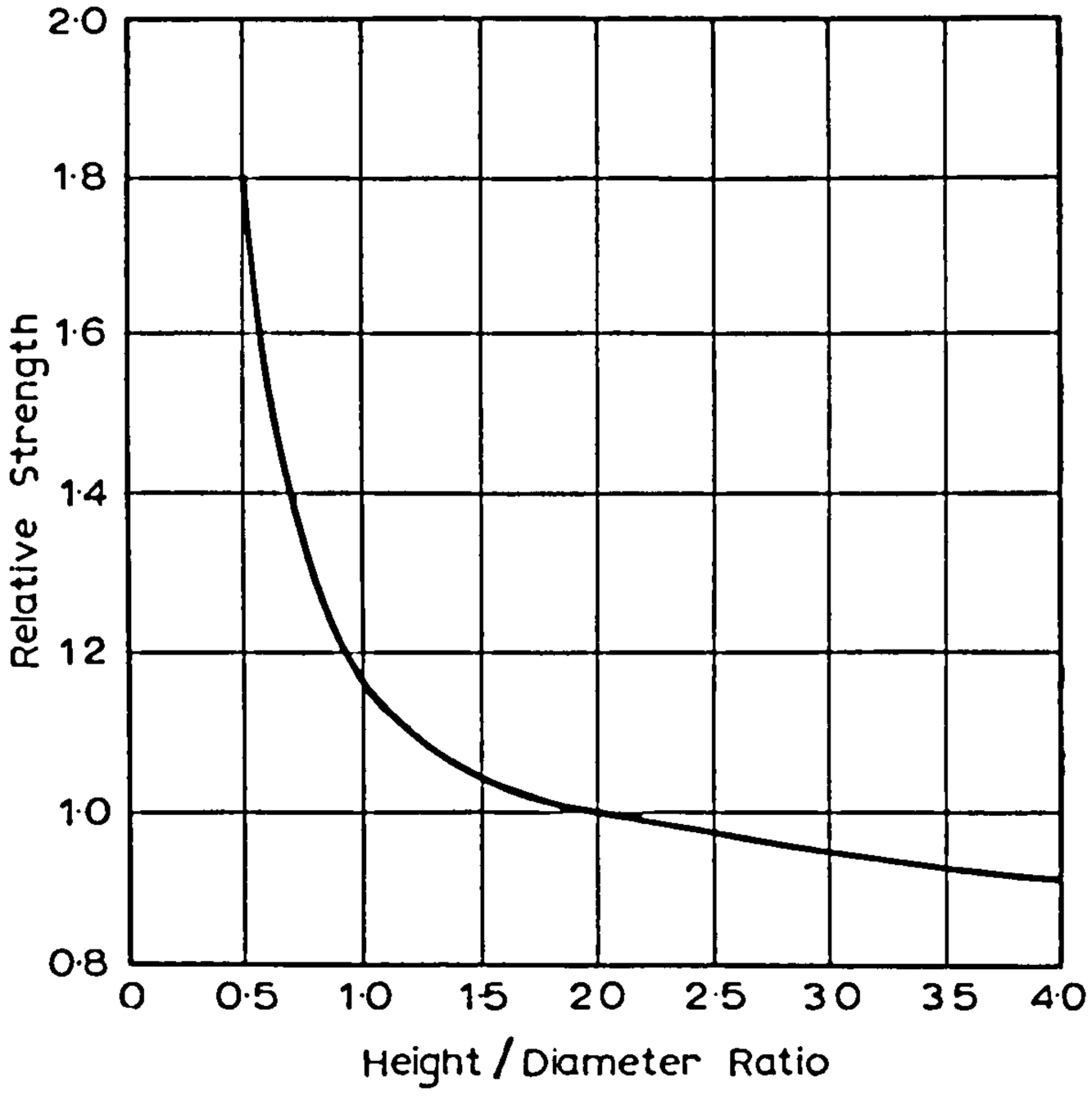

Figure 3.7 Influence of height/diameter ratio on the apparent strength of a cylinder (Gonnerman, 1925).

The addition of steel fibres can increase the compressive strength, the elastic modulus and the strain at peak stress (Balaguru and Shah, 1992). However, for fibre volumes less than 1.5% (i.e. less than 120kg/m^3), the effect of steel fibres on these properties can be regarded as negligible as shown in Figure 3.5. In contrast, this figure also shows that steel fibres have been shown to make a considerable contribution to the shape and magnitude of the post-peak compressive response even at low fibre volumes. Similar results have also been reported by (Fanella and Naaman, 1985; and Hannant, 1978).

Matrix strength also influences the shape of the stress-strain curve for a given fibre volume fraction. An increase in matrix strength increases the modulus of elasticity and the strain at peak stress, but also results in a more brittle failure causing a steeper descending post-peak curve (Balaguru and Shah, 1992).

Theoretical evaluation of the compressive stress-strain curve

Numerous models are available for predicting the stress-strain curve of plain concrete (Neville, 1995) but only a few are available for fibre reinforced concrete (Soroushian and Lee, 1989; Fanella and Naaman, 1985; Balaguru and Shah, 1992). Generally,

these models are empirical and are expressed as a function of various material parameters, which include: peak stress, strain at peak stress, modulus of elasticity, and fibre volume. However, none of these models account for the many other parameters influencing the shape of the curve (e.g. matrix composition and fibre geometry). Therefore, for design purposes an idealised stress-strain curve is commonly used, which for low volume fibre reinforced concrete is essentially the same as that used in conventional reinforced concrete design (Kong and Evans, 1987).

A few analytical expressions are also available for predicting the modulus of elasticity (Neville, 1995) and the strain at peak stress (Balaguru and Shah, 1992).

3.3.4 Stress-strain behaviour in tension

General

The tensile stress-strain curve for steel fibre reinforced concrete can be characterised by three main regions (Balaguru and Shah, 1992): (1) a linear elastic region up to about 80% of the tensile strength; (2) a region of non-linear deformation between first cracking and peak stress; and (3) a post-peak region. Fibre volume additions at up to 1.5% (i.e. 120kg/m^3) have been shown to increase both the peak tensile stress and the strain at peak stress by up to 25-30%, and the elastic modulus by up to 10% (Gopalaratnam and Shah, 1987; Hannant, 1978). Similarly, post-peak toughness can be significantly enhanced by the addition of steel fibres (Balaguru and Shah, 1992).

It is generally accepted that the elastic moduli in tension and compression, for both plain and fibre reinforced concrete, have essentially the same value (Hannant, 1978; Gopalaratnam and Shah, 1985a; Gopalaratnam and Shah, 1987).

Experimental evaluation

No standard test exists to determine the stress-strain curve of fibre reinforced concrete in direct tension (ACI 544.4R, 1988). This is mainly due to the difficulty in producing a uniform tensile stress distribution. Common problems include: stress concentrations at the gripping points causing premature specimen failure; misalignment of the test specimen and test equipment centrelines causing eccentricities; and the inability to obtain a stable post-peak response (Toutanji and El-Korchi, 1994; Gopalaratnam and Shah, 1985a).

Various types of gripping devices are available which can be categorised as follows: clamping by means of embedded steel bars (Evans and Marathe, 1968); clamping by means of gluing (Karihaloo, 1995; Li *et al.*, 1993; Toutanji and El-Korchi, 1994); clamping by means of wedge action or friction (Gopalaratnam and Shah, 1985a; Phillips and Binsheng, 1993; Green *et al.*, 1978); and clamping by means of scissor action (Johnson and Gray, 1978). Although some of these methods have been shown to minimise stress concentrations and eccentricities, Toutanji and El-Korchi (1994) suggest that none of them can totally eliminate these problems.

A stable post-crack response has generally been achieved by adopting two main systems of testing: (1) cross-head deflection control system incorporating a stiff steel loading frame around the specimen (Phillips and Binsheng, 1993; Shah *et al.*, 1978); or (2) a closed-loop testing system using notched specimens, in which the test control parameter is the specimen notch-opening displacement (Li *et al.*, 1993; Gopalaratnam and Shah, 1985a; Mobasher and Shah, 1989).

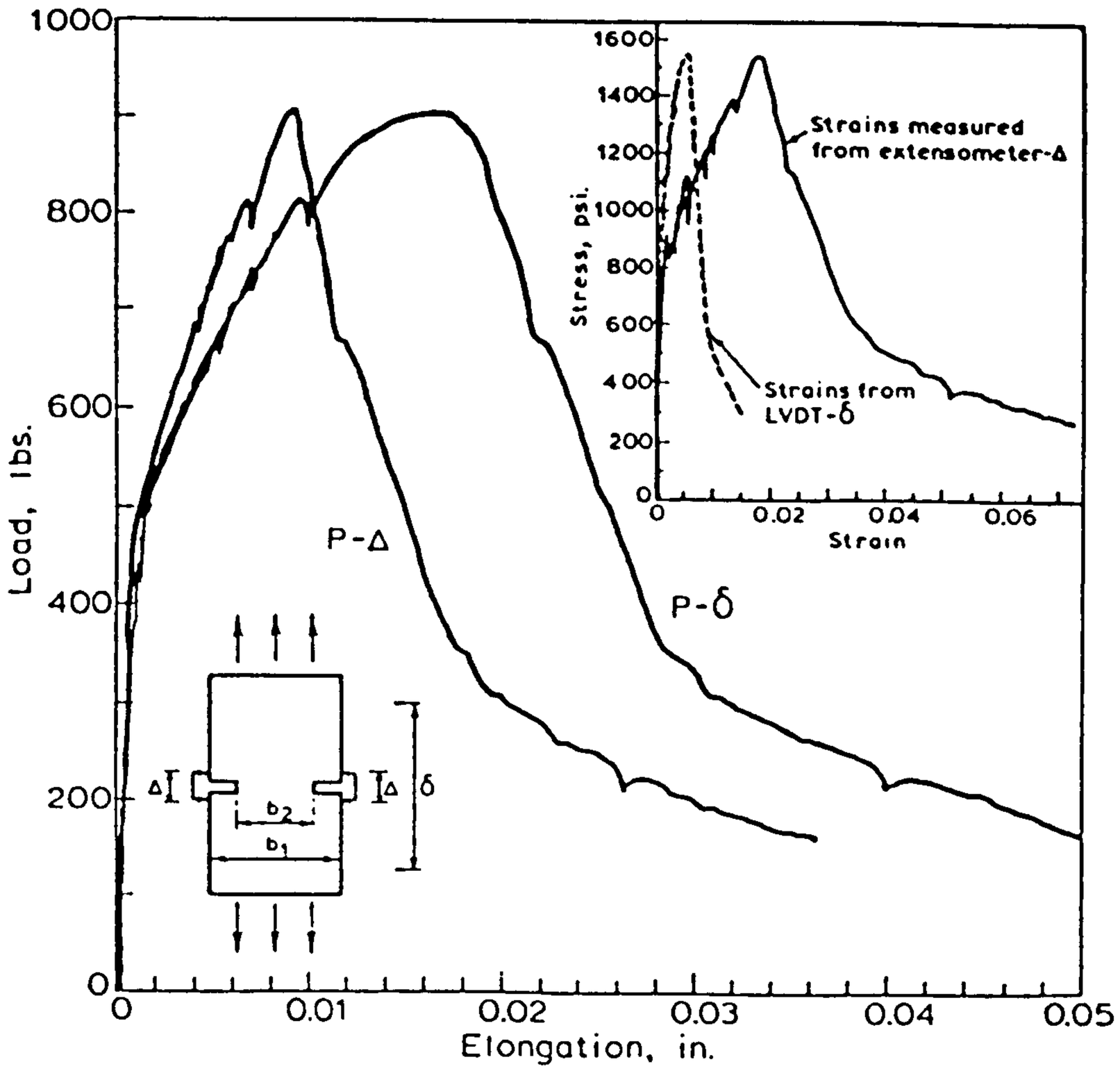

Figure 3.8 **Gauge length dependency of the stress-strain curve in tension (Mobasher and Shah, 1989) - 1 lb = 4.448N; 1 in. = 25.4mm.**

The method of strain measurement and the associated gauge length must also be carefully considered as shown in Figure 3.8. Gopalaratnam and Shah (1987) have shown using measurements of optical crack-widths, local strains, and residual deformations that the gauge length dependency observed in Figure 3.8 is due to a highly non-linear localised strain distribution that occurs in the vicinity of the cracked section just prior to peak stress. Furthermore, the results show that the total post-peak specimen deformation is equal to the width of a widening crack regardless of the gauge length. Hence, the post-peak response can be regarded as a function of a single tensile stress versus crack-width relationship regardless of the length of the specimen (Gopalaratnam and Shah, 1985; Gopalaratnam and Shah, 1987).

The tensile stress-strain curve is also influenced by other factors - similar to those influencing the compressive stress-strain curve: loading rate (Glinicki, 1994), specimen size (Neville, 1995), fibre type and geometry (Balaguru and Shah, 1992), fibre volume (Gopalaratnam and Shah, 1987), and matrix composition (Phillips and Binsheng, 1993).

Theoretical evaluation of the tensile stress-strain curve

Some models are available for predicting the tensile response curve of both plain (Gopalaratnam and Shah, 1985a; Phillips and Binsheng, 1993) and fibre reinforced concrete (Gopalaratnam and Shah, 1987; Li *et al.*, 1993). To overcome the problems associated with the non-uniform strain distribution occurring prior to peak load and the localised deformations which occur in the post-peak region, these models consider the tensile response as two separate curves (Hillerborg, 1980):

- a stress-strain curve ($\sigma - \varepsilon$) in the pre-peak region - that is up to the tensile strength, f_t; and
- a stress-crack width curve ($\sigma - w$) in the post-peak region.

Although empirical expressions are available for predicting the shape of the $\sigma - \varepsilon$ curve (Gopalaratnam and Shah, 1985a; Phillips and Binsheng, 1993), Balaguru and Shah (1992) and Karihaloo (1994) suggest that for fibre volumes less than 2% this curve can be approximated by a straight line, with a gradient equal to the elastic modulus of the material (E_t) as shown in Figure 3.9a.

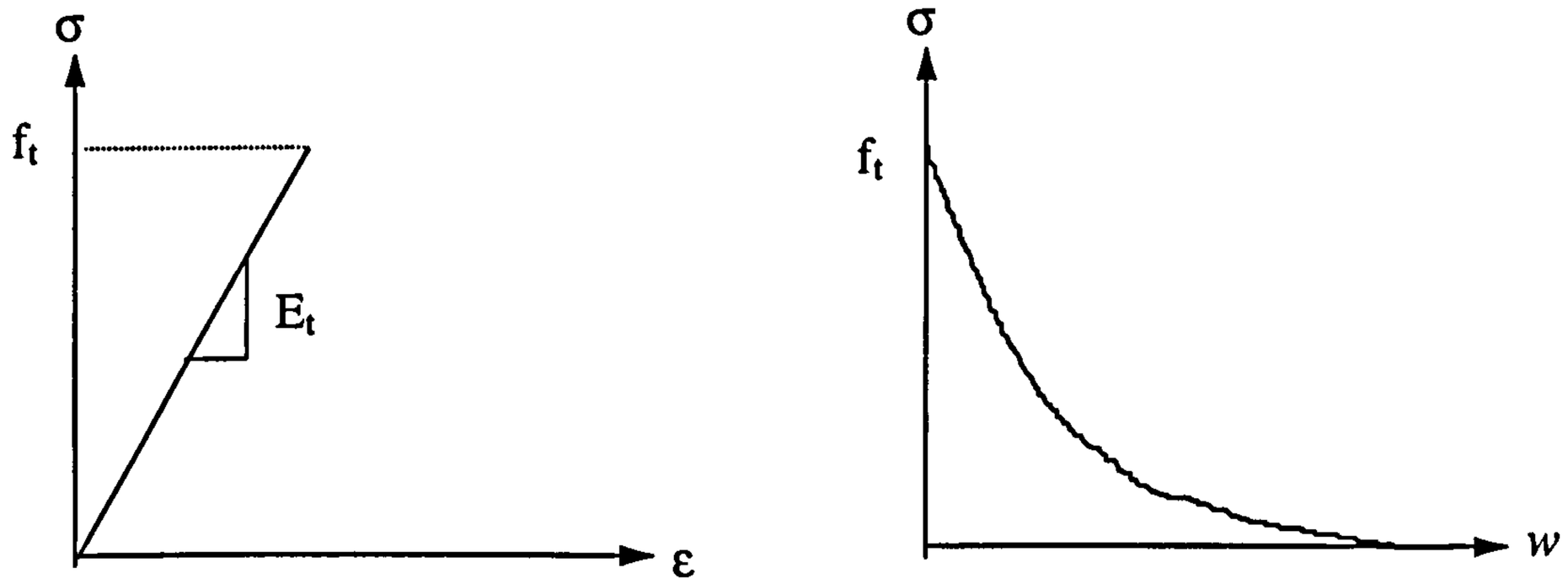

(a) stress-strain (σ–ε) curve (b) stress-crack width (σ-*w*) curve

Figure 3.9 Tensile stress distributions in the vicinity of a crack: (a) pre-crack region; and (b) post-crack region.

In the case of plain concrete, various relationships and shapes have been proposed for the σ – w curve (Gopalaratnam and Shah, 1985; Hillerborg *et al.*, 1976; Cotterell *et al.*, 1992; Phillips and Binsheng, 1993; Li *et al.*, 1993) including linear, bilinear and polynomials. However, it is thought by some researchers (Armelin and Banthia, 1997; Gopalaratnam and Shah, 1985) to be best described using an exponential relationship, as shown in Figure 3.9b, of the form:

$$\sigma = f_t (e^{-\lambda \eta w}) \qquad \text{equation 3.3}$$

where f_t is peak tensile stress (MPa), λ and η are empirical constants, and *w* is the crack width in millimetres.

The prediction of the σ – w curve for fibre reinforced concrete is not so simple, because the shape of the curve is influenced by the type and amount of fibres used. For smooth fibres, Wecharatana and Shah (1983) propose an empirical relationship of the form:

$$\frac{\sigma_{(w)}}{\sigma_{max}} = \left[1 - \frac{w}{w_{max}} \right]^n \qquad \text{equation 3.4}$$

where σ_{max} is the maximum tensile stress (determined from the law of mixtures), *w* is the crack width, w_{max} is the maximum crack-width (i.e. half the fibre length), and *n* is a constant which depends on the geometry of the fibres. A similar expression has also been proposed by Stang (1992). Others have attempted to predict the σ – w curve by

superimposing the fibre pull-out response curve on the $\sigma - w$ curve of a plain matrix (Li *et al.*, 1993; Gopalaratnam and Shah, 1987; Hillerborg, 1980). Li *et al* (1993) used this approach to predict the $\sigma - w$ curve for smooth steel fibres at small crack widths (less than 0.3mm). Their model considers the following stresses as a function of crack width, w : (1) aggregate bridging stress, $\sigma_a(w)$; (2) fibre bridging stress, $\sigma_f(w)$; and (3) fibre prestress, $\sigma_{ps}(w)$. Expressions were developed to predict these individual stress-crack width relations, which were then superimposed on each other to determine the total post-peak tensile stress versus crack-width relationship $\sigma_c(w)$:

$$\sigma_c(w) = \sigma_a(w) + \sigma_f(w) + \sigma_{ps}(w) \qquad \text{equation 3.5}$$

Finally, it must be emphasised that the above models have been developed predominantly for predicting the behaviour of concrete reinforced with straight steel fibres. As such, further research is required to modify them for use with deformed steel fibre concrete.

3.3.5 Strain and crack-width profiles

General

The motion of a beam in bending is the sum of two parts:

- a translation and rotation of the beam as a whole - rigid body motion; and
- the movement of points on the beam relative to each other - deformation.

Strain is a geometric quantity that depends on the relative movements of two or more points in the beam and is related to deformation of the beam (i.e. displacements due to rigid body motion do not produces strains). In the case of a beam under four-point loading, the middle-third of the beam is considered to be in a state of pure bending. That is, the bending moment is constant, the shearing force is zero and the bending stresses induced by the bending moment act parallel to the longitudinal axis of the beam. Hence, strains associated with the bending stresses are essentially uniaxial, and can be expressed as:

$$\varepsilon_x = du / dx \qquad \text{equation 3.6}$$

where ε_x is the uniaxial strain in the x direction, du is the deformation of an arbitrary line in the x direction, and dx is the original length of that line. Elastic theory approximates the state of stress in this situation as:

$$\sigma_x = \varepsilon_x \cdot E \qquad \text{equation 3.7}$$

where E is the static modulus of elasticity. However, equations 3.6 and 3.7 are only valid for the portion of the load-deflection curve up to the first-cracking point (i.e. the elastic region). Once the beam begins to crack elastic theory is not sufficient to predict the behaviour of the beam. In this case, the stress transferred across the crack must be expressed in terms of the tensile σ-w curve and fibre pull-out behaviour.

A model that predicts the complete load-deflection behaviour of a steel fibre reinforced concrete beam - based on the stress-block approach - will require data relating to a wide range of strain and crack-width measurements:

- in the uncracked regions of the beam - tensile strains up to approximately 200-250 microstrain and compressive strains up to approximately 5000 microstrain; and
- in the cracked regions of the beam - crack-widths up to 5-6mm.

There are a wide range of experimental methods available for determining strain distributions and crack-width profiles in flexure (Dally and Riley, 1991). However, in order to choose the most appropriate for a particular problem the following factors must first be considered for each method:

- What is the range of strain (or crack-widths) that can be measured ?
- What is the accuracy or sensitivity of the measurements obtained ?
- What is the maximum specimen size that can be analysed ?
- Does the method provide a full-field solution or point by point measurements ?
- What are the requirements for time and cost ?
- What equipment is required to perform the analysis ?
- Has the method been used in the past for similar work ?

This section reviews the main methods available, and discusses their respective advantages and disadvantages in relation to the above factors.

Electrical resistance strain gauges

This is the most widely used strain analysis technique. A strain gauge is a length of wire or metal foil of known resistance fixed to a non-conductive backing, which is rigidly bonded to the surface of the specimen. Any change in the length of the specimen is transmitted directly to the gauge, which then changes in length and cross-

sectional area. These dimensional changes cause a change in the resistance of the gauge (dR/R), which can be related to strain (ε) by the following relationship:

$$\varepsilon = S_g \, . \, dR/R \qquad \text{equation 3.8}$$

where S_g is a calibration constant known as the gauge factor and provided by the strain gauge manufacturer.

The quality of a strain gauge installation is dependent on many factors which need careful consideration. These include: strain gauge size and type; bonding adhesive; temperature compensation; environmental protection; strain limits; cost; circuit design; and strain recording instrumentation. Detailed advice on all these factors can be found in Daly and Riley (1991) and Hearn (1968).

The main advantages of strain gauges include:

- Simple and quick method of strain measurement, which is relatively cheap.
- Strains can be read directly from the recording instrumentation.
- Accurate to 5 microstrain with excellent repeatability.
- The method has been used on numerous occasions for obtaining strain measurements from conventional steel bar and steel fibre reinforced concrete specimens in flexure (Purkiss and Blagojevic, 1993; Babut and Brandt, 1978; Gopalaratnam and Shah, 1985a; Sturman *et al.*, 1965).

The main disadvantages include:

- Crack-widths cannot be measured, and strain readings are generally limited to 2% strain.
- Strain gauges only measure strain at the point of fixing and in the direction of the gauge alignment. Therefore, they do not provide a full-field analysis.
- The size, and geometry, of the specimen can limit the number of gauges that can be attached.
- The gauges must be carefully and correctly bonded to the specimen to ensure accurate strain measurements.

Grid methods

The grid method is one of the oldest strain analysis techniques available. The method requires the placement of a well defined grid of spots or lines on the surface of the

specimen, which is then photographed before and after loading to determine specimen distortion. The distances between pre-determined points on the grid before and after loading can then be used to calculate surface strains from equation 3.9, as illustrated in Figure 3.10 (Sevenhuijsen, 1993):

$$\varepsilon_{PQ} = (P^*Q^* - PQ) / PQ \qquad \text{equation 3.9(a)}$$

$$\varepsilon_{PR} = (P^*R^* - PR) / PR \qquad \text{equation 3.9(b)}$$

$$\gamma_{QPR} = \alpha + \beta \qquad \text{equation 3.9(c)}$$

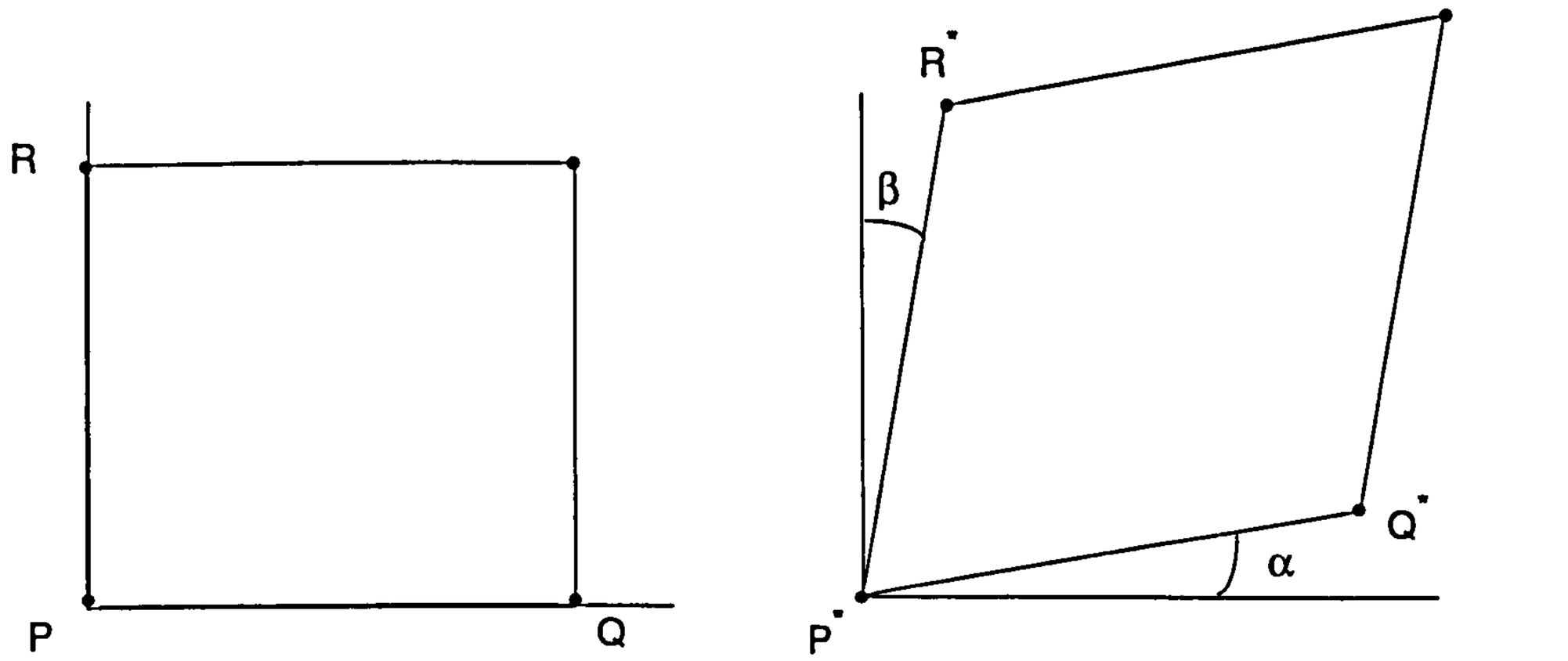

Figure 3.10 Schematic illustration of the in-plane deformation of a grid (after).

Unfortunately, early applications of the grid method were limited by three main problems:

a) It was difficult to apply a well defined grid onto the specimen.
b) The analysis was performed manually by eye, and so the accuracy and precision of the results were poor.
c) The manual analysis of the deformed grid could be very time consuming.

However, with recent advancements in photographic and computer technology, a new automated approach to the grid method has been developed using digital image processing techniques (Sevenhuijsen, 1993; Gonzalez and Woods, 1992). In this method, a photo-electronic camera, digitising (A/D) board and a computer based image-processing system are used to capture a digital image of the grid. The digital image is then analysed, using grey-level threshold techniques and centroid algorithms (Fail and Taylor, 1990), in order to determine the positions of the centroids of the grid spots in terms of (x,y) co-ordinates. This process is repeated on different images of the

grid under different loads, and grid deformations and strains are then computed from the differences in the centroid positions of each grid spot. Various methods are available for applying the grid (Parks, 1982; Sevenhuijsen, 1993), which must have high contrast (e.g. black dots on a white background) in order that it can be analysed by the image processing software. In addition, the following factors must be considered in the analysis: calibration of the camera lens to minimise distortion effects (Sirkis and Lim, 1991); image resolution - the number of pixels making up the image (Gonzalez and Woods, 1992); the grid spot size and pitch (Sirkis, 1990; Parks, 1982); the image grey level difference (Sirkis, 1990; Fail and Taylor, 1990); and system noise (Sirkis, 1990; Fail and Taylor, 1990).

The main advantages of the automated grid method include:

- Large strains (greater than 5%) and crack-widths can be measured.
- The upper limits of strain and crack-width measurement are unlimited.
- The analysis is fully automated and, therefore, not influenced by operator error.
- This method provides a full-field analysis over a large area of the specimen.

The main disadvantages include:

- Accuracy can be poor (typically around 500 microstrain).
- The method requires expensive state-of-the-art equipment, including a photoelectronic camera, a digitising board, and a high performance computer with the capability to analyse and store the digital images.
- Photoelectronic camera technology currently limits the size of the analysed grid to individual areas of approximately 200mm^2.

Note that this method has not previously been used to analyse plain or fibre reinforced concrete specimens in flexure.

Moire methods

The mechanical Moire method is a special form of grid method, in which a fine grid (termed the specimen grating) is glued to or formed on the surface of the specimen to be analysed, and after loading is superimposed on a copy of the undeformed grid (master grating). When viewed with light the superimposed grids produce an interference pattern consisting of Moire fringes, which can be analysed to yield strain values from the simple expression:

$$\varepsilon_x = a / p_x \qquad \text{equation 3.10}$$

where a is the pitch of the undeformed grating, and p_x is the distance between the fringes. A full derivation of this expression is given by Dally and Riley (1991).

Various types of grating are available (Dally and Riley, 1991), but for strain analysis work they generally consist of straight parallel lines - ideally, opaque bars with transparent interspaces of equal width - with a maximum density of 40 lines per millimetre (i.e. a pitch of 0.025mm). The master grating is usually produced by photoplotting on to a glass plate, which is then used to print or etch a copy of the grating onto the specimen. However, when using these gratings, it is difficult to measure strains of less than 200 microstrain on anything but large specimens. (For example, a grating with a density of 40 lines/mm and deformed to 200 microstrain will produce Moire fringes at 125mm centres). However, the technique is effective at measuring high levels of strains in the plastic strain range (i.e. strains exceeding 10-30%), and provides a full-field analysis.

In an attempt to increase the sensitivity of this technique Moire interferometry has been developed to enable gratings with densities of up to 2000 lines/mm to be used. The master grating is produced by a laser which is reflected by mirrors on to the specimen and a photographic plate placed in front of the specimen. The light reflected from the specimen then combines with the master grating on the photographic plate to form the fringe pattern.

The main advantages of Moire interferometry include:

- The method provides a full-field analysis, over a large area of the specimen, to an accuracy of less than 5 microstrain. It has, therefore, proved to be a very powerful method for analysing the fracture process of fibre reinforced concrete (Oplinger, 1982; Rastogi and Denarie, 1994; Balaguru and Shah, 1992).
- Unlimited range of strain measurement.
- The analysis can be automated.

However, the main disadvantage of the method is that accuracy is dependent on the need for expensive and highly sophisticated equipment to be able to produce high density gratings, obtain clear and well defined fringe pattern and analyse the fringes.

Photoelasticity

Photoelasticity involves analysing a transparent model of the actual specimen under investigation, where the model is made from a material that exhibits bi-refringent properties when stressed; that is, the material splits a ray of polarised light into two components at right angles corresponding to the planes of principal strain. By placing the model under stress in the path of a beam of polarised light it is possible to observe an interference pattern between these light components. These patterns can then be analysed to determine the strain distribution. A full description of the theory and experimental technique is given by Dally and Riley (1991).

The main advantages of photoelasticity include:

- Both two and three dimensional strain fields can be determined.
- The method provides a full-field stress analysis over a large area.
- The strain measurements can be accurate to 10 microstrain.

The main disadvantages include:

- It is an expensive technique requiring specialised equipment (e.g. the manufacture of specimen models).
- The range of strain measurement is limited to less than 1% strain.
- Scaling factors are required to convert the model strains to those expected in the actual specimen.
- The method is not suitable for analysing the anisotropic response of composites.

Photoelastic reflective method

This method is an extension of photoelasticity as described above, whereby the actual specimen under investigation is coated with a layer of photelastic material. Polarised light is reflected off the surface of the specimen and the resulting interference pattern is analysed by viewing the specimen through an analyser (Hearn, 1968; Dally and Riley, 1991).

The main advantages include:

- The method provides a full-field strain distribution to an accuracy of less than 10 microstrain.
- The method provides a relatively simple and quick method of establishing a general picture of the strain distribution over a large area of the specimen.

- It has been used for determining strain distributions and crack-width profiles of reinforced concrete beams (Lierse and Ringkamp, 1983; Babut and Brandt, 1978).

The main disadvantages include:

- Strains are measured at the centre of the coating and not at the surface of the specimen. Therefore, correction factors must be applied to the measured strains.
- The range of strain measurement is limited to 4% strain.
- Specialised and expensive equipment is required to perform the analysis.

Brittle lacquer coatings

This method involves applying a strain-sensitive coating over the surface of the specimen. The coating cracks when the strain in the specimen reaches a certain critical value, and in a direction normal to the axis of maximum principal strain. By using a calibration test on a simple cantilever, it is possible to determine the approximate value of strain which produces the crack (Hearn, 1968; Dally and Riley, 1991).

The main advantage of this method is that it provides a quick and cheap qualitative visualisation of the strain distribution over the surface of the specimen. However, it is not recommended for quantitative strain analysis due to its poor level of accuracy (between 500-1000 microstrain) and low range of strain measurement (up to 0.3% strain).

Manual crack-width measurements

Optical crack-width measurement techniques are also available (Purkiss and Blagojevic, 1993; Gopalaratnam and Shah, 1987). However they can only measure crack-widths at single points and are not practical for determining crack-width profiles during a flexural beam test. Therefore, their use will not be discussed further.

3.4 MODELLING THE LOAD-DEFLECTION CURVE

A variety of models have been proposed for predicting the flexural behaviour of steel fibre reinforced concrete. These can be categorised by their basic underlying modelling concept, as follows: a law of mixtures approach; a fracture mechanics approach; and a stress-block approach (using simple beam theory). This section reviews the main models available in each of these categories.

3.4.1 Law of mixtures type models

The earliest attempts at modelling flexural behaviour were based on a law of mixtures approach (Hannant, 1978) to derive expressions for the first crack and ultimate flexural strength (Mandel, 1985). Swamy and Mangat (1974) used this concept, in combination with regression analysis on a wide range of flexural strength data, to derive the following equation for flexural strength σ_{fu} (MPa) which was later recommended by ACI Committee 544 (1988):

$$\sigma_{fu} = 0.97\sigma_m(1- V_f) + 3.41 V_f (l/d)_f \qquad \text{equation 3.11}$$

where σ_m is the flexural strength of the plain matrix (MPa), V_f is the fibre volume fraction and $(l/d)_f$ is the fibre aspect ratio.

Although this type of model is simple to understand, and can estimate the effect of material properties on the performance of the composite, its main disadvantages include:

- The predictions are based on average fibre bond stresses and, therefore, the actual fibre pull-out behaviour is not considered.
- The load-deflection curve cannot be predicted.

3.4.2 Fracture mechanics models

General

It is now generally held that linear elastic fracture mechanics theories (LEFM), originally developed for analysing the fracture of brittle materials (e.g. glass) and elastic-plastic materials (e.g. metals), are not applicable to plain or fibre reinforced concrete (Hillerborg, 1983; Karihaloo, 1995). The main reason for this is that plain concrete is regarded as a quasi-brittle material that has no well defined crack tip during fracture (as is found in glass and metals), but develops an extensive fracture process zone (FPZ) ahead of the visible crack which gradually softens due to progressive matrix microcracking (Figure 3.11). In fibre reinforced concrete the FPZ is even larger as it comprises the additional fibre bridging zone, and has recently been observed using Moire interferometry techniques (Rastogi and Denarie, 1994).

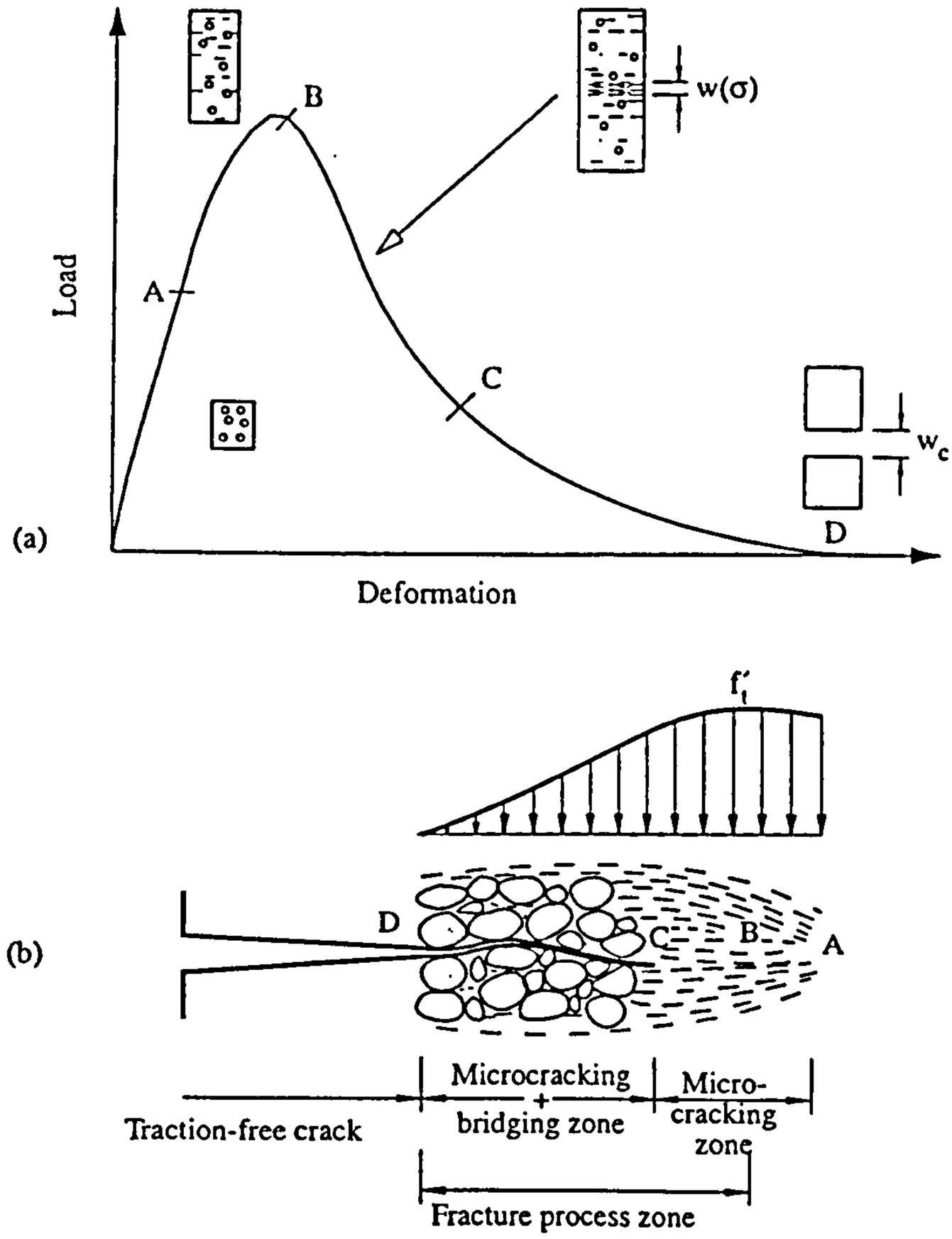

Figure 3.11 Typical tensile load-deformation response of a pre-cracked concrete specimen (a) and the fracture process zone ahead of a real traction-free crack (b) (Karihaloo, 1995).

Hillerborg (1983) has shown that the applicability of LEFM to a given material depends on a parameter termed the brittleness ratio, B:

$$B = \frac{d}{l_{ch}} \qquad \text{equation 3.12}$$

where d is the depth of the specimen, and l_{ch} the characteristic length of the material (Hillerborg *et al.*, 1976). l_{ch} is a material property that crudely approximates to the length of the FPZ. Typical values of l_{ch} for a variety of cementitious materials are compared with glass in Table 3.1. Hence, the brittleness of a material (and, therefore, its suitability to be modelled using LEFM) increases with an increase in specimen size, or a decrease in the length of the FPZ. It was subsequently suggested by Hillerborg (1983) that LEFM is only applicable when the brittleness ratio is greater than 5 (which equates to a beam depth of between 1-2m for concrete and an even greater beam depth for fibre reinforced concrete) otherwise non linear fracture

mechanics should be adopted. The brittleness ratio has also been used to explain the size effect associated with flexural strength (Maalej and Li, 1994; Karihaloo, 1995).

Given the above, the fracture analysis of plain and fibre reinforced concrete requires the use of non linear fracture mechanics theories for the typical beam sizes used in research and design (Karihaloo, 1995). In this section the two main non-linear fracture mechanics models are reviewed: (1) the fictitious crack model; and (2) the effective crack model.

Material	l_{ch}
Cement paste	5-15mm
Mortar	100-200mm
Concrete	200-400mm
Steel fibre reinforced concrete	2-20m
Glass	10^{-6}mm

Table 3.1 Typical values for l_{ch} (after Hillerborg, 1983)

Fictitious crack model

The fictitious crack model (FCM), was first suggested by Hillerborg *et al* (1976) for modelling the fracture of plain concrete beams. It assumes that no singularity exists at the crack tip, the FPZ has negligible thickness, and fracture is initiated when the uniaxial tensile strength (f_t) of the concrete is reached. As the fracture zone develops the concrete stress does not immediately fall to zero, but is assumed to gradually decrease with an increasing crack width, w. Only when the critical crack width w_c is reached (approximately 0.01-0.02mm according to Hillerborg *et al.*, 1976) is the concrete stress assumed to be zero. The length of crack up to w_c corresponds to the fracture zone and is termed the *fictious crack*, or fracture zone; and the remaining portion of crack is called the *real crack* (zero stress transfer). The fracture zone is thus a fictitious crack which transfers stress according to the σ-w relationship (Figure 3.9b).

Hillerborg subsequently developed the FCM to predict the load-deflection curve of steel fibre reinforced concrete beams. Initially he derived the σ-w curve using the law of mixtures (Hillerborg, 1980), by combining the σ-w curve of the plain concrete matrix with a simplified theoretical σ-w curve for the fibre pull-out stress. This was used in combination with a finite element analysis to produce load-deflection curves for 100mm deep notched and unnotched beams with 1-2% (i.e. 80-160kg/m^3) of straight steel fibres. However, in a more recent paper (Hillerborg, 1985) an idealised σ-w curve was used, based on a range of experimentally obtained σ-w curves for different fibre types and volume contents. Unfortunately, in both these studies no validation of the predicted curves with experimental results was presented.

Maalej and Li (1994) also adopted the FCM concept to derive an analytical model to predict the flexural strength of straight steel fibre reinforced composites. In their model the σ-w curve is related to the composite's micromechanical properties (such as fibre length, fibre diameter, fibre/matrix interfacial bond strength, and fibre and matrix moduli) through explicit analytical expressions. Although the flexural strength predictions compare well with experimental results their model is unable to predict the load-deflection curve.

The crack-band model, proposed by Bazant and Oh (1983), adopts a similar concept to the FCM except that a stress-strain relationship is used in place of the σ-w curve. This model assumes that the FPZ is distributed over a band width h^*, hence the name crack-band model. The parameter h^* is effectively a gauge length that relates inelastic strain to inelastic deformation.

Effective crack model

Effective crack models have also been used to predict the load-deflection curve of notched steel fibre reinforced concrete beams. These models represent the FPZ by an elastically equivalent effective crack, which incorporates the bridging effect of the fibres and assumes that crack tip singularity exists. Fracture properties and flexural capacities can be obtained using various non-linear (and linear) fracture mechanics theories, as discussed by Shah (1990), Balaguru and Shah (1992), and Mandel (1985). Among these type of models are those proposed by Jenq and Shah (1986), and Wecharatana and Shah (1983) for predicting the flexural response of notched beams.

However, it is not clear whether effective crack models can be used for predicting the flexural behaviour of unnotched beams, and they use theories, parameters and procedures which are not readily understood by civil engineers. Therefore, it is unlikely that a design rationale based on this concept could be universally accepted in the foreseeable future, and so their use as flexural modelling tools for steel fibre reinforced concrete will not be discussed further.

3.4.3 Stress-block models

General

Stress-block models use simple principles of mechanics to determine the moment of resistance (and hence flexural load capacity) of a steel fibre reinforced concrete beam under investigation. These principles are equally applicable to both uncracked and cracked sections providing the size and shape of the stress-block can be evaluated, and the equilibrium of the section is maintained.

The earliest models predicted ultimate flexural strengths using assumed stress blocks. Hannant (1978) used a rectangular tensile stress block with a neutral axis depth of D/4. His approach assumed that at ultimate stress the matrix is fully cracked and, therefore, the tensile stress block is purely a function of the pull-out resistance of the fibres. This concept was later extended by Mangat and Gurusamy (1987), who modified the rectangular tensile stress block to include a matrix contribution. An expression was derived for the modulus of rupture of the composite σ_{fu}, which was almost identical to equation 3.11. More recently, Dwarakanath and Nagaraj (1991) used a similar concept to predict the flexural strength of a steel fibre reinforced concrete beam using just three empirically obtained parameters: (1) uniaxial compressive stress-strain curves; (2) uniaxial tensile stress-strain curves; and (3) maximum compressive and tensile strains measured from the extreme faces of a flexural test beam. Although these models are useful for predicting first crack or ultimate stress conditions they are unable to predict the complete post-crack load-deflection behaviour.

The prediction of the load-deflection curve, using the stress-block approach, requires a knowledge of the following: (1) the influence of beam deflections on both the strain distribution and the crack-width profile; and (2) the stress-strain relationships that

occur at the critical section of the beam prior to, and following cracking. Such an approach has been considered by various researchers (Swift and Smith, 1978; Sakai *et al.*, 1986; Armelin and Banthia, 1997) as discussed below.

The model proposed by Swift and Smith (1978) uses a zonal concept to represent the various kinds of stress-strain behaviour that occur at the critical section, as follows: (i) plastic compression; (ii) elastic compression; (iii) uncracked tension; (iv) cracked tension; and (v) fibre pull-out. Simplified stress-strain relationships for each zone are determined from a number of theoretical and empirical parameters, and assumed strain limits. However, the resulting flexural load predictions are not related to the load-deflection curve but to a dimensionless measure of the local curvature of the beam. As a result, the use of this model in design appears limited.

More recently Armelin and Banthia (1997) have proposed a model to predict the post-cracking load-deflection response of a beam tested in accordance with ASTM C1018 (1992). By dividing the cracked section into discrete zones (similar to the model proposed by Swift and Smith (1978) as described above), the section forces are determined by applying theoretical and experimental stress-strain relations to the respective zones. An iterative process is then used to determine the neutral axis position, crack-width profile and moment of resistance in relation to mid-span deflection, from an assumed value of maximum compressive strain. Both simple beam theory and approximate flexural mechanics relationships (for a cracked beam section) form the basis of the iterative calculations. The process is repeated for a range of increasing compressive strain values in order to obtain points on the post-cracking load-deflection curve. Compressive and tensile stress-strain relationships are based on established uniaxial stress-strain expressions for plain concrete found in the literature, while pull-out forces are related to crack opening displacements using an average single fibre pull-out curve and average fibre densities obtained experimentally.

A similar modelling concept, using an assumed value for maximum compressive strain in combination with an iterative process, has also been proposed by Sakai *et al* (1986) in which the various stress-strain relationships at the cracked section are predicted from theoretical expressions. However, this model uses only two stress-strain relationships to model the forces across the crack: (1) a compressive stress-strain relationship; and (2) a tensile stress-strain relationship. As a result, the model

cannot fully differentiate between the uncracked and cracked states of stress that occur at the critical section of a beam subject to flexural loads.

Both the above models are simple to understand, use conventional principles of flexural mechanics and material parameters, and appear to predict the post-cracking load-deflection curve for a selection of experimental data reasonably well. However, their main limitation is that crack-width profiles, neutral axis positions, and mid-span deflections are determined theoretically, using approximate expressions and assumed strain values, without any apparent justification for their use, or accuracy.

Author's Note: Although the model proposed by Armelin and Banthia (published in March 1997) is similar in concept to the model developed and presented in this thesis, it must be noted that their work was undertaken totally independent of the work presented in this thesis.

3.5 RESEARCH AND DEVELOPMENT NEEDS

This chapter has shown that the flexural behaviour of steel fibre reinforced concrete can only be fully understood, and thereby predicted, if crack formation and the associated reinforcing mechanisms at the critical section are explicitly considered in terms of the strain distribution, crack-width profile and the deflection of the beam. To this end, the stress-block concept potentially offers the most universally acceptable flexural modelling approach for the following reasons: (1) it is simple to understand; (2) it uses conventional principles of flexural mechanics; and (3) it could be incorporated into a design rationale similar to that used for conventional reinforced concrete.

In order to predict the load-deflection curve in flexure, the main requirements of a stress-block model are: (1) an ability to predict the strain-distribution (and associated crack-width profile) in terms of the mid-span beam deflection; and (2) an ability to relate the strain distribution and crack-width profile to the corresponding stress-block, by applying stress-strain relations to the various reinforcing mechanisms that occur at the critical section.

However, the stress-block models developed to date have used either an assumed stress-block, or an assumed strain profile from which the stress-block is obtained. No

attempt has been made to ascertain the actual stress-block from strain distributions measured during a flexural beam test. Furthermore, the actual fibre numbers and distributions existing at a cracked section have not been related to the actual response of the beam under investigation. This may be because no experimental data appears to exist for these parameters. Consequently, the stress-block models currently available cannot fully explain why a certain failure occurs, or provide experimental evidence to validate the assumptions used in their formulation.

Research is therefore needed to fully develop a design rationale for steel fibre reinforced concrete based on the stress-block modelling concept. This should focus on the following: (1) predicting the actual strain-distributions, crack-width profiles and, hence, stress-distributions for any given beam deflection; (2) investigating the influence of the fibres bridging the cracked section on the resulting flexural load-deflection response, and in particular the influence of fibre numbers, orientations and embedment lengths; and (3) validating the use of the stress-block modelling concept to predict flexural behaviour (and in particular the load-deflection response).

This thesis aims to address these research needs in order to develop the basis of a universally accepted design rationale for both sprayed and cast steel fibre reinforced concrete.

4. RESEARCH METHODOLOGY

4.1 INTRODUCTION

This chapter - which draws on the research needs identified in chapters 2 and 3 - presents the research methodology adopted. Initially it describes the aims and objectives of this thesis, which centres around the development of a model to predict the flexural load-deflection response of a steel fibre reinforced sprayed concrete beam. The concepts of the model are then described together with its principal parameters and data requirements. A brief outline of the experimental investigation undertaken to obtain the data for the model, and the potential implications of the model on the future design and quality control of steel fibre reinforced sprayed concrete are also discussed.

The principles described in this chapter were published and presented by the author at the International Conference on Sprayed Concrete - 'Sprayed concrete technology for the 21st century' - held at Edinburgh University in September 1996 and jointly organised by the American Concrete Institute and the Sprayed Concrete Association (Robins, Austin and Jones, 1996).

4.2 RESEARCH AIMS AND OBJECTIVES

The literature review presented in Chapters 2 and 3 identified the following research needs relating to the development of steel fibre reinforced sprayed concrete:

1. To advance our current knowledge of the reinforcing mechanisms associated with steel fibre reinforced sprayed concrete (particularly under flexural loads), in order to better understand the micromechanics of the fracture process.
2. To develop analytical models and design rationales, using conventional fibre reinforced concrete material parameters, which are universally accepted for the prediction of flexural behaviour.
3. To develop flexural toughness characterisation procedures which can provide toughness parameters readily obtained from the load-deflection response and that can be used quantitatively in structural design and quality control.

In an attempt to address these needs, the principal aims and objectives of this thesis can be stated as follows:

AIMS

To investigate experimentally the reinforcing mechanisms and fracture processes associated with a steel fibre reinforced sprayed concrete beam under flexural load, in order to develop a model based on conventional principles of mechanics - using a stress-block diagram approach - to predict the flexural load-deflection response and thereby predict flexural toughness performance.

OBJECTIVES

To test the following hypothesis:

Given the compressive strength, fibre volume, fibre type, cross-section dimensions and loading geometry of a steel fibre reinforced sprayed concrete beam, the flexural load-deflection response curve of the beam can be predicted, using a stress-block diagram approach, if the following principal parameter relationships are known:

- ***the uniaxial compressive stress-strain relationship;***
- ***the uniaxial tensile stress-strain relationship;***
- ***the single fibre pull-out load versus crack-width relationship;***
- ***the number, distribution, embedment lengths and orientations of the fibres bridging the cracked beam;***
- ***the strain profile (and associated neutral axis position) of the uncracked beam in relation to the mid-span beam deflection; and***
- ***the crack-width profile of the cracked beam in relation to the mid-span beam deflection.***

4.3 THE PROPOSED MODEL

4.3.1 Overview

The proposed model centres around predicting the stress-block diagram at the critical section of a steel fibre reinforced sprayed concrete beam in flexure, for a given mid-span deflection. If the shape and magnitude of the stress-block diagram can be

ascertained then it can be used to estimate the flexural capacity of the beam in a similar way that stress-block diagrams are used in conventional reinforced concrete design. Thus, flexural loads can be calculated for any given beam deflection and the complete load-deflection response curve can be predicted. In this way a direct link can be established between structural design and flexural toughness performance.

The main objectives of the model can thus be summarised as follows:

- the prediction of the stress-block diagram for a given beam deflection, matrix strength, fibre type, fibre volume content, beam size and loading geometry;
- the estimation of the flexural capacity of the beam under investigation from the stress block diagram; and
- the prediction of the complete load-deflection response and thereby flexural toughness performance.

4.3.2 Concepts

The concept of the model is illustrated in Figure 4.1 (a) to (d), which shows an idealised representation of a propagating crack at the critical section of a steel fibre reinforced sprayed concrete beam under increasing mid-span deflection, together with the corresponding stress-block diagram. At the early stages of loading the beam is uncracked and behaves elastically (Figure 4.1(a)). Once the matrix tensile strength is exceeded matrix microcracking develops at the tensile face, initiating fibre-matrix debonding and causing the neutral axis to move towards the compression face of the beam (Figure 4.1(b)). Further increases in the mid-span deflection cause the microcracks to widen, and eventually this results in the development of a macro-crack and further movements of the neutral axis (Figure 4.1(c)). This process continues until the fibres start being pulled out from the matrix across the macrocrack (initially at the extreme tensile face) resulting in the subsequent failure of the beam (Figure 4.1(d)). These four stages of crack development and propagation can be related to separate regions of the load-deflection response curve as shown in Figure 4.2.

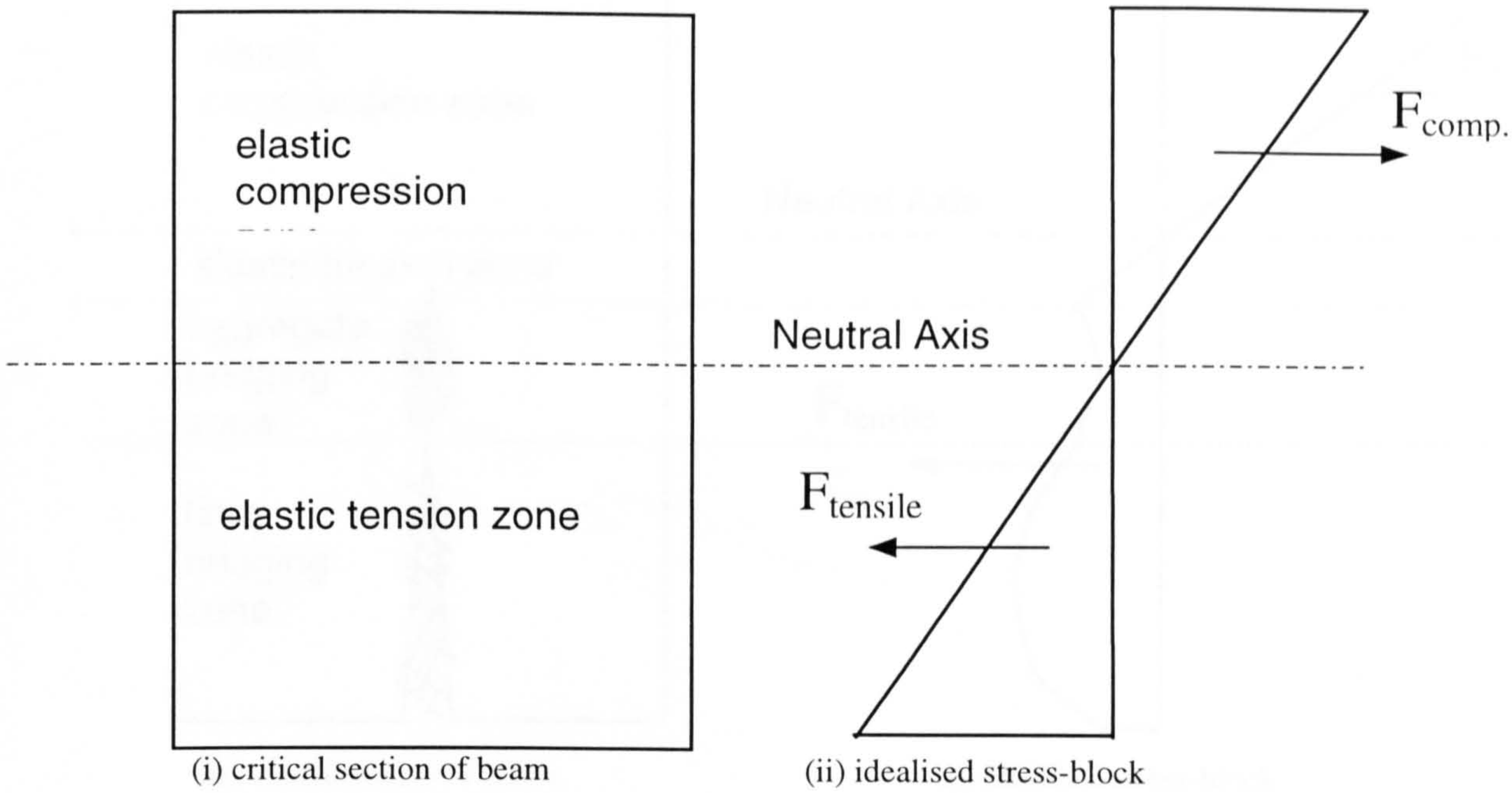

Figure 4.1(a) Schematic representation of a steel fibre reinforced concrete beam under flexural loading: Stage 1 - uncracked elastic response.

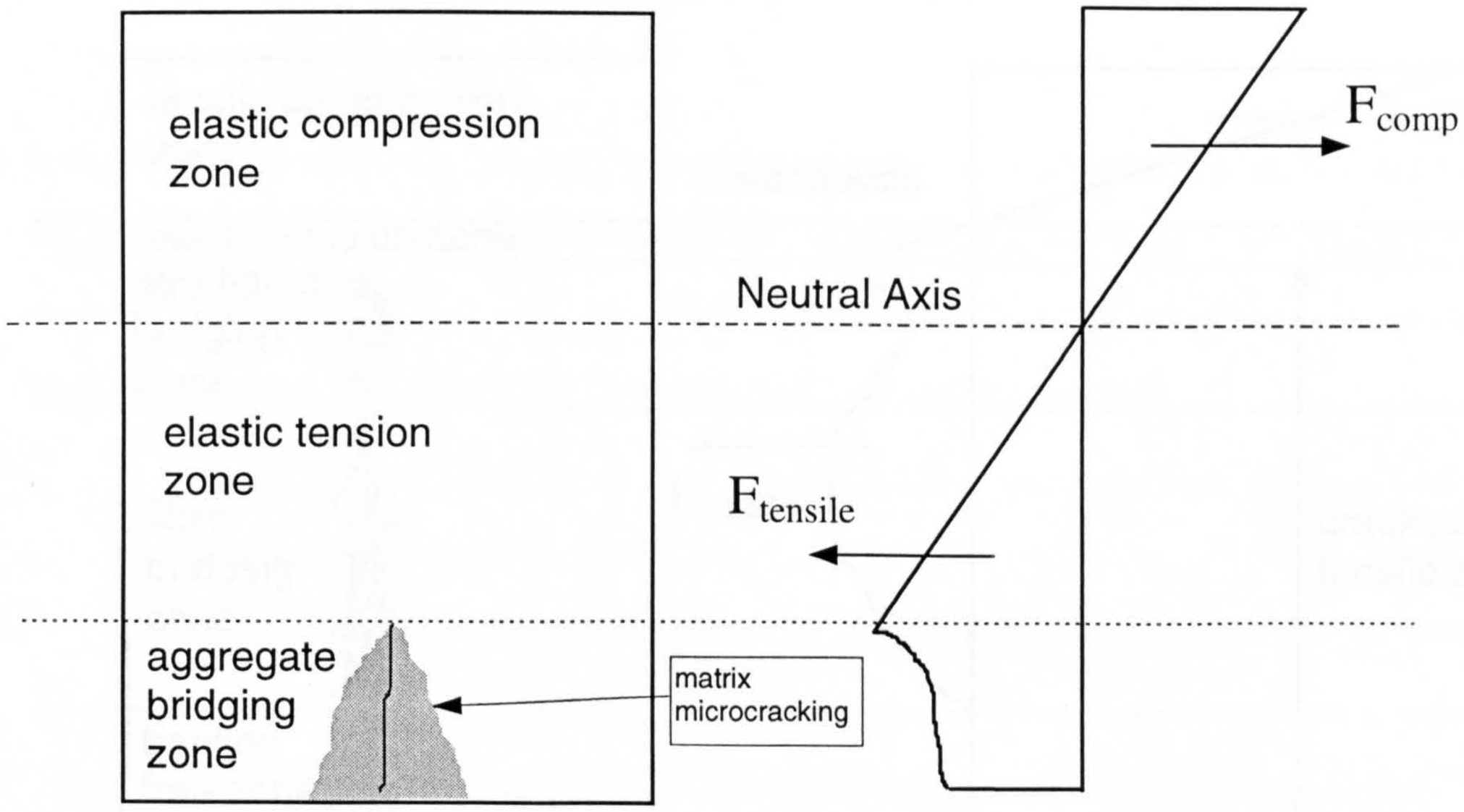

Figure 4.1(b) Schematic representation of a steel fibre reinforced concrete beam under flexural loading: Stage 2 - initial cracked response.

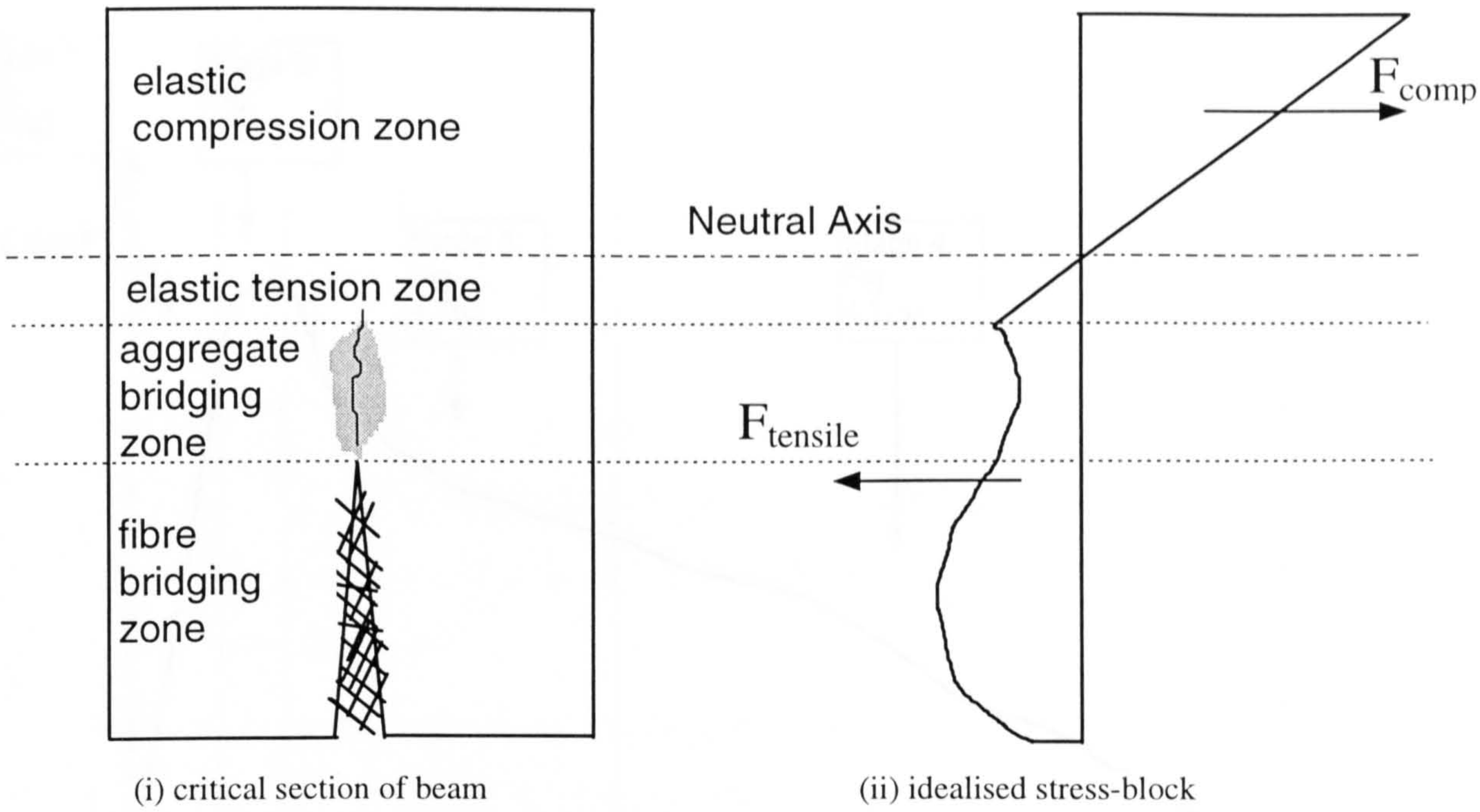

(i) critical section of beam (ii) idealised stress-block

Figure 4.1(c) Schematic representation of a steel fibre reinforced concrete beam under flexural loading: Stage 3 - development of macro-crack.

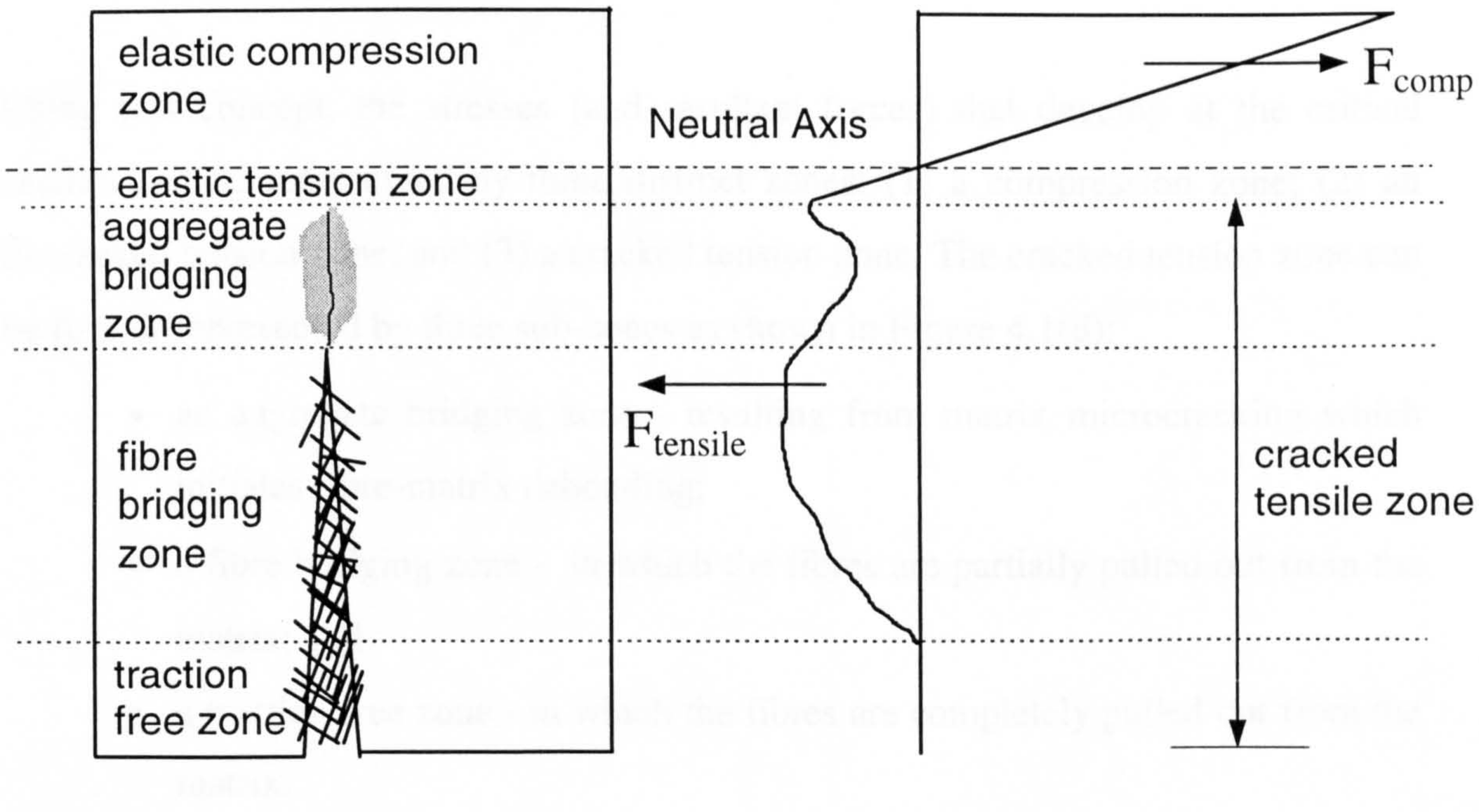

(i) critical section of beam (ii) idealised stress-block

Figure 4.1(d) Schematic representation of a steel fibre reinforced concrete beam under flexural loading: Stage 4 - development of traction free zone.

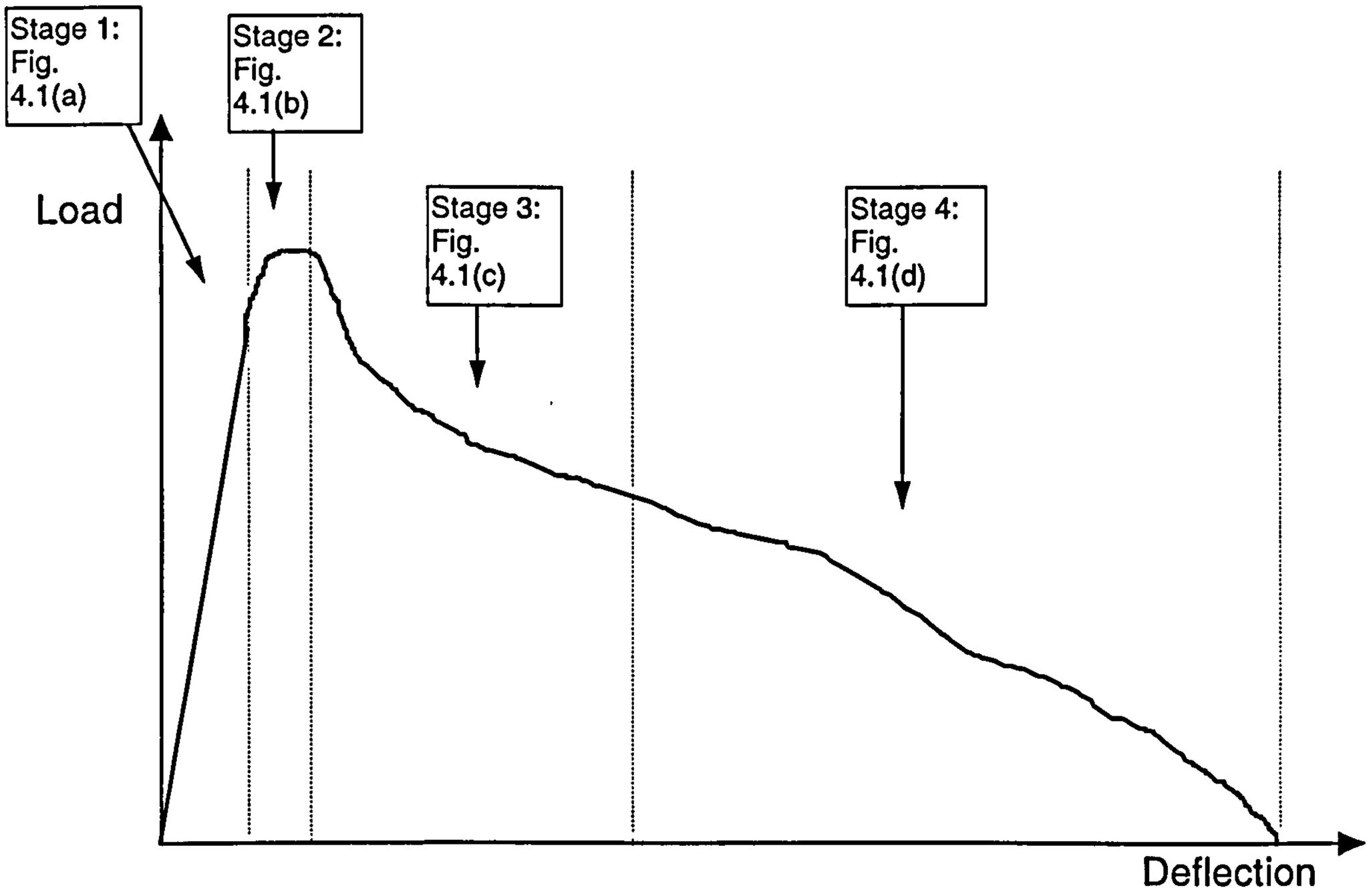

Figure 4.2 Relationship between the four stages of crack-propagation and the flexural load deflection response of a steel fibre reinforced concrete beam.

Using this concept, the stresses (and resultant forces) that develop at the critical section can be represented by three distinct zones: (1) a compression zone; (2) an uncracked tension zone; and (3) a cracked tension zone. The cracked tension zone can be further represented by three sub-zones as shown in Figure 4.1(d):

- an aggregate bridging zone - resulting from matrix microcracking which initiates fibre-matrix debonding;
- a fibre bridging zone - in which the fibres are partially pulled out from the matrix; and
- a traction free zone - in which the fibres are completely pulled out from the matrix.

It is can also be seen from Figure 4.1 (a) to (d) that the shape of the stress-block diagram changes as the crack propagates over the depth of the beam. By using this concept the flexural capacity of the critical section can be related to the following principal parameters:

- the uniaxial compressive stress-strain relationship;
- the uniaxial tensile stress-strain relationship;
- the single fibre pull-out load versus crack-width relationship;
- the number, distribution, embedment lengths and orientations of the fibres bridging the cracked section;
- the strain profile (and associated neutral axis position) of the uncracked section in relation to the mid-span beam deflection; and
- the crack-width profile of the cracked section in relation to the mid-span beam deflection.

If relationships for these parameters can be established, then the shape and magnitude of the stress-block diagram can be predicted for a given beam deflection. Hence, providing the internal force equilibrium of the section is satisfied, the flexural moment capacity of the beam can be computed for a given beam deflection.

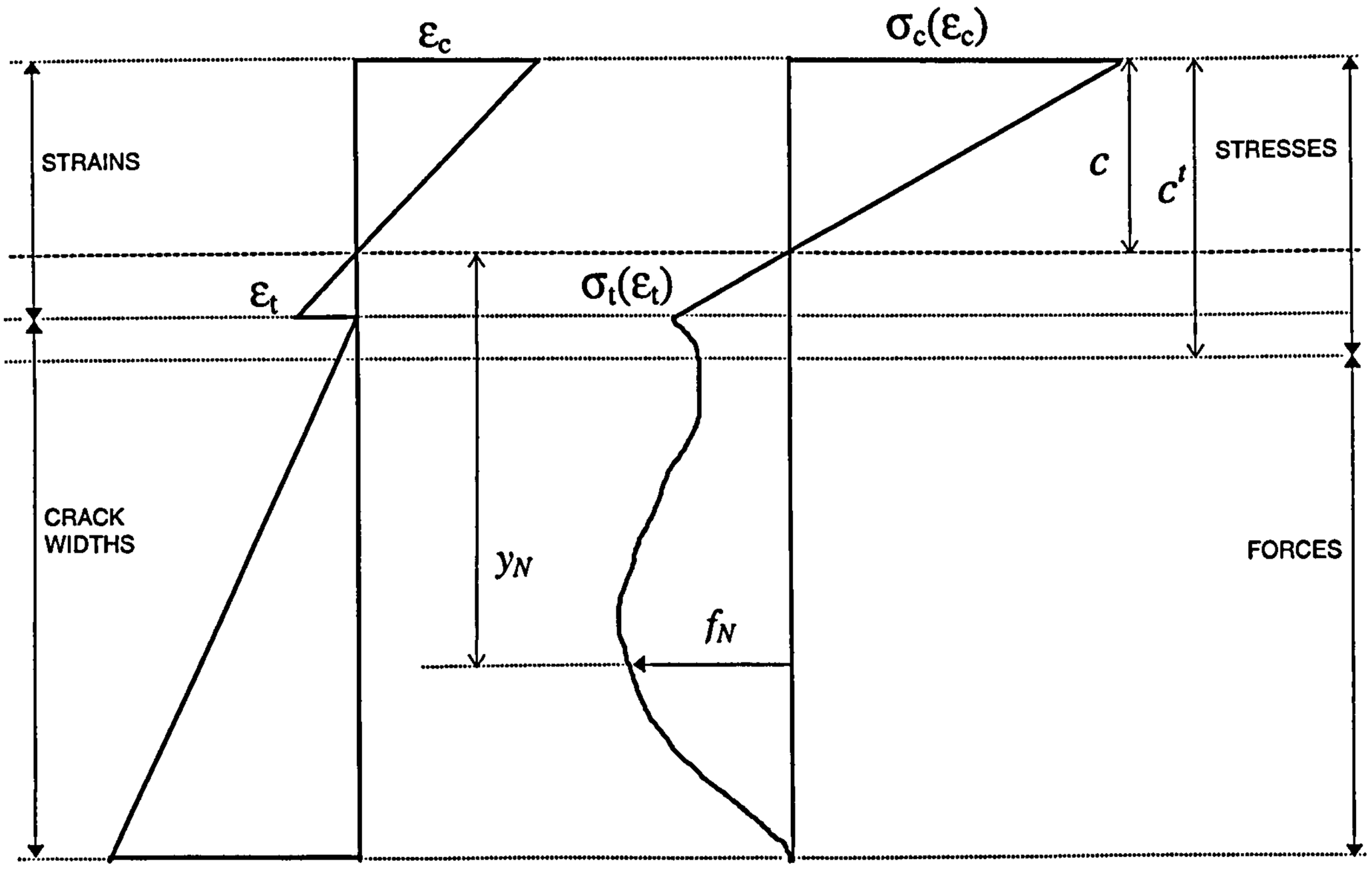

(a) strain/crack-width diagram (b) stress-block diagram

Figure 4.3 Schematic representation of the strain and stress blocks across the cracked section of a steel fibre reinforced concrete beam.

The equilibrium of internal forces is satisfied if the total resultant compressive forces (F_{comp}) and tensile forces ($F_{tensile}$) are equal - see Figure 4.1 - or, in terms of the individual components of the stress-block diagram (Figure 4.3)

$$\int_0^c \sigma_c(b.dy) + \int_{c'-c}^{c'} \sigma_t(b.dy) + \sum_1^N f_N = 0 \qquad \text{equation 4.1}$$

where σ_c and σ_t are the compressive and tensile stresses respectively, b is the width of the beam, and f_N is the force carried by each of the N individual fibres bridging the cracked tensile zone. Note from Figure 4.3 that concrete stresses are related to strains, and fibre pull-out forces are related to crack opening displacements (i.e. crack-widths).

The internal moment capacity M_e of the section is computed by summing all the moments generated by the pull-out forces of the individual fibres, with respect to their positions relative to the neutral axis, together with the moments generated by the concrete stresses (Figure 4.3)

$$\int_0^c \sigma_c(b.dy).y_c + \int_{c'-c}^{c'} \sigma_t(b.dy).y_t + \sum_1^N (f_N.y_N) = M_e \qquad \text{equation 4.2}$$

where y_c, y_t and y_N are the respective lever arms of the individual forces relative to the neutral axis.

The flexural load capacity P is obtained by equating the externally applied moment to the internal moment capacity of the section. For a beam tested in four point loading (at third-span points) over a span l, this equates to

$$P = \frac{6M_e}{l} \qquad \text{equation 4.3}$$

By repeating this process for various mid-span beam deflections, the flexural load-deflection response curve can be determined for the given beam under investigation.

4.3.3 Experimental investigation and data requirements

An experimental investigation was undertaken, using typical wet process steel fibre reinforced sprayed concrete mix designs, to obtain the data for the development and implementation of the model. Five different tests were identified and developed for use in the investigation:

(1) Single fibre pull-out tests

These tests were used to establish the fibre pull-out load versus crack-width relationship for a wide range of fibre embedment lengths and orientations. The results were used to predict the forces transferred by the fibres bridging the cracked tensile zone (Figure 4.1).

(2) Compression tests

These tests were used to establish uniaxial compressive stress-strain relationship for a range of different fibre volume contents. The results were used to model the compressive stress-block diagram (Figure 4.1). Elastic secant modulus values were also determined from the stress-strain relationships to model the uncracked tensile stress-block diagram (Figure 4.1).

(3) Strain analysis tests

These tests were used to determine the strain gradients and crack-width profiles at the critical beam section, in relation to mid-span deflection, for a range of different fibre volume contents.

Note that the results of these tests are central to the successful implementation of the model, as it is the strain gradients and crack-width profiles against which all the other test data is applied in order to predict the stress-block diagram for a given mid-span beam deflection.

(4) Flexural toughness tests

These tests were used to obtain typical flexural load-deflection curves for a series of beams of various depths and fibre volumes tested under four point loading. The principal beam size investigated was a 75mm deep x 100mm wide x 450mm span, although data was also obtained from beams with depths of 50mm and 100mm. Both notched and unnotched beams were investigated. The results were used to compare with, and verify, the model predictions.

(5) Fibre distribution analysis

This analysis was required to determine fibre distribution data relating to the individual fibres bridging the critical section of the beams under investigation. The results included: (1) an analysis of the actual number and distribution of

fibres bridging the cracked section; and (2) the establishment of statistical probability distributions relating to the fibre embedment lengths and fibre orientations of the fibres bridging the cracked section. The results were used in combination with the single fibre pull-out test data to predict the forces transferred by the fibres bridging the cracked tensile zone (Figure 4.1).

Since a large number of tests were required to obtain the necessary data for the model, it was decided that only one fibre type would be used in the experimental work. The fibre type chosen was a 30mm long (0.5mm diameter) collated hooked-end steel fibre, which is typical of the fibre type currently used in a large proportion of wet process steel fibre reinforced sprayed concrete applications.

The majority of the experimental investigation used cast (as opposed to sprayed) specimens so that the test variables and material parameters under investigation could be better controlled. However, spraying trials were also undertaken to demonstrate the pumpability and sprayability of the concrete mixes used in the experimental investigation. These trials provided sprayed test specimens for comparison with the cast specimens, and for verifying the use of the model to predict the flexural load-deflection response of both cast and sprayed specimens.

4.3.4 Assumptions

Certain assumptions must be made in order to use the proposed model.

a) Failure occurs at a single crack within the middle third of a four-point loaded beam.
b) The stress zones detailed in Figure 4.1 are separated by discrete boundaries.
c) The cracked tensile zone in Figure 4.1 represents a fictious crack in accordance with the Fictious Crack Model (see Section 3.4.2). Hence, there is no singularity at the crack-tip, the fracture process zone is of negligible thickness, and the concrete matrix cracks when its tensile strength f_t is exceeded.
d) The stresses and pull-out forces acting across the critical section are purely uniaxial.
e) The beam is in a state of pure bending within the middle third, and the effects of shearing stresses and strains are negligible.
f) The beam is of homogenous material, which is elastically isotropic and has the same value of elastic modulus in both tension and compression.

g) Lateral cross-sections remain plane.

4.3.5 Implications of the proposed model

If the proposed model can be shown to predict accurately the load-deflection response curve, then it can provide an explanation for the shape characteristics of load-deflection curve and, thereby, help to further our understanding of the reinforcing mechanisms associated with the flexural behaviour of both cast and sprayed steel fibre reinforced concrete.

Consequently, the model could form the basis of a design rationale to predict the load-deflection response of a structural member given only the matrix strength, fibre type, fibre volume content, beam size and loading geometry. In this way it would provide a much needed link between structural design and flexural toughness performance and thereby provide a means of incorporating toughness parameters into the design process.

4.4 CHAPTER SUMMARY

This chapter has described the research methodology adopted in this thesis in order to address the research needs identified in Chapters 2 and 3. The main aims and objectives of the research were shown to centre around the testing of a hypothesis relating to the development of a model (based on the stress-block diagram approach) to predict the flexural load-deflection response curve of a steel fibre reinforced sprayed concrete beam. A variety of experimental tests were identified as being necessary to obtain the data for the development and implementation of the model: single fibre pull-out tests, compression tests, strain analysis tests, flexural toughness tests, and fibre distribution analysis tests.

The remainder of this thesis describes how this methodology was implemented to achieve the stated aims and objectives.

5. CONCRETE MIX DEVELOPMENT AND PRODUCTION

5.1 INTRODUCTION

The first stage of the experimental investigation involved the development of appropriate concrete mix designs and production methods for the testing programme. The main precondition of this work was to develop concrete mix designs that complied with recommendations for typical wet process steel fibre reinforced sprayed concrete in terms of the constituent material types, properties and proportions. In addition, because this thesis is primarily aimed at predicting the flexural response of fibre reinforced sprayed concrete, the pumpability and sprayability of the concrete mixes also had to be demonstrated.

This chapter discusses the development, production and quality control of the concrete mixes used in the experimental testing programme, together with details of the spraying trials undertaken to demonstrate their pumpability and sprayability.

5.2 CONSTITUENT MATERIALS

5.2.1 General

The constituent materials used in the development of the concrete mixes were chosen as being typical of those used in wet process fibre reinforced sprayed concrete as discussed in Chapter 2.

5.2.2 Cement

The cement was Class 42.5N Ordinary Portland Cement (OPC) conforming to BS12 (1991) and supplied by Castle Cement Limited. Some of its main chemical and physical properties are given in Table 5.1.

5.2.3 Condensed Silica Fume Slurry

The condensed silica fume slurry was EMAC 500 S supplied by Elkem Materials. This is a water-based slurry with a 50% silica fume content by weight. Prior to its addition to a concrete mix it was thoroughly agitated to ensure a 50:50 (water-to-silica fume) consistency. Its chemical composition and some of its main physical properties are detailed in Table 5.2.

Class	Fineness	Soundness	Compressive strength (40mm x 40mm x 160mm mortar prisms)			Chloride content	Alkali content
(BS12)	Specific surface (m^2/kg)	Initial set (mins)	2 days (MPa)	7 days (MPa)	28 days (MPa)	%	Average % Na_2O equivalent
42.5N	400	100	25.0	40.0	56.5	0.02	0.56

Table 5.1 Physical and chemical properties of the Ordinary Portland Cement used in the experimental investigation.

Type	Specific surface (m^2/kg)	Average particle size (μm)	Coarse particles >45μm (%)	Dry solids by weight (%)	pH value	SiO_2 content (%)	Colour
EMSAC 500S	20000	0.15	max. 2.0	50 (± 2)	5.0 - 7.0	> 86	Grey

Table 5.2 Physical and chemical properties of the silica fume slurry used in the experimental investigation.

5.2.4 Aggregate

The aggregate was a 6mm maximum sized uncrushed river gravel supplied by Porterway Limited from a source in Derby. Particle size analysis, determined in accordance with BS812: Part103.1 (1985), showed that its grading curve complied with a Zone M sand in accordance with BS882 (1992). The aggregate grading curve is compared in Figure 5.1 with the recommended grading curve for wet process sprayed concrete as given in the EFNARC (1996) specification. It can be seen that the aggregate generally falls within the limits of the recommended grading curve, except for the following discrepancies:

- the fractions passing the 600 microns and 150 microns sieves lie outside the recommended limits by approximately +3% and -4% respectively; and

- the fraction retained by the 300 microns sieve is marginally greater than 30% of the total (see Section 2.3.3).

However, these discrepancies were considered not to merit changing the aggregate type. Therefore, the aggregate was considered to be potentially suitable for use in wet process sprayed concrete.

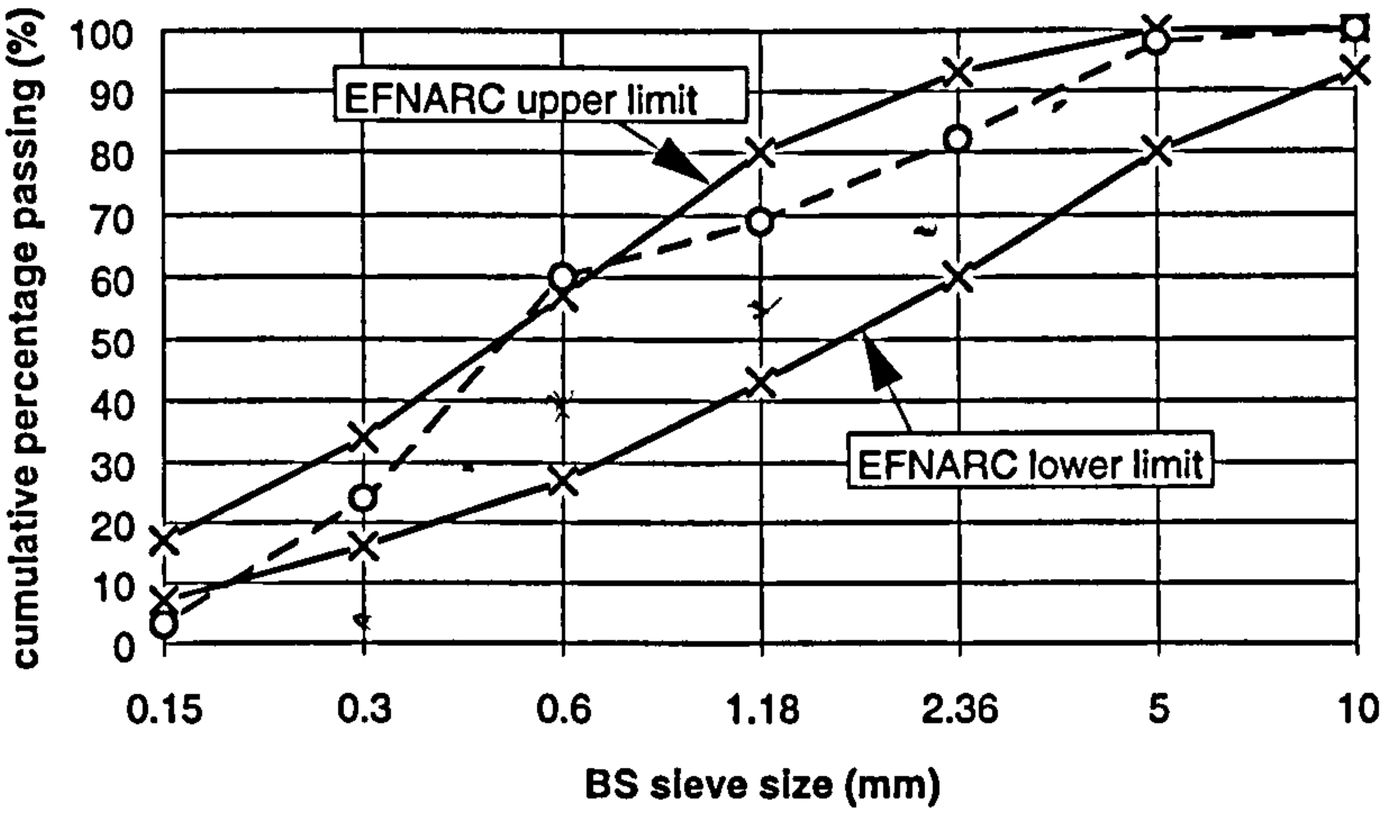

BS Sieve size	EFNARC (1996)	Aggregate used in the experimental work	
	cumulative percentage passing	cumulative percentage passing	percentage retained
10 mm	93-100	100	0
5 mm	80-100	98	2
2.36 mm	60-93	82	16
1.18 mm	43-80	69	13
600 µm	27-57	60	9
300 µm	16-34	25	35
<150 µm	7-17	3	22

Figure 5.1 Graphical and tabular comparisons between the particle size analysis of the aggregate used in the experimental investigation and the EFNARC (1996) recommended grading limits.

5.2.5 Superplasticiser

The superplasticiser was Sikament FF (based on melamine-formaldehyde) supplied by Sika Limited. Some of its chemical and physical properties are detailed in Table 5.3.

Type	Form	Colour	Specific gravity	Chloride content (%)	Alkali - equivalent Na_2O (%)	Solids content (%)	Cement suitability
Sikament FF	Liquid	Colourless	1.25	<0.2	5.9	40± 1.0	All OPC

Table 5.3 Chemical and physical properties of the superplasticiser used in the experimental investigation.

5.2.6 Steel fibres

The steel fibre was Dramix® ZP 30/.50 (30mm long and 0.5mm diameter), a collated hooked-end fibre supplied by N.V.Bekaert S.A. Some of its main physical properties are detailed in Table 5.4.

Type (Dramix®)	Steel quality	Diameter (mm)	Total fibre length (mm)	Length of hooked-end (mm)	Min. Tensile strength (MPa)	Modulus of elasticity (GPa)
ZP 30/.50	Low carbon	0.5±0.02	30 +2/-3	4.0±1.0	1150	205

Table 5.4 Physical properties of the steel fibres used in the experimental investigation.

5.3 QUALITY CONTROL

5.3.1 Concrete quality and batch variations

Variations in the fresh and hardened properties of concrete can arise from variations in the properties of the constituent materials and from variations in the batching, mixing, placing, curing and testing procedures (Neville, 1995). The need to minimise these variations in the experimental work was considered critical for ensuring consistent concrete quality, in order that repeatable experimental results were obtained for use in the model. To this end, the following quality control measures were adopted.

1. All the cement, silica fume, superplasticiser and steel fibres used in the experimental work came from a single batch of each material, and were all stored in air-tight containers.
2. All the aggregate used in the experimental work came from a single delivery. The moisture content of the aggregate was controlled by drying it in the laboratory, using a heat bed, to ensure a 'bone-dry' moisture condition (Neville, 1995). The dry material was then stored in sealed containers prior to batching.
3. Standard procedures for batching, mixing, placing, curing and testing were developed and stringently adhered to throughout the experimental work.
4. All the test specimens requiring the same concrete mix were made using the same batch of concrete wherever possible.
5. All the specimens were tested at an age of 28days.

5.3.2 Aggregate water absorption

A modified version of the aggregate water absorption test in accordance with BS812: Part 2 (1985) was developed to determine the average quantity of water absorbed in 30 minutes by the bone-dry aggregate. This quantity of water was added to the free (or effective) water content of the mix design to obtain the total mixing water requirements, and thereby control the water content of the concrete mixes used in the experimental investigation.

This particular value of water absorption was used because dry aggregate particles become quickly coated with cement paste which prevents further water absorption after about 20-30 minutes (Neville, 1995). This results in: (i) the aggregate particles never actually achieving the saturated surface-dry condition required by the mix design; and (ii) a higher free water-cement ratio in the concrete than if full water absorption by the aggregate had been possible. The test, therefore, provides a more realistic measurement of the water absorbed by the dry aggregate during the mixing process.

From tests on fifteen representative samples of aggregate (each weighing approximately 0.5kg) the average 30 minute water absorption was measured at 1.4% by weight of aggregate with a standard deviation of 0.2%.

5.4 MIX DESIGN AND PROPORTIONING

5.4.1 General requirements

The design of the concrete mixes used in the experimental work was based on the following criteria:

- composition of the constituent materials must comply with the recommendations for a typical wet mix steel fibre reinforced sprayed concrete as detailed in published literature;
- mixes with fibre contents less than 80kg/m^3 (approximately 1.0% by volume) must be pumpable and sprayable - having a slump of between 40-120mm (Neville, 1995); and

- the mixes must display no segregation or bleeding during external vibration and placement.

Strength was not a main criteria of the mix design. A standard method of production, which minimised the variability in the properties of the concrete mixes, was considered more important for the development and implementation of the proposed model.

Three base concrete mixes, designated Matrix A, Matrix B and Matrix C, were developed for the experimental investigation. The design of these three mixes only differed in the proportion of silica fume they contained. This enabled the influence of silica fume on the properties of the mixes to be investigated as part of the experimental investigation. The principal mix used in the development of the proposed model was Matrix C which contained a silica fume content of 10% by weight of cement. Matrix B was a secondary mix containing a silica fume content of 5% by weight of cement, and Matrix A was a control mix containing no silica fume.

In addition to the plain base mixes, steel fibres were also added to the base mixes in quantities of 40, 80 and 120kg/m^3 (approximately 0.5, 1.0 & 1.5% by volume respectively) to provide the full range of concrete mixes used in the experimental investigation. However, only fibre additions up to 80kg/m^3 (1.0% by volume) were verified for pumpability and sprayability; fibre contents greater than 80kg/m^3 are generally difficult to spray using conventional spraying equipment and are, therefore, not commonly used in steel fibre reinforced sprayed concrete applications.

5.4.2 Mix development

Following a review of the wet process mix designs discussed in Section 2.5, an initial mix specification was formulated for the principal mix (Matrix C) as detailed in Table 5.5.

Cementitious content (cement + silica fume)	450kg/m^3
Silica fume	10% by weight of cement
Aggregate/cementitious ratio	3.8:1
Water/cementitious ratio	0.44
Superplasticiser	as required to achieve specified slump
Slump	120-40mm

Table 5.5 Initial mix design specification for the principal mix (Matrix C).

A trial mixing study was undertaken to test the suitability of this mix design for use in the experimental investigation. Unfortunately, this initial mix design was found to be problematic, which resulted in significant changes being made before an acceptable mix could be established The main problems encountered, together with the solutions adopted, are discussed below.

- A relatively high aggregate-cementitious ratio of 3.8:1 combined with a low water-cementitious ratio (less than 0.50) caused the mix to be very sandy and harsh. This resulted in poor workability, even at very high superplasticiser contents (up to 10% by weight of cementitious material), and poor compaction. Furthermore, increasing the water-cementitious ratio to 0.5, to increase workability, made the mix less stable during compaction, resulting in severe bleeding.
- The aggregate-cementitious ratio was subsequently reduced to 3:1 - with a corresponding increase in total cementitious content (cement plus silica fume) to 500kg/m^3 - and the water-cementitious ratio set at 0.45. These changes had the effect of:
    i. increasing the water content of the mixes, thus increasing workability, without significantly effecting strength;
    ii. increasing the 'fines' content, thus making the mix less harsh and less prone to bleeding; and
    iii. providing the mixes with a more balanced and cohesive appearance.
- This mix was subsequently assessed in a spraying trial using a low capacity worm pump as shown in Figure 5.2. This trial was undertaken by Fosroc International Limited at their in-house concrete spraying facility in Birmingham. Unfortunately the mix did not perform very well causing sand blocks in the delivery hose. As a consequence, the mix design was modified by gradually reducing the aggregate-cementitious ratio until a sprayable mix was achieved. This was found to occur at an aggregate-cementitious ratio of 2.8:1.

As a result of the trial mixing study and the preliminary spraying trial, a mix design was eventually developed which complied with all the criteria detailed in Section 5.4.1. This mix design was based on a total cementitious content (cement plus silica fume) of 540kg/m^3, an aggregate-cementitious ratio of 2.8:1 and a water-cementitious ratio of 0.45.

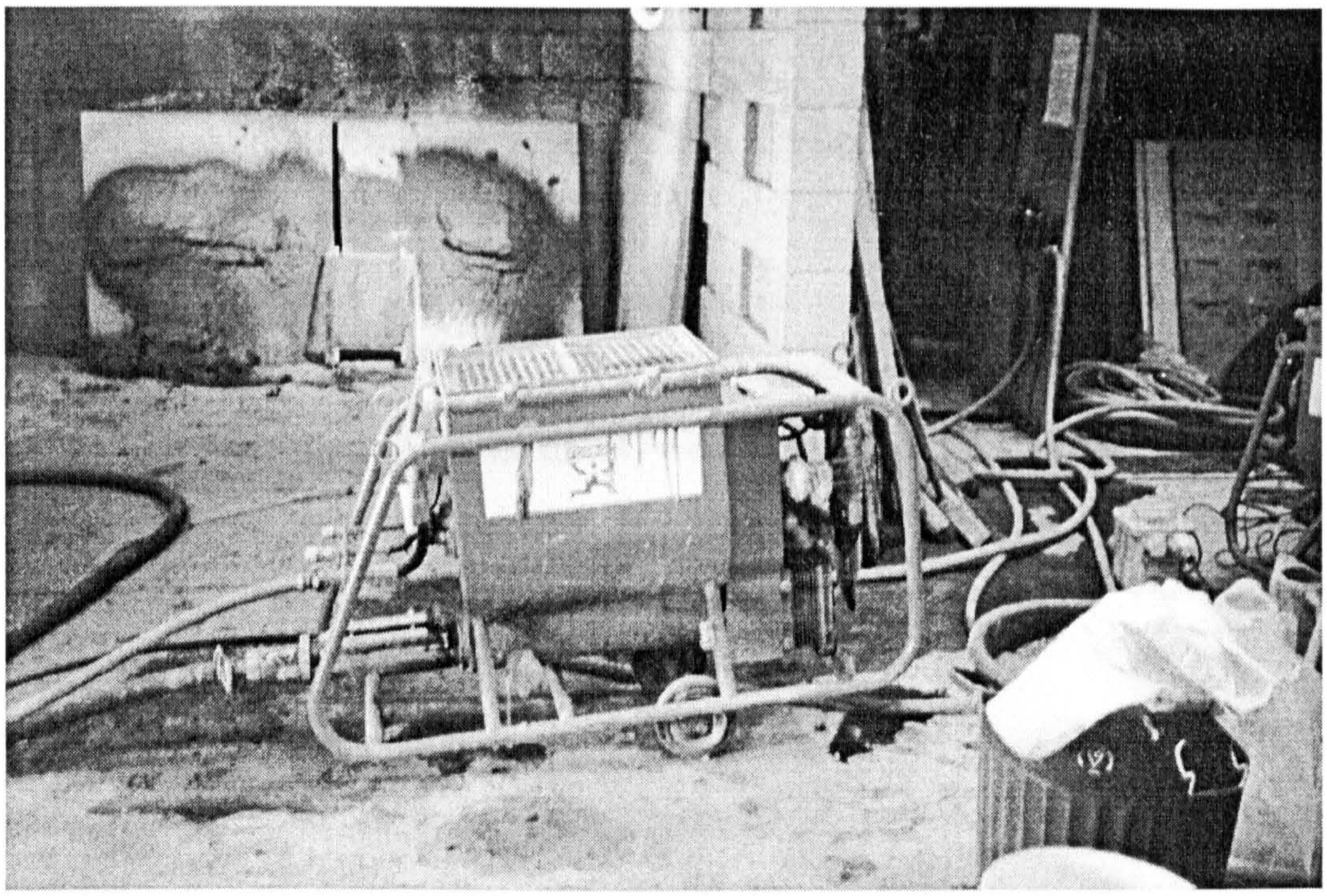

Figure 5.2 Worm pump used in the preliminary spraying trial.

The final compositions of the three base mixes used in the experimental investigation are detailed in Table 5.6. The pumpability and sprayability of all these mixes was subsequently demonstrated in a further spraying trial (see Section 5.7).

Constituents	MIX REFERENCE		
	Matrix A	**Matrix B**	**Matrix C**
Cement (kg/m^3)	540	515	490
Silica Fume (kg/m^3)	0	25	50
Water (kg/m^3)	245	245	245
Aggregate (kg/m^3)	1510	1510	1510
Superplasticiser (% by weight of cementitious)	0.65	1.0	1.5
Steel Fibres (kg/m^3)	0, 40, 80 & 120	0, 40, 80 & 120	0, 40, 80 & 120
Specification			
Silica fume (% by weight of cement)	**0**	**5**	**10**
Water/cementitious ratio	0.45	0.45	0.45
Aggregate/cementitious ratio	2.8:1	2.8:1	2.8:1
Slump (mm)	40-120	40-120	40-120

Table 5.6 Composition and specification of the concrete mixes used in the experimental investigation.

5.5 MIXING PROCEDURE

A standard batching and mixing procedure was developed for use in the experimental investigation, as described below.

i. The mix constituents were weigh batched using the same electronic weighing device throughout the investigation.
ii. All the aggregate (and any steel fibres) were then added to the mixer together with half of the total water (absorbed + free water) and mixed for two minutes. The contents were then left covered for 10 minutes. This was to allow for some water absorption by the aggregate.
iii. The silica fume slurry (if required) was then added and mixed for approximately one minute until the mix appeared homogenous.
iv. The cement was then added and mixed for approximately 30 seconds. The remaining water (containing the superplasticiser) was then added over the next 30 seconds and mixed for a further two minutes.
v. The concrete was then ready to use.

5.6 PRODUCTION OF CAST SPECIMENS

5.6.1 Batching and mixing

The mixes were batched and mixed in the laboratory in accordance with the standard procedure detailed in Section 5.5. Two types of mechanical pan mixers were used: (1) a small capacity mixer ($0.008m^3$) for the production of the single fibre pull-out test specimens; and (2) a medium capacity mixer ($0.045m^3$) for the production of all the other test specimens.

5.6.2 Placing

Specimens were compacted using table vibration. The moulds were clamped to the top surface of the table and filled in two equal layers (generally between 35-50mm depending on the depth of the mould). Vibration continued until bubbles ceased to appear at the surface of the specimens. This usually took between 1 to 1.5 minutes depending upon the size and number of specimens cast. The same vibration setting was used throughout the investigation. All specimens were finished using a steel float.

5.6.3 Curing

Specimens were cured in accordance with BS1881: Part 111 (1983). Immediately following the casting operations the specimens were placed under damp hesian, wrapped in polythene, and stored in a controlled temperature of $20 \pm 5^{o}C$ for 24 hours. They were then demoulded, labelled and placed in a curing tank at $20 \pm 2^{o}C$ until they were tested.

5.6.4 Fresh properties

The workability of each mix was determined using a standard slump test in accordance with BS1881: Part 102 (1983). The average workabilities of all the mixes used in the experimental investigation are given in Table 5.7(a).

5.6.5 Hardened properties

In addition to the hardened properties investigated as part of the main experimental investigation (see Chapter 6), the following hardened properties were also determined for each mix: (1) the 28 day compressive cube strength in accordance with BS1881: Part 116 (1983); and (2) the saturated hardened density in accordance with BS1881: Part 114 (1983). The average values of both these properties for all the mixes used in the experimental investigation are given in Table 5.7(b) and (c) respectively.

5.7 SPRAYING TRIAL AND PRODUCTION OF SPRAYED SPECIMENS

5.7.1 General

This section describes the spraying trial undertaken by Gunform Limited on the site of a wet process steel fibre reinforced concrete project in Falmouth, Cornwall. The main aims of these trials were twofold:

- to demonstrate the pumpability and sprayability of the plain and fibre reinforced concrete mixes used in the experimental investigation; and
- to produce the sprayed test specimens for use in the experimental investigation.

The trial involved six mixes as detailed in Table 5.8.

Fibre content (kg/m^3)	MIX REFERENCE		
	Matrix A	Matrix B	Matrix C
0	80	90	90
40	75	80	85
80	60	60	65
120	55	50	55

(a) Average workability determined using a standard slump test (mm).

Fibre content (kg/m^3)	MIX REFERENCE					
	Matrix A		Matrix B		Matrix C	
	Average	Standard deviation	Average	Standard deviation	Average	Standard deviation
0	59	2	71	1	74	2
40	60	4	68	1	72	2
80	58	1	70	1	72	2
120	59	1	70	2	73	3

(b) 28 day compressive cube strengths (MPa).

Fibre content (kg/m^3)	MIX REFERENCE					
	Matrix A		Matrix B		Matrix C	
	Average	Standard deviation	Average	Standard deviation	Average	Standard deviation
0	2240	10	2225	20	2230	15
40	2255	10	2260	10	2240	20
80	2280	20	2290	10	2280	20
120	2320	10	2310	10	2300	30

(c) Hardened saturated densities (kg/m^3).

Table 5.7 Fresh and hardened properties of the cast mixes used in the experimental investigation.

5.7.2 Batching and mixing

The mixes were batched off-site in the laboratory and then transported to site where they were mixed, in accordance with the standard procedure detailed in Section 5.5, using a mobile pan mixer ($0.05m^3$ capacity) prior to discharging directly into the pump of the spraying machine. Unfortunately, it was not until the mixing of the first trial commenced that it became apparent that the capacity of the mixer was not large enough to hold the full quantity of concrete required for each trial. Therefore, the concrete for each trial was mixed in two separate halves before discharging into the pump. Fortunately, the majority of mix constituents had been previously batched in

two halves. However, this was not the case for the steel fibres which had been batched into single bags. As a result the quantity of fibres in each mix had to be approximately halved prior to mixing, which under site conditions proved very difficult. This is reflected in some of the in-situ fibre contents detailed in Table 5.8, which show measured in-situ fibre contents greater than the theoretical as-batched fibre contents. Although this did not effect the usefulness of the sprayed specimen test results in the context of this thesis, it did mean that fibre rebound quantities could not be determined.

Sprayed mix reference	Matrix type	Theoretical as-batched fibre content (kg/m^3)	Measured in-situ fibre content (kg/m^3)		Hardened saturated density (kg/m^3)	
			Average	Stand. dev.	Average	Stand. dev.
1	C	0	-	-	2210	20
2	C	40	26	5	2260	10
3	C	80	66	4	2300	10
4	B	40	53	6	2285	10
5	B	80	65	3	2285	10
6	A	40	56	6	2255	15

Table 5.8 Properties of the spraying trial mixes.

5.7.3 Plant and equipment

A 'Reed B10' double-piston pump wet process spraying machine, with a maximum capacity of $8m^3$/hour, was used in the trial (Figure 5.3). The freshly mixed concrete was conveyed through a standard 50mm diameter rubber hose, 10m in length, to the nozzle.

5.7.4 Preparation and curing of test specimens

Each mix was sprayed by an experienced and certified nozzle operator to produce a vertical 600 x 600 x 100 mm test panel as shown in Figures 5.4 and 5.5. Following the completion of the spraying of each mix, the exposed concrete surface of the panel was lightly finished with a steel float and then immediately sealed with a sprayed curing membrane. Each panel was then covered with polythene sheeting and stored on-site for approximately 48 hours. All the panels were then transported back to the laboratory and de-moulded. Figure 5.6 shows a representative panel from the spraying trial following de-moulding. Each panel was then sawn into three 75mm x 125mm x

500mm test beams in accordance with EFNARC (1996), which were then labelled and placed in a curing tank at $20 \pm 2^{o}C$ until they were tested.

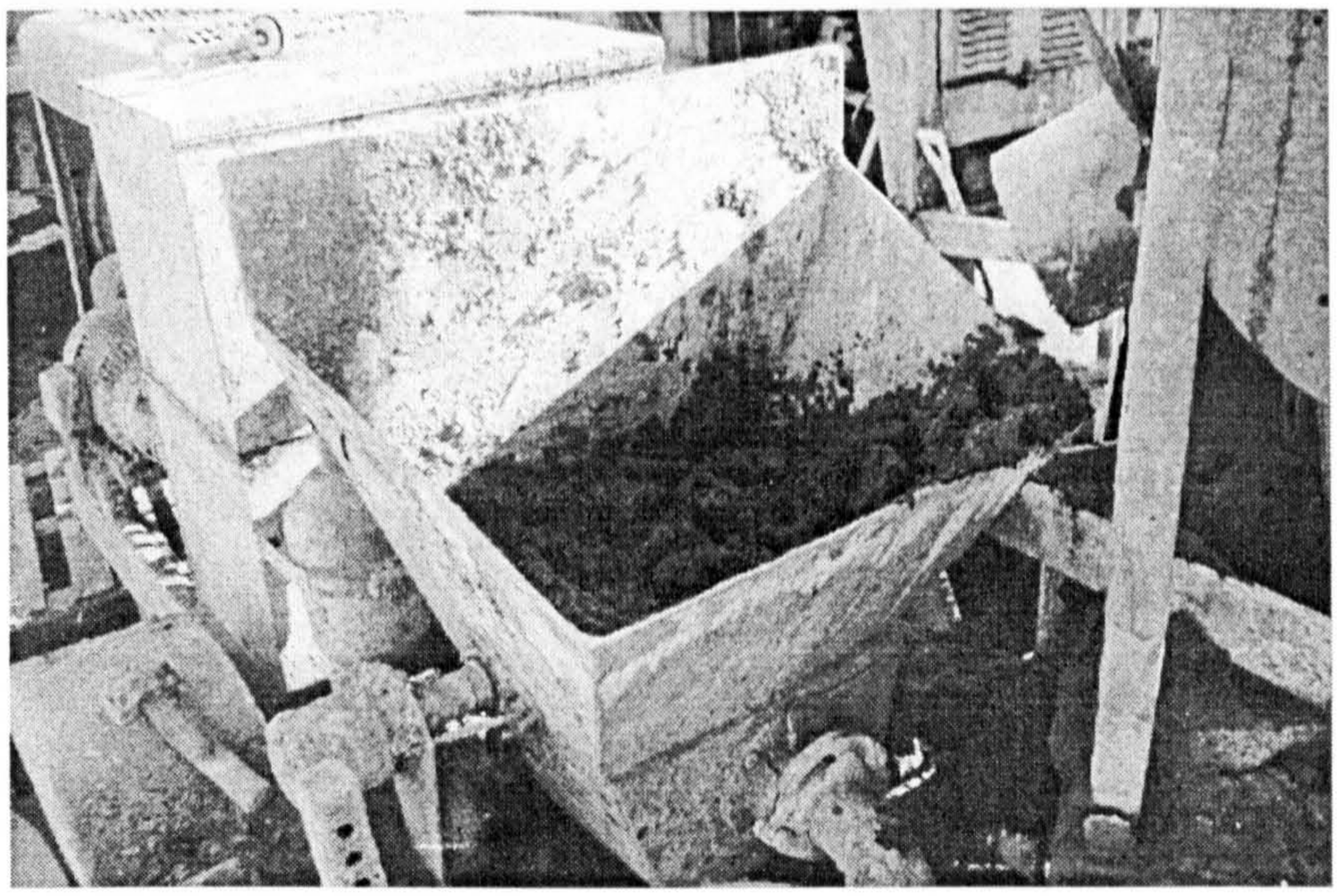

Figure 5.3 Double-piston pump used in the spraying trial.

5.7.5 Results of the spraying trial

All six mixes investigated as part of the spraying trial were both pumpable and sprayable (Figures 5.4 and 5.5). No blockages occurred and all the mixes appeared to display virtually no sloughing or material rebound.

5.7.6 Hardened properties

In addition to the hardened properties investigated as part of the main experimental investigation (see Chapter 6), the following were also determined - using three 75mm diameter cores cut from the test beams - for each of the sprayed mixes: (1) the in-situ fibre content in accordance with Clause 10.9 (Method A) of EFNARC (1996); and (2) the saturated hardened density in accordance with BS1881: Part 114 (1983). The average results from both these tests for all six sprayed mixes are detailed in Table 5.8.

Standard compressive cube specimens could not be obtained using the spraying process - although 75mm x 75mm x 225mm prisms were cut from the test panels and tested in compression (see Chapter 6). Therefore, 28 day compressive cube strengths for the sprayed mixes do not appear in Table 5.8. However, the similarities in the

hardened saturated densities between the sprayed mixes (Table 5.8) and the cast mixes (Table 5.7) suggest a similar degree of compaction.

Figure 5.4 A test panel being sprayed during the spraying trial.

Figure 5.5 A reverse view of a test panel being sprayed during the spraying trial.

5.8 CHAPTER SUMMARY

This chapter has described the development of the concrete mixes used in the experimental investigation, together with the development of the concrete production methods used to obtain both the cast and sprayed test specimens. In addition, it has described the successful spraying trials undertaken on plain and fibre reinforced

versions of the concrete mixes to demonstrate their pumpability and sprayability, and thereby verify their use in this thesis for the development and implementation of the proposed model.

The next stage of the experimental investigation was to undertake the experimental testing programme in order to collect the data for use in the development and implementation of the proposed model. This is described in Chapter 6.

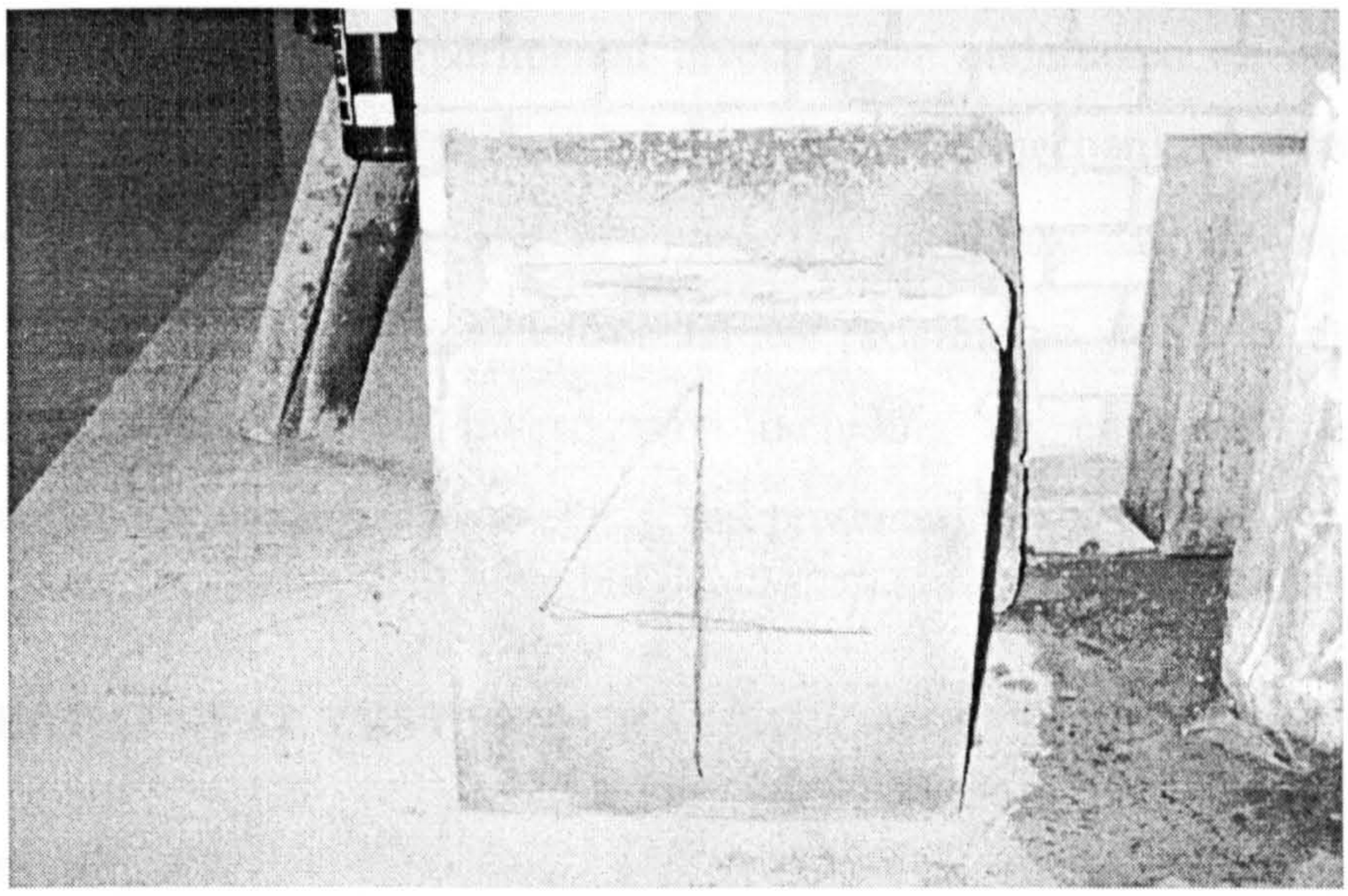

Figure 5.6 Representative test panel from the spraying trial.

6. EXPERIMENTAL TESTING PROGRAMME AND DATA COLLECTION

6.1 INTRODUCTION

This chapter describes the experimental investigation undertaken on both cast and sprayed specimens, in order to investigate the reinforcing mechanisms associated with steel fibre reinforced concrete and to obtain the necessary data for the proposed model. It initially describes the experimental test programme, and then describes the various tests adopted in the investigation including for each test: test method development and procedure, data analysis, and presentation and discussion of results.

6.2 EXPERIMENTAL TEST PROGRAMME

6.2.1 General

The experimental investigation involved five different tests and three concrete matrices (as described in Chapter 5). The test programme for each test, together with the test variables investigated, are summarised in Tables 6.1 to 6.3 and are described in the following sections. All specimens were tested at an age of 28 days.

6.2.2 Single fibre pull-out tests

The test programme comprised 41 cast test series as shown in Table 6.1, consisting of four test specimens per series. Tests were only performed on cast specimens due to the difficulties associated with the preparation of sprayed specimens containing single fibres (see Section 6.3).

Test variables investigated:

- matrix type — A, B and C
- fibre embedment length — 5, 10, 15 and 20mm
- fibre orientation — 0, 10, 20, 30, 40, 50 and 60 degrees

6. EXPERIMENTAL TESTING PROGRAMME AND DATA COLLECTION

6.1 INTRODUCTION

This chapter describes the experimental investigation undertaken on both cast and sprayed specimens, in order to investigate the reinforcing mechanisms associated with steel fibre reinforced concrete and to obtain the necessary data for the proposed model. It initially describes the experimental test programme, and then describes the various tests adopted in the investigation including for each test: test method development and procedure, data analysis, and presentation and discussion of results.

6.2 EXPERIMENTAL TEST PROGRAMME

6.2.1 General

The experimental investigation involved five different tests and three concrete matrices (as described in Chapter 5). The test programme for each test, together with the test variables investigated, are summarised in Tables 6.1 to 6.3 and are described in the following sections. All specimens were tested at an age of 28 days.

6.2.2 Single fibre pull-out tests

The test programme comprised 41 cast test series as shown in Table 6.1, consisting of four test specimens per series. Tests were only performed on cast specimens due to the difficulties associated with the preparation of sprayed specimens containing single fibres (see Section 6.3).

Test variables investigated:

- matrix type — A, B and C
- fibre embedment length — 5, 10, 15 and 20mm
- fibre orientation — 0, 10, 20, 30, 40, 50 and 60 degrees

Series Ref.	Matrix Type	Fibre embedment length /mm				Fibre orientation /degrees						
		5	10	15	20	0	10	20	30	40	50	60
A/01	C	✓				✓						
A/02	C		✓			✓						
A/03	C			✓		✓						
A/04	C				✓	✓						
A/05	C	✓					✓					
A/06	C		✓				✓					
A/07	C			✓			✓					
A/08	C				✓		✓					
A/09	C	✓						✓				
A/10	C		✓					✓				
A/11	C			✓				✓				
A/12	C	✓							✓			
A/13	C		✓						✓			
A/14	C			✓					✓			
A/15	C				✓				✓			
A/16	C	✓								✓		
A/17	C		✓							✓		
A/18	C			✓						✓		
A/19	C	✓									✓	
A/20	C		✓								✓	
A/21	C			✓							✓	
A/22	C				✓						✓	
A/23	C	✓										✓
A/24	C		✓									✓
A/25	C			✓								✓
A/26	B	✓				✓						
A/27	B			✓		✓						
A/28	B	✓					✓					
A/29	B			✓			✓					
A/30	B	✓							✓			
A/31	B			✓					✓			
A/32	B	✓									✓	
A/33	B			✓							✓	
A/34	A	✓				✓						
A/35	A			✓		✓						
A/36	A	✓					✓					
A/37	A			✓			✓					
A/38	A	✓							✓			
A/39	A			✓					✓			
A/40	A	✓									✓	
A/41	A			✓							✓	

Table 6.1 Single fibre pull-out test programme.

6.2.3 Compression tests

The test programme comprised 12 cast and 6 sprayed test series as shown in Table 6.2, consisting of three test specimens per series.

Test variables investigated:

- matrix type — A, B and C
- fibre contents — cast - 0, 40, 80 and 120kg/m^3
  sprayed - as per in-situ contents detailed in Table 5.8

Series Ref.		Matrix Type	Fibre volume (kg/m^3)			
			0	40	80	120
CAST	B/01	C	✓			
	B/02	C		✓		
	B/03	C			✓	
	B/04	C				✓
	B/05	B	✓			
	B/06	B		✓		
	B/07	B			✓	
	B/08	B				✓
	B/09	A	✓			
	B/10	A		✓		
	B/11	A			✓	
	B/12	A				✓
SPRAYED	MIX 1	C	0kg/m^3 - as per Table 5.8			
	MIX 2	C	26kg/m^3 - as per Table 5.8			
	MIX 3	C	66kg/m^3 - as per Table 5.8			
	MIX 4	B	53kg/m^3 - as per Table 5.8			
	MIX 5	B	65kg/m^3 - as per Table 5.8			
	MIX 6	A	56kg/m^3 - as per Table 5.8			

Table 6.2 Compression test programme.

6.2.4 Flexural toughness tests

The test programme comprised 34 cast and 6 sprayed test series as shown in Table 6.3, consisting of three test specimens per series. Cast beams were nominally 100mm wide by 500mm long with a variable depth (as detailed below). Sprayed beams were nominally 75mm deep by 125mm wide by 500mm long.

Test variables investigated:

- matrix type — A, B and C

- fibre contents — cast - 0, 40, 80 and 120kg/m^3
  sprayed - as per in-situ contents detailed in Table 5.8
- beam depth (cast only) — unnotched - 100, 75 and 50mm
  notched - 85 and 60mm (including a 10mm deep notch)

A full investigation involving all three matrix types and fibre volumes was undertaken on 75mm deep beams, and a limited investigation on the 50 and 100mm deep beams. Therefore, the investigation concentrated on a similar size beam (i.e. with the same span/depth ratio) as that adopted by EFNARC (1996).

6.2.5 Strain analysis tests

Strain analysis tests were undertaken in conjunction with the flexural toughness tests detailed in Section 6.2.4 above. The test programme comprised 8 cast and 2 sprayed test series as shown in Table 6.3. Each series consisted of only two specimens due to the relatively high cost associated with specimen preparation (see Section 6.4). For the same reason only the principal matrix (Matrix C) was investigated.

Test variables investigated:

- matrix type — C only
- fibre contents — cast - 40, 80 and 120kg/m^3
  sprayed - as per in-situ contents detailed in Table 5.8
- beam depth (cast only) — unnotched - 100 and 75 mm
  notched - 85 and 60mm (including a 10mm deep notch)

6.2.6 Fibre distribution analysis

Fibre distribution analysis was undertaken on a selection of flexural toughness beam specimens following the completion of the flexural toughness tests. Two methods of analysis were used: (1) an X-ray photographic method to determine the spatial distributions associated with fibre embedment length and fibre orientation; and (2) a manual counting method to obtain the actual fibre numbers and fibre distributions across the cracked section of the beams.

(a) UNNOTCHED BEAMS

Series Ref.		Matrix Type	Beam Depth (mm)			Fibre volume (kg/m^3)				Strain analysis tests	Fibre distribution analysis	
			50	75	100	0	40	80	120		manual	X-ray
CAST	U/01	C		✓		✓						
	U/02	C		✓			✓			SA.1	✓	✓
	U/03	C		✓				✓		SA.3		✓
	U/04	C		✓					✓	SA.4	✓	✓
	U/05	B		✓		✓						
	U/06	B		✓			✓				✓	
	U/07	B		✓				✓				
	U/08	B		✓					✓			
	U/09	A		✓		✓					✓	
	U/10	A		✓			✓					
	U/11	A		✓				✓				
	U/12	A		✓					✓			
	U/13	C	✓				✓					
	U/14	C	✓					✓				
	U/15	A	✓				✓					
	U/16	A	✓					✓				
	U/17	C			✓		✓			SA.8	✓	
	U/18	C			✓			✓		SA.10	✓	
	U/19	A			✓		✓					
	U/20	A			✓			✓				
SPRAYED	S/01	C		✓		0kg/m³ - as per Table 5 8						
	S/02	C		✓		26kg/m³ - as per Table 5.8				SA.5	✓	✓
	S/03	C		✓		66kg/m³ - as per Table 5.8				SA.6	✓	✓
	S/04	B		✓		53kg/m³ - as per Table 5.8						
	S/05	B		✓		65kg/m³ - as per Table 5.8						
	S/06	A		✓		56kg/m³ - as per Table 5.8						

(b) NOTCHED BEAMS

Series Ref.		Matrix Type	Beam depth (mm)		Fibre volume (kg/m^3)				Strain analysis tests	Fibre distribution analysis	
			60	85	0	40	80	120		manual	X-ray
CAST	N/01	C		✓	✓						
	N/02	C		✓		✓			SA.2	✓	
	N/03	C		✓			✓			✓	
	N/04	C		✓				✓			
	N/05	B		✓	✓						
	N/06	B		✓		✓				✓	
	N/07	B		✓			✓			✓	
	N/08	B		✓				✓			
	N/09	A		✓	✓						
	N/10	A		✓		✓				✓	
	N/11	A		✓			✓			✓	
	N/12	A		✓				✓			
	N/13	C	✓			✓			SA.7	✓	
	N/14	C	✓				✓		SA.9	✓	

Table 6.3 Flexural toughness test, strain analysis and fibre distribution analysis programme.

The X-ray analysis programme comprised 3 cast and 2 sprayed test series, and the manual counting analysis comprised 14 cast and 2 sprayed test series as shown in Table 6.3. Both methods consisted of two specimens per series. Matrix type was assumed to be independent of fibre distribution for the three matrices used. Test variables investigated included: fibre volume, beam depth and the method of placement (i.e. casting and spraying).

6.3 SINGLE FIBRE PULL-OUT TESTS

6.3.1 Background

In Chapter 3, it was noted that all the single fibre pull-out tests reported to date have involved fibre pull-out across an artificial crack. Such tests do not take into account the pre-crack fibre-matrix interface stress distribution or the change in this distribution which occurs at the instant the matrix cracks. In an attempt to overcome this shortcoming, a single fibre pull-out test was developed which casts the fibre in an uncracked matrix and thereby enabled the complete load versus pull-out response to be recorded.

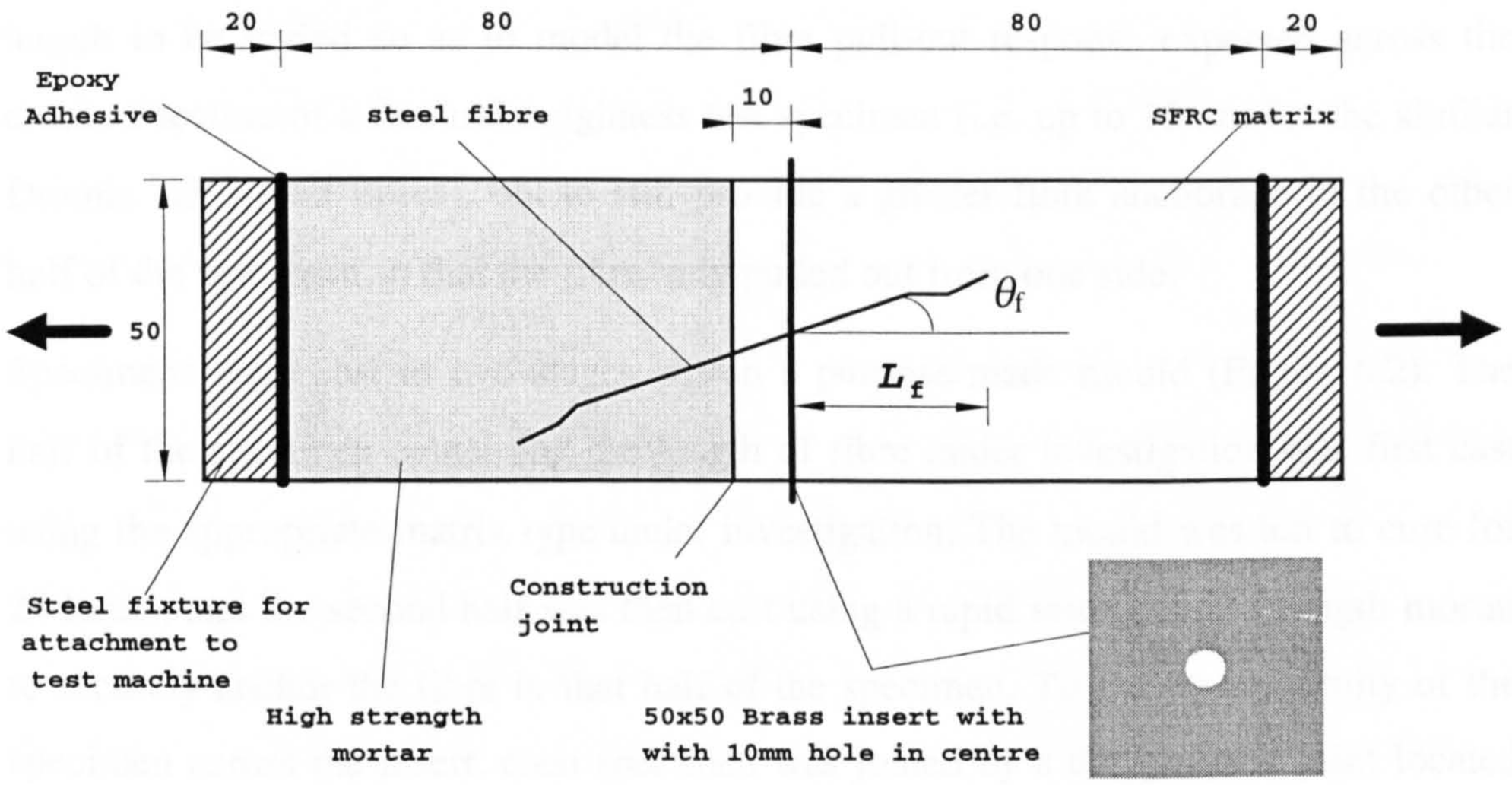

Figure 6.1 Schematic illustration of a single fibre pull-out test specimen (all dimensions in millimetres).

6.3.2 Specimen preparation and test procedure

A schematic illustration of a typical test specimen is shown in Figure 6.1. Encasement of the fibre within the uncracked matrix was achieved by casting a brass insert, with a 10mm hole located at its centre, at the mid-length of each specimen. This hole served two purposes: (1) to provide continuity of the specimen across the insert; and (2) to form a reduced section at which the specimen cracked during the test. The size of the hole was determined from the relationship proposed by Krenchel

P 68

(1975) - equation 3.2 - for the prediction of average fibre spacing in a random 3-D fibre composite. For the concrete mixes used this relationship predicted an average fibre spacing of between 7-10mm for fibre contents between 40-80kg/m^3 (i.e. 0.5-1.0% by volume).

To prevent a bond forming between the insert and the specimen, a thin layer of PTFE spray was applied to one side of the insert. Preliminary tests showed PTFE spray to be the most suitable debonding agent for this purpose when compared with a variety of alternatives, which included mould oil, lithium grease and polythene sheet.

Dramix ZC 50/0.50 (50mm long and 0.5mm diameter) hooked-end steel fibres were used in the pull-out tests. The length of these fibres allowed the fibre embedment length to be varied so as to model the fibre pull-out response expected across the cracked section of a flexural toughness test specimen (i.e. up to 15mm for the similar Dramix ZP 30/0.5 fibres), but to still provide a greater fibre anchorage in the other half of the specimen so that the fibre only pulled out from one side.

Specimens were cast in two stages within a purpose-made mould (Figure 6.2). The half of the specimen containing the length of fibre under investigation was first cast using the appropriate matrix type under investigation. The mould was left to cure for 24 hours, and the second half was then cast using a rapid setting high strength mortar to securely anchor the fibre in that half of the specimen. To ensure continuity of the specimen across the insert, each specimen was joined by a construction joint located 10mm to one side of the insert (Figure 6.1). This was prepared by roughening the joining surface of each specimen with a wire brush before casting the second half. Once hardened the completed specimens were carefully demoulded and placed in a curing tank until the time of testing. Four identical specimens were cast for each combination of embedment length and orientation. A specially designed block was

used to position the fibre accurately at the centre of the specimen during the first stage of casting, and to obtain the correct fibre orientation (θ_f in Figure 6.1) and embedment length (L_f in Figure 6.1).

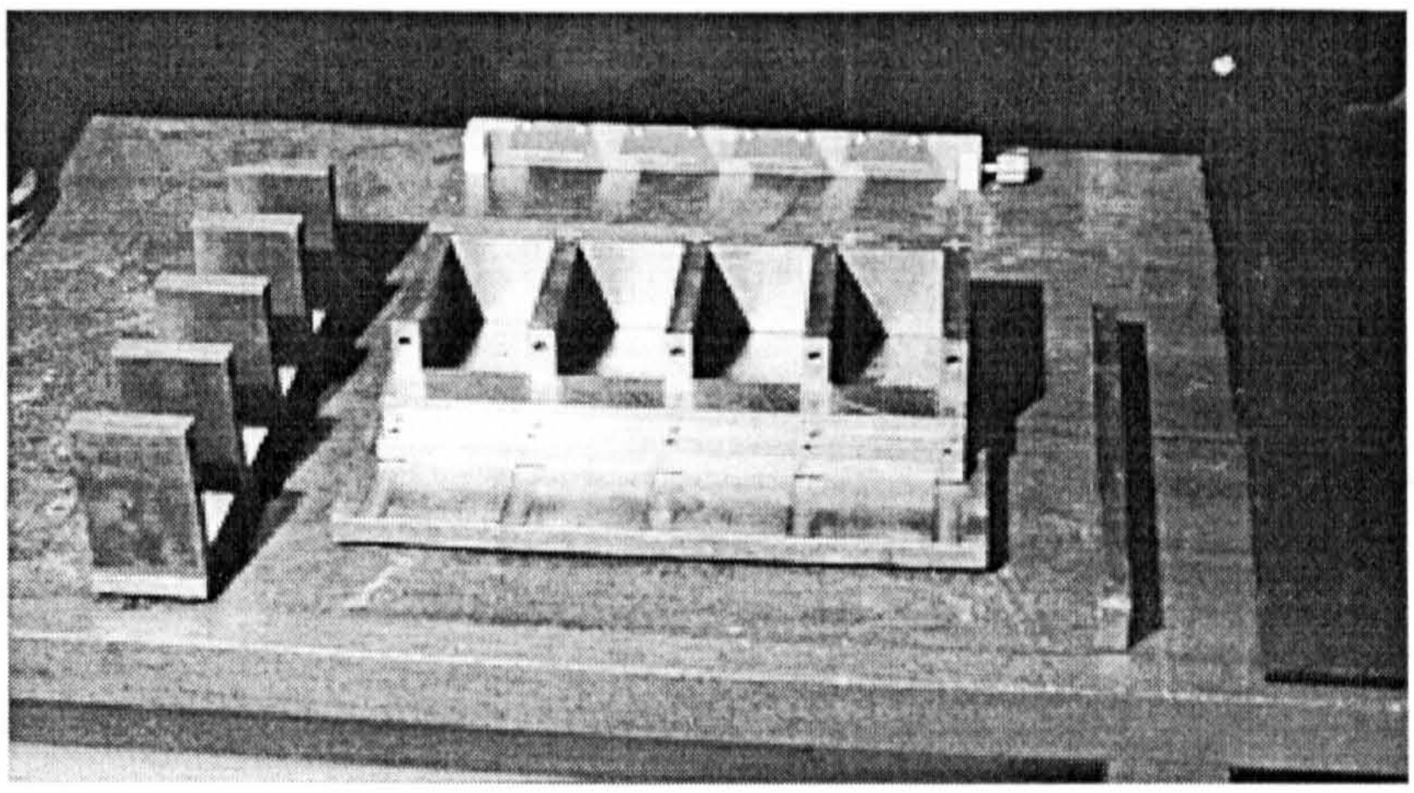

Figure 6.2 Fibre pull-out test specimen mould.

Prior to the day of testing, the specimens were removed from the curing bath and dried at room temperature. 50 x 50 x 20mm steel fixtures were then glued to the ends of each specimen, using a two-part epoxy adhesive, to facilitate attachment to the loading rig. An even and continuous layer of adhesive was applied to the grip interface to provide a homogenous stress field across which the pull-out load was transferred to the specimen. To minimise the eccentricity between the centreline of the grips and the centreline of the specimen, a straight edge was used to abut against the grips and specimen during the gluing process. Each specimen was held securely in place until the glue had cured, and then placed back in the curing room until they were tested.

The tests were performed under cross-head deflection control with an Instron 6025 screw driven testing machine using a 1kN load cell. Specimen deformation, and crack widths, were measured over a gauge length of 85mm using four LVDTs mounted on a purpose made aluminium frame, such that the gauge points were equidistant from the ends of the specimen (Figure 6.3). One LVDT was located on each side of the specimen to enable an average deformation reading to be determined. The aluminium frame consisted of two removable square collars, similar to a frame used by Johnston and Gray (1978). The top collar was clamped to the specimen using four conical tipped bolts set into Demec strain gauge pips, which were accurately positioned and glued onto the specimen beforehand. The lower collar was supported in a similar fashion, although the conical tipped bolts were set in to small aluminium pads as

opposed to gauge points. The gauge length was set accurately by a removable spacer bar which fitted between the upper and lower collars. Load and deformations were digitally recorded using a six channel data acquisition system operating at a frequency of 0.2Hz. An X-Y plotter was also used to record the real time pull-out response as a check that the test was progressing correctly.

Load was applied at a cross-head travel rate, as follows:

- 0.03mm/min up to the specimen fracture point;
- 0.08mm/min between the fracture point and 1.2mm crack-width; and
- 1.0mm/min between 1.2mm crack-width and complete fibre pull-out.

Pull-out rates up to a 1.2mm crack-width were calculated to be equivalent of the strains developed in the extreme fibre of a 75 x 100 x 500mm beam, when tested over a span of 450mm in third-point loading with a mid-span deflection of 0.1mm/min. Beyond this crack-width a nominal pull-out rate was adopted so as not to unduly prolong the duration of each test.

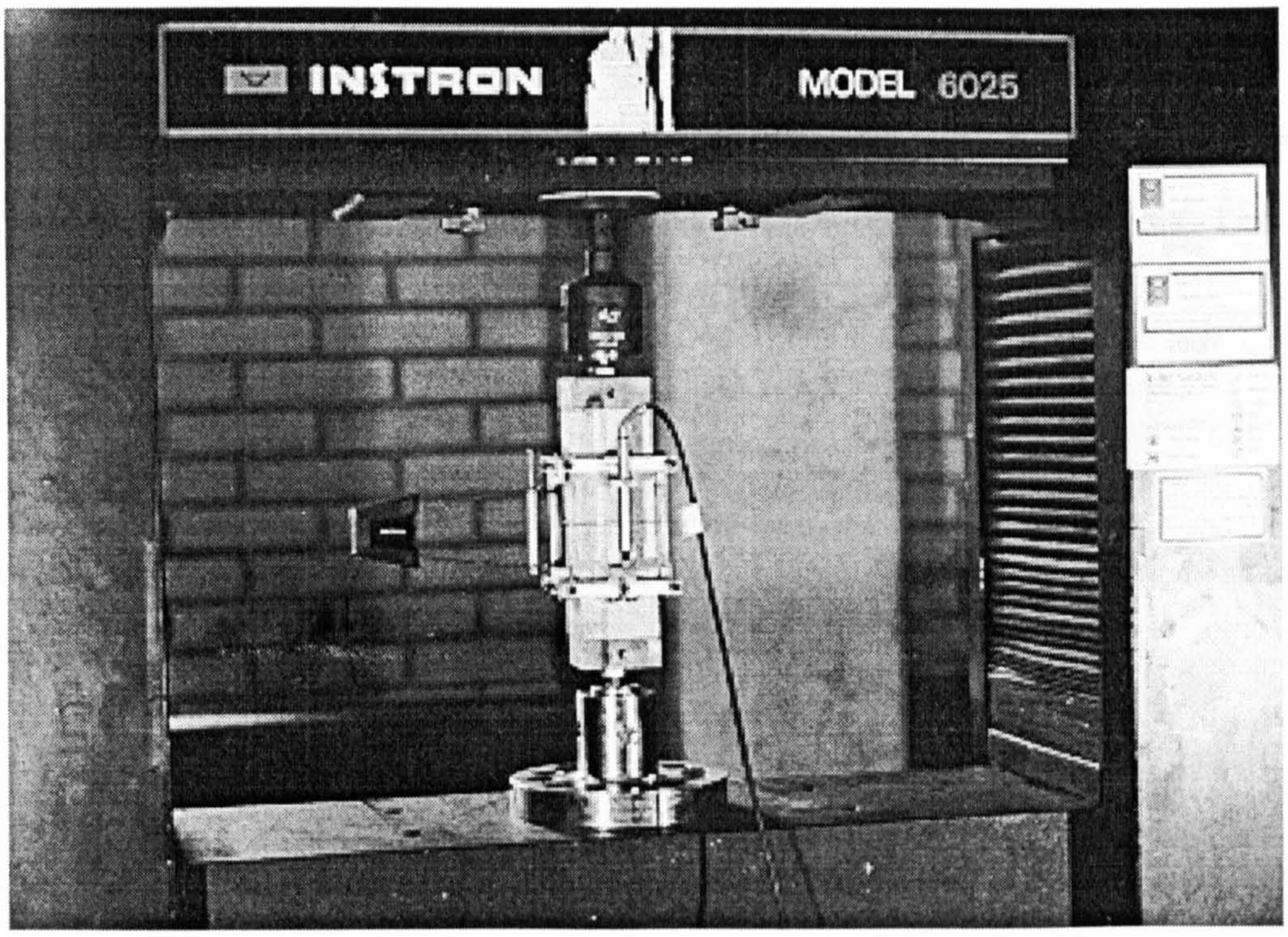

Figure 6.3 Fibre pull-out specimen showing aluminium frame.

For the tests with a fibre embedment length up to 10mm, two LVDTs were used with a total travel of 5mm and two with a total travel of 10mm. For fibre embedment lengths greater than 10mm, the two LVDTs with a total travel of 10mm were replaced with two LVDTs having a total travel of 20mm. The calibration factor, sensitivity and accuracy of the LVDTs and the 10kN Instron load cell are detailed in Table 6.4.

Recording device		Sensitivity (Volts per unit measurement)	Accuracy over full range (%)
Type	Range		
LVDT	5mm	2V/mm	0.5
	10mm	2V/mm	0.5
	20mm	0.5V/mm	0.5
Extensometer	10mm	1V/mm	0.1
Load Cell	1kN	10V/kN	0.1
	100kN	0.1V/kN	0.5
	5000kN	0.02V/kN	1.0

Table 6.4 Sensitivity and accuracy of the load and deflection transducers.

6.3.3 Development of the test procedure

General

The test procedure detailed in Section 6.3.2 was the result of a systematic process of development based on published literature and a series of preliminary tests. The main issues relating to the development of the test are discussed below.

Specimen design

The design of the test specimen was based on the following criteria:

- the test should ideally simulate a random fibre located across the cracked section of a beam under flexural load;
- the test should be capable of varying the fibre embedment length and fibre orientation as required;
- the test should allow for the full length of the fibre to be embedded in the matrix;
- the width of specimen should be able to accommodate the most onerous fibre embedment length and fibre orientation combination required by the test programme (that is, a 20mm embedment length orientated at 50 degrees);

- the test should allow for the fibres to be positioned securely and accurately during specimen manufacture; and
- the specimens should be easy to handle with the minimum risk of damage.

Test control

Closed-loop testing using specimen strain as the control parameter is considered to be the preferred method for controlling single fibre pull-out tests (Section 3.3.1). However, following a series of preliminary tests, the use of closed-loop testing was found to be difficult to achieve. The main reason for this appeared to result from an inability of the test machine to react to the sudden change in specimen stiffness that occurred at the instant the specimen fractured. Although a stable pre-crack response was achieved, the post-crack response was always found to be erratic and unstable. Therefore, following a series of further unsuccessful attempts to control both the pre- and post-crack responses via a closed-loop system, the less favoured cross-head deflection control system was eventually adopted.

6.3.4 Results and discussion

Curve averaging

The data from each pull-out test was initially processed to determine an applied load versus specimen displacement (determined from the four LVDT readings). This data was then used to obtain an average load versus displacement response for each series of four specimens (that is, for each combination of matrix type, fibre embedment length and fibre orientation). These average responses were used in the analysis of the test results as presented in this section.

Characteristics of the single fibre pull-out response curve

A typical pull-out load versus displacement curve is shown in Figure 6.4. The shape of the curve can be characterised by four principal points (labelled A to D in Figure 6.4.): (A) specimen fracture; (B) initial post-fracture fibre pull-out load; (C) peak fibre pull-out load; and (D) complete fibre pull-out. During the tests it was observed that when the matrix fracture point was reached the applied load dropped suddenly to an initial post-fracture pull-out load (Point B in Figure 6.4) of between 10-40N - equivalent to a stress in the fibre of between 50-200 MPa - and the deflection jumped by an order of magnitude to 0.02-0.05 mm before the test re-stabilised. This instability appeared to

be caused by the release of strain energy from the test machine as it compensated for the sudden loss of load capacity in the test specimen at matrix fracture and, therefore, as a direct result of the cross-head control used in the tests. However, this change in the load-deflection response did not appear to affect the subsequent fibre pull-out response. As previously discussed a more stable response might have been obtained if closed-loop deflection control had been possible.

The portion of the pull-out response of most interest for the development of the proposed model is the post-fracture pull-out load versus crack-width response - curve BCD in Figure 6.4. Hence, the majority of results presented in this section relate specifically to the characteristics of this response in terms of matrix type, fibre embedment length and fibre orientation.

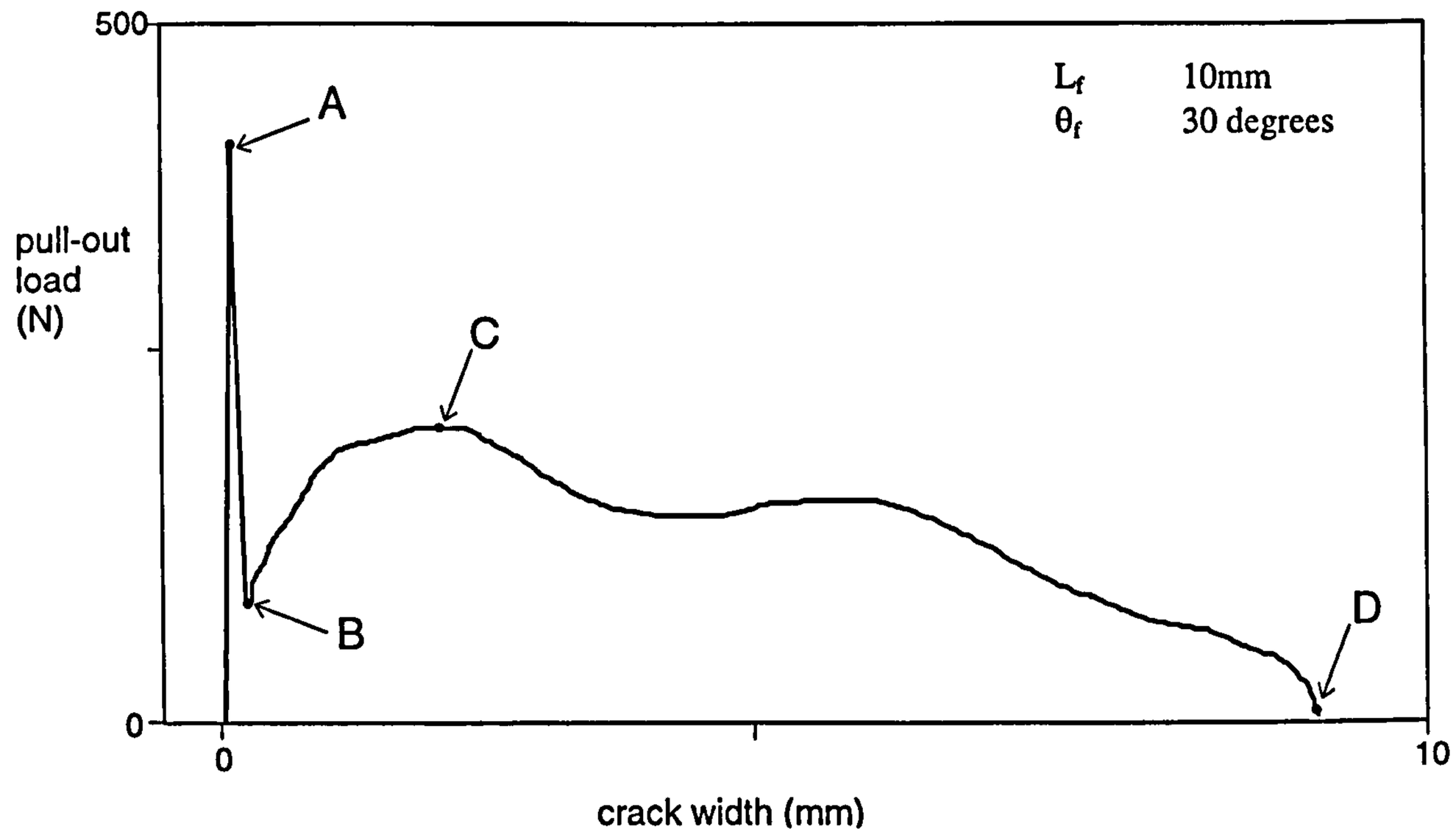

Figure 6.4 Typical single fibre pull-out load versus crack-width response.

Test repeatability

The coefficient of variation (CoV) associated with the average specimen fracture stress (Point A in Figure 6.4) for the Matrix C test series, as a function of fibre embedment length and orientation, is shown in Figure 6.5. It can be seen that its value generally varies between 0-30%. This high variability is most likely the result of specimen eccentricities, as a result of the misalignment of the specimen end-fixing plates during specimen preparation.

The CoV associated with the average fibre pull-out load for the Matrix C test series is presented in Figure 6.6 as a function of crack-width for fibre orientations of 0, 20, 40 and 60 degrees, at fibre embedment lengths of 5, 10 and 15mm respectively. These figures show two main trends: (1) for a fibre embedment length of 5mm the CoV generally varies between 10-60 % irrespective of fibre orientation; and (2) for embedment lengths of 10 and 15mm the CoV increases with an increasing fibre orientation - between 5-15% at 0 and 20 degrees, between 5-30% at 40 degrees, and between 25-50% at 60 degrees.

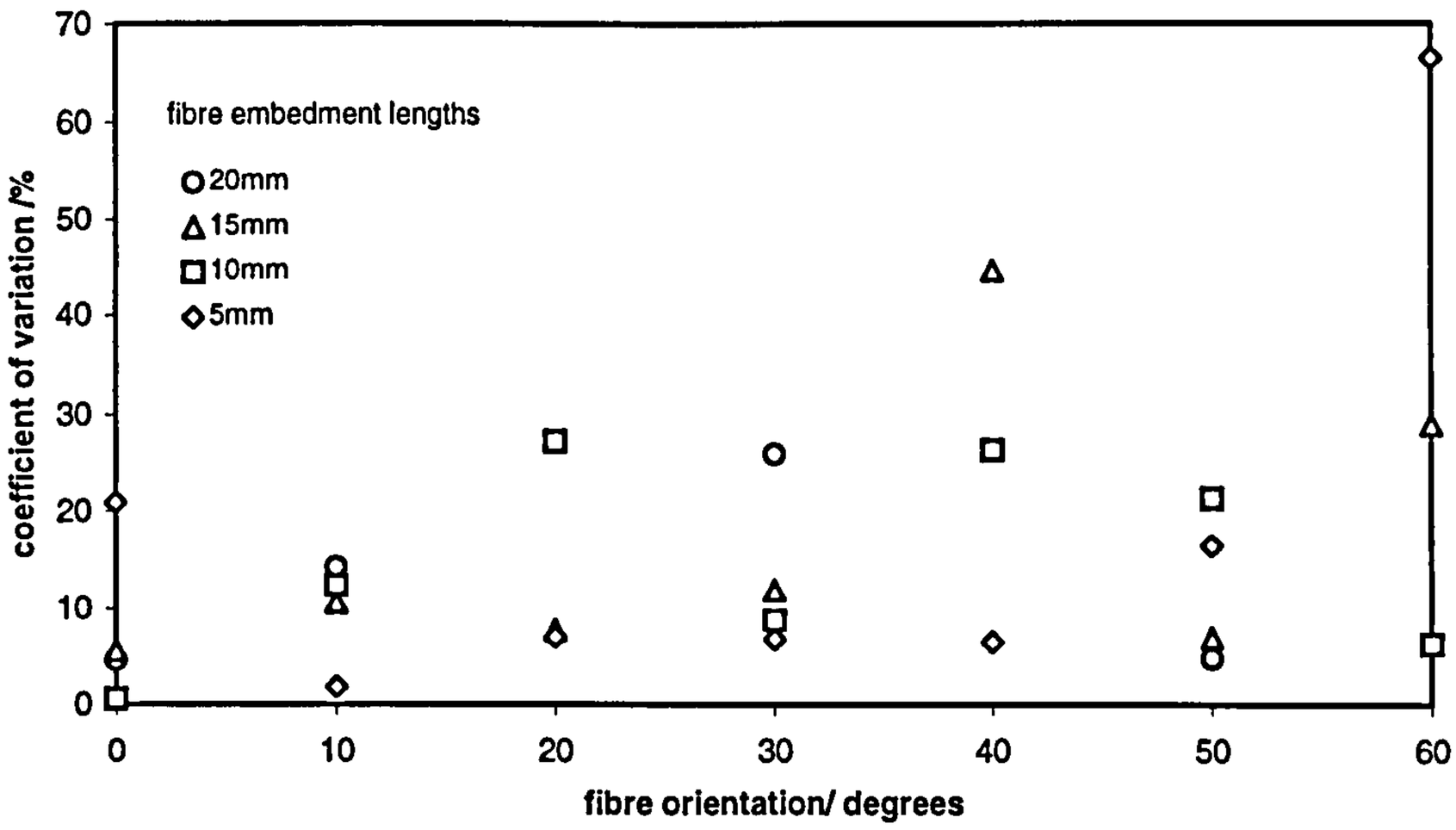

Figure 6.5 Coefficient of variation associated with the specimen fracture stress (Matrix C).

Specimen fracture stress

The specimen fracture stress (Point A in Figure 6.4) for Matrix C is shown in Figure 6.7 as a function of fibre orientation and embedment length. As might be expected, it can be seen that the value of matrix fracture stress (4-6 MPa) does not appear to be influenced by either fibre embedment length or orientation. A similar trend was also observed in the Matrix A and B data.

Fibre orientation and embedment length

The average fibre pull-out response (curve BCD in Figure 6.4) in terms of fibre orientation are shown in Figure 6.8 for Matrix C at fibre embedment lengths of 5, 10, 15 and 20mm, in Figure 6.9 for Matrix B at fibre embedment lengths of 5 and 15mm, and in Figure 6.10 for Matrix A at fibre embedment lengths of 5 and 15mm. Note that

although the load versus crack-width responses were recorded for each test up to the point where the fibre completely pulled-out from the specimen (Point D in Figure 6.4), only the pull-out responses up to a crack-width of 5mm are shown. This is because crack-widths greater than 5mm are generally not relevant in flexural toughness testing and design.

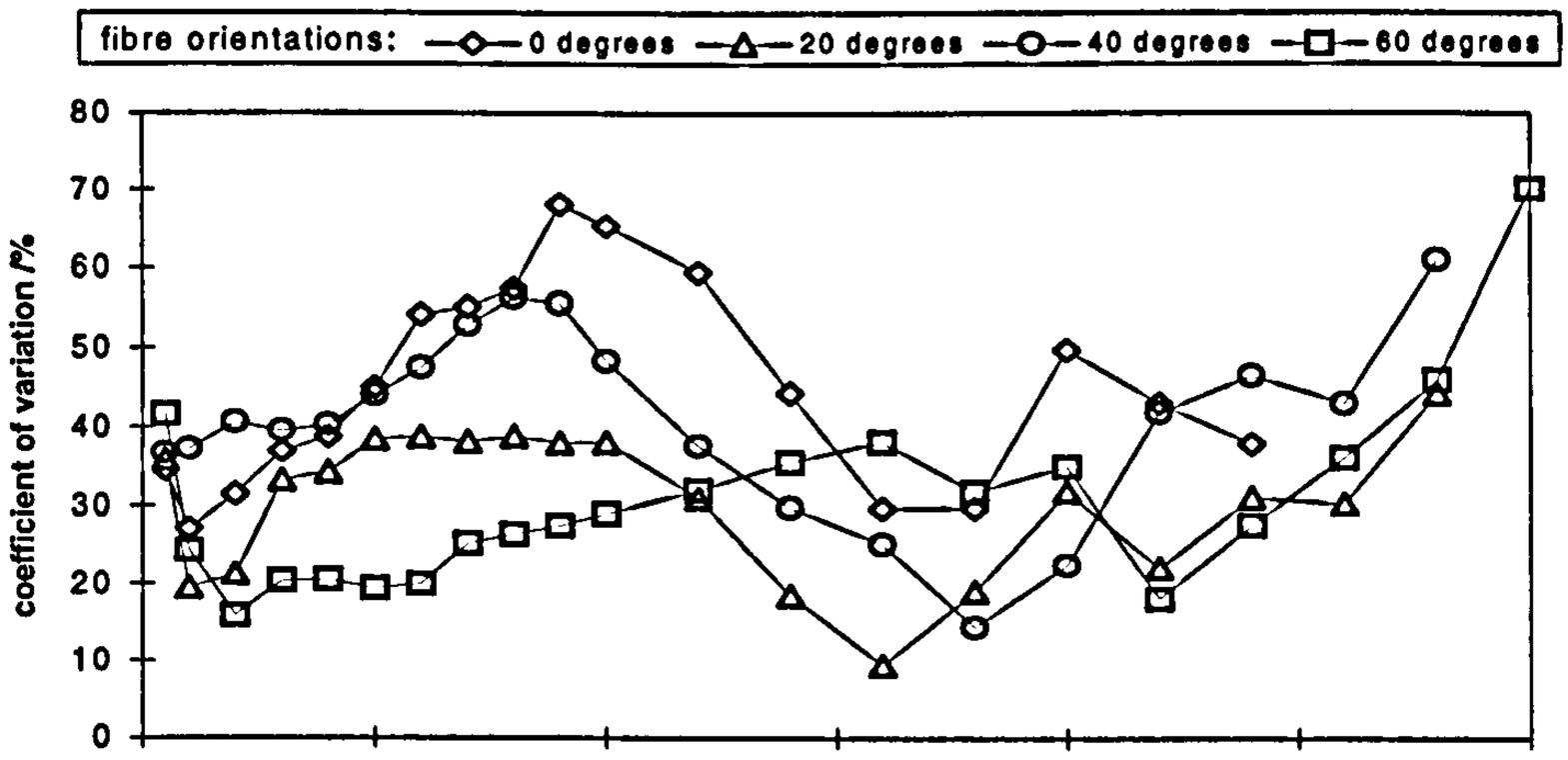

(a) L_f = 5mm

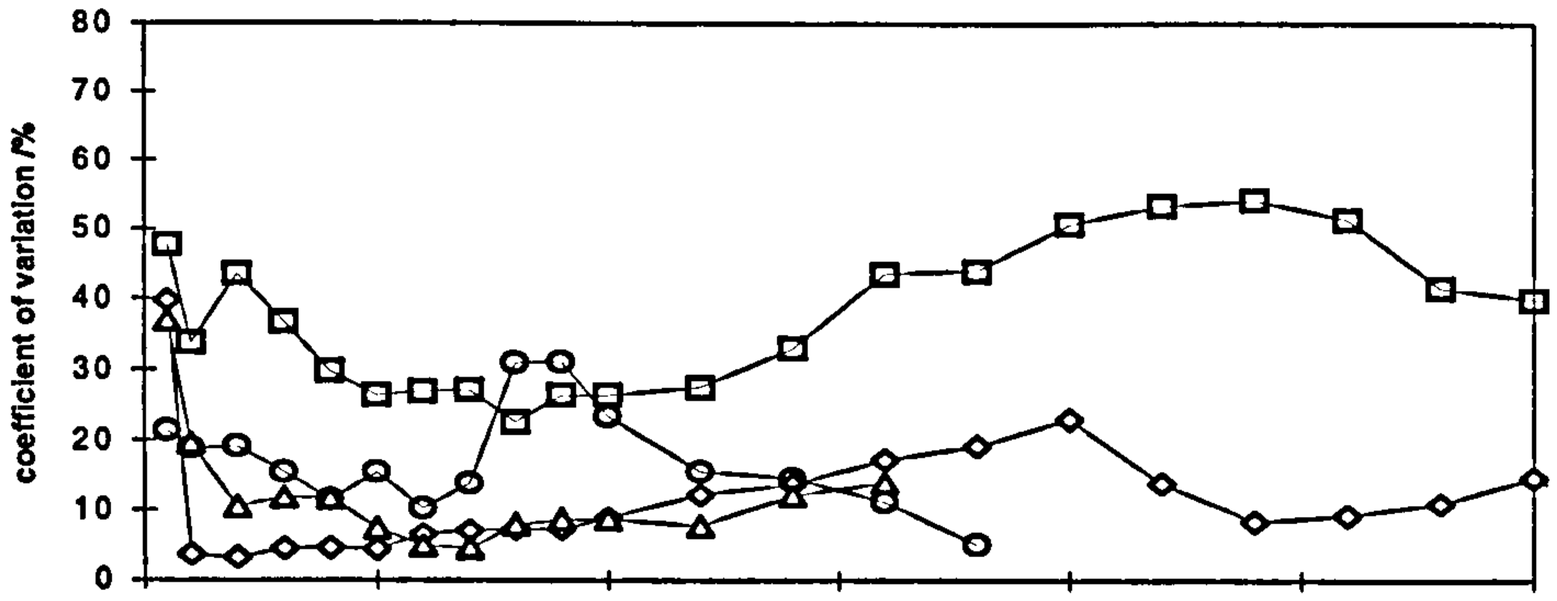

(b) L_f = 10mm

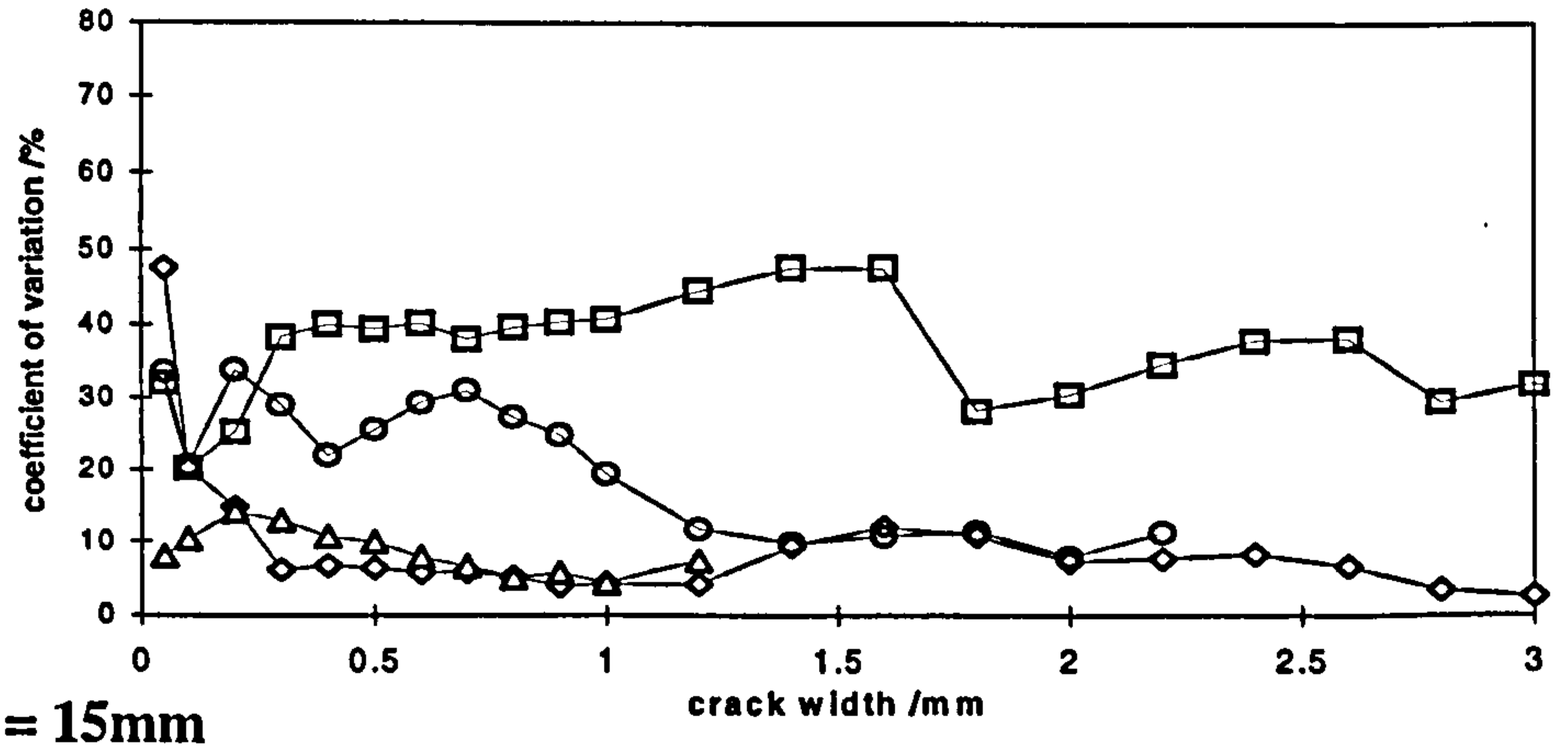

(c) L_f = 15mm

Figure 6.6 Coefficient of variation associated with the fibre pull-out load (Matrix C).

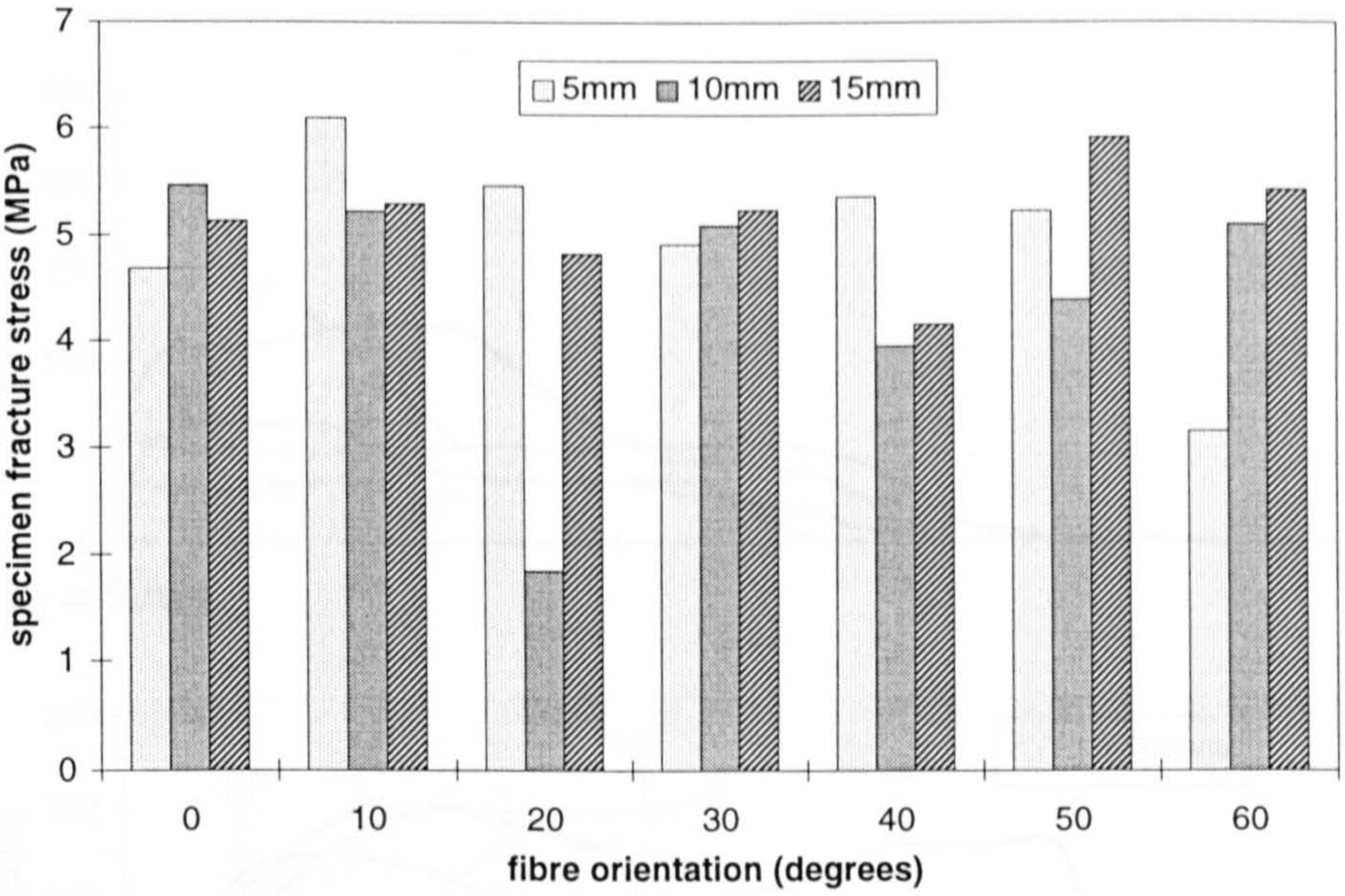

Figure 6.7 Influence of fibre orientation and embedment length on specimen fracture stress (Matrix C).

Two distinctive fibre pull-out modes were observed during the tests. Either the hooked-end straightened and subsequently pulled out from the specimen, or the fibre fractured. From Figures 6.8-6.10 it appears that fibre fracture (marked with an 'x') was most likely to occur in the specimens with fibre embedment lengths greater than 5mm in combination with fibre orientations greater than 20 degrees.

It can also be seen from the results that fibre orientation has a definite influence on fibre pull-out behaviour at embedment lengths of 10, 15 and 20mm. In all cases the action of the mechanical anchorage (provided by the hooked-end) appears to be mobilised at greater crack-width for an increasing fibre orientation. This trend is in accordance with the findings of Banthia and Trottier (1994) who reported similar results for a 30mm long hooked-end fibre with an embedment length of 15mm and orientated at 0, 22.5, 45 and 67.5 degrees to the direction of the pull-out force. However, this trend is not so clear at an embedment length of 5mm. In this case, the magnitude and shape of the pull-out response curve is essentially the same irrespective of fibre orientation.

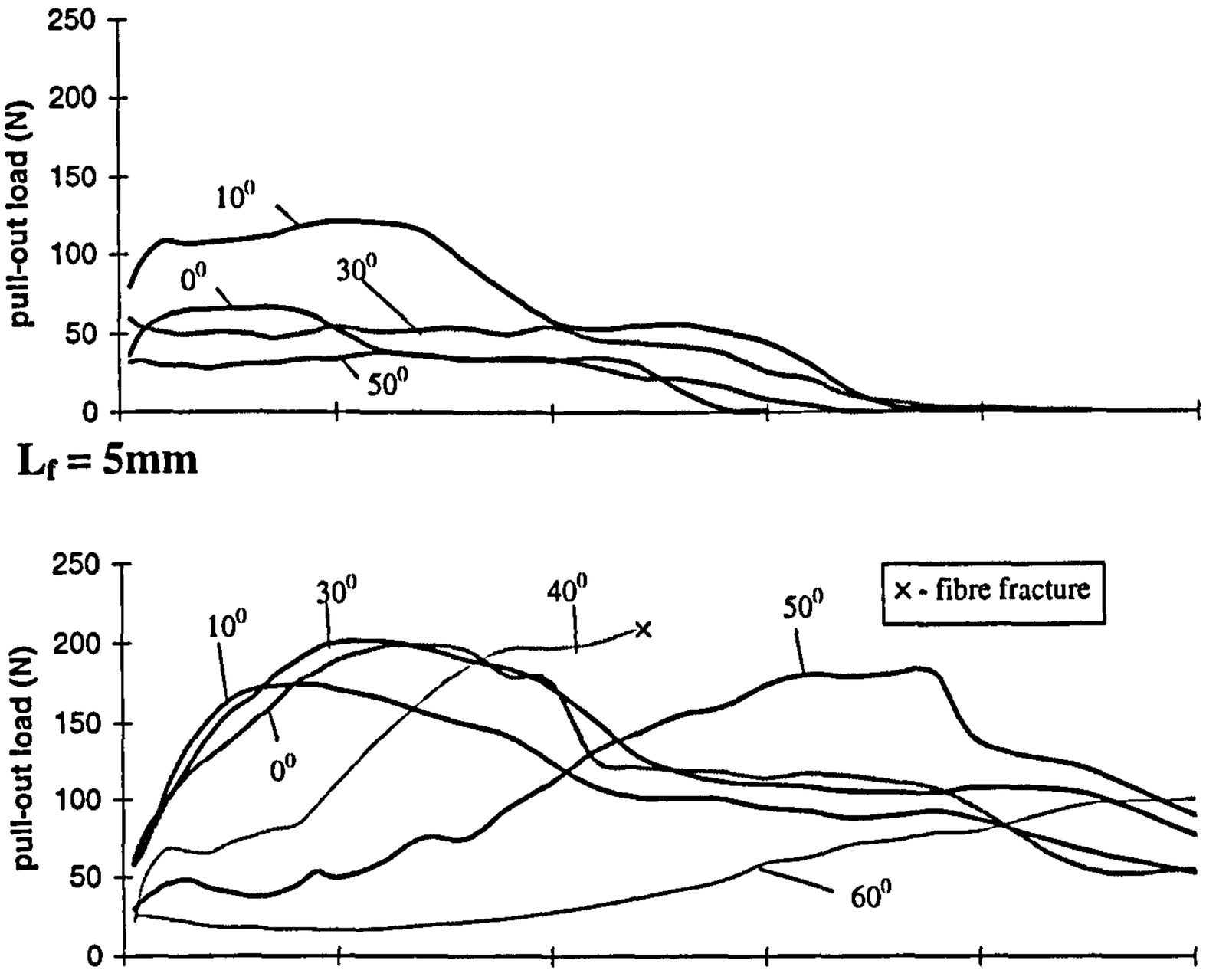

(a) L_f = 5mm

(b) L_f = 10mm

(c) L_f = 15mm

(d) L_f = 20mm

Figure 6.8 Average fibre pull-out responses (Matrix C).

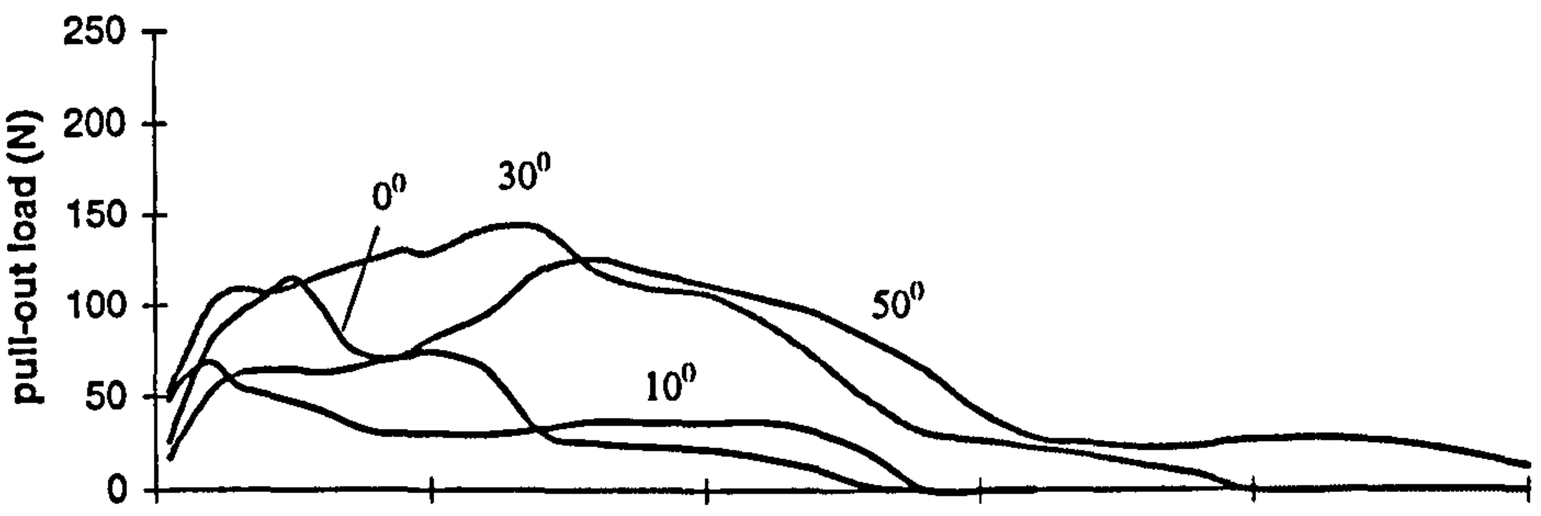

(a) $L_f = 5mm$

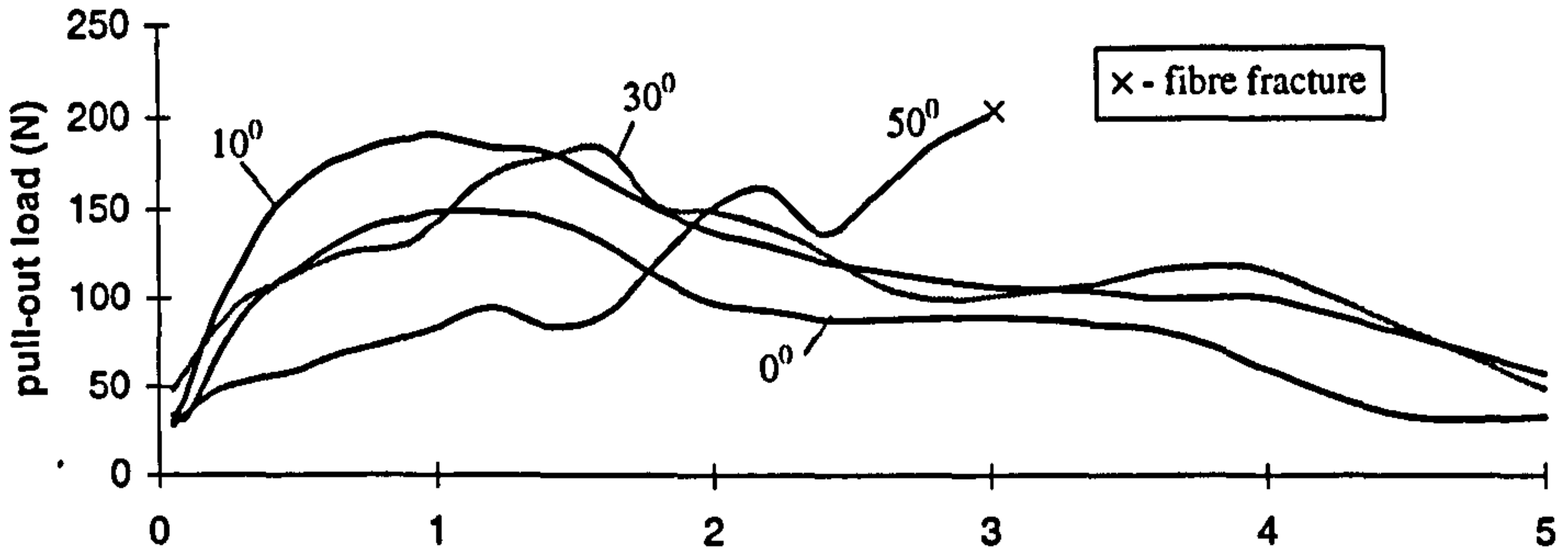

(b) $L_f = 15mm$

Figure 6.9 Average fibre pull-out responses (Matrix B).

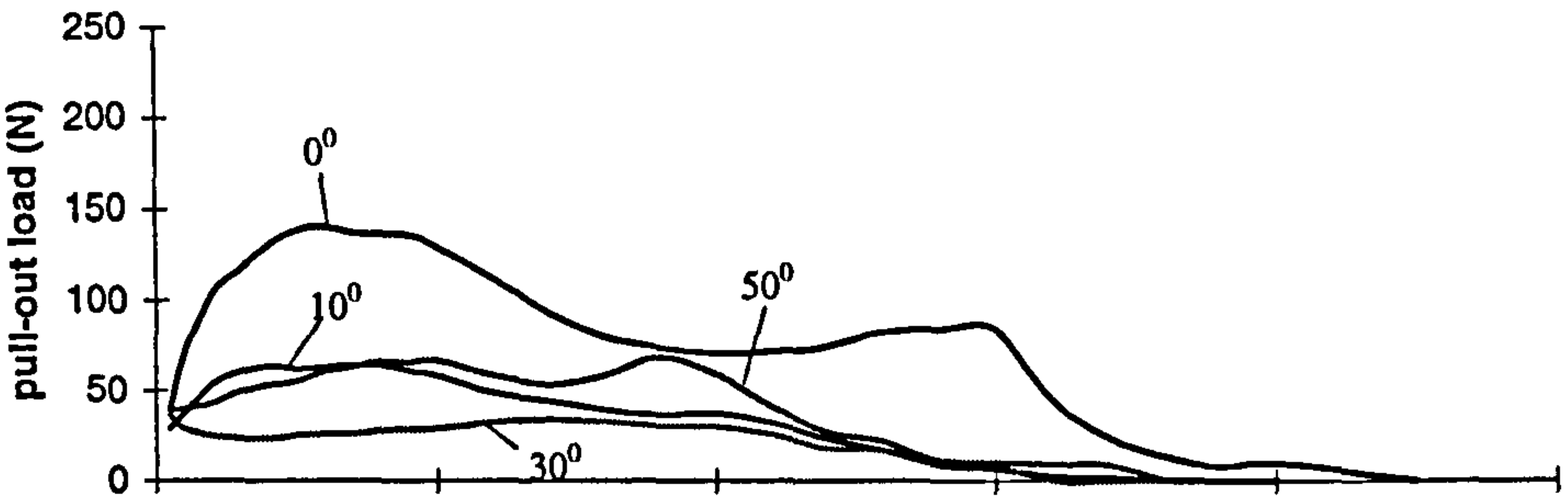

(a) $L_f = 5mm$

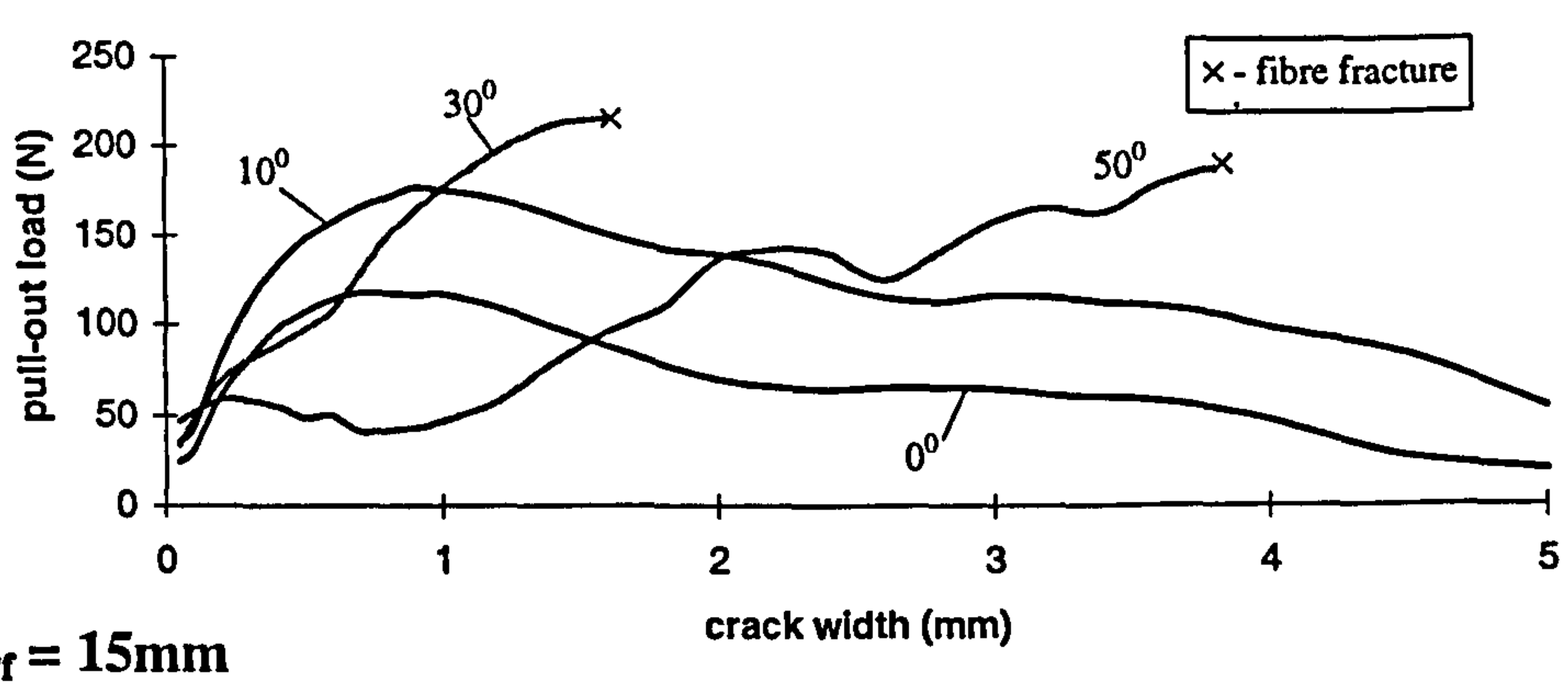

(b) $L_f = 15mm$

Figure 6.10 Average fibre pull-out responses (Matrix A).

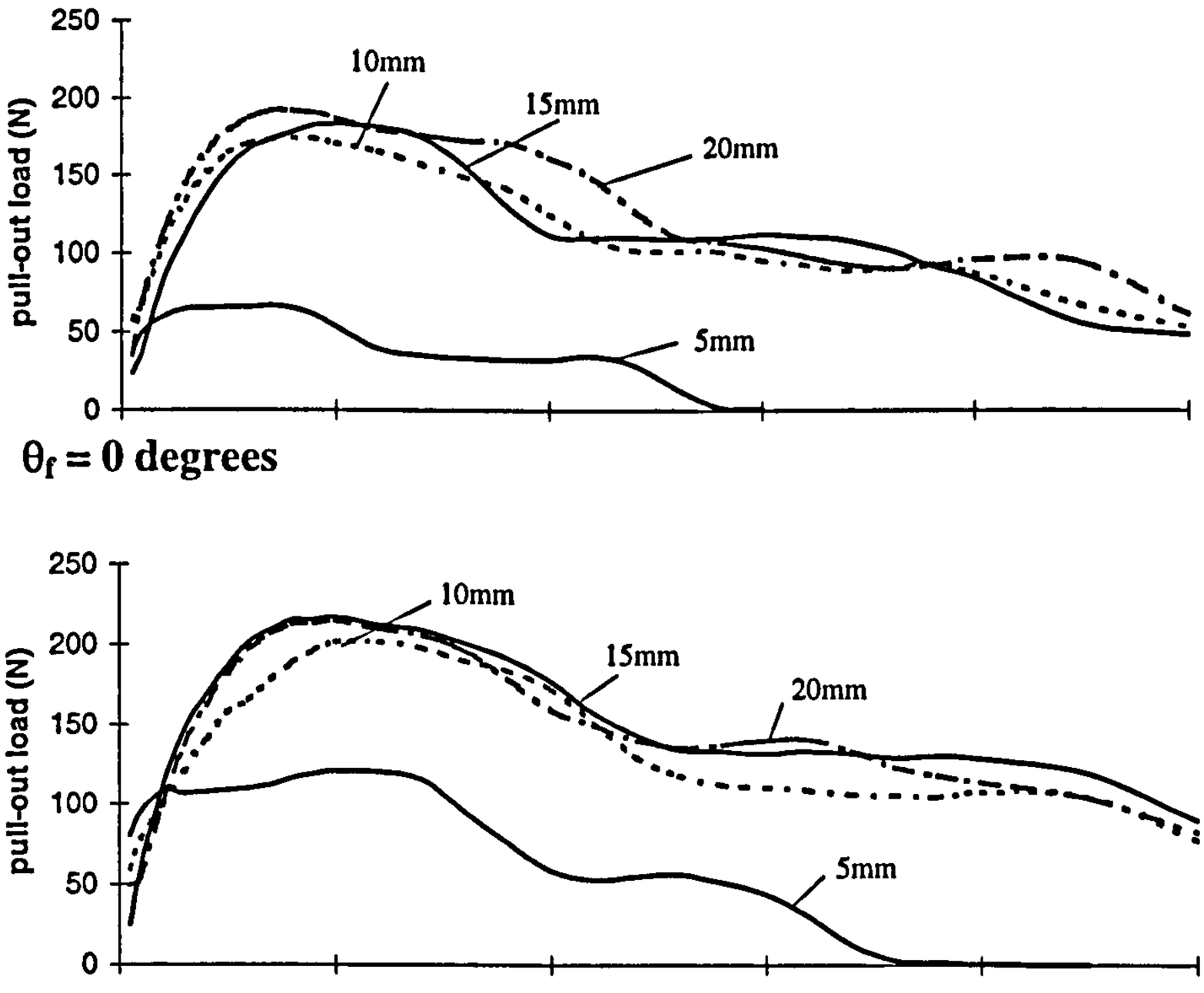

(a) $\theta_f = 0$ degrees

(b) $\theta_f = 10$ degrees

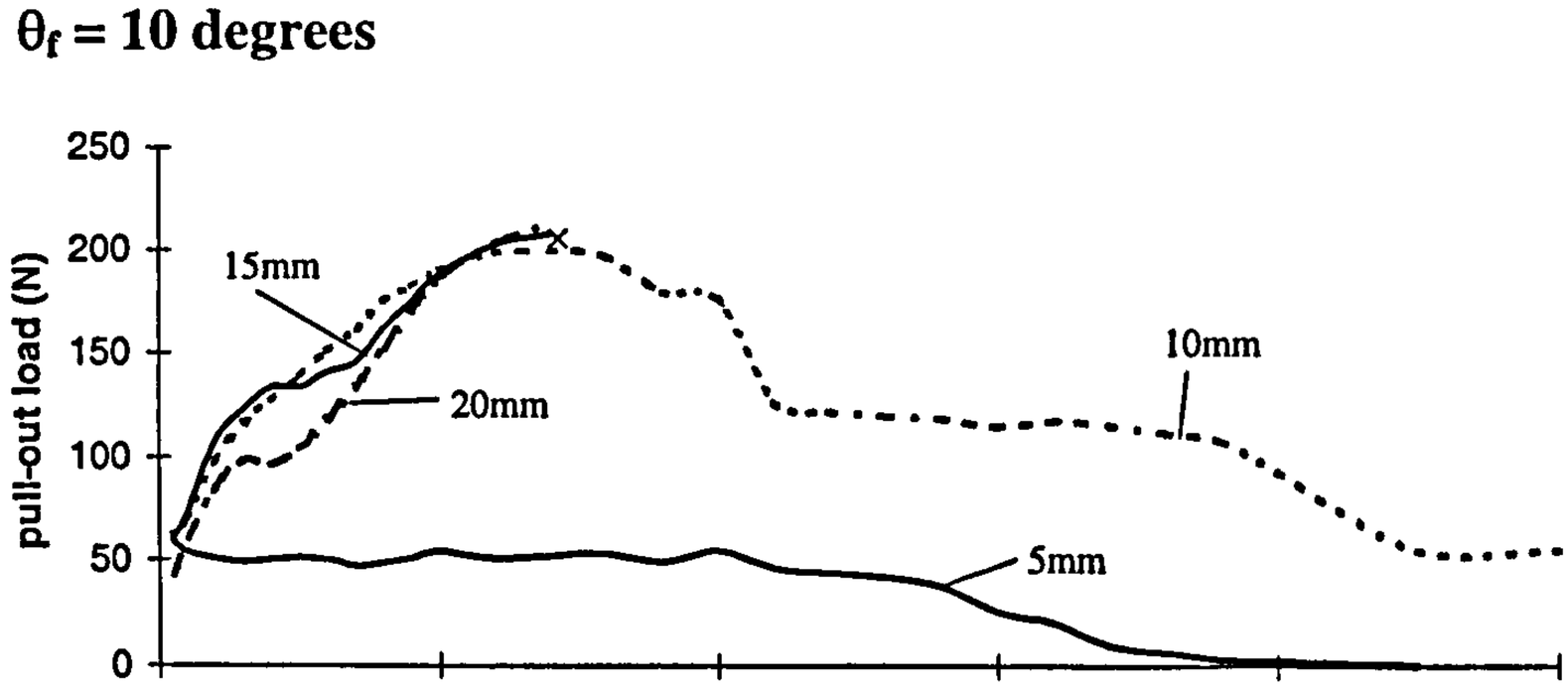

(c) $\theta_f = 30$ degrees

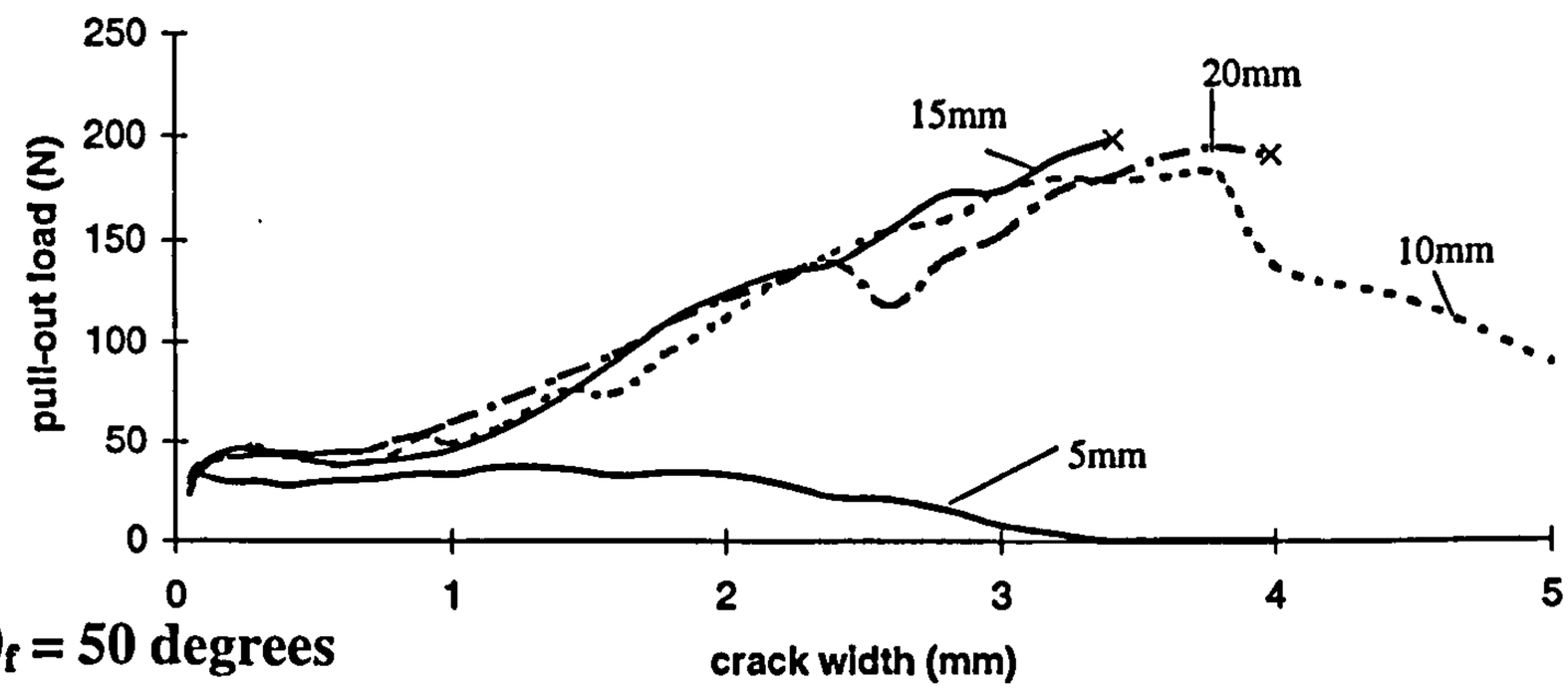

(d) $\theta_f = 50$ degrees

Figure 6.11 Influence of fibre embedment length on pull-out behaviour (Matrix C).

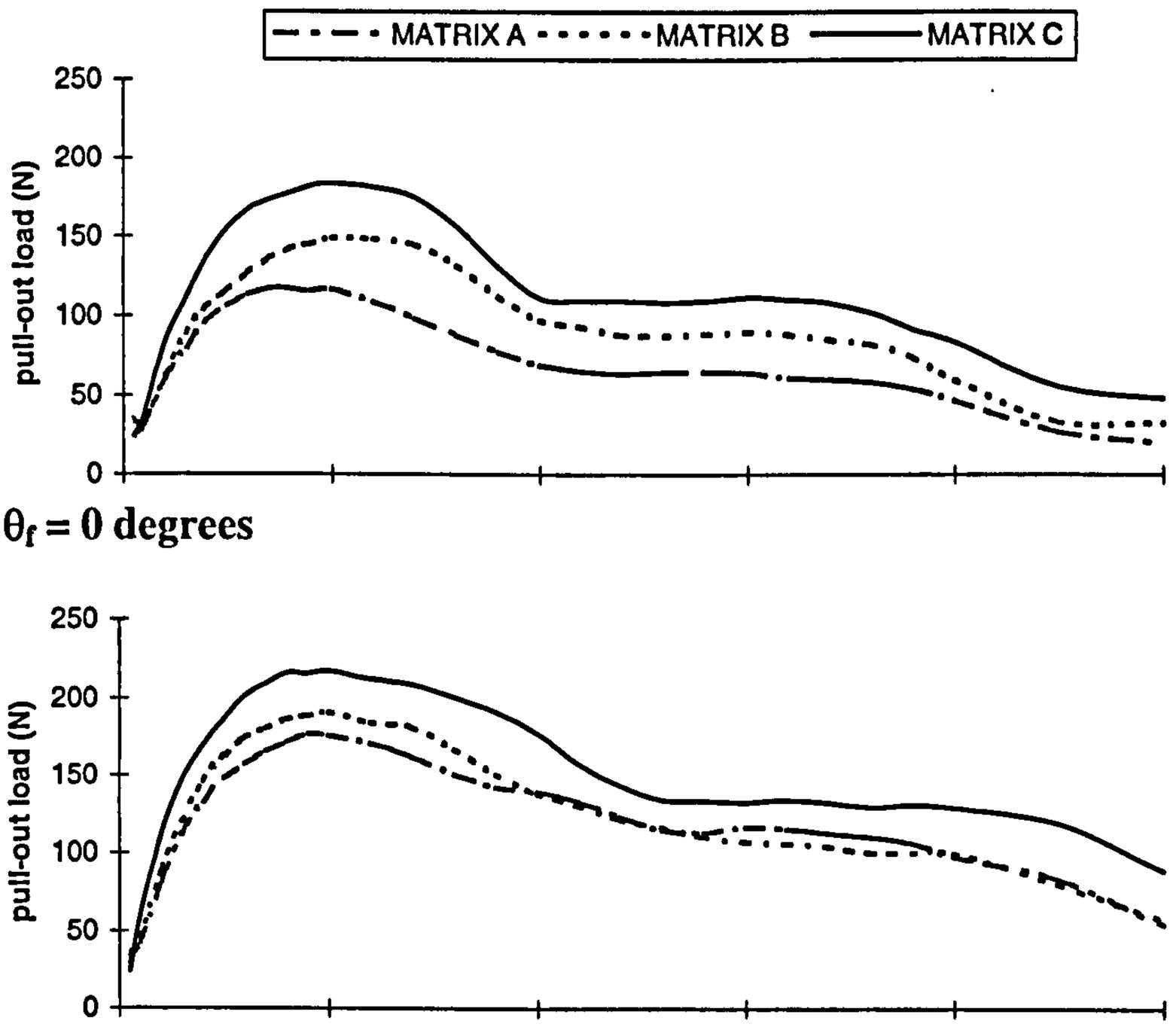

Figure 6.12 Influence of matrix strength on pull-out behaviour (fibre embedment length = 15mm).

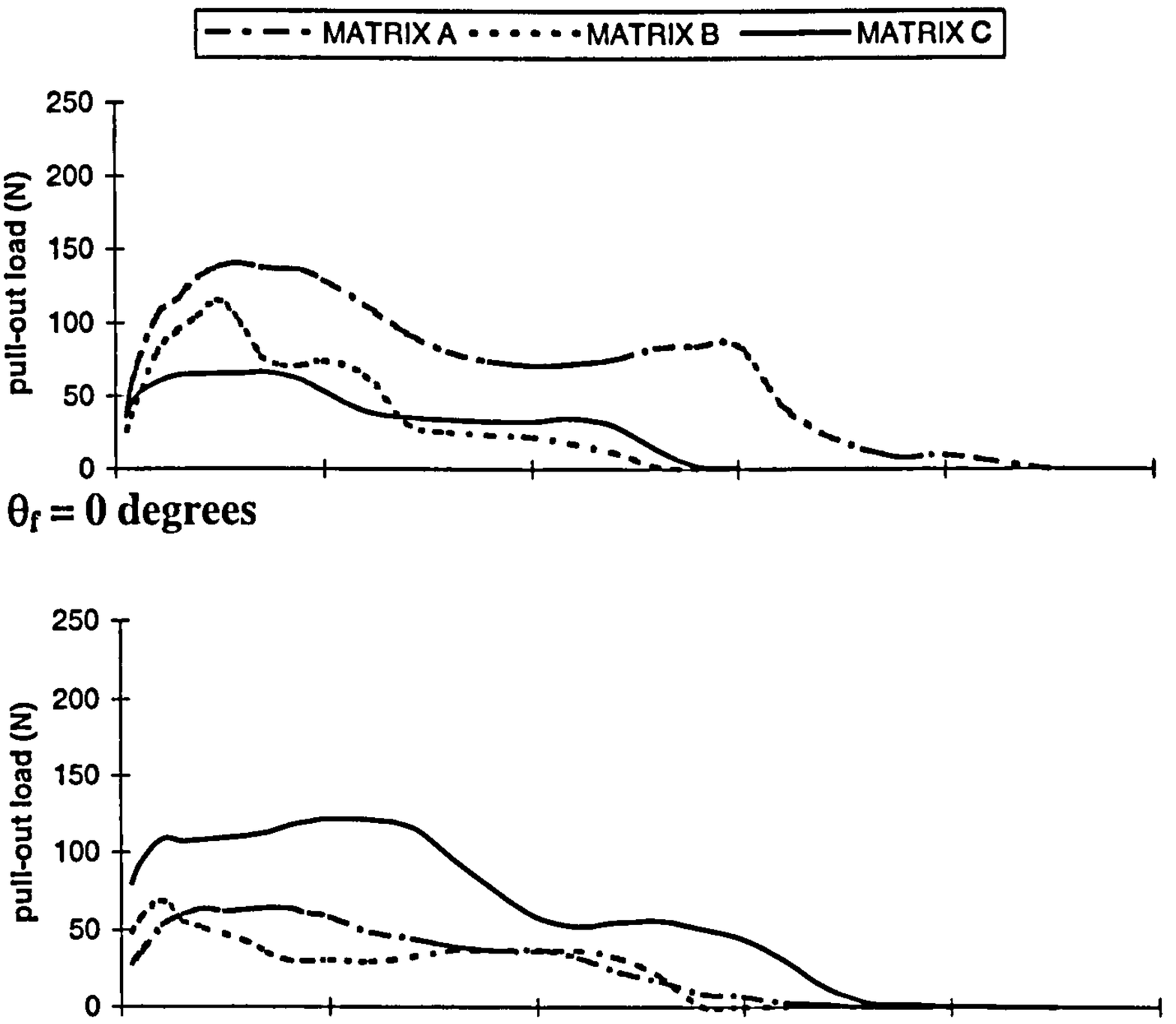

(a) θ_f = 0 degrees

(b) θ_f = 10 degrees

(c) θ_f = 30 degrees

(d) θ_f = 50 degrees

Figure 6.13 Influence of matrix strength on pull-out response (fibre embedment length = 5mm).

The influence of fibre embedment length can be more easily observed in Figure 6.11, which shows for Matrix C the pull-out responses in terms of fibre embedment length at fibre orientations of 0, 10, 30, and 50 degrees. Similar trends were also displayed by Matrix A and B. In general the response of the fibres with embedment lengths of 10, 15 and 20mm are essentially the same at each respective fibre orientation, with the maximum pull-out load occurring close to the ultimate tensile strength of the fibres (≅225N or 1150MPa). However, in the case of the fibres with a 5mm embedment length the magnitude and shape of the pull-out response curves are significantly different, with the maximum pull-out load occurring at a much reduced value between 40-120 N.

In addition, the full embedded fibre length was rarely pulled-out. More commonly the fibres were pulled out completely at crack-widths between 1-2mm less than the embedment length set during specimen manufacture. This indicated that the position and profile of the specimen fracture was rarely coincident with the face of the brass insert (that is, the point from which embedment lengths were set during specimen manufacture).

These results suggest that the pull-out response of a hooked-end fibre, at a given fibre orientation, is predominantly influenced by the mobilisation and straightening of the hooked-end. Full mobilisation and straightening can only occur if the fibre embedment length is greater than the length of the hooked-end. Given that the length of the hooked-end is typically 4mm long (Table 5.4), fibres with embedment lengths less than this value will not be fully mobilised, resulting in a reduced pull-out response

Matrix strength

The influence of matrix strength on pull-out behaviour is shown in Figure 6.12 for a 15mm fibre embedment length at orientations of 0, 10, 30 and 50 degrees. It can be seen that the magnitude of the pull-out response appears to be directly related to matrix strength at fibre orientations of 0 and 10 degrees; that is a higher matrix strength results in a higher pull-out load at a given crack-with. However, at fibre orientations of 30 and 50 degrees there is no distinguishable matrix strength influence on the pull-out response. This suggests that as fibre orientation increases, fibre pull-out behaviour becomes increasingly more influenced by the metallurgical properties of

the steel fibres as they attempt to straighten in-line with the direction of the pull out force, and increasingly less influenced by the strength of the cementitious matrix. In contrast, the corresponding curves for a 5mm embedment lengths shown in Figure 6.13 - where the hooked-end is not fully mobilised - show no such trend, and the magnitude of the pull-out response appears to be influenced by the actual length of fibre remaining in the specimen following matrix fracture, irrespective of matrix strength or fibre orientation.

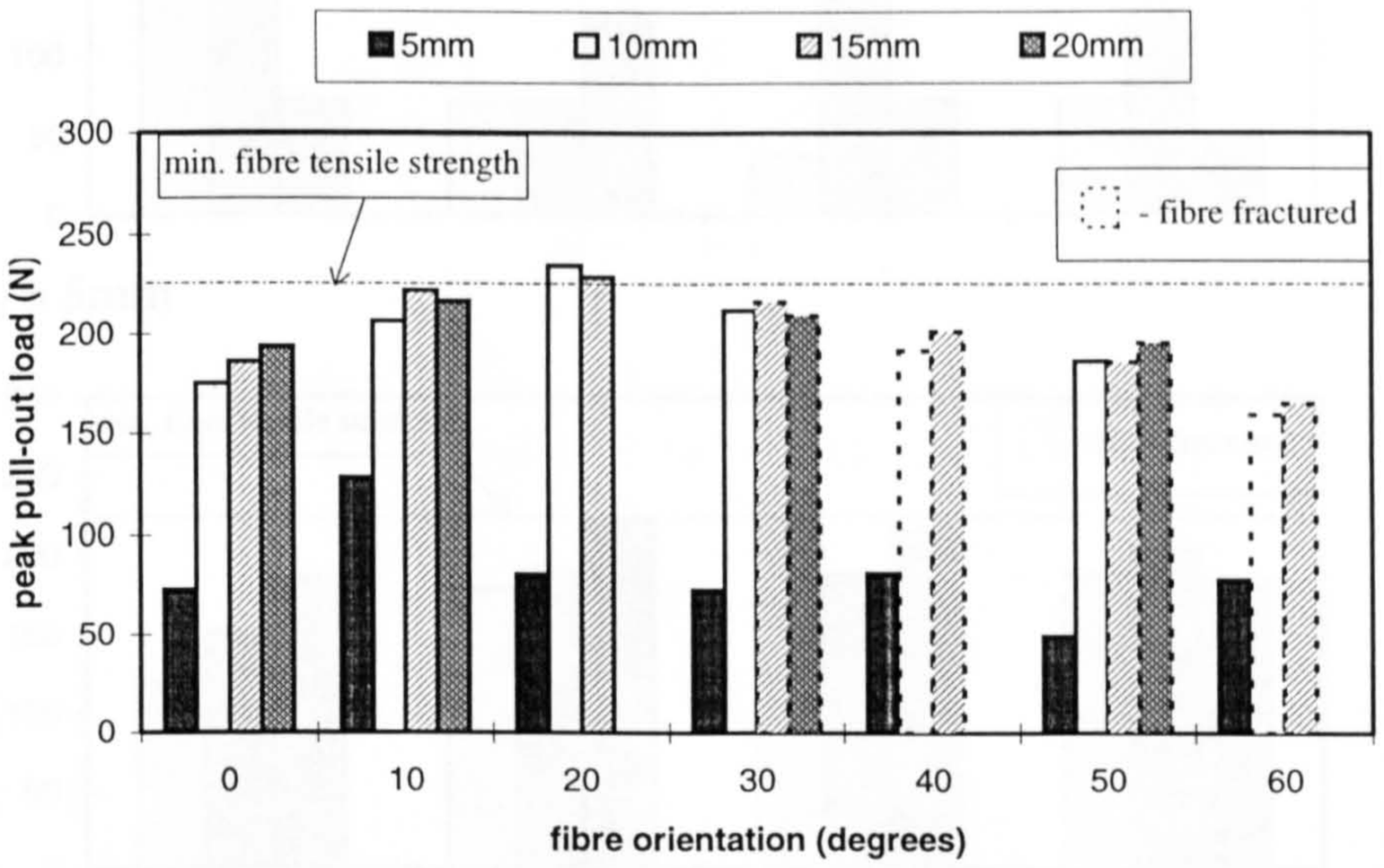

Figure 6.14 Influence of fibre orientation and embedment length on peak pull-out load (Matrix C).

Peak fibre pull-out load and crack-width

Figure 6.14 shows the peak fibre pull-out load (Point C in Figure 6.4) for Matrix C as a function of fibre orientation at embedment lengths of 5, 10, 15 and 20mm. Also indicated in this figure is the minimum ultimate tensile strength of the fibres as provided by the fibre manufacturer (that is, 1150MPa ≈ 225N). Similar trends were also displayed by Matrix A and B (Figure 6.15). The results indicate that providing the hooked-end is fully mobilised (that is, the embedment length is greater than 5mm) the peak pull-out load, at a given fibre orientation, essentially displays the same value irrespective of embedment length, and is maximised at approximately 20 degrees. However, at orientations greater than 20 degrees the fibre is more likely to fracture (shown dotted in Figures 6.14 and 6.15), with the fracture load appearing to decrease as fibre orientation increases. This apparent dependency of fibre orientation on peak

load is in accordance with the findings of Banthia and Trottier (1994) who reported the peak-load of hooked-end fibres (with an embedment length of half the total fibre length) to maximise at between 15-30 degrees.

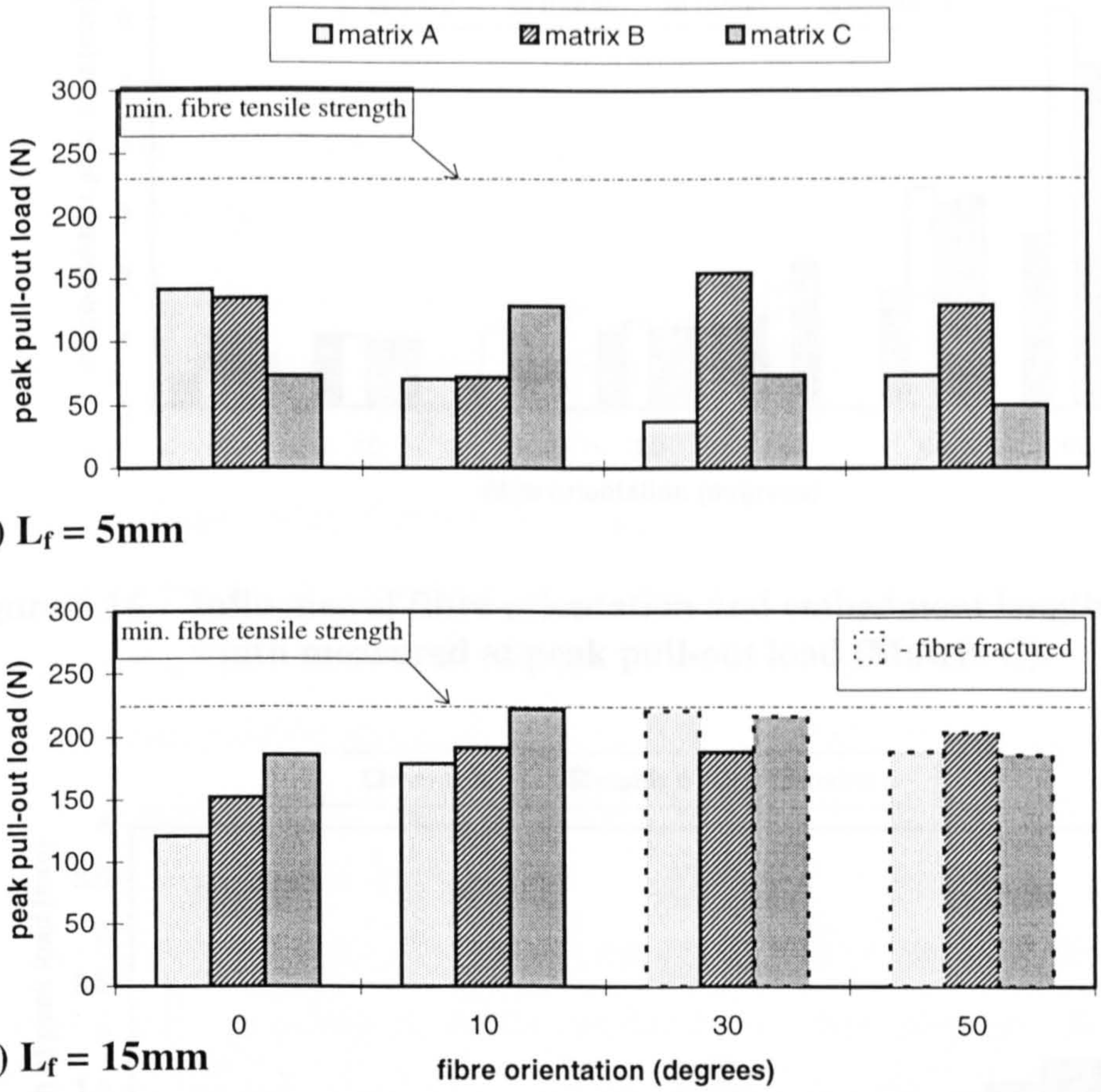

(a) L_f = 5mm

(b) L_f = 15mm

Figure 6.15 Influence of matrix strength on peak pull-out load.

In contrast, the peak load for the fibres with an embedment length of 5mm generally remains unchanged (Figure 6.14) irrespective of fibre orientation, which suggests that fibre orientation has a minor influence on pull-out behaviour when the hooked-end is not fully mobilised.

The average crack-widths measured at the peak pull-out load for Matrix C as a function of fibre orientation at embedment lengths of 5, 10, 15 and 20mm are shown in Figure 6.16. Similar trends were also displayed by Matrix A and B (Figure 6.17). In general, the crack-width at peak load increases as the inclination angle increases for all the fibre embedment lengths investigated. This is also in accordance with the findings of Banthia and Trottier (1994). Furthermore, the crack-width at peak load is

generally independent of fibre embedment length providing the hooked-end is fully mobilised.

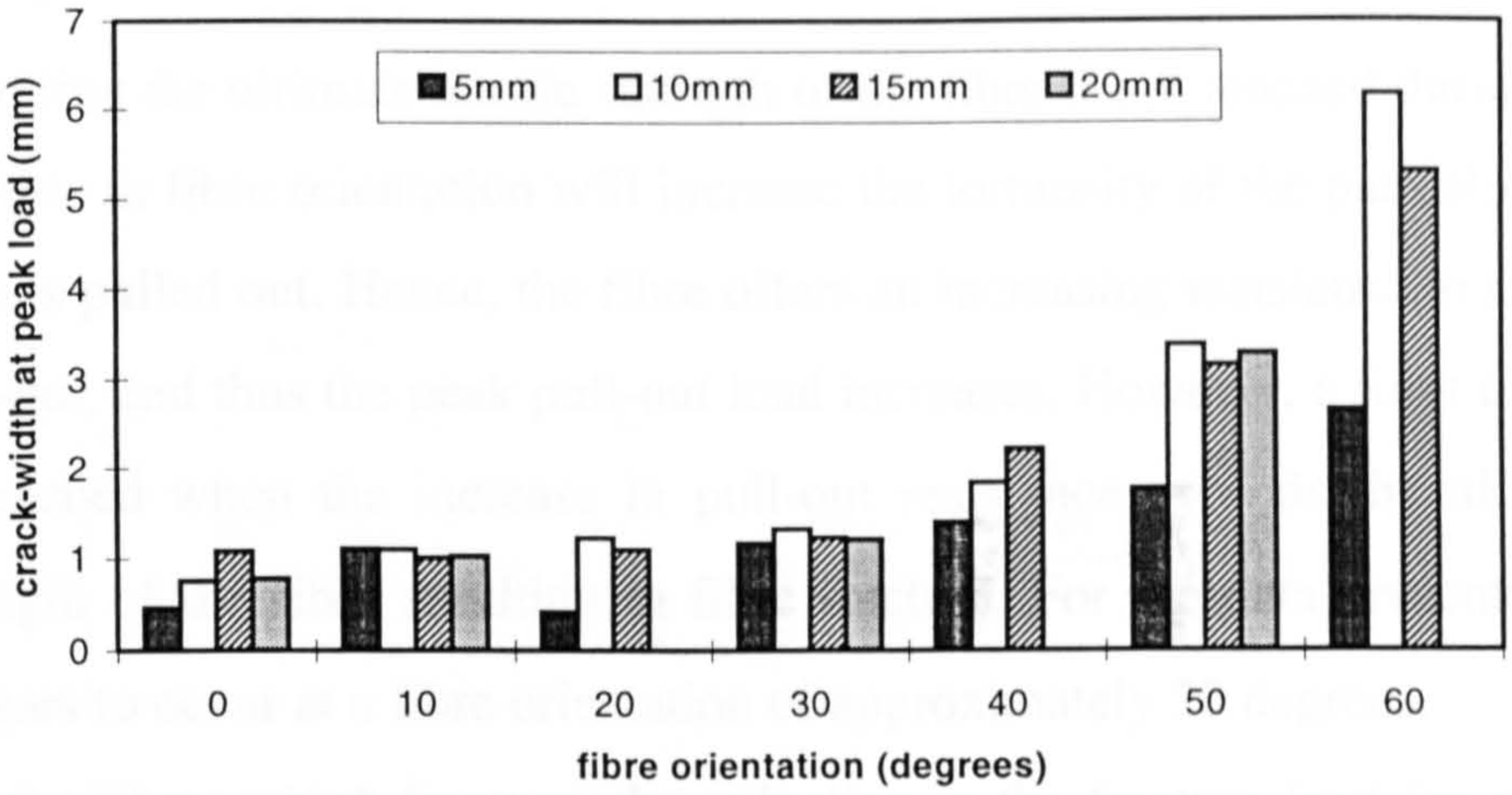

Figure 6.16 Influence of fibre orientation and embedment length on the crack-width measured at peak pull-out load (Matrix C).

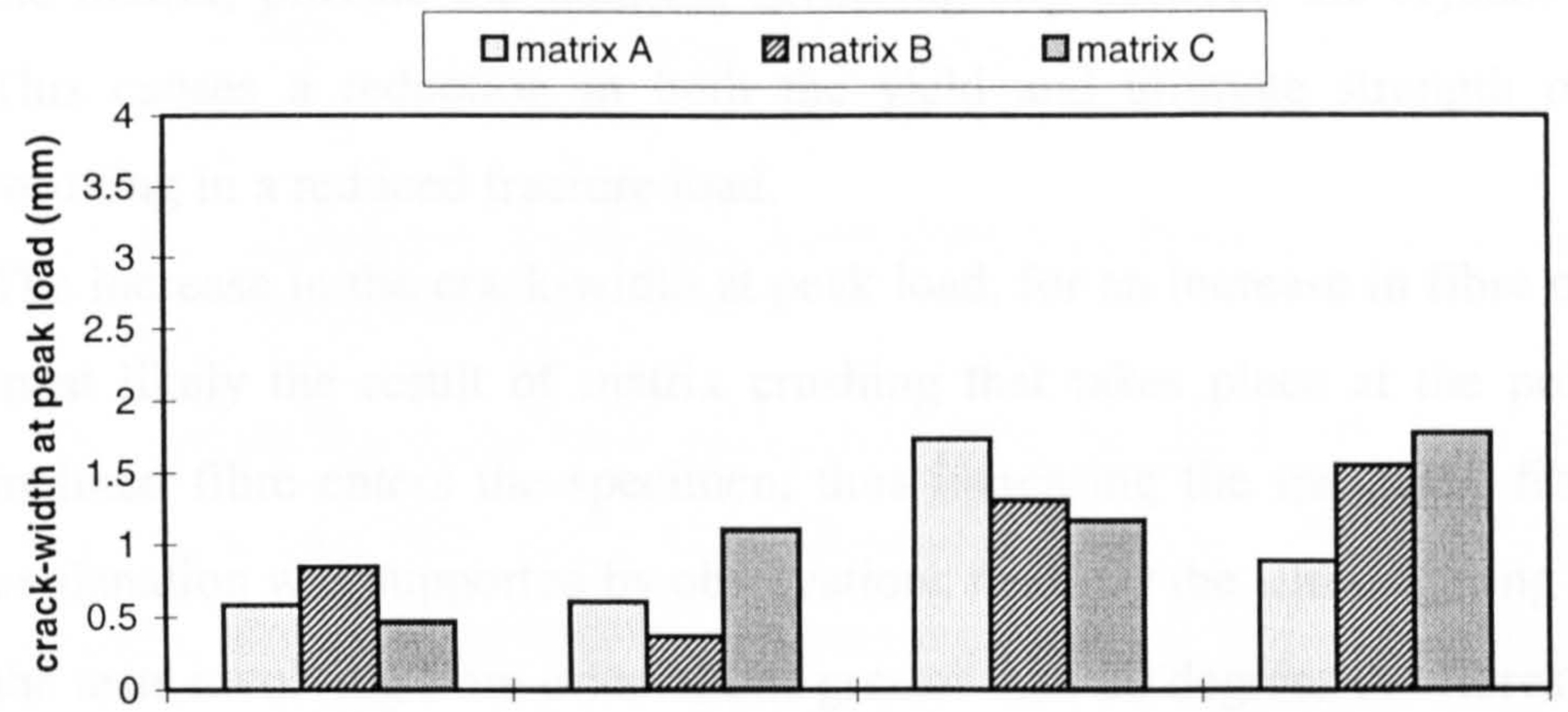

(a) L_f = 5mm

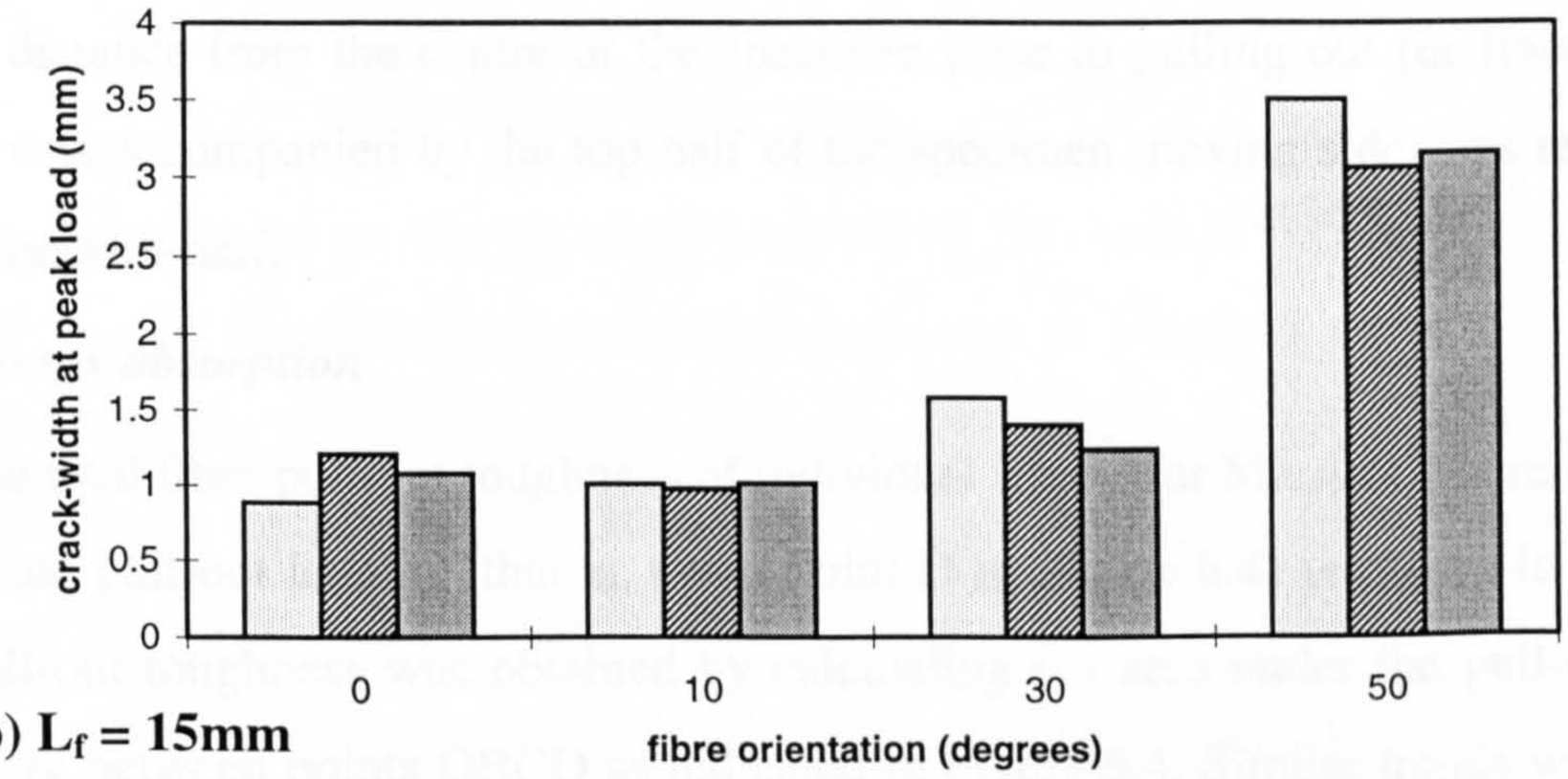

(b) L_f = 15mm

Figure 6.17 Influence of matrix strength on the crack-width measured at peak pull-out load.

The influence of fibre orientation on peak pull-out load, and on the crack-width at peak pull-out load, indicated by the pull-out test results can be explained by the following.

i. Providing the ultimate tensile strength of the fibre is not reached during the test, an increase in fibre orientation will increase the tortuosity of the path along which the fibre is pulled out. Hence, the fibre offers an increasing resistance to straighten and pull-out, and thus the peak pull-out load increases. However, a limit to this process is reached when the increase in pull-out resistance exceeds the ultimate tensile strength of the fibre resulting in fibre fracture. For the data presented, this limit appears to occur at a fibre orientation of approximately 20 degrees.
ii. For the fibres which fracture, the reduction in the fracture load for an increase in fibre orientation is probably best explained by Banthia and Trottier (1994). They suggest that additional shear stresses imposed on inclined fibres, where they enter the matrix, provide mechanisms favouring slip between the crystals in the steel. This causes a reduction in both the yield and ultimate strength of the fibres, resulting in a reduced fracture load.
iii. The increase in the crack-width at peak load, for an increase in fibre orientation, is most likely the result of matrix crushing that takes place at the point where an inclined fibre enters the specimen, thus increasing the measured fibre slip. This explanation was supported by observations made by the author during the tests. For the tests involving fibre orientations greater than 20 degrees the fibres did not pull-out from the centre of the specimen, but crushed the matrix to a point at some distance from the centre of the specimen prior to pulling-out (or fracturing). This was accompanied by the top-half of the specimen moving sideways relative to the bottom-half.

Energy absorption

The total fibre pull-out toughness of individual fibres, for Matrix C, in relation to their actual pull-out lengths (that is, up to Point D in Figure 6.4) is shown in Figure 6.18. Pull-out toughness was obtained by calculating the area under the pull-out response curve between points OBCD as indicated in Figure 6.4. Similar trends were observed for Matrix A and B. In general Figure 6.18 shows that as the total pull-out length increases so the total pull-out toughness increases, but the relationship is non-linear up

to an embedment length of approximately 5mm. However, at greater fibre embedment lengths the relationship appears to be linear. This suggests that the energy required to straighten the hooked-end has a constant value, and that once the hooked-end is straightened the additional energy required to completely pull-out the fibre is linearly proportional to the fibre embedment length remaining in the specimen.

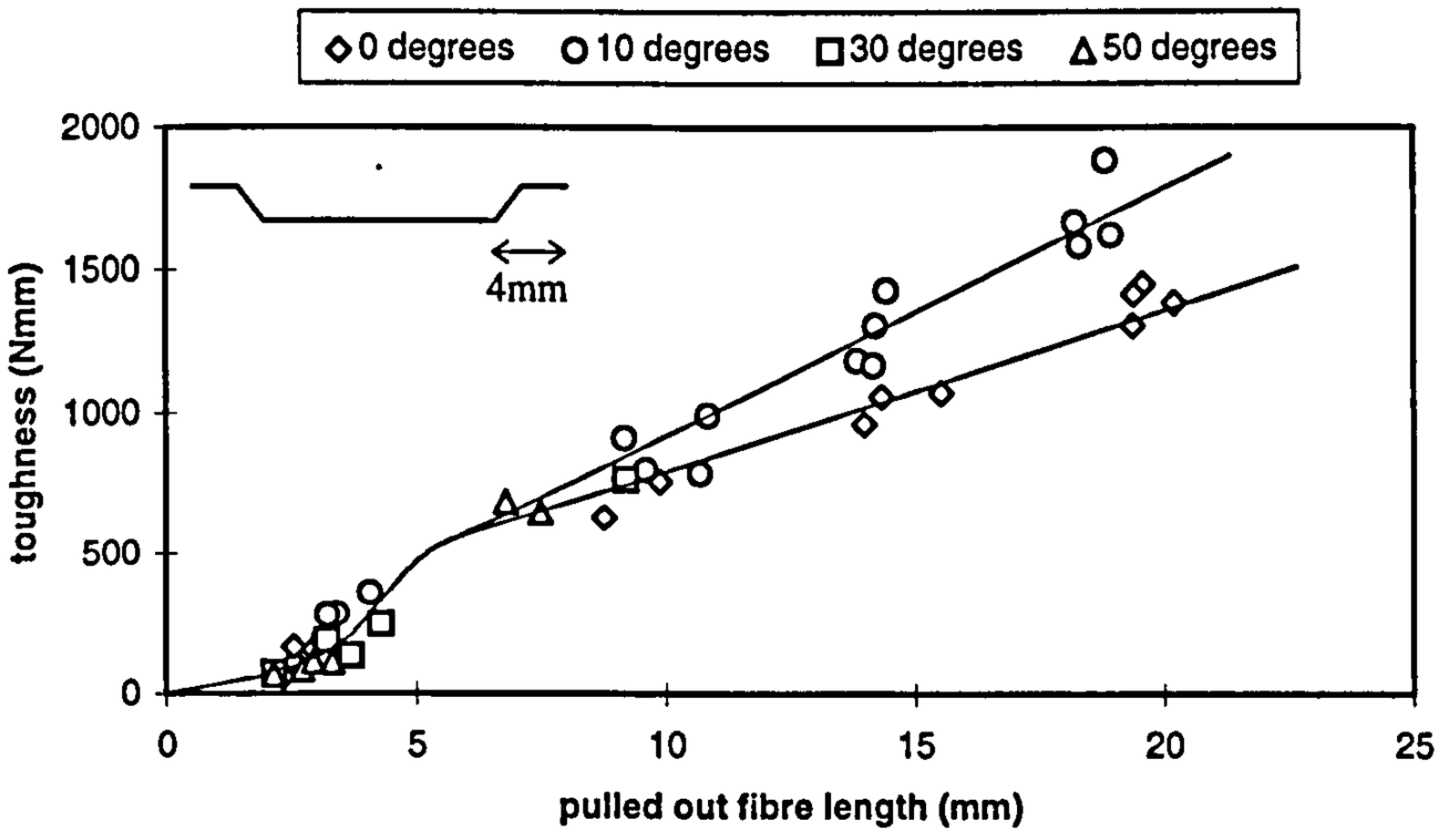

Figure 6.18 Influence of the pulled out fibre length on total fibre pull-out toughness (Matrix C).

Note the variability in the total pull-out lengths for the 5, 10, 15 and 20mm fibre embedment shown in Figure 6.18: 2-4mm, 7-12mm, 13-16mm and 17-21mm respectively. As previously mentioned, this is caused by the exact position and profile of the specimen fracture being rarely coincident with the face of the brass insert (the point from which embedment lengths were measured during specimen casting), thus affecting the actual pulled out fibre lengths.

In addition to measuring the total toughness of the fibres in pulling out along their full embedment lengths, a measure of toughness up to a certain value of crack-width is more relevant to the proposed model. Average values of pull-out toughness up to a crack-width of 1.2mm and 4.0mm as a function of fibre orientation for Matrix C specimens with fibre embedment lengths of 5, 10, 15 and 20mm, are shown in Figure 6.19. Note the reduction in toughness values indicated by Figure 6.19(b), due to an increase in the number of fibre fractures, for fibre embedment lengths greater than 5mm and fibre orientations greater than 20 degrees. The influence of fibre orientation on the energy absorbed is clearly observed in these figures, with a maximum

toughness value occurring at approximately 10-20 degrees. A similar trend was also displayed by Matrix A and B (Figure 6.20). Note these results are consistent with the findings of Banthia and Trottier (1994) who reported the maximum pull-out toughness of hooked-end fibres to occur at approximately 15-30 degrees. In addition, providing the hooked-end is fully mobilised (that is, the fibre embedment length is greater than 5mm), the fibre embedment length does not appear to influence the value of toughness for a given fibre orientation. Toughness also appears to converge towards a constant value, as fibre orientation increases, irrespective of fibre embedment length.

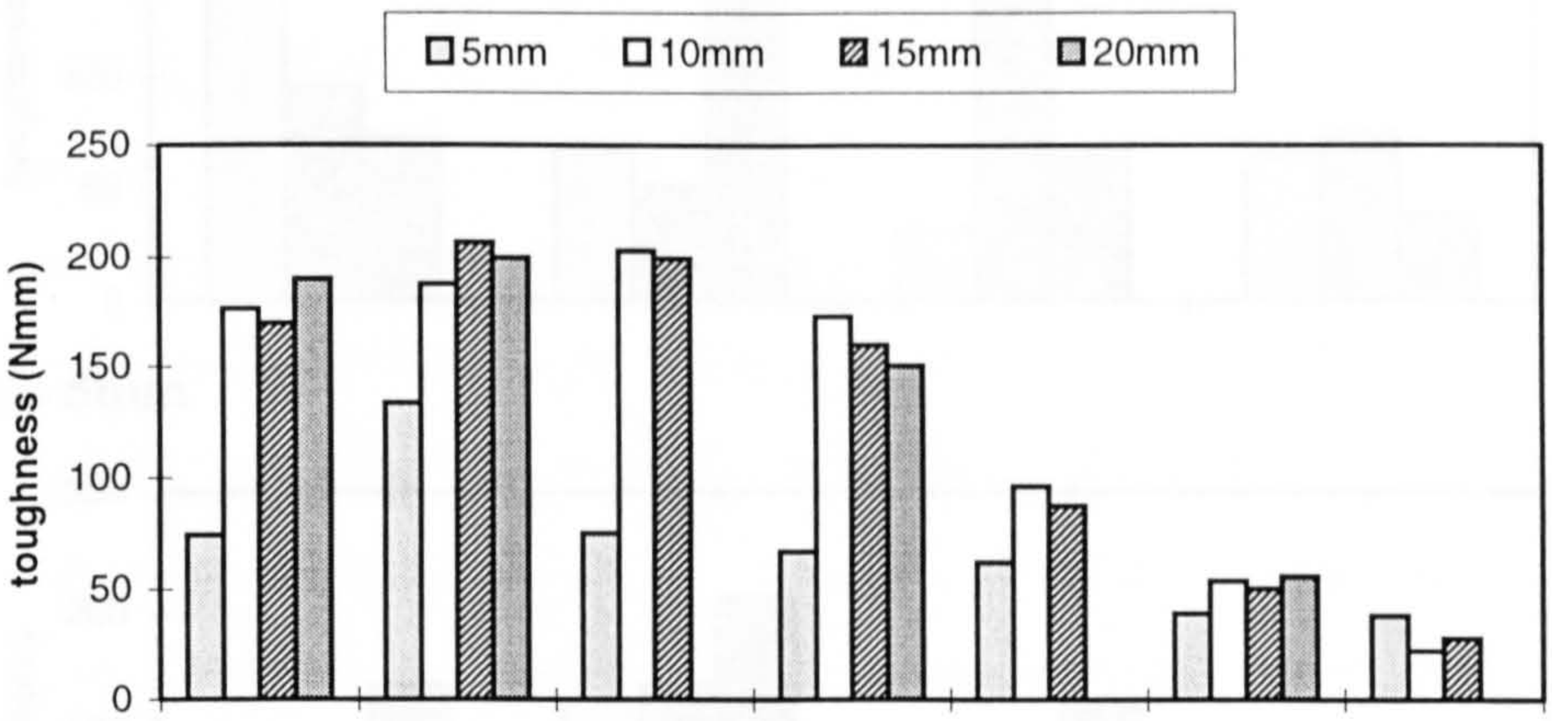

Figure 6.19 Influence of fibre orientation and embedment length on fibre pull-out toughness up to a crack-width of (a) 1.2mm and (b) 4.0mm (Matrix C).

Also note from Figure 6.20 the effect of matrix strength on the post fracture toughness of individual fibres with embedment lengths of 5mm and 15mm. It can be seen that at fibre orientations of 0 and 10 degrees the pull-out toughness appears to be directly related to matrix strength when the hooked-end is fully mobilised (Figure 6.20(b));

that is a higher matrix strength results in a higher pull-out toughness. However, when the hooked-end is not fully mobilised (Figure 6.20(a)) or at orientations greater than 30 degrees (Figure 6.20(b)) there is no distinguishable matrix strength influence. This result is in accordance with the trends observed in Figure 6.12.

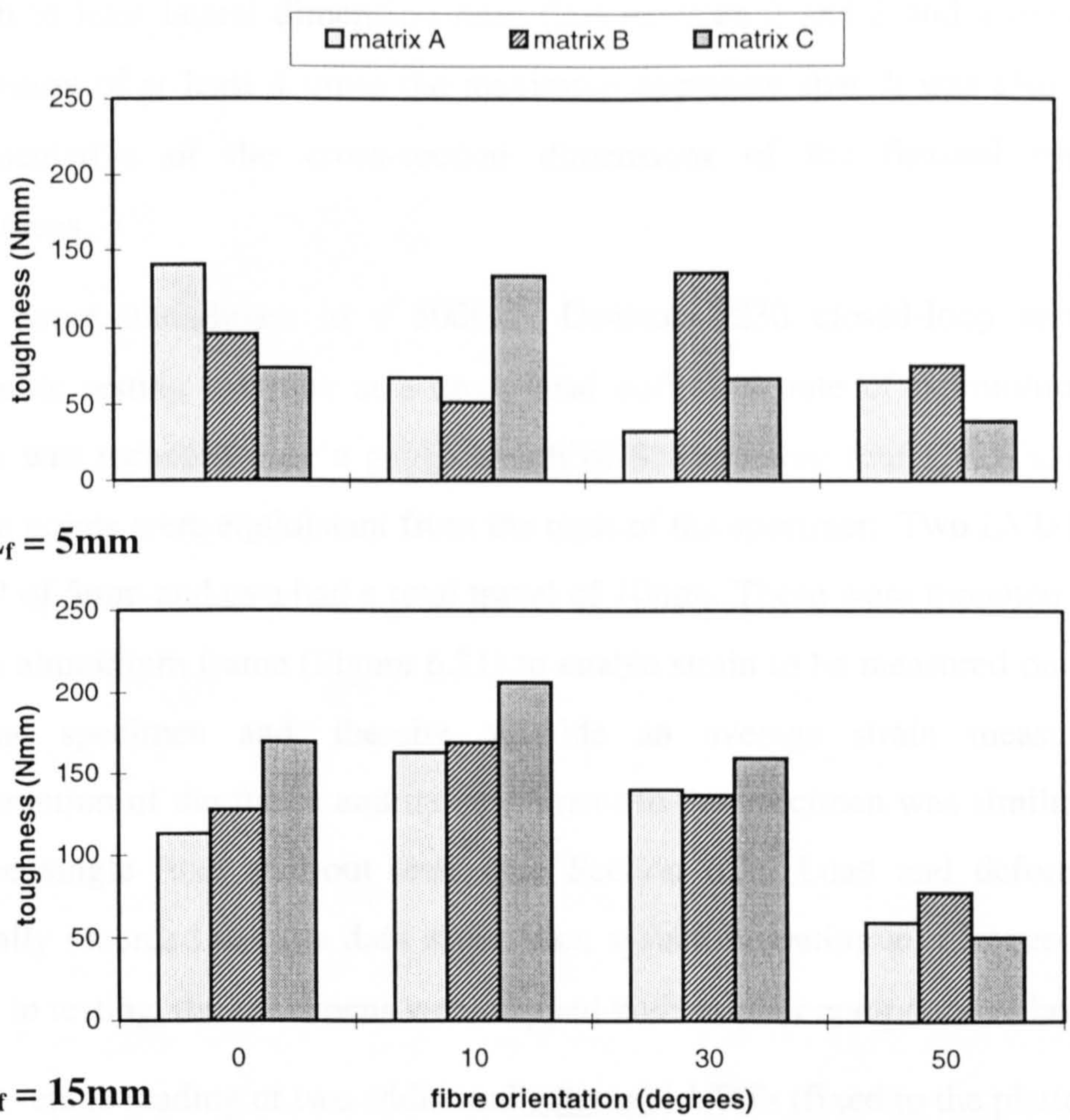

(a) L_f = 5mm

(b) L_f = 15mm

Figure 6.20 Influence of matrix strength on fibre pull-out toughness up to a crack-width of 1.2mm at embedment lengths of (a) 5mm and (b) 15mm.

6.4 COMPRESSIVE STRESS-STRAIN TESTS

6.4.1 Background

The main objective of these tests was to determine the stress-strain properties of the plain and fibre reinforced mixes under investigation. A test was developed based on the recommendations detailed in Section 3.3.3 and BS1881: Part 121 (1983) for the determination of the static modulus of elasticity in compression.

6.4.2 Test procedure

Prism specimens nominally measuring 76 x 76 x 229 mm were either cast using steel moulds or sawn from sprayed concrete panels. This specimen size was chosen to comply with the recommendations given in Section 3.3.3 in terms of a specimen length to least lateral dimension ratio (l/d) between 2 and 5 and a minimum lateral dimension of at least 4 times the maximum aggregate size. It was also chosen to be representative of the cross-section dimensions of the flexural toughness test specimens.

Tests were undertaken in a 5000kN Denison 7230 closed-loop servo-controlled hydraulic testing machine at a cross-head deflection rate of 0.5mm/min. Specimen strain was recorded over a gauge length of 85mm using four LVDTs, such that the gauge points were equidistant from the ends of the specimen. Two LVDTs had a total travel of 5mm and two had a total travel of 10mm. These were mounted on a purpose made aluminium frame (Figure 6.21) to enable strain to be measured on all four sides of the specimen and, thereby, provide an average strain measurement. The construction of the frame and its attachment to the specimen was similar to that used in the single fibre pull-out tests (see Section 6.3). Load and deformations were digitally recorded using a data acquisition system operating at a frequency of 0.2Hz. Prior to testing, the specimens were capped with sulphur compound at both ends.

The average reading of two additional external LVDTs (fixed to the plattens of the test machine) was used as the feedback signal to control the closed-loop test system and maintain the predetermined cross-head deflection rate.

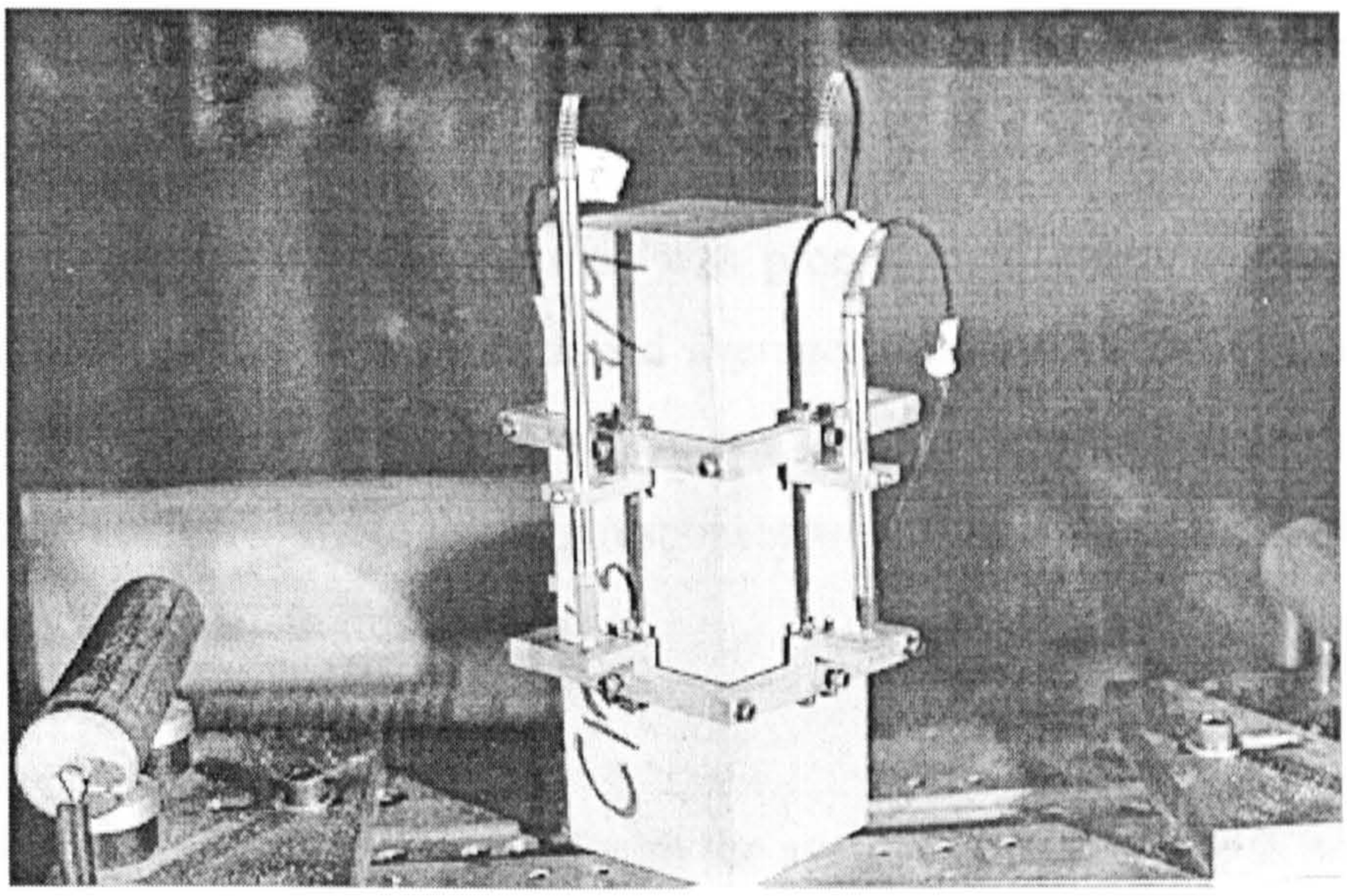

Figure 6.21 Compression specimen showing the LVDT mounting frame.

The test procedure was based on the standard procedure for the determination of the static secant modulus of elasticity as detailed in BS1881: Part 121 (1983) as follows.

- The compressive strength of the concrete mix under investigation was initially determined from three standard cubes in accordance with BS 1881: Part 116 (1983).
- The test specimen was then located centrally in the test machine, a basic stress of 0.5MPa was applied and the LVDT readings zeroed.
- Further stress was then applied until one-third of the compressive strength of the concrete was reached $\sigma_{1/3}$. This stress was maintained for 60 seconds and the LVDT readings recorded during the succeeding 30 seconds.
- The individual LVDT readings were then checked to be within $\pm 10\%$ of their mean value at $\sigma_{1/3}$. If they were not the specimen was recentered and the test repeated.
- Once the specimen was sufficiently centred the applied stress was reduced back to zero, and after an interval of 60 seconds the test started.
- Specimens were generally tested up to a maximum strain of 3500 microstrain.

The sensitivity and accuracy of the LVDTs and the 5000kN load cell are detailed in Table 6.4.

6.4.3 Results and discussion

Curve averaging

The data obtained from each specimen was processed to obtain an applied stress versus strain. From this data a combined average stress versus strain response was determined for each series of three specimens (i.e. for each combination of matrix type and fibre content). These average responses were then used in the analysis of the test results as presented in this section.

Test repeatability

The coefficient of variation associated with the average applied stress as a function of strain for all the cast and sprayed test series is presented in Figure 6.22. In general the coefficient of variation varied between 1-4% for the cast specimens and between 2-5% for the sprayed specimens, which indicates excellent test repeatability. The slightly higher variability associated with the sprayed specimens was most likely caused by a higher variability in specimen dimensions, squareness and parallelism, as a result of being sawn from sprayed panels and not cast in moulds.

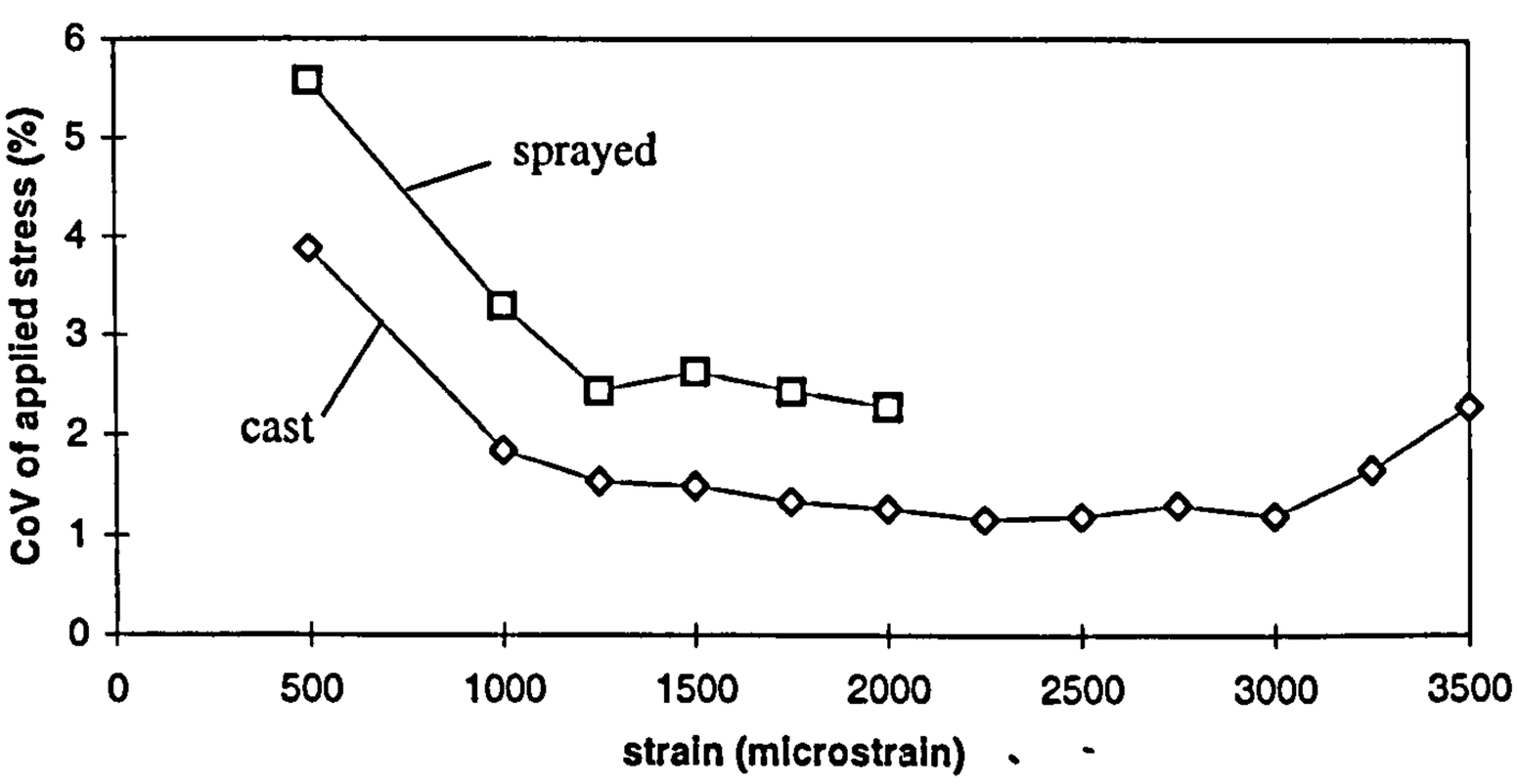

Figure 6.22 Influence of casting method on the coefficient of variation associated with the applied compressive stress.

Fibre content and matrix strength

Figure 6.23 shows the influence of fibre content on the compressive stress versus strain responses for Matrix A, B and C. For each matrix type, it can be seen that the influence of hooked-end steel fibres on the shape and magnitude of the compressive

response up to a strain of 3500 microstrain can be considered negligible for fibre contents less than 120kg/m^3 (i.e. 1.5% by volume).

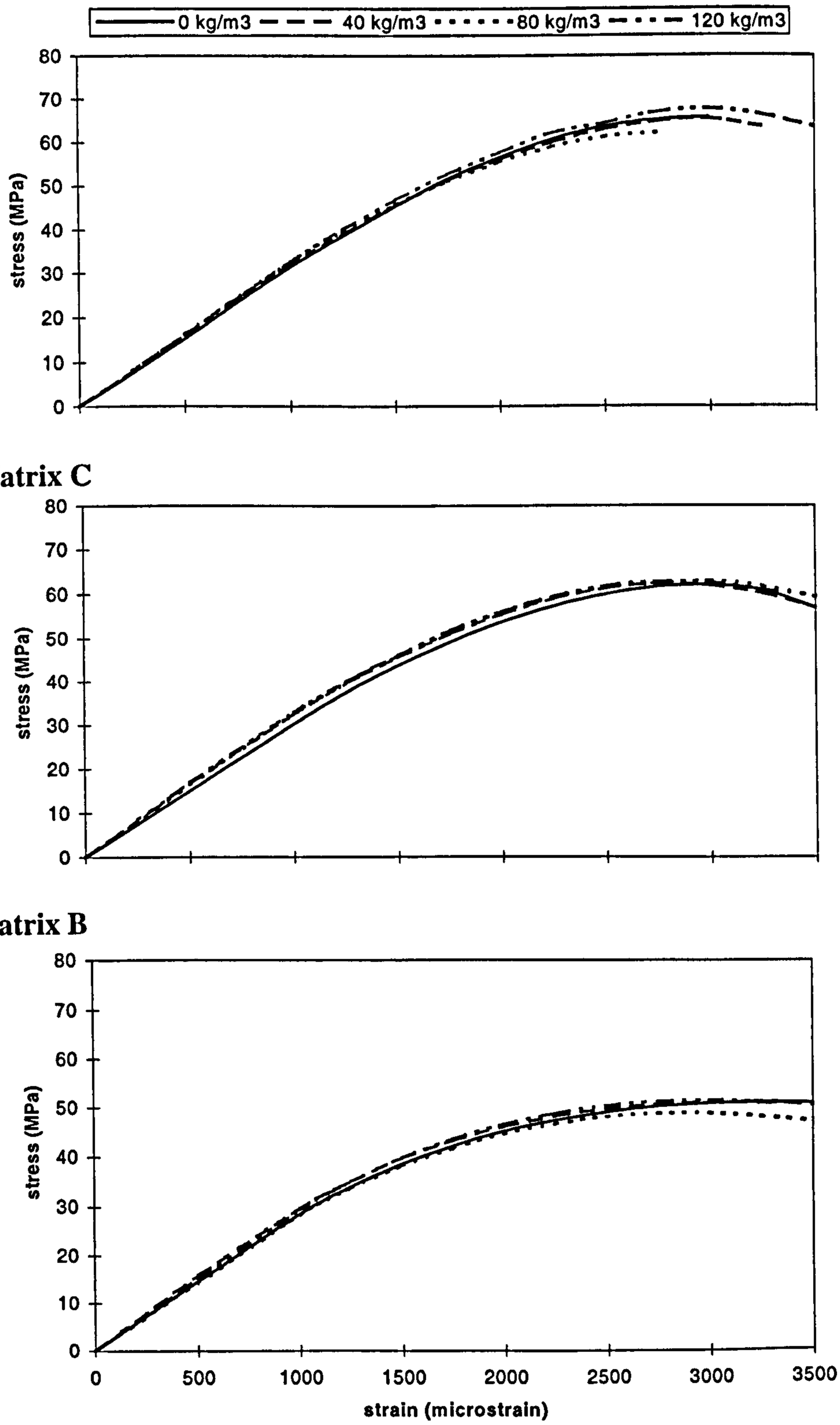

(a) Matrix C

(b) Matrix B

(c) Matrix A

Figure 6.23 Influence of fibre content on the compressive stress-strain response for Matrix A, B and C.

Figure 6.24 shows the influence of matrix type on the shape and magnitude of the compressive stress versus strain curve at a fibre content of 40kg/m^3. Similar trends were observed with fibre contents of 0, 80 and 120kg/m^3. As expected the higher strength matrices Matrix B and Matrix C, containing silica fume additions of 5 and 10% respectively, produced the greatest compressive responses for all the fibre contents considered. However, note the enhancement in compressive behaviour between Matrix A and Matrix B is significantly greater than between Matrix B and Matrix C. This is discussed later under 'peak stress and strain at peak stress'.

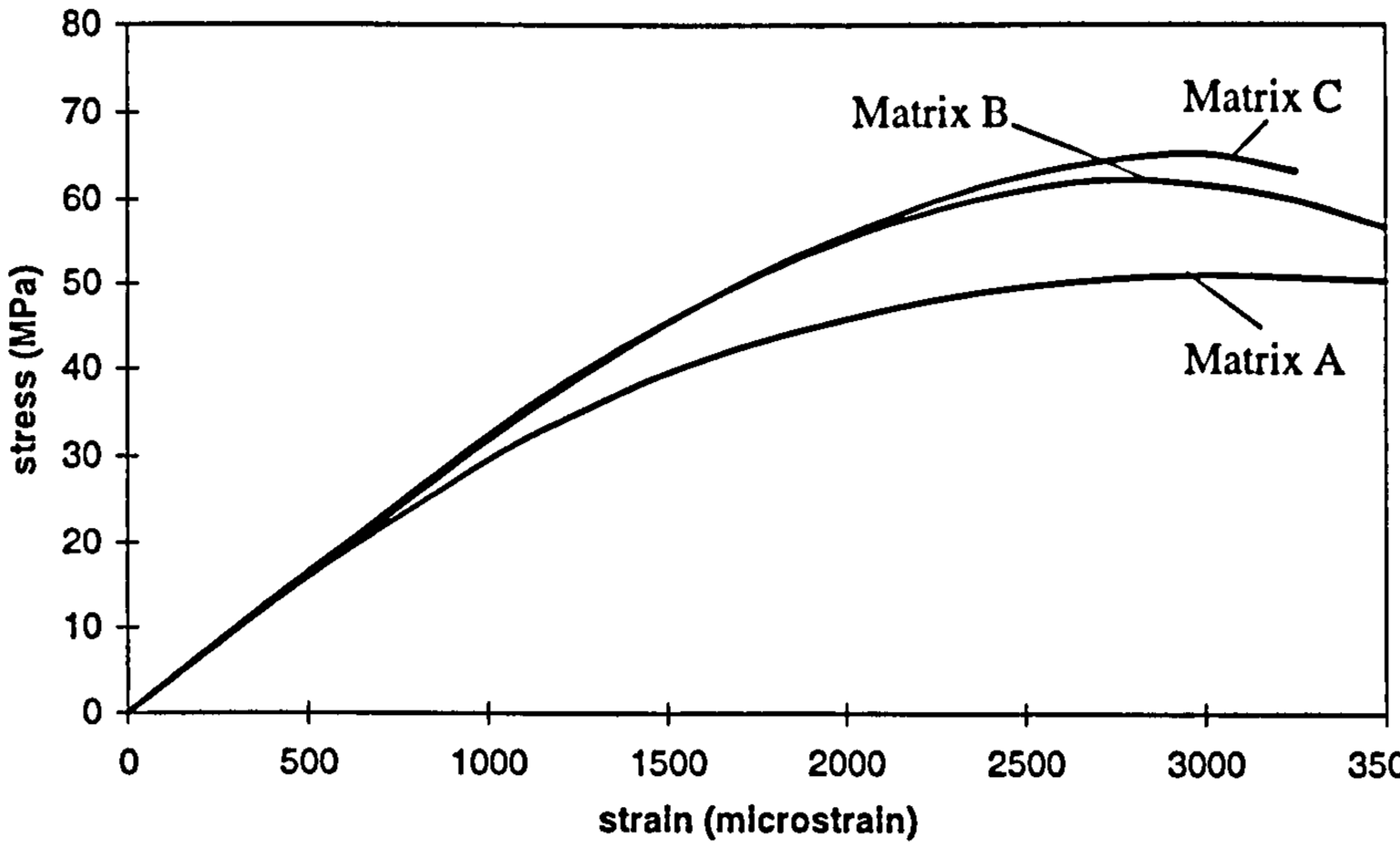

Figure 6.24 Influence of matrix strength on compressive stress-strain behaviour (fibre content - 40kg/m^3 equivalent to 0.5% by volume).

Cast versus sprayed

Figure 6.25 compares the compressive behaviour of the cast and sprayed specimens for Matrix A, B and C. Note that the sprayed specimens were more prone to a premature splitting failure mode (as opposed to the conventional crushing failure mode) than the cast specimens. This seemed to be caused by the poor squareness and parallelism of the sprayed specimens as a result of them being sawn. Therefore, a complete stress-strain response up to a strain of 3500 microstrain was not always obtained from the sprayed specimens (Figure 6.25). Nevertheless, the results show for all three matrix types that there was essentially no difference between the compressive behaviour of the cast and sprayed specimens used in this investigation. This is an important result in the context of this thesis, as it provides evidence to indicate similar behaviour between cast and sprayed steel fibre reinforced concrete made using

equivalent mix designs. However, this result does not agree with the findings of Banthia *et al.* (1994b) who reported wet process steel fibre reinforced sprayed concrete specimens developing higher compressive strengths than equivalent cast specimens.

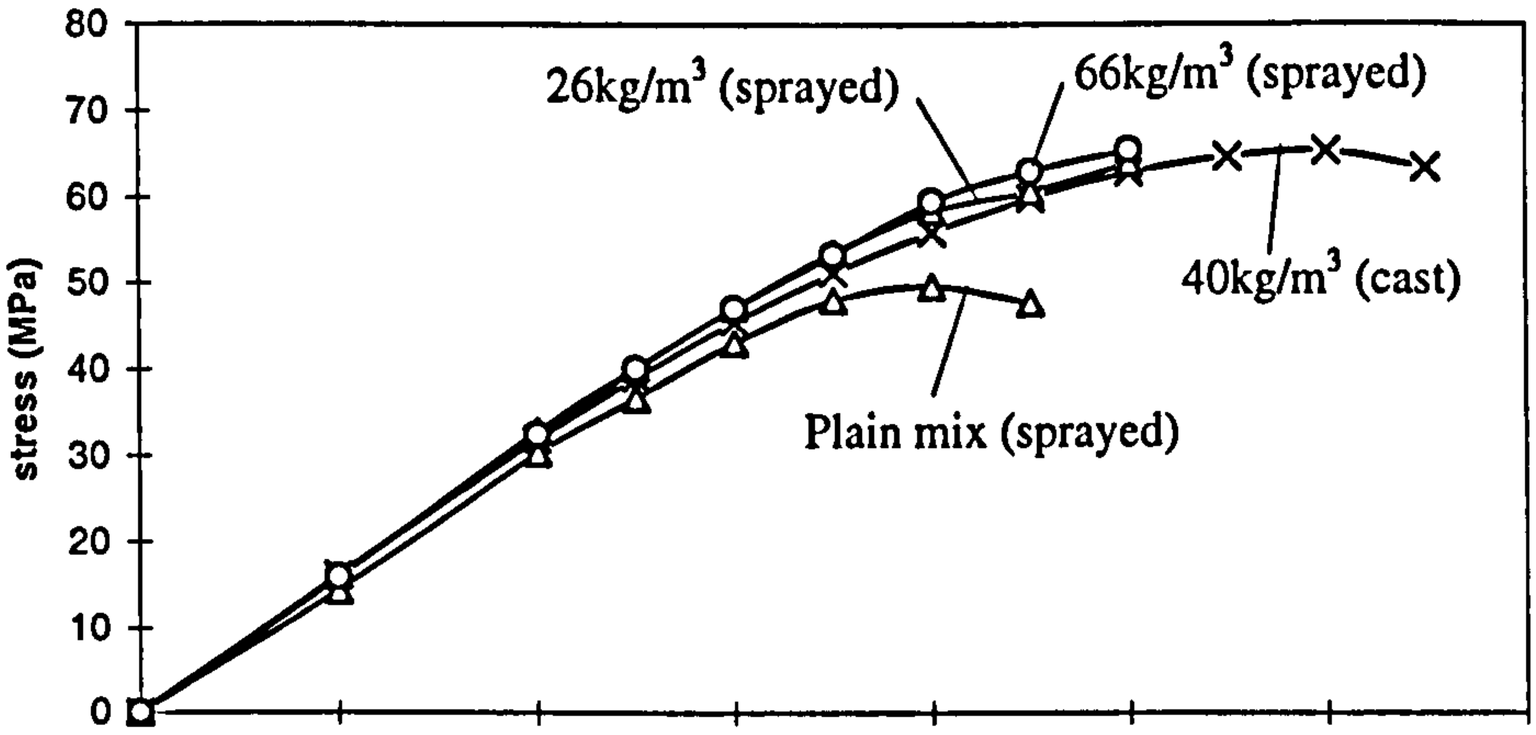

(a) Matrix C

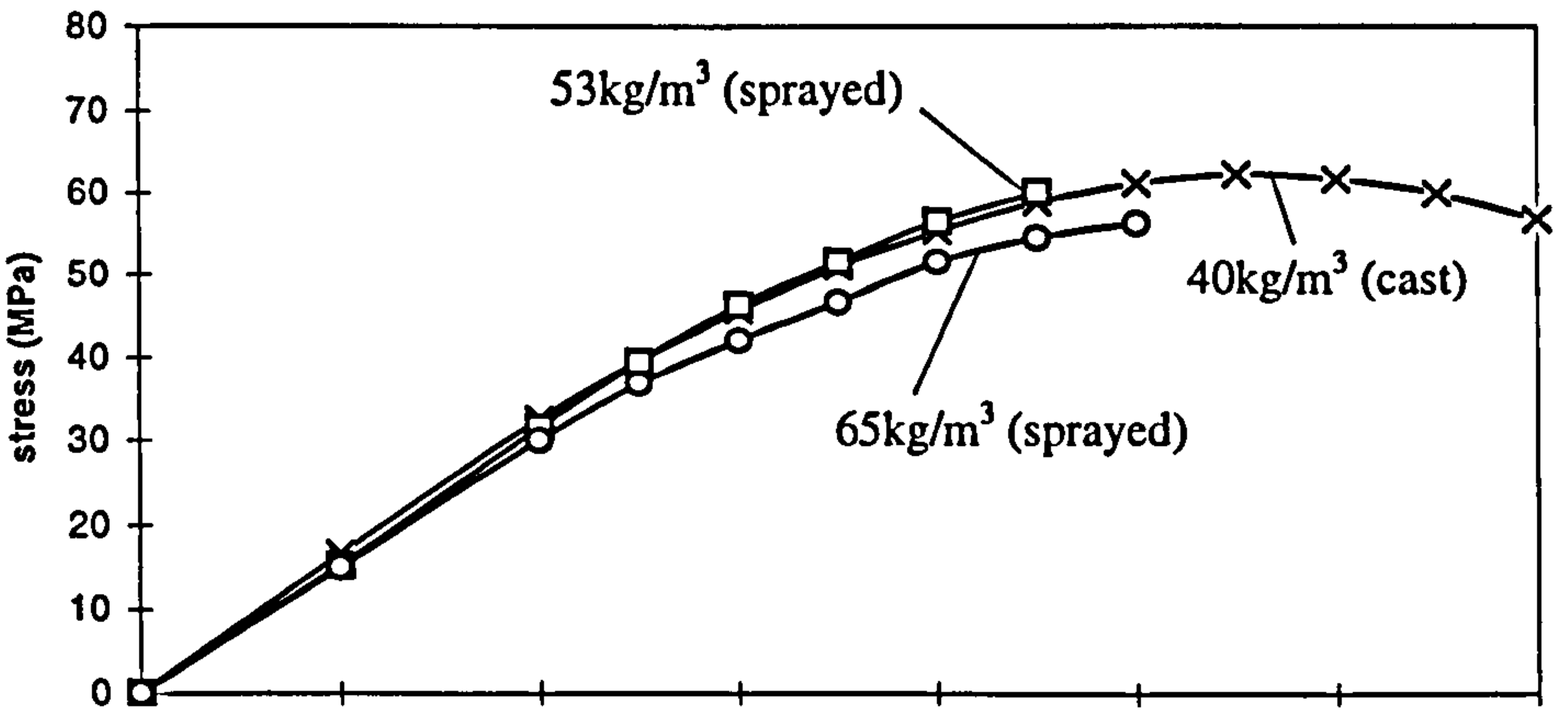

(b) Matrix B

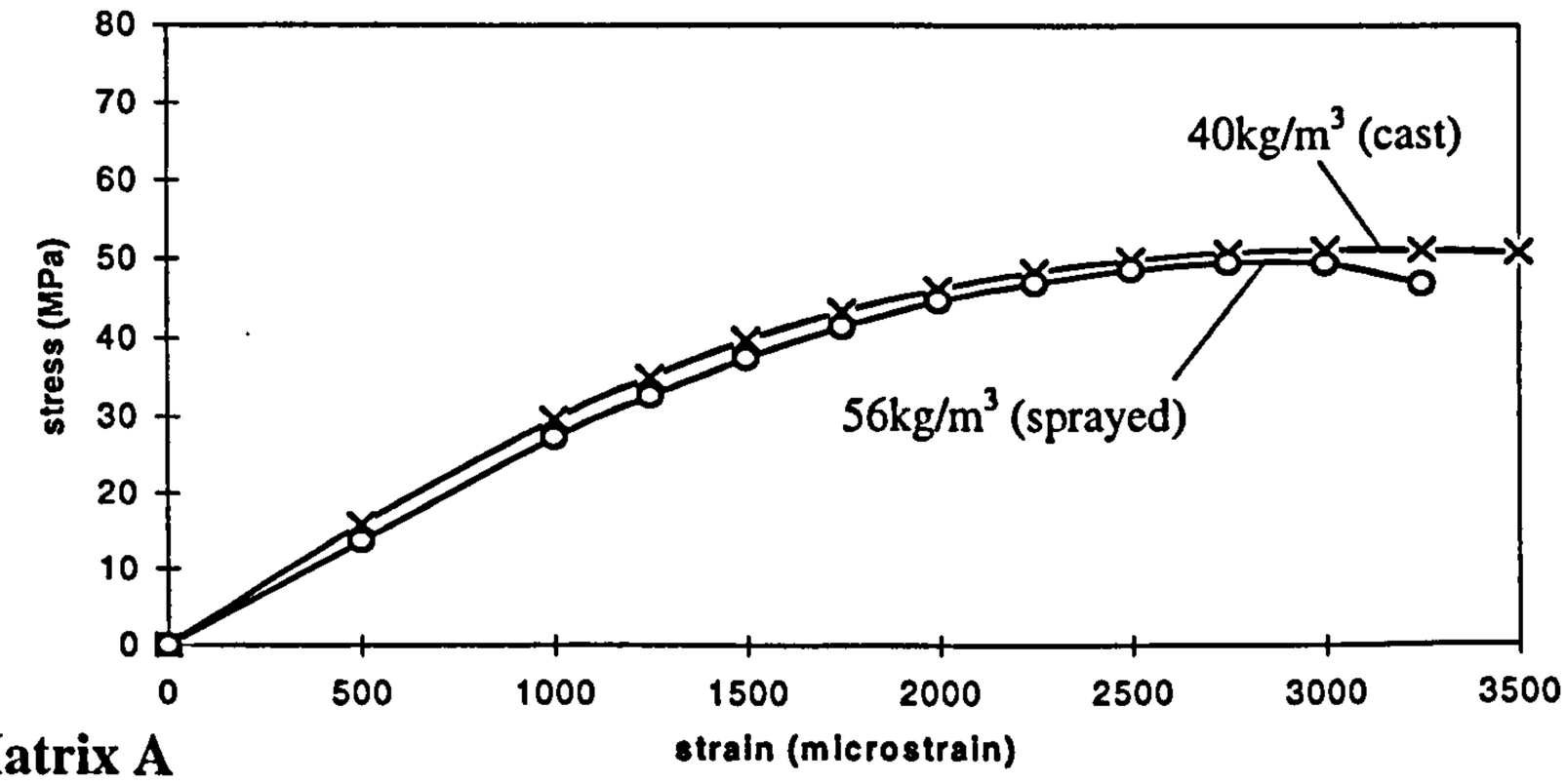

(c) Matrix A

Figure 6.25 Comparison between the compressive behaviour of sprayed and cast specimens made using an equivalent concrete mix.

Peak stress and strain at peak stress

Peak stress (or compressive strength) as a function of fibre content is shown in Figure 6.26 for Matrix A, B and C. The results show, for each matrix type, that peak stress is generally not influenced by fibre content up to 120kg/m^3. Average values for each matrix type are: Matrix A - 51 MPa (SD 1.2); Matrix B - 62 MPa (SD 0.4); and Matrix C - 65MPa (SD 1.8). These results are in accordance with the findings of other researchers (Section 3.3.3) who also reported that peak strength is not significantly influenced by the addition of fibres at contents less than 120kg/m^3. Furthermore, the data shows an increase in peak stress with an increase in silica fume addition. The magnitude of the strength increase is greater between Matrix A and B (between 0 and 5% addition of silica fume) than between Matrix B and C (between 5 and 10% addition of silica fume).

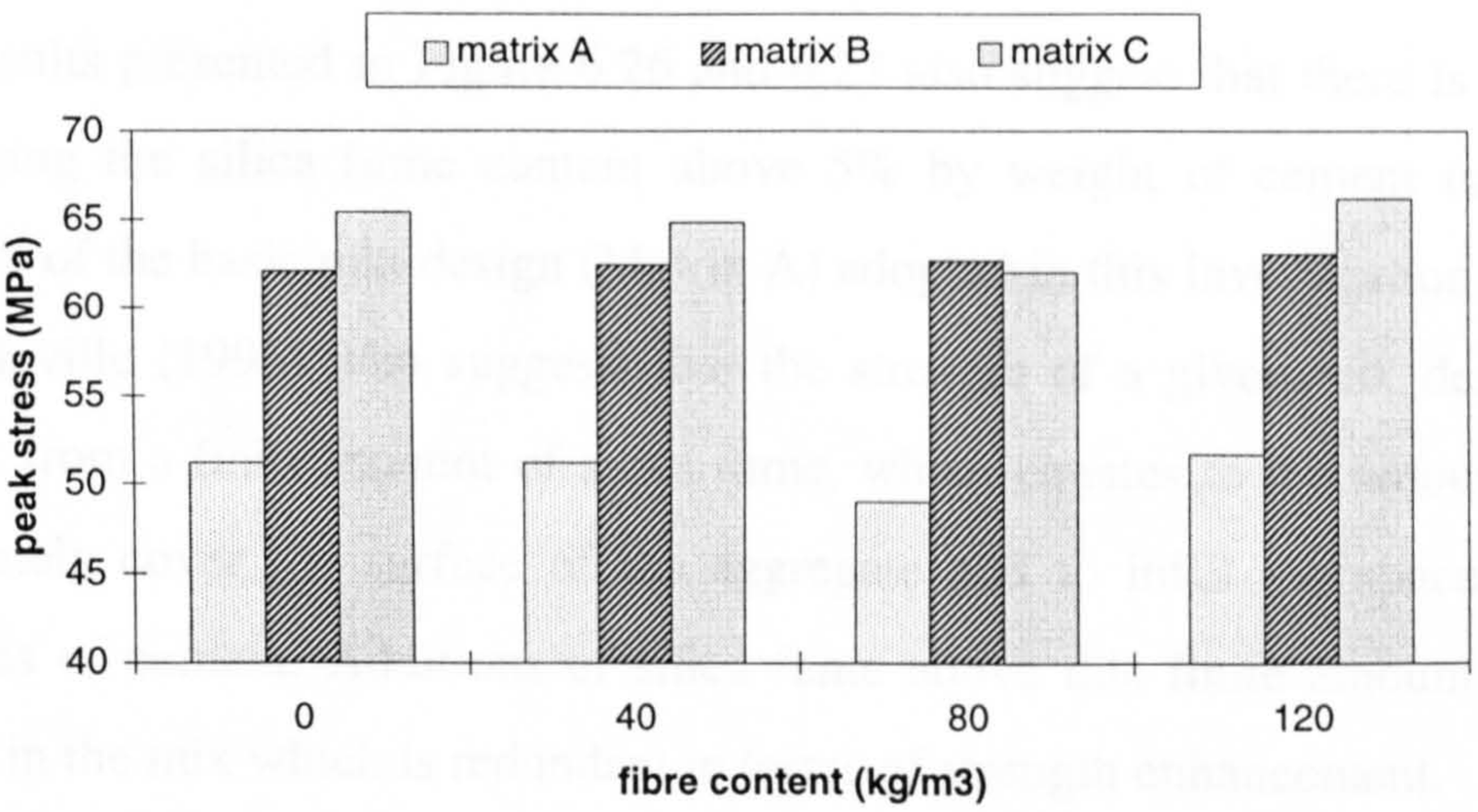

Figure 6.26 Influence of fibre content on peak compressive stress (76 x 76 x 229mm prism specimens).

Figure 6.27 shows the strain at peak stress as a function of fibre content for Matrix A, B and C. The results show, for each matrix type, that strain at peak stress remains virtually unchanged up to a fibre content of 120kg/m^3. Average strain values for each matrix type are: Matrix A - 3055 microstrain (SD 137); Matrix B - 2865 microstrain (SD 84); and Matrix C - 2815 microstrain (SD 58). These values indicate that an

increase in the silica fume content may also increase the brittleness of the matrix and thereby reducing the strain measured at peak stress.

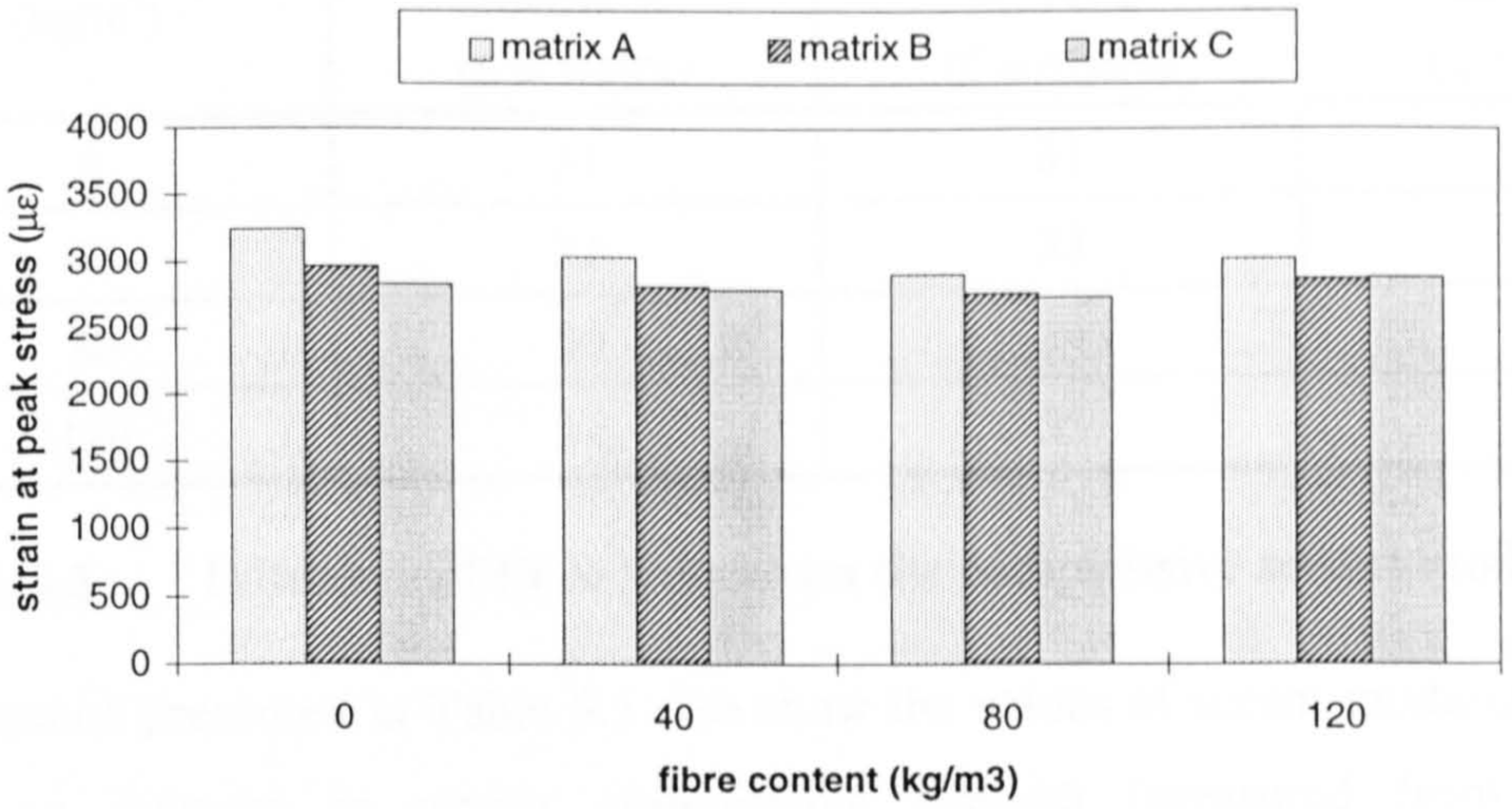

Figure 6.27 Influence of fibre content on the strain measured at peak stress (76 x 76 x 229mm prism specimens).

The results presented in Figure 6.26 and 6.27 also suggest that there is little value in increasing the silica fume content above 5% by weight of cement to enhance the strength of the basic mix design (Matrix A) adopted in this investigation. This accords with Neville (1995) who suggests that the strength of a given mix design can only benefit from a finite amount of silica fume, which equates to the amount required to completely cover the surface of the aggregate and to infill the space between the particles of cement. Additions of silica fume above this finite amount result in an excess in the mix which is redundant in terms of strength enhancement.

Elastic modulus

Table 6.5 shows the compressive secant modulus - determined from the test data in accordance with BS1881: Part 121 (1983) - for all the cast matrices used in the investigation. It can be seen that for all the mixes investigated the value of secant modulus remains virtually unchanged up to a fibre content of 120kg/m^3. Average values for each matrix are: Matrix A - 31 GPa (SD 0.8); Matrix B - 33GPa (SD 1.3); and Matrix C 33 GPa (SD 0.9). Corresponding values for the sprayed specimens could not be determined because the stress versus strain response up to peak load was not always recorded. However, an inspection of Figure 6.25 shows similar gradients in the

initial portion of the curves for both cast and sprayed specimens indicating similar values for the secant modulus.

Fibre content (kg/m^3)	Secant modulus (GPa)		
	Matrix A (f_c = 51MPa)	Matrix B (f_c = 63MPa)	Matrix C (f_c = 65MPa)
0	31	31	33
40	31	33	32
80	30	34	33
120	32	35	34

Table 6.5 Influence of fibre volume on the compressive secant modulus.

The results presented in Table 6.5 also show the values of secant modulus increasing with an increase in matrix compressive strength (measured from the prism specimens), although the relative increase in the value of secant modulus (≈10%) is much lower than the corresponding increase in compressive strength (≈27%). This result is in accordance with the results of other researchers who have found the modulus of elasticity (E_c) to be approximately related to compressive strength (f_c) by the expression:

$$E_c = A\sqrt{f_c} \qquad \text{equation 6.1}$$

where E_c is expressed in GPa, f_c in MPa and A is an empirical constant which is influenced by the type and proportion of aggregate in the mix and the type of test specimen used to obtain f_c (Neville, 1995). For the type of mixes and prism specimens investigated here the results showed a value of 4.1 as being the most appropriate value for this constant.

Cubes versus prisms

A comparison of the average compressive strengths obtained from the 100 x 100 x 100mm cubes (h/d ratio of 1) with the average compressive strengths obtained from the 75 x 75 x 225 mm prisms (h/d ratio of 3), for each of the cast mixes used in the investigation, is shown in Table 6.6. Note that the cube data presented in Table 6.6 has been copied from Table 5.7. It can be seen that the cube strength is consistently higher than the prism strength. For the mixes investigated the average ratio of cube strength to prism strength is 1.13 (SD 0.03). This difference in compressive strength

can be attributed to the different restraining effects of the test plattens as a result of differences in the size, shape and height to least lateral dimension ratio between the two specimen types. This is discussed in more detail by Neville (1995). However, the value of this ratio appears to agree with that expected from the relationships presented in Figure 3.6 and 3.7: (1) the size effect is negligible for specimens sizes between 100mm and 75mm (Figure 3.6); and (2) the ratio of the relative strengths between a height-diameter ratio of 1 and 3 is approximately 1.15 (Figure 3.7).

Fibre content (kg/m^3)	Cube strength (MPa)			Prism strength (MPa)		
	Matrix A	Matrix B	Matrix C	Matrix A	Matrix B	Matrix C
0	59	71	74	51	62	65
40	60	68	72	51	62	65
80	58	70	72	49	63	62
120	59	70	73	52	63	66
Average	59	69	72	51	63	65

Table 6.6 Comparison between the compressive strengths of 100mm cube and 76 x 76 x 229mm prism specimens.

6.5 FLEXURAL TOUGHNESS TESTS

6.5.1 Background

The main objectives of the flexural toughness testing programme were threefold:

- to obtain typical load-deflection curves for the plain and fibre reinforced concrete mixes used in the investigation;
- to analyse the flexural toughness performance of sprayed and cast mixes adopted in the investigation; and
- to provide specimens for the post-test fibre distribution analysis described in Section 6.7.

At the time the methodology for this thesis was being developed the flexural toughness test described in the final EFNARC specification (1996) was still under development and, therefore, had not been published. As a result, the test procedure and set-up adopted in this investigation was primarily developed by combining the recommendations detailed in Section 2.8.3 with the test described in the draft EFNARC specification (1993), and consequently it does not conform to any particular test standard.

6.5.2 Test procedure

Unnotched beam specimens were either cast in 100 x 100 x 500mm steel moulds or sawn from sprayed panels. Unnotched beam depths of 50, 75 and 100mm were achieved in the cast specimens by fixing an appropriate number of 25 x 100 x 500mm timber inserts into the mould prior to casting. In the case of the notched beams, a 10mm notch was cast into the tensile face of each beam at mid-span by attaching a 1mm thick brass plate to an appropriately sized timber insert prior to casting. The purpose of the notch was to act as a crack inducer such that the specimens cracked at the notch. Preliminary investigations using notch sizes of 2.5, 5, 10 and 15mm showed that a 10mm notch was the most suitable for the beam dimensions used in the investigation. The use of this notch size was further justified from the work of Gopalaratnam et al (1991) who reported that for a notch to beam depth ratio of less than 0.125, notched beams exhibit no noticeable notch sensitivity. Incidentally, in their study they compared notched and unnotched beams of equal depth. As a result, the ligament depth (total beam depth less notch depth) of each notched beam was smaller than the unnotched beam depth. Therefore, a true comparison of the results could not be made. In the investigation reported here the total depth of the notched beams were made 10mm greater than the equivalent unnotched beams, in order that the ligament depths were the same in both beam types. Details relating to the full range of beam sizes used in the investigation are given in Table 6.7.

Specimens were tested over a span of 450mm in third-point loading using a 100kN capacity floor-mounted Instron 6025 testing machine. Average mid-span beam deflections were measured using two LVDTs (5mm total travel) mounted on a yoke around the specimen (Figure 6.28). This enabled net mid-span deflections to be recorded exclusive of any extraneous deflections caused by seating or twisting of the

specimen on its supports. The yoke was also designed to accommodate the full range of beam sizes used in the investigation.

Specimen type		Length L (mm)	Width b (mm)	Depth d (mm)	Notch size d^* (mm)	Ligament depth $d - d^*$ (mm)
CAST	unnotched	500	100	50	0	50
	unnotched	500	100	75	0	75
	unnotched	500	100	100	0	100
	notched	500	100	60	10	50
	notched	500	100	85	10	75
SPRAYED	unnotched	500	125	75	0	75

Table 6.7 Range of beam types and sizes used in the flexural toughness tests.

Tests were performed under closed-loop deflection control using the net mid-span beam deflection as the feedback signal, which was monitored by a single Instron extensometer (10mm total travel) attached to one of the LVDTs (Figure 6.29). A mid-span deflection rate of 0.1mm/min was used to control the test up to a mid-span deflection of 1.0mm. After this, the rate was increased to 1.0mm/min. The test ended at a mid-span deflection of 4.0mm. Load and deflections were digitally recorded using a data acquisition system operating at a frequency of 0.2Hz. In addition an X-Y plotter was used to record the real time load-deflection curve as a further check that the test was progressing correctly.

In the case of the notched beams, an additional extensometer (10mm total travel) was attached across the notch (Figure 6.30) to measure the crack-mouth-opening-displacement (CMOD) during the test. Hence, load, average mid-span deflection and CMOD were measured during the notched beam tests.

The sensitivity and accuracy of the LVDTs and Instron load cell are detailed in Table 6.4.

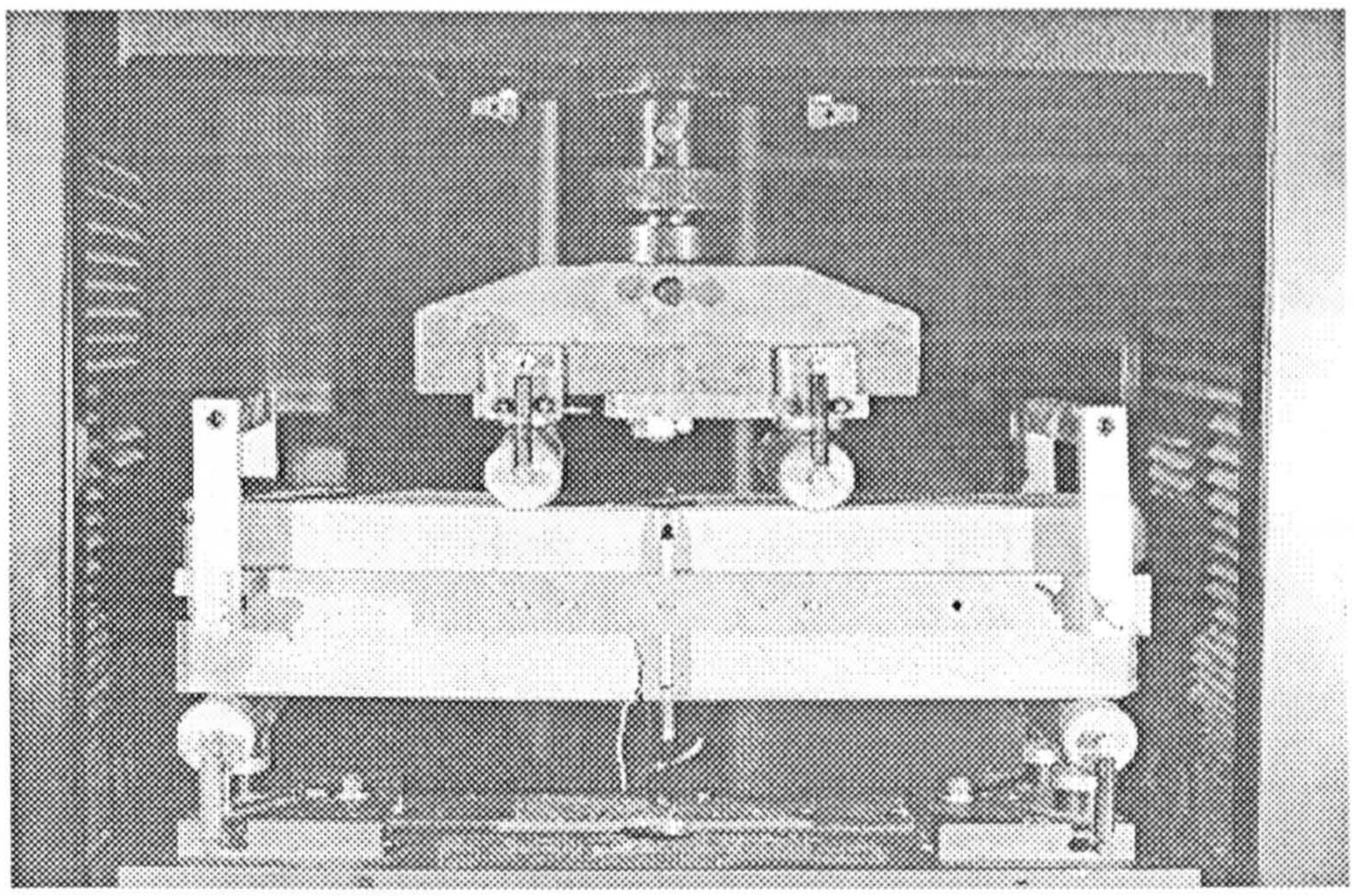

Figure 6.28 Flexural toughness specimen - front view showing the yoke and LVDT attachment.

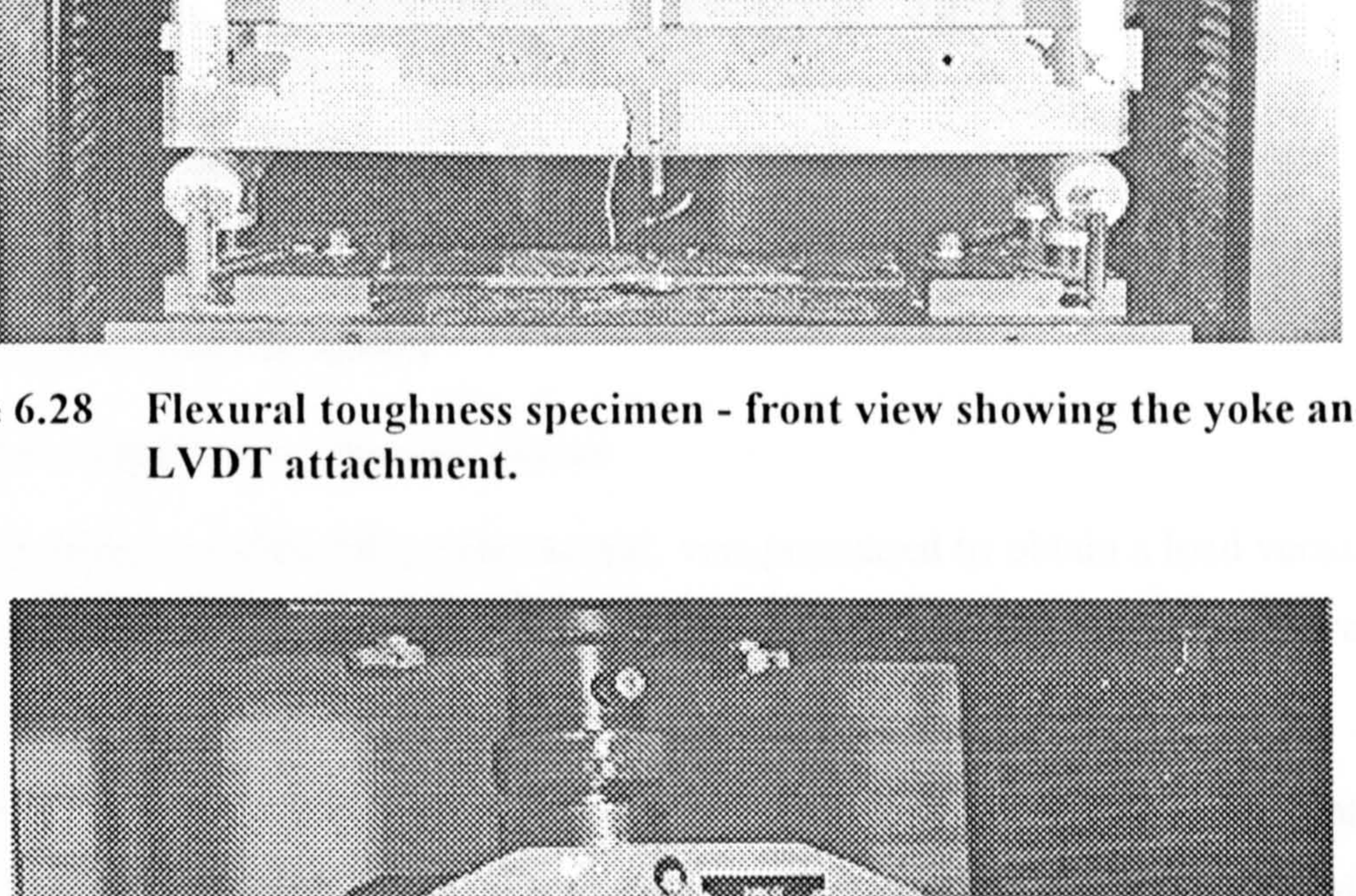

Figure 6.29 Flexural toughness specimen - rear view showing the yoke and LVDT/extensometer attachment.

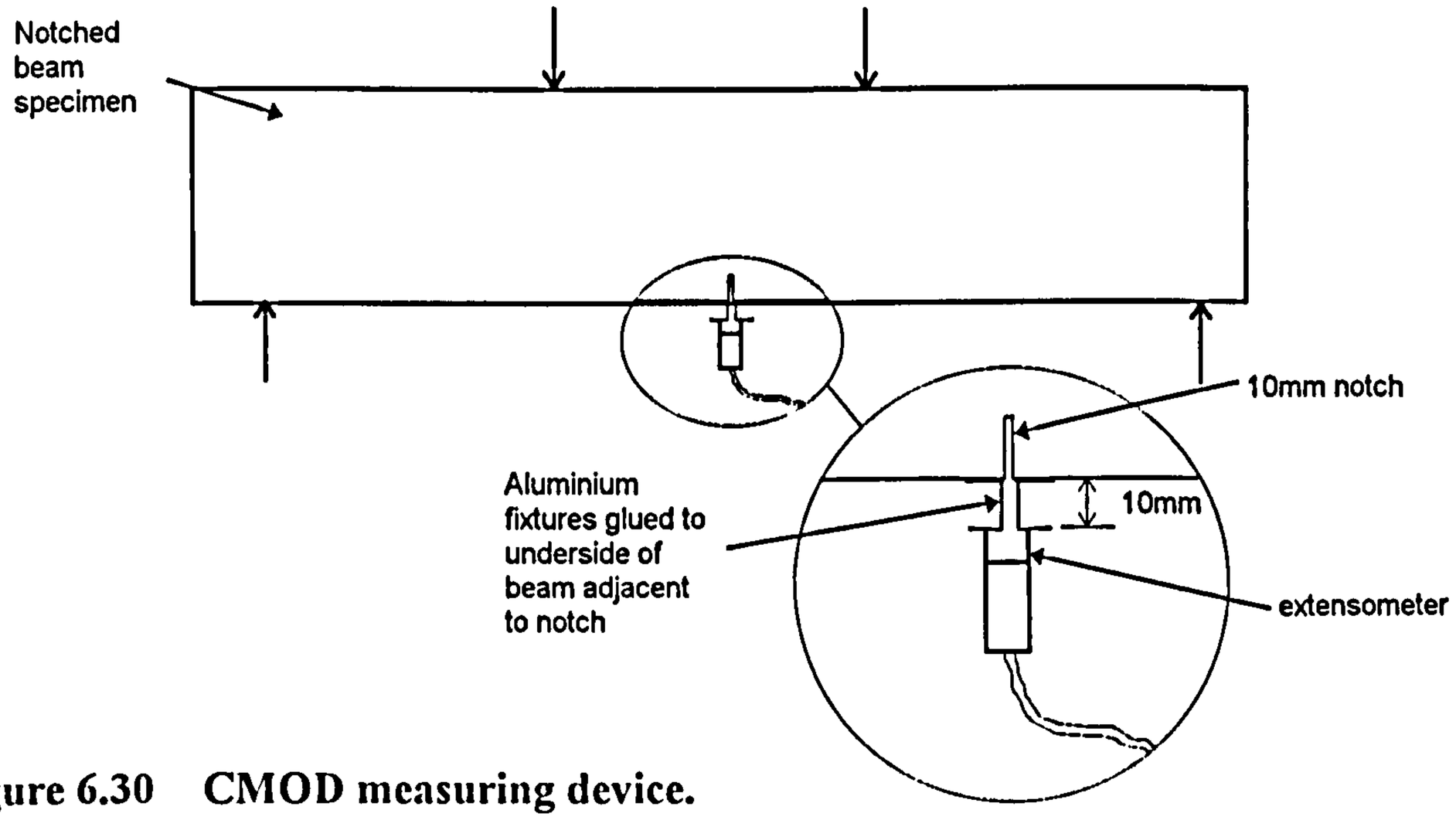

Figure 6.30 CMOD measuring device.

6.5.3 Results and discussion

Load versus deflection response curves

The data from each flexural toughness test was processed to obtain a load versus mid-span deflection response curve. Note that the proposed model attempts to predict a selection of these curves (Chapter 7).

Figures 6.31-6.34 show representative load versus deflection responses for Matrix A, B and C in terms of the various beam sizes, types and fibre contents investigated. Figure 6.31 shows the responses from cast 75mm deep unnotched beams; Figure 6.32 shows the responses from cast 85mm deep notched beams; Figure 6.33 compares the response from cast unnotched beams with depths of 50, 75 and 100mm; and Figure 6.34 shows the responses from the sprayed beams. The following trends can be observed from these figures, which are generally in accordance with the findings of other researchers (as discussed in Section 3.2.3).

i. There is no appreciable difference in the initial slope of the load deflection curves for similar size beams with fibre contents up to 120 kg/m^3.
ii. An increase in fibre content results in an increase in ductility and energy absorption. Improvements between 0-40kg/m^3 are much greater than those associated with further increases in fibre content.
iii. At the higher fibre contents investigated (80 and 120kg/m^3) the peak strength and the first-crack strength are quite distinct; with peak strength increasing with

increasing fibre content, but at lower fibre contents the two strengths appear to generally coincide.

iv. As the size of a beam reduces from 100mm to 50mm the load-deflection response appears to change from a brittle/unstable response (i.e. relatively large post-crack load drop) to a more ductile/stable response (i.e. no post-crack load drop) as shown in Figure 6.33.

In addition, the following observations were made during the tests.

iv. The test allows the complete strain-softening response of a plain beam to be recorded without the need for a notch.

v. Unnotched beams generally failed at a single crack for fibre contents less than 80 kg/m^3 (1% by volume). At higher fibre contents multiple cracking generally occurred, the extent of which increased as fibre content increased.

vi. Notched beams generally failed at single crack located at the notch irrespective of fibre content. However, for a small number of specimens with fibre contents between 80-120 kg/m^3 the crack did not occur at the notch. In these isolated cases, the resulting flexural response curve was not used in the subsequent analysis.

Test repeatability

Figure 6.35 shows the average coefficient of variation of the flexural load as a function of the mid-span deflection for all the notched, unnotched and sprayed test series. The results show relatively high levels of variability. In general, the notched specimens displayed less variability (5-10%) than either of the unnotched (5-20%) or sprayed specimens (10-35%). The higher variability associated with the unnotched specimens was most likely caused by them having a variable crack position (not always at mid-span) and inherent multiple cracking, whereas the notched beams consistently failed at a single crack located at the notch.

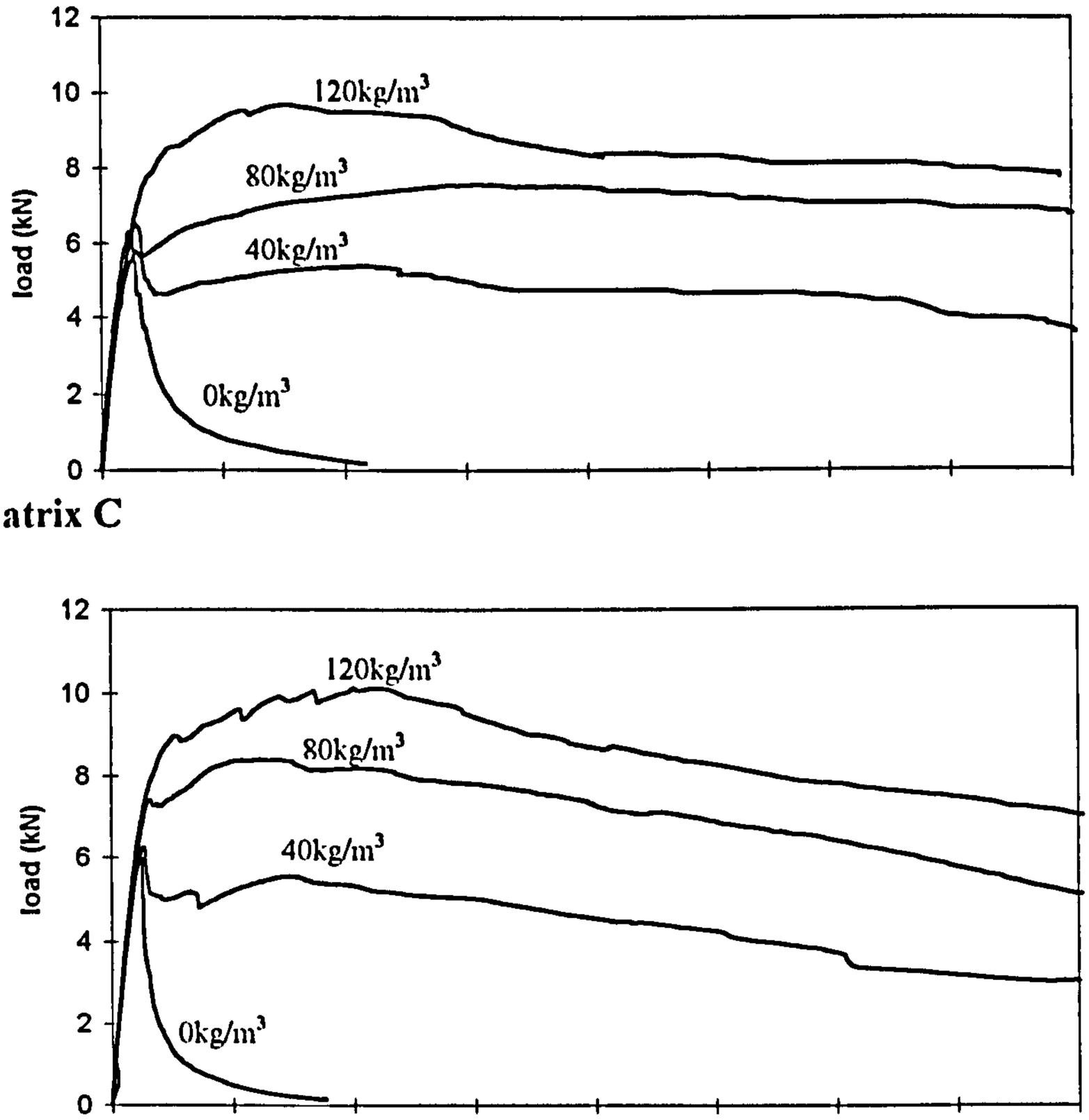

(a) Matrix C

(b) Matrix B

(c) Matrix A

Figure 6.31 Representative load-deflection responses for the 75mm unnotched beams.

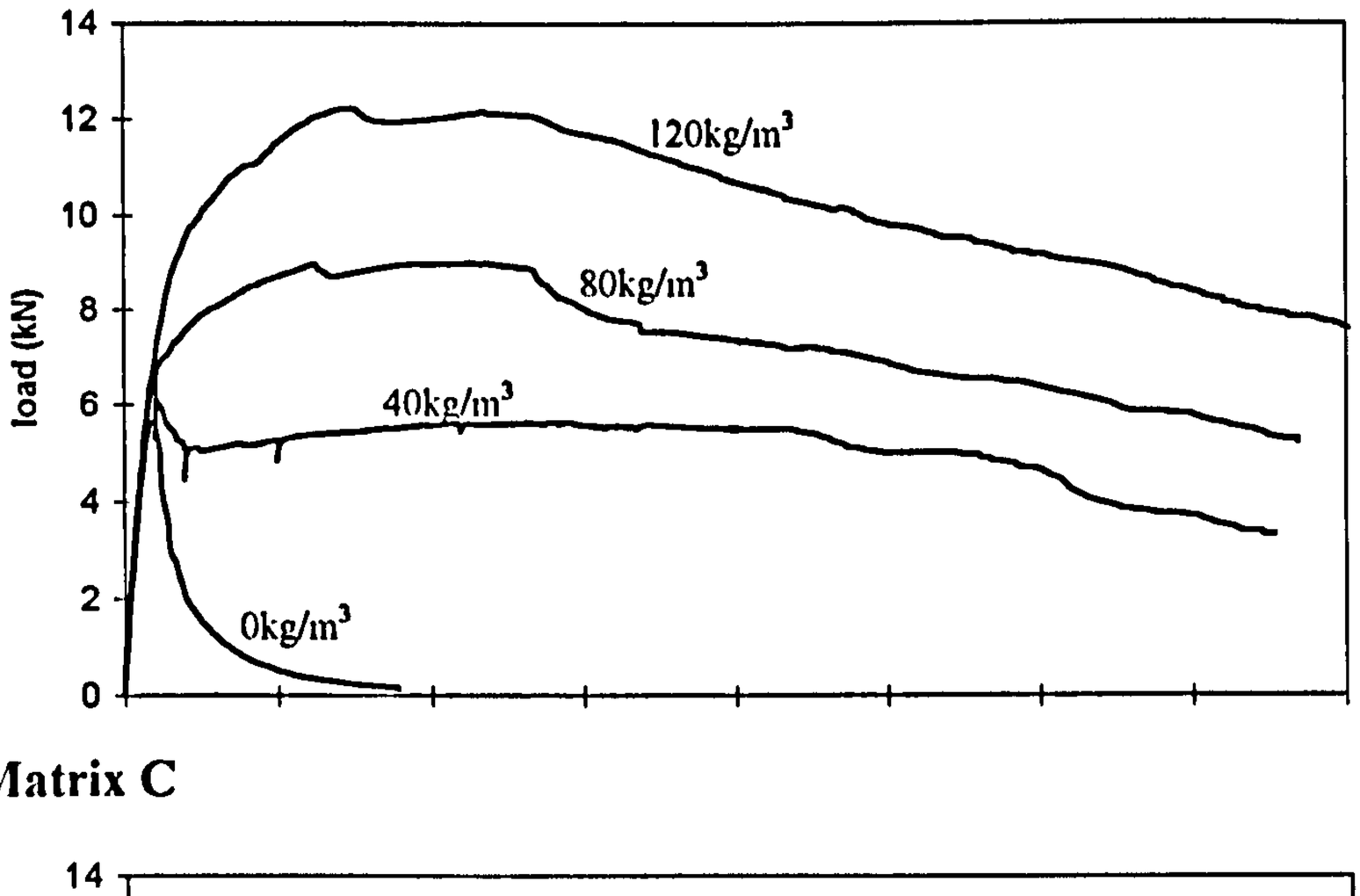

(a) Matrix C

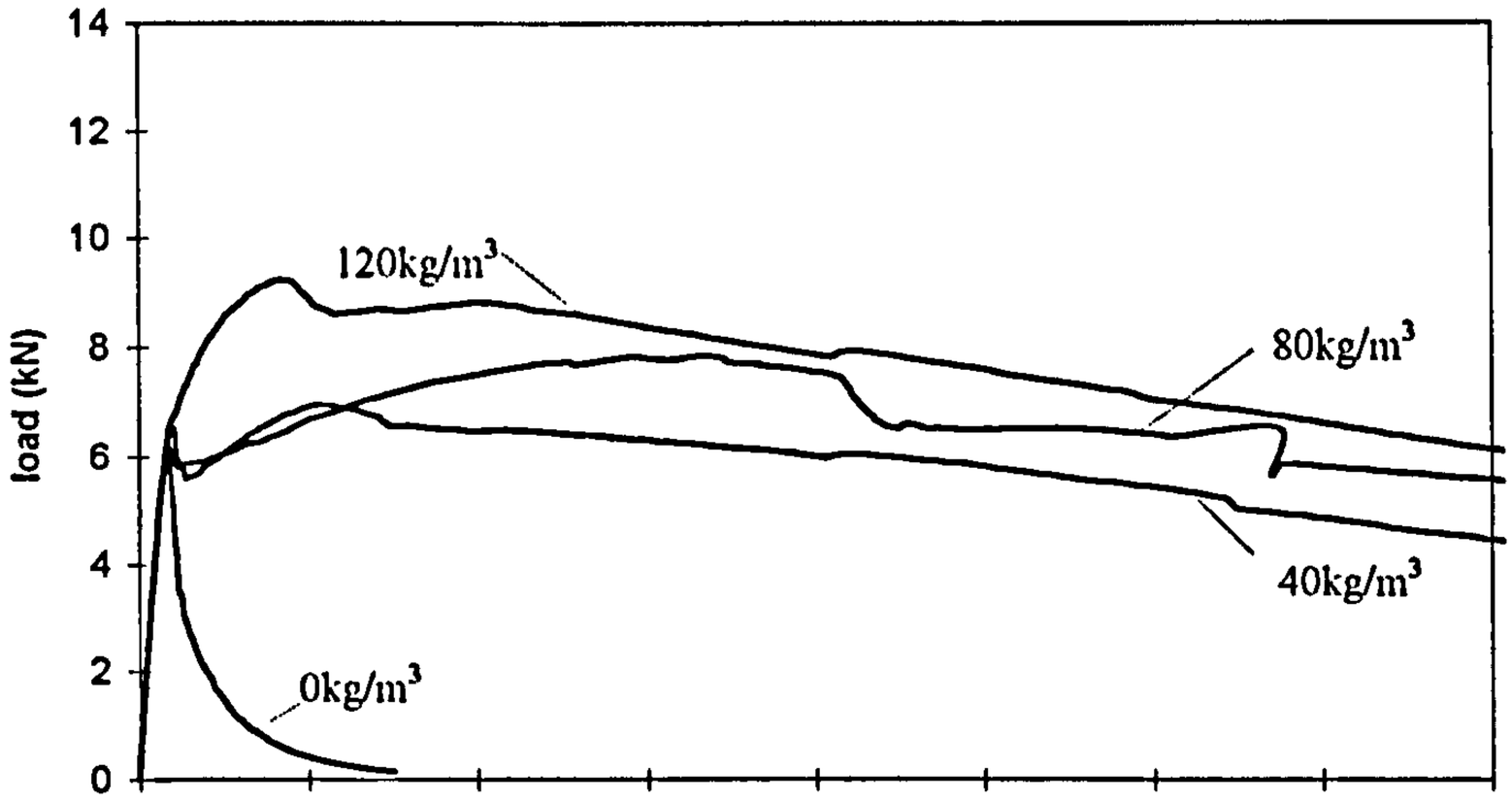

(b) Matrix B

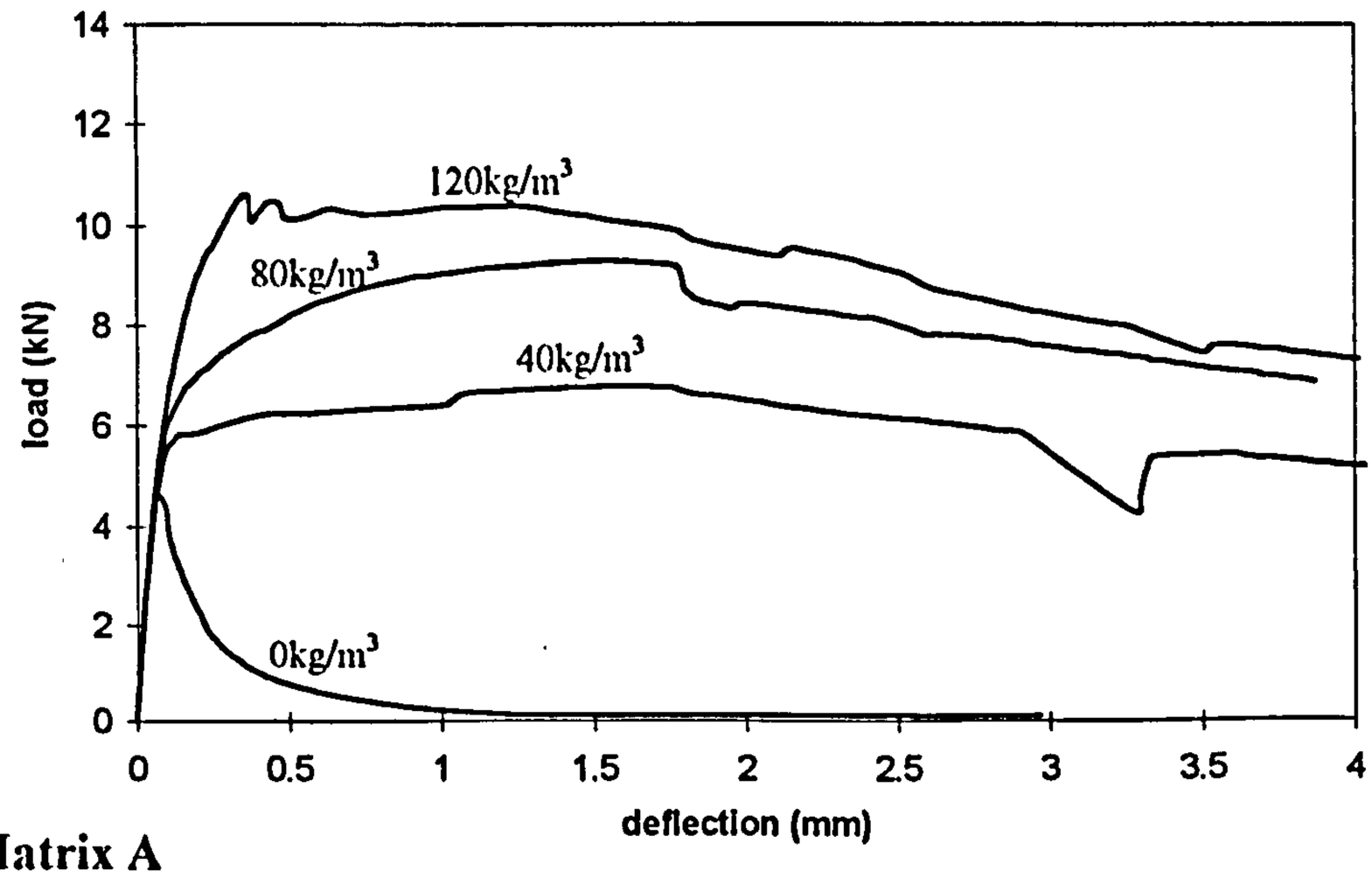

(c) Matrix A

Figure 6.32 Representative load-deflection responses from the 85mm notched beam specimens.

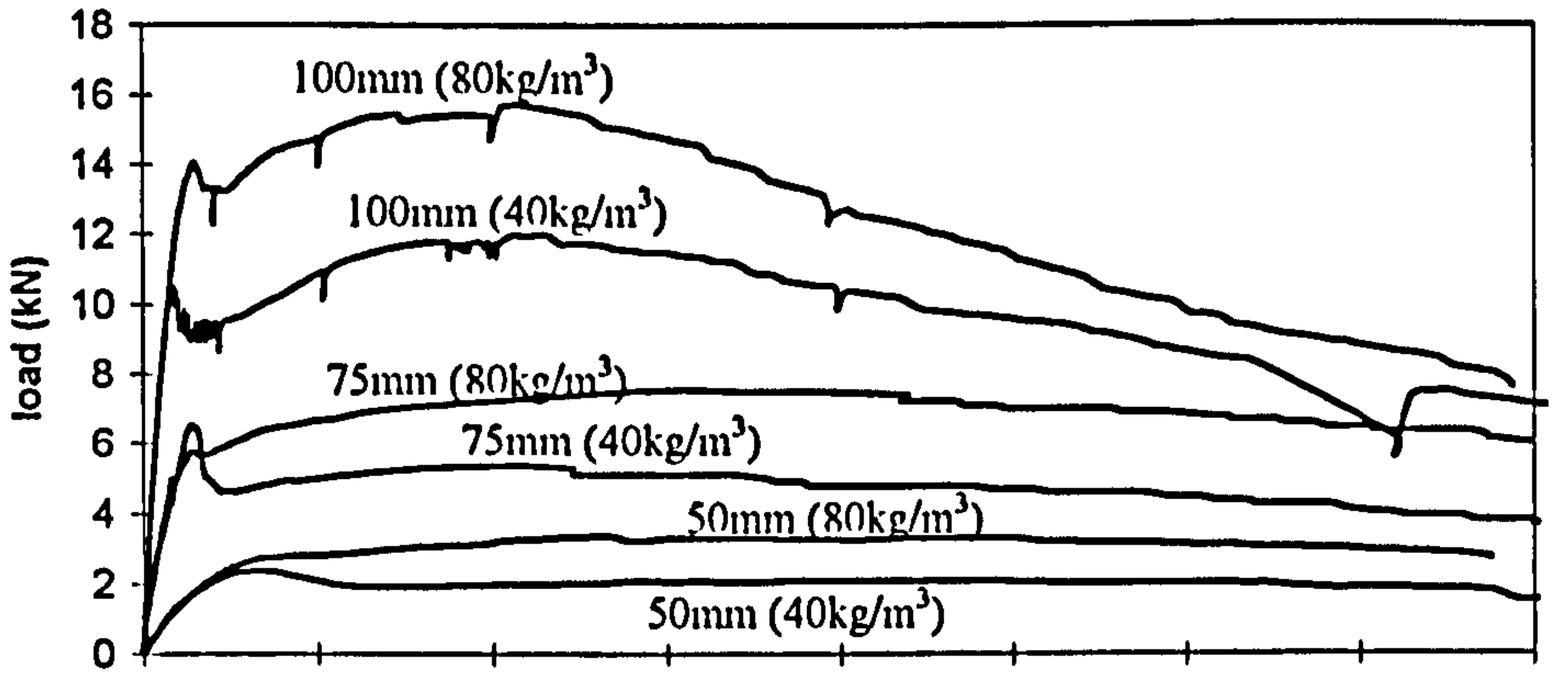

Figure 6.33 Influence of beam depth on load-deflection response - Matrix C

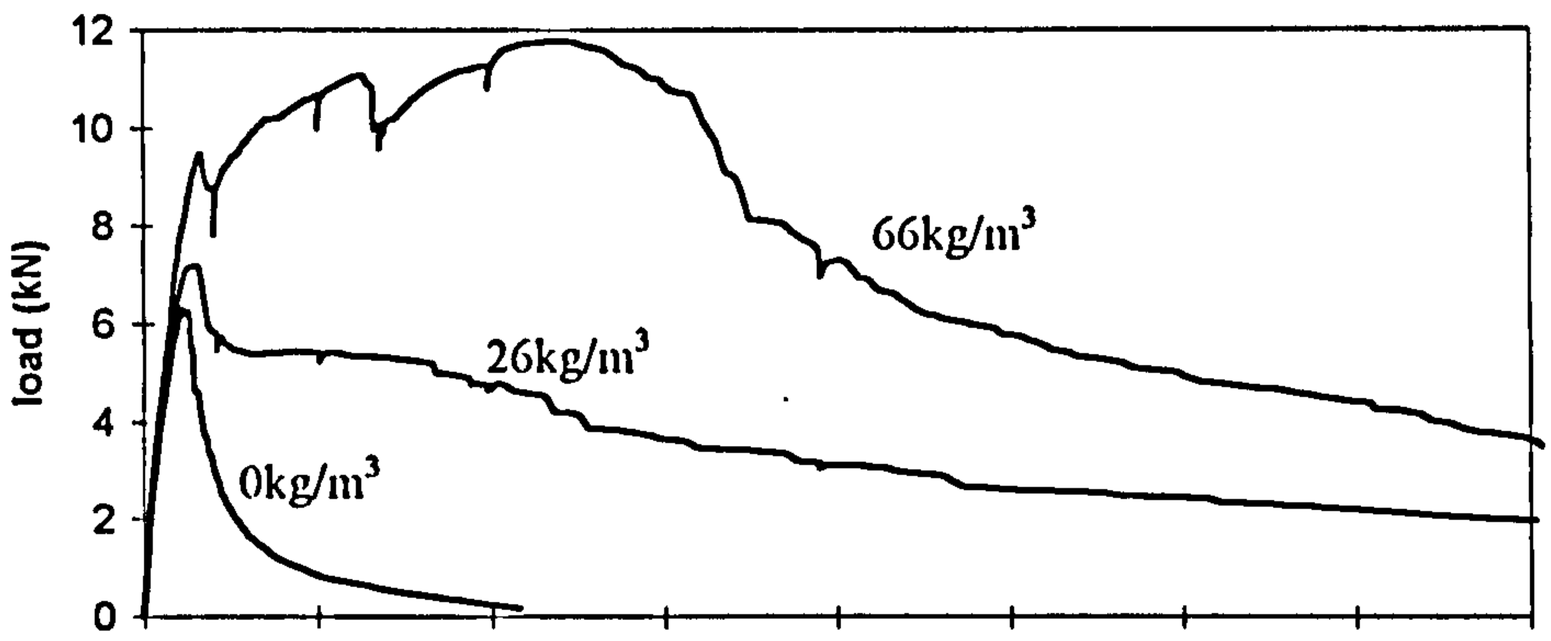

(a) Matrix C

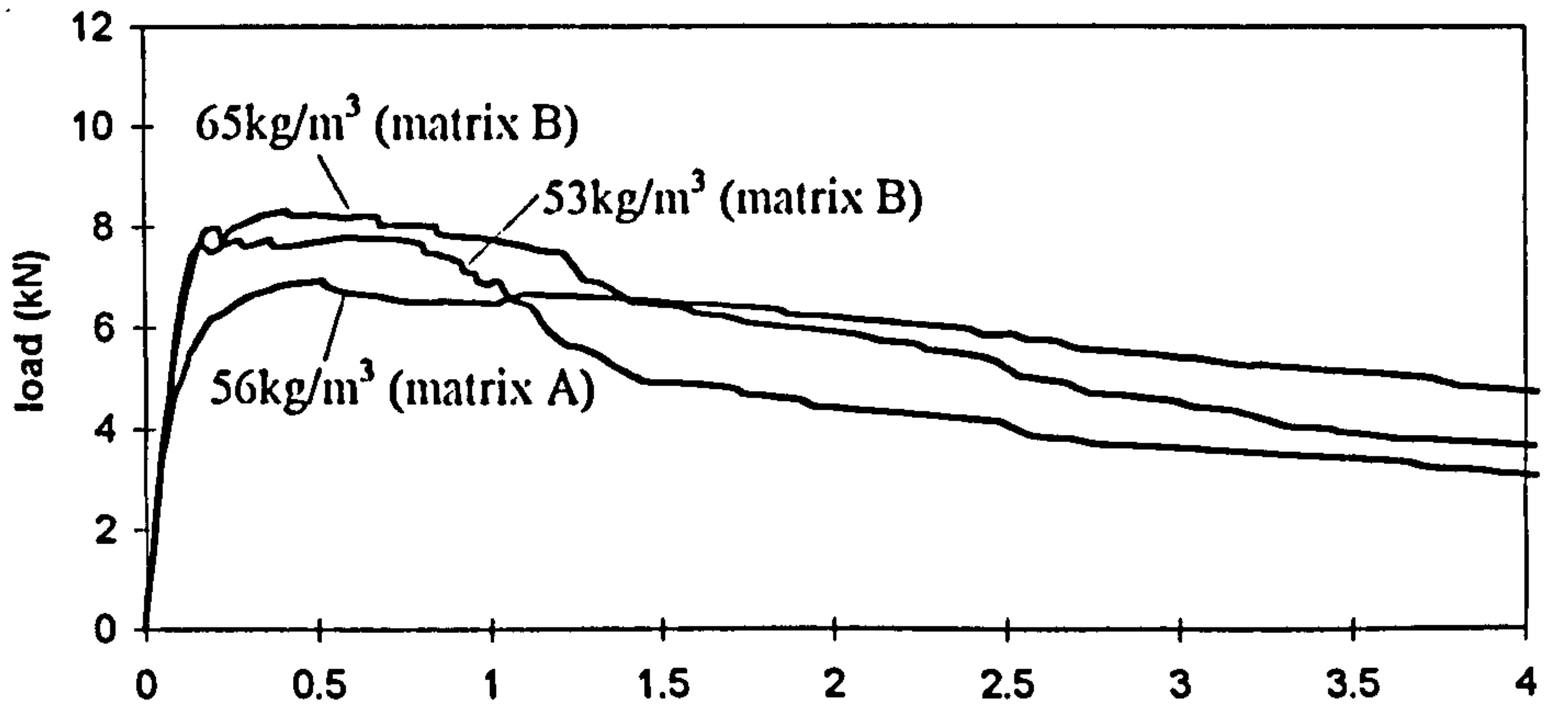

(b) Matrix A & B

Figure 6.34 Representative load-deflection responses from the sprayed beams.

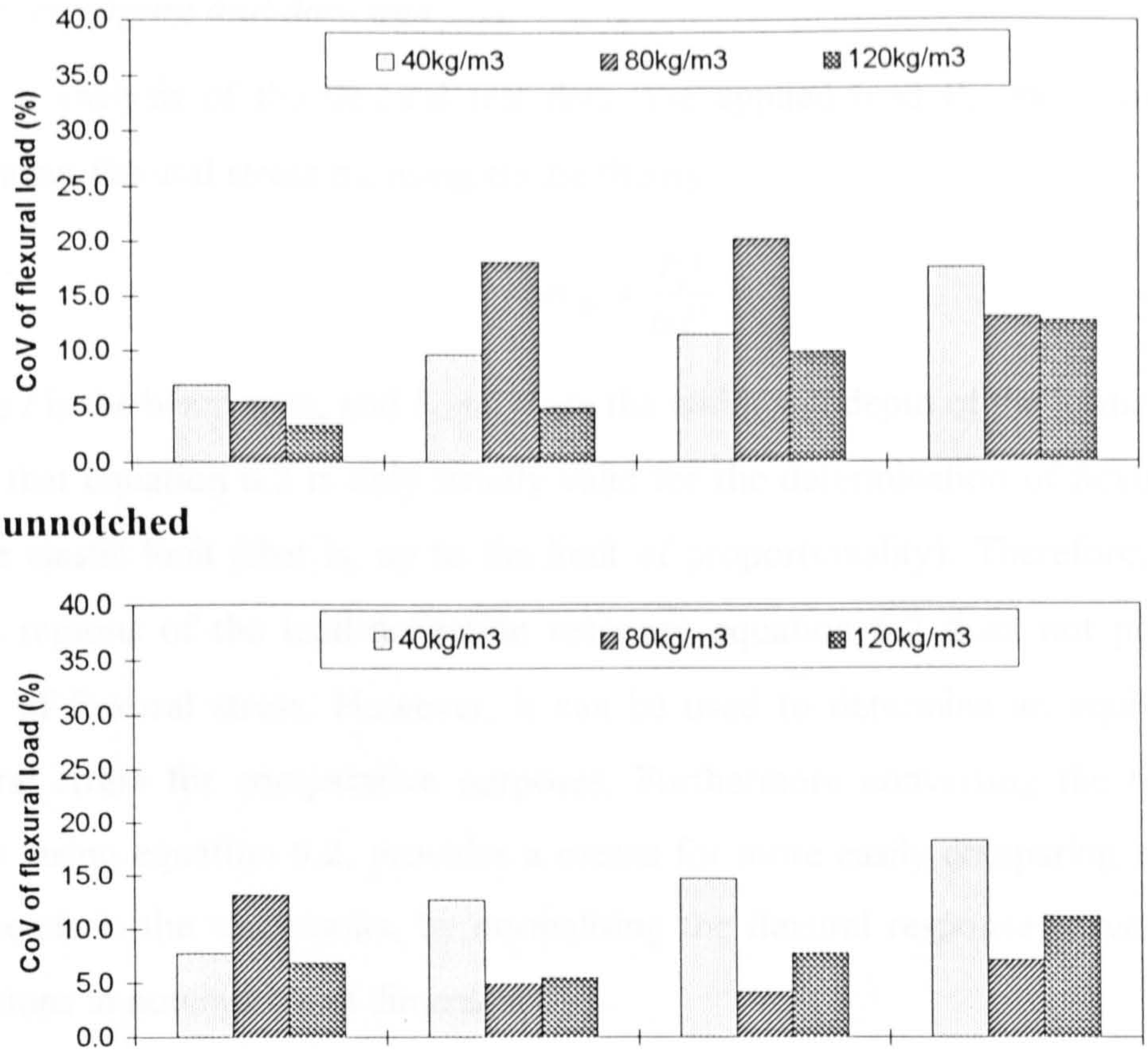

Figure 6.35 Influence of fibre content and beam type on the coefficient of variation of the flexural load.

Curve averaging and data analysis

For the analysis of the flexural test data, the applied load P_a was converted to an equivalent flexural stress σ_{fe} using elastic theory:

$$\sigma_{fe} = \frac{P_a l}{bd^2} \qquad \text{equation 6.2}$$

where l is the beam span, and b and d are the width and depth of the beam respectively. Note that equation 6.2 is only strictly valid for the determination of flexural stress up to the elastic limit (that is, up to the limit of proportionality). Therefore, in the post-crack regions of the load-deflection response equation 6.2 does not provide a true value of flexural stress. However, it can be used to determine an equivalent elastic flexural stress for comparative purposes. Furthermore converting the test data into stress, using equation 6.2, provides a means for more easily comparing and analysing the trends in the test results, by normalising the flexural response curves in terms of variations in nominal beam dimensions.

An average equivalent flexural stress versus mid-span deflection curve was thus determined for each series of three specimens (that is, for each combination of beam type and size, matrix type, and fibre content). These curves were then analysed in accordance with EFNARC (1996) to determine the flexural strength, and the residual flexural strengths and associated classifications at deflections of 0.5, 1.0. 2.0 and 4.0mm. The results of this analysis are summarised in Table 6.8 and Table 6.9, and the individual results from each test series are presented in Appendix I.

Flexural strength

In terms of matrix strength, the results show, as expected, that the higher strength matrices Matrix B and C produced the highest flexural strengths. The increase in flexural strength appears to be greater between Matrix A and B (0 and 5% silica fume) than between Matrix B and C (5 and 10% silica fume), which is in accordance with the trend observed in the compressive strengths results (Section 6.4.3). Furthermore, the increase in flexural strength of the plain Matrix C and B compared with Matrix A, as a result of silica fume additions, is of similar magnitude to the increase in the flexural strength of Matrix A resulting from an 80 kg/m^3 steel fibre addition. This supports the findings of Wolsiefer and Morgan (1993) discussed in Section 2.7.3, who suggested

for some applications (which do not require high flexural toughness characteristics) that flexural strength may be more economically increased by the addition of silica fume as opposed to steel fibres.

Matrix	Silica fume content /%	Fibre content /kgm-3	Nom. beam width /mm	Nom. beam depth /mm	EFNARC		RESIDUAL STRENGTHS /MPa			
					Deflection at peak strength /mm	Flexural strength/ MPa	0.5mm	1.0mm	2.0mm	4.0mm
A	0	0	100	75	0.10	3.7	0.3	0.0	0.0	0.0
A	0	40	100	75	0.14	4.6	4.6	4.5	4.1	3.4
A	0	80	100	75	0.19	5.3	6.1	6.3	6.0	4.4
A	0	120	100	75	0.21	5.6	6.3	6.9	6.6	5.4
B	5	0	100	75	0.12	4.8	0.5	0.0	0.0	0.0
B	5	40	100	75	0.14	5.2	3.9	4.1	3.6	2.7
B	5	80	100	75	0.16	5.9	6.7	7.0	6.6	4.9
B	5	120	100	75	0.20	6.7	7.6	7.9	7.3	5.4
C	10	0	100	75	0.12	4.8	0.4	0.0	0.0	0.0
C	10	40	100	75	0.13	5.2	3.9	4.1	3.7	2.9
C	10	80	100	75	0.19	6.2	6.3	6.5	6.5	4.7
C	10	120	100	75	0.24	6.7	7.7	8.4	7.4	4.8
A	0	40	100	50	0.14	4.0	4.0	4.1	3.5	3.1
A	0	80	100	50	0.25	5.3	5.6	5.5	5.5	4.9
C	10	40	100	50	0.26	4.4	3.7	3.6	3.7	3.1
C	10	80	100	50	0.31	5.5	6.0	6.6	7.1	6.1
A	0	40	100	100	0.08	4.2	3.7	3.6	3.3	2.3
A	0	80	100	100	0.12	4.6	5.5	6.0	5.4	3.3
C	10	40	100	100	0.11	4.9	4.6	4.4	3.8	2.7
C	10	80	100	100	0.13	5.5	5.9	6.3	5.4	3.3

Table 6.8(a) Summary of flexural toughness tests - unnotched beams.

A comparison of the plain matrix flexural strengths from the unnotched beams in Table 6.8(a) with the corresponding notched beams in Table 6.8(b) shows that there is generally no significant difference. This result should be expected given that both beam types have similar ligament depths. However the results also show, for an increase in fibre content between 0-120kg/m^3, a general increase in flexural strength of between 30-40% for the unnotched specimens and between 60-80% for the notched specimens (Figure 6.36). The higher strength associated with the notched specimens may be

explained by relating the results to the higher values of flexural strength observed from centre-point loaded beams when compared with the flexural strength observed from third-point loaded beams of similar size (Neville, 1995). In a third-point loaded beam the whole of the middle third section is subjected to the maximum stress, so that the critical crack may develop at any point within that section. However, if the beam is notched the notch acts as a crack inducer. Therefore, the probability of the weakest section being subjected to the critical stress is lower in a notched beam tested in third-point loading than in an unnotched beam, and so the notched beam will generally give a higher value of flexural strength.

Matrix	Silica fume content /%	Fibre content /kgm-3	Nom. beam width /mm	Nom. beam depth /mm	EFNARC		RESIDUAL STRENGTHS /MPa			
					Deflection at peak strength /mm	Flexural strength/ MPa	0.5mm	1.0mm	2.0mm	4.0mm
A	0	0	100	75	0.07	3.5	0.5	0.1	0.0	0.0
A	0	40	100	75	0.13	4.7	5.3	5.4	5.1	3.8
A	0	80	100	75	0.18	5.3	6.2	6.9	6.6	5.4
A	0	120	100	75	0.21	6.5	7.7	8.2	7.4	5.8
B	5	0	100	75	0.08	4.7	0.4	0.0	0.0	0.0
B	5	40	100	75	0.09	5.1	5.2	5.4	5.2	4.1
B	5	80	100	75	0.11	5.3	6.6	6.4	6.1	4.1
B	5	120	100	75	0.20	7.3	8.2	8.6	8.2	6.5
C	10	0	100	75	0.10	4.6	0.4	0.0	0.0	0.0
C	10	40	100	75	0.10	5.0	5.2	5.4	5.1	-
C	10	80	100	75	0.21	6.6	7.2	7.4	6.2	-
C	10	120	100	75	0.24	7.5	8.8	9.1	7.9	-
C	0	40	100	50	0.18	5.8	5.6	6.2	6.4	5.6
C	0	80	100	50	0.23	6.3	6.9	7.6	7.9	6.3

Table 6.8(b) Summary of flexural toughness tests - notched beams.

A comparison of the flexural strengths of the cast and sprayed beams made with Matrix A, B and C as a function of fibre content is shown in Figure 6.37. The results indicate slightly lower flexural strengths for the sprayed specimens, which is not in accordance with the findings of Banthia *et al.* (1994b) who reported wet process steel fibre reinforced sprayed concrete specimens developing slightly stronger flexural strengths than equivalent cast specimens.

Matrix	Silica fume content /%	In-situ fibre content /kgm-3	Nom. beam width /mm	Nom. beam depth /mm	EFNARC		RESIDUAL STRENGTHS /MPa			
					Deflection at peak strength /mm	Flexural strength/ MPa	0.5mm	1.0mm	2.0mm	4.0mm
A	0	56	125	75	0.19	4.1	4.6	4.5	4.5	3.4
B	5	53	125	75	0.17	5.1	5.1	4.7	3.0	2.0
B	5	65	125	75	0.20	5.0	4.5	4.3	3.1	1.9
C	10	0	125	75	0.12	4.1	0.4	0.1	0.0	0.0
C	10	26	125	75	0.16	4.8	3.5	3.0	2.1	1.4
C	10	66	125	75	0.16	5.7	6.6	6.5	3.7	1.9

Table 6.8(c) Summary of flexural toughness tests - sprayed beams.

Matrix	Silica fume content /%	Fibre content /kgm-3	Nom. beam width /mm	Nom. beam depth /mm	RESIDUAL STRENGTH CLASSES (EFNARC)			
					0.5mm	1.0mm	2.0mm	4.0mm
A	0	0	100	75	0	0	0	0
A	0	40	100	75	4	4	4	3
A	0	80	100	75	4	4	4	4
B	5	0	100	75	0	0	0	0
B	5	40	100	75	3	3	3	3
B	5	80	100	75	4	4	4	4
C	10	0	100	75	0	0	0	0
C	10	40	100	75	3	3	3	3
C	10	80	100	75	4	4	4	4

(a) CAST

A	0	56	125	75	4	4	4	3
B	5	53	125	75	4	4	3	2
B	5	65	125	75	4	4	3	2
C	10	0	125	75	0	0	0	0
C	10	26	125	75	3	2	2	1
C	10	66	125	75	4	4	3	2

(b) SPRAYED

Table 6.9 EFNARC residual strength classes.

In terms of the influence of beam depth on flexural strength, the results indicate that flexural strength remained virtually unchanged for the range of beam depths investigated (Figure 6.38). This is surprising given that size effect laws and numerous

experimental results (Neville, 1995; Karihaloo, 1995) show that flexural strength decreases with an increase in beam depth. However, there does not appear to be any obvious explanation for this anomaly.

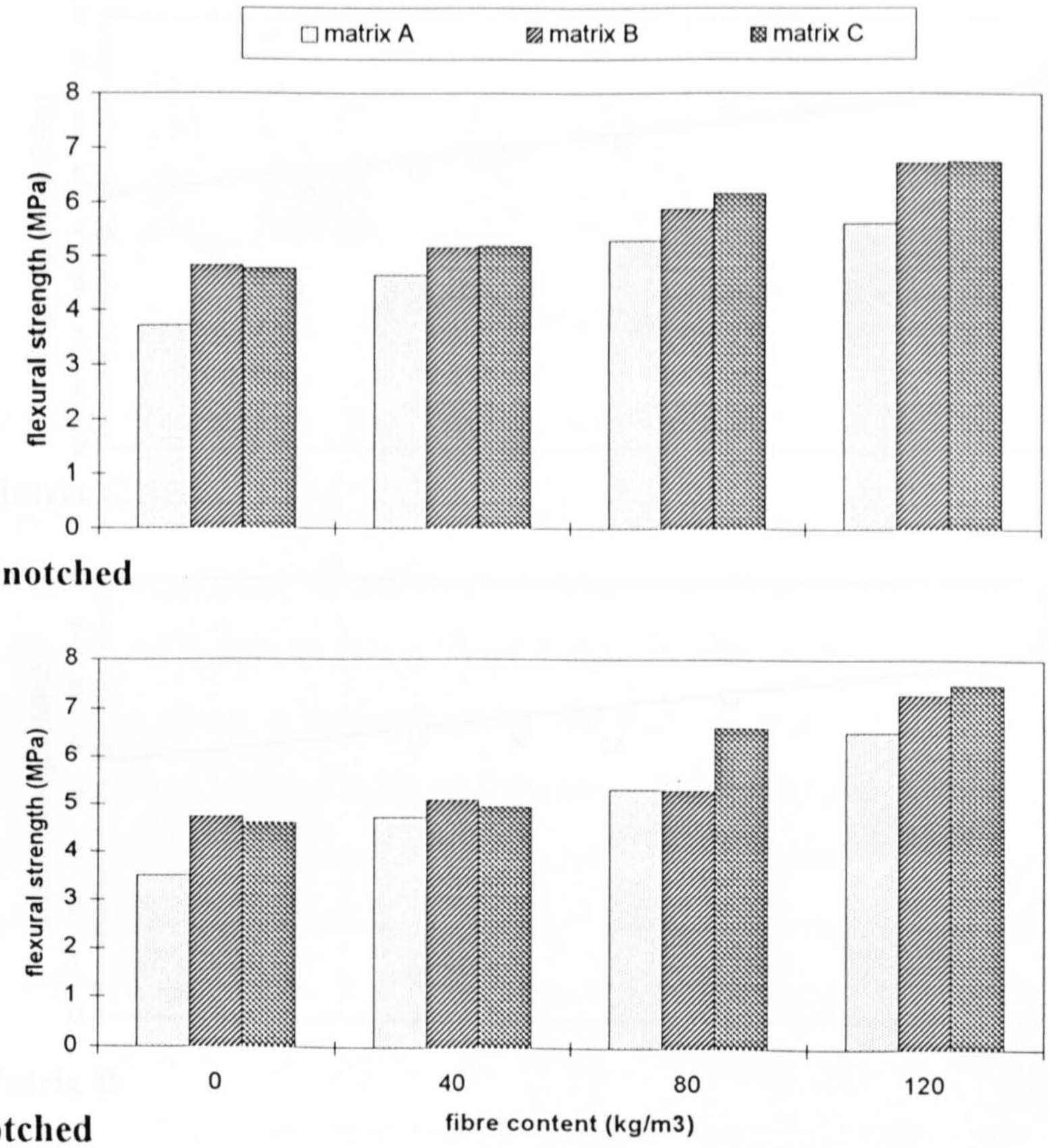

(a) unnotched

(b) notched

Figure 6.36 Influence of fibre content on flexural strength.

Residual strengths

The influence of matrix strength on residual strength is shown in Figure 6.39 for 75mm deep unnotched beams with fibre content of 40, 80 and 120kg/m^3. The results show that at fibre contents of 80 and 120kg/m^3 there is a general increase in residual strength corresponding to an increase in matrix strength. This result is in accordance with the trend observed in the flexural strength data. However, this does not appear to be the case at a fibre content of 40 kg/m^3, which shows the reverse; Matrix A displays higher residual strengths than either Matrix B and C. These findings suggest that the higher strength (and, therefore, more brittle) matrices display a greater post-peak load drop,

the magnitude of which decreases as fibre content increases. Similar trends can also be observed in the notched beam data detailed in Table 6.8(b).

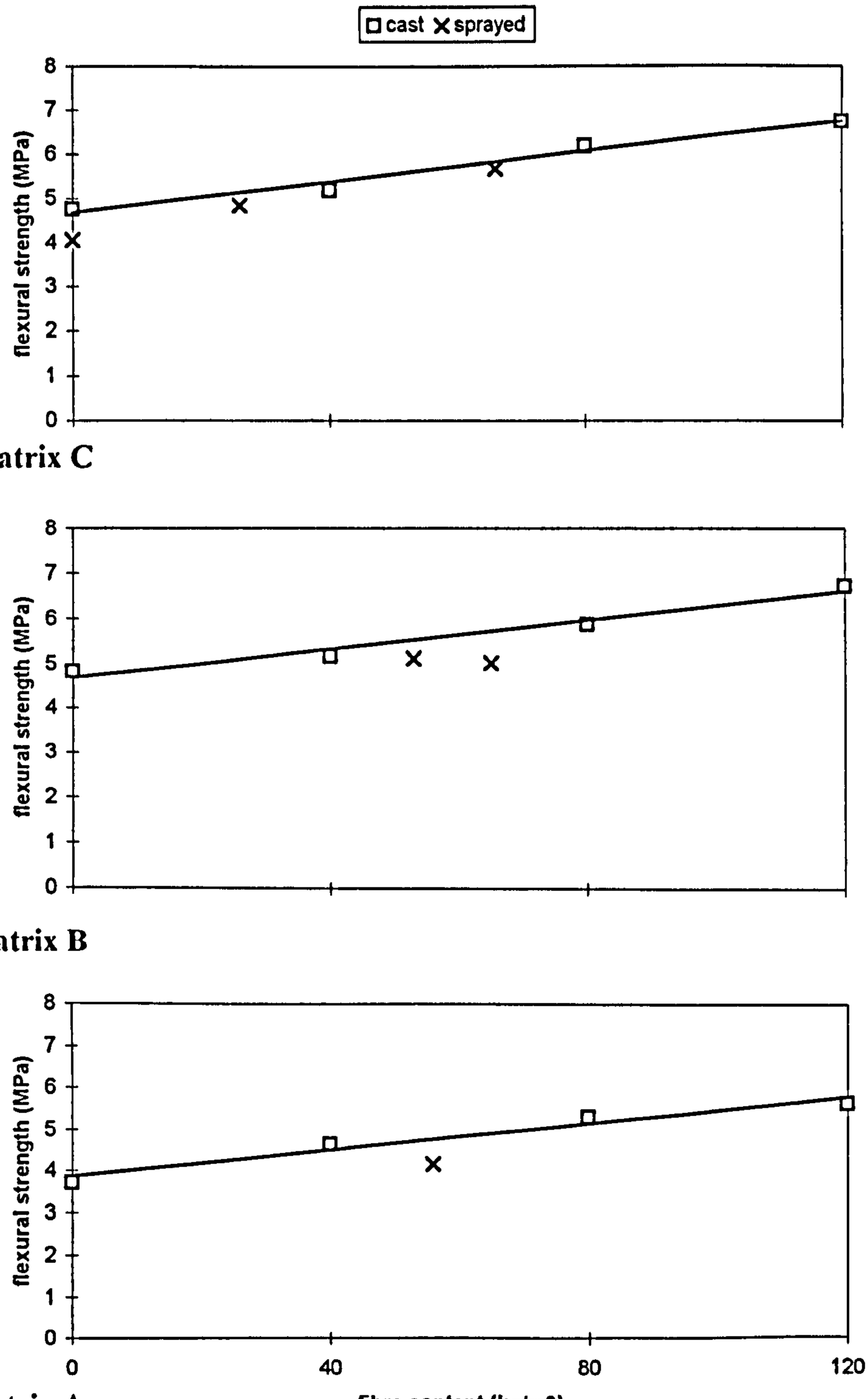

(a) Matrix C

(b) Matrix B

(c) Matrix A

Figure 6.37 Flexural strength comparison of cast and sprayed specimens.

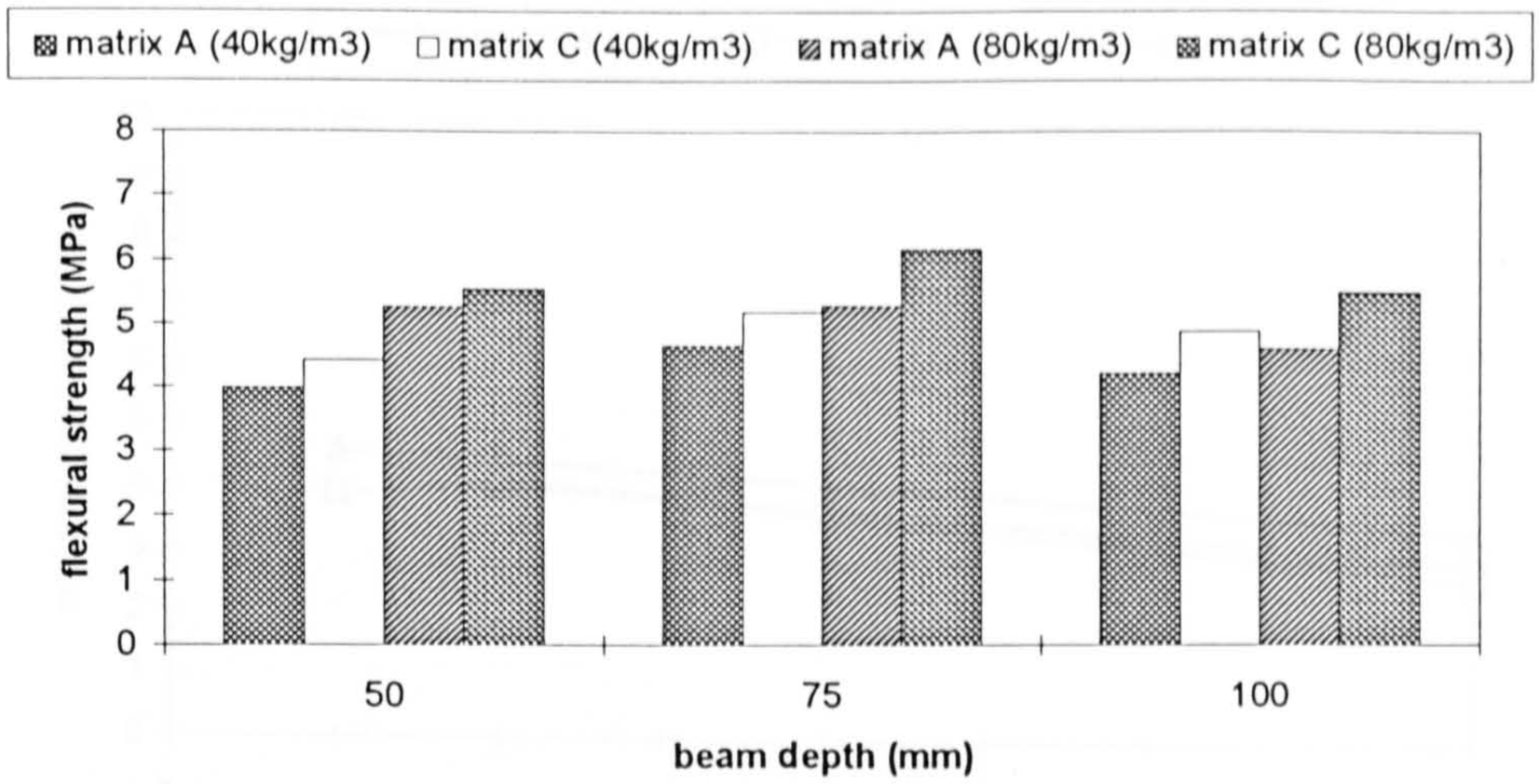

Figure 6.38 Influence of beam depth on flexural strength (unnotched beams).

The influence of fibre content on the residual strength of 75mm deep cast unnotched beams made using Matrix C is shown in Figure 6.40. Similar trends can also be seen in the Matrix A and B data shown in Table 6.8(a). In general the results show, for a given deflection, that residual strength increases with an increase in fibre content. The increase appears to be greater for an increase in fibre content between 0-40 kg/m^3 than for further increases in fibre content. This trend suggests that the relative improvement in flexural toughness as a result of increased fibre additions diminishes above a certain fibre content. Similar trends can be observed in the notched specimen data (Table 6.8(b)). Figure 6.40 also shows that residual strengths change very little between deflections of 0.5-2.0mm - with a slight peak at 1.0mm deflection - and only begin to reduce in value between deflections of 2.0-4.0mm.

A comparison of the unnotched beam data with the corresponding notched beam data shows that the notched specimens generally display greater residual strengths than the unnotched beams (Figure 6.41). This result suggests that the presence of the notch provides a more stable failure process. Consequently, this produces a more stable and ductile post-peak response, which helps to mobilise the fibres across the cracked section more effectively. Linking this result with the higher flexural strengths observed in the notched beams (Figure 6.36) suggests that the overall flexural response of a fibre reinforced concrete notched beam is greater than an unnotched beam with a similar fibre content.

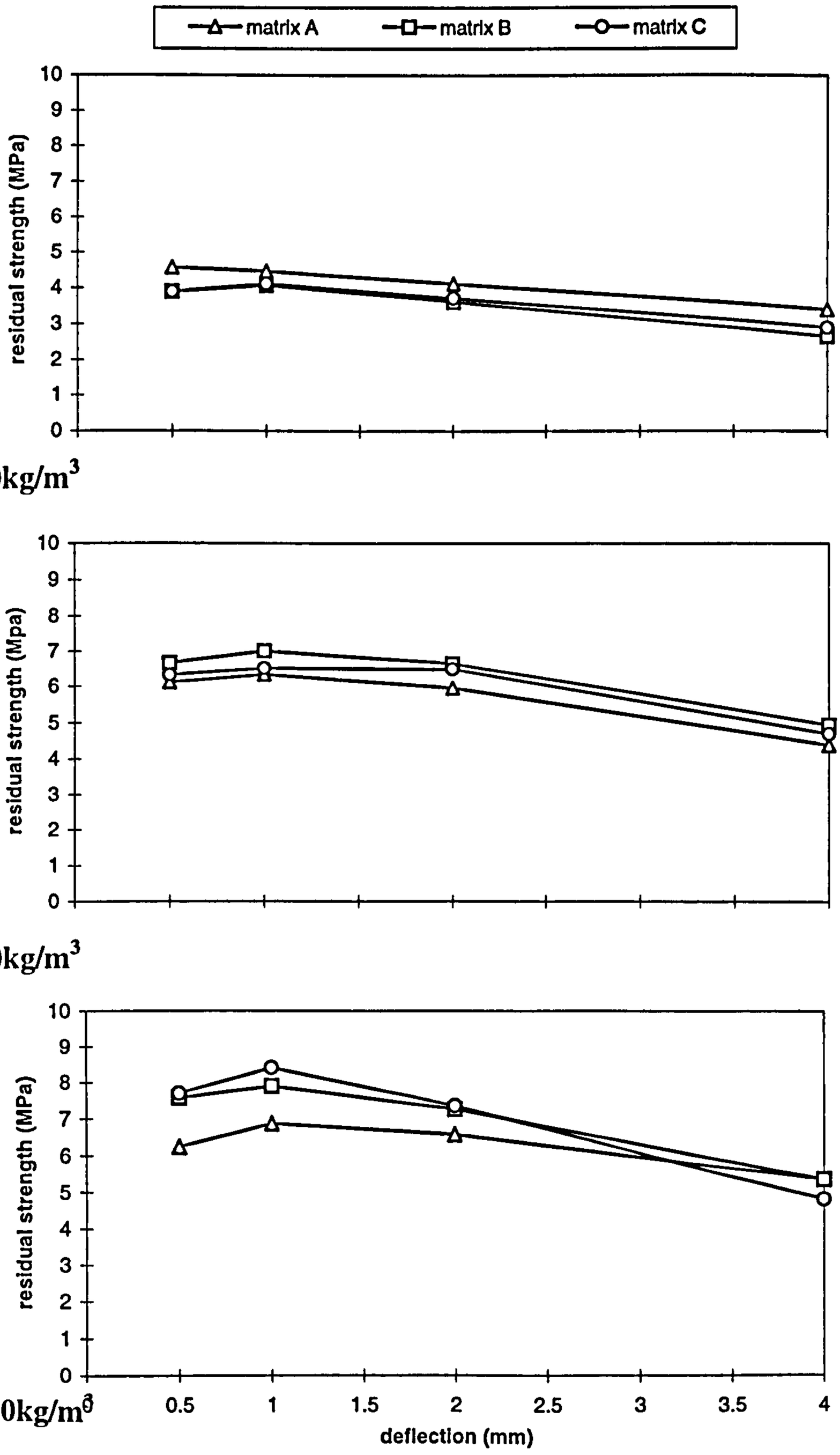

Figure 6.39 Influence of matrix strength on residual strength (unnotched).

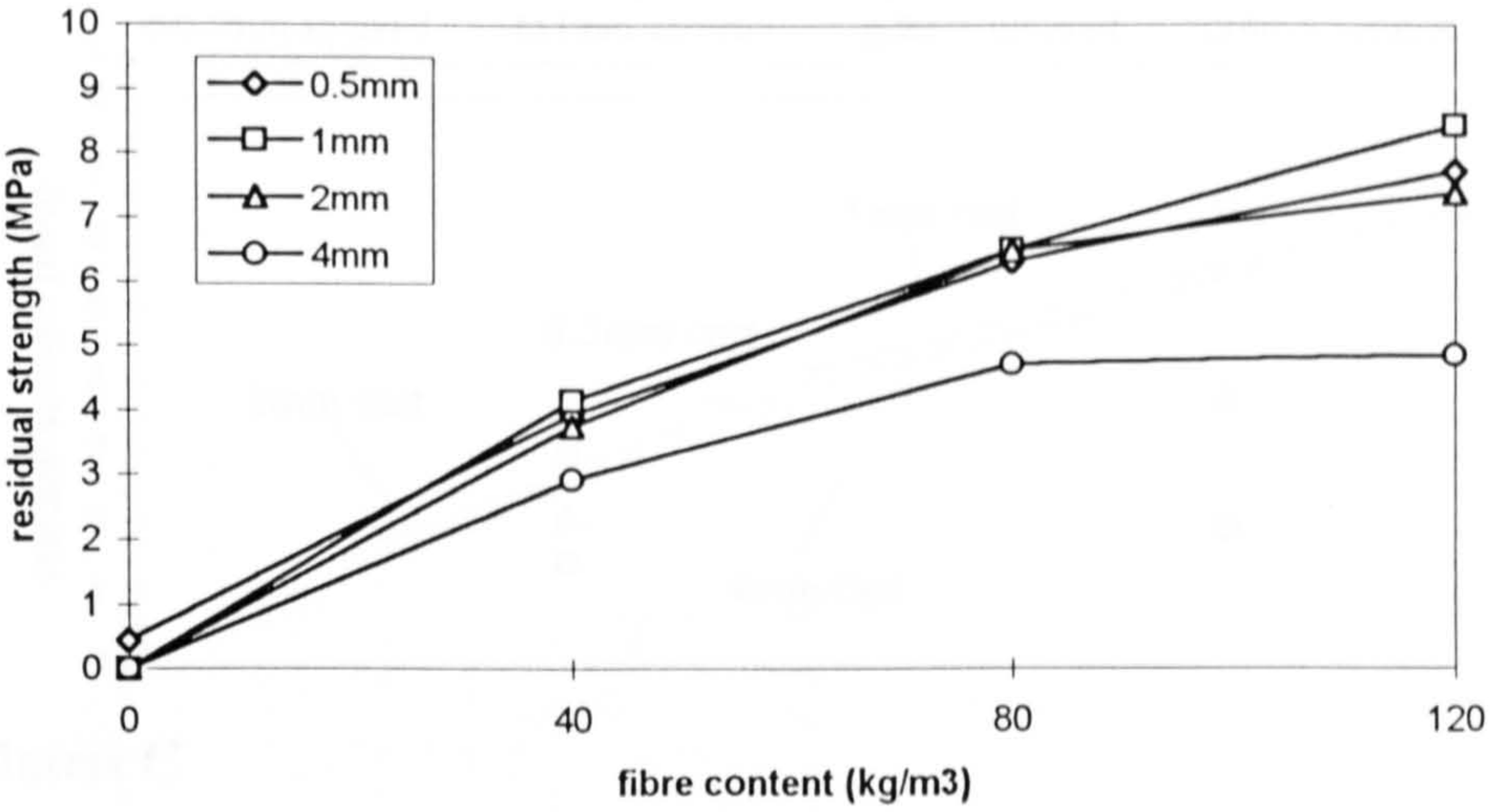

Figure 6.40 Influence of fibre content on residual strength (Matrix C - unnotched).

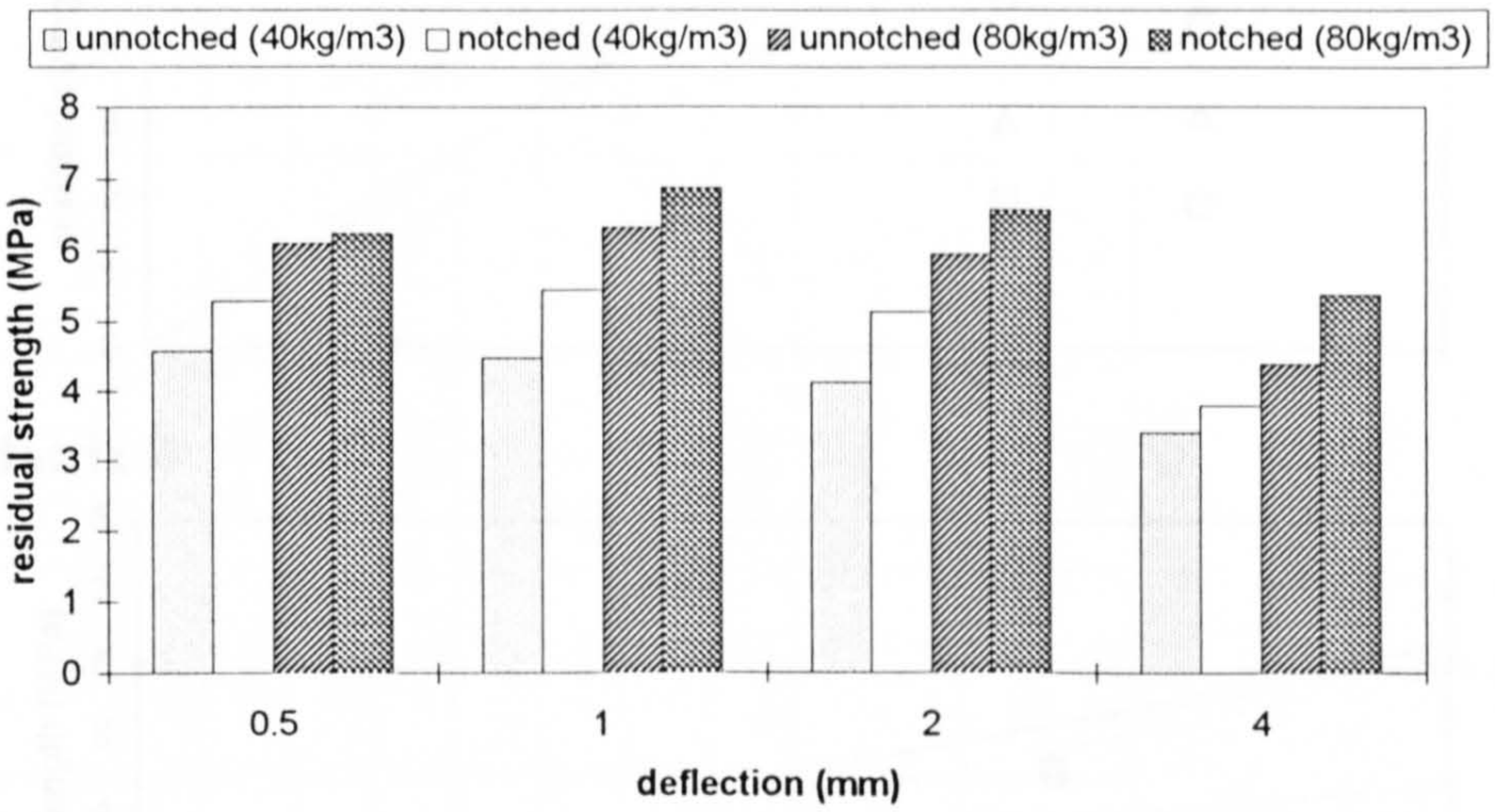

Figure 6.41 Residual strength comparison between cast unnotched and notched beams (Matrix A).

Figure 6.42 compares the residual strengths of the cast and sprayed specimens as a function of fibre content for Matrix A, B and C. The results indicate that the residual strengths of the sprayed specimens are generally lower than the cast specimens. This is not surprising given that the flexural strengths of the sprayed specimens were also lower than the equivalent cast specimens (Figure 6.37). These results are further highlighted in Table 6.9, which shows the corresponding EFNARC (1996) residual strength classes for the sprayed and cast specimens up to a fibre content of 80kg/m^3. In Section 6.7 it is shown that the lower residual strengths associated with the sprayed specimens may be caused by a reduced fibre density close to the tensile face of the sprayed specimens.

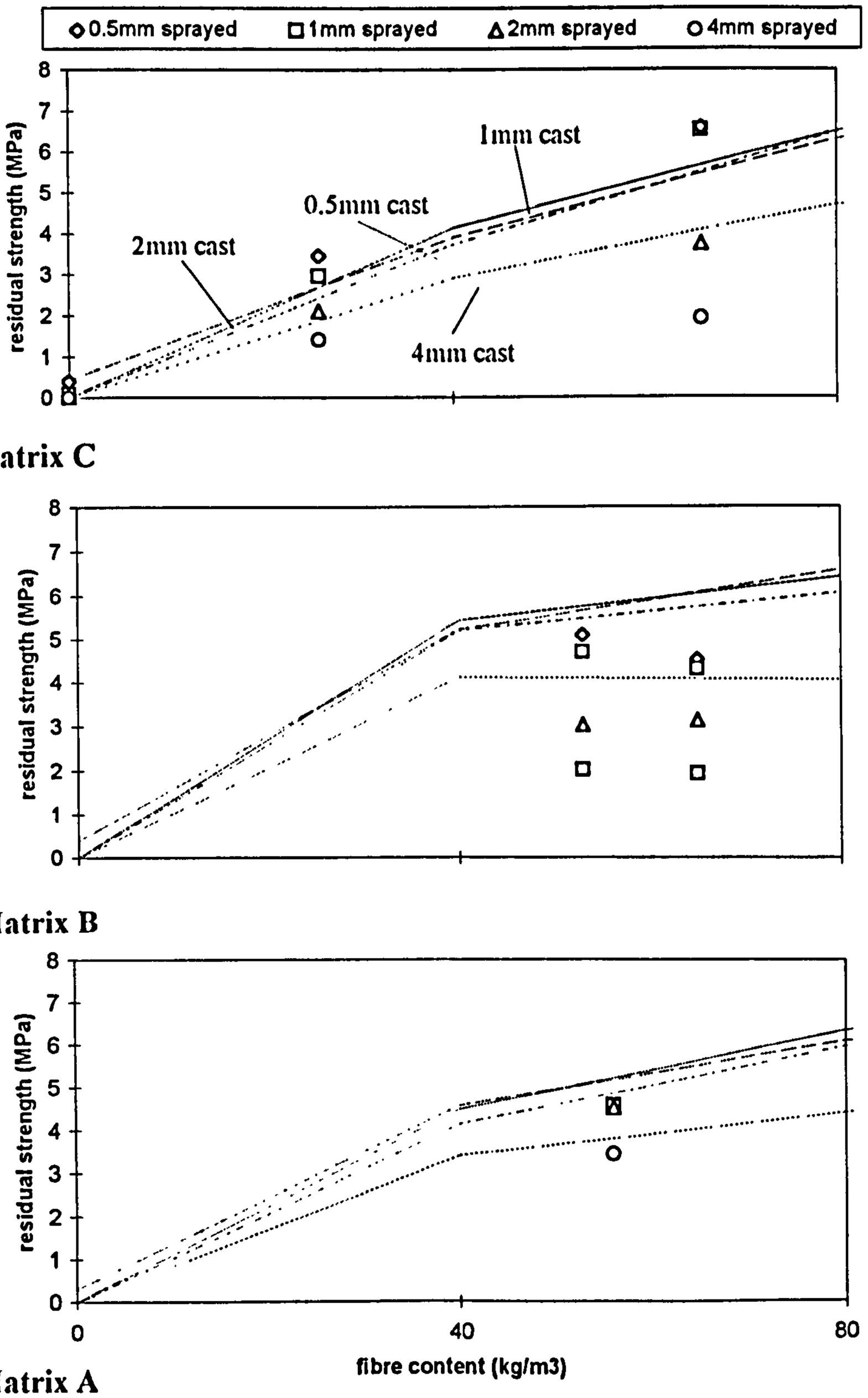

(a) Matrix C

(b) Matrix B

(c) Matrix A

Figure 6.42 Residual strength comparison between cast and sprayed unnotched beams.

Also note that the residual strengths detailed in Table 6.8(a) do not show any significant trends in terms of beam depth for either Matrix A or C.

Matrix	Silica fume content /%	Fibre content /kgm-3	Nom. beam width /mm	Nom. beam depth /mm	EFNARC		CMOD (mm)				DEFLECTION/CMOD RATIO (MEASURED)				
					Deflection at peak load /mm	CMOD at peak load /mm	0.5mm	1.0mm	2.0mm	4.0mm	At deflection at peak load	0.5mm	1.0mm	2.0mm	4.0mm
A	0	0	100	75	0.07	0.03	0.42	0.89	-	-	2.42	1.20	1.13	-	-
A	0	40	100	75	0.13	0.06	0.35	0.75	1.61	3.40	2.29	1.44	1.33	1.24	1.18
A	0	80	100	75	0.18	0.09	0.33	0.74	1.61	3.36	2.03	1.51	1.34	1.24	1.19
A	0	120	100	75	0.21	0.10	0.29	0.69	1.71	3.75	2.04	1.71	1.44	1.17	1.07
B	5	0	100	75	0.08	0.02	0.41	-	-	-	3.53	1.22	-	-	-
B	5	40	100	75	0.09	0.03	0.36	0.82	1.81	3.65	3.40	1.41	1.22	1.10	1.10
B	5	80	100	75	0.11	0.04	0.37	0.80	1.67	3.54	2.80	1.35	1.26	1.20	1.13
B	5	120	100	75	0.20	0.09	0.28	0.67	1.62	3.60	2.14	1.81	1.50	1.23	1.11
C	10	0	100	75	0.10	0.03	0.43	0.95	-	-	2.94	1.16	1.05	-	-
C	10	40	100	75	0.10	0.04	0.39	0.84	1.73	-	2.89	1.29	1.19	1.16	-
C	10	80	100	75	0.21	0.09	0.33	0.80	1.65	-	2.21	1.54	1.25	1.21	-
C	10	120	100	75	0.24	0.09	0.22	0.63	1.51	-	2.64	2.27	1.58	1.32	-

Table 6.10 Measured deflection/CMOD ratios.

Flexural stress versus CMOD curves

The notched beam specimens were further analysed in terms of flexural stress versus crack-mouth-opening-displacements (CMOD), and the results compared with the corresponding mid-span deflection responses. A summary of this analysis is presented in Table 6.10, which shows: (1) average measurements of the deflection and CMOD at peak load; (2) average CMOD measurements at deflections of 0.5, 1.0, 2.0 and 4.0mm; and (3) deflection/CMOD ratios at deflections of 0.5, 1.0, 2.0 and 4.0mm.

In terms of the influence of fibre content on the measured CMOD, the results indicate a reduction in CMOD for an increase in fibre content. This suggests that an increase in fibre content may restrict the propagation and widening of the crack. In contrast, matrix strength does not appear to influence the value of CMOD at a given deflection.

Analysis of the CMOD/deflection ratios in Table 6.10 shows that its value reduces as mid-span deflection increases; at the deflection at peak load (generally between 0.1-0.2mm) the ratio varies between 2.0-3.5, but at a deflection of 4.0mm it has reduced to a value between 1.1-1.2. This reduction is significantly greater between a deflection of 0-0.5mm than for further increases in deflection.

Armelin and Banthia (1997) recently showed that, by considering the mechanics of a cracked beam, a change in mid-span deflection $d\delta$ can be related to a change in crack mouth opening displacement $dCMOD$ by the following equation

$$\frac{d\delta}{dCMOD} = \frac{l}{4(d-c)} \qquad \text{equation 6.3}$$

where d is the depth of the beam, c is the depth of the neutral axis measured from the compressive face of the beam, and l is the span (assuming third-point loading). By using equation 6.3, and assuming that prior to the beam cracking the neutral axis is at mid-depth and at a 4.0mm mid-span deflection it has moved close to the compressive face ($c \rightarrow 0$), theoretical upper and lower bound deflection/CMOD ratios can be determined. For the beam size and geometry used in this investigation (that is, l = 450mm, d = 95mm and c varies between 0-42.5mm), the lower bound ratio (c = 0) equates to 1.18, and the upper bound ratio (c = 42.5mm) to 2.65. Note that a 95mm beam depth was used in these calculations corresponding to the distance, relative to the compressive face of the beam, at which CMOD was measured during the tests (see

Figure 6.30). A comparison of the theoretical upper and lower bound deflection/CMOD ratios with the measured ratios for Matrix A, B and C, as detailed in Table 6.10, indicates: (1) a reasonable agreement between the theoretical lower bound ratio (c = 0) and the measured values at deflections of 2 and 4mm; and (2) a reasonable agreement between the theoretical upper bound value (neutral axis located at mid-depth) and the measured values at the flexural strength deflection.

In terms of the fracture processes associated with the flexural behaviour of steel fibre reinforced concrete, these findings indicate that, as expected, the neutral axis is located close to the mid-depth when the flexural strength is reached. But once the beam cracks it then moves quickly to a position close to the compressive face of the beam as the mid-span deflection continues to increase. Further data relating to the actual position of the neutral axis relative to mid-span deflection is discussed in Section 6.6.

6.6 STRAIN ANALYSIS TESTS

6.6.1 Background

In Chapter 3 various methods of strain analysis were described for measuring the strain and crack-width profiles of a steel fibre reinforced concrete beam in flexure. A comparison of these methods showed that Moiré interferometry offered the most accurate and versatile technique for analysing fibre reinforced concrete due to the following: (1) its high level of accuracy; and (2) an unlimited range of full-field elastic and plastic strain measurement. However, it was also shown that the use of this method is severely limited because of the expensive and sophisticated equipment required for its implementation including: a laser, an optical bench, and the production of high density interference gratings (2000 lines/mm).

Therefore, an alternative strain analysis technique was developed for use in this investigation, which combined electrical resistance strain gauges with a semi-automated grid method using digital image processing. The main criteria dictating the development of the test method included: low cost, the need to use readily available equipment, and the ability to measure a wide range of strain and crack-widths.

6.6.2 Test development: grid method

General

The four main stages considered in the development of the strain analysis grid method using digital image processing were:

a) application of the grid;

b) image acquisition;

c) image processing; and

d) image analysis.

The accuracy of the method depends on a variety of factors which also required careful consideration. These included the size and spacing of the grid points, image resolution, image contrast, and camera lens distortion.

A digital image is an approximation of a real image in which segments of the image are represented by individual digital elements (pixels) in an array of size X,Y, where X and Y are the dimensions of the image in pixels. The light intensity of each element is given by a discrete value termed a 'grey level' in the range [0,G], where level 0 corresponds to zero or minimum light intensity (black) and G corresponds to the maximum light intensity (white). The resolution of a digital image depends on these three parameters (X, Y and G), and as their values increase so the approximation of the digital image to the real image improves (Gonzalez and Woods, 1992).

The contrast of a digital image is measured by a parameter termed the grey level difference. This is determined by computing a histogram of grey level frequencies from all the pixels making up the image (Figure 6.43), and then calculating the number of grey levels between the average local black grey level and the average local white grey level (Fail and Taylor, 1990). An increase in the value of grey level difference corresponds to an increase in contrast, which also corresponds to an increase in the accuracy of strain measurements obtained from an image. This is because the centroids of high contrast grid spots can be more accurately determined by digital image processing software. Note that a high contrast grid is most commonly obtained by applying a black grid of spots on to a white background.

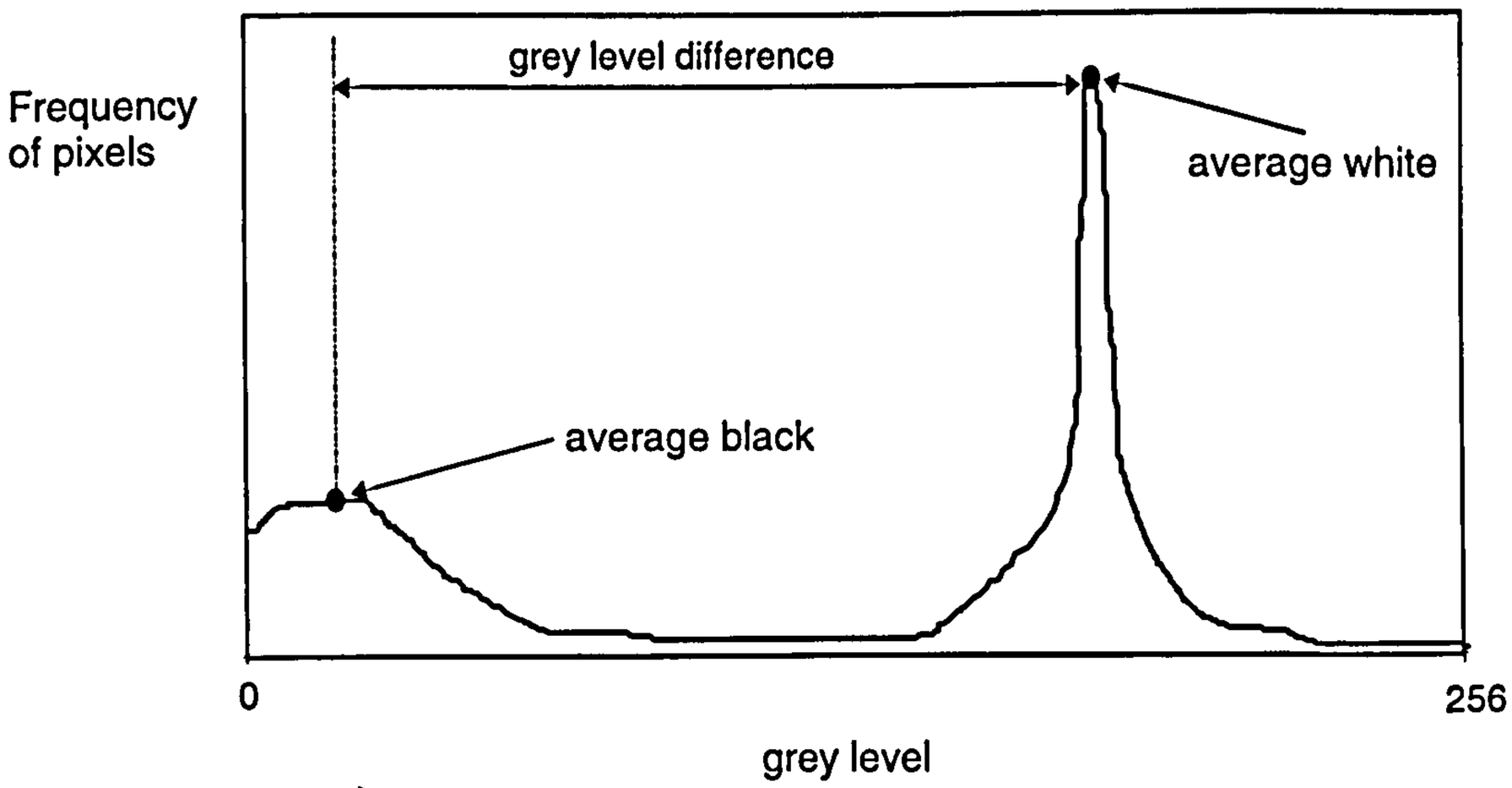

Figure 6.43 Typical histogram of grey levels from a digital image of a grid of black spots on a white background.

The size of the grid spots, and hence the number of pixels making up a spot, is also a limiting factor on the accuracy of the method. This is because the measurement of grid deformations relies on the precision to which the centroids of the grid spots can be located. The spacing of the grid spots (or pitch), which essentially equates to gauge length, must also be chosen such that individual grid spots can be easily distinguished. Hence, in order to obtain reliable results, Sirkis and Taylor (1990) recommend a grid spot diameter of at least 10 pixels and a lower limit on the grid spacing of between 2-3 times spot diameter. In this investigation these recommendations were achieved by using a grid of 2.5mm diameter spots at 5mm centres.

Application of the grid

There are several methods available for applying a black grid of spots onto a white background including stencilling, etching and cementing (Sevenhuijsen, 1993). Of these stencilling was considered the most versatile and economical for the size and number of specimens to be tested in this investigation. Thus, a series of trials were undertaken to assess a variety of stencilling methods: (1) inking using a fine fibre-tipped permanent marker pen; (2) painting using black emulsion; and (3) spraying using a black acrylic primer. Each trial consisted of stencilling a regular circular spot

grid on to a test beam which had previously been sprayed with two coats of a white acrylic primer.

Both the spraying and painting methods were found to be unsatisfactory for the following reasons: the application was messy; it was difficult to apply the paint/spray evenly; it required at least 24 hours drying time; and the roundness of the spots was poor. In contrast, the inking method was found to be very effective as it provided a quick drying application with complete control over the quality of the applied grid spots. As a result this method was adopted in the investigation.

Image acquisition

A photoelectronic camera (for example, a charged couple device (CCD) camera) is normally recommended for acquiring a digital image of the grid for strain analysis measurements. This is because the relatively high degree of accuracy that can be achieved with this type of camera due to the minimal image distortion resulting from the acquired images not being subjected to photographic developing procedures. However, the use of these cameras is restricted by their high cost (in excess of £10,000) and limited field of view, approximately 200mm^2 (Sevenhuijsen *et al.*, 1993). Furthermore, they require an on-line analogue-to-digital converter to transform the acquired analogue image (consisting of a matrix of numbers representing the recorded image) into a digital image prior to image processing.

In this study, an alternative method of digital image acquisition was developed which used a conventional 35mmm SLR camera to photograph the grid in combination with proprietary electronic digital scanning technology. This method offered significant advantages over photoelectronic image acquisition including: relatively low cost, use of readily available equipment, and a virtually unlimited field of view. However, it was also recognised that the accuracy of the method would be compromised by an increase in image distortion due to the photographic developing and scanning processes.

The conversion of the photographic negatives to digital format using electronic scanning represents a critical step in which various systematic errors may be introduced. A variety of technologies are available and these have recently been

reviewed by Chandler and Padfield (1996). At one end of the price/precision range are the high precision systems designed for photogrammetric productions capable of scanning full aerial format imagery at resolutions as low as 7μm and with high geometric accuracy. At the other extreme are desktop systems designed for scanning A4 documents at resolutions of 60μm with a consequential degradation of accuracy. However, an alternative and recent scanning technology is Kodak Photo CD (Chandler and Padfield, 1996). This system has been developed for both consumer and commercial use, primarily for digitising photographic material for publishing and presenting on a computer, and offers the following benefits:

- photographic negatives can be scanned at a variety of resolutions (Table 6.11);
- all the digital image data is stored on CD ROM which solves a common storage problem associated with digital image processing (that is, storing digital image files of sizes up to 72Mb);
- it is relatively cheap - twenty four 35mm photographic negatives can be scanned and stored for less than £20; and
- each image is scanned with up to 256 grey levels.

Therefore, it was decided to adopt this system in this investigation.

Type	Base/16	Base/4	Base (TV resolution)	Base x 4	Base x 16	Base x 64
Resolution (lines x pixels)	128 x 192	256 x 384	512 x 768	1024 x 1536	2048 x 3072	4096 x 6144
File size (Mb)	0.02	0.09	0.38	1.50	6.00	24.00
Grey levels	256	256	256	256	256	256

Table 6.11 Range of scanning resolutions using Kodak Photo-CD (Chandler and Padfield, 1996).

Image processing

Visilog, a digital image processing software package developed by Noessis, was used to determine the centroid co-ordinates (in units of pixels) of the grid spots for each of the digital grid images analysed. This software is available under one of the CHEST (Combined Higher Education Software Team) agreements at a reduced price for

academic usage. It is supported in both the Microsoft Windows and UNIX environments, and includes a comprehensive suite of digital image processing techniques including: frequency histogram processing, pattern recognition, segmentation, thresholding, labelling, filtering and grid spot image analysis (i.e. computation of centroid co-ordinates, spot sizes and shape factors). Furthermore, it allows the digital image processing to be automated so as to minimise operator error.

Image analysis

Image analysis consisted of two main stages: (1) transforming the digital image co-ordinates, in units of pixels, into 'real' two-dimensional photo image co-ordinates in units of millimetres; and (2) determining grid deformations to enable strain and crack-widths profiles to be computed.

A six parameter affine transformation, using least squares, was used to transform the measured pixel co-ordinates system (XY) into the photo co-ordinate system (xy). This transformation consists of three basic steps: (1) a correction for size differences by means of scale factors; (2) a translation to shift the origin of the grid from the XY digital co-ordinate system to the xy photo system; and (3) a rotation of the XY axis to correspond with the xy axis. Computer software developed by Chandler and Padfield (1996) was used to carry out the least squares calculations associated with the transformation. The results consisted of the xy photo co-ordinates for the centroid of each grid spot together with the residual errors associated with the least squares solution. These residual errors represented the closing errors of the transformation as a result of the distortion of the grid images by the camera lens and photographic development processes.

In order to undertake the transformation the co-ordinates of at least four fixed points had to be known in both the XY digital image co-ordinate system and the xy photo image co-ordinate system. This was achieved by stencilling 20mm diameter reference grid spots on to a rigid steel target that was placed on the cross-head of the test machine (Figure 6.44). The target was first sprayed with white acrylic primer and then the reference spots were stencilled using a black fibre-tipped permanent marker pen. Note that the stencil was machined to an accuracy of 1/1000th of an inch. The setting-out of the reference spots is detailed in Figure 6.45.

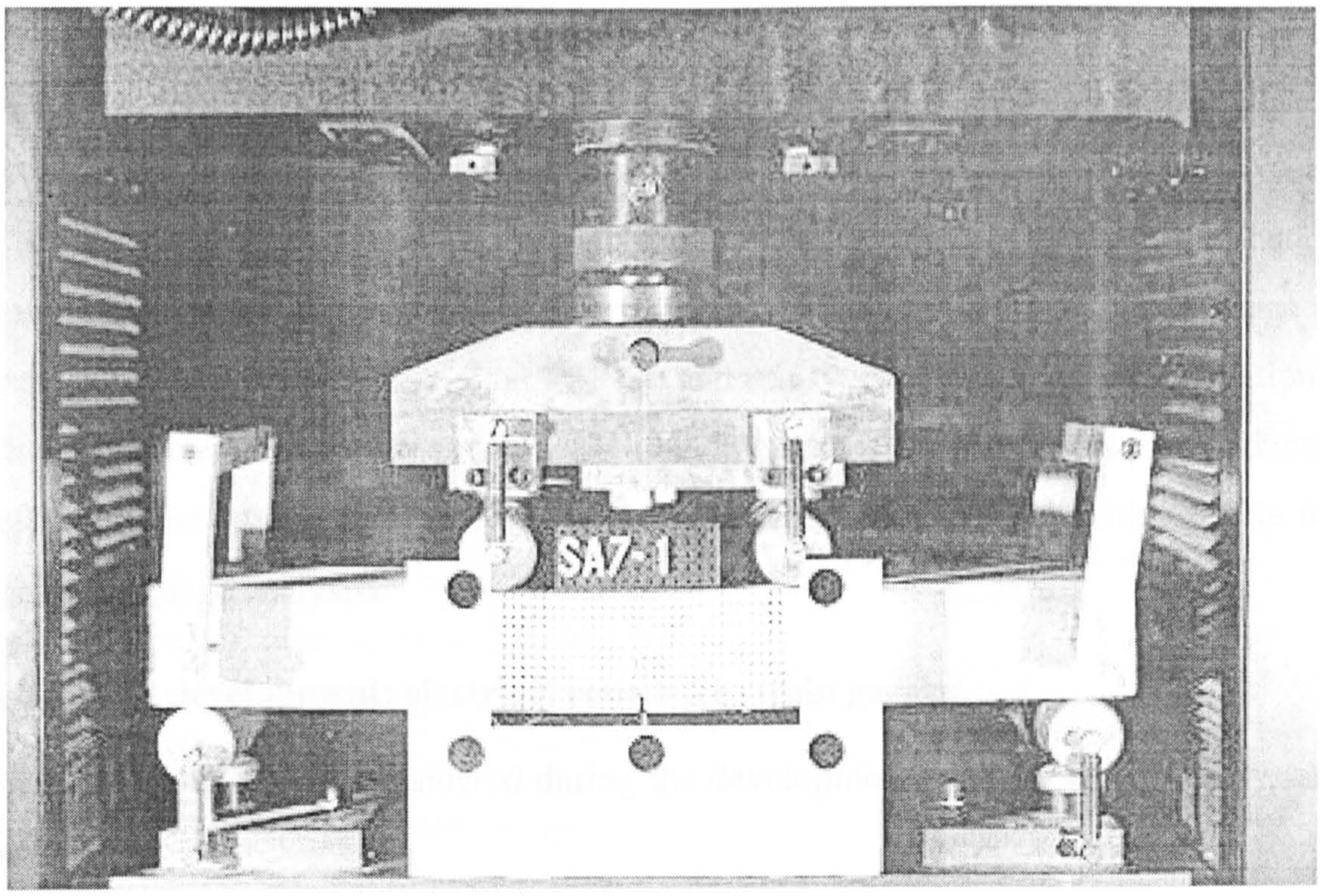

Figure 6.44 Grid method test specimen and target.

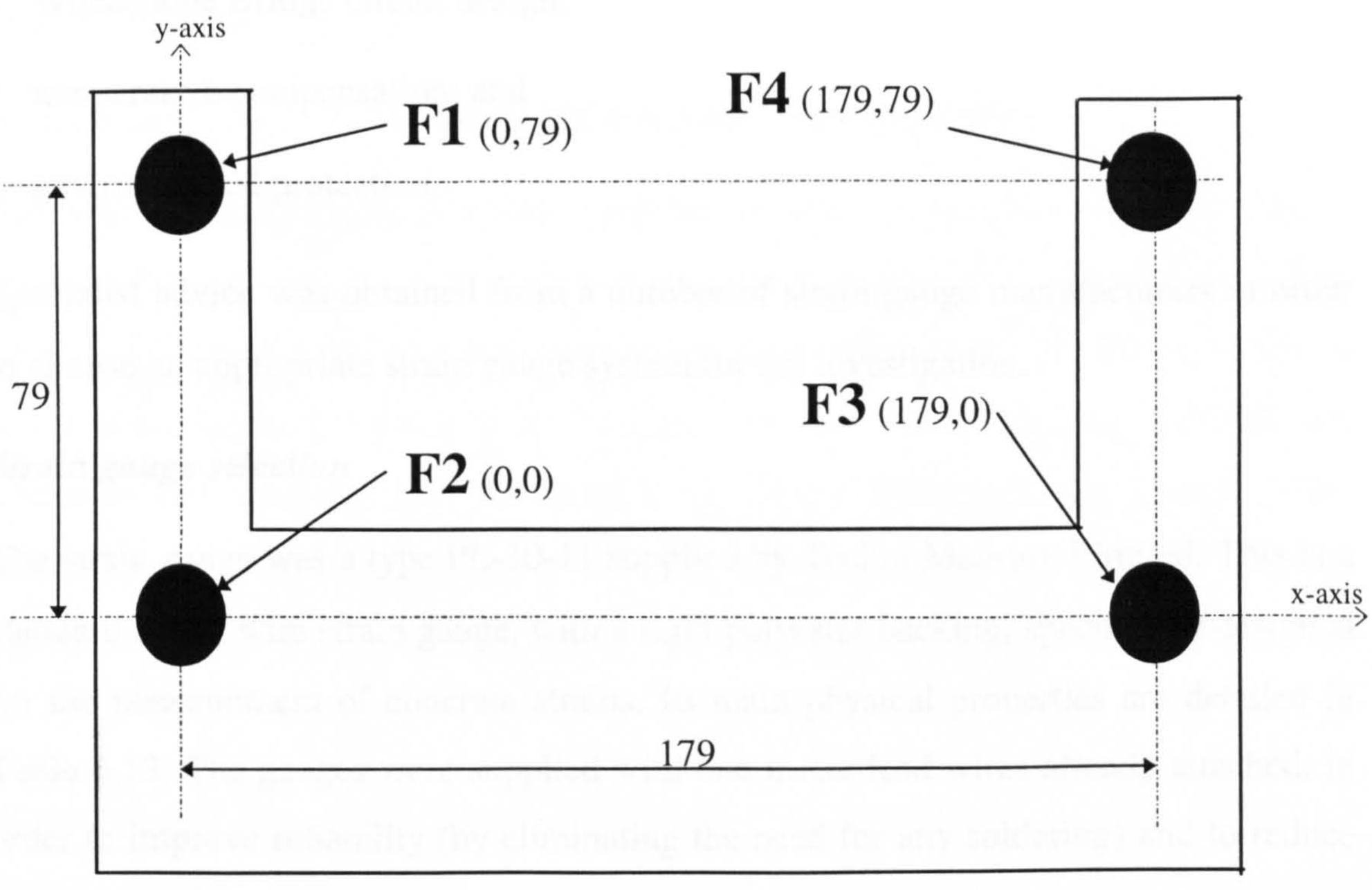

Figure 6.45 Setting-out of target reference points (all dimensions in mm).

The transformed xy photo co-ordinates for the centroid of each grid spot was used to determine the deformation of the grid. This was achieved by determining the distance between the centroids of adjacent grid spots for both the undeformed and deformed grid images using equation 3.9. The distances between adjacent spots in the loaded images were then compared with the corresponding distances in the unloaded image to determine the relative longitudinal (x-axis) and transverse (y-axis) grid deformations. These relative grid deformations were then plotted as a function of beam depth, relative to the compressive face of the beam, to determine the crack-width profile for each grid image analysed.

6.6.3 Test development: electrical resistance strain gauges

Five main stages were considered during the development of the strain gauge system were:

- strain gauge type and size;
- bonding adhesive and procedure;
- Wheatstone Bridge circuit design;
- temperature compensation; and
- environmental protection.

Specialist advice was obtained from a number of strain gauge manufacturers in order to choose an appropriate strain gauge system for the investigation.

Strain gauge selection

The strain gauge was a type PL-30-11 supplied by Techni Measure Limited. This is a standard single wire strain gauge, with a rigid polyester backing, specifically designed for the measurement of concrete strains. Its main physical properties are detailed in Table 6.12. The gauges were supplied with one metre lead wires already attached, in order to improve reliability (by eliminating the need for any soldering) and to reduce installation time.

	Dimensions (mm)						
Type	Gauge length	Gauge width	Backing	Nominal resistance (ohms)	Gauge factor	Strain limit (%)	Operating temperature (C°)
PL-30-11	30	2	43 x 8	120	2.1	2	+10 ~ +80

Table 6.12 Physical properties of the strain gauges used in the investigation.

Bonding adhesives and procedures

The strain gauge bonding adhesives were those recommended by the strain gauge manufacturer for attachment to concrete:

- a polyester precoat - type PS supplied by Techni Measure Limited; and
- a polyester bonding adhesive - type RP-2 supplied by Techni Measure Limited.

The purpose of the precoat was twofold: (1) to seal the specimen surface and fill surface voids, thus forming a desirable surface for gauge bonding; and (2) to prevent the deterioration of electrical insulation due to moisture penetrating from the reverse side of the gauge.

Wheatstone bridge circuit design and temperature compensation

The effect of temperature is a major problem in strain gauge measurements. This is because strain gauges show resistance changes (and hence a strain reading) as a result of changes in both strain and temperature. The main cause of this problem is temperature-induced resistance changes in the leadwires. Various methods are available for compensating for temperature effects (Measurements Group, 1992) including: (a) using a dummy gauge in a two-wire Wheatstone bridge circuit (known as the active-dummy method); (b) using a three-wire Wheatstone bridge circuit; or (c) using temperature compensating strain gauges.

In this investigation, the effects of temperature were compensated by using the active-dummy method. A schematic illustration of the Wheatstone bridge circuit adopted is shown in Figure 6.46. Note that the active and dummy (or compensating) gauges were of identical construction (that is, the same gauge type and lead wire length). In each test the required number of active gauges were bonded to the test specimen and a

single common dummy gauge was bonded to a separate identical specimen. This dummy specimen was placed adjacent to the test specimen during the test but was not subjected to an applied load.

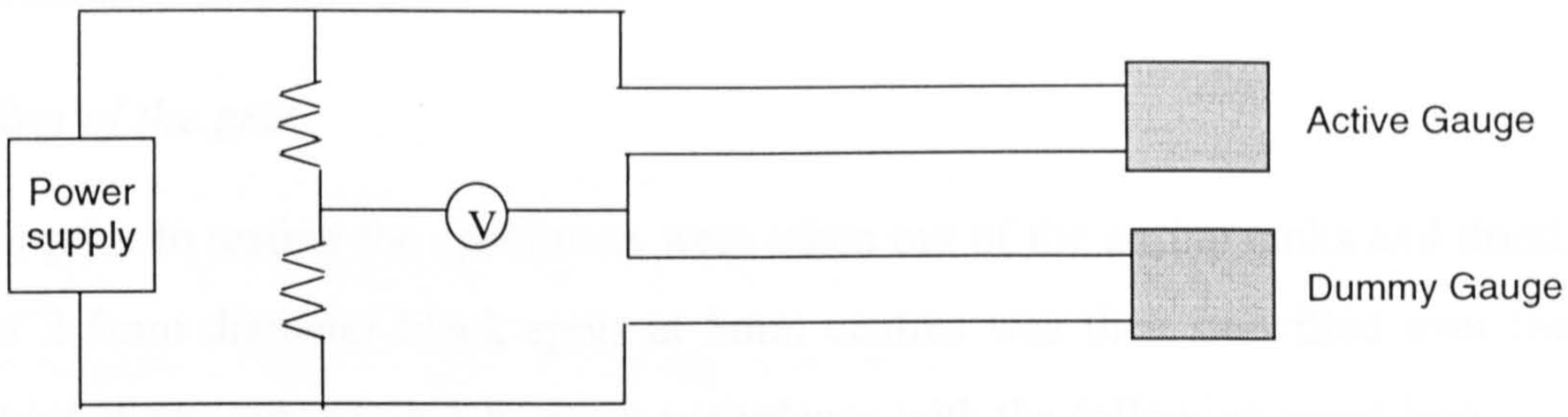

Figure 6.46 Half-bridge Wheatstone bridge circuit.

Environmental protection

Waterproofing of strain gauges is usually recommend for external applications and internal applications over a prolonged period in order to minimise the effects of moisture ingress. However, given that the tests in this investigation were of short duration and performed indoors, it was decided that additional environmental protection was not required.

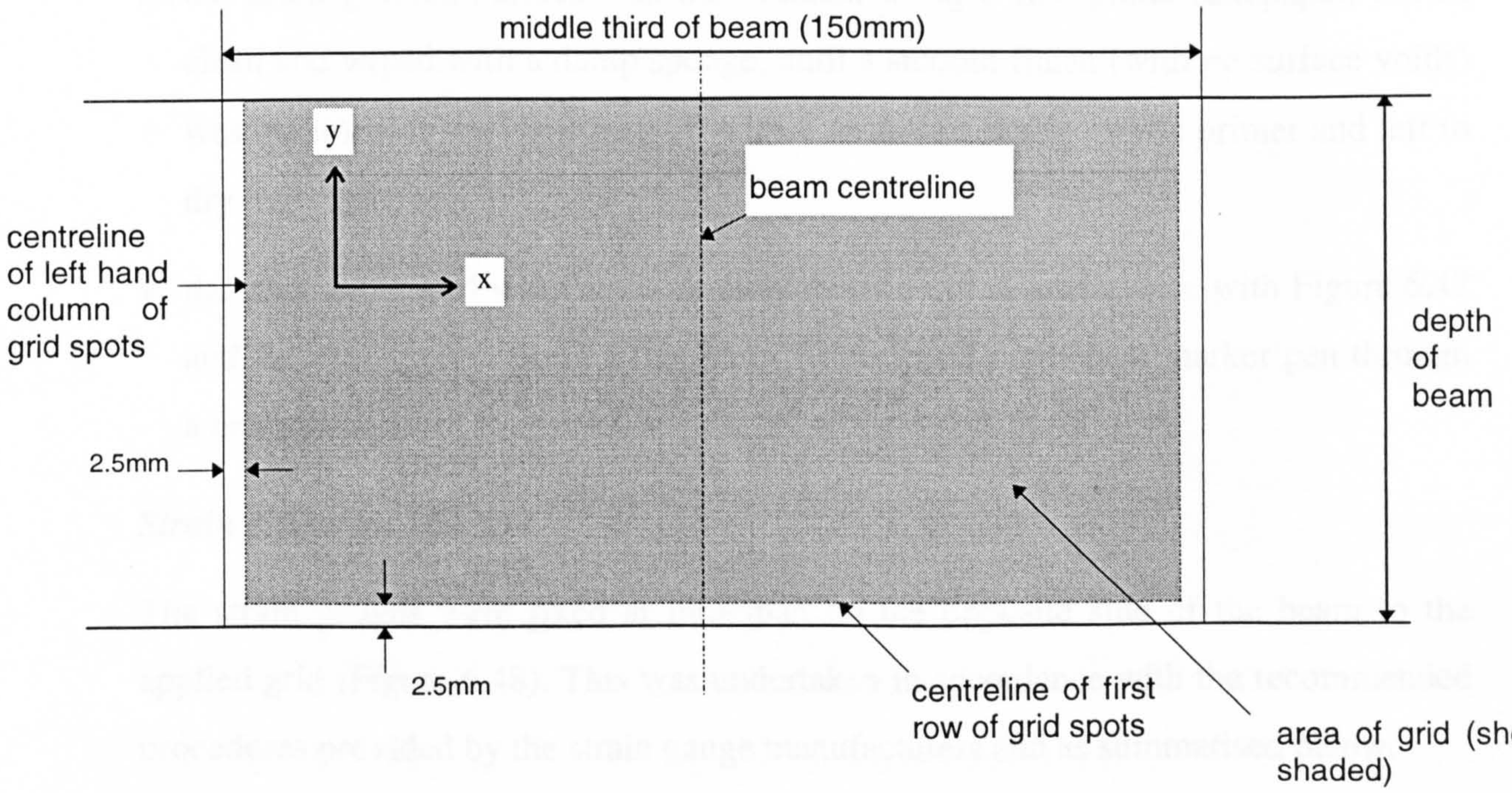

Figure 6.47 Setting-out of grid.

6.6.4 Test procedure

General

Strain analysis tests were performed on a selection of the flexural toughness test beams as detailed in Table 6.3.

Application of the grid

Four days prior to testing the specimens were taken out of the curing tanks and dried. A grid of 2.5mm diameter black spots at 5mm centres was then stencilled over the middle-third of one side of each beam in accordance with the following procedure:

i. the area of the grid was roughly marked-out with a pencil and sanded down to remove any loose material;

ii. the sanded area was then blown clean with a high pressure air hose and wiped with a damp sponge;

iii. this area was then covered with a pre-mixed grout which was worked into all the surface voids with a palette knife, smoothed off with a steel float and left to dry for six hours. The mix design for the grout was based on Matrix C (Table 5.6) except the aggregate was sieved through a standard 600 micron sieve prior to mixing;

iv. the dried grouted surface was then sanded using a fine grade sandpaper, blown clean and wiped with a damp sponge, until a smooth finish (with no surface voids) was obtained. It was then sprayed with 4 coats of a white acrylic primer and left to dry overnight; and

v. the area of the grid was then accurately marked out in accordance with Figure 6.47 and the grid applied using a fine black fibre-tipped permanent marker pen through a brass stencil.

Strain gauge installation

The strain gauges were fixed at mid-span on the opposite side of the beam to the applied grid (Figure 6.48). This was undertaken in accordance with the recommended procedures provided by the strain gauge manufacturers and as summarised below.

i. The area of the gauge installation was abraded with a wire brush to remove any loose particles. It was then blown clean with an air hose, thoroughly washed with distilled water and left to dry.

ii. The gauge positions were then accurately set-out and the centrelines of each gauge marked with a pencil.

iii. As soon as the prepared area was dry, the PS precoat adhesive was applied in accordance with the manufacturer's instructions. The specimen was then left for approximately 2 hours to allow the adhesive to harden.

iv. Each gauge was then fixed in position using the RP-2 bonding adhesive in accordance with the manufacturers instructions, and the specimen left overnight.

v. Finally, the strain gauge lead wires were connected to the data logger.

The number and positions of the strain gauges for each beam size and type investigated are detailed in Table 6.13. Note that a single gauge (SG1) was installed on the compressive face of each specimen to measure the maximum compressive strain throughout each test.

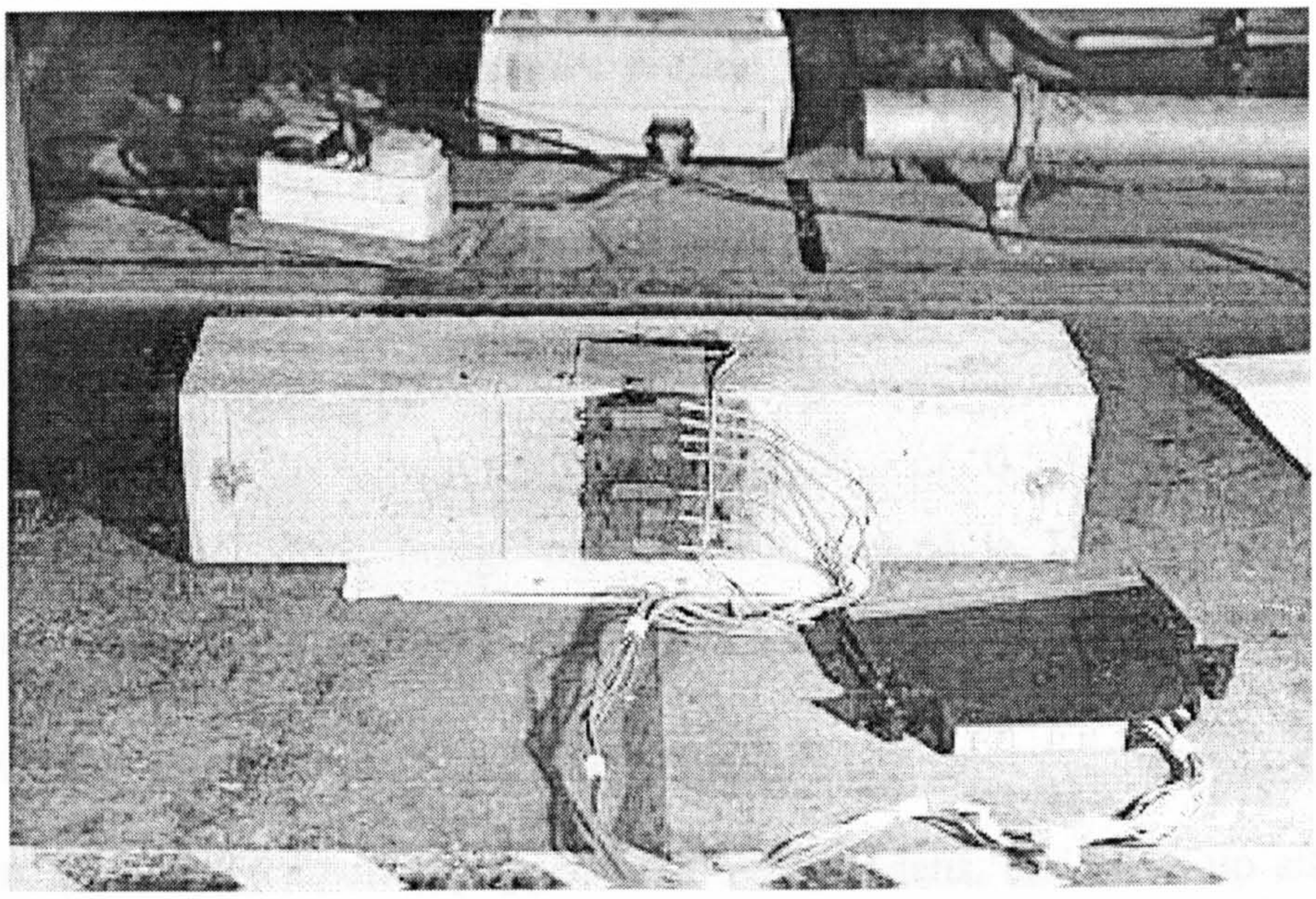

Figure 6.48 Showing strain gauges attached to test specimen.

Strain gauge reference	Distance from compressive face of beam to the centreline of the gauge (mm)			
	100mm unnotched beams	75mm unnotched/ 85mm notched cast beams	75mm unnotched sprayed beams	60mm notched beams
SG1	0	0	0	0
SG2	6	6	6	6
SG3	16	16	16	16
SG4	26	26	26	26
SG5	36	36	36	40
SG6	60	46	52	-
SG7	75	56	68	-
SG8	94	68	-	-

Table 6.13 Number and position of strain gauges for each beam size and type investigated.

Test procedure

Tests were performed in an Instron 6025 screw driven testing machine using a 10kN load cell in accordance with the flexural toughness test procedure detailed in Section 6.5. However, in order for the specimen grid to be photographed during the test only one arm of the yoke and, hence, one LVDT could be used to measure mid-span deflection.

Load, deflection and strain gauge readings were digitally recorded using a 24 channel data acquisition system operating at a frequency of 0.5Hz. The data logger incorporated a Wheatstone bridge circuit as illustrated in Figure 6.46, and was programmed to record strain directly in units of microstrain.

Photographic acquisition of the specimen grid

A Cannon T-90 SLR camera equipped with a 50mm lens, and close-up attachment, was used to acquire the 35mm photographic negatives of the grid. Kodak TMax Pro 100 ASA (black and white) film was used, with a fixed aperture of f/11 and shutter speed of 1/125s. A 0.5 exposure compensation, with centre weighted average

metering, was also used to enhance contrast. The specimen was illuminated by two helium spot lamps placed at predetermined positions either side of the camera. The camera was mounted on a tripod and fixed in position at a predetermined height and off-set from the face of the specimen (Figure 6.49). This provided a field of view which just encapsulated the grid and reference grid spots (Figure 6.50) without the need to adjust the position of the camera during the test. The camera shutter was controlled by remote control, via a shutter lead, to minimise camera vibrations.

The camera and lighting set-up was the result of a systematic test development involving a series of preliminary tests to determine the optimum set-up to produce the highest contrast (determined by size of the grey level difference) and highest image clarity (determined by the size of the resolved grid spots). The set-up variables investigated were: aperture f/11 and f/13; exposure compensation of 0 and 0.5; and four different light settings producing shutter speeds between 1/45-1/180s.

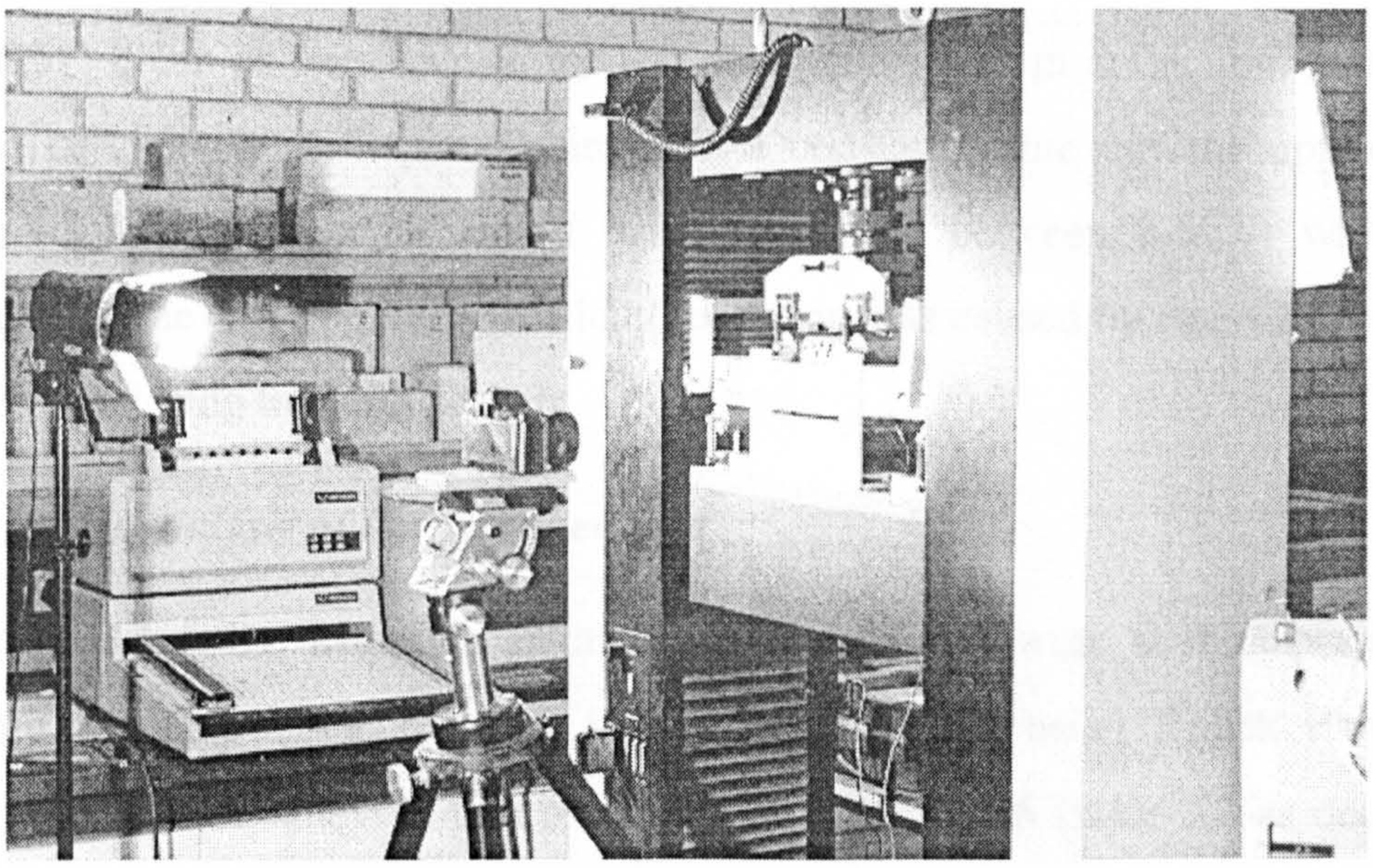

Figure 6.49 Strain analysis test set-up.

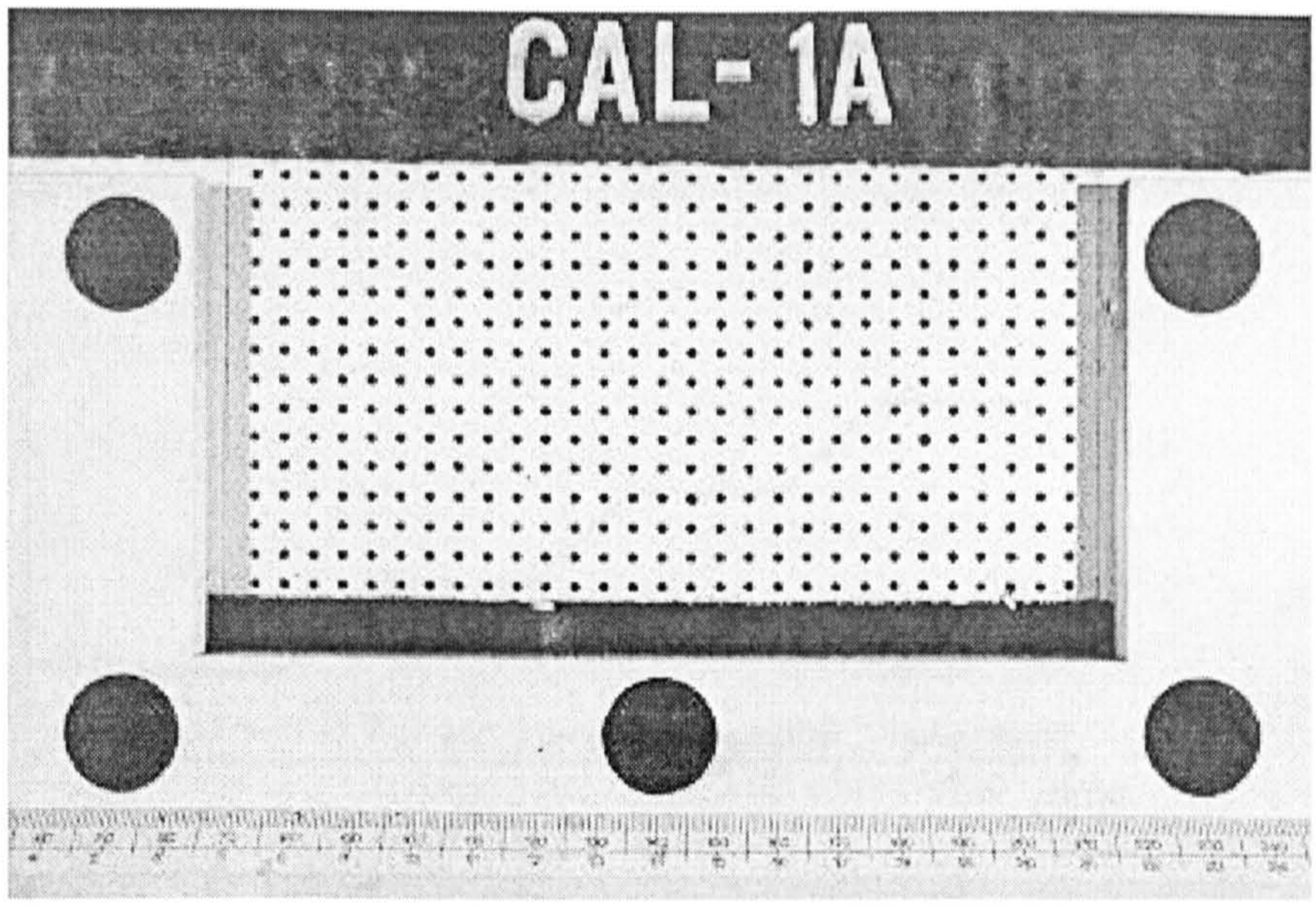

Figure 6.50 Typical grid method photograph showing the field of view.

During each test, the specimen grid was photographed at six different mid-span deflections: 0, 0.2, 0.5, 1.0, 2.0 and 4.0mm. The test was held at each deflection for 10 seconds to allow the photographs to be taken. A typical deflection-versus-time plot obtained from the tests and the corresponding load-versus-time plot are shown in Figure 6.51. It can be seen, due to the test being controlled in deflection, that during the hold periods the deflection maintained a constant value but the applied load displayed a temporary reduction in value (generally between 2-5kN) which was regained once the test restarted. This load reduction was caused by stress relaxation in the specimen during the hold periods.

Digital image analysis of the specimen grid

The six photographic negatives obtained from each test were first dispatched for electronic scanning and conversion into a digital format using Kodak Photo CD. Digital images were analysed at a resolution of 1024 x1536 (Base X4 as detailed in Table 6.11) corresponding to a file size of approximately 1.50Mb per image.

The Visilog software, running on a 128Mb SUN-UNIX Ultrasparc 140 computer, was used to analyse the digital images. Table 6.14 shows representative size and shape characteristics for both the 25mm diameter specimen grid spots and 20mm diameter reference spots as determined from the analysis. The spot size is a measure of the

number of pixels making-up the spot, and the shape factor is a measure of roundness of the spot (that is, a perfect circle has a shape factor of unity).

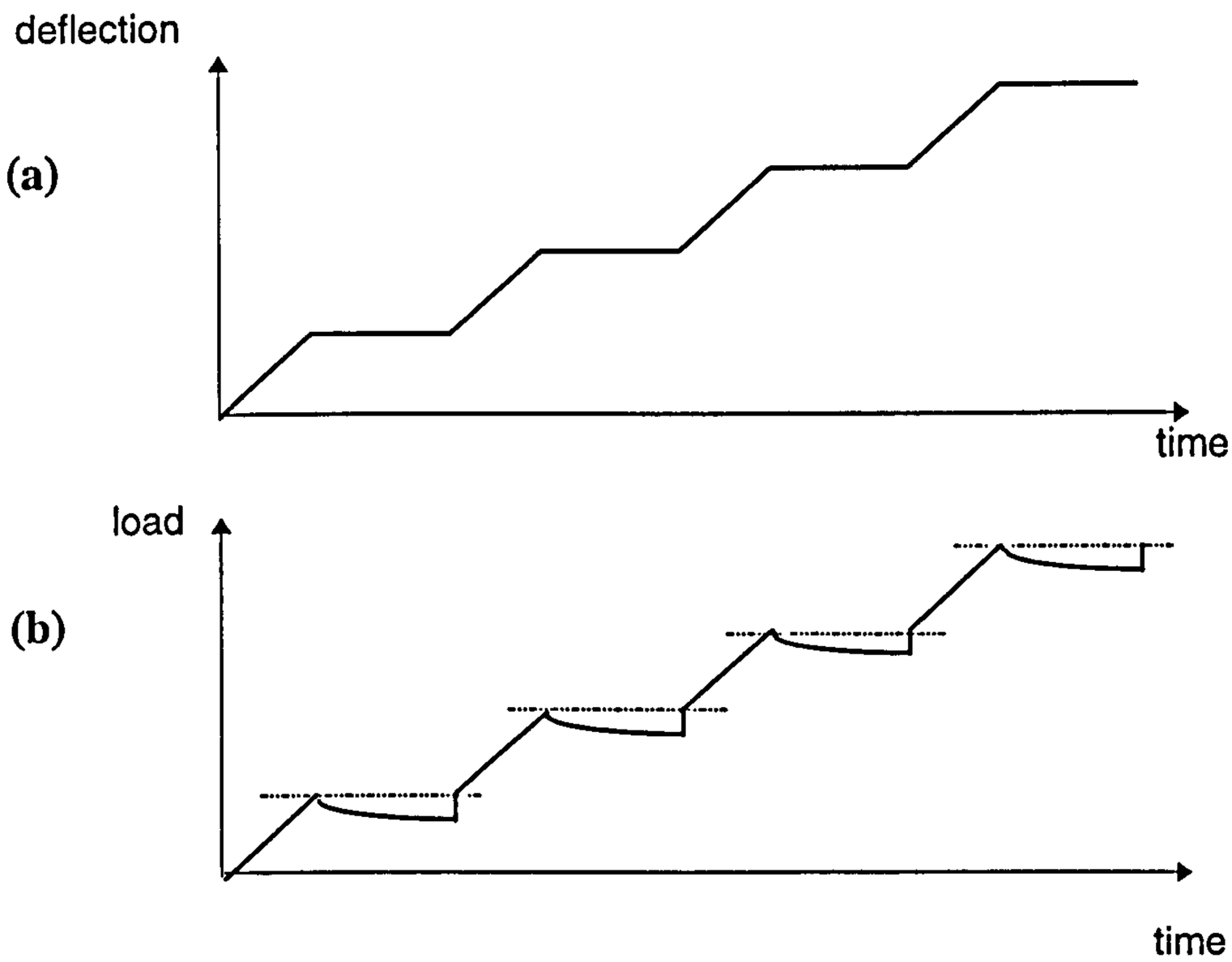

Figure 6.51 Typical plots of (a) deflection versus time, and (b) load versus time from the strain analysis tests.

The Visilog software determined the centroid co-ordinates of each grid and reference spot using automatic thresholding techniques which incorporated the following centroid algorithm functions (Sirkis, 1990):

$$\overline{Y} = \frac{\sum_{k=k_0}^{k_f}\sum_{l=l_0}^{l_f} k(T - G_{kl})}{\sum_{k=k_0}^{k_f}\sum_{l=l_0}^{l_f}(T - G_{kl})} \qquad \text{equation 6.4}$$

$$\overline{X} = \frac{\sum_{k=k_0}^{k_f}\sum_{l=l_0}^{l_f} k(T - G_{kl})}{\sum_{k=k_0}^{k_f}\sum_{l=l_0}^{l_f}(T - G_{kl})}$$

where k_0, k_f, l_0, and l_f define the X,Y window of pixels containing the grid spots, T is the threshold level, and G_{kl} is the grey level of each pixel. Hence, only pixels with a grey level less than T (i.e. black) are included in the determination of the grid spot centroids.

The digital image centroid co-ordinates were then transformed into photo image centroid co-ordinates using the 6 parameter affine transformation detailed in Section 6.6.2. The co-ordinates of the grid spot centroids were then saved in a Microsoft Excel file where they were automatically sorted in terms of their respective row and column positions within the grid.

		Typical spot characteristics	
Spot diameter (mm)	Spot type	Area (pixels)	Shape factor
2.5	grid spot	100-150	1.02-1.10
20	reference spot	11500-12500	1.01-1.06

Table 6.14 Grid spot characteristics (image resolution of 1024 x 1536)

A master Microsoft Excel file was set-up to analyse the grid spots in order to determine the deformation of the grid at each of the six mid-span deflections investigated. A summary of the analysis procedure is detailed below.

i. The distances between adjacent grid spots were calculated at each of the six deflections investigated using equation 3.9. (p.79)

ii. Using the distances between the grid spots in the undeformed grid (that is, at zero mid-span deflection) as the base data, the relative changes in the corresponding grid spot distances in the five deformed grids (at deflections of 0.2, 0.5, 1.0, 2.0 and 4.0mm) were calculated. These relative changes in the distance between adjacent grid spots represented the deformations of the grid.

iii. Grid deformations were then plotted as a function of their location within the grid. From this plot the position and profile of the crack was determined. Finally, knowing the depth to each row position relative to the compressive face of the beam, the crack-width profile was plotted as a function of beam depth.

The above grid analysis procedure assumes that the rotation of the beam is small compared to the deformations of the grid. Hence, strain is calculated as:

$$\varepsilon_x = \frac{\Delta l_x}{l_i} \qquad \text{equation 6.6}$$

where ε_x is the average strain between adjacent grid spots in the x-direction, l_i is the initial distance between adjacent grid spots, and Δl_x is the change in the distance between adjacent grid spots in the x-direction. Thus, across the cracked section of a beam Δl_x corresponds to crack-width (assuming zero strain in the concrete).

	95% confidence interval of significant movement (mm)			
	50mm Lens		28mm lens	
Cross-head movement (mm)	5mm gauge length	30mm gauge length	5mm gauge length	30mm gauge length
0.2	± 0.09	± 0.09	± 0.10	± 0.11
0.5	± 0.08	± 0.09	± 0.10	± 0.14
1.0	± 0.07	± 0.08	± 0.10	± 0.14
2.0	± 0.10	± 0.16	± 0.10	± 0.15
4.0	± 0.09	± 0.18	± 0.11	± 0.14
Average	± 0.09	± 0.12	± 0.10	± 0.14

Table 6.15 Influence of lens size on the accuracy of grid method.

6.6.5 Grid method: accuracy and calibration

Accuracy

The accuracy of the grid method was determined by undertaking a series of controlled tests under zero strain conditions to establish the following:

i. How well do the measured grid deformations compare with actual grid deformations?

ii. What is the smallest grid deformation that can be measured?; and

iii. What effect does camera lens size have on the accuracy of the method?

Tests were undertaken using a 50mm and a 28mm camera lens in accordance with the test procedure described in Section 6.6.4, but no load was applied to the beam. The undeformed grid was photographed at cross-head movements of 0, 0.2, 0.5, 1.0, 2.0

and 4.0mm to simulate the deflection limits used in the main test series. The digital images of the grid were then analysed to establish a statistical distribution for the deformations between adjacent grid spots for each relative cross-head movement. From the data a 95% confidence interval of significant grid deformation was determined, which represented the smallest grid deformation that could be measured.

Table 6.15 shows the results of the analysis for both the 50mmm and 28mm camera lens over a gauge length of 30mm (i.e. between grid spots seven columns apart) and a gauge length of 5mm (i.e. between adjacent grid spots) in the x-direction. It can be seen from the results that the 95% confidence interval is approximately 0 ± 0.1mm, irrespective of camera lens size, gauge length or cross-head movement. Over a gauge length of 30mm this error equates to a strain of approximately $\pm 3500\mu\varepsilon$.

Residual errors

The residual error resulting from the least squares transformation of the digital image grid co-ordinates to the photo grid co-ordinates, for all the specimens analysed, had a mean value of 0.2mm and a standard deviation of 0.1mm. This error corresponds to a maximum grid distortions of approximately 5% over the depth of the grid and 2.5% over the width of the grid, indicating only moderate distortions as a result of the camera lens and photographic processing. However, it is not clear what effect this error has on the measured grid deformations obtained from the analysis due to the following: (a) the residual error is a function of the test set-up and therefore shows only a small variation between different images of the same specimen grid; and (b) because the analysis determines relative grid deformations (based on the undeformed grid image) the residual errors may have a nullifying effect on the grid deformation measurements.

Calibration

Scale factors were also determined from each test series in order to calibrate the measured grid deformations. These factors account for the effects of grid distortion and variations in the test set-up as a result of: least squares residuals; camera lens distortion; photographic processing and development; and variations in the camera and lighting set-up. For each test, the image of the undeformed grid (that is, at a zero deflection) was analysed to obtain the average distances between adjacent grid spots

centroids in both columns (x-direction) and rows (y-direction). These distances were then compared with the theoretical spot spacing of 5mm to determine the scale factors. The results from all the beams analysed showed the average distance between adjacent spots varied between 4.65-4.90mm (in both the vertical and horizontal directions) indicating a scale factor of between 1.08-1.02.

6.6.6 Strain gauges: accuracy and calibration

General

A series of tests were undertaken to establish the following strain gauge characteristics:

i. The accuracy of the gauge readings under steady state conditions and no applied load.

ii. The accuracy of the gauge readings under an applied load.

Accuracy under steady-state conditions

Eight strain gauges fixed on two 75mm deep test beams and prepared in accordance with the procedures described in Section 6.6.4 were monitored for a 20 minute interval (i.e. 600 readings per gauge) in steady-state conditions without any applied flexural load. The time interval was chosen to simulate the duration of a flexural toughness test. The variation in the strain gauge readings, calculated as a sample standard deviation, was found to vary between $\pm 1\mu\varepsilon$.

Accuracy under an applied load

The accuracy of the strain gauges under an applied load was determined by comparing measured strains, up to an assumed deflection within the elastic limit, with theoretical strains calculated from elastic theory. For the third point loaded beams investigated, the elastic strain ε at any point within the middle third region was determined from the equation:

$$\varepsilon = \frac{8.y_g.\delta^*}{L_p^2} \qquad \text{equation 6.6}$$

where y_g is the distance from the neutral axis to the position of the strain gauge, δ^* is the mid-span deflection measured relative to the load points (approximately 0.13

times the mid-span deflection measured relative to the support points), and L_p is taken as the distance between the load points. Note that the deflection at the elastic limit was assumed to occur at 0.1mm in the 75 and 60mm deep beams, and at 0.07mm in the 100mm beams. In general, for all the beams tested, the mean difference between measured and theoretical strains ranged between ±12 με (SD 10με). This difference can be attributed to various factors associated with strain gauge measurement including: (1) operator error during gauge installation in terms of gauge location, orientation and poor adhesive bond; (2) errors in the strain measurement system due to heat dissipation, electrical noise and a non-linear output from the Wheatstone bridge; and (3) variations in measured strain due to local stress fluctuations occurring within the concrete matrix over the 30mm gauge length. In the isolated cases where the mean differences were greater than 15με, the quality of gauge installation was considered unacceptable and the strain readings discarded from the subsequent strain analysis. Thus, the accuracy of the strain gauge measurements under an applied load was considered to be within ± 15με.

6.6.7 Results and discussion: grid method

General

Figure 6.52 represents a series of photographs showing the development of a crack during a typical grid method test. Note that some specimens cracked outside the area of the grid (Figure 6.53(a)), which prevented the grid analysis from being undertaken, and others developed multiple cracking (Figure 6.53(b)). In both cases the results were not used in the subsequent crack width analysis or model development. From the 20 beams tested, 6 cracked outside the area of the grid and 5 displayed multiple cracking. A summary detailing the crack locations relative to the mid-span for all the beams tested, and whether or not multiple cracking occurred, is given in Table 6.16. The variability in the position of the crack in the unnotched beams as highlighted in this data is discussed in the next section. It can be seen from this table that out of all the beams tested only six failed at a single crack located close to mid-span: (a) three 60mm deep notched specimens; (b) two 85mm deep notched specimens: and (c) a 100mm deep unnotched specimen.

Crack-width profiles

Representative crack-width profiles for the beams failing at a single crack are shown in Figure 6.54 for the four different beam sizes investigated. It can be seen that the crack-width profiles are represented by straight lines obtained by linear regression analysis. The results also indicate the following observations:

- as the beam deflection increases, the crack widens and its origin moves towards the compressive face of the beam;
- the CMOD at a given deflection increases with an increase in beam depth;
- the linear regression coefficient (R^2) increases with increasing beam deflection, indicating a closer linear fit to the data;
- the value of R^2 generally only exceeds 0.95 (indicating a near perfect linear fit) for beam deflections greater than 0.5mm; and
- crack widths less than 0.2mm cannot be measured accurately.

Figure 6.55 shows the variation in CMOD (obtained from the crack-width profiles) as a function of the distance the crack occurred from mid-span for the 75 and 100mm deep unnotched beams. Note that because the notched beams cracked at mid-span (i.e. at the notch) the equivalent figures for the notched beams are not shown. The results show a general increase in the value of CMOD for an increase in the distance the crack occurred from mid-span. At a deflection of 4mm the results indicate an increase in CMOD between mid-span and the limit of the middle-third region of approximately 1mm for the 75mm deep beams and approximately 2.5mm for the 100mm deep beams.

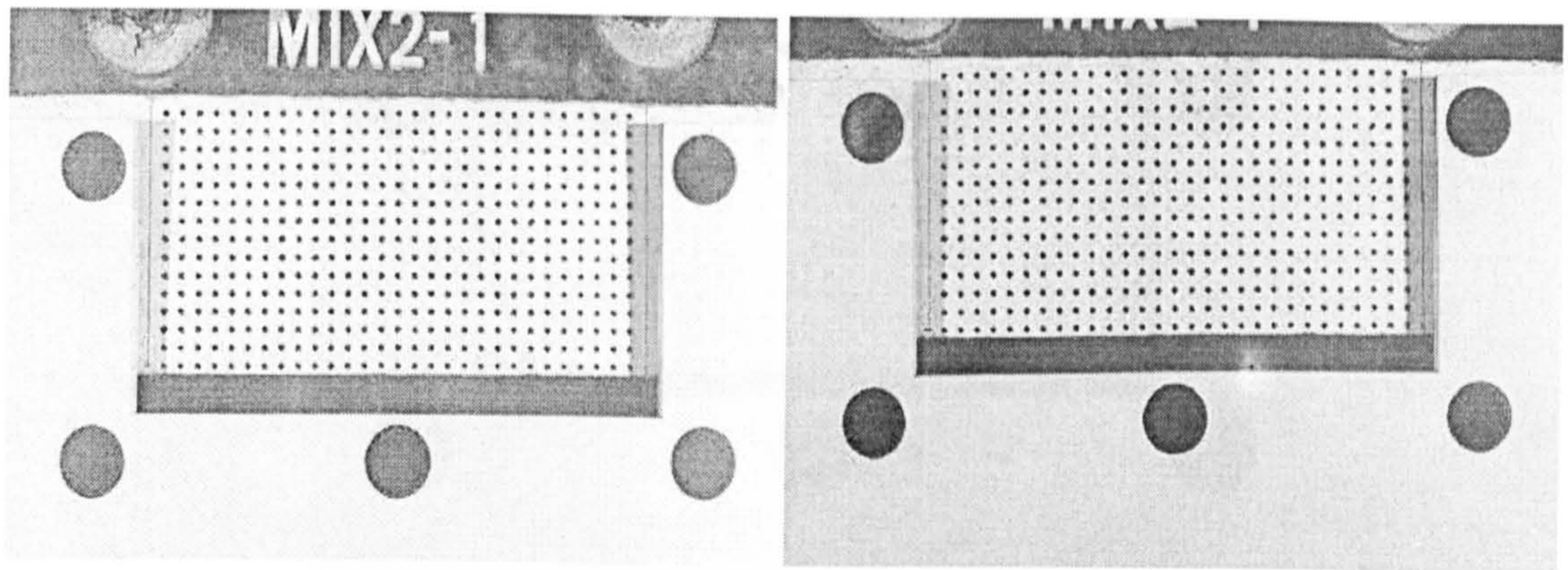

(a) unloaded specimen.

(b) 0.2mm deflection.

(c) 0.5mm deflection.

(d) 1.0mm deflection.

(e) 2.0mm deflection.

(f) 4.0mm deflection.

Figure 6.52 Development of a crack during a grid method test on an unnotched beam specimen.

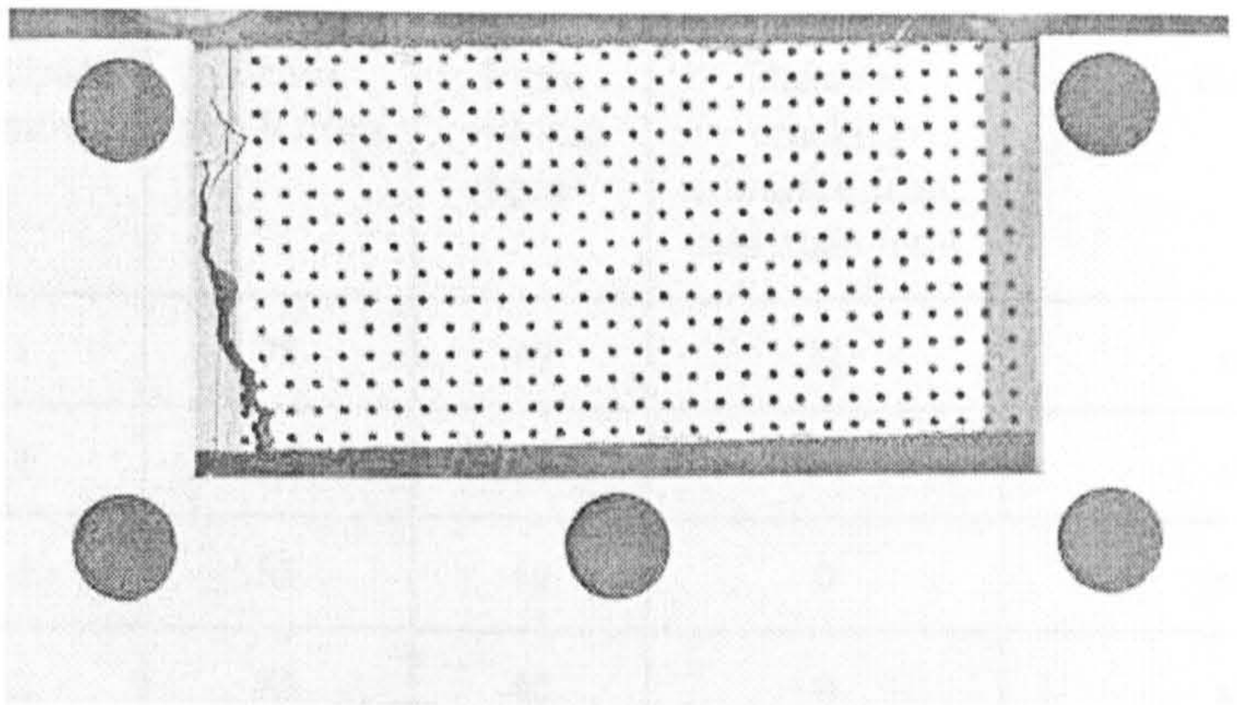

(a) Specimen cracked outside area of grid.

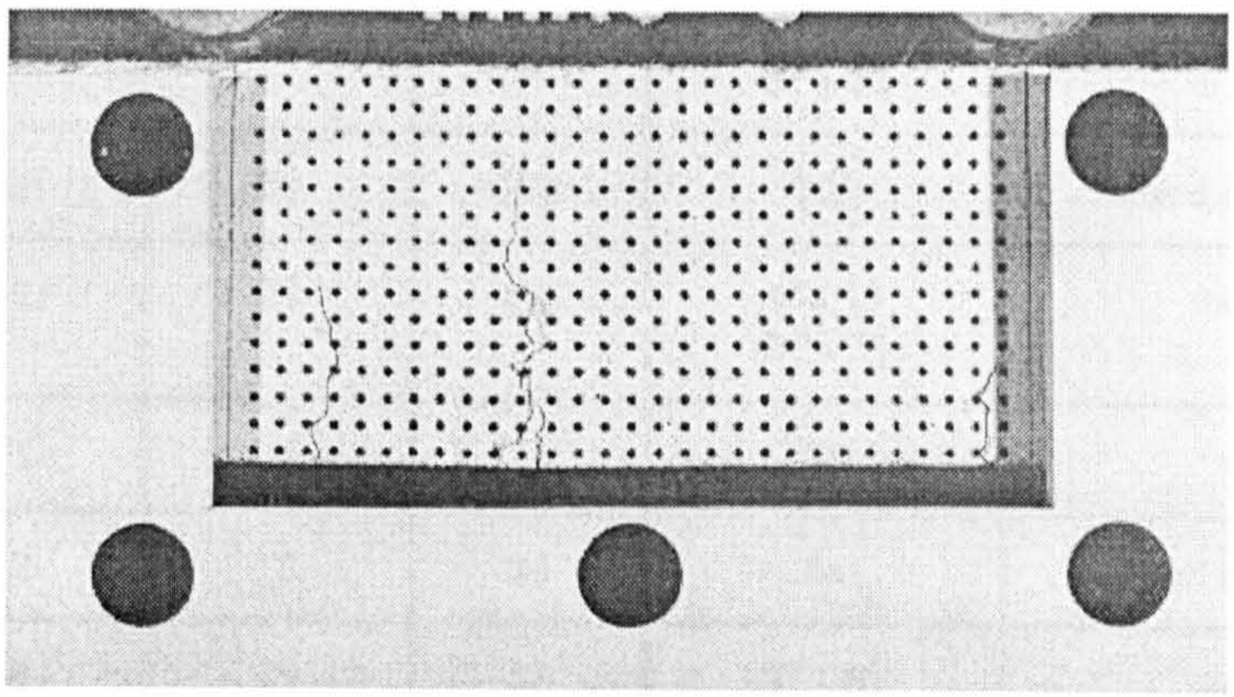

(b) Multiple cracked specimen.

Figure 6.53 Examples of grid method test results that could not be analysed.

Test reference	Specimen number	Beam depth /mm	Fibre volume /kgm^{-3}	Distance crack(s) occurred from mid-span /mm	Failure mode
SA1 unnotched	1	75	40	31	single crack
	2	75	40	64	single crack
SA2 notched	1	85	40	0	single crack
	2	85	40	0	single crack
SA3 unnotched	1	75	80	82	cracked outside middle third
	2	75	80	1st - 22 2nd - 75 3rd - 10	multiple cracks
SA4 unnotched	1	75	120	105	cracked outside middle third
	2	75	120	1st - 15 2nd - 75	multiple cracks
SA5 sprayed	1	75	26	56	single crack
	2	75	26	84	cracked outside middle third
SA6 sprayed	1	75	66	1st - 65 2nd - 25	multiple cracks
	2	75	66	1st - 86 2nd - 26	multiple cracks
SA7 notched	1	60	40	0	single crack
	2	60	40	1st - 0 2nd - 50	multiple cracks
SA9 notched	1	60	80	0	single crack
	2	60	80	0	single crack
SA8 unnotched	1	100	40	1st - 5 2nd - 65	multiple cracks
	2	100	40	15	single crack
SA10 unnotched	1	100	80	1st - 0 2nd - 75	multiple cracks
	2	100	80	43	single crack

Table 6.16 Summary of results from strain analysis tests.

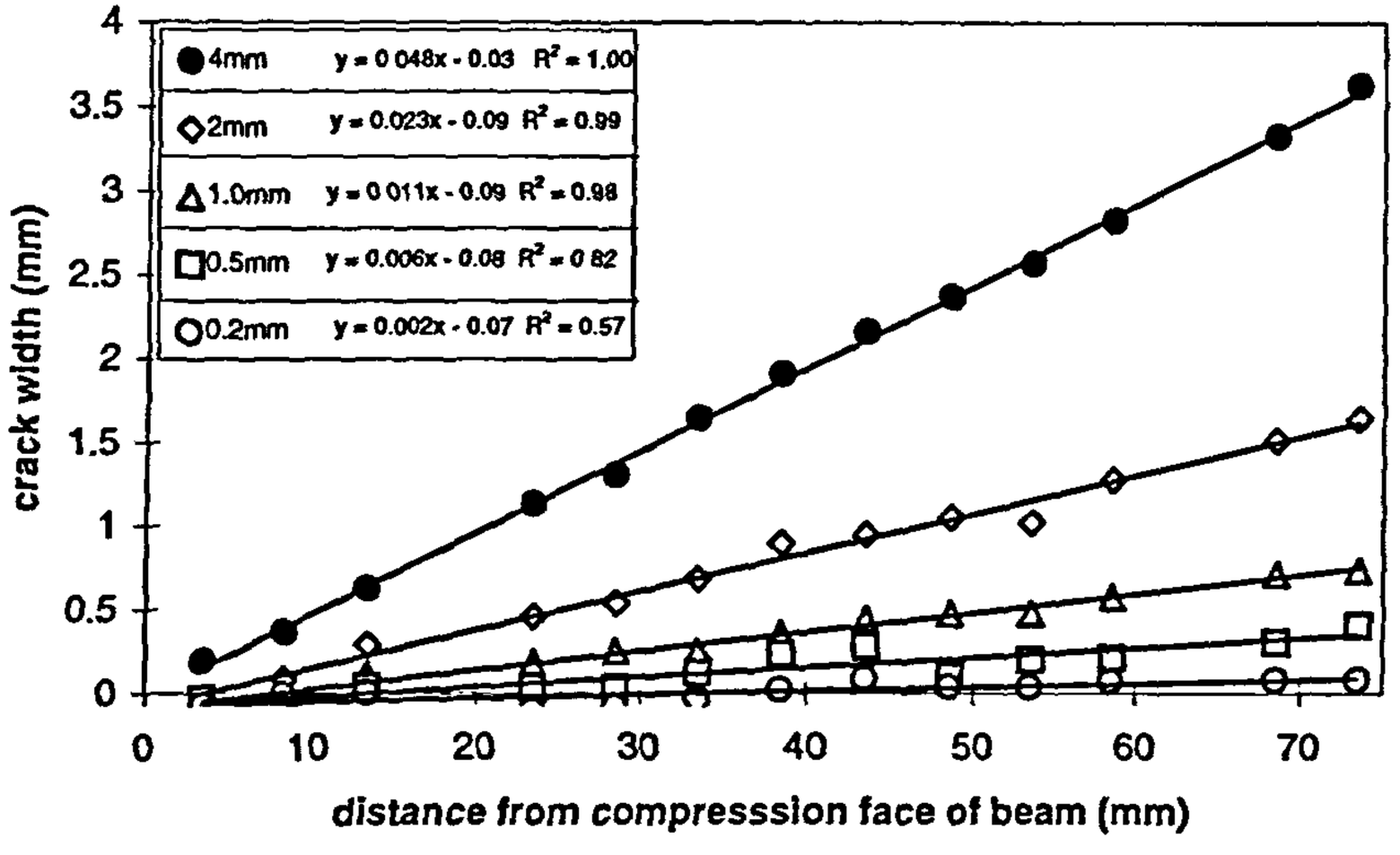

(a) SA5/1 - 75mm unnotched.

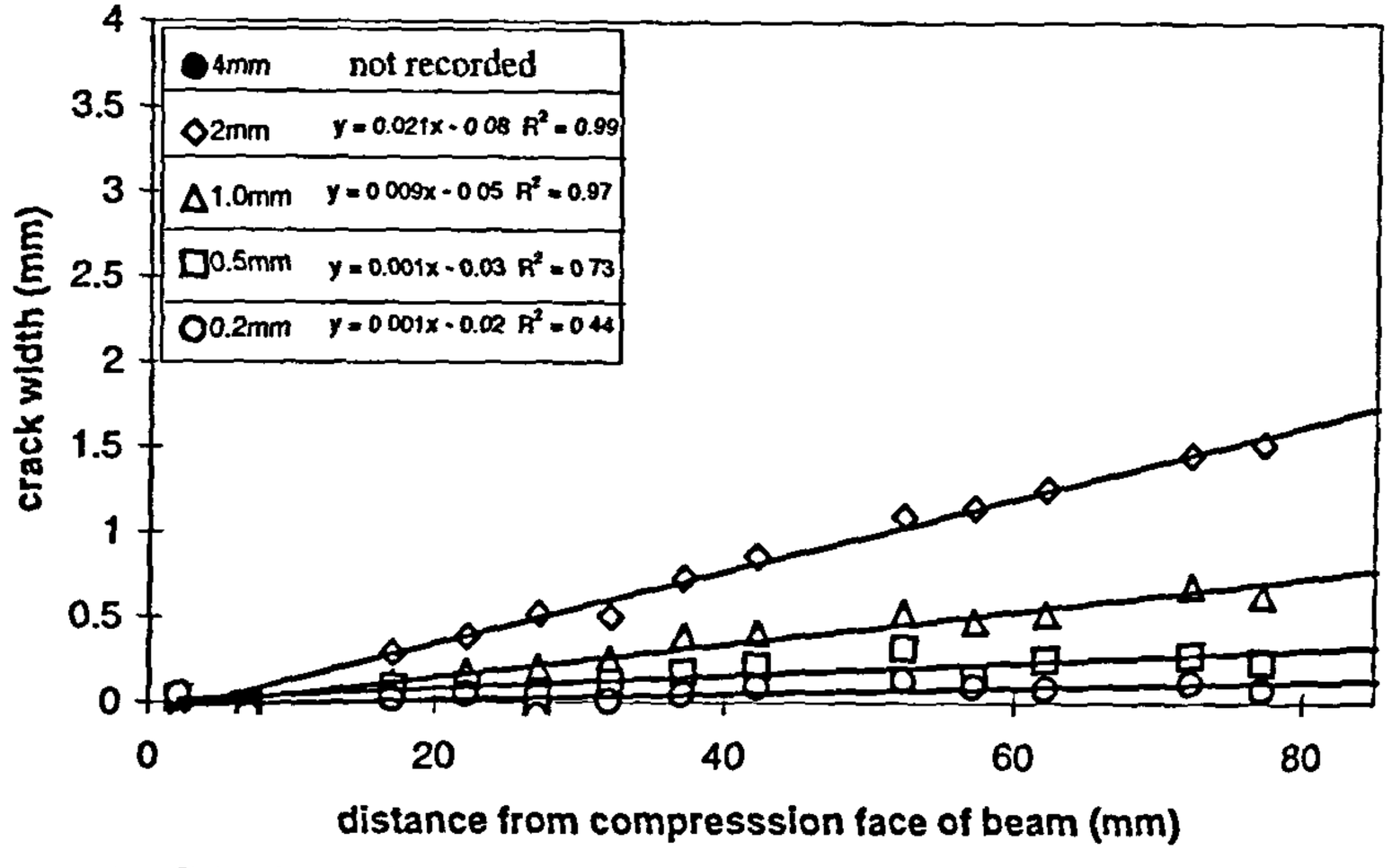

(b) SA2/1 - 85mm notched.

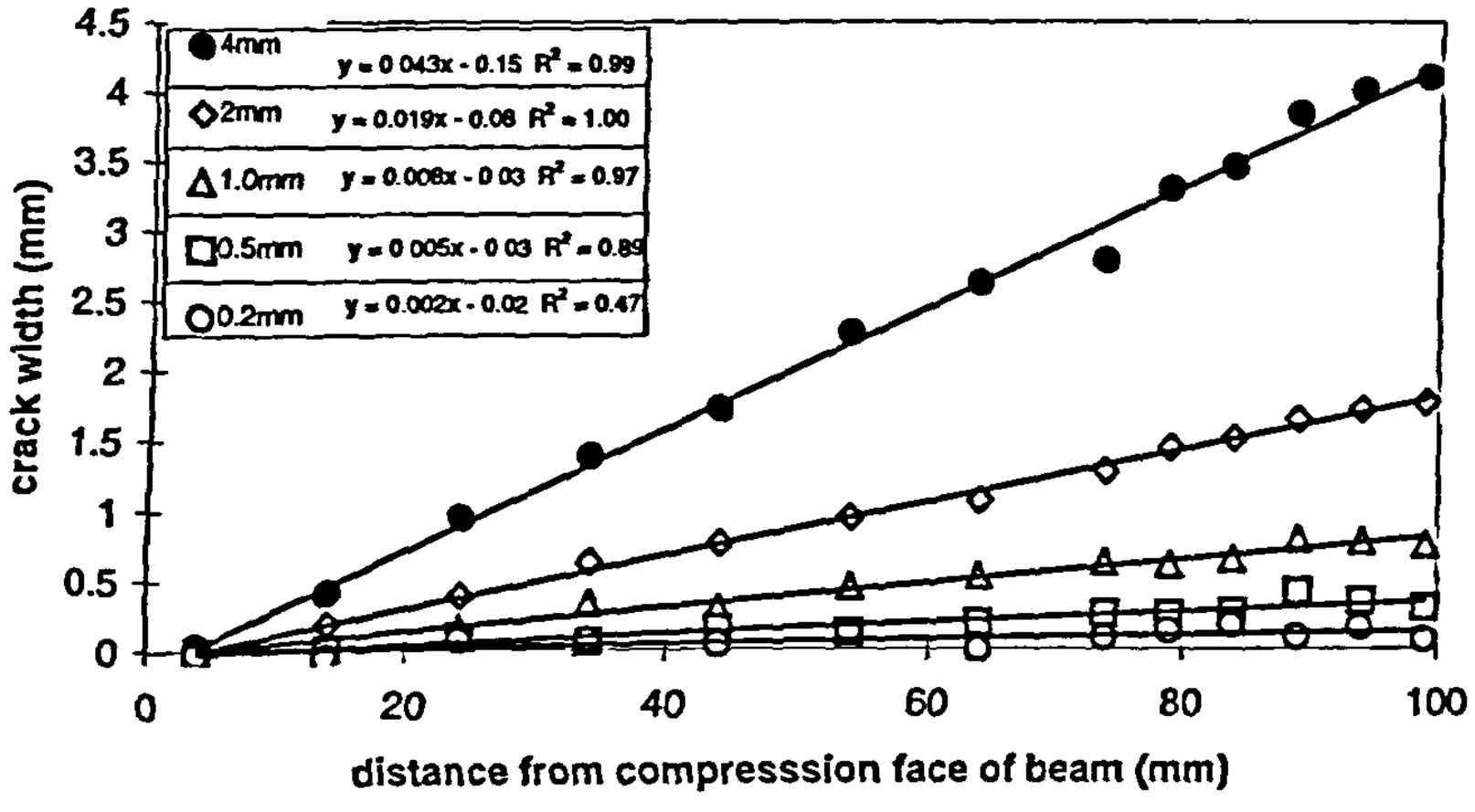

(c) SA8/2 - 100mm unnotched.

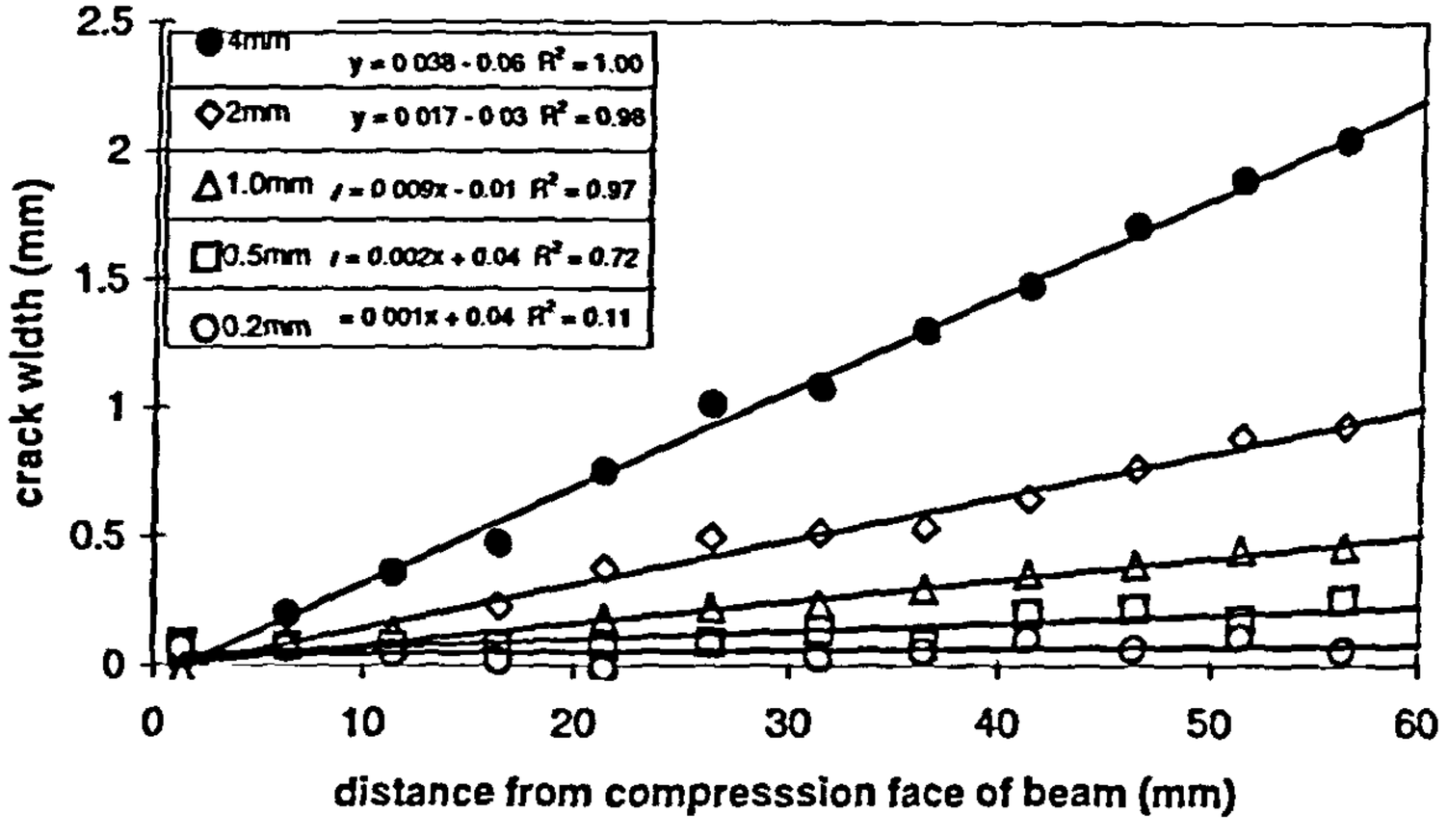

(d) SA7/1 - 60mm notched.

Figure 6.54 Representative crack-width profiles from grid method analysis.

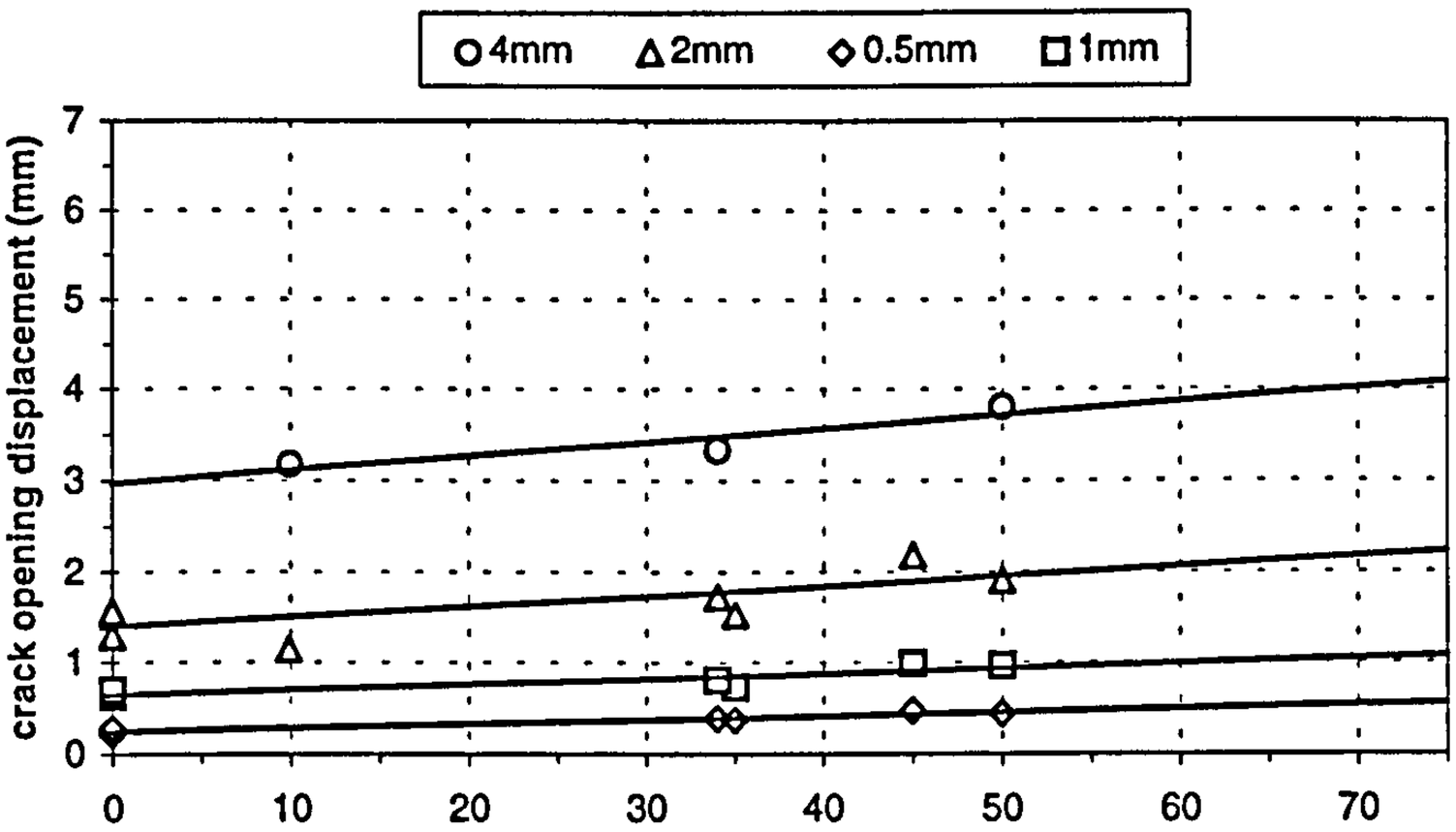

(a) 75mm unnotched and 85mm notched specimens.

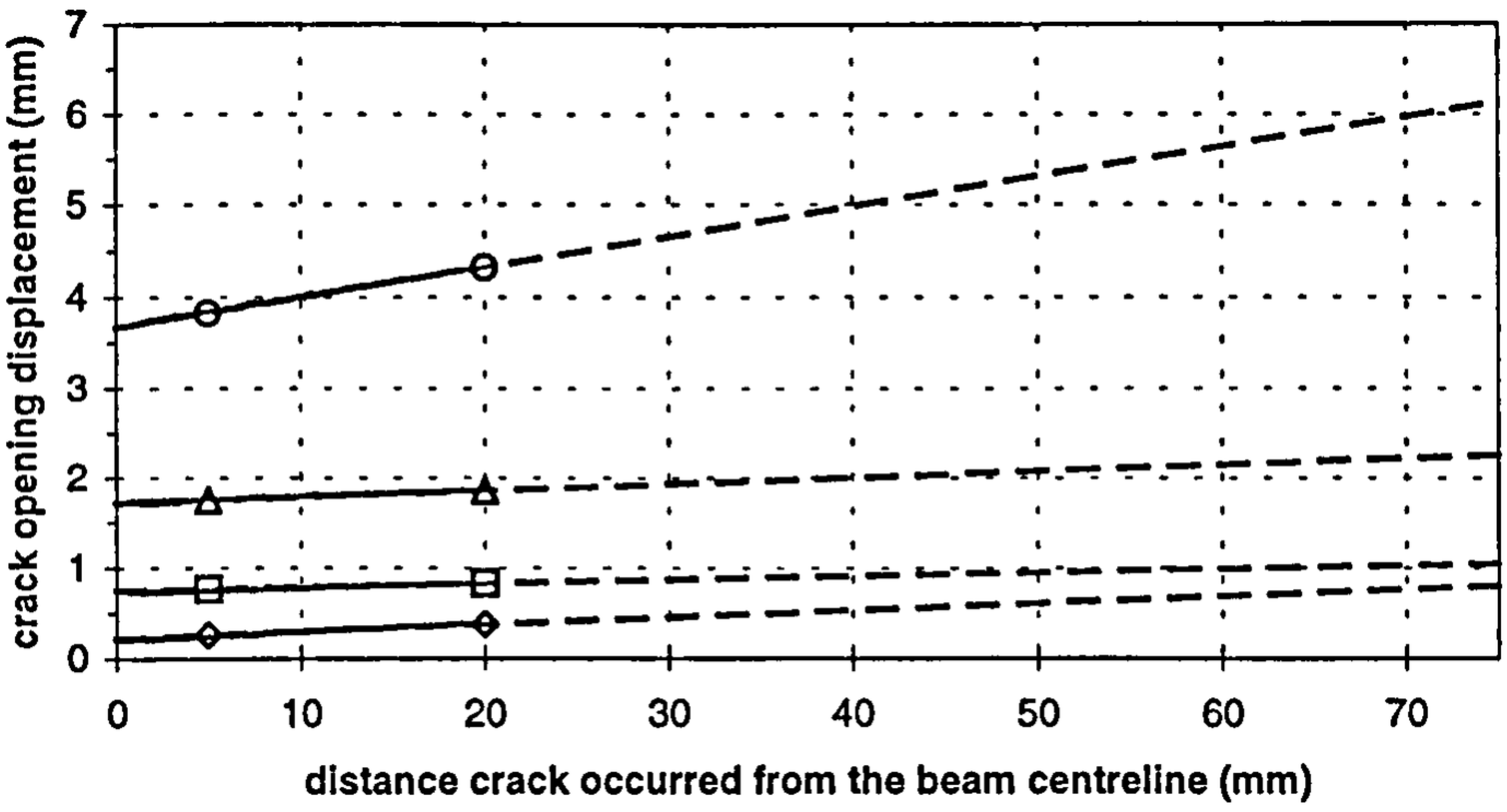

(a) 100mm unnotched specimens.

Figure 6.55 Variation in CMOD with distance crack occurred from mid-span.

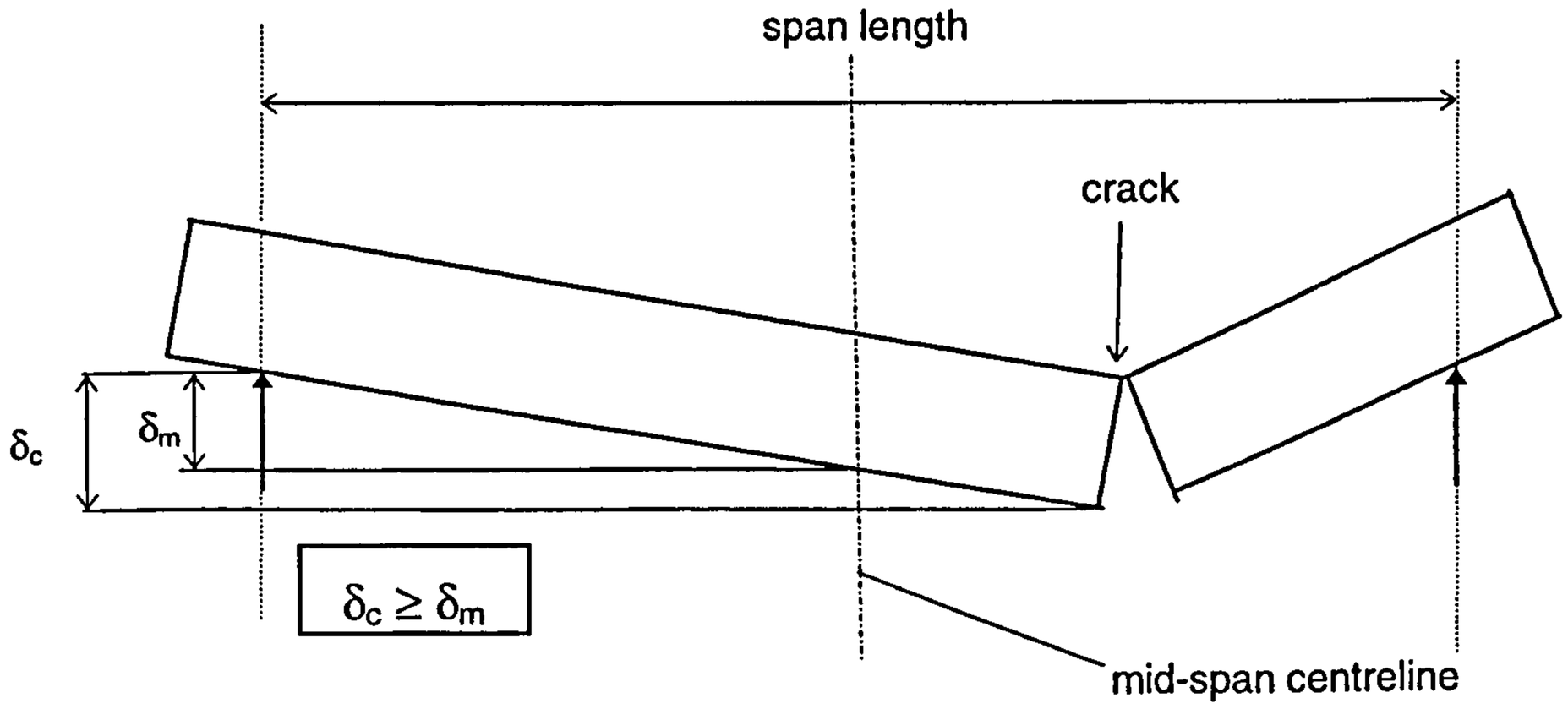

Figure 6.56 Relationship between deflection at mid-span (δ_m) and the deflection at the crack (δ_c).

These findings may have implications for third-point flexural toughness testing of unnotched fibre reinforced concrete beams which are controlled by mid-span beam deflection. They may also provide an explanation for the high variability observed in the flexural toughness test results detailed in Figure 6.35 and as reported by Armelin and Banthia (1997). For an unnotched beam tested in third-point loading, and controlled by mid-span deflection, the failure crack can occur anywhere within the middle third without the test being invalidated. However, for a beam not cracking at mid-span the load-deflection response may be affected by the following inter-dependent factors:

i. The 'true' deflection of the beam at the crack will be greater than the deflection at mid-span (Figure 6.56).

ii. As a result of the increase in beam deflection at the crack (relative to the beam deflection at mid-span) the CMOD will be greater at the crack (Figure 6.55).

iii. Regardless of the position of the crack, the deflection at mid-span will continue to increase at the controlled rate of deflection increase required by the test. However, for a crack not occurring at mid-span, the rate of deflection increase at the crack will be greater than the rate of deflection increase at mid-span (Figure 6.56). And the difference in the respective deflection rates will increase the further the crack occurs from mid-span (up to the limit of the middle third region).

iv. Thus, the rate of deflection increase (and the corresponding CMOD) at the crack may vary between two identical test specimens depending upon the location of the crack relative to mid-span.

The combined effect of these factors will cause greater variability in the recorded load-deflection responses between identical test specimens. However, none of the current standard flexural toughness tests appear to address this issue.

In the case of notched beam tests, these influencing factors are minimised because the crack always occurs at the notch (i.e. mid span). Hence, the variability in the load-deflection responses will be reduced (Figure 6.35). Notched beams, therefore, appear to offer an advantage for flexural toughness tests controlled by mid-span deflection.

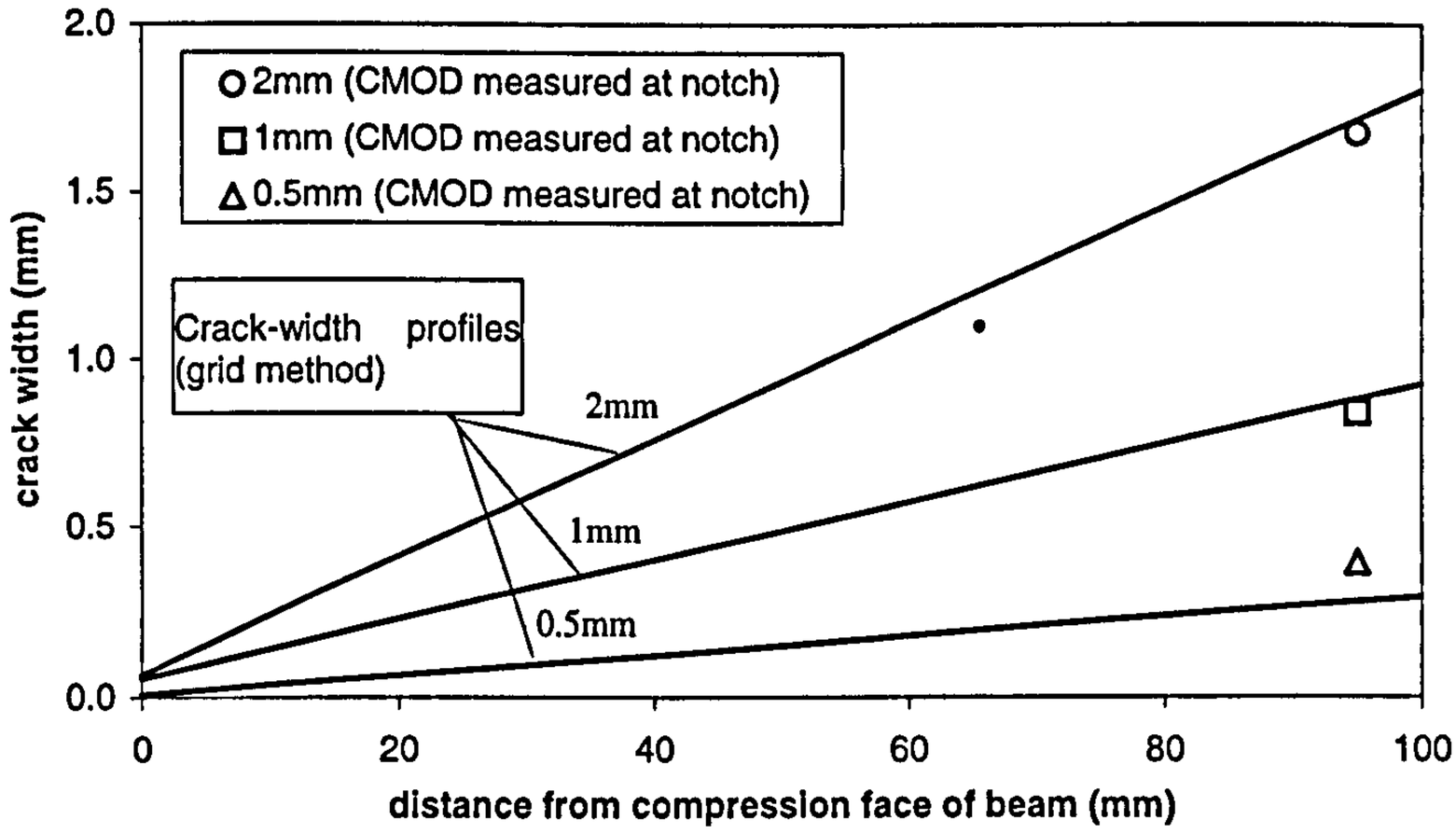

Figure 6.57 Comparison between crack-width profiles obtained from grid method with CMODs measured using an extensometer at the notch (85mm deep notched beam).

Further validation of the crack width measurements obtained from the grid method are shown in Figure 6.57, which compares the crack-width profiles obtained from the grid method with average CMODs measured using an extensometer fixed at the notch. Note that the crack profiles in Figure 6.57 have been extrapolated to the point at which CMOD was measured during the flexural toughness tests (that is, at a distance of 95mm from the compressive face of the beam as shown in Figure 6.30). A good agreement between the results can be seen, providing validation of the crack width measurements obtained using the grid method.

Note that the influence of fibre content on the crack-width profiles could not be analysed. This was mainly because there was not enough data due to the relatively high number of beams cracking outside the middle third or displaying multiple cracking, and the difficulty in comparing the crack-width profiles of beams that did not crack at mid-span. Similarly, comparisons could not be made between the crack-width profiles obtained from cast and sprayed specimens.

The combining of the crack-width profiles with the strain profiles (Section 6.6.8), for use in the proposed model, is discussed in Section 6.6.9.

6.6.8 Results and discussion: strain gauges

General

Unlike the grid method which is able to measure the crack-widths across the cracked section of a beam, providing that that the beam cracks within the middle third, the strain gauges measure strain at fixed points located at mid-span irrespective of the crack position. Therefore, if a beam does not crack at mid-span (and thus the crack passes through the strain gauges) the measured strain values and corresponding strain profiles are significantly affected. This is illustrated in Figures 6.58 and 6.59 which show the strain gauge readings in terms of their position relative to the compressive face of two test specimens: Figure 6.58 shows a beam that cracked at mid-span and Figure 6.59 shows a beam that cracked at a distance of approximately 65mm from mid-span. The corresponding load response is also indicated in these figures. Note the magnitude of the strain gradient in Figure 6.58, which displays tensile strains of up to 7000με before failure of the gauge occurs (characterised by a sudden drop in the strain reading) and a rapid movement of the neutral axis towards the compressive face of the beam over an initial deflection of 0.2mm. In contrast, the tensile strains shown in Figure 6.59 never exceeds 200με and the neutral axis hardly moves from its initial mid-depth position. Hence, the strain gauge responses shown in Figure 6.59 are not representative of the strain distribution occurring in the vicinity of a crack.

The influence of crack position relative to the strain gauges is further illustrated in Figure 6.60, which shows the neutral axis depth (relative to the compressive face of the beam) as a function of the distance from the crack at deflections of 0.05, 0.1, 0.2. 0.5, 1, and 2mm. It can be seen that prior to the beam cracking (i.e. at deflections up to approximately 0.15mm) the neutral axis is located at mid-depth across the whole middle third region of the beam. However, following cracking there is a shift in the neutral axis position towards the compressive face of the beam, which increases as the distance between the crack and the strain gauges reduces. For example, at a deflection of 2mm the neutral axis depth is within 5mm of the compressive face of the beam at the crack, but close to mid-depth at a distance of 75mm from the crack.

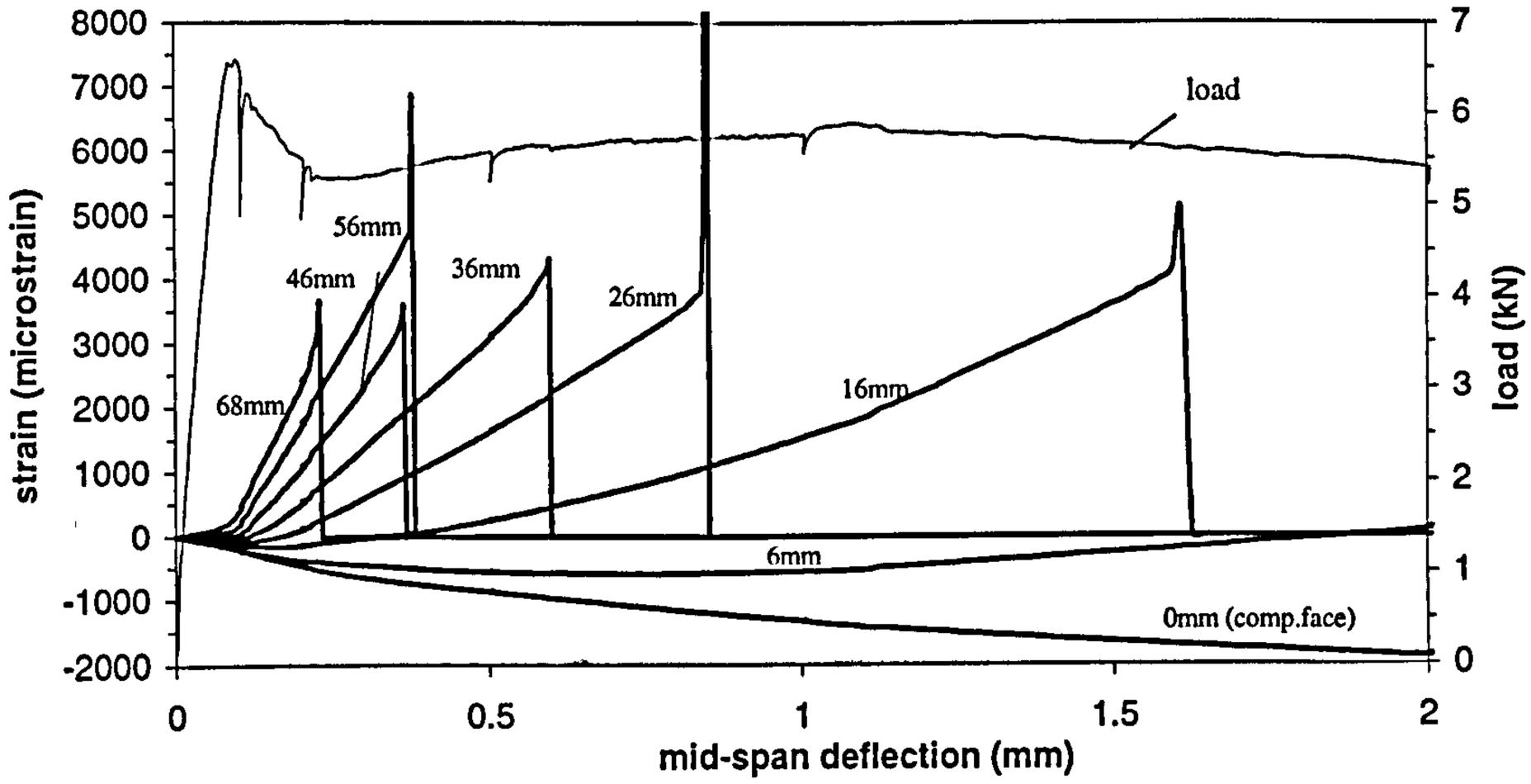

Figure 6.58 **Influence of strain gauge reading relative to compression face of a 85mm deep notched beam - crack occurring close to mid-span (compressive strain negative).**

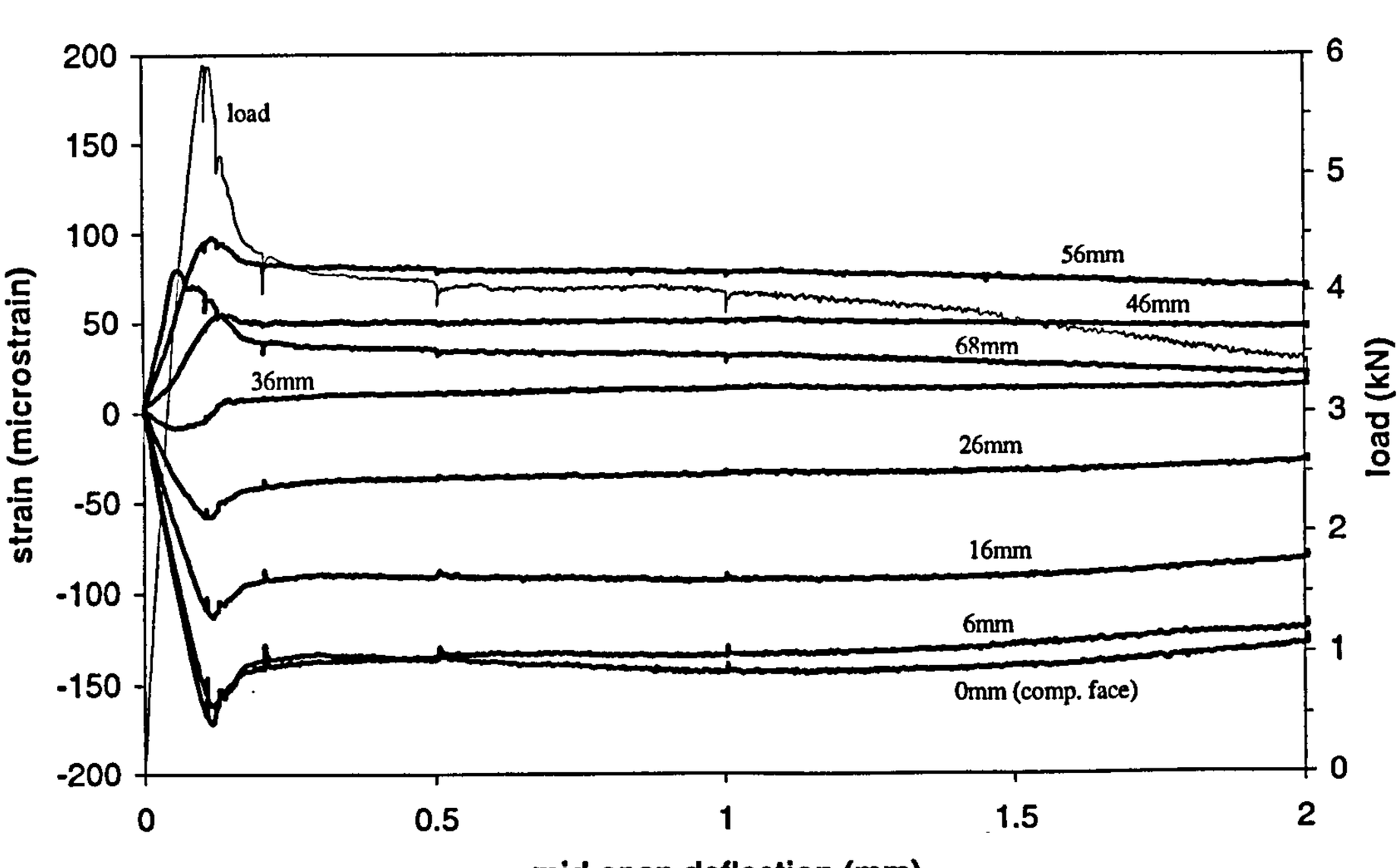

Figure 6.59 **Influence of strain gauge reading relative to compression face of a 75mm deep unnotched beam - crack occurring away from mid-span (compressive strain negative).**

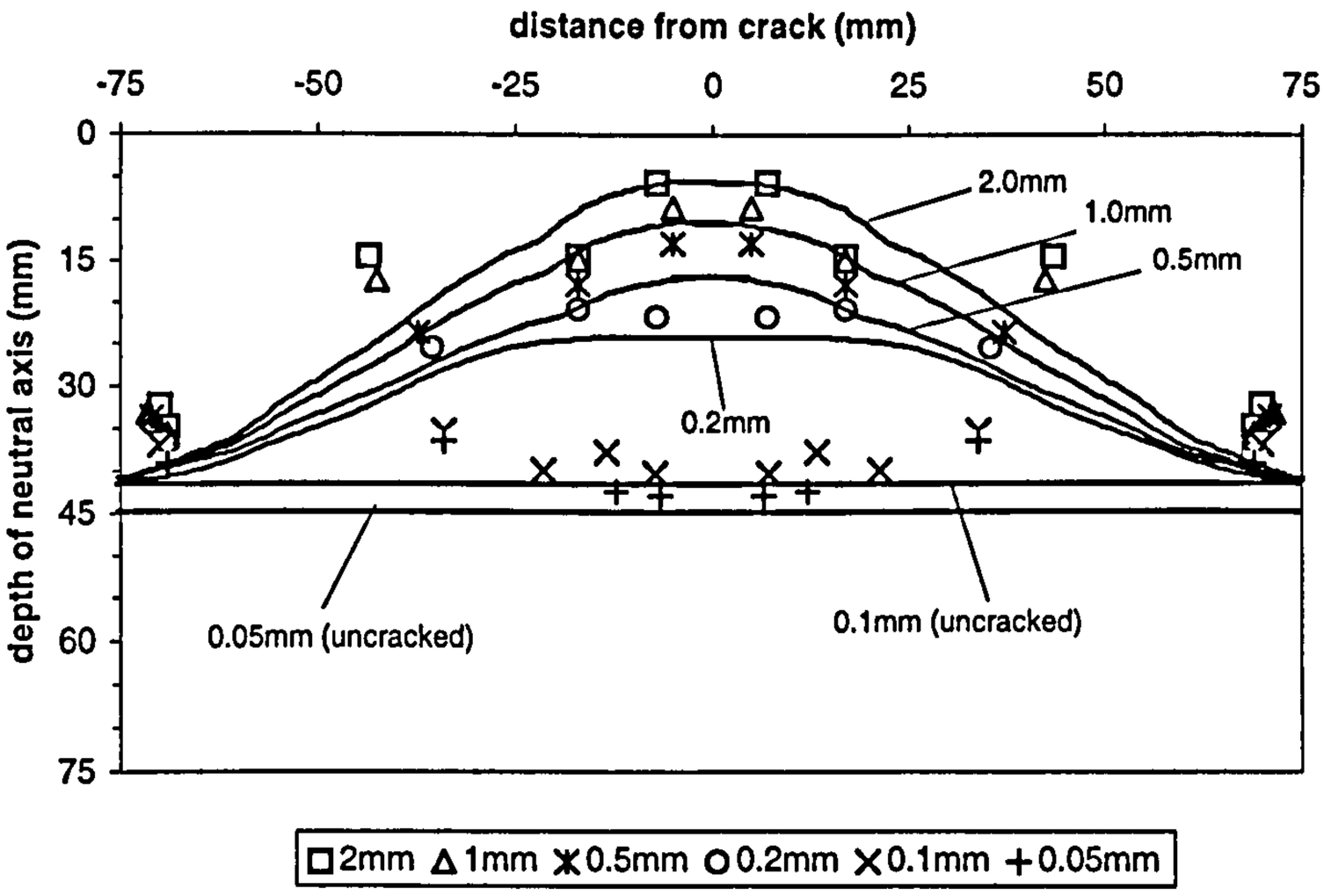

Figure 6.60 Distribution of neutral depth either side of a crack (75mm deep unnotched & 85mm deep notched beams).

To take account of the effects illustrated in Figures 6.58-6.60 the strain gauge data had to be further manipulated, in order to determine the strain profiles for use in the proposed model. The philosophy adopted was based on extrapolating the strain readings from each specimen to determine an average strain profile (at each deflection) for a crack occurring at mid-span. In the case of the uncracked beams (i.e. at deflections of 0.05mm and 0.1mm) the strain readings at each deflection were simply averaged to determine the value of strain at each gauge location (see Appendix II.A). However, in the case of the cracked beams (i.e. at deflections between 0.2-4.0mm) the determination of the strain profiles was not so simple due to the variable crack location relative to the strain gauge positions. Thus, the following procedure was developed for determining the average strain profiles at the crack.

i. The test results were grouped and analysed separately by beam depth (that is, 75mm deep unnotched, 85mm deep notched beams, 100mm deep unnotched beams, and 60mm deep notched).

ii. For each specimen the strain gauge readings were carefully examined and any extraneous data discarded. This included strain readings associated with: (a) multiple cracked beams; (b) beams which cracked outside the middle third region;

(c) uncharacteristic or highly variable gauge readings; and (d) strain readings from gauges either destroyed by, or affected by, their close proximity to the crack tip.

iii. The distance from the centreline of the crack to the centreline of each strain gauge was plotted against the measured strain reading for each beam tested. These individual plots were then combined into a single plot for each beam depth under investigation (see Appendix II.B). From the resulting plots a regression analysis was performed on the data to obtain a line of best-fit for each strain gauge position. The relationships obtained from this analysis were then used to predict a strain value, for each strain gauge position, for a crack located at mid-span (i.e. a crack propagating through the centreline of the gauges).

iv. These strain predictions were then plotted as a function of their position relative to the compressive face of the beam. A linear regression analysis was then performed on the data to obtain the strain profile for each deflection investigated.

The resulting plots together with the lines of best-fit for each gauge position are shown in Appendix II and the predicted strain profiles for each beam type investigated are shown in Appendix III. Note that if a crack occurred close to the centreline of the gauges, then as it propagated over the depth of the beam it would gradually eradicate each gauge. This can be seen in the data presented in Appendix II.B, which shows all the gauges recording strain at a deflection of 0.2mm but only the top two gauges recording strain at a deflection of 4mm. In addition, note from the predicted strain profiles in Appendix III that the linear regression coefficients are all greater than 0.95, which suggests that the strain gradient in front of a crack tip remains linear throughout a flexural toughness test.

Neutral axis depth, maximum compressive strain and mid-span deflection

The strain profile data presented in Appendix III is summarised in Table 6.17, in terms of the neutral axis depth and maximum compressive strain, for each beam depth and mid-span deflection investigated. Using this data Figures 6.61-6.63 show for each beam depth under investigation, the relationships between neutral axis depth, mid-span deflection and maximum compressive strain. Note that in these figures neutral axis depth is plotted as fraction of the corresponding overall beam depth, *d*. It can be seen that in general, the shapes and magnitudes of the relationships indicated by these

figures are similar irrespective of beam depth. The poor correlation associated with the 75mm deep unnotched beam data is probably the result of none of these beams cracking within 30mm of the strain gauges (Table 6.16), which compromised the accuracy of the predicted strain profiles (see Appendix III). These findings suggest that a fibre reinforced concrete beam, with a relatively low fibre content, may have a distinct failure mode irrespective of beam depth. This failure mode can be summarised as follows:

i. Once the beam cracks the neutral axis moves towards the compressive face of the beam. The rate of movement appears to gradually reduce with increasing deflection, suggesting an exponential relationship as shown in Figure 6.61. For example, between the first crack and a deflection of 1mm the neutral axis moves from mid-depth to a position, relative to the compressive face of the beam, corresponding to approximately 15% of the overall beam depth. However between a deflection of 1 and 4mm it only moves by a further 5-10% of the overall beam depth.

ii. The maximum compressive strain increases non-linearly with an increase in deflection (Figure 6.62) and a corresponding movement in the neutral axis position towards the compressive face of the beam (Figure 6.63). Over the deflection range investigated, the value of maximum compressive strain never exceeded 3200με which suggests that none of the beams failed in compression.

It is hoped that the relationships indicated by Figures 6.61-6.63 can be developed as design tools, from which the maximum compressive strain, neutral axis depth and thereby the strain profile can be predicted as a function of mid-span deflection (or angular deformation) for a range of beam sizes and loading geometry. This is discussed further in Chapter 7.

	60mm notched		85m notched		75mm unnotched		100mm unnotched	
Deflection (mm)	neutral axis depth (mm)	max. comp. strain (με)	neutral axis depth (mm)	max. comp. strain (με)	neutral axis depth (mm)	max. comp. strain (με)	neutral axis depth (mm)	max. comp. strain (με)
0.05	23.5*	74	41.7*	107	37.3	84	45.1	100
0.1	22.7*	145	38.5*	230	37	155	43.9	195
0.2	18.9	281	21.9	527	35.1	307	22.9	409
0.5	9.3	704	12.1	985	23.4	721	18.9	675
1.0	4.4	1207	10.5	1352	17.6	1137	12.8	1037
2.0	3.2	2035	5.1	1888	15.2	1500	9.3	1897
4.0	2.4	3140	-	-	13.6	2045	5.7	2895

Depths marked with a * are measured relative to the total notched depth (i.e. notch + ligament).

Table 6.17 Summary of strain gauge analysis.

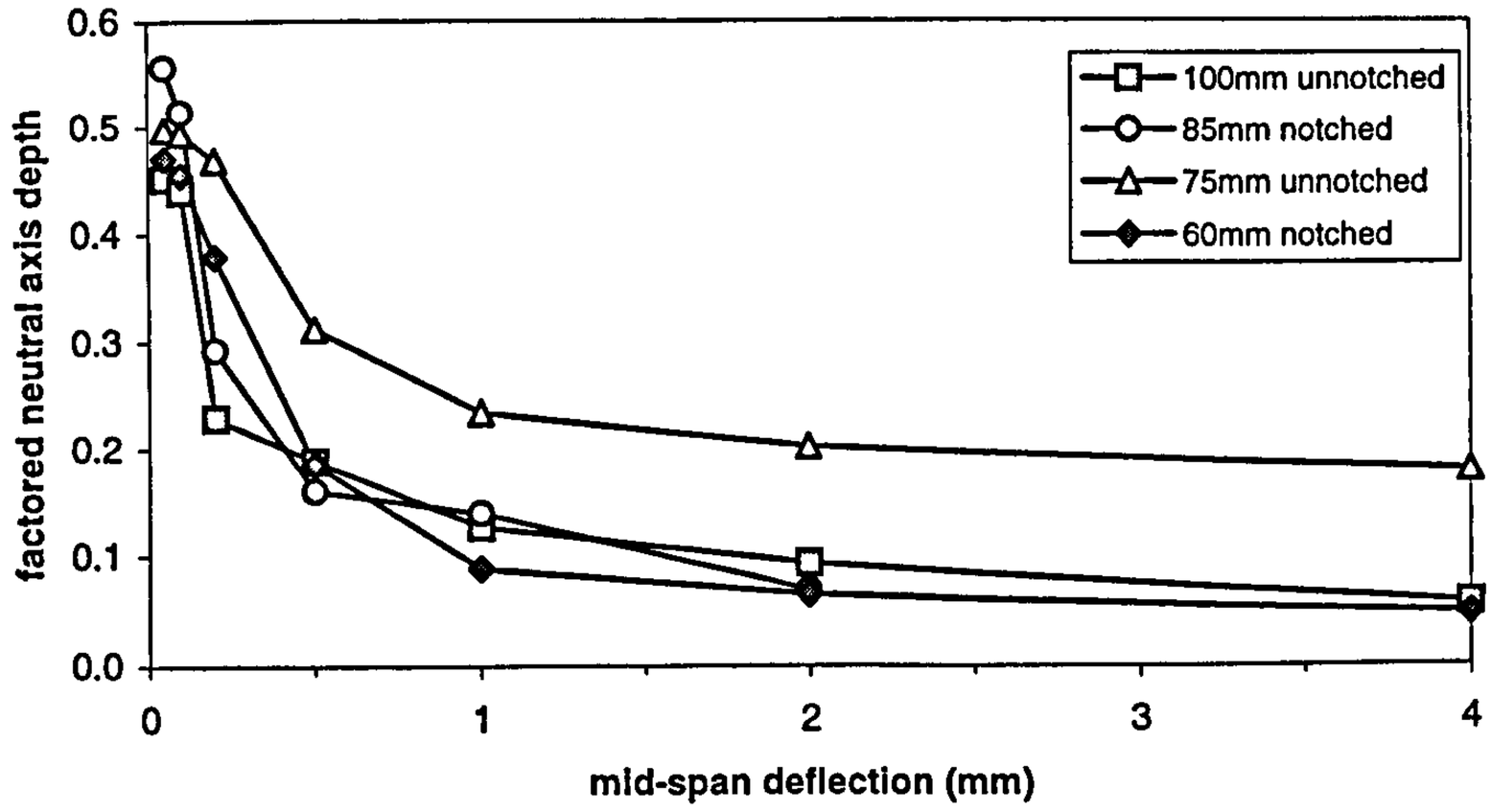

Figure 6.61 Relationship between neutral axis depth and mid span deflection.

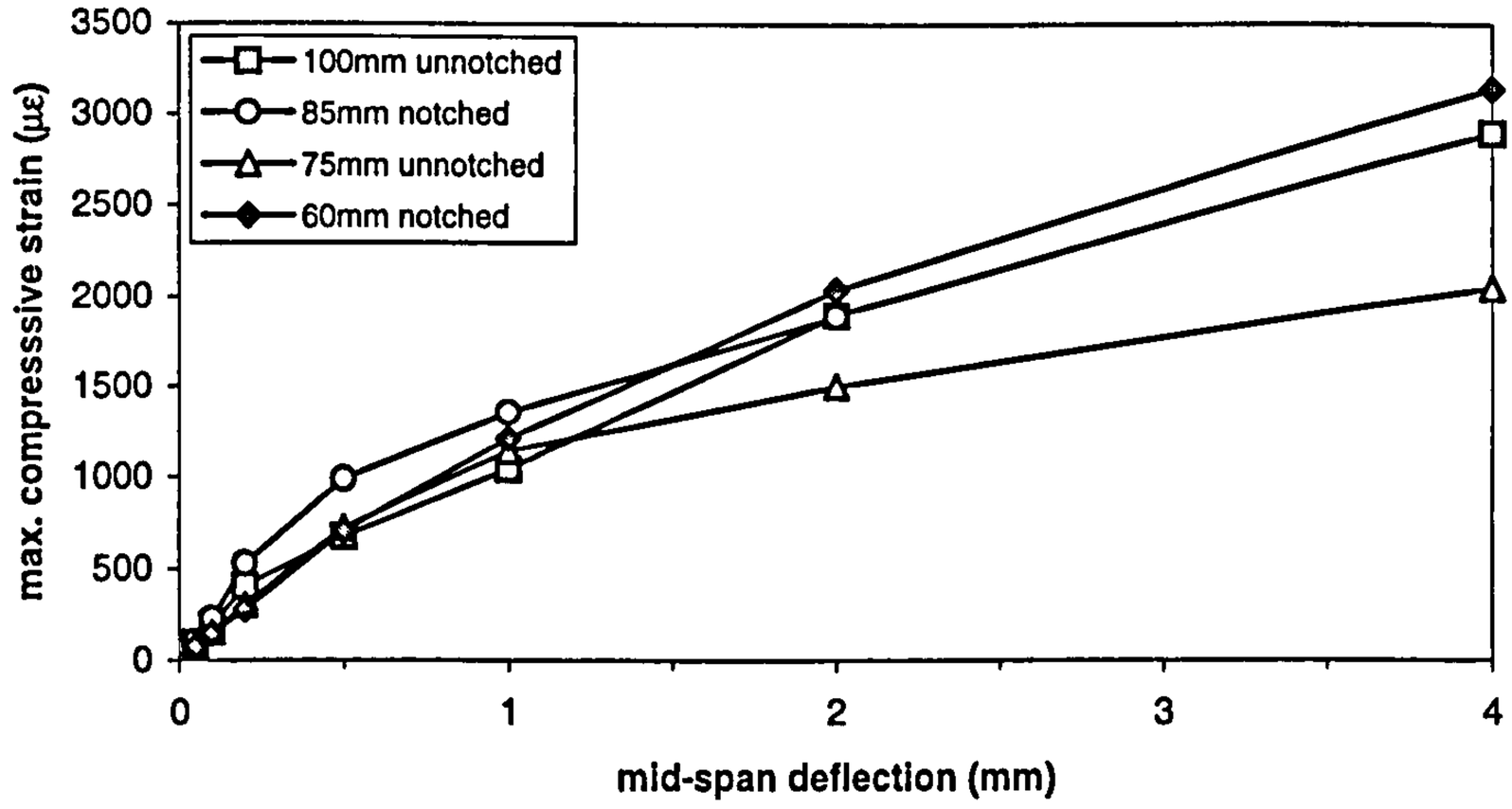

Figure 6.62 Relationship between strain measured at the compressive face of a beam and mid-span deflection.

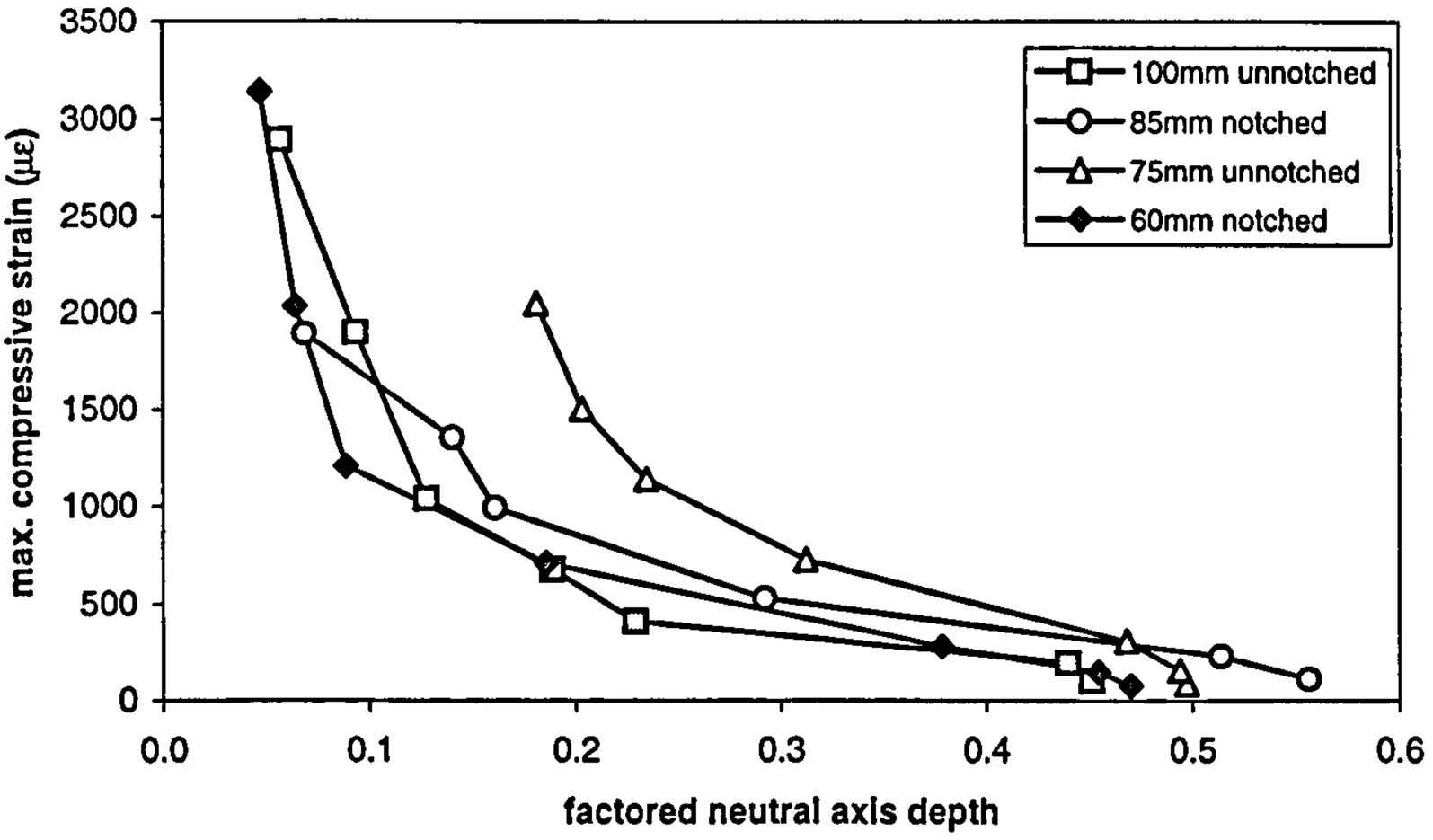

Figure 6.63 Relationship between strain measured at the compressive face of a beam and the neutral axis depth.

Location of the first crack using the strain gauge data

An attempt was also made to determine the occurrence of the first crack in terms of the flexural stress, strain and deflection using the strain gauge readings. However, this was found to be very difficult because the occurrence of the first crack was not clearly defined by the strain gauge readings, which made the analysis extremely subjective. The lack of a clearly defined first crack location on the load-deflection response curve appears to agree with Morgan *et al.* (1995) who suggest that there is no such thing as a

discrete first crack point in a flexural toughness test due to progressive matrix microcracking which occurs as the beam deflects.

Although the results of the analysis, shown in Table 6.18, are not conclusive they do indicate a first crack tensile strain of between 130-250με for all the beams tested, with an average of approximately 190με. In the case of the 75mm deep unnotched beams, this average strain value corresponds to a first crack deflection, flexural stress and elastic modulus of between 0.1-0.2mm, 4.4-4.6 MPa, and 24-26 kN/mm^2 respectively.

Test reference	specimen	ligament depth (mm)	first crack deflection (mm)	first crack tensile strain (με)	first crack flexural stress (MPa)	average flexural E-value (GPa)
SA1	1	75	0.11	166	4.4	26
	2	75	0.11	193	4.6	24
SA2	1	75	0.09	173	5.2	30
	2	75	0.08	129	4.7	37
SA3	1	75	0.20	216	6.2	28
	2	75	0.12	184	5.6	30
SA4	1	75	-	-	-	-
	2	75	0.09	177	4.5	25
SA7	1	50	0.17	245	5.9	24
	2	50	0.16	224	5.5	25
SA9	1	50	0.17	214	6.0	28
	2	50	0.12	172	4.7	27
SA8	1	100	0.10	205	5.2	25
	2	100	0.08	185	4.5	25
SA10	1	100	0.10	208	5.1	24
	2	100	0.10	195	5.3	27

Table 6.18 Summary of first-crack analysis results.

6.6.9 Combining the grid method and strain gauge results for use in the proposed model

The final stage of the strain analysis investigation was to combine the crack-width profiles obtained from the grid method with the strain profiles obtained from the strain gauge analysis, in order to determine the complete strain/crack-width profiles for use in the proposed model. The interface between the strain and crack-width profiles was assumed to occur at the point along the strain profile where the matrix cracking strain (ε_{cr}) is first exceeded, corresponding to a zero-crack-width (Figure 6.64). Hence, the depth to this interface, relative to the compressive face of the beam, was termed the 'zero crack-width depth'.

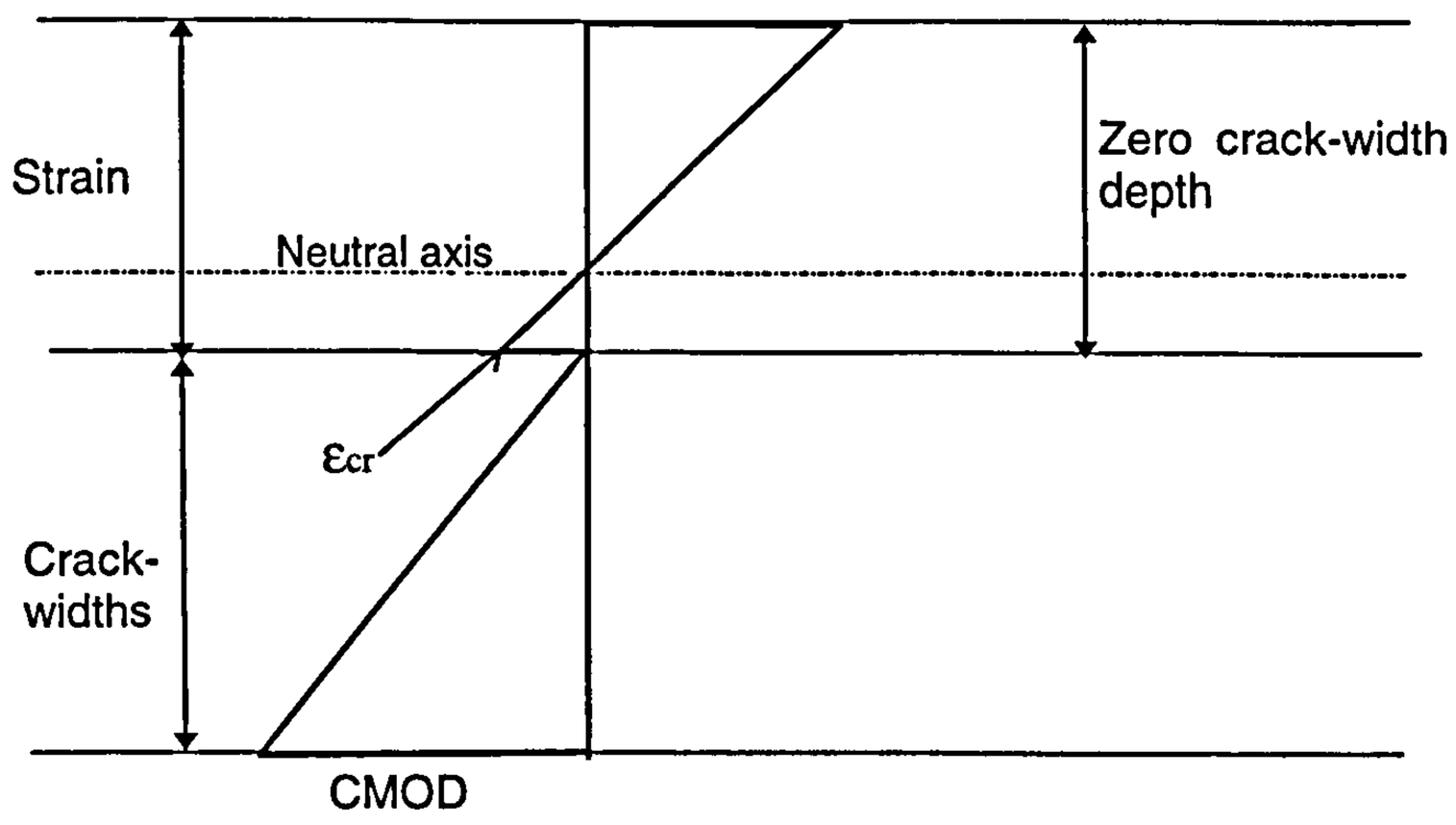

Figure 6.64 Typical strain/crack-width profile showing zero crack-width depth.

Using this concept, the zero crack-width depths determined from both the grid method and the strain gauges were compared to see if there was any agreement between the two sets of data; this is shown in Table 6.19. Note that for this comparative analysis the concrete matrix cracking strain was assumed to be 190με (as indicated by the strain gauge data in Table 6.18). Furthermore, because of the poor correlation shown by the strain data obtained from the 75mm deep unnotched beams (Figure 6.61-6.63), the zero crack-width depths associated with these beams were determined from the strain data associated with the 85mm notched beam data (i.e. the beam size with a similar ligament depth of 75mm as shown in Table 6.7).

		Zero crack-width depth (mm)					Zero crack-width depth (mm)		
Specimen reference	deflection (mm)	grid method A	strain gauges B	diff. A-B	Specimen reference	deflection (mm)	grid method A	strain gauges B	diff. A-B
SA1-1 75mm	0.5	8.4	14.4	**-6.0**	SA1-2 75mm	0.5	6.3	14.4	**-8.1**
	1.0	6.7	12.0	**-5.3**		1.0	13.3	12.0	**1.3**
	2.0	6.5	5.7	**0.8**		2.0	5.6	5.7	**-0.1**
SA2-1 75mm	0.5	3.0	14.4	**-11.4**	SA2-1 75mm	0.5	4.2	14.4	**-10.2**
	1.0	6.0	12.0	**-6.0**		1.0	6.4	12.0	**-5.6**
	2.0	3.7	5.7	**-2.0**		2.0	3.7	5.7	**-2.0**
SA5-1 75mm	0.5	13.6	14.4	**-0.8**	SA7-1 50mm	0.5	7.5	11.8	**-4.3**
	1.0	8.0	12.0	**-4.0**		1.0	2.6	5.1	**-2.5**
	2.0	3.8	5.7	**-1.9**		2.0	0.7	3.5	**-2.8**
	4.0	-	-	**-**		4.0	1.5	2.5	**-1.0**
SA8-2 100mm	0.5	26.6	24.2	**2.4**	SA10-1 100mm	0.5	29.4	24.2	**5.2**
	1.0	1.1	15.1	**-14.0**		1.0	20.4	15.1	**5.3**
	2.0	3.5	10.3	**-6.8**		2.0	12.5	10.3	**2.2**
	4.0	3.5	6.0	**-2.5**		4.0	7.7	6.0	**1.7**
SA9-1 50mm	0.5	25.9	11.8	**14.1**	SA9-2 50mm	0.5	27.5	11.8	**15.7**
	1.0	26.2	5.1	**21.1**		1.0	21.2	5.1	**16.1**
	2.0	12.3	3.5	**8.8**		2.0	13.6	3.5	**10.1**
	4.0	9.4	2.5	**6.9**		4.0	-	-	**-**

Table 6.19 Comparison between zero crack-width depths determined from both the grid method and the strain gauges.

Also note that the 0.2mm deflection data has been omitted from Table 6.19. This is because of the poor regression coefficients displayed by the crack-width profiles at this deflection limit.

The results shown in Table 6.19 generally indicate a poor agreement between the zero crack-width depth determined from the grid method and the strain gauges; with the difference generally varying between 5-10mm. This discrepancy can be attributed to a number of factors associated with the strain analysis methodology and from observations made during the tests, including:

- variations in the crack location and profile either side of the beam under test;
- the generalised approach that was used to manipulate the strain gauge data, in order to predict the strain profile for a crack occurring at mid-span;
- poor crack definition in some of the grid method specimens (Figure 6.65) which affected the accuracy of the digital image analysis; and
- the low sensitivity of the grid method which made it difficult to determine crack-width profiles for crack-widths less than 0.2mm - this was particularly significant at deflections less than 0.5mm.

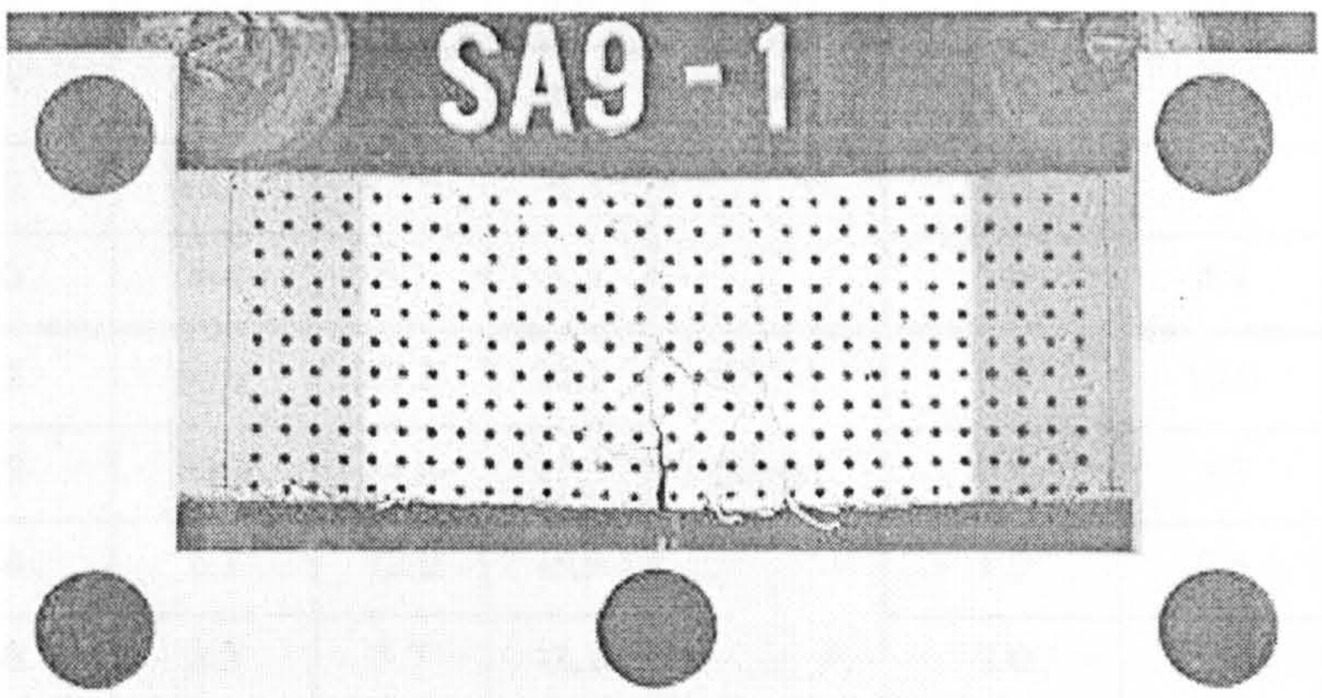

Figure 6.65 An example of poor crack definition in a grid method specimen.

In order to improve the correlation between the grid method data and the strain gauge data for use in the model, the crack-width profiles obtained from the grid method were modified by incorporating the zero crack-width depths obtained from the strain profiles. A linear regression analysis was then repeated on the combined data in order to obtain modified crack-width profiles (shown in Appendix IV).

Table 6.20 compares the modified crack-width profiles (Appendix IV) with the strain profiles (Appendix III), at mid-span deflections of 0.2, 0.5. 1.0, 2.0 and 4.0mm for all the beams that failed at a single crack within the middle-third region. Overall, these results show a much improved correlation between the zero crack-width depths determined from the strain gauges and crack-widths profiles. A comparison of Table 6.20 with Table 6.19 also shows that, as expected, there is a noticeable improvement in the correlation of the zero crack-width depth data at deflections of 0.2, 0.5 and 1.0mm, but virtually no effect at deflections of 2mm and 4mm.

		Zero crack-width depth (mm)					Zero crack-width depth (mm)		
Specimen reference	deflection (mm)	grid method A	strain gauges B	diff. A-B	Specimen reference	(mm)	grid method A	strain gauges B	diff. A-B
SA1-1 75mm	0.2	28.4	29.8	**-1.4**	SA1-2 75mm	0.2	32.0	29.8	**2.2**
	0.5	10.9	14.4	**-3.5**		0.5	11.4	14.4	**-3.0**
	1.0	8.6	12.0	**-3.4**		1.0	10.4	12.0	**-1.6**
	2.0	7.1	5.7	**1.4**		2.0	5.6	5.7	**-0.1**
SA2-1 75mm	0.2	30.6	29.8	**0.8**	SA2-1 75mm	0.2	26.9	29.8	**-2.9**
	0.5	14.2	14.4	**-0.2**		0.5	14.1	14.4	**-0.3**
	1.0	11.7	12.0	**-0.3**		1.0	4.9	12.0	**-7.1**
	2.0	4.4	5.7	**-1.3**		2.0	4.4	5.7	**-1.3**
SA5-1 75mm	0.2	55.9	29.8	**26.1**	SA7-1 50mm	0.2	19.9	31.7	**-11.8**
	0.5	32.3	14.4	**17.9**		0.5	7.3	11.8	**-4.5**
	1.0	6.1	12.0	**-5.9**		1.0	2.5	5.1	**-2.6**
	2.0	3.5	5.7	**-2.2**		2.0	2.4	3.5	**-1.1**
	4.0	-	-	-		4.0	2.0	2.5	**-0.5**
SA8-2 100mm	0.2	31.7	33.5	**-1.8**	SA10-1 100mm	0.2	31.1	33.5	**-2.4**
	0.5	25.0	24.2	**0.8**		0.5	25.0	24.2	**0.8**
	1.0	6.5	15.1	**-8.6**		1.0	16.3	15.1	**1.2**
	2.0	5.6	10.3	**-4.7**		2.0	11.9	10.3	**1.6**
	4.0	4.3	6.0	**-1.7**		4.0	7.3	6.0	**1.3**
SA9-1 50mm	0.2	32.4	31.7	**0.7**	SA9-2 50mm	0.2	30.0	31.7	**-1.7**
	0.5	21.3	11.8	**9.5**		0.5	29.1	11.8	**17.3**
	1.0	14.6	5.1	**9.5**		1.0	22.0	5.1	**16.9**
	2.0	11.6	3.5	**8.1**		2.0	13.6	3.5	**10.1**
	4.0	7.6	2.5	**5.1**		4.0	-	-	-

Table 6.20 Comparison between zero crack-width depths determined from the modified grid method data and the strain gauge data.

The results presented in Table 6.20 indicate a close correlation between the strain profiles obtained from the strain gauges, and the crack-width profiles obtained from the grid method. Furthermore, they indicate the suitability of the strain analysis method described herein for measuring the strain and crack-width profiles of a steel fibre reinforced concrete beam in flexure, particularly at deflections greater than 0.5mm.

6.6.10 Limitations of the strain analysis tests for measuring the complete strain/crack-width profiles

The strain gauges were shown to be suitable for measuring both the compressive and tensile strain profiles to an accuracy of $\pm 15\mu\varepsilon$ up to a strain limit of $200\mu\varepsilon$ in tension and $3500\mu\varepsilon$ in compression, and the grid method was shown to be suitable for measuring crack-widths greater than 0.2mm to an accuracy of ± 0.1mm. Thus, when using this method, a range of specimen deformation exists - between a strain of $200\mu\varepsilon$ (equivalent to 0.006mm over a gauge length of 30mm) and a crack-width of 0.2mm (equivalent to $6500\mu\varepsilon$ over a gauge length of 30mm) - which cannot be accurately measured. The implications of this limitation on the accuracy of the proposed model, particularly in the region of the load-deflection response between the first crack deflection (i.e. between 0.1-0.2mm) and a deflection of 0.5mm, are discussed in Chapter 7.

6.7 FIBRE DISTRIBUTION ANALYSIS

6.7.1 Background

A knowledge of the fibre distribution across the cracked section of a steel fibre reinforced concrete beam is an important element of the proposed model. It is hoped that the fibre bridging forces across the cracked zone can be predicted by combining the single fibre pull-out test data (Section 6.3) with fibre distribution data relating to fibre numbers, embedment lengths and orientations.

This section describes two methods of analysis used to obtain the necessary fibre distribution data for use in the model: (1) an X-ray photograph method to obtain probability distributions relating to fibre embedment lengths and orientations

occurring across the cracked zone for the concrete mixes used in the investigation; and (2) a manual fibre counting method to obtain the actual fibre numbers and fibre distributions across the cracked zone for a selection of the flexural toughness test specimens.

6.7.2 X-ray analysis: test procedure

Specimen preparation

The X-ray analysis specimens were sawn from cast and sprayed beam specimens - as detailed in Table 6.3 - following flexural toughness testing. Three 125 x 75 x 30mm specimens were sawn from each beam in an orientation parallel to the direction of casting/spraying as illustrated in Figure 6.66. The thickness of the specimens was limited to 30mm, in accordance with the recommendations given by Kasperkiewicz *et al.* (1978), in order to obtain readable X-ray photographs for use in the analysis.

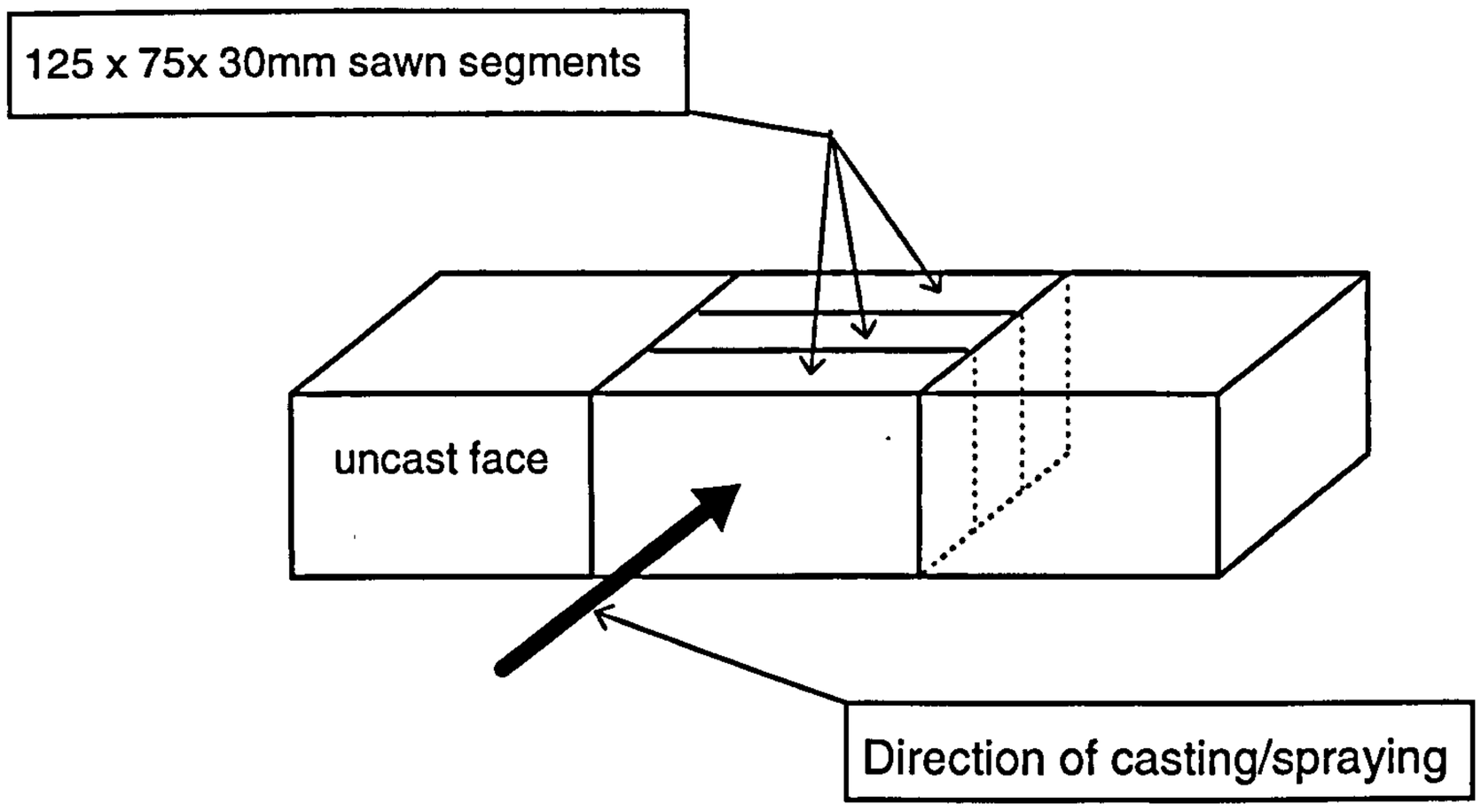

Figure 6.66 Preparation of X-ray analysis specimens.

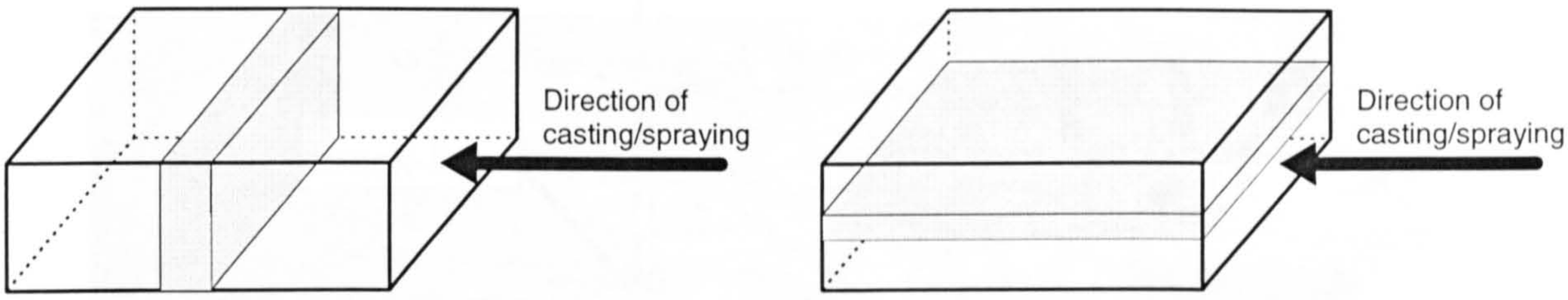

(a) Parallel to the direction of casting/spraying.

(b) Normal to the direction of casting/spraying.

Figure 6.67 Orientation of X-ray analysis specimens.

A further set of single 125 x 75 x 30mm specimens was analysed to compare qualitatively the global fibre distributions of cast and sprayed specimens in terms of fibre content and the direction of casting and spraying. Two orientations with respect to the direction of casting and spraying were investigated as shown in Figure 6.67: (a) parallel to the direction of casting/spraying; and (b) normal to the direction of casting/spraying.

A typical X-ray analysis specimen is shown in Figure 6.68. Note the lead scale (of known length) which was placed on the surface of the specimen. The purpose of this scale was to relate the actual size of the specimen to that indicated by the X-ray photograph.

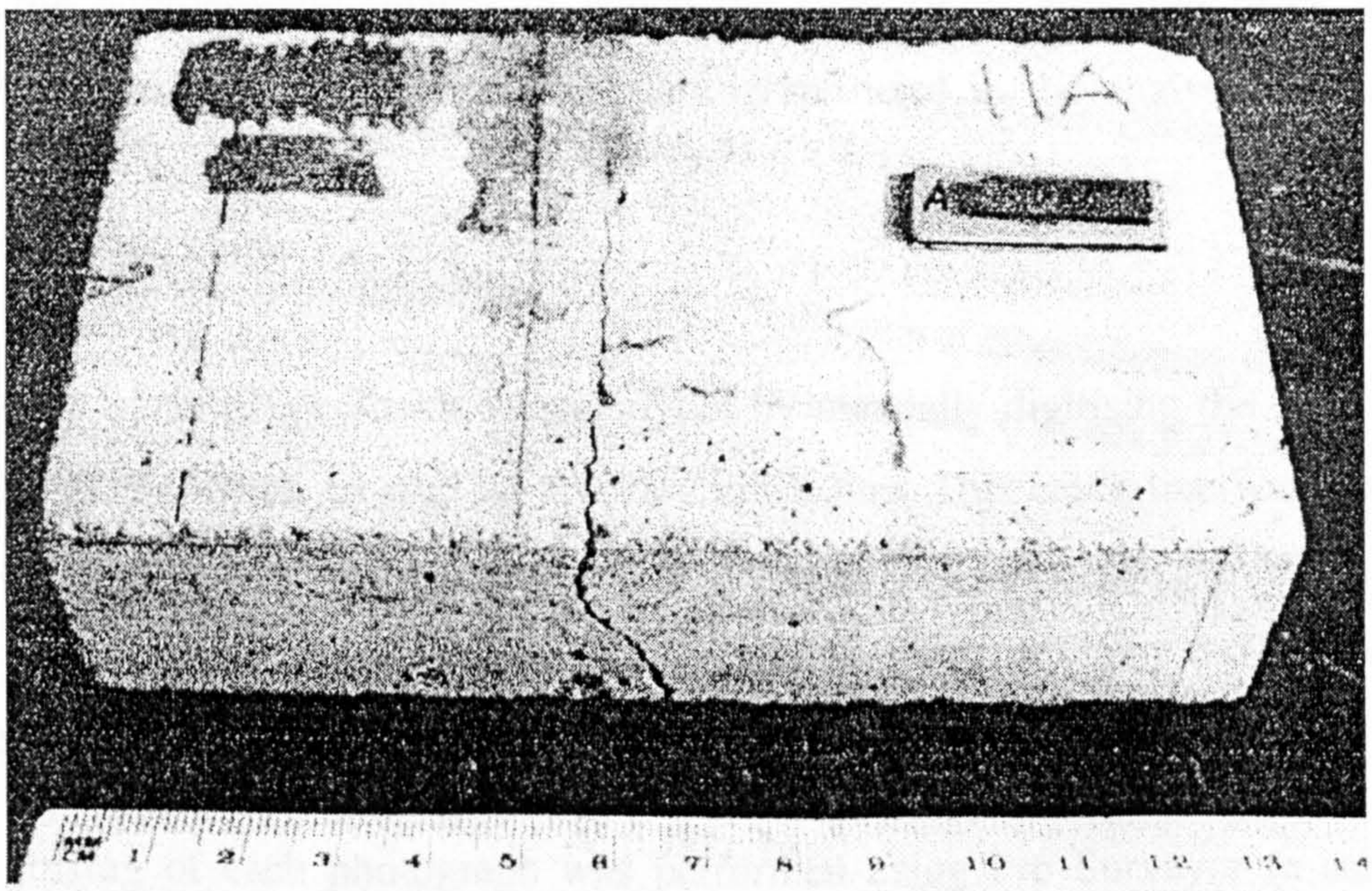

Figure 6.68 Typical X-ray analysis specimen.

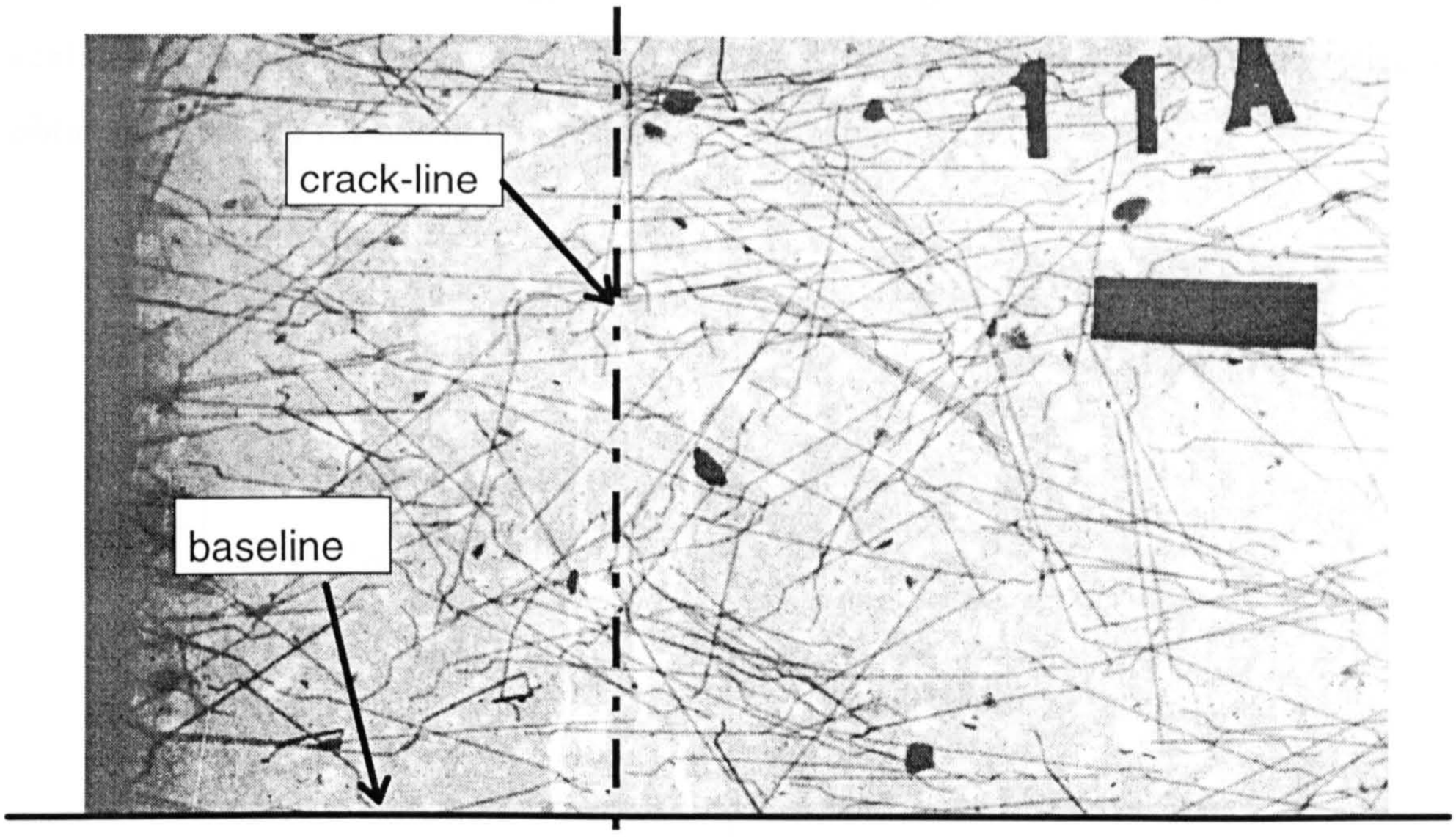

Figure 6.69 Typical X-ray photograph used in the analysis showing a superimposed crack-line and baseline.

Acquisition of X-ray photographs

A 125 kV 5mA X-ray source was used to obtain the X-ray photographs. Each specimen was placed on a photographic film emulsion and exposed to the source for 35 seconds. This exposure time was determined from a series of trials to optimise the clarity and readability of the photographs. The X-ray negatives were contact printed to obtain the photographic images in which the steel fibres appeared black and the concrete matrix grey. A typical X-ray photograph used in the analysis is shown in Figure 6.69.

Analysis of the X-ray photographs

Each series of three specimens was analysed by manually digitising the co-ordinates of all the fibres which crossed an arbitrary crack-line. This crack-line was drawn on the photographs, in a concordant position for each test series, perpendicular to the tensile face of the specimen (termed the baseline) as shown in Figure 6.69. It therefore represented the best-fit straight line through the centre of an arbitrary crack.

The digitising of each photograph was performed using Pro Surveyor (a surveying software package produced by AiC Ltd) linked to a digitising board. Each fibre was

digitised at three points - F1, F2 and FC - as illustrated in Figure 6.70. The length of the lead scale (S1 to S2 on Figure 6.70) was also digitised in order to calculate the scaling factor for each specimen. The digitising of each point was repeated twice to obtain an average for use in the analysis.

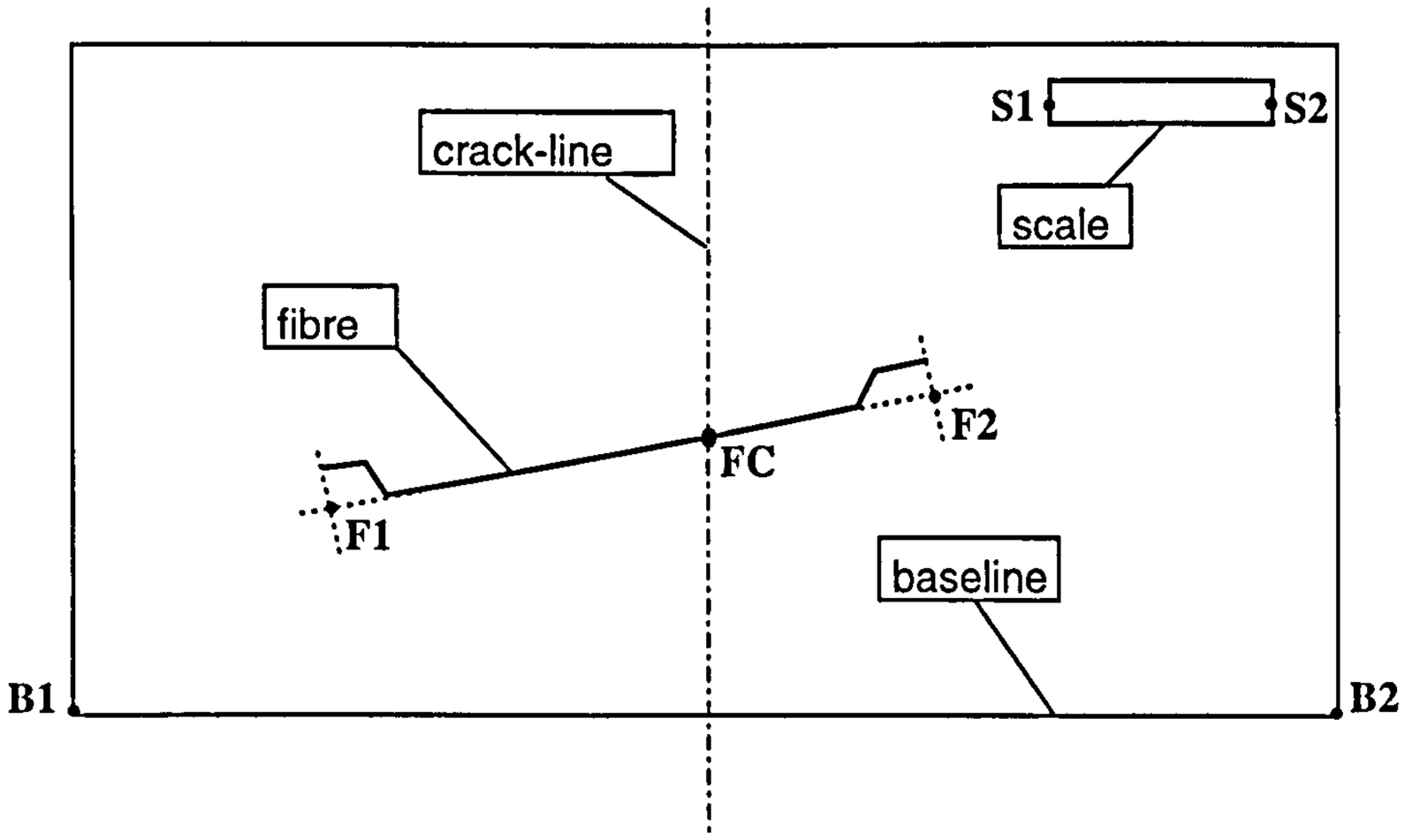

Figure 6.70 Schematic illustration of the key digitising points.

Each photograph was digitised on a arbitrary local grid (E,N) system which was set by the digitiser. Therefore, the digitised data had to be transformed from the local digitised grid system into a specimen grid system (x,y) in which the tensile face of the specimen corresponded with the x-axis. This was achieved by digitising the baseline of each specimen (B1 to B2 on Figure 6.70) to obtain a whole circle bearing (WCB), and then calculating the angles between the WCB of the baseline and the WCB of each fibre. These angles represented the 2D orientation of the fibres relative to the x-axis of the specimen grid system.

The digitised data for each photograph was referenced and saved as a text file. The data was then processed (in accordance with the theory described below) using a spreadsheet designed in Microsoft Excel to obtain fibre distribution data relating to fibre orientations and embedment lengths across the crack-line. The digitising and processing of the photographs was undertaken by a Civil Engineering undergraduate student, under the supervision of the Author, as part of a final year project (Payton, 1997).

Calculation of fibre distribution parameters from the digitised data

The following is a description of the theory developed by the Author for determining the 3D spatial properties (that is, fibre orientation and embedment length) from a 2D X-ray photograph of fibres crossing an arbitrary crack.

(A) FIBRE ORIENTATION

In the 2D case, the apparent total fibre length L^{tot}_{2D}, the fibre embedment length L^{*}_{2D} (measured to the right of the crack-line) and fibre orientation θ_{2D} relative to the tensile face of the specimen can be determined from the digitised Points F1, F2 and FC (Figure 6.71(a)) as:

$$L^{tot}_{2D} = \sqrt{(x_2 - x_1)^2 + (y_2 - y_1)^2} \qquad \text{equation 6.7(a)}$$

$$L^{*}_{2D} = \sqrt{(x_c - x_1)^2 + (y_c - y_1)^2} \qquad \text{equation 6.7(b)}$$

$$\theta_{2D} = \tan^{-1}\left(\Delta y_{c-2} / \Delta x_{c-2}\right) \qquad \text{equation 6.7(c)}$$

where x and y are the co-ordinates of the digitised points F1, F2 and FC on the specimen grid system, and Δx and Δy are the corresponding differences in the x and y co-ordinates.

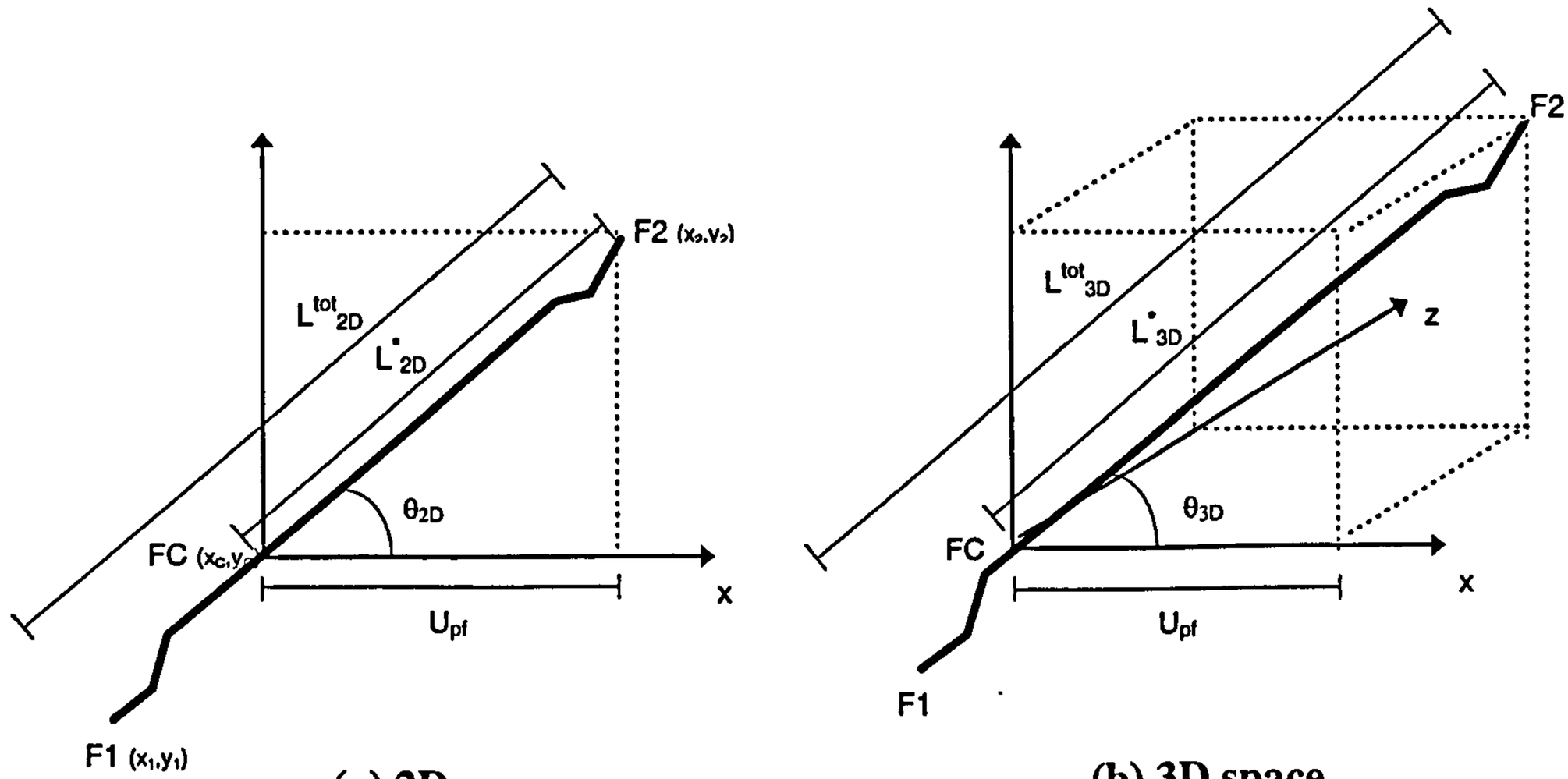

(a) 2D space. **(b) 3D space.**

Figure 6.71 Comparison between a fibre in 2D and 3D space.

Hence, the projected length of the 2D fibre onto the x-axis, termed U_{pf} (Figure 6.71(b)), is given by

$$U_{pf} = \cos \theta_{2D} \, . \, L^{*}_{2D} \, . \, \alpha \qquad \text{equation 6.8}$$

Where α the scale factor relating the size of the specimen in the photograph to the actual size of the specimen;

$$\alpha = \frac{\textit{actual length of lead scale (mm)}}{\textit{digitised length of lead scale (mm)}}$$

Knowing the actual 3D length of the fibre L^{tot}_{3D} (nominally 30mm for the fibres used in the investigation), the actual 3D fibre embedment length to the right of the arbitrary crack L^{*}_{3D} can be determined from similar triangles as:

$$L^{*}_{3D} = (L^{*}_{2D} / L^{tot}_{2D}) \, . \, L^{tot}_{3D} \qquad \text{equation 6.9}$$

Hence, the 3D fibre orientation angle θ_{3D}, relative to the uniaxial tensile force across the cracked zone (assumed to be parallel with the x-axis), is thus given by (Figure 6.71(b))

$$\theta_{3D} = \cos^{-1} (U_{pf} / L^{*}_{3D}) \qquad \text{equation 6.10}$$

This process is repeated for all the fibres digitised.

(B) FIBRE EMBEDMENT LENGTH

The embedded length of each fibre is taken as the fibre length which is most likely to pull-out under a tensile load (that is, the lesser of the two fibre lengths either side of the crack-line). Hence, for the 30mm long fibres used in this investigation the fibre embedment length $|L|$ is given by

$$|L| = L^{*}_{3D} \qquad \text{for } L^{*}_{3D} \leq 15\text{mm} \qquad \text{equation 6.11(a)}$$

$$|L| = 30 - L^{*}_{3D} \qquad \text{for } L^{*}_{3D} > 15\text{mm} \qquad \text{equation 6.11(b)}$$

6.7.3 Manual analysis: test procedure

Following the flexural toughness tests a selection of beam specimens were loaded to failure to break them in two at the flexural crack. The fractured surfaces were then analysed by dividing them into 10mm wide zones across the depth of the beam - using a purpose made grid of elastic bands - and then manually counting the number of fibres occurring in each zone. The total number of fibres in each zone (per beam) was then determined by summing the corresponding zonal numbers from both crack surfaces. In addition to obtaining the total number of fibres occurring across the cracked zone for use in the proposed model, the data was also used to investigate fibre density and fibre distribution in terms of different fibre volume contents and beam depths.

The width and layout of the fibre counting zones used in this analysis correspond to the 'fibre zones' used in the implementation of the proposed model as described in Chapter 7.

An additional investigation was also undertaken to observe the effect of casting orientation and placing technique (cast and sprayed) on fibre distribution. Three different orientations were investigated as illustrated in Figure 6.72: cast Orientation 1 - beams cast on their side; cast Orientation 2 - beams cast flat; and Orientation S - sprayed beams. Note that flexural toughness test beams described in Section 6.5 were either cast using Orientation 1 or sprayed using Orientation S.

6.7.4 X-ray analysis: results and discussion

Qualitative investigation

Figures 6.73-6.77 show representative X-ray photographs indicating the effect of casting (using table vibration) and spraying on the fibre distribution: (a) parallel to the direction of casting and spraying; and (b) normal to the direction of casting and spraying. Figures 6.73-76 show cast beams with fibre volumes of 0.5%, 1.0% and 1.5% respectively, and Figures 6.76-78 show sprayed beams with fibre volumes of 0.34% and 0.87% respectively. It can be seen that there is essentially no discernible visible difference between casting (using surface vibration) and spraying on the resulting fibre distributions and orientations for all the fibre volumes investigated. Both methods tend to cause the fibres to align in a 2D plane at right angles to the

direction of casting and spraying. These findings are in accordance with the results of other researchers who reported similar observations regarding fibre orientations as a result of table vibration (Edgington and Hannant, 1972; Soroushian and Lee, 1990) and spraying (Austin, 1984; Austin and Robins, 1993).

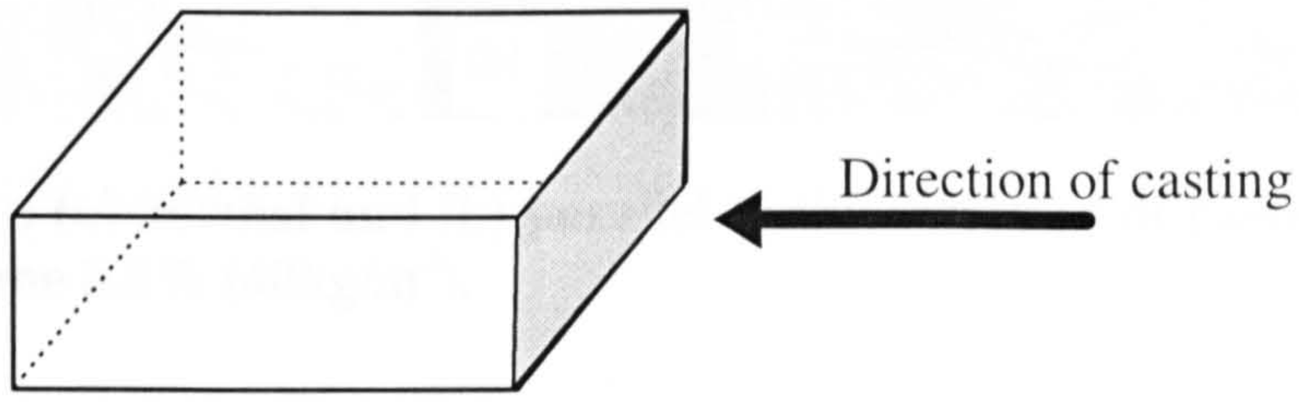

(a) Orientation 1.

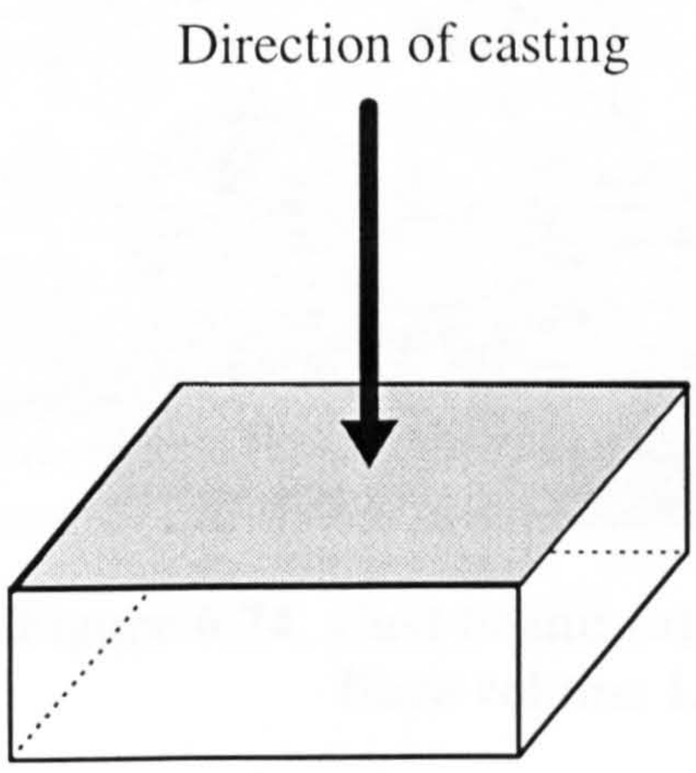

(b) Orientation 2.

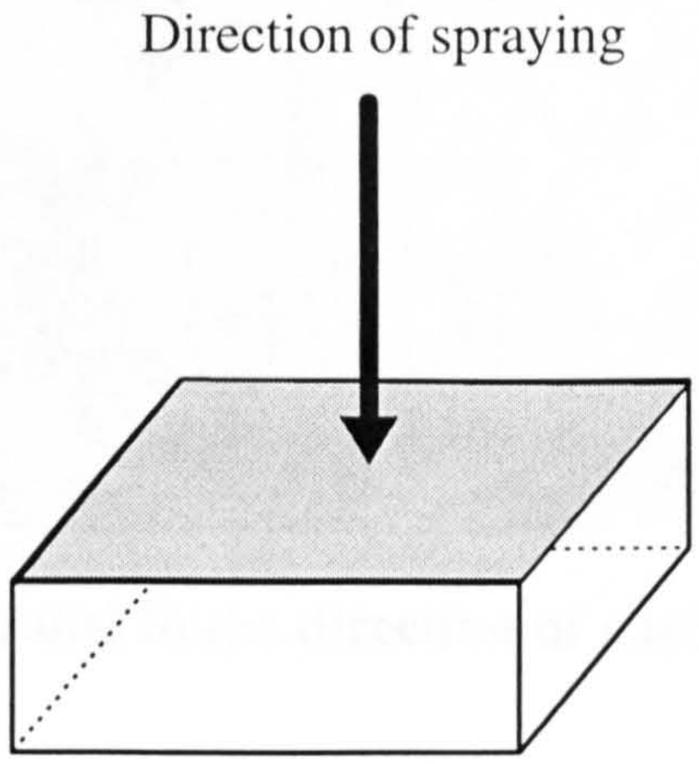

(c) Orientation S.

Figure 6.72 Casting orientations investigated.

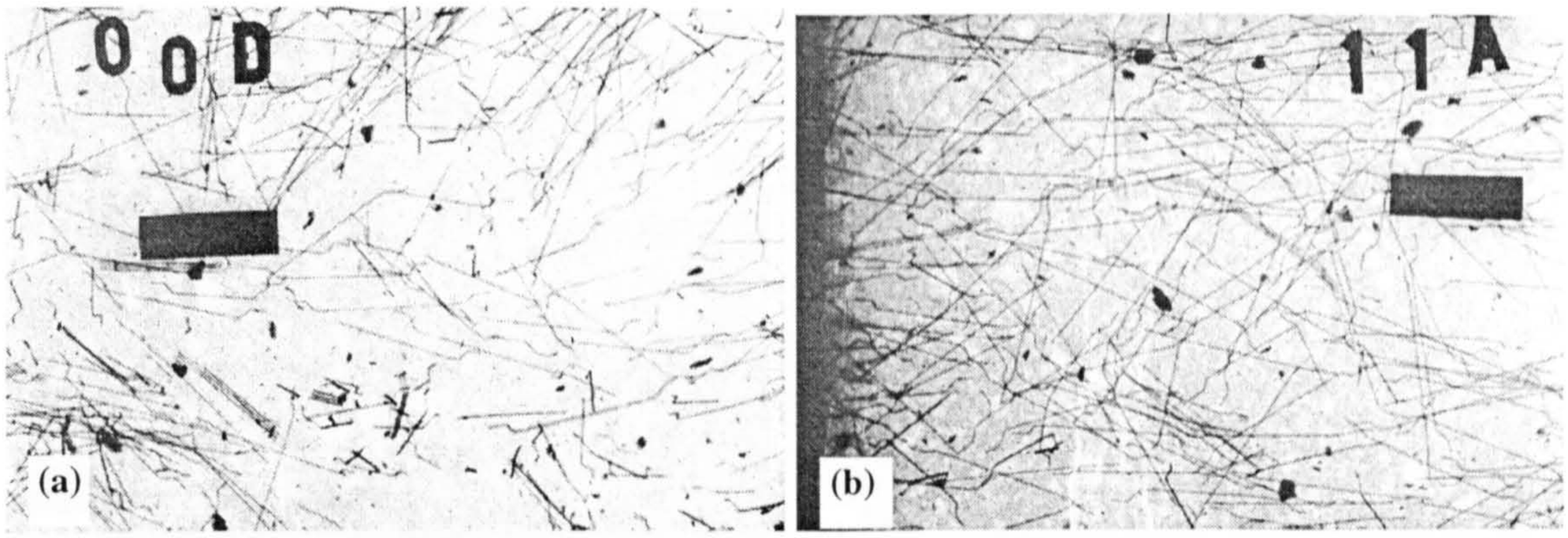

Figure 6.73 Cast beam: (a) normal and (b) parallel to the direction of casting - fibre volume 0.5% (40kg/m^3).

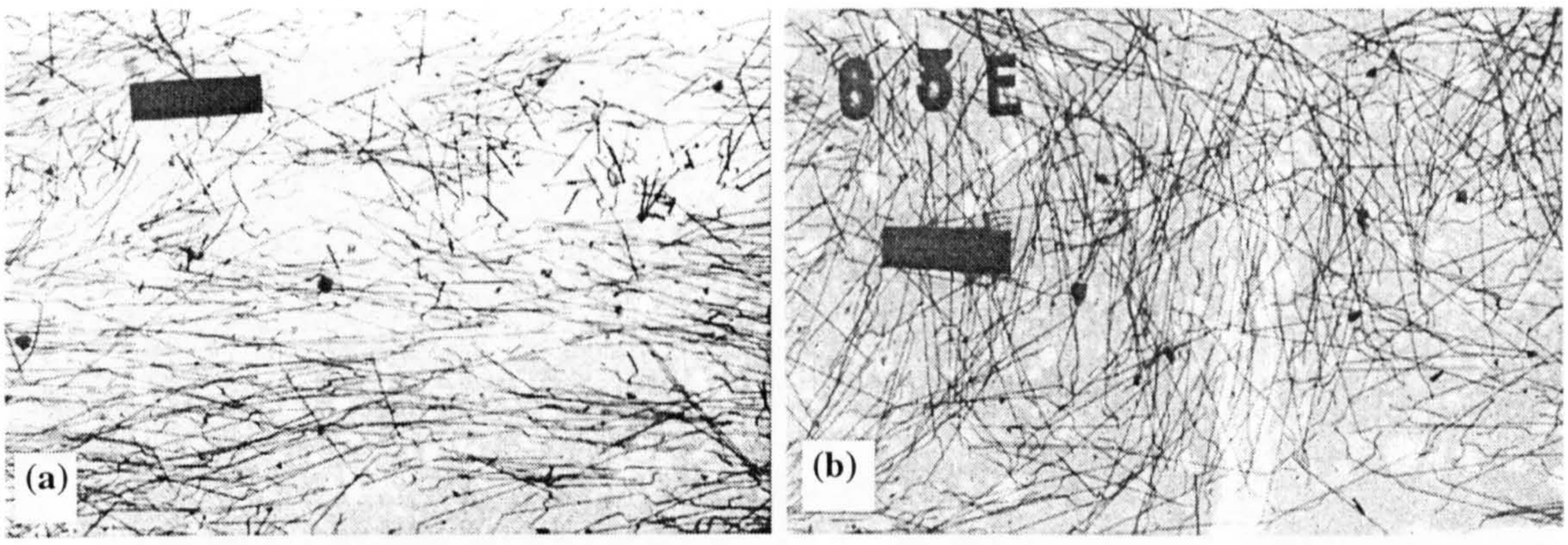

Figure 6.74 Cast beam: (a) normal and (b) parallel to the direction of casting - fibre volume 1.0% (80kg/m^3).

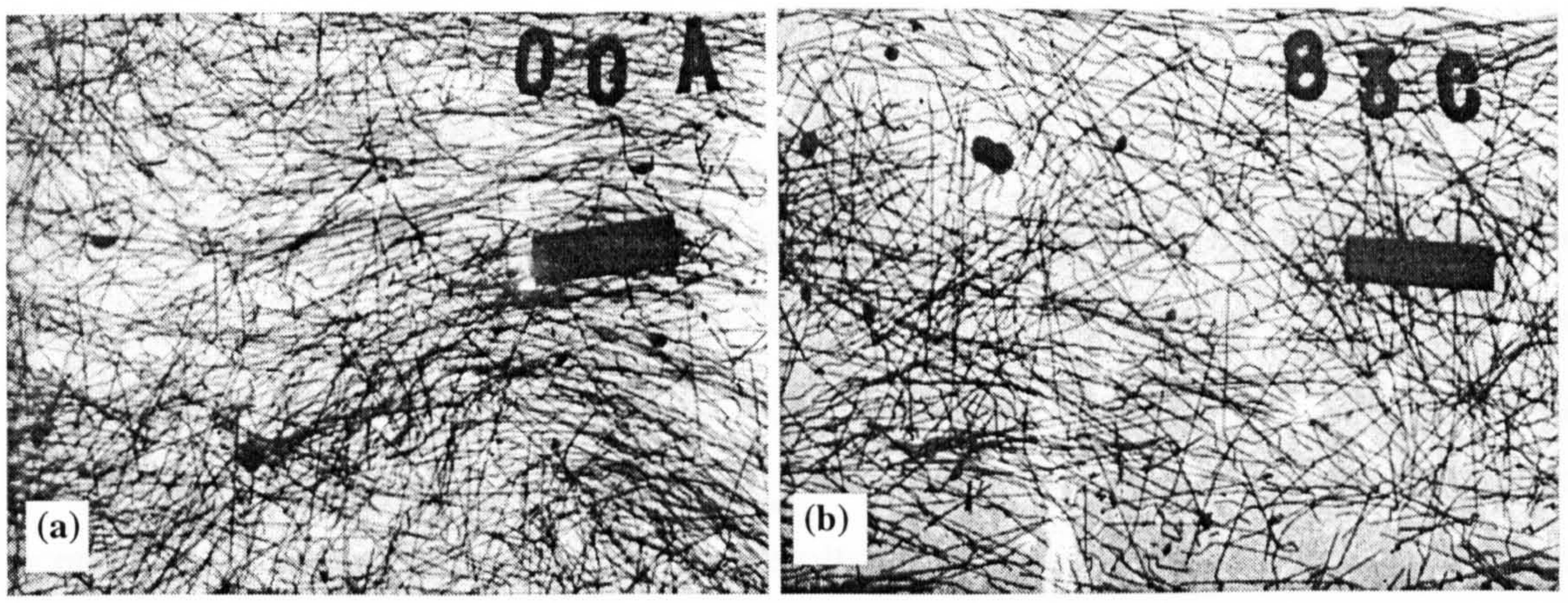

Figure 6.75 Cast beam: (a) normal and (b) parallel to the direction of casting - fibre volume 1.5% (120kg/m^3).

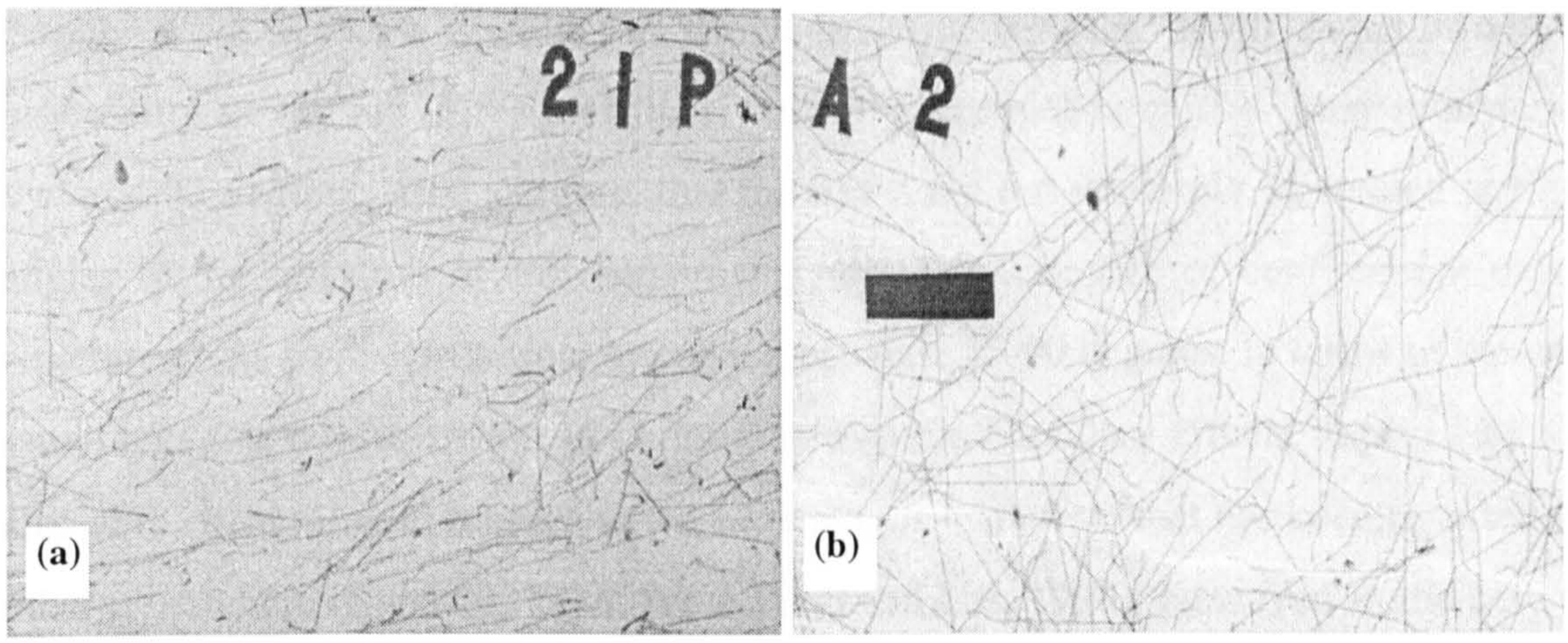

Figure 6.76 Sprayed beam: (a) normal and (b) parallel to the direction of casting - fibre volume 0.34% (26kg/m^3).

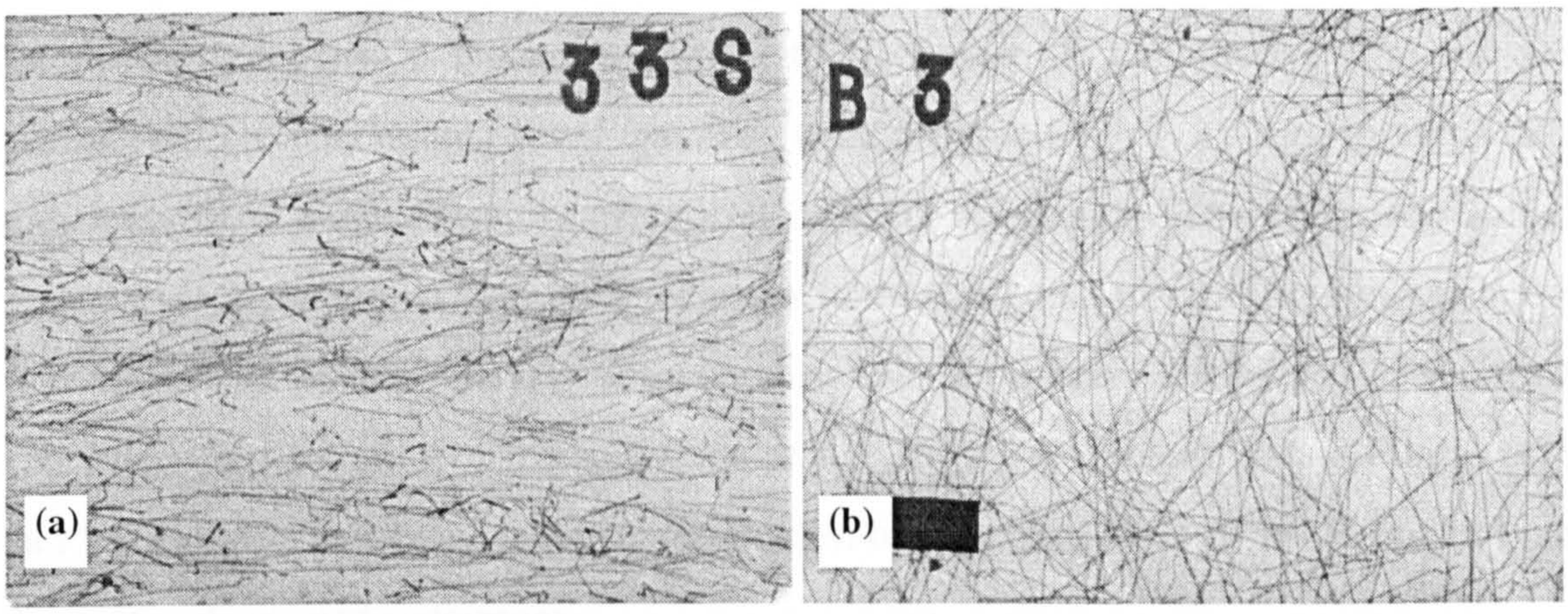

Figure 6.77 Sprayed beam: (a) normal and (b) parallel to the direction of casting - fibre volume 0.87% (66kg/m^3).

Quantitative investigation

Table 6.21 summarises the results from the quantitative analysis on both the cast and sprayed specimens in terms of average fibre embedment lengths and fibre orientation occurring across an arbitrary crack. And Figure 6.78 shows the corresponding probability distributions for the fibre embedment length and fibre orientation occurring across an arbitrary crack. The results indicate that there is little difference in the distribution of fibre embedment length and orientation between the cast and sprayed specimens. Figure 6.78(a) indicates fibre embedment lengths are uniformly distributed, which is reflected in a mean value of approximately one quarter of the overall fibre length in Table 6.21. In contrast, fibre orientations (Figure 6.78(b))

display a non-uniform distribution which peaks at between 20-40 degrees (with a probability of around 20%) and then gradually diminishes as the orientation tends towards 90 degrees. This suggests that the fibres are not randomly orientated at right angles to the direction of casting/spraying, but that a degree of confinement exists which restricts fibre orientations occurring between 45-90 degrees. In terms of the cast specimens this confinement can be attributed to the boundary effects imposed by the size of the beam mould relative to the fibre length - an effect that has been reported by other researchers (Hannant, 1978; Soroushian and Lee, 1990). However, in the case of the sprayed specimens, which were sprayed into 500mm square moulds, no confining effect should exist. Hence, the non-uniform fibre orientations are probably the result of the spraying process or the particular spraying technique adopted by the nozzleman.

Incidentally, note from Figures 6.73-6.77 that because the quantitative analysis was performed on specimens sawn parallel to the direction of casting/spraying the digitised fibres were generally orientated in a 2D orientation. Therefore, the 30mm width restriction imposed on the specimens (although equal to the fibre length) had a minimal effect on the analysis because very few fibres were cut by the saw during specimen preparation. Consequently, the results shown in Table 6.21 and Figure 6.78 can be regarded as a reasonable representation of the actual fibre distributions in both the cast and sprayed specimens.

	Fibre embedment length/mm		Fibre orientation /degrees		
	average	standard dev.	average	standard dev.	sample size
CAST	7.9	4.2	35.2	16.9	354
SPRAYED	7.3	4.2	38.7	19.5	328
OVERALL	7.6	4.2	36.9	18.2	682

Table 6.21 Summary of X-ray analysis on both cast and sprayed beams.

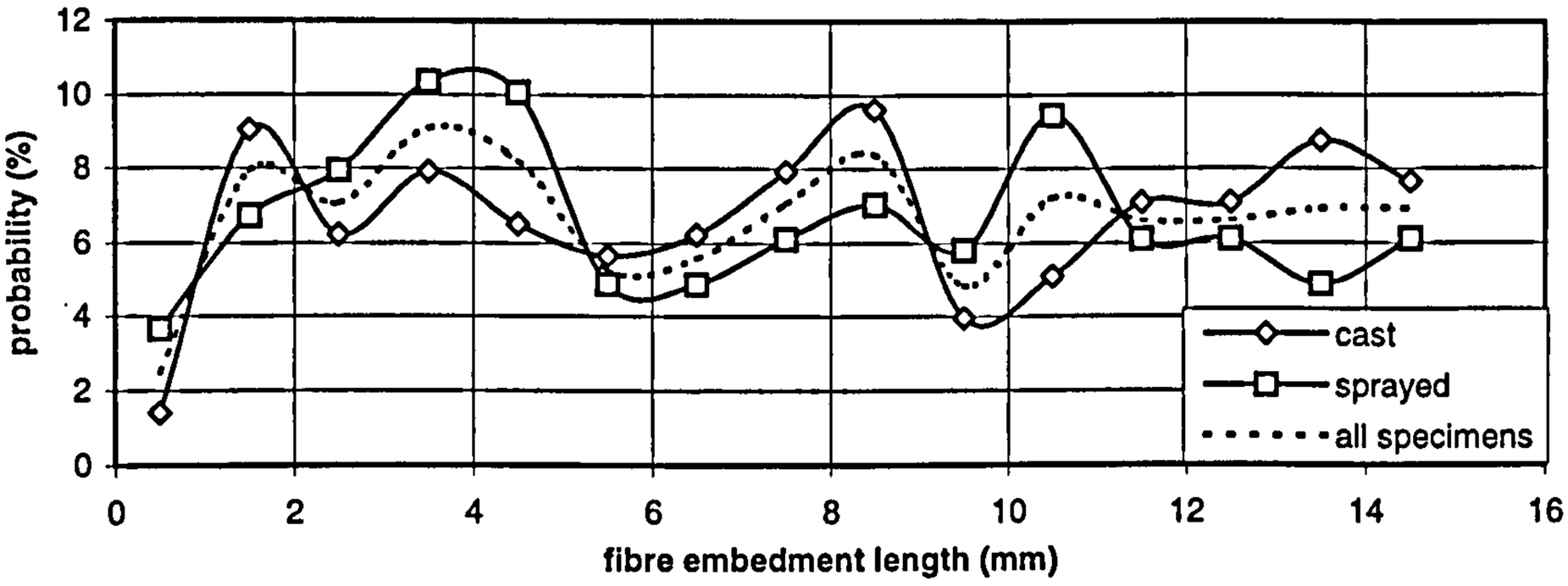

(a) Fibre embedment length.

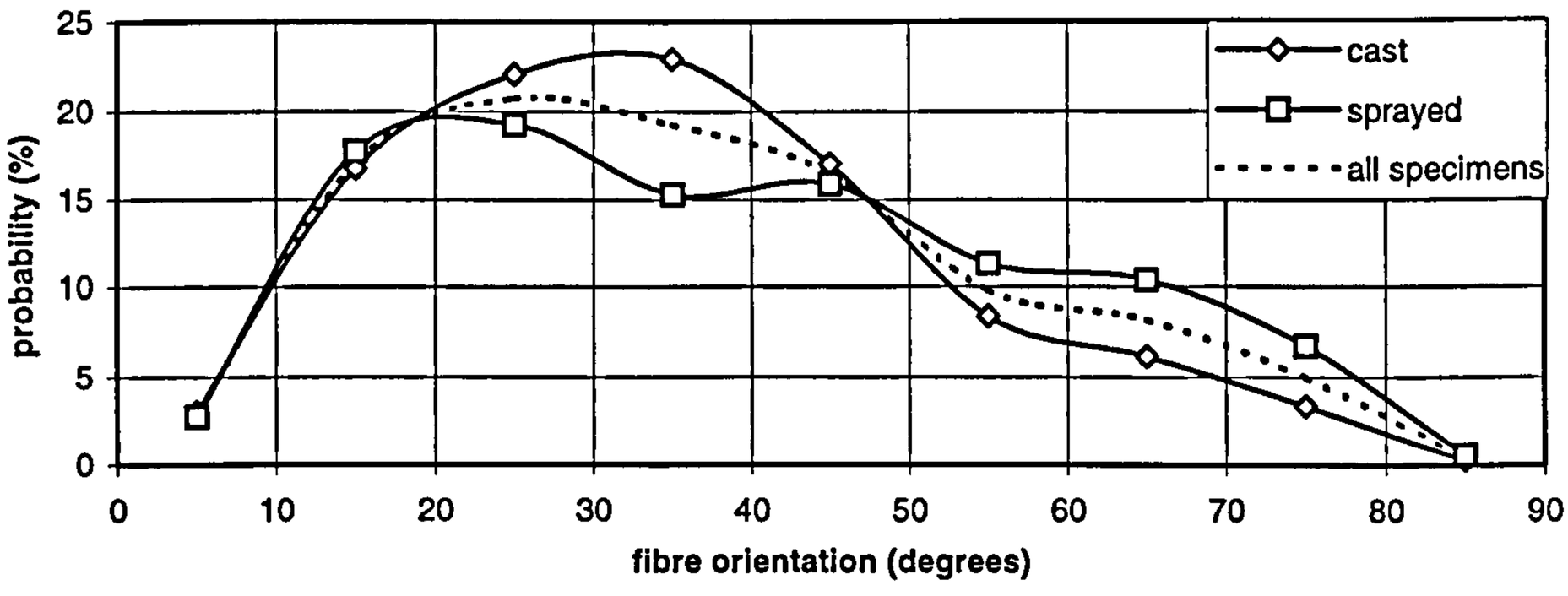

(b) Fibre orientation.

Figure 6.78 Probability distributions determined from X-ray analysis data.

Cast versus sprayed

The results from both the qualitative and quantitative investigations provide strong evidence that the fibre distribution associated with a table vibrated cast specimen is similar to the fibre distribution of a wet process sprayed specimen. This is an important finding in the context of this thesis, as it suggests that fibre distribution data obtained from cast specimens may be appropriate for modelling the behaviour of sprayed specimens made using an equivalent mix design.

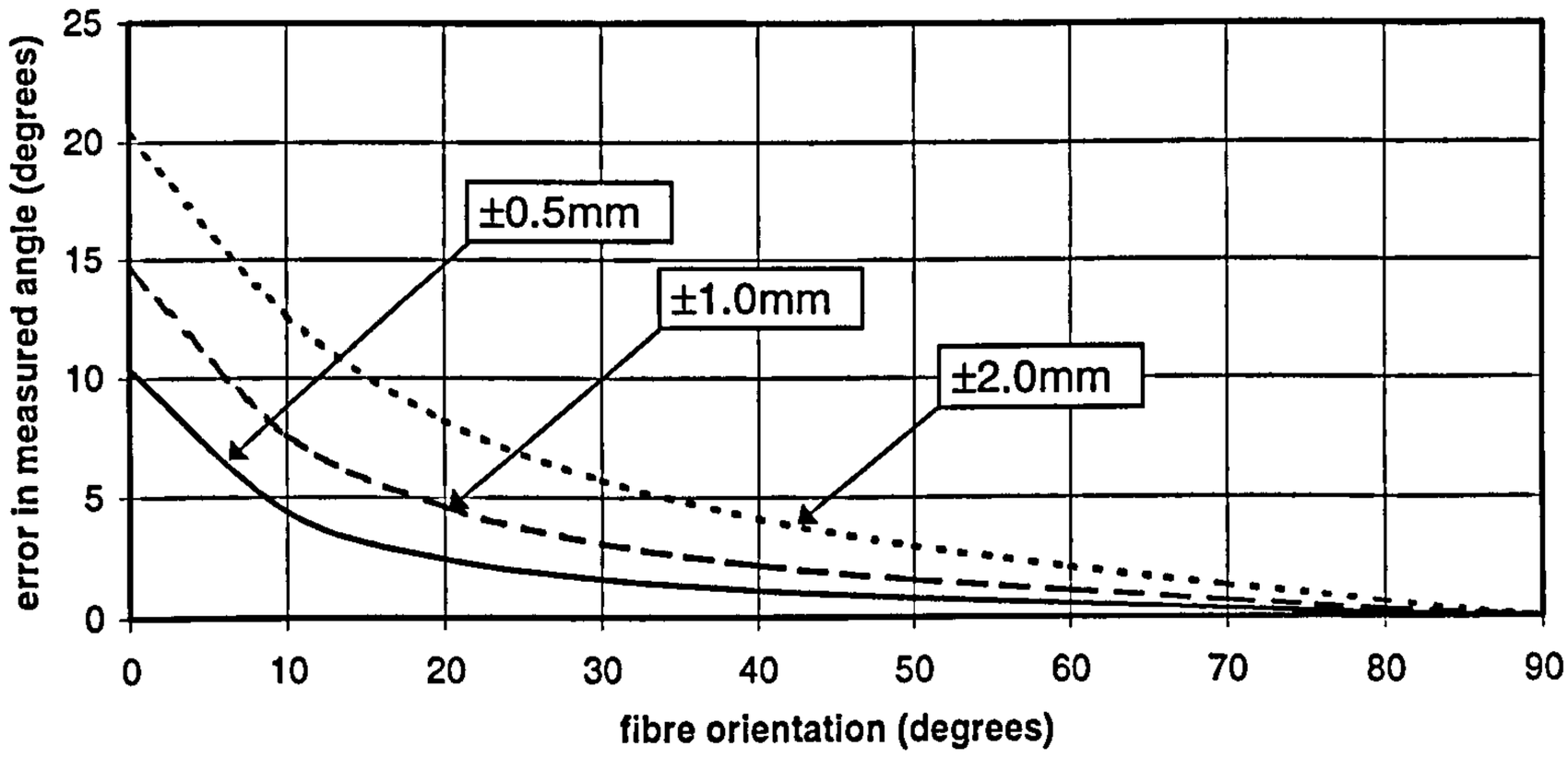

Figure 6.79 Influence of the variation in fibre length on the accuracy of the X-ray analysis.

Accuracy issues

Two aspects relating to the accuracy of the x-ray analysis results must be mentioned.

Firstly, the manufacturer of the 30mm long steel fibres used in this investigation quote fibre length tolerances of between +2 and -3mm (Table 5.4). These tolerances effect the accuracy of the X-ray analysis which assumes that the actual length of each fibre is known. A theoretical study undertaken to investigate these effects indicated that variations in the length of a 30mm long fibre by $\pm$2mm cause errors in the measured orientation angle of up to 20 degrees (Figure 6.79). However, a fibre length analysis on a sample of 100 fibres from the batch used in the experimental investigation, assuming fibre lengths are normally distributed, indicated a 95% confidence interval of 29.7$\pm$0.5mm. Hence, the length tolerances of the actual fibres used, and therefore the magnitude of the potential errors on the measured fibre orientation angles, can be expected to be significantly less than indicated by the fibre manufacture (i.e. less than 10 degrees from Figure 6.79).

Secondly, the accuracy of the digitising procedure was assessed by digitising a sample of ten fibres eight times. The results were used to calculate the standard error relating to the measured fibre lengths and digitised co-ordinates. The results indicated a spatial accuracy in the order of $\pm$0.1mm.

Beam type	Fibre content (kgm^{-3})	Fibre volume (%)	Beam depth (mm)	Fibre density (fibres per cm^2) Average	Fibre density (fibres per cm^2) Standard deviation	Orientation factor (β)
CAST	40	0.5	100	1.06	0.10	0.42
	80	1.0	100	1.95	0.10	0.38
CAST	40	0.5	75	1.33	0.25	0.52
	80	1.0	75	2.27	0.22	0.44
CAST	40	0.5	50	1.38	0.16	0.54
	80	1.0	50	2.64	0.08	0.52
SPRAYED	26	0.34	75	0.85	0.08	0.49
	66	0.87	75	2.17	0.40	0.49

Table 6.22 Influence of beam depth, fibre content and method of manufacture on fibre distribution.

6.7.5 Manual analysis: results and discussion

Fibre density

Table 6.22 compares the average fibre densities and orientation factor β (determined from equation 3.1) at the cracked section for both cast and sprayed specimens, in terms of beam depth (50, 75 and 100mm) and in-situ fibre volume (0.5 and 1.0% for the cast beams, and 0.34 and 0.87% for the sprayed beams). The corresponding relationship between fibre density and fibre volume for each of the beam types investigated is graphically illustrated in Figure 6.80. It can be seen that fibre density appears to be linearly related to fibre volume for both the cast and sprayed beams (that is, a 1.0% mix provides an average fibre density roughly twice as large as a 0.5 % mix), which is in accordance with the theoretical relationship given in equation 3.1 (Section 3.3.2).

The orientation factors shown in Table 6.22 (calculated from the average fibre densities intercepting a cracked section) display similar values for both the sprayed (0.49) and cast specimens (0.38-0.52), which indicates a similar fibre distribution in both types of specimen. In terms of the cast specimens, there appears to be a reduction

in orientation factor with increasing beam depth (or mould size). The results indicate average orientation factors of 0.53, 0.48 and 0.40 for beam depths of 50, 75 and 100mm respectively. These findings are in accordance with the work of Soroushian and Lee (1990) who showed, using a theoretical model, that for a constant specimen-width-to-fibre-length ratio the orientation factor reduces as the height-to-width ratio of the specimen mould increases. They suggested the reduction is caused by the fibre distribution moving from a 2D distribution towards a 3D random distribution as the height-to-width ratio of the mould increases. As a result, less fibres are aligned parallel with the sides of the mould, and hence, the fibre density across the crack and the orientation factor reduces.

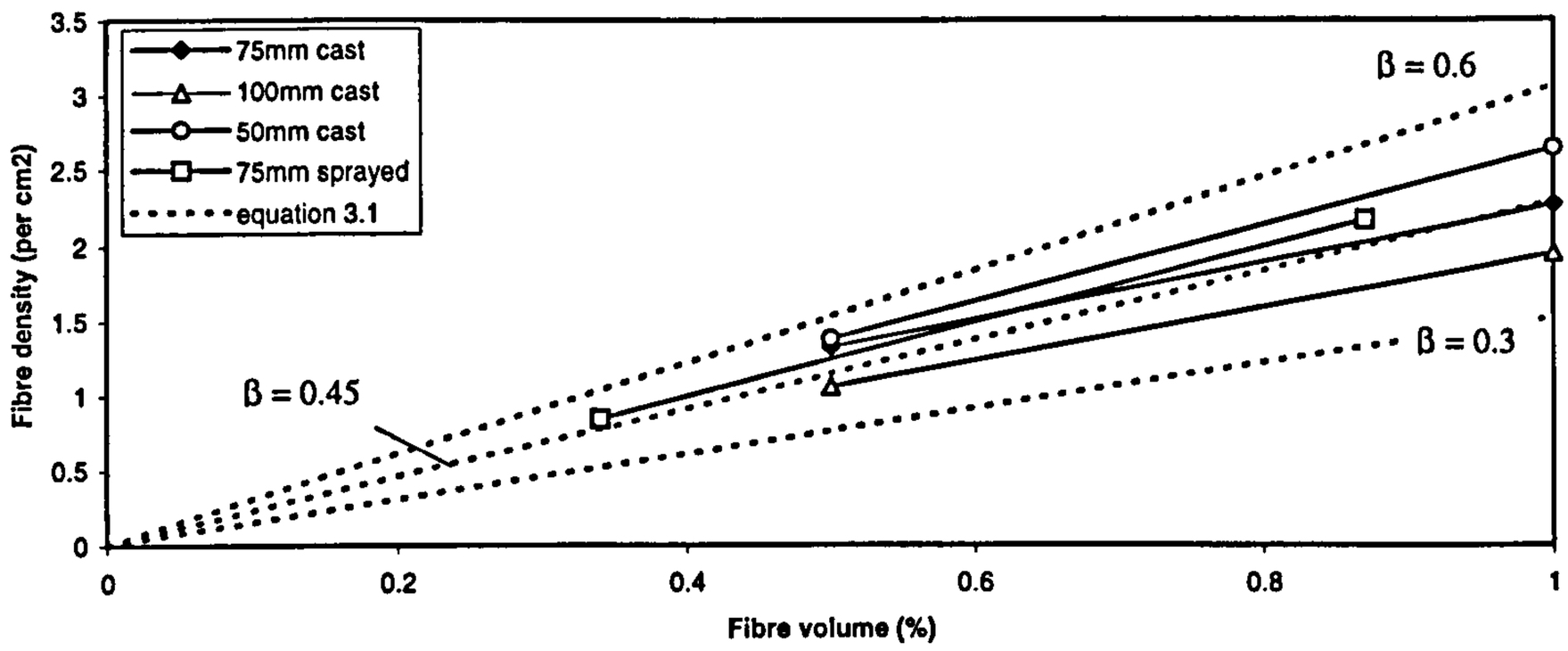

Figure 6.80 Relationship between fibre density and fibre volume.

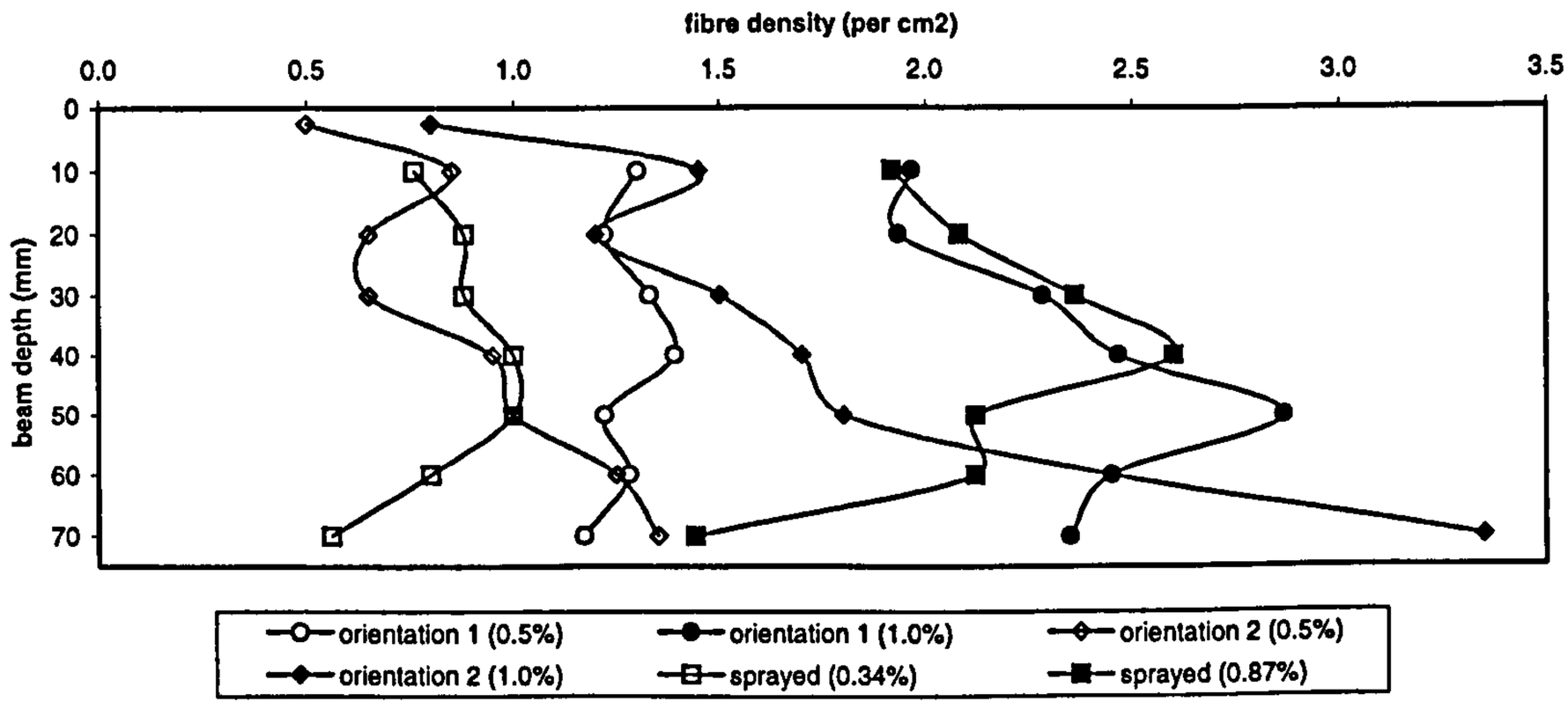

Figure 6.81 Fibre density as a function of beam depth (75mm unnotched beams).

In the case of the sprayed specimens - which were sprayed into moulds with a relatively small height-to-width ratio compared with the cast specimens, but with a significantly larger mould-width-to-fibre-length ratio - the work of Soroushian and Lee (1990) suggests that a small height-to-width ratio tends to result in a 2D fibre distribution (and thus an increase in orientation factor), which is counterbalanced by the large mould-width-to-fibre-length ratio (causing a reduction in orientation factor). As a result, it is possible for the orientation factors associated with both the cast and sprayed specimens to have similar values indicating similar fibre distributions. Incidentally, note that out of the three cast beam sizes investigated, the orientation factor of 75mm deep beams most closely matches that of the sprayed beams.

Fibre distribution relative to beam depth and cast orientation

Figure 6.81 shows average fibre density, of the 75mm deep unnotched beams, as a function of beam depth for a range of cast orientations and fibre volumes. The results indicate two main trends:

i. Casting using table vibration tends to cause the fibres to settle under gravity in the direction of casting. In the case of cast Orientation 2 (beams cast flat) this causes a fibre density gradient over the beam depth, with higher values towards the bottom of the beam. However, in the case of cast Orientation 1 (beams cast on their side) the resulting fibre distribution gradient is orientated across the width of the beam, and hence, the value of fibre density appears uniform over the beam depth.

ii. Spraying generally results in an uniform distribution of fibres over the beam depth, with a slight reduction in fibre density near the base of the beam. This reduction may be caused by higher fibre rebound in the initial layers of sprayed concrete (Austin, 1995a). Thus, the general shape of the fibre density distribution associated with a sprayed beam is essentially the same as that associated with a beam cast and table vibrated on its side (cast Orientation 1).

These findings may provide an explanation for the differences in the shape of the flexural load versus deflection curves for the cast and sprayed specimens discussed in Section 6.5. In particular, the reduction in fibre content near the base of the sprayed beams may explain the lower residual strengths associated with the sprayed specimens shown in Figures 6.42.

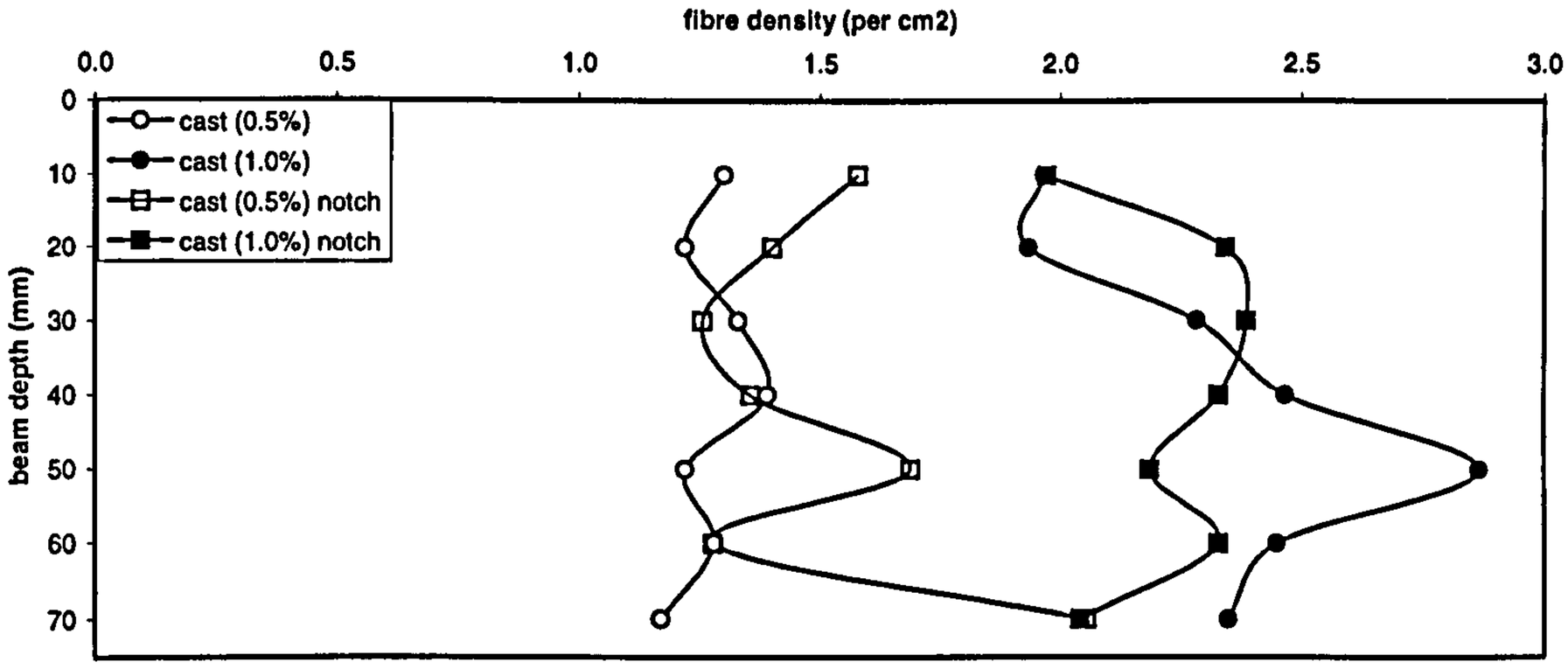

Figure 6.82 Fibre density as a function of beam depth (75mm unnotched and 85mm notched beams).

Incidentally, the presence of a notch does not appear to affect the average fibre density distribution over the beam depth when compared with an equivalent unnotched beam. This is illustrated in Figure 6.82, which compares the average fibre density distributions of 75mm deep unnotched beams with 85mm deep notched beams with fibre volumes of 0.5 and 1.0%.

6.8 CHAPTER SUMMARY

This chapter has described the experimental investigation undertaken to investigate the reinforcing mechanisms associated with steel fibre reinforced concrete and to obtain the necessary data and parameter relationships for use in the development and implementation of the proposed model. Furthermore, it has highlighted some important similarities between the strength, structural behaviour and fibre distributions of wet process sprayed and cast specimens made with equivalent steel fibre reinforced concrete mixes. These similarities are of importance for the implementation and validation of the methodology used in this thesis. A summary of the main conclusions drawn from this investigation in terms of the implication of the results on the proposed model, and more generally in terms of the reinforcing mechanisms associated with fibre reinforced concrete, is presented in Chapter 8.

The final stage of this thesis was to develop, implement and check the accuracy of the proposed model by combining the data obtained from the experimental investigation to predict flexural load-deflection curves for the range of beam sizes used in the investigation. This is described in Chapter 7.

7. MODEL DEVELOPMENT, IMPLEMENTATION AND RESULTS

7.1 INTRODUCTION

This chapter describes the development and testing of the proposed model, in order to confirm the hypothesis stated in Chapter 4. It describes how the experimental data (presented in Chapter 6) was applied to the model, and then how the model was implemented to obtain predictions of the flexural load-deflection response. Finally the predicted data is compared with the experimental data to assess the validity and accuracy of the model.

The testing of the model centred around the prediction of the flexural load-deflection response for the principal matrix (Matrix C) using two modelling approaches:

i. Modelling the load-deflection responses associated with the strain analysis test beams that failed at a single crack within the middle-third region, and then comparing the results with the measured responses. In total ten beams were analysed, comprising five unnotched beams and five notched beams, as detailed in Table 7.1.
ii. Modelling generalised load-deflection responses for the different beam sizes investigated in the experimental programme, assuming the cracked section occurs at mid-span, and then comparing the results with the corresponding average responses obtained from the flexural toughness tests. In total twelve beams were analysed, as detailed in Table 7.2.

In each case, flexural loads were predicted at mid-span deflections of 0.05, 0.1, 0.2, 0.5, 1.0, 2.0 and 4.0mm.

7.2 DEVELOPMENT OF MODEL

7.2.1 General

This section describes how the experimental data was applied to the model to enable the stress block diagram to be predicted at each mid-span deflection for a beam of known size, loading geometry, fibre content and matrix compressive strength. It is presented as four sub-sections corresponding to the main elements of the stress block diagram (Figure 4.1): (i) the strain and crack-width profile; (ii) the compression zone; (iii) the uncracked tensile zone; and (iv) the cracked tensile zone.

Beam reference	Notched/ unnotched	depth mm	width mm	Fibre content kg/m^3	cast/ sprayed
SA8-2	unnotched	100	100	40	cast
SA10-3	unnotched	100	100	40	cast
SA1-1	unnotched	75	100	40	cast
SA1-2	unnotched	75	100	40	cast
SA5-1	unnotched	75	125	26	sprayed
SA2-1	notched	85*	100	40	cast
SA2-2	notched	85*	100	40	cast
SA7-1	notched	60*	100	40	cast
SA9-1	notched	60*	100	80	cast
SA9-2	notched	60*	100	80	cast

* depth includes 10mm notch.

Table 7.1 Summary of modelling analysis to predict *actual* load-deflection responses of the flexural test beams.

7.2.2 Strain and crack-width profile

The strain/crack-width profiles, determined from the strain analysis tests (Section 6.6), were central to the successful implementation of the model. This was because it was these profiles against which all the other test data was applied, in order to predict the stress-block diagram at each mid-span deflection.

It was originally envisaged that the measured strain/crack-width profiles would be applied directly to the model. However, early modelling trials showed that the measured neutral axis depth always had to be altered slightly in order to satisfy equilibrium of the internal forces at the section under investigation. Therefore, later trials only used measured values for the maximum compressive strain and corresponding CMOD, so that during the modelling analysis the position of the neutral axis was altered by trial-and-error until equilibrium of the internal forces was satisfied. Hence, only the extreme values of the measured strains and crack-widths were used in the model. By using this approach, equilibrium of the internal forces at the section under investigation was always satisfied.

Beam reference	Notched/ unnotched	depth mm	width mm	Fibre content kg/m^3	cast/ sprayed
100C (40)	unnotched	100	100	40	cast
100C (80)	unnotched	100	100	80	cast
75C (40)	unnotched	75	100	40	cast
75C (80)	unnotched	75	100	80	cast
50C (40)	unnotched	50	100	40	cast
50C (80)	unnotched	50	100	80	cast
75S (26)	unnotched	75	125	26	sprayed
75S (66)	unnotched	75	125	66	sprayed
60C (40)	notched	85*	100	40	cast
60C (80)	notched	85*	100	80	cast
85C (40)	notched	60*	100	40	cast
85C (80)	notched	60*	100	80	cast

* depth includes 10mm notch.

Table 7.2 Summary of modelling analysis to predict *generalised* load-deflection responses for the range of beams investigated.

	SA1-1		SA1-2		SA2-1		SA2-2		SA5-1		SA8-2		SA10-3		SA7-1		SA9-1		SA9-2	
deflection (mm)	ε_{max} (με)	cmod (mm)	ε_{max} (με)	cmod (mm)	ε_{max} (με)	cmod (mm)	ε_{max} (με)	cmod (mm)	ε_{max} (με)	cmod (mm)	ε_{max} (με)	cmod (mm)	ε_{max} (με)	cmod (mm)	ε_{max} (με)	cmod (mm)	ε_{max} (με)	cmod (mm)	ε_{max} (με)	cmod (mm)
0.05	85	-	85	-	110	-	110	-	85	-	100	-	100	-	75	-	75	-	85	-
0.1	155	-	155	-	230	-	230	-	155	-	195	-	195	-	145	-	145	-	155	-
0.2	530	0.09	530	0.15	530	0.05	530	0.10	530	0.11	410	0.14	410	0.07	280	0.09	280	0.02	280	0.11
0.5	985	0.36	985	0.47	985	0.22	985	0.27	985	0.40	675	0.37	675	0.26	705	0.15	705	0.09	705	0.40
1.0	1350	0.73	1350	0.99	1350	0.64	1350	0.70	1350	0.79	1040	0.84	1040	0.74	1210	0.31	1210	0.28	1210	0.79
2.0	1890	1.54	1890	2.19	1890	1.29	1890	1.58	1890	1.72	1900	1.88	1900	1.75	2035	0.69	2035	0.70	2035	1.72
4.0	-	-	-	-	-	-	-	-	3020	3.83	2895	4.34	2895	3.83	3140	1.42	3140	-	3140	3.83

Table 7.3 **Summary of maximum compressive strains (ε_{max}) and crack-mouth-opening-displacements (CMOD) used in the modelling analysis to predict the *actual* load-deflection responses of the strain analysis test beams.**

	Beam Reference (see Table 7.2)									
	50/60C		50/60C		75/85C		100C		75S	
	40kg/m^3		80kg/m^3		40 & 80kg/m^3		40 & 80kg/m^3		26 & 66kg/m^3	
deflection (mm)	ε_{max} (με)	cmod (mm)	ε_{max} (με)	cmod (mm)	ε_{max} (με)	cmod (mm)	ε_{max} (με)	cmod (mm)	ε_{max} (με)	cmod (mm)
0.05	75	-	75	-	85	-	100	-	85	-
0.1	145	-	145	-	155	-	195	-	155	-
0.2	280	(0.07)	280	(0.05)	530	(0.05)	410	(0.07)	530	(0.05)
0.5	705	0.25	705	0.15	985	0.25	675	0.25	985	0.25
1.0	1210	0.45	1210	0.30	1350	0.65	1040	0.75	1350	0.65
2.0	2035	0.85	2035	0.70	1890	1.40	1900	1.70	1890	1.40
4.0	3140	1.90	3140	1.45	<u>3020</u>	3.00	2895	3.65	<u>3020</u>	3.00

Note: (1) Figures given in brackets are extrapolated from crack-width profiles;
(2) underlined figures are extrapolated from strain profiles.

Table 7.4 Summary of maximum compressive strains (ε_{max}) and crack-mouth-opening-displacements (CMOD) used in the *generalised* modelling analysis.

When modelling the load-deflection responses of the strain analysis test beams, the maximum compressive strains were determined from the strain-block data given in Table 6.17, and the CMOD values from the crack-width data given in Appendix IV. A summary of this data is given in Table 7.3.

When modelling the generalised load-deflection responses the maximum compressive strains were also determined from the data presented in Table 6.17, but the CMODs were determined by estimating average values for a crack occurring at mid-span. For the notched beams (which always cracked at mid-span) the CMODs were simply obtained by averaging the data in Appendix IV. However, for the unnotched beams (which invariably did not crack at mid-span) the CMODs at mid-span were determined by extrapolating the best-fit lines in Figure 6.55. A summary of this data is given in Table 7.4. Notice that, except for the 60mm notched/50mm unnotched beams (i.e. 50/60C), the same values of maximum compressive strain and CMOD were used

to model the responses of both fibre volumes investigated. Furthermore, the analysis used the same strain/crack-width profiles to model the responses of both the 75mm unnotched and the 85mm notched beams (i.e. 75/85C).

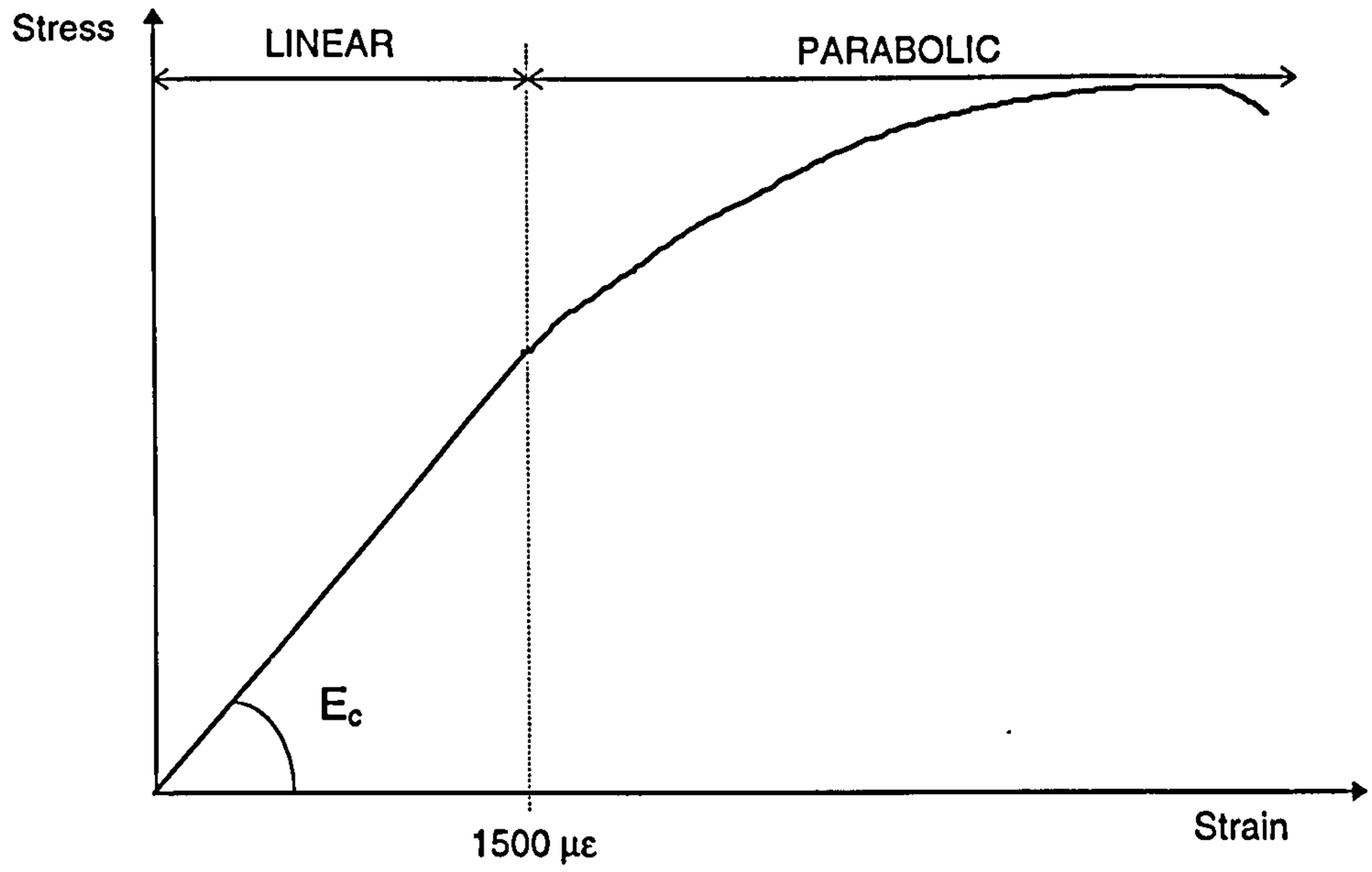

Figure 7.1 Idealised compressive stress-strain curve used in model.

7.2.3 Compression zone

The compressive stress-block was predicted by applying the appropriate measured compressive stress versus strain relationship directly to the compressive strain block determined from the strain/crack-width profile.

The calculation of the stress block area per unit beam width (A_c) and the distance from its centroid to the neutral axis (x_c), was simplified in the model by adopting the idealised stress-strain relationship shown in Figure 7.1.

Thus, for a compressive strain up to 1500με, the stress-strain relationship was assumed to be linear, and so:

$$A_c = \frac{1}{2} c\sigma_c \quad \text{and} \quad x_c = \frac{2}{3} c \qquad \text{equation 7.1}$$

where c is the depth of the neutral axis and σ_c is the value of stress measured at the extreme compressive face of the beam.

For a compressive strain greater than 1500με, the stress-strain relationship was assumed to be parabolic, and so:

$$A_c = \frac{2}{3} c\sigma_c \quad \text{and} \quad x_c = \frac{5}{8} c \qquad \text{equation 7.2}$$

Initial modelling trials showed that the compressive stress-strain relationships, obtained from the compression tests, were overestimating the strength of the concrete matrix by up to 30%. This suggested that the measured compressive strengths were artificially high as a result of the following factors: (i) the relatively small cross-section dimensions of the test specimens; and (ii) the fundamental differences between the strain gradients and failure modes associated with a prism tested in uniaxial compression and a beam tested in pure bending. Hence, a compressive strength reduction factor of 0.76 was applied to the measured compressive stress-strain relationships in order to compensate for these differences and, thereby, to provide a more realistic compressive stress block for use in the model. The value of this factor was estimated from Figure 3.6.

Note that the compressive strength reduction factor also corresponds to a reduction in the value of Young's modulus. In the case of Matrix C, this factor reduces the value of Young's modulus from 33GPa to 25GPa, which incidentally compares favourably with the Young's modulus values determined from the first-crack flexural analysis (as detailed in Table 6.18).

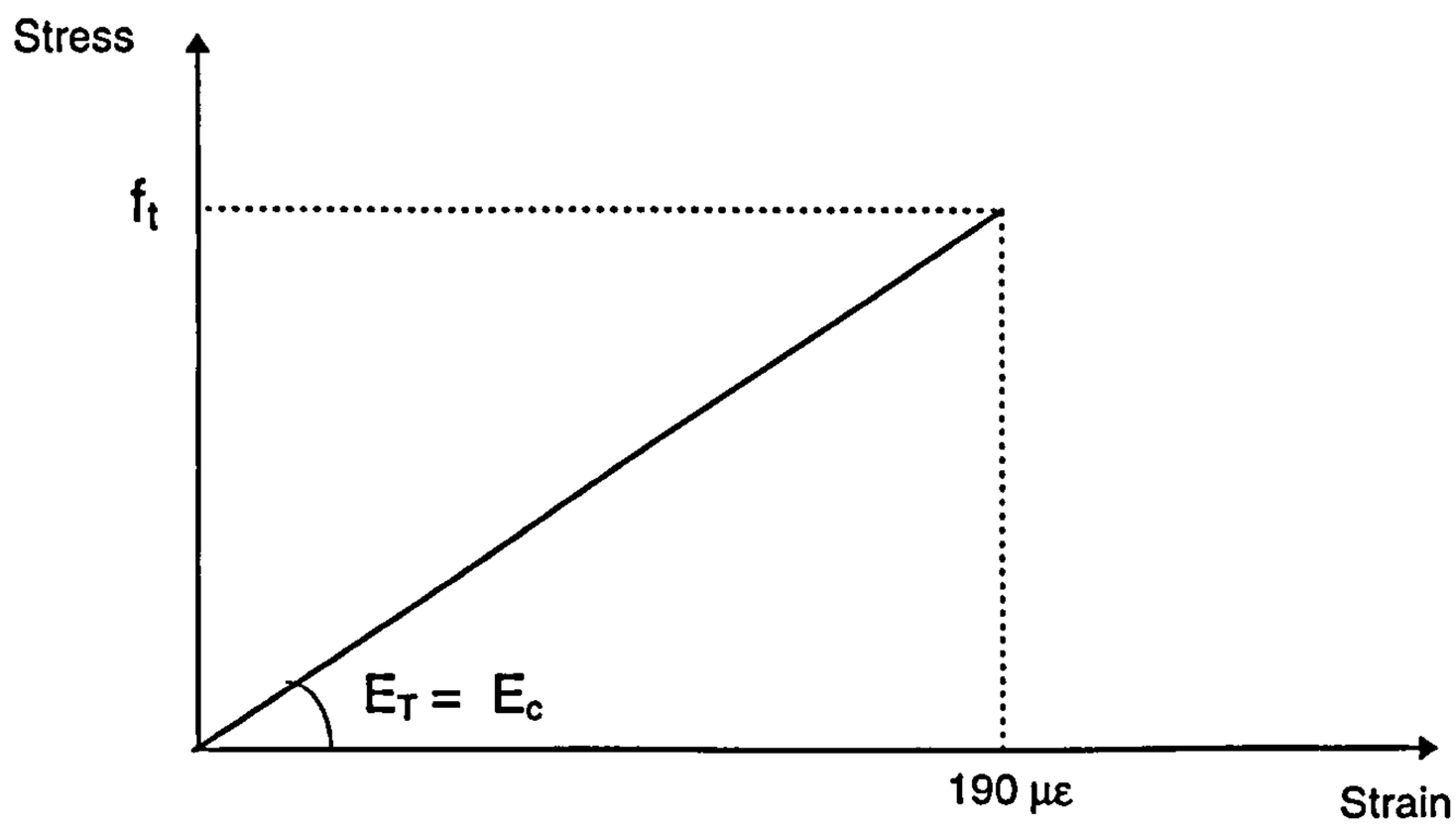

Figure 7.2 Idealised tensile stress-strain curve used in the model.

7.2.4 Uncracked tensile zone

The uncracked tensile stress-block was predicted by applying the tensile stress-strain relationship (Figure 7.2) directly to the uncracked tensile strain block determined from

the strain/crack-width profile. Note that the following assumptions were made in the prediction of the uncracked tensile stress block:

- the beam is of a homogenous material which has the same value of Young's modulus in both compression (E_c) and tension (E_t);
- the tensile stress-strain relationship is linear up to the matrix cracking strain (ε_{cr}) - assumed to be 190με for the concrete matrices used in the experimental investigation; and
- the matrix cracking stress (f_t) is determined as

$$f_t = E_c \times \varepsilon_{cr} \qquad \text{equation 7.3}$$

7.2.5 Cracked tensile zone

General

In Chapter 4 the cracked tensile zone was shown to consist of three sub-zones (Figure 4.1): an aggregate bridging zone, a fibre bridging zone and a traction free zone. It was also proposed that the forces transferred across the cracked tensile zone are mainly dependent on the pull-out behaviour of the individual fibres bridging the crack, which can be modelled using single fibre pull-out test data in combination with the fibre distribution data measured across the crack. Therefore, two main problems had to be overcome in order to predict the forces across the cracked tensile zone:

i. how many fibres bridge the cracked section ?; and
ii. what is the fibre embedment length and fibre orientation of each fibre bridging the cracked section ?

The first problem was overcome by using the results from the manual fibre counting analysis (Section 6.7) to provide data relating to both the number and distribution of the fibres bridging the cracked section. However, because it was not possible to apply a separate pull-out response curve to each fibre, an alternative approach (based on a probability analysis) was developed to combine statistically all the single fibre pull-out test responses (that is, for all the different combinations of fibre embedment length l_f and fibre orientation θ_f) into a single pull-out response curve. This curve, hereafter termed the *probabilistic fibre pull-out curve*, represents the most probable pull-out response of each fibre bridging the cracked section.

The method developed for determining the probabilistic fibre pull-out curve from the fibre pull-out test data is summarised below.

- The probabilities relating to each value of l_f and θ_f investigated in the single fibre pull-out tests (column A and B in Table 7.5) were first determined from the results of the X-ray analysis as described in Section 6.7. Therefore, in order to incorporate the full range of l_f and θ_f (that is, 0-15mm and 0-90 degrees, respectively) into the probabilistic fibre pull-out curve, the individual values of l_f and θ_f investigated in the pull-out tests had each to represent a continuous range of values. These are shown in Table 7.6, together with their corresponding probabilities determined from the X-ray analysis results (Figure 6.78).
- The probabilities shown in Table 7.6 were then used to determine a combined probability associated with each combination of l_f and θ_f, by calculating the product of the probabilities for each combination of l_f and θ_f - as shown in column C of Table 7.5.
- Average fibre pull-out loads were then determined from the single fibre pull-out tests, up to a crack-width of 5mm (in increments of 0.05mm), for each combination of l_f and θ_f - as shown in columns $D_{0.05}$ to $D_{5.0}$ of Table 7.5.
- For each combination of l_f and θ_f, the average fibre pull-out loads were multiplied by their probability of occurrence to obtain 'weighted fibre pull-out loads' - as shown in columns $E_{0.05}$ to $E_{5.0}$ of Table 7.5.
- The weighted fibre pull-out loads were then summed together to obtain a total 'probabilistic fibre pull-out load' for each crack-width value.
- Finally, the probabilistic fibre pull-out loads were plotted against the corresponding crack-widths to obtain the resulting probabilistic fibre pull-out curve.

Lf	θf	A	B	C	$D_{0.05}$	$D_{0.1}$	$D_{0.15}$	$D_{0.2}$		$D_{5.0}$	$E_{0.05}$	$E_{0.1}$	$E_{0.15}$	$E_{0.2}$		$E_{5.0}$
fibre length (mm)	fibre orientation (degrees)	probability of Lf	probability of θf	combined probability of Lf and θf	Average fibre pull-out loads between crack-widths of 0.05-5.0mm for each combination of Lf and θf (N)						Weighted fibre pull-out loads between crack-widths of 0.05-5.0mm for each combination of Lf and θf (N)					
-	-	-	-	col. A x col B.	-						col. C x col.($D_{0.05}$ - $D_{5.0}$)					
					0.05	0.1	0.15	0.2		5.0	0.05	0.1	0.15	0.2		5.0
5	0	0.27	0.04	0.01	36	50	60	64		0	0.4	0.5	0.6	0.7		0.0
5	10	0.27	0.17	0.05	80	94	108	107		0	3.6	4.3	4.9	4.8		0.0
5	20	0.27	0.21	0.06	36	60	74	69		0	2.0	3.3	4.1	3.9		0.0
5	30	0.27	0.19	0.05	59	54	51	49		0	3.0	2.8	2.6	2.5		0.0
5	40	0.27	0.16	0.04	28	35	43	45		0	1.2	1.5	1.8	1.9		0.0
5	50	0.27	0.10	0.03	32	33	30	30		0	0.9	0.9	0.8	0.8		0.0
5	60-90	0.27	0.13	0.03	32	35	36	36		4	0.6	0.6	0.6	0.6		0.1
10	0	0.47	0.04	0.02	57	67	106	133		53	1.1	1.3	2.0	2.5		1.0
10	10	0.47	0.17	0.08	59	78	99	120		77	4.7	6.2	7.8	9.5		6.1
10	20	0.47	0.21	0.10	51	76	115	138		44	5.0	7.4	11.3	13.5		4.3
10	30	0.47	0.19	0.09	62	70	98	116		54	5.5	6.2	8.7	10.3		4.8
10	40	0.47	0.16	0.07	22	49	67	66		0	1.6	3.6	5.0	5.0		0.0
10	50	0.47	0.10	0.05	30	36	45	48		90	1.4	1.7	2.1	2.2		4.2
10	60-90	0.47	0.13	0.06	26	26	23	21		100	0.8	0.8	0.7	0.7		3.0
15	0	0.27	0.04	0.01	24	39	84	111		49	0.3	0.4	0.9	1.2		0.5
15	10	0.27	0.17	0.05	25	60	111	147		89	1.1	2.7	5.0	6.6		4.0
15	20	0.27	0.21	0.06	47	71	115	140		91	2.6	4.0	6.4	7.8		5.1
15	30	0.27	0.19	0.05	60	73	108	123		0	3.0	3.7	5.5	6.2		0.0
15	40	0.27	0.16	0.04	41	55	66	68		0	1.8	2.3	2.8	2.9		0.0
15	50	0.27	0.10	0.03	24	39	46	46		0	0.6	1.0	1.2	1.2		0.0
15	60-90	0.27	0.13	0.03	31	30	25	25		150	0.5	0.5	0.4	0.4		2.6
	Totals	1.00	1.00	1.00	-						42	56	75	85		36

Table 7.5 Determination of a probabilistic fibre pull-out load curve.

Fibre embedment lengths studied in pull-out tests (mm)	Range of values represented by each embedment length (mm)	Probability of occurrence
5	$0 \leq 4.5$	0.267
10	$4.5 \leq 11.5$	0.466
15	$11.5 \leq 15.0$	0.267

(a) Fibre embedment lengths (probabilities determined from Figure 6.78).

Fibre orientations studied in pull-out tests (degrees)	Range of values represented by each orientation (degrees)	Probability of occurrence
0	$0 \leq 10$	0.04
10	$10 \leq 20$	0.17
20	$20 \leq 30$	0.21
30	$30 \leq 40$	0.19
40	$40 \leq 50$	0.16
50	$50 \leq 60$	0.10
60	$60 \leq 90$	0.13

(b) Fibre orientations (probabilities determined from Figure 6.78).

Table 7.6 Probabilities of occurrence used in the determination of the probabilistic fibre pull-out curve used in the model.

Figure 7.3 compares the probabilistic fibre pull-out curve used in the model (as determined from the probabilities given in Table 7.6) with a corresponding curve determined by assuming a random fibre distribution (that is, assuming all the combinations of l_f and θ_f have an equal probability of occurrence). A significant difference in the magnitude of these curves can be seen, particularly up to a crack-width of 2mm where the loads associated with the random distribution curve are up to 40% lower than the actual curve used in the model. The greater pull-out loads associated with the actual curve are the result of the measured fibre distribution being skewed towards fibre orientations between 0-30 degrees, which corresponds to the pull-out tests that generally displayed the highest peak pull-out loads (see Section 6.3).

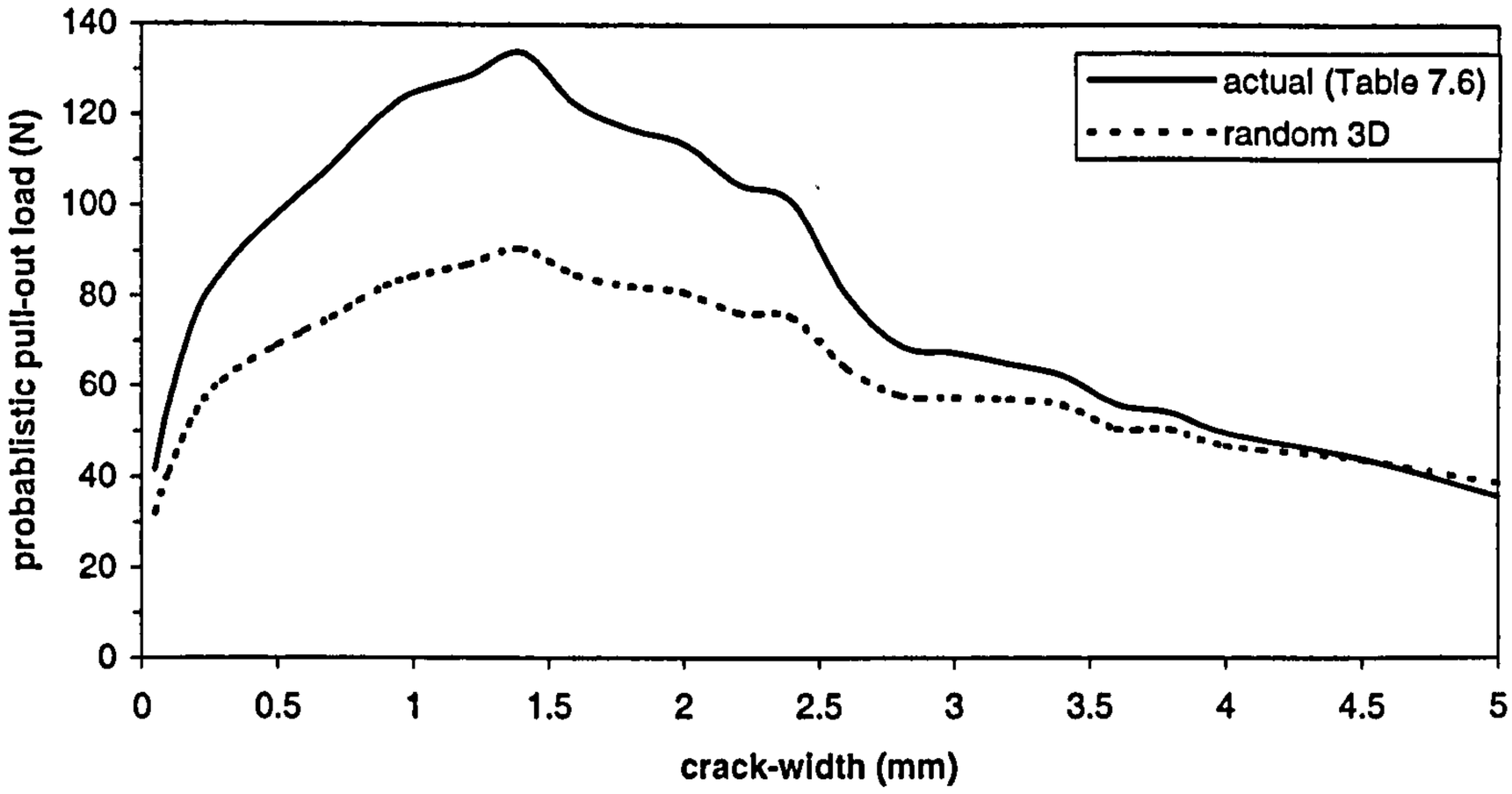

Figure 7.3 Probabilistic fibre pull-out curves.

Aggregate bridging zone

It was originally envisaged that the single fibre pull-out test data would be used to predict both the aggregate and fibre bridging zones in the model. However, because the tests could not be undertaken using a closed-loop system of strain the post-crack fibre pull-out responses were characterised by a sudden drop in load and a 'jump' in the crack-width measurement (to approximately 0.02-0.05mm) at the instant the specimen fractured. Consequently, between the specimen fracture point and a crack width of approximately 0.05mm the pull-out response could not be recorded and, hence, there was no fibre pull-out data available to model the aggregate bridging zone.

To overcome this problem, a stress versus crack-width relationship (σ–w curve) was derived, for crack-widths up to 0.05mm, using the law of mixtures (Figure 7.4). This was achieved by combining a theoretical tensile σ–w curve for the plain concrete matrix with the probabilistic fibre pull-out curve (converted to fibre stresses).

The theoretical tensile σ–w curve for the plain matrix was assumed to decrease exponentially in accordance with Equation 3.3 - using values of 1.0 and 60.8 for the exponential shape factors λ and η respectively (Gopalaratnam and Shah, 1985).

The fibre pull-out σ–w curve was obtained by first calculating a value for the stress in the fibres at the instant the matrix cracks (σ_{ps}), and then extrapolating the probabilistic fibre pull-out curve between this value of fibre stress (at a zero crack-width) and the probabilistic fibre stress at a crack-width of 0.05mm. For the 0.5mm diameter fibres

used in the experimental investigation, assuming a Young's modulus and matrix cracking strain of 205GPa and 190με respectively, the stress in the fibres at the instant the matrix cracks equates to approximately 40MPa.

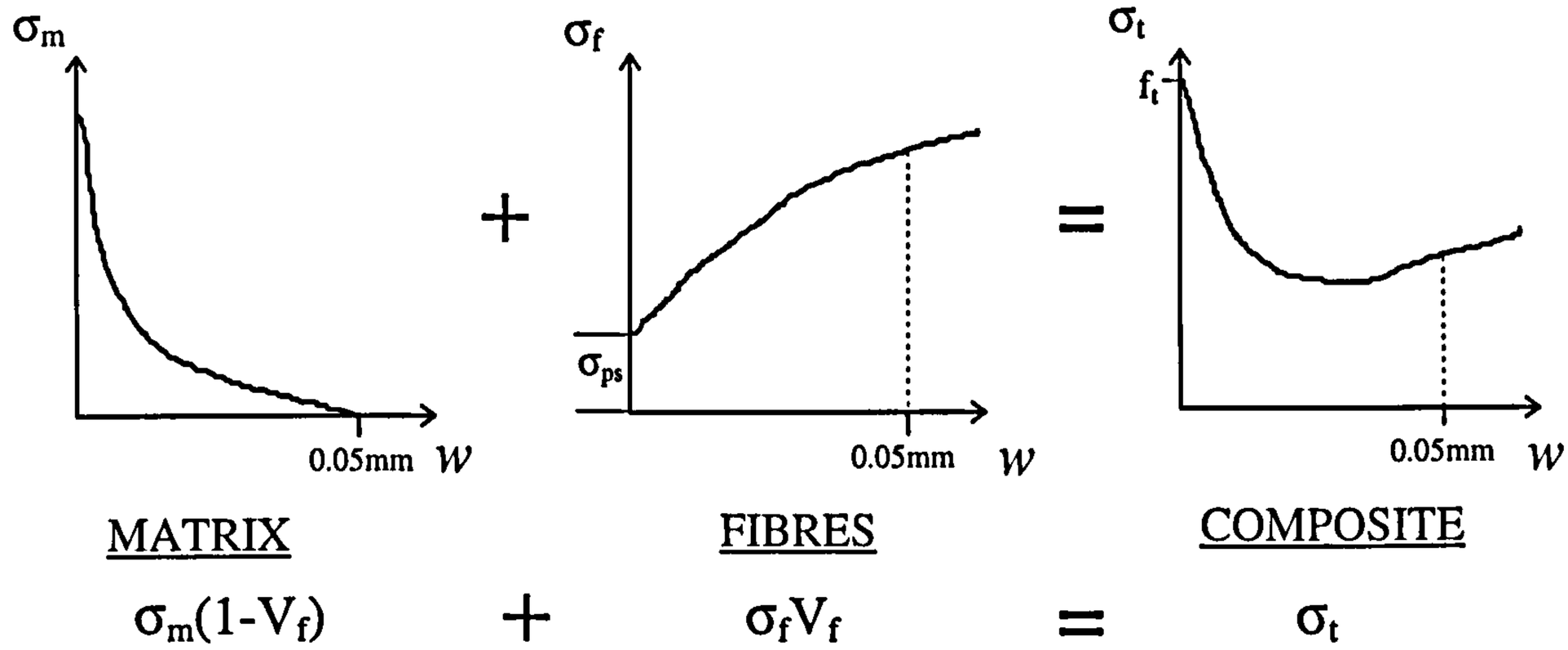

Figure 7.4 Schematic illustration showing the determination of the tensile σ–*w* curve using the law of mixtures.

Figure 7.5 shows the resulting tensile σ–w curves for fibre volumes of 0.5 and 1.0% (40 and 80kg/m^3 respectively). Similar curves (not shown) were also determined for the values of insitu fibre volume associated with the sprayed specimens. These curves were used to predict the aggregate bridging stress-block by applying them directly to the crack-width profiles, determined from the strain/crack-width profiles. By using this approach, the boundary between the aggregate bridging zone (modelled using a stress versus crack-width relationship) and the fibre bridging zone (modelled using a fibre pull-out load versus crack-width relationship) was assumed to occur at a crack-width of 0.05mm.

Fibre bridging zone

The fibre bridging forces were predicted by relating the probabilistic fibre pull-out curve to the crack-width profile at each mid-span deflection, and then combining the resulting single fibre pull-out loads with the fibre distribution data obtained from the manual fibre counting analysis (Section 6.7).

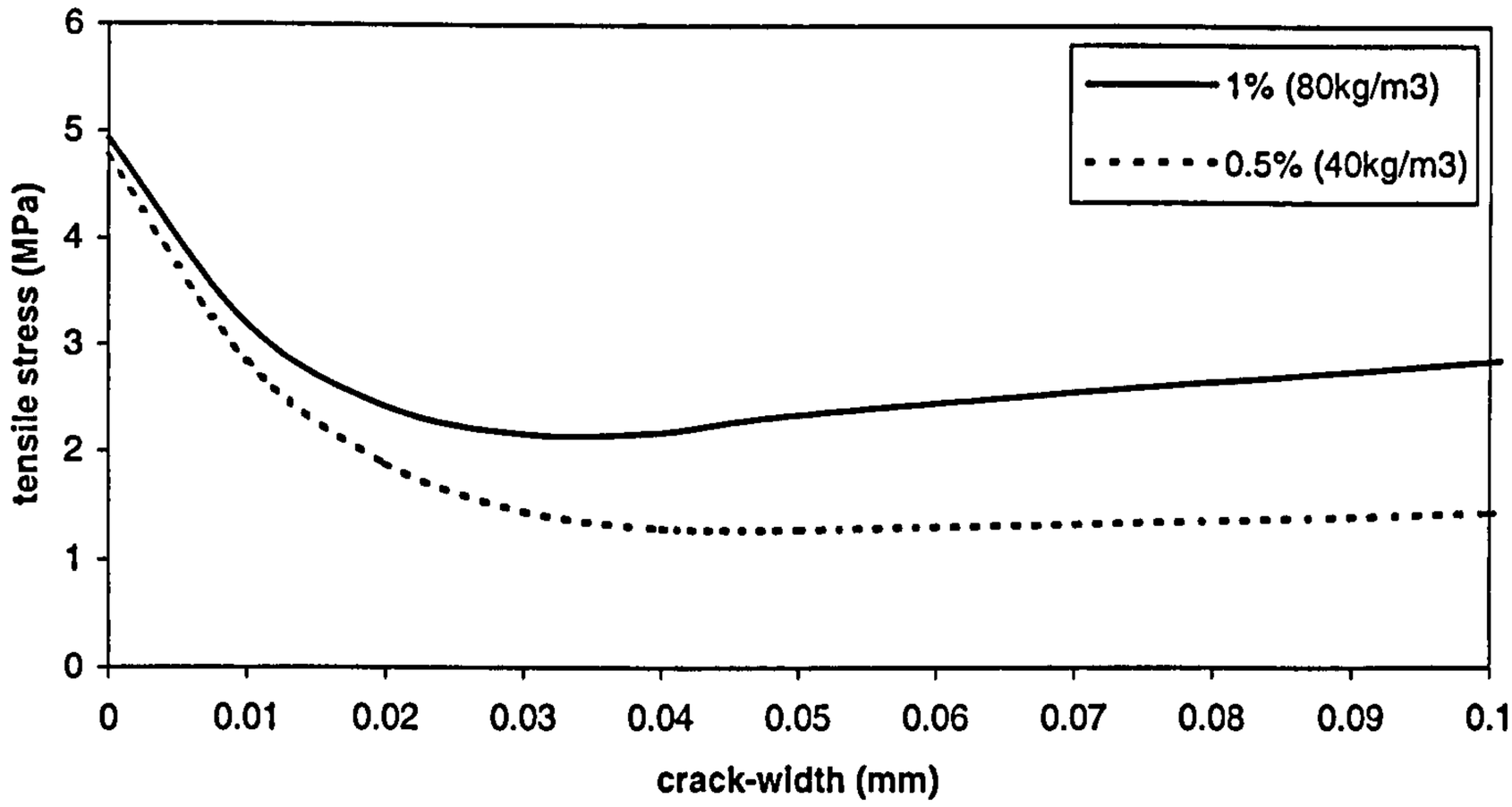

Figure 7.5 Tensile stress versus crack-width (σ–*w*) curves used in the model.

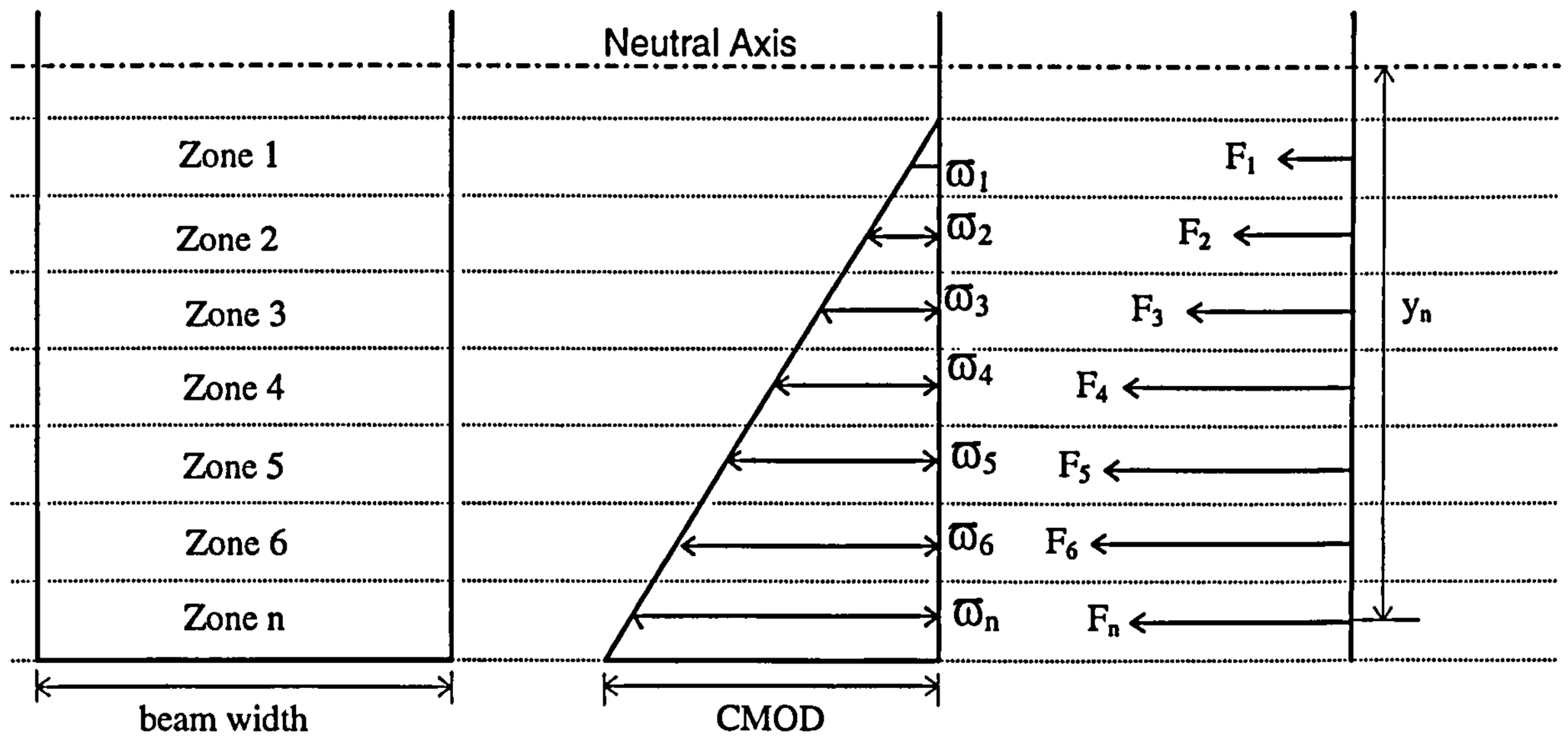

(a) Fibre zones. **(b) Crack-widths.** **(c) Probabilistic fibre pull-out forces.**

Figure 7.6 Schematic illustration of the average crack-widths (ϖ_n) and the total fibre pull-out forces (F_n) associated with each fibre zone across a crack.

The cracked section was first divided into 10mm thick layers, termed *fibre zones* (Figure 7.6(a)), corresponding to the fibre counting zones used in the manual fibre counting analysis. The average crack-widths ϖ_n (measured at the mid-point) of each fibre zone were determined by superimposing the crack-width profile onto the fibre zone layout (Figure 7.6(b)). The single fibre pull-out force P_n associated with each

fibre zone could then be determined by relating the probabilistic fibre pull-out curve to each value of ϖ_n (Figure 7.6(c)).

The total fibre pull-out force F_n transferred across the crack by each fibre zone was determined by multiplying the values of P_n by the total number of fibres occurring in each fibre zone:

$$F_n = P_n .(N_f)_n . b \qquad \text{equation 7.4}$$

where $(N_f)_n$ is the fibre density (measured as fibres/cm^2) associated with each fibre zone and b is the width of the beam.

Thus, the moment generated by each fibre zone M_n was determined as

$$M_n = F_n . y_n \qquad \text{equation 7.5}$$

where y_n is the lever arm measured from the neutral axis to the mid-point of each fibre zone.

When modelling the actual load-deflection responses for the strain analysis test beams, the values of $(N_f)_n$ were determined from the actual fibre densities (fibres/cm^2) measured across the cracked section of each specimen as summarised in Table 7.7.

When modelling the generalised load-deflection responses, the values of $(N_f)_n$ were determined from the average fibre densities (fibres/cm^2) measured across the cracked section of the flexural toughness test specimens as summarised in Table 7.8.

Traction free zone

Theoretically, the boundary between the traction free zone and the fibre bridging zone occurs at a crack-width of 15mm (that is, a crack-width corresponding to half the length of a 30mm long fibre). It is only then that all the fibres will have been completely pulled-out, and no force will be transferred across the cracked section. However, the crack-widths associated with the test beams investigated here never exceeded 5mm, and so the traction free zone did not develop. Therefore it does not appear in the modelling analysis.

Fibre zone	Depth to midpoint of zone (mm)	fibre densities per cm2				
		SA1-1	SA1-2	SA2-1	SA2-2	SA5-1
1	10	1.1	0.6	1.3	0.5	1.1
2	20	0.7	0.6	0.5	1.1	0.7
3	30	0.6	0.7	0.7	1.1	0.7
4	40	0.9	1.0	1.7	1.0	1.0
5	50	1.1	0.9	1.1	0.8	1.0
6	60	1.0	1.5	1.0	1.1	1.0
7	70	1.2	1.5	1.6	2.0	0.8

(a) 75mm deep beams.

Fibre zone	Depth to midpoint of zone (mm)	fibre densities per cm2		
		SA7-1	SA9-1	SA9-2
1	5	1.2	1.4	3.6
2	15	2.2	0.6	1.4
3	25	1.2	1.3	3.4
4	35	0.9	2.0	3.3
5	45	2.0	1.4	1.8

(b) 50mm deep beams.

Fibre zone	Depth to midpoint of zone (mm)	fibre densities per cm2	
		SA8-2	SA10-3
1	5	1.2	1.6
2	15	1.6	2.1
3	25	1.1	1.8
4	35	0.7	1.6
5	45	1.2	0.7
6	55	0.6	2.4
7	65	0.9	2.0
8	75	0.9	2.4
9	85	1.5	2.2
10	95	0.8	2.8

(c) 100mm deep beams.

Table 7.7 Actual fibre densities used in the modelling analysis.

7.2.6 Summary

A summary of the modelling philosophy indicating the demarcations and the main modelling parameters associated with each stress zone is given in Figure 7.7. Table 7.9 gives a summary of the sources of data used in the implementation of the model.

		fibre densities per cm2											
		CAST				CAST				SPRAYED			
		75mm (unnotched)				75mm (notched)				75mm (unnotched)			
		0.5% fibres by vol.		1.0% fibres by vol.		0.5% fibres by vol.		1.0% fibres by vol.		0.34% fibres by vol.		0.87% fibres by vol.	
Fibre zone	Depth to midpoint of zone (mm)	mean	stan. dev.	mean	stan. dev.	mean	stan. dev.	mean	stan. dev.	mean	stan. dev.	mean	stan. dev.
1	2.5	1.8	0.6	2.9	1.2	1.7	1.3	2.5	1.2	1.0	0.0	3.3	1.6
2	10	1.3	0.3	2.0	0.8	1.6	0.4	2.0	0.6	0.8	0.6	1.9	0.7
3	20	1.2	0.4	1.9	0.6	1.4	0.4	2.3	0.8	0.9	0.3	2.1	1.0
4	30	1.3	0.6	2.3	0.4	1.3	0.5	2.4	0.7	0.9	0.3	2.4	0.4
5	40	1.4	0.3	2.5	0.6	1.4	0.3	2.3	0.5	1.0	0.1	2.6	0.4
6	50	1.2	0.3	2.9	0.4	1.7	0.5	2.2	0.5	1.0	0.1	2.1	0.6
7	60	1.3	0.3	2.5	0.6	1.3	0.5	2.3	0.6	0.8	0.4	2.1	0.2
8	70	1.2	0.5	2.4	0.5	2.1	0.5	2.0	0.6	0.6	0.4	1.4	0.8

(a) 75mm unnotched and 85mm notched beams.

fibre densities per cm2					
		50mm (unnotched)			
		0.5% fibres by vol.		1.0% fibres by vol.	
Fibre zone	Depth to midpoint of zone (mm)	mean	stan. dev.	mean	stan. dev.
1	5	1.3	0.1	3.8	0.3
2	15	1.4	1.1	1.8	0.5
3	25	1.3	0.1	2.9	0.8
4	35	1.5	0.8	2.3	1.5
5	45	1.7	0.4	2.6	1.1

(b) 50mm deep beams.

fibre densities per cm2					
		CAST			
		100mm (unnotched)			
		0.5% fibres by vol.		1.0% fibres by vol.	
Fibre zone	Depth to midpoint of zone (mm)	mean	stan. dev.	mean	stan. dev.
1	5	1.1	0.1	1.9	0.4
2	15	1.2	0.6	2.1	0.0
3	25	1.0	0.1	1.5	0.5
4	35	0.6	0.1	1.7	0.1
5	45	0.8	0.6	1.2	0.7
6	55	0.8	0.2	2.3	0.2
7	65	1.1	0.2	1.8	0.4
8	75	1.6	0.9	2.6	0.2
9	85	1.5	0.0	2.3	0.1
10	95	1.1	0.4	2.5	0.5

(c) 100mm deep beams

Table 7.8 Average fibre densities used in generalised modelling analysis.

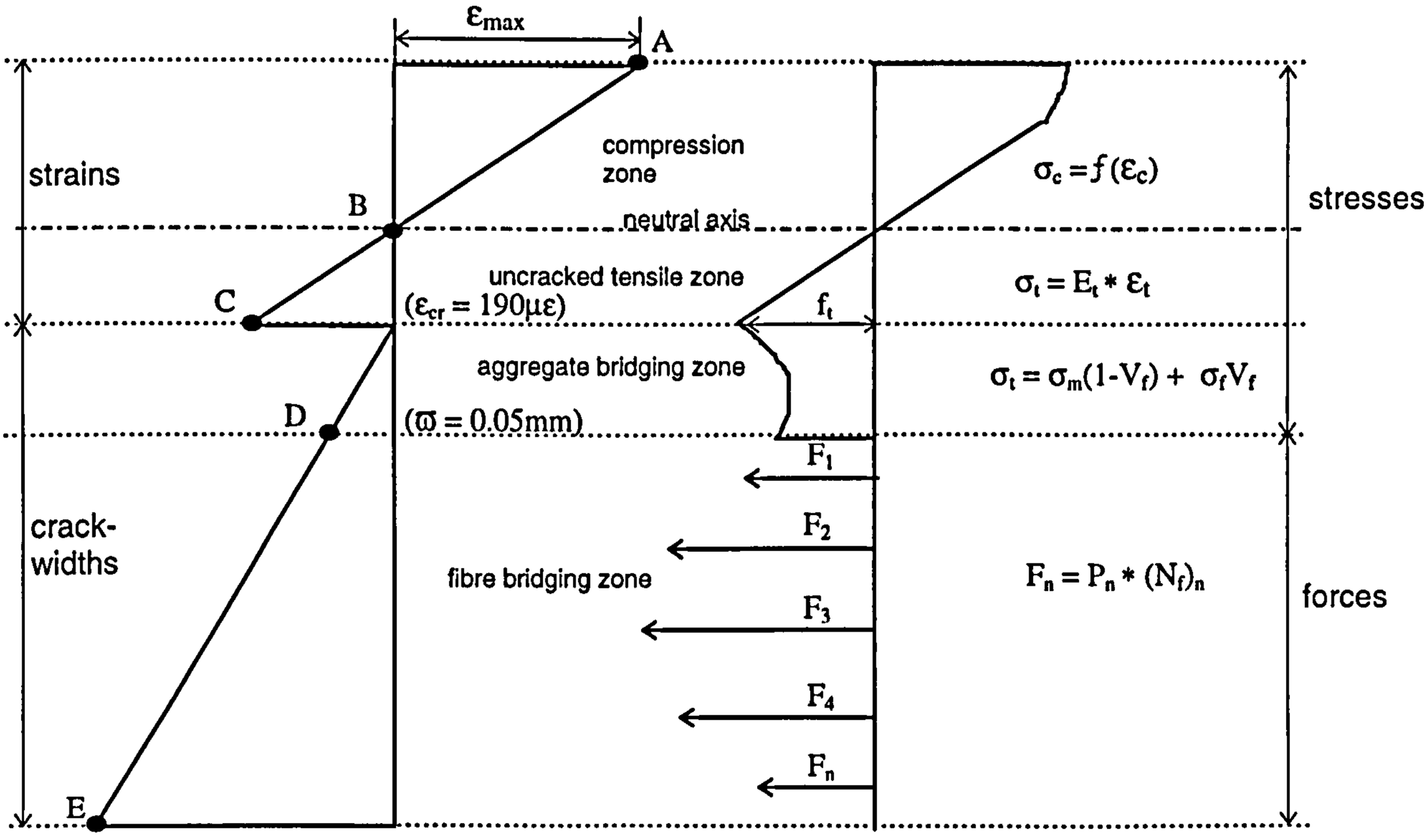

(a) strain/crack-width profile. **(b) stress block.**

Figure 7.7 Summary of the modelling philosophy.

	SOURCE OF MODEL DATA	
Model parameters	individual beam analysis	generalised beam analysis
strain/crack-width profile	Table 7.1	Table 7.2
compressive stress/strain	Figure 6.23 & 7.1	Figure 6.23 & 7.1
tensile stress/strain	Figure 7.2	Figure 7.2
tensile stress/crack-width	Figure 7.5	Figure 7.5
probabilistic fibre pull-out curve	Figure 7.3	Figure 7.3
fibre distribution across crack	Table 7.7	Table 7.8

Table 7.9 Summary of the sources of data used in model.

7.3 IMPLEMENTATION OF MODEL

7.3.1 General

The model was implemented by setting up a computer generated spreadsheet for each beam analysed. This spreadsheet consisted of 8 worksheets as follows:

DATASHEET (sheet 1) - containing general input data for the model including: beam dimensions, fibre content, maximum compressive strain versus mid-span deflection relationship; CMOD versus mid-span deflection relationship; compressive modulus value, compressive stress reduction factor, compressive stress versus strain relationship (compression zone); tensile stress versus strain relationship (uncracked tensile zone); tensile stress versus crack-width relationship (aggregate bridging zone); the probabilistic fibre pull-out load versus crack-width relationship (fibre bridging zone); and the fibre densities occurring across the cracked section.

ANALYSIS (sheets 2-8) - containing the calculation of the predicted flexural load at each mid-span deflection (0.05, 0.1, 0.2, 0.5, 1.0, 2.0 and 4.0mm respectively) using the input data from the datasheet.

Table 7.10 shows a typical analysis worksheet used in the implementation of the model. A description of the data shown under each column is described below.

Column (a) - The model analysis is based on establishing five principal points, associated with the strain/crack-width profile, which provide the boundaries between the different stress zones (Figure 7.7):

A - maximum compressive strain

B - neutral axis

C - zero crack-width (corresponding to the matrix cracking strain)

D - zero matrix tensile stress

E - crack mouth opening displacement

beam deflection 0.5mm

	gradient	constant
strain block	156.3	-985
crack width	0.0037	

a	b	c	d	e	f	g	h	i	j	k	l	m	n	o
principal points	distance from comp. face/mm	strain/ micro strain	crack-width/ mm	stress/ N/mm2	prob. pull-out load /N	section	cross-section area / cm2	mid-point of section from comp. face /mm	lever arm /mm	av.stress of section/ N/mm2	av. pull-out load of section/ N	fibre density per fibre zone /cm2	total force per section/ kN	moment per section/ kNm
A	0.00	-985	0	23.82										
						C	6.30	2.10	0.00	11.91			-7.51	0.0000
B	6.30	0	0	0.00		NA		6.30						
						T1	1.22	7.11	5.01	2.38			0.29	0.0014
C	7.52	190	0	4.76										
						T2	2.70	8.87	6.77	3.80			1.03	0.0069
	10.22		0.01	2.84										
						T3	2.70	11.57	9.47	2.36			0.64	0.0060
	12.92		0.02	1.88										
						T4	2.70	14.27	12.17	1.66			0.45	0.0054
	15.62		0.03	1.44										
						T5	2.70	16.97	14.86	1.36			0.37	0.0055
	18.31		0.04	1.28										
						T6	2.70	19.66	17.56	1.28			0.34	0.0061
D	21.01		0.05	1.27	41.67									
						2	3.99	23.01	20.91		43.73	1.22	0.21	0.0044
	25		0.06		45.79									
						3	10	30	27.90		50.89	1.33	0.68	0.0189
	35		0.10		55.99									
						4	10	40	37.90		59.66	1.39	0.83	0.0314
	45		0.14		63.34									
						5	10	50	47.90		67.01	1.22	0.82	0.0392
	55		0.18		70.69									
						6	10	60	57.90		73.72	1.28	0.94	0.0546
	65		0.21		76.75									
						7	10	70	67.90		78.59	1.17	0.92	0.0624
E	75		0.25		80.42									
												totals	0.01	0.2424
												predicted load=		3.23 kN

Table 7.10 Typical analysis worksheet used in model.

Notice that the aggregate bridging zone (between points C and D) is further divided into sub-sections to represent crack-widths between 0-0.05mm; and the fibre bridging zone (points D to E) is further divided into sub-sections to represent the fibre zones.

Column (b) - This column shows the positions of each principal point, and sub-section boundaries, relative to the compressive face of the beam. During the analysis the gradient of the strain profile is changed systematically until axial equilibrium is achieved (indicated by the total of the forces in column (n) equating to zero). Since the values of maximum compressive strain (Point A) and the value of crack-width at Point E are fixed, a change in the gradient of the strain profile causes a corresponding change in the position of the neutral axis (Points B), the zero crack-width (Point C) and the zero matrix tensile stress (Point D). Hence, Points B, C and D are termed 'floating-points' and Points A and E 'fixed points'.

Column (c) and (d) - These columns show the strain and crack-widths respectively, corresponding to the distances from the compressive face of the beam given in column (b).

Column (e) - This column shows the stress values corresponding to the strains and crack-widths given in column (c) and (d) respectively. The stress at Point A is determined from the appropriate compressive stress versus strain relationship (incorporating the compressive stress reduction factor), and the stresses between Points C and D are determined from the appropriate tensile stress versus crack-width relationship.

Column (f) - This column shows the probabilistic fibre pull-out loads, determined from the probabilistic fibre pull-out curve, corresponding to the crack-widths given in column (d).

Column (g) - This column gives the reference numbers for each element making-up the analysis.

Column (h) - This column shows the cross-sectional area of each element, determined by multiplying the element heights (determined from column (b)) by the width of the beam (obtained from the datasheet).

Column (i) - This column shows the distance from the centroid of each element to the compressive face of the beam. Except for the compressive and uncracked tensile stress

blocks, which were assumed to have shapes represented by either a triangle or parabola (see Section 7.2.3 and 7.2.4), the centroid of each element was assumed to occur at the mid-height of each element.

Column (j) - This column shows the lever arm of each element, determined as the distance between the centroid of each element to the centroid of the compressive stress-block.

Column (k) and (l) - These columns show the average stresses and average probabilistic fibre pull-out forces of each element, calculated from the values of stress and pull-out force at the boundaries of each element as given in column (e) and (f) respectively.

Column (m) - This column shows the values of fibre density occurring in each fibre zone (between Points D and E).

Column (n) - This column shows the total force transferred by each element. Between Points A and D, the element forces are obtained by multiplying the stresses in column (k) by the cross-sectional areas in column (h), and between Points D and E by multiplying the fibre pull-out forces in column (l) by the product of the fibre densities in column (m) and the cross-sectional areas in column (h). Note that compressive forces have a negative sign in the model.

Column (o) - This column shows the moment capacities of each element, obtained by multiply the element force in column (n) by the corresponding lever arm in column (j).

Finally, the flexural load capacity of the beam is calculated by summing all the element moment capacities in column (o), and converting the total moment into a load using equation 4.3.

7.3.2 Modelling procedure

The implementation of the model, using the spreadsheet described in Section 7.3.1, can be illustrated by the flow chart shown in Figure 7.8.

Stage 1 Specify the main parameters of the beam under investigation including: matrix strength; fibre type; fibre content; beam size; and beam geometry.

Stage 2 Specify the principal parameter relationships for the beam under investigation: maximum compressive strain versus mid-span deflection; CMOD

versus mid-span deflection; compressive stress versus strain; tensile stress versus strain; tensile stress versus crack-width; probabilistic fibre pull-out curve; fibre densities versus beam depth; and the value of Young's modulus.

Stage 3 Choose a mid-span deflection and determine the values of maximum compressive strain (ε_{max}) and CMOD from the appropriate relationships.

Stage 4 Guess a value for the gradient of the strain profile, and determine the positions of the principal points A to E relative to the compressive face of the beam. Note that some principal points (for example Points C, D and E) will only be present once the beam has cracked.

Stage 5 Determine the compressive stress block (and, hence, the resultant compressive force) by applying the compressive stress-strain relationship to the compressive strain block.

Stage 6 Determine the uncracked tensile stress block (and, hence, the resultant tensile force) by applying the tensile stress-strain relationship to the tensile strain block.

Stage 7 Determine the aggregate bridging stress block (and, hence, the resultant tensile force) by applying the tensile stress versus crack-width relationship to the crack-width profile.

Stage 8 Determine the total force in each 'fibre zone', by first applying the probabilistic fibre pull-out curve to the crack-width profile, and then multiplying the resulting forces by the number of fibres in each fibre zone.

Stage 9 Equate the equilibrium of forces (equation 4.1). If equilibrium is not satisfied, change the gradient of the strain profile and repeat stages 4 to 9 until it is satisfied.

Stage 10 Determine the lever arm of each force, relative to the neutral axis (or alternatively the centroid of the compressive stress block), and calculate the moment capacity of the section (equation 4.2). Hence, determine the flexural load capacity of the beam (equation 4.3).

Stage 11 Repeat stages 3 to 10 for a range of mid-span deflections.

Stage 12 Plot the predicted loads against the corresponding mid-span deflections, to obtain the flexural load-deflection response.

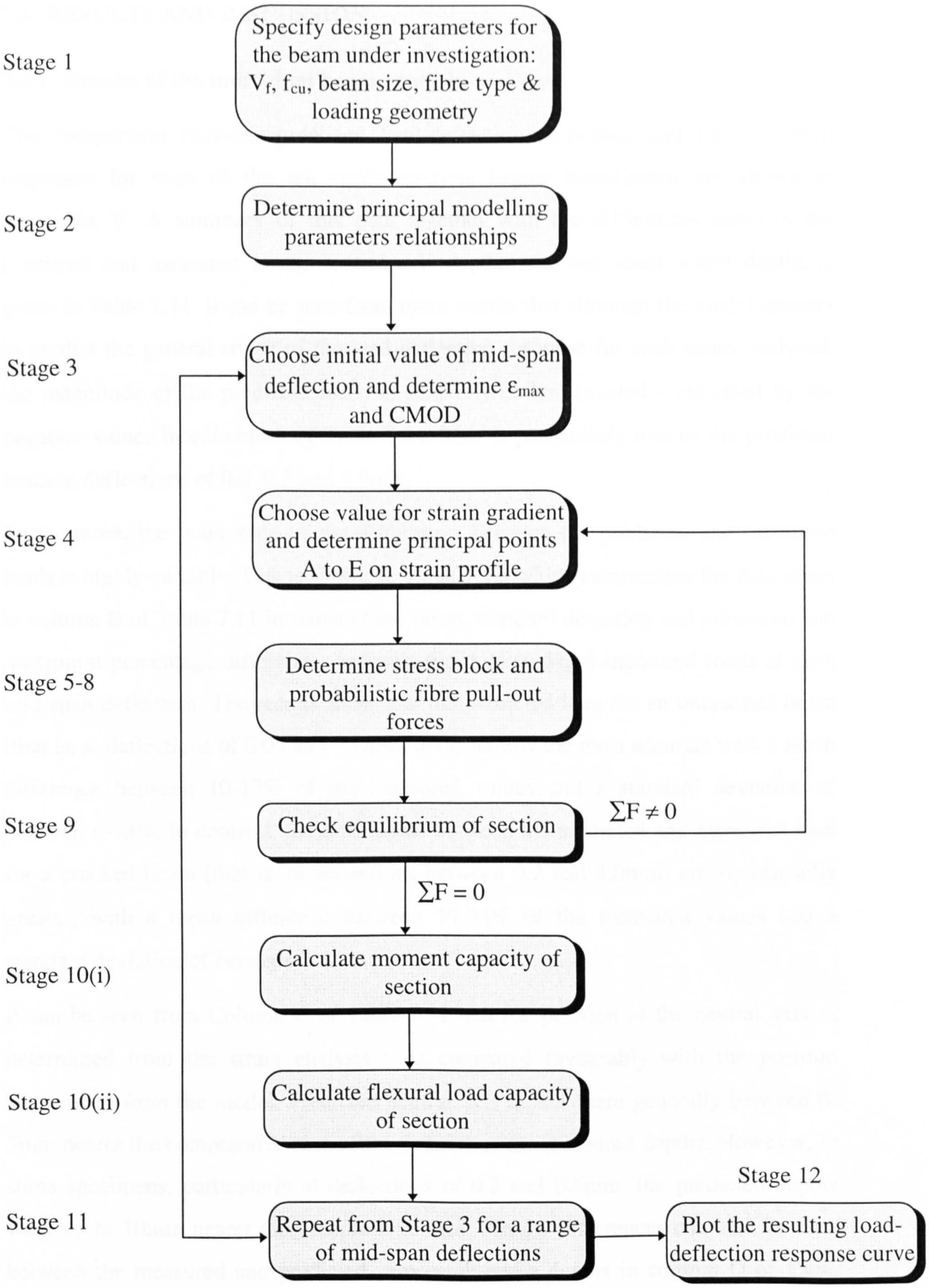

Figure 7.8 Flow chart showing modelling procedure.

7.4 RESULTS AND DISCUSSION

7.4.1 Results of the individual beam analysis

The comparison between predicted load-deflection responses and the measured responses for each of the ten strain analysis beams investigated are shown in Appendix V. A summary of this data together with the differences between the predicted and measured loads, neutral axis depths and zero crack-width depths is given in Table 7.11. It can be seen from these results that although the model appears to predict the general shape of the load-deflection response for each beam analysed, the magnitude of the predicted loads is generally underestimated - indicated by the negative values in column A of Table 7.11. This is particularly true of the predicted loads at deflections of 0.2, 0.5 and 1.0mm.

Furthermore, the magnitude of the differences between the predicted and measured loads is highly variable. This is shown in Table 7.12, which summarises the data given in column B of Table 7.11 in terms of the mean, standard deviation and minimum and maximum percentage differences between the predicted and measured loads at each mid-span deflection. The results show that the predicted load for an uncracked beam (that is, at deflections of 0.05 and 0.1mm) are generally the most accurate with a mean difference between 10-17% of the measured values and a standard deviation of between 6-13%. In contrast, the differences between the predicted and measured load for a cracked beam (that is, at deflections between 0.2 and 4.0mm) are significantly greater, with a mean difference between 19-34% of the measured values and a standard deviation of between 7-15%.

It can be seen from Column C of Table 7.11 that the position of the neutral axis as determined from the strain analysis tests compared favourably with the position determined from the model. Predicted neutral axis depths were generally between 0-5mm nearer the compressive face of the beam than the measured depths. However, in some specimens, particularly at deflections of 0.2 and 0.5mm, the predicted depths were up to 10mm nearer the compressive face. Similar differences can also be seen between the measured and predicted zero crack-width depths in column D of Table 7.11.

SPECIMEN REFERENCE					EXPERIMENTAL			PREDICTED			ERRORS (experimental v.predicted)			
											A	B	C	D
beam ref	depth (mm)	width (mm)	fibre content (kgm-3)	mid-span deflection (mm)	load (kN)	neutral axis depth (mm)	zero crack width depth (mm)	load (kN)	neutral axis depth (mm)	zero crack width depth (mm)	load (kN)	load (%)	neutral axis depth (mm)	zero crack width depth (mm)
CAST														
sa1-1	75	100	40	0.05	3.3	37.3	-	2.6	37.7	-	-0.7	21	0.4	-
				0.1	5.5	37.0	-	4.9	38.4	-	-0.6	12	1.3	-
				0.2	4.1	21.9	29.1	3.7	14.3	19.4	-0.5	11	-7.6	-9.7
				0.5	4.2	12.1	12.7	2.9	5.3	6.3	-1.2	29	-6.8	-6.4
				1	4.2	10.5	10.3	3.5	4.4	5.1	-0.6	15	-6.1	-5.2
				2	3.8	5.1	6.4	4.3	3.9	4.2	0.6	15	-1.3	-2.2
sa1-2	75	100	40	0.05	3.7	37.3	-	2.6	37.7	-	-1.1	30	0.4	-
				0.1	5.8	37.0	-	4.8	37.7	-	-1.1	18	0.7	-
				0.2	4.3	21.9	30.9	3.2	12.1	16.5	-1.1	26	-9.8	-14.4
				0.5	4.1	12.1	12.9	3.7	5.9	7.0	-0.4	10	-6.2	-5.9
				1	3.8	10.5	11.2	4.5	5.0	5.8	0.7	19	-5.5	-5.4
				2	3.4	5.1	5.6	4.8	4.0	4.4	1.4	42	-1.1	-1.2
sa8-2	100	100	40	0.05	7.7	45.1	-	5.5	50.3	-	-2.3	29	5.2	-
				0.1	10.1	43.9	-	10.7	50.2	-	0.5	5	6.3	-
				0.2	9.2	22.9	32.6	6.5	22.1	32.3	-2.8	30	-0.8	-0.3
				0.5	10.9	18.9	28.3	6.6	11.9	15.2	-4.3	39	-7.0	-13.1
				1	11.7	12.8	10.6	8.2	8.7	10.3	-3.5	30	-4.1	-0.3
				2	10.4	9.3	6.9	9.7	5.9	6.5	-0.7	6	-3.4	-0.4
				4	7.0	5.7	3.3	5.6	3.3	3.6	-1.4	20	-2.4	0.3
sa10-3	100	100	80	0.05	7.6	45.1	-	5.5	50.3	-	-2.1	28	5.2	-
				0.1	12.2	43.9	-	10.8	50.7	-	-1.4	12	6.8	-
				0.2	13.3	22.9	44.7	10.5	31.1	45.6	-2.8	21	8.2	0.9
				0.5	14.8	18.9	28.3	9.2	16.8	21.6	-5.6	38	-2.0	-6.7
				1	15.6	12.8	10.6	12.0	12.7	15.1	-3.6	23	-0.1	4.5
				2	12.7	9.3	6.9	15.2	9.7	10.6	2.5	20	0.4	3.7
				4	7.6	5.7	3.3	10.7	6.5	6.9	3.1	41	0.8	3.6
SPRAYED														
mix2-1	75	125	26	0.05	3.3	37.3	-	3.2	37.7	-	-0.1	3	0.4	-
				0.1	5.3	37.0	-	6.0	37.7	-	0.7	14	0.7	-
				0.2	6.7	21.9	42.8	3.4	11.7	15.9	-3.4	50	-10.2	-26.9
				0.5	5.3	12.1	23.4	3.3	4.9	5.8	-2.0	38	-7.2	-17.6
				1	4.9	10.5	9.1	4.0	4.2	4.8	-0.9	19	-6.3	-4.3
				2	3.5	5.1	4.6	4.9	3.6	4.0	1.4	41	-1.5	-0.6
				4	2.4	-	-	3.4	2.4	2.5	1.0	41	-	-

Table7.11(a) Summary of individual beam analysis: unnotched beams.

SPECIMEN REFERENCE					EXPERIMENTAL			PREDICTED			ERRORS (experimental v.predicted)			
beam ref	depth (mm)	width (mm)	fibre content (kgm-3)	mid-span deflection (mm)	load (kN)	neutral axis depth (mm)	zero crack width depth (mm)	load (kN)	neutral axis depth (mm)	zero crack width depth (mm)	A load (kN)	B load (%)	C neutral axis depth (mm)	D zero crack width depth (mm)
CAST														
sa2-1	75	100	40	0.05	4.4	41.7	-	4.2	42.7	-	-0.2	3	1.0	-
				0.1	6.6	38.5	-	6.8	36.7	-	0.2	3	-1.8	-
				0.2	5.5	21.9	30.2	5.7	18.6	25.3	0.1	3	-3.3	-4.9
				0.5	5.6	12.1	14.3	3.2	6.2	7.4	-2.4	43	-5.9	-6.9
				1	5.8	10.5	11.8	4.1	5.1	5.8	-1.6	28	-5.4	-6.0
				2	5.4	5.1	5.0	5.1	4.5	4.9	-0.2	5	-0.6	-0.1
sa2-2	75	100	40	0.05	4.5	41.7	-	4.2	42.7	-	-0.3	6	1.0	-
				0.1	6.7	38.5	-	6.8	36.7	-	0.0	0	-1.9	-
				0.2	5.1	21.9	28.3	3.7	13.9	19.0	-1.4	28	-8.0	-9.3
				0.5	5.3	12.1	14.2	3.4	6.2	7.4	-1.9	35	-5.9	-6.8
				1	5.6	10.5	8.4	4.4	5.3	6.0	-1.2	22	-5.2	-2.4
				2	5.5	5.1	5.0	5.4	4.5	5.0	-0.1	1	-0.6	0.0
sa7-1	50	100	40	0.05	1.5	23.5	-	1.0	25.1	-	-0.5	32	1.6	-
				0.1	2.5	22.7	-	2.0	25.1	-	-0.5	19	2.4	-
				0.2	3.1	18.9	43.8	2.2	18.3	30.7	-0.9	28	-0.6	-13.1
				0.5	2.9	9.3	22.1	1.6	6.3	8.0	-1.2	43	-3.0	-14.1
				1	3.1	4.4	5.6	2.0	4.4	5.1	-1.1	35	0.0	-0.5
				2	3.4	3.2	3.5	2.4	3.3	3.5	-1.0	29	0.1	0.0
				4	2.6	2.4	1.5	2.8	3.2	3.4	0.2	8	0.8	1.9
sa9-1	50	100	80	0.05	1.2	23.5	-	1.0	25.1	-	-0.2	18	1.6	-
				0.1	2.2	22.7	-	2.0	25.1	-	-0.2	8	2.4	-
				0.2	3.4	18.9	43.8	2.8	20.7	34.8	-0.6	18	1.8	-9.0
				0.5	3.8	9.3	22.1	2.3	8.6	11.0	-1.5	40	-0.7	-11.1
				1	4.3	4.4	5.6	2.8	5.9	6.8	-1.5	36	1.5	1.2
				2	4.7	3.2	3.5	3.5	4.4	4.9	-1.2	26	1.2	1.4
				4	3.8	2.4	1.5	4.3	4.7	5.0	0.5	14	2.3	3.5
sa9-2	50	100	80	0.05	1.0	23.5	-	1.0	25.1	-	0.0	2	1.6	-
				0.1	2.2	22.7	-	2.0	25.1	-	-0.2	11	2.4	-
				0.2	3.0	18.9	43.8	3.2	22.8	38.2	0.3	9	3.9	-5.6
				0.5	3.4	9.3	22.1	2.4	9.6	12.1	-1.0	29	0.3	-10.0
				1	3.6	4.4	5.6	2.8	6.3	7.4	-0.8	22	1.9	1.8
				2	3.5	3.2	3.5	3.7	4.9	5.3	0.1	4	1.7	1.8

Table 7.11(b) Summary of individual beam analysis: notched beams.

deflection (mm)	Percentage differences between measured and predicted loads (%)			
	mean	stand. dev.	min. value	max. value
0.05	17	13	2	32
0.1	10	6	0	19
0.2	22	13	3	50
0.5	34	10	10	43
1	25	7	15	36
2	19	15	1	42
4	25	15	8	41

Table 7.12 Summary of the individual beam analysis.

7.4.2 Results of the generalised beam analysis

The comparisons between the modelled load-deflection responses and the measured responses obtained from the flexural toughness tests are shown in Appendix VI. A summary of the predicted data, together with the values of neutral axis depth and zero crack-width depth are given in Table 7.13.

Notice that the measured responses shown in Appendix VI also include data from Matrix B. This data was included in these figures because the flexural load-deflection responses for Matrix C and B specimens were similar in shape and magnitude (see Table 6.8) and, therefore, by incorporating the Matrix B data a better representation of the variability associated with the flexural toughness tests was provided.

For the cast specimens, it can be seen from Appendix VI that the predicted responses generally fall within the limits of variation indicated by the measured responses, except at a deflection of between 0.5-1.0mm where the predicted loads are consistently underestimated. In contrast, the predicted responses for the sprayed specimens are not so good (Appendix VI - Figures 9 and 10). In particular, there appears to be a fundamental difference between the shapes of the predicted and measured responses.

SPECIMEN REFERENCE				FIBRE VOLUME					
				40 kg/m3			80 kg/m3		
beam ref	ligament depth (mm)	width (mm)	mid-span deflection (mm)	load (kN)	neutral axis depth (mm)	zero crack width depth (mm)	load (kN)	neutral axis depth (mm)	zero crack width depth (mm)
50&60C	50.0	100.0	0.05	1.0	25.1	-	1.0	25.1	-
			0.1	2.0	25.1	-	2.0	25.1	-
			0.2	2.2	18.2	30.6	2.9	21.5	36.0
			0.5	1.7	6.2	7.9	2.3	8.9	11.3
			1.0	2.0	4.3	4.9	2.8	6.1	7.1
			2.0	2.4	3.1	3.4	3.6	4.7	5.1
			4.0	2.8	3.1	3.3	4.4	4.7	5.1
75&85C	75.0	100.0	0.05	2.6	37.7	-	2.6	37.7	-
			0.1	4.8	37.7	-	4.8	37.7	-
			0.2	5.7	18.5	25.1	7.4	21.9	29.7
			0.5	3.2	6.3	7.5	6.0	10.0	12.0
			1.0	4.2	5.4	6.2	7.7	9.1	10.4
			2.0	5.2	4.8	5.3	9.8	8.4	9.2
			4.0	4.6	3.8	4.0	8.7	6.7	7.1
100C	100.0	100.0	0.05	5.5	50.3	-	5.5	50.3	-
			0.1	10.7	50.3	-	10.7	50.3	-
			0.2	7.8	26.0	38.1	10.6	31.3	45.7
			0.5	5.4	11.2	14.3	9.4	17.0	21.8
			1.0	6.9	7.6	9.0	12.4	12.9	15.2
			2.0	8.7	5.6	6.2	15.6	9.8	10.7
			4.0	6.1	3.8	4.0	11.3	6.8	7.3

(a) Cast beams.

SPECIMEN REFERENCE				IN-SITU FIBRE VOLUME					
				26 kg/m3			66 kg/m3		
beam ref	ligament depth (mm)	width (mm)	mid-span deflection (mm)	load (kN)	neutral axis depth (mm)	zero crack width depth (mm)	load (kN)	neutral axis depth (mm)	zero crack width depth (mm)
75S	75.0	125.0	0.05	3.3	37.7	-	3.3	37.7	-
			0.1	6.0	37.7	-	6.0	37.7	-
			0.2	6.3	17.3	23.5	8.7	21.1	28.6
			0.5	2.7	4.9	5.8	6.1	8.9	10.6
			1.0	3.4	4.0	4.5	8.0	8.0	9.2
			2.0	4.3	3.3	3.7	10.1	7.4	8.2
			4.0	3.9	2.7	2.8	9.4	6.2	6.5

(b) Sprayed beams.

Table 7.13 Summary of generalised modelling analysis.

Figure 7.9 compares the relationship between neutral axis depth and mid-span deflection for the predicted data given in Table 7.13 and the measured data given in Table 7.11. From the results two main trends can be observed:

- the shape and magnitude of the predicted neutral axis depths compare favourably with the measured data for all the beam sizes investigated; and
- the beams with lower fibre contents show greater shifts in the position of the neutral axis towards the compressive face for a given mid-span deflection.

The latter of these trends suggests that a higher fibre content restricts the rate of crack propagation over the depth of a beam depth, due to a greater number of fibres occurring across the crack, which has the effect of increasing the post-peak flexural response of a beam.

7.4.3 Discussion

Although the model appears to predict the general shape of the load-deflection responses for the range of beam sizes and fibre volumes investigated, the overall accuracy of the model is currently unacceptable for use in design. Therefore, this section discusses the results in terms of the parameters used in the model, in order to highlight where improvements could be made.

Figure 7.10 shows the individual contributions of the matrix and fibres in the tensile zone to the predicted flexural load capacity of a 75mm unnotched beam (calculated about the centroid of the compressive stress-block), for an increasing mid-span deflection. It can be seen that up to the first cracking point (approximately 0.15mm) the flexural capacity is dominated by the matrix stresses. However once the beam cracks the matrix contribution diminishes and the fibre contribution increases, so that at a deflection of approximately 0.5mm (equivalent to a CMOD of approximately 0.25 from the data given in Table 7.3 and 7.4) the flexural capacity is dominated by the fibre pull-out forces. In between, there appears to be a transition region between the first crack deflection and a deflection of 0.5mm, where the moment capacity is a function of by both the matrix stresses (provided by the uncracked tensile zone and the aggregate bridging zone) and the fibre pull-out forces (provided by the fibre bridging zone).

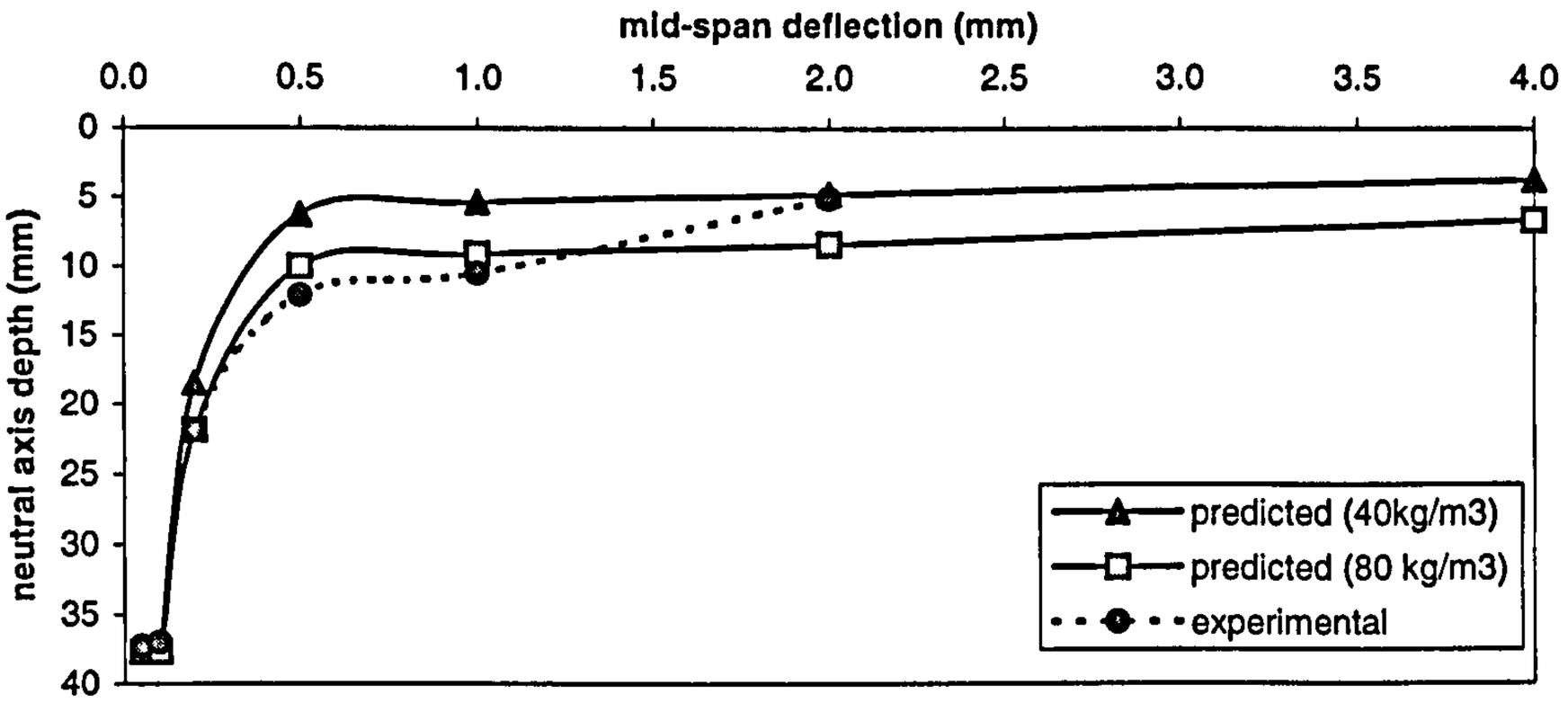

(a) 75mm unnotched and 85mm notched.

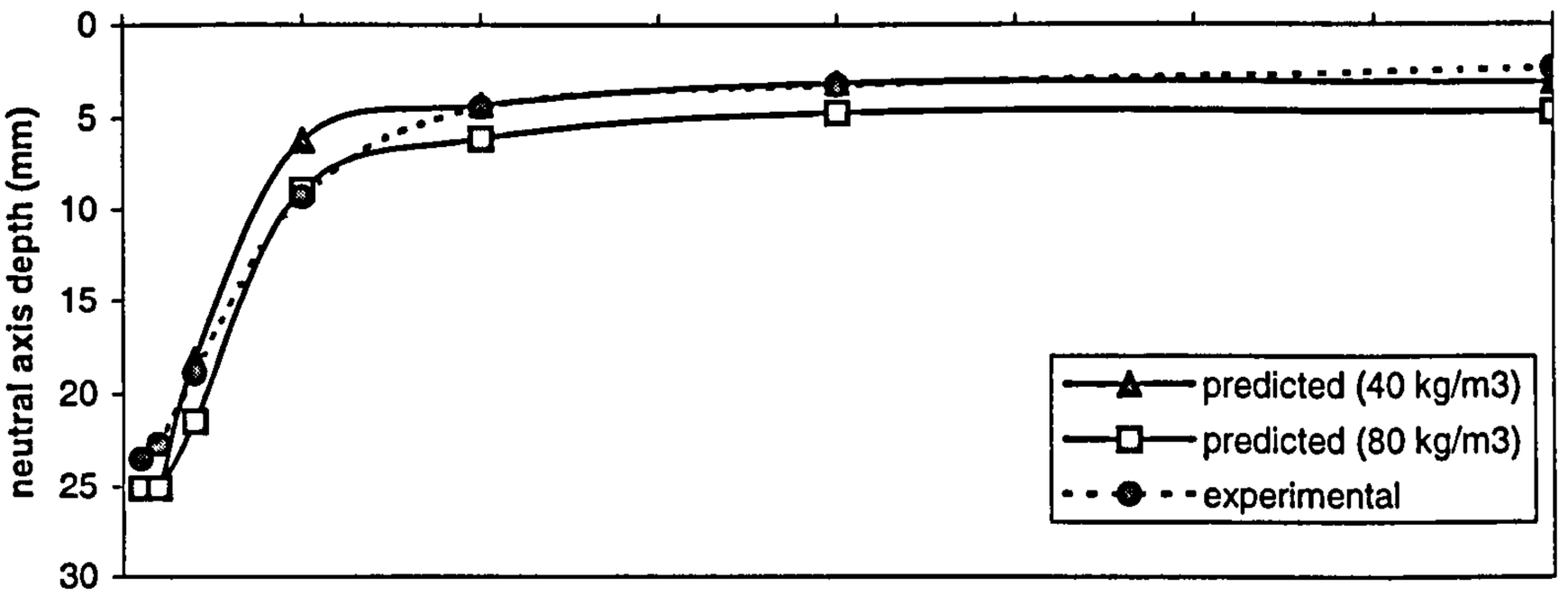

(b) 50mm unnotched and 60mm notched.

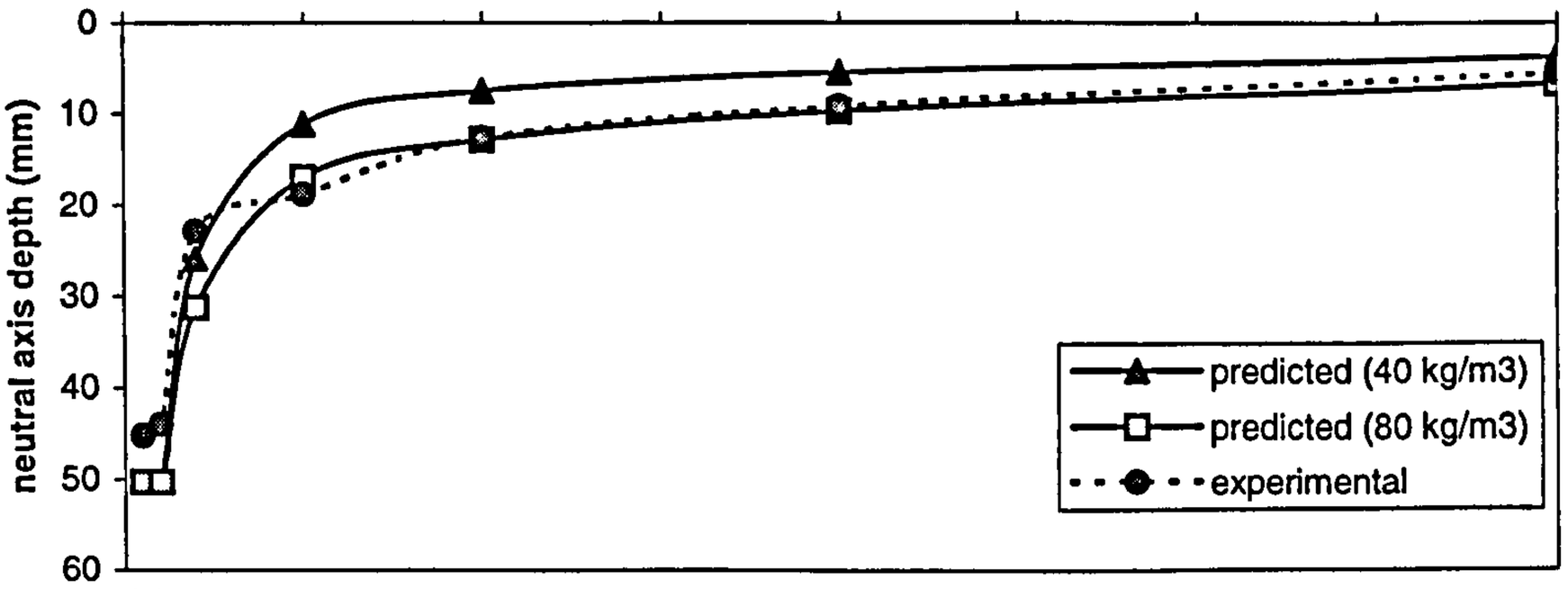

(c) 100mm unnotched.

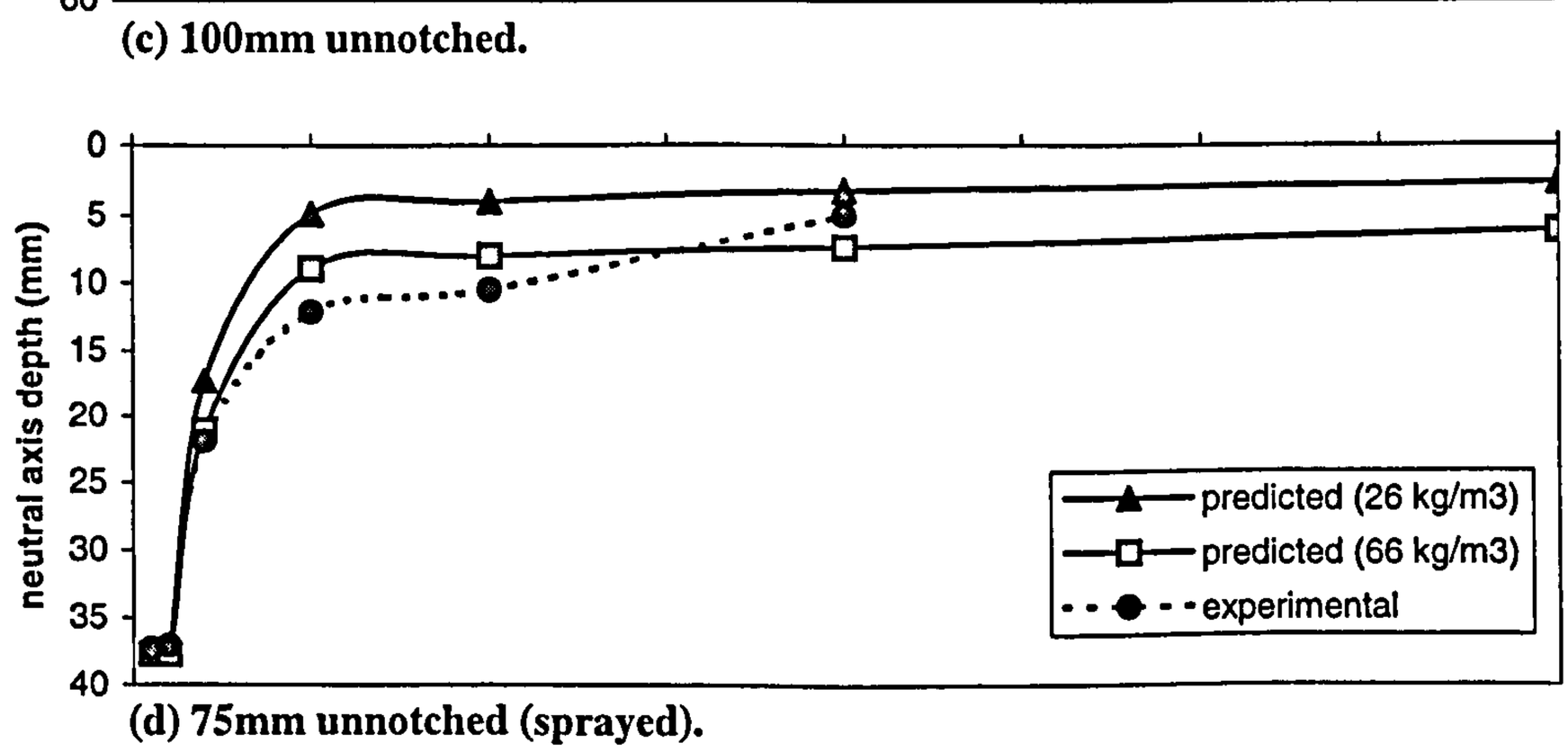

(d) 75mm unnotched (sprayed).

Figure 7.9 Comparison between predicted and measured neutral axis depths from the generalised modelling analysis.

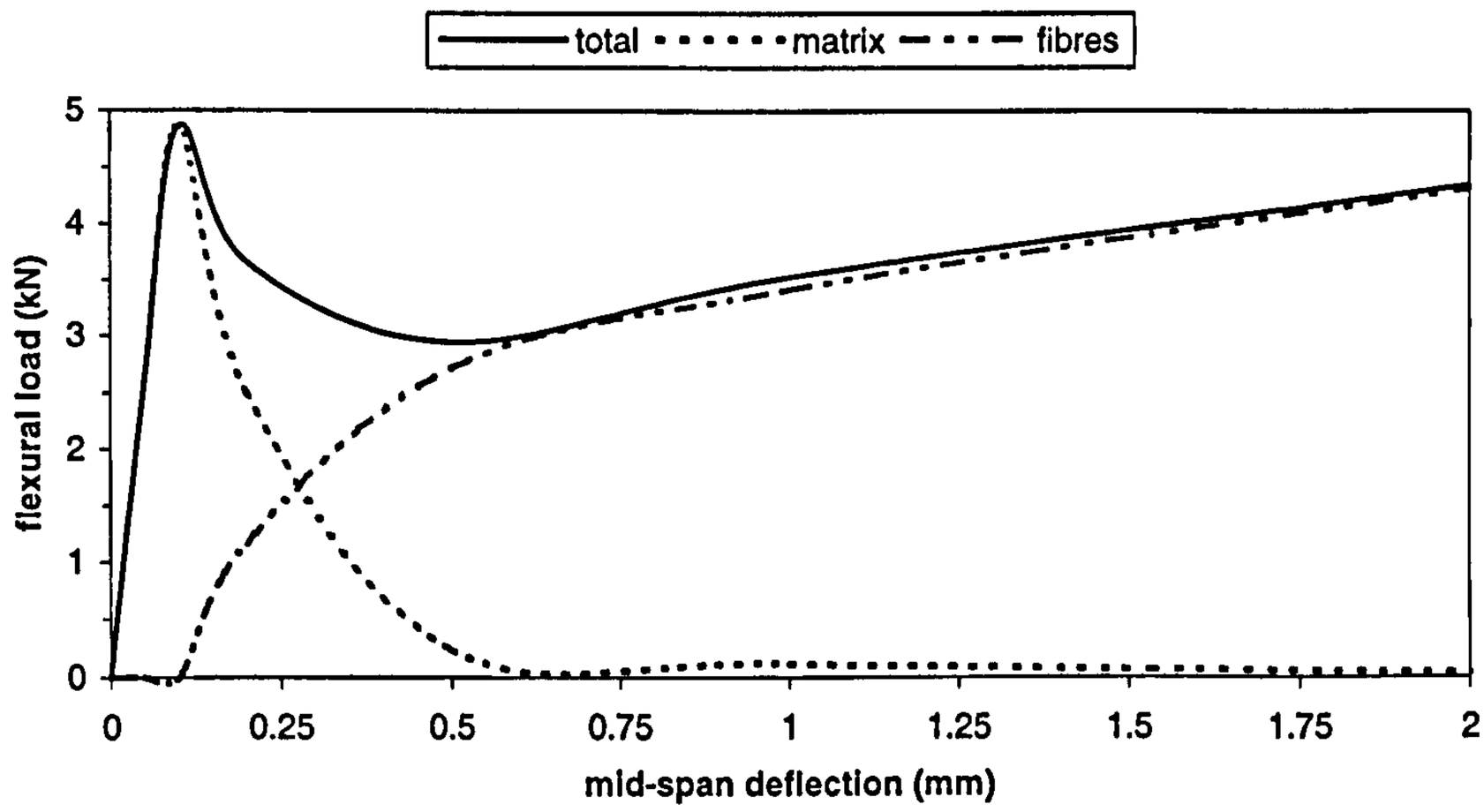

Figure 7.10 Contribution of the fibres and matrix to the total flexural capacity of a fibre reinforced concrete beam (SA1-1).

	mid-span deflection (mm)						
principal model parameter	0.05	0.1	0.2	0.5	1.0	2.0	4.0
strain profile	✔	✔	✔	✔	✔	✔	✔
crack-width profile			✔	✔	✔	✔	✔
compressive σ–ε	✔	✔	✔	✔	✔	✔	✔
uncracked tensile σ–ε	✔	✔					
cracked tensile σ–*w*			✔				
probabilistic fibre pull-out curve			✔	✔	✔	✔	✔
fibre numbers and distribution			✔	✔	✔	✔	✔

Table 7.14 Principal model parameters having the greatest influence on the load capacity at each mid-span deflection.

By using Figure 7.10, and the results from the modelling analysis, the principal model parameters which have the greatest influence on the load capacity at each deflection can be deduced. These are summarised in Table 7.14.

Given that the loads in the uncracked region of the load-deflection response (at deflections of 0.05 and 0.1mm) were generally predicted to within 10-17% of the their actual values, it appears that the uncracked compressive and tensile stress zones

modelled reasonably well by the experimental data. Thus, the strain profiles (which were shown to be within 15με of their theoretical values in Chapter 6) and the factored compressive stress-strain relationships appear to be appropriate for use in the model. Furthermore, because the number and distribution of the fibres were obtained by analysing the actual cracked section of the beams under investigation, it is unlikely that this data adversely affected the model predictions. Thus, the model deficiencies appear to be caused by either (or a combination) of the following: (i) the crack-width profiles; (ii) the tensile stress versus crack-width relationship (σ-*w* curve); and (iii) the probabilistic fibre pull-out curve.

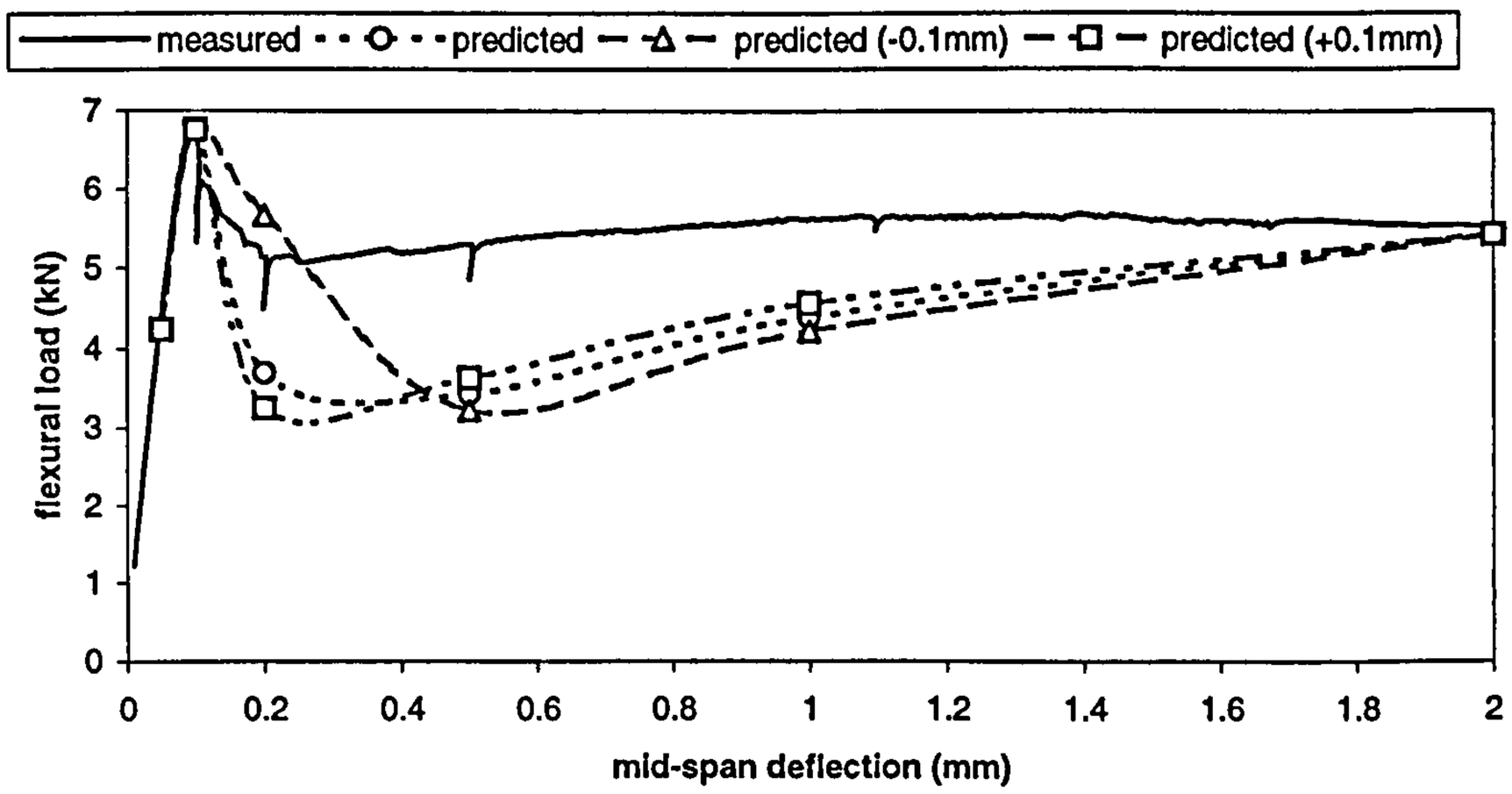

(a) 85mm notched beam (SA2-2).

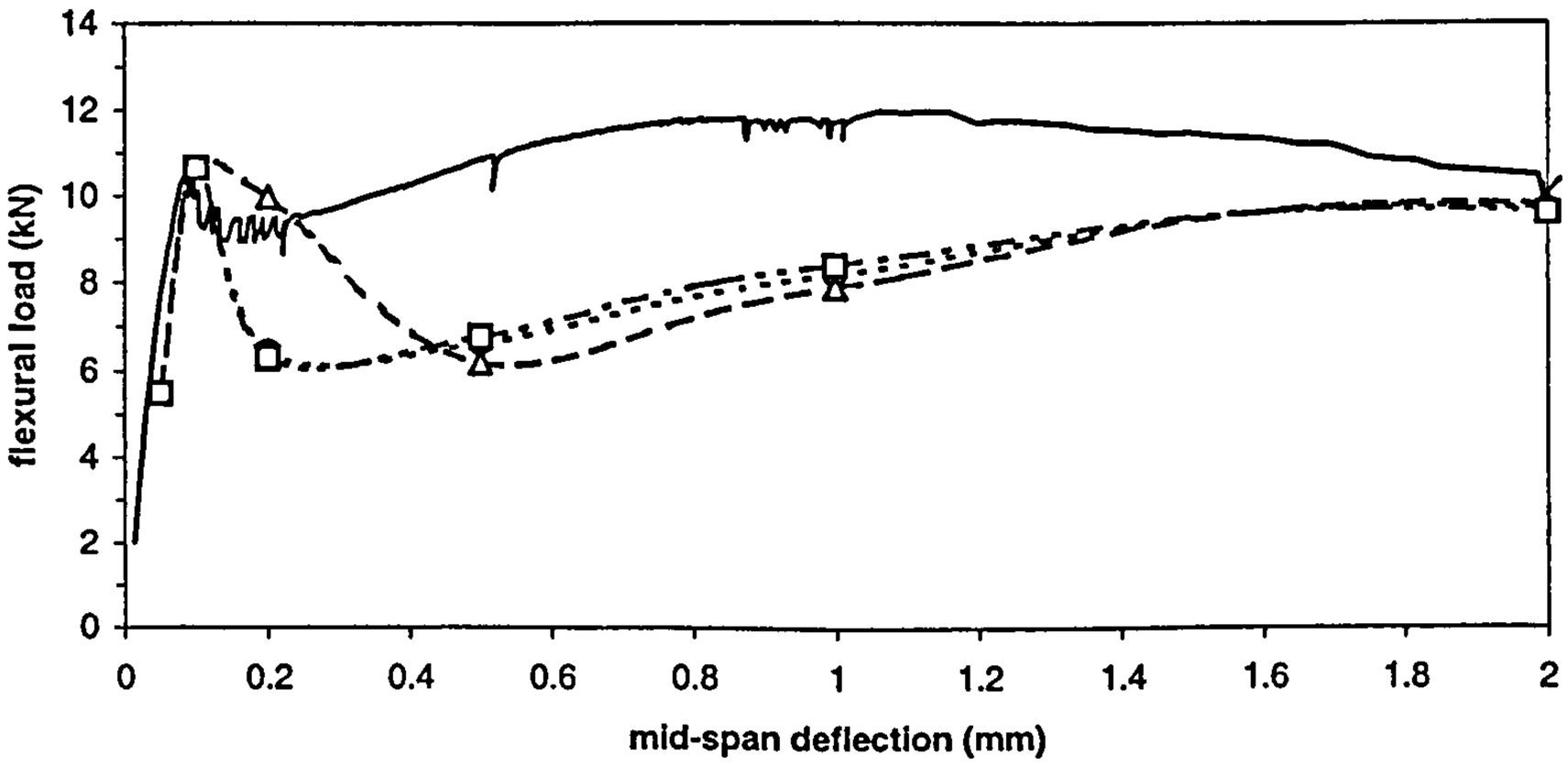

(b) 100mm unnotched beam (SA8-2).

Figure 7.11 Influence of changing the value of CMOD on the predicted load-deflection response.

In terms of the crack-width profiles, it was shown in Chapter 6 that the grid method was only suitable for measuring crack-widths greater than 0.2mm. As a result, the load predictions where the CMOD is less than 0.2mm (equivalent to a mid-span deflection of approximately 0.4mm) will generally be unreliable. This is illustrated in Figure 7.11, which shows the effect on the predicted responses of a 85mm deep notched beam and a 100mm deep unnotched beam caused by altering the measured CMOD values by an amount equivalent to the accuracy of the grid method (that is, by ±0.1mm). In both cases a reduction of 0.1mm in the CMOD at a deflection of 0.2mm significantly increases the value of the predicted loads, to an extent that they compare favourably with the measured loads. However more interestingly, an increase in CMOD by the same amount has virtually no effect. Similarly, there is virtually no effect on the predicted loads due to an increase or decrease in the measured CMOD at deflections greater than 0.2mm. Given that the measured CMOD values at a 0.2mm deflection were less than 0.2mm for all the beams analysed (see Table 7.3), it appears that the limitations of the grid method (in terms of its accuracy and sensitivity) is the main cause of the differences between the predicted and measured loads in the deflection range between 0-0.2mm. These findings show that the crack-width data obtained from the grid method tests is only suitable for use in the model when the value of CMOD is greater than 0.2mm, which for the beam sizes investigated correspond to mid-span deflections greater than 0.5mm.

Given that the CMOD values at deflections less than 0.5mm will generally be unreliable, the CMOD values at a 0.2mm deflection used in the generalised modelling analysis (shown in Table 7.4) were estimated by extrapolating the CMOD values between deflections of 0.5-4.0mm back to a deflection of 0.2mm. As a result, the predicted loads at the 0.2mm deflection generally compared well with the measured loads (Appendix VI). Given that the extrapolated CMOD values at the 0.2mm deflection ranged between 0.05-0.07mm, the moment capacity of the beams (taken about the centroid of the compressive stress-block) at this deflection will be dominated by the tensile stress versus crack-width relationship. Consequently, it appears that the tensile stress versus crack-width relationships (Figure 7.5) obtained from the law of mixtures are appropriate for use in the model.

From the foregoing discussions, it appears that the probabilistic fibre pull-out curve is causing the main discrepancies associated with the model predictions between mid-span deflections of 0.5-4.0mm. In particular, the results shown in Appendix VI indicate that the shape and magnitude of this curve may be inappropriate, as it generally underestimates the flexural loads at deflections of 0.5 and 1.0mm but overestimates the flexural loads at greater deflections.

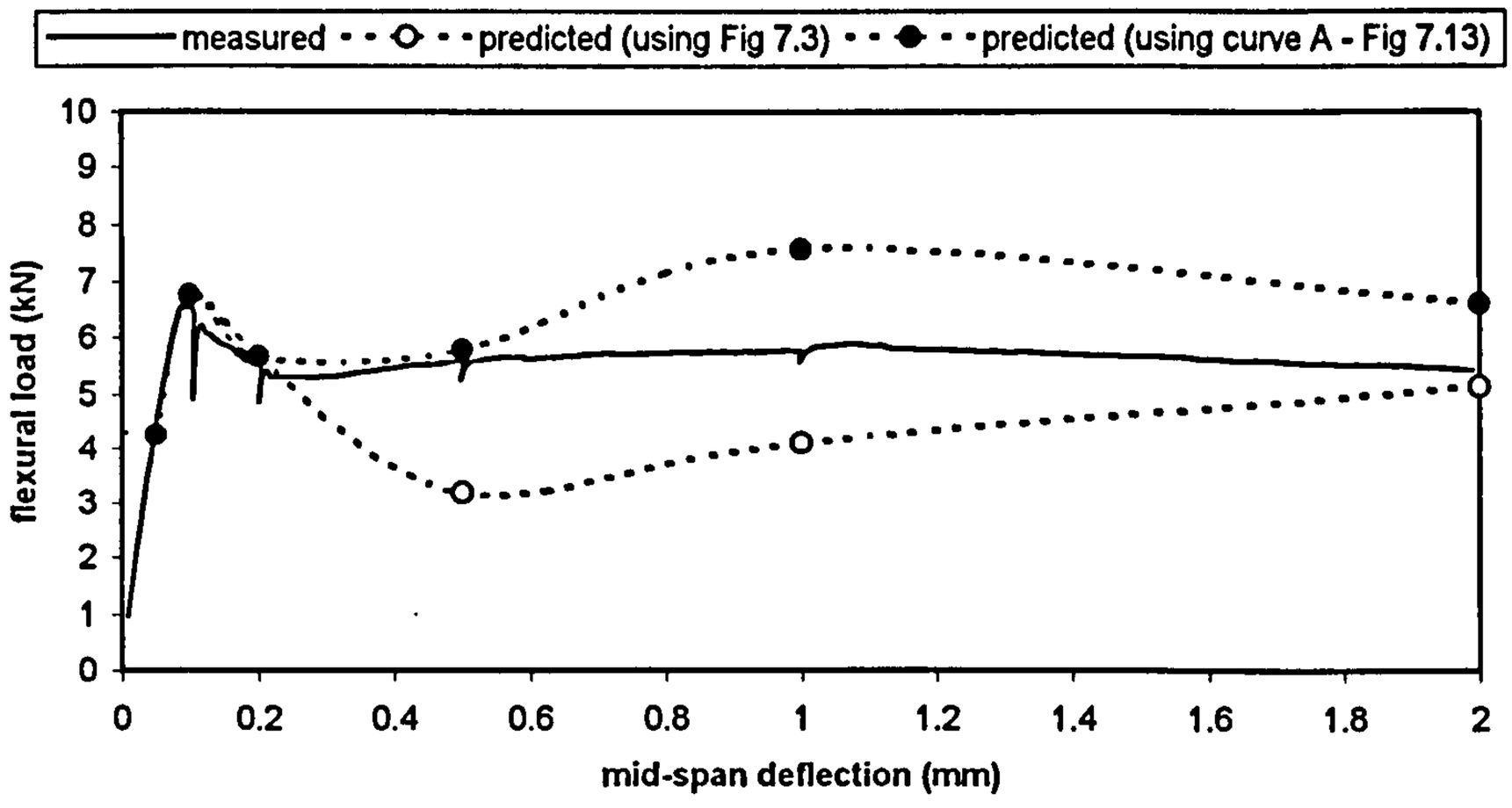

Figure 7.12 Influence of altering the shape of the probabilistic fibre pull-out curve to achieve an agreement between the predicted and measured load at a deflection of 0.5mm.

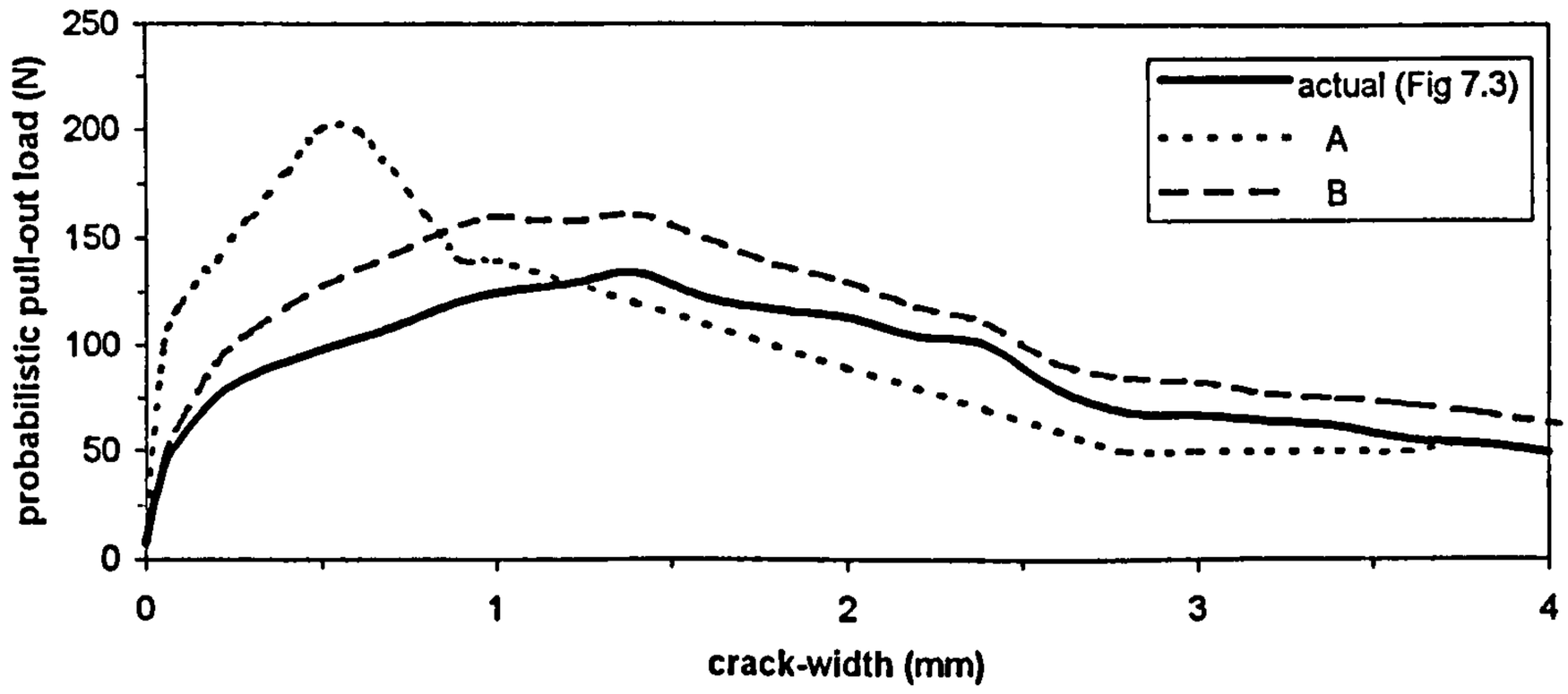

Figure 7.13 Shape and magnitude of different probabilistic fibre pull-out curves used in analysis of the predicted loads as shown in Figures 7.12 and 14.

In Section 7.2.5 it was shown that the probabilistic fibre pull-out curve is primarily a combination of two sets of experimental data: (i) the single fibre pull-out test results associated with different combinations of fibre embedment length and fibre orientation;

and (ii) the probability distributions associated with the fibre embedment lengths and fibre orientations occurring across a crack. Therefore, in an attempt to determine which set of data was causing the discrepancies a sub-analysis was undertaken in which the shape and magnitude of the probabilistic fibre pull-out curve was altered. The results of this analysis are discussed below.

Figure 7.12 shows the effect of altering the shape and magnitude of the probabilistic pull-out curve (as per curve A in Figure 7.13) to achieve an agreement between the predicted and measured loads at a deflection of 0.5mm. Notice from Figure 7.13, the significant increase in the fibre pull-out loads over the initial portion of the probabilistic pull-out curve (up to a crack-width of 0.5mm), when compared with the probabilistic pull-out curves shown in Figure 7.3. It appears, therefore, that the discrepancies associated with the model predictions may be due to the single fibre pull-out test data. In particular, the test seems to underestimate the fibre pull-out loads up to a crack-width of 1mm. This may be the result of the following factors associated with the single fibre pull-out tests:

i. the cross-head deflection control, used in the tests, which caused a sudden and unstable drop in pull-out load at the instant the specimen fractured;
ii. fundamental differences in the pull-out behaviour of single fibres in a uniaxial pull-out test, compared with the pull-out behaviour of a group of fibres subjected to a strain gradient across the cracked section of a beam; and
iii. the observed sideways movement between the two halves of the test specimens, particularly at orientations greater than 40 degrees, which delayed the full mobilisation of the fibres until a crack-width of approximately 2mm was reached (see Section 6.3). This movement appeared to be caused by the fibres crushing the matrix at the point at which the fibre entered the specimen. However in hindsight, if the test specimen could be laterally restrained then the extent of matrix crushing would be minimised, and the measured fibre pull-out load may increase more rapidly over the initial portion of the pull-out response curve.

Figure 7.14 shows the effect of weighting the fibre distribution probabilities towards fibre orientations between 0-30 degrees (as shown in Table 7.15). It can be seen from Figure 7.13 and 7.14, that these changes did not effect the general shape of the probabilistic fibre pull-out curve or the predicted load-deflection response, but they did

increase the relative magnitudes of both these curves. This result suggests that the model predictions are also strongly influenced by the fibre distribution probabilities used in the formulation of the probabilistic fibre pull-out curve.

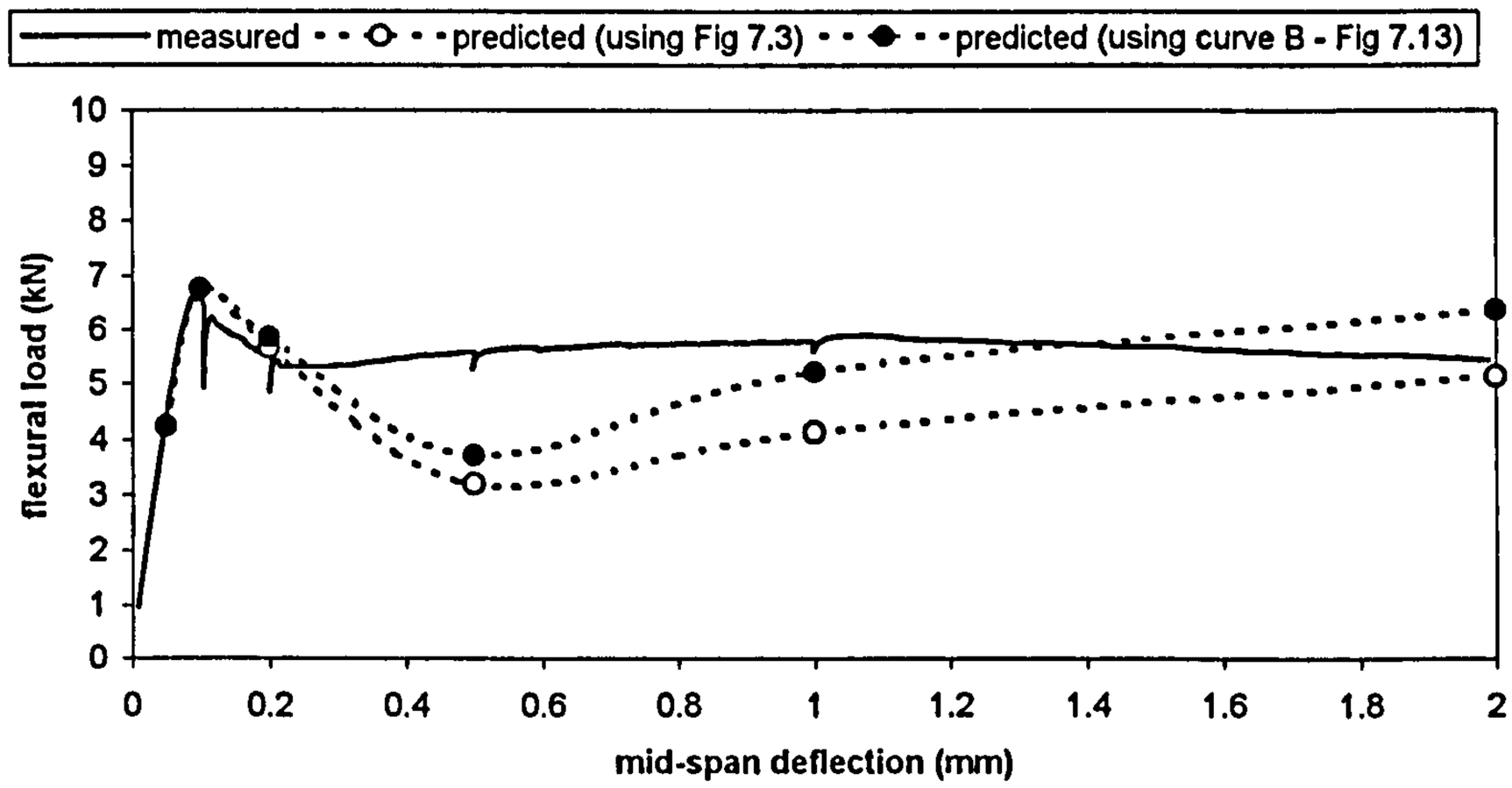

Figure 7.14 Influence of weighting the fibre distribution probabilities towards fibre orientations between 0-30 degrees.

fibre embedment lengths		fibre orientations	
range (mm)	probability	range (degrees)	probability
$0 \leq 4.5$	0.2	$0 \leq 10$	0.15
$4.5 \leq 11.5$	0.6	$10 \leq 20$	0.15
$11.5 \leq 15.0$	0.2	$20 \leq 30$	0.40
		$30 \leq 40$	0.15
		$40 \leq 50$	0.05
		$50 \leq 60$	0.05
		$60 \leq 90$	0.05

Table 7.15 Fibre distribution probabilities used in the determination of the probabilistic fibre pull-out curve B shown in Figure 7.13.

A further influence on the model predictions may also result from the generalised approach used in applying the probabilistic fibre pull-out curve to the fibre distribution data across the cracked section. This is because the accuracy of the model is dependent on how well the distribution of fibres in each fibre zone compares with the fibre distribution represented by the probabilistic fibre pull-out curve. In particular, the fibre distribution probabilities used in the determination of the probabilistic fibre pull-out curve were obtained from analysing over 600 individual fibres. However, in reality the number of fibres occurring in each fibre zone for a beam containing a fibre content of

between 40-80kg/m^3, varies between 10-30 fibres (Table 7.7 and 7.8). Consequently, the distribution of such a small sample of fibres, in terms of the individual values of fibre embedment length and orientation, will vary considerably between the fibre zones and, therefore, may not be representative of the fibre distribution associated with the probabilistic fibre pull-out curve. As a result, the probabilistic fibre pull-out curve may be over generalising the pull-out behaviour of the fibres across the cracked beam section. This problem might be overcome if the pull-out behaviour of each fibre could be individually modelled, although this would only be possible if the actual fibre embedment length and orientation of each fibre across the cracked section could be determined. In this respect, the X-ray analysis procedures described in Section 6.7 may provide the basis for such a measuring device.

7.5 TOWARDS A DESIGN RATIONALE FOR STEEL FIBRE REINFORCED CONCRETE IN FLEXURE

The results of the modelling analysis have shown the hypothesis stated in Chapter 4 to be correct in principal. It therefore appears that the flexural load-deflection response (and hence flexural toughness performance) of a given cast, or sprayed, steel fibre reinforced concrete beam can be predicted from conventional principles of mechanics if the stress-block diagram can first be determined for a given mid-span deflection.

In this thesis, the stress-block at each mid-span deflection was established using a limited range of experimental data. However, for the model to be of value as a design tool it must also allow the designer to predict the stress-block analytically using specified design criteria (for example: the matrix compressive strength; the type and size of fibre; the in-situ fibre content; the beam size; and the applied loading geometry). In order to achieve this, analytical expressions and/or design curves would need to be developed - using the design criteria as input values - to allow the designer to predict values for the principal model parameters (see Table 7.14), from which the stress-block could be predicted, for a given mid-span deflection.

In view of the above need, the following sections provide an initial attempt to develop analytical expressions and design curves for each principal parameter used in the model. In each case, the relationships have been determined from the experimental data

reported in Chapter 6 (and as summarised in Section 7.2). Note that the model already uses analytical expressions for the tensile stress-strain and tensile stress versus crack-width relationships, and so these parameters are omitted from the following discussion.

CMOD and maximum compressive strain

Figure 7.15 shows the relationship between maximum compressive strain (ε_{max}) and mid-span deflection (δ_m) for the three beam sizes investigated. It can be seen that the resulting relationship appears to be independent of beam size, and follows a simple power curve of the form:

$$\varepsilon_{max} = K_1 \delta_m^{3/4} \qquad \text{equation 7.6}$$

where K_1 is an empirical constant which equates approximately to 1.1×10^{-3} for the data presented here.

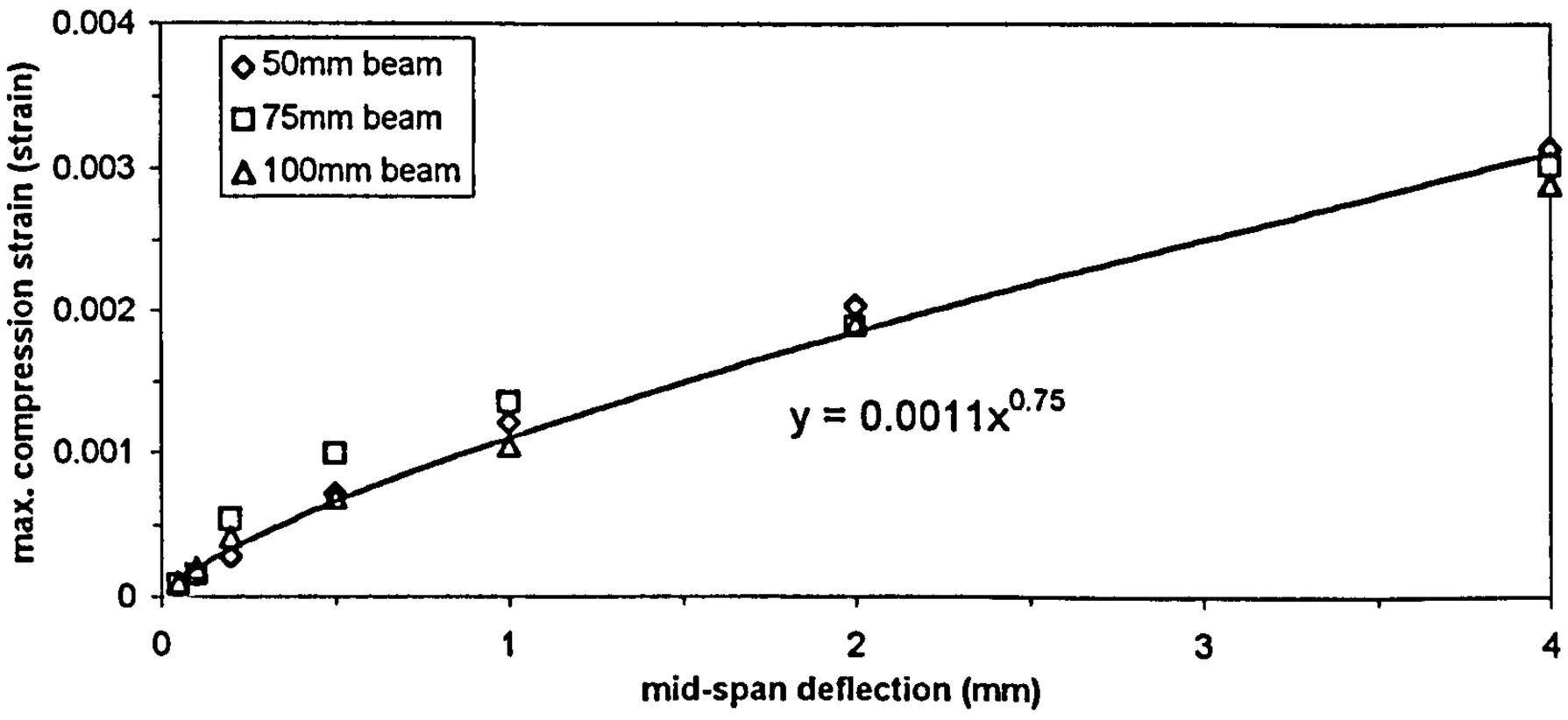

Figure 7.15 Relationship between maximum compressive strain and mid-span deflection (using the data presented in Table 7.4).

Figure 7.16 shows the relationship between crack-mouth-opening-displacement (*CMOD*) and mid-span deflection (δ_m) for the three beam sizes investigated. It can be seen that the resulting relationship appears to be linearly related to both mid-span deflection and beam depth (d), and follows the approximate expression:

$$CMOD \cong K_2 d \delta_m \qquad \text{equation 7.7}$$

where is K_2 is an empirical constant which equates approximately to 9.4×10^{-3} for the data presented here.

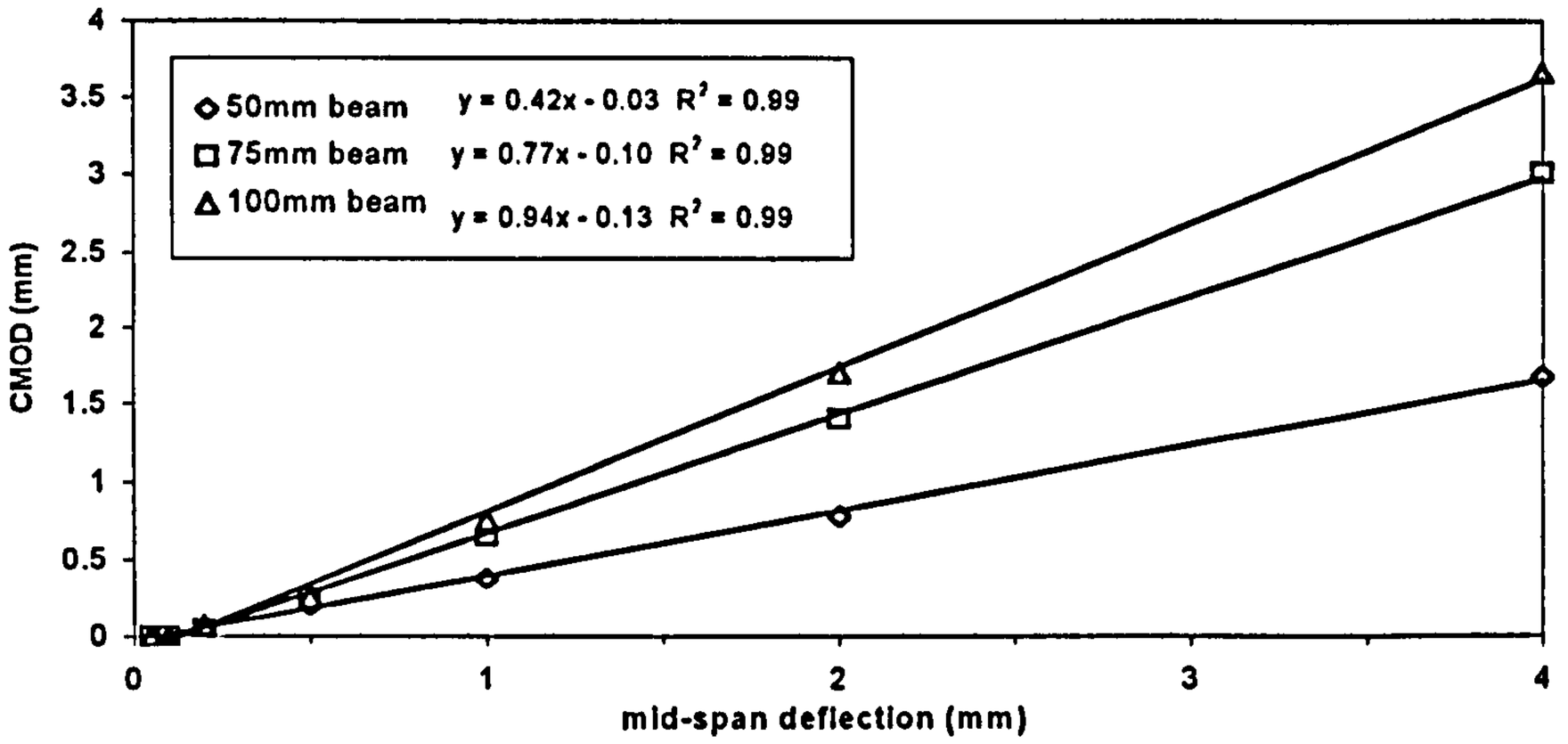

Figure 7.16 Relationship between CMOD and mid-span deflection (using the data presented in Table 7.4).

By combining Figure 7.15 with Figure 7.16 results in the set of curves shown in Figure 7.17 for the relationship between CMOD and maximum compressive strain, which from equations 7.7 and 7.6 is shown to follow a power curve of the form:

$$CMOD = (K_2 / K_1^{4/3})\, d\, \varepsilon_{max}^{4/3} \qquad \text{equation 7.8}$$

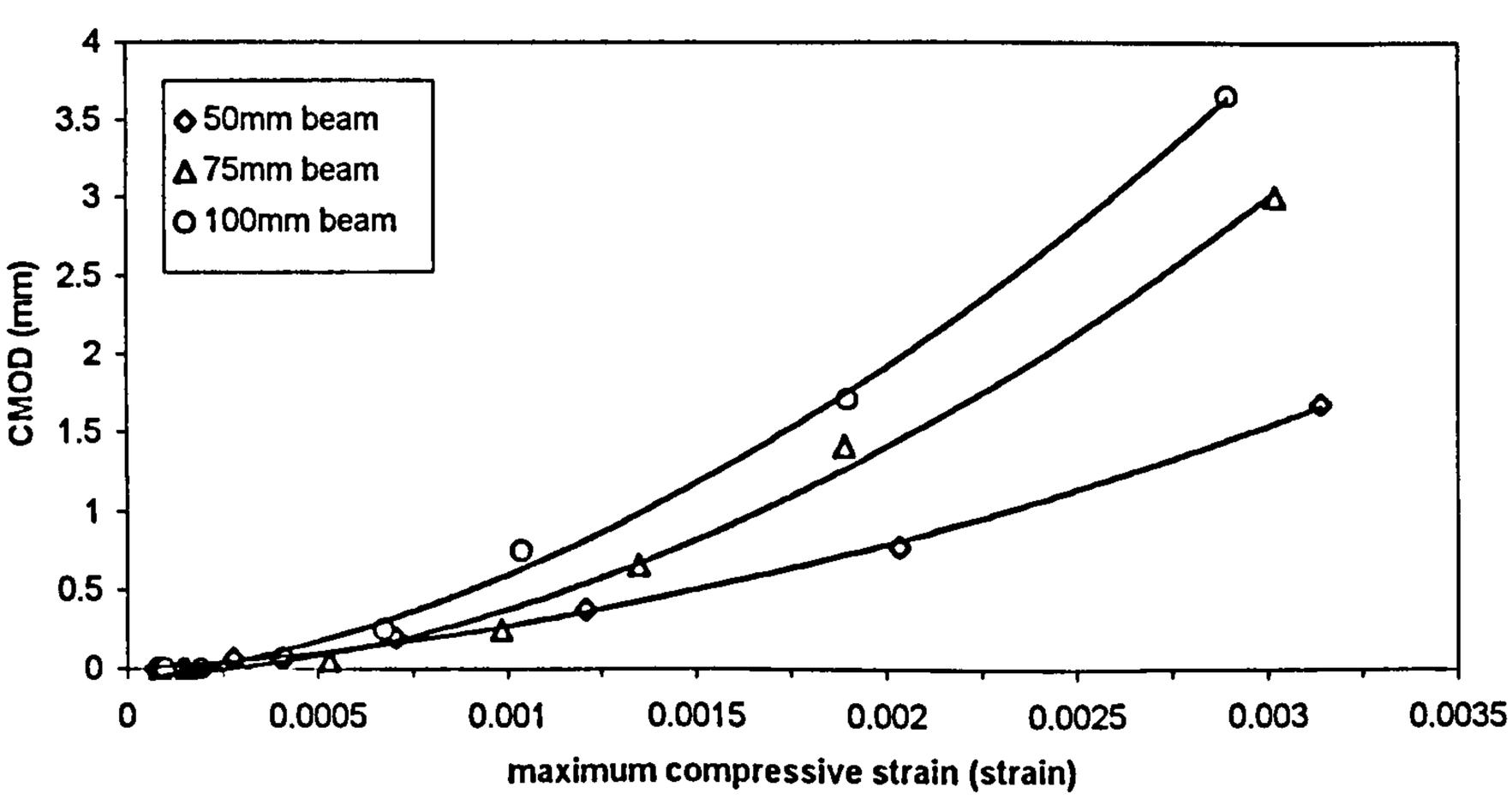

Figure 7.17 Relationship between CMOD and maximum compressive strain.

It is proposed that, if used together, equations 7.6, 7.7 and 7.8 may provide a means of predicting the strain/crack-width profile, at a given mid-span deflection, for a beam of known size and fibre content. However, further work is required to develop the equations for a wider range of loading geometry, matrix strengths and fibre contents.

(B) Compressive stress-strain behaviour

Under compression, it has been suggested by Armelin and Banthia (1997), that concrete behaves according to a parabolic stress-strain relationship of the form:

$$\sigma_c = f_c \left[2\frac{\varepsilon_c}{\varepsilon_c^{*\prime}} - \left(\frac{\varepsilon_c}{\varepsilon_c^{*}}\right)^2 \right] \quad \text{where} \quad \varepsilon_c^{*} = K^{*}\frac{f_c}{E_c} \qquad \text{equation 7.9}$$

and where σ_c is the concrete compressive stress at strain ε_c, f_c is the matrix compressive strength (in MPa), ε_c^{*} is the strain corresponding to f_c and K^{*} is a constant relating the initial tangent modulus to the secant modulus measured at f_c. In their study K^{*} was given a value of 2, in accordance with the Canadian Standards Association (1984), but a value of 1.6 was found to be more appropriate for the experimental data applied here. Note that the modulus of elasticity E_c for use in equation 7.9 was determined from equation 6.1.

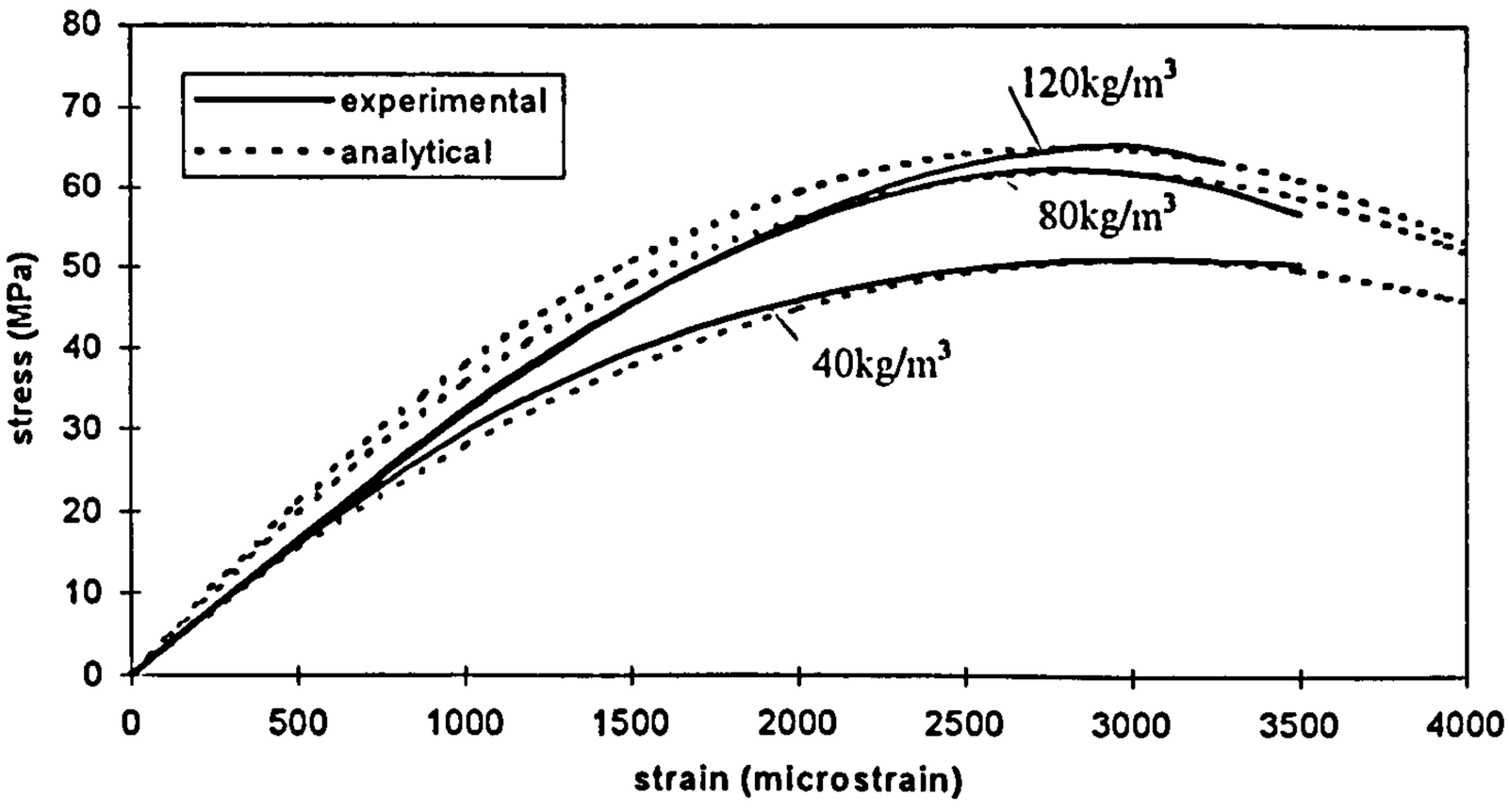

Figure 7.18 Comparison between measured and analytical compressive stress-strain relationships (Matrix C).

Figure 7.18 compares the compressive stress-strain curves obtained from the compression tests on Matrix C specimens with the corresponding analytical curves determined from equation 7.9. It can be seen that, in general, there is a reasonable agreement between the curves, suggesting that equation 7.9 may provide a means of predicting the compressive stress-strain for use in the model. Note that this equation has the advantage of requiring only a single parameter to be determined experimentally (i.e. matrix compressive strength).

(C) Fibre density distribution, orientation and embedment length

The probabilistic fibre pull-out curve (Figure 7.3) has been shown to be a powerful tool for representing statistically the pull-out forces of individual fibres occurring across a cracked section of a beam. However, it is also likely that the shape and magnitude of this curve may be unique for a given fibre type, matrix strength and method of placement. Therefore, further work is required on a wider range of fibre types and matrix strengths before a generalised curve can be developed for use in design and which can be related to the properties of the fibre, the matrix strength, and the method of placement.

It is also apparent from this study, that the fibre density distribution over the depth of a beam has a major influence on the predicted load-deflection response. It would therefore be appropriate in design, if a method could be developed for predicting the fibre density distribution from a specified value of fibre content. From the data presented in Chapter 6, it appears that this might best be achieved by adopting the linear relationship between fibre density and in-situ fibre content as given in equation 3.1. It is further proposed that values of orientation factor (β) for use in this equation could be determined (for use in design) for a given specimen size, fibre length and method of placement.

7.6 CHAPTER SUMMARY

This chapter has presented the procedures developed for testing the proposed model, in order to confirm the hypothesis stated in Chapter 4. The results show that in general the model is capable of predicting the general shape of the load-deflection response associated with a steel fibre reinforced concrete beam. Unfortunately, the relative accuracy of the model is currently unacceptable for it to be used in design. A subsequent analysis of the principal model parameters highlighted the single fibre pull-out tests, the probabilistic fibre pull-out curve, and the limitations associated with the crack-width measurements obtained from the grid method, as being the main causes of the discrepancies between the predicted and measured loads. A framework for the development of the model as the basis of a design rationale has also been proposed.

8. CONCLUSIONS AND RECOMMENDATIONS

8.1 INTRODUCTION

This last chapter presents the conclusions drawn from the results of the thesis together with the recommendations for further study. The conclusions are presented as two main sections: (a) in terms of the results from the five test programmes undertaken as part of the experimental investigation; and (b) in terms of the model development, testing and analysis. The recommendations are principally aimed at the future development of the model: (a) in terms of improving the precision of the model parameters obtained from experimental tests; and (b) in terms of developing the model as part of a design rationale for sprayed and cast steel fibre reinforced concrete.

8.2 CONCLUSIONS

8.2.1 Experimental investigation

In terms of the overall behaviour and reinforcing mechanisms associated with sprayed and cast steel fibre reinforced concrete, the main conclusions drawn from the experimental investigation undertaken are:

Single fibre pull-out tests

- A single fibre pull-out test has been developed in which the fibre is embedded within an uncracked matrix. The test allows the complete fibre pull-out response to be recorded (i.e. for both the uncracked and cracked specimen) and, thereby, provides a truer representation of fibre pull-out behaviour when compared with previous pull-out tests.
- The pull-out response of a hooked-end fibre is predominantly influenced by three parameters: fibre embedment length, fibre orientation and matrix strength. Furthermore, the response can be characterised by one of two pull-out modes: either the hooked-end is straightened as it is pulled out from the matrix or the fibre fractures. Full straightening of the hooked-end (resulting in the maximisation of peak pull-out load and pull-out toughness) can only occur if the total fibre

embedment length is greater than the length of the hooked-end, otherwise the hooked-end will only be partially straightened resulting in a considerable reduction in pull-out performance.

- For a hooked-end fibre orientated to the direction of loading, increasing the matrix strength increases the magnitude and toughness of the pull-out response. However, as fibre orientation increases the pull-out response becomes increasingly less influenced by matrix strength and increasingly more influenced by the mechanical properties of the fibre as it attempts to straighten in line with the direction of loading.
- The peak pull-out load and pull-out toughness of a hooked-end fibre is maximised at a non-zero fibre orientation providing the fibre is fully straightened and does not fracture during the pull out process. In addition, the crack-width at which peak-load occurs increases with increasing fibre orientation.
- Increasing the embedment length and orientation of a hooked-end fibre (with respect to the direction of loading), increases the magnitude and toughness of the pull-out response. A limit to this process is reached when the increase in pull-out resistance exceeds the ultimate tensile strength of the fibre causing the fibre to fracture prematurely. For fibres that fracture, the fracture load decreases as fibre orientation increases.
- In terms of the pull-out energy-absorption of a hooked-end fibre, the following conclusions were drawn: (a) the energy required to fully straighten the hooked-end has a constant value irrespective of fibre orientation; (b) once the hooked-end has been fully straightened the additional energy required to completely pull-out the fibre is linearly related to the remaining length of fibre embedded in the specimen; and (c) an inclined fibre with respect to the loading direction absorbs a greater amount of energy at a given slip than one that is aligned.

Compressive stress-strain tests

- For a given matrix strength, the influence of hooked-end fibres on the compressive stress-strain response can be considered to be negligible for fibre contents less than 120 kg/m^3 (equivalent to 1.5% by volume).

- From the results presented here, there is no significant difference between the compressive behaviour of cast and wet process sprayed steel fibre reinforced concrete made using equivalent mix designs.
- For a given water-cementitious ratio (i.e. cement plus silica fume), an increase in the addition of silica fume has an effect of increasing matrix strength and the value of secant modulus, but it also increases the brittleness of the matrix leading to a reduction in the value of strain at which peak stress occurs. A given mix design can only benefit from a finite addition of silica fume, which is equivalent to the amount required to completely cover the surface of the aggregate particles and infill the spaces between cement particles. Additions in excess of this amount lead to a surplus in the mix which is redundant in terms of strength enhancement.

Flexural toughness tests

- A flexural toughness test has been developed which allows the complete strain-softening response of a plain beam to be recorded without the need for a notch. This high degree of post-crack test stability suggests that the test set-up is appropriate for use in standard test methods for flexural toughness characterisation.
- In terms of flexural strength and flexural toughness performance, the response of a wet processed steel fibre reinforced sprayed concrete specimen is lower than a cast specimen made using an equivalent mix design. In addition, the flexural behaviour of sprayed concrete is more variable than its cast counterpart.
- In terms of flexural strength and flexural toughness performance, the response of a notched beam is greater than an unnotched beam having a similar ligament depth, width and loading geometry and it is less variable.
- The use of residual strength (measured in units of equivalent stress or a residual load capacity) as specified in EFNARC (1996), provides a relatively simple method of characterising the flexural behaviour and flexural toughness of fibre reinforced concrete when compared with other standard test methods. In particular, a residual strength can be more readily related to structural design than other flexural toughness measurements based on, for example, dimensionless indices of energy absorption capacity.
- The use of notched beams may offer significant advantages over unnotched beams for reducing the high variability associated with flexure toughness testing. In

particular, notched beams help to minimise the variability resulting from unnotched beams not always failing at mid-span: an issue that is not currently addressed by any of the current flexural toughness test standards.

Strain analysis tests

- A strain analysis test has been developed, which combines electrical resistance strain gauges with a semi-automated grid method (using digital image processing) for measuring and monitoring the strain and crack-width profile over the depth of a beam during a flexural test. The main merits of the test are: (a) its ability to measure a wide range of full-field strain and crack-widths using simple techniques of analysis; (b) its relatively low cost; and, (c) its use of readily available equipment. The test has been shown capable of measuring strain to an accuracy of ±15με over a range between 200με in tension and 3500με in compression, and crack-widths greater than 0.2mm to an accuracy of ±0.1mm. The test is capable of determining the following relationships, which potentially could be used in design:
    * CMOD versus mid-span deflection;
    * maximum compressive strain versus mid-span deflection;
    * neutral axis depth versus mid-span deflection;
    * CMOD versus maximum compressive strain;
    * CMOD versus beam depth.
- In terms of the strain profiles the results show that a fibre reinforced concrete beam, with a given test geometry and fibre content, has a common failure mode in terms of the movement in the neutral axis position (measured as a fraction of beam depth) and the associated values of maximum compressive strain measured at the compressive face of the beam, which appears to be independent of beam depth.
- In terms of the crack-width profiles the results show that, for a given deflection, the width of a propagating crack increases linearly over the depth of a beam. In terms of the crack-mouth-opening-displacement (CMOD), the results show that: (i) the CMOD increases linearly with increasing mid-span deflection, and (ii) the CMOD at a given deflection increases linearly with an increase in beam depth.

Fibre distribution analysis

- A test procedure has been developed, which uses X-ray photographs to determine the 3D spatial properties of the fibres bridging the cracked section of a fibre

reinforced concrete beam. The test is capable of determining the probability distributions associated with a particular fibre embedment length and fibre orientation combination occurring across the cracked section. The merits of the test are: (a) its simplicity in formulation; (b) the measurements are made directly from X-ray photographs of the specimen under investigation; and (c) the analysis only requires the average fibre length as an input parameter.

- The results of this study showed that there is no significant difference between casting (using table vibration) and spraying (using the wet process) on the resulting fibre distribution properties. In both cases, the method of placement tends to cause the fibres to align in a partially random 2D plane at right angles to the direction of casting or spraying. The probability distributions of fibre embedment length and orientation across a crack were also shown to be similar in both sprayed and cast specimens. Fibre embedment lengths were uniformly distributed indicating a high degree of randomness, and the distribution of fibre orientations was skewed towards an angle of 10-30 degrees suggesting that fibre orientation is influenced by the confining effect of the specimen mould.
- Fibre density measured on a 2D plane cut through a specimen is linearly related to fibre volume within the specimen. This relationship was further shown to be influenced by a parameter known as the orientation factor (β) which is a function of the height-to-width ratio of the specimen mould and the mould-width-to-fibre-length ratio.
- Casting using table vibration tends to cause the fibres to settle under gravity in the direction of casting, resulting in a fibre density gradient over the depth of the specimen. In contrast, spraying tends to cause a uniform fibre density gradient over the depth of the specimen with a slight reduction near the base of the specimen, suggesting higher values of fibre rebound in this region. These differences may provide an explanation for the lower flexural performance of sprayed specimens when compared with cast specimens, as noted above.

8.2.2 Model development and analysis

A semi-analytical model has been proposed for predicting the load-deflection response (and hence the flexural toughness performance) of both sprayed and cast steel fibre reinforced concrete beams in flexure. The main merits of the model are:

i. its simplicity in formulation;

ii. its use of conventional principles of mechanics;

iii. its use of parameters obtained from tests on laboratory specimens; and

iv. its potential for incorporating into a design rationale for fibre reinforced concrete.

The model has been shown capable of predicting the load-deflection response for a variety of beam sizes (ranging between a depth of 50-100mm and a span-to-depth ratio of 9-4.5 respectively) and fibre contents (up to 1.0% by volume) to within 30% of the measured response. Thus, in principle, the hypothesis stated in Chapter 4 - that the flexural load-deflection response can be predicted from conventional principles of mechanics if the stress-block can first be determined for a given mid-span deflection - appears to be valid for the range of beam sizes, matrix strengths, fibre volumes and the fibre type investigated.

Although the overall accuracy of the model is probably unacceptable for it to be currently used in design, this study has contributed to current knowledge by providing a further understanding of the reinforcing mechanisms, fracture processes and kinematics of failure associated with sprayed and cast steel fibre reinforced concrete in flexure. In particular, it has shown that flexural behaviour (and hence toughness performance) can be regarded as a function of six principal parameters: the pull-out behaviour of individual fibres; the distribution of fibres bridging the cracked section in terms of fibre density, orientation and embedment length; uniaxial compressive and tensile stress-strain relationships; and the strain and crack-width profiles in relation to mid-span deflection.

In terms of predicting relationships for these parameters from laboratory tests, the main conclusions drawn from this study are:

- The pull-out behaviour of individual fibres can be related to the overall post-crack flexural performance (i.e. flexural toughness) if a statistical approach is used to account for the variability associated with the embedment length and orientation of the fibres bridging the cracked section. In this respect, the use of probability distributions in combination with fibre pull-out data has been shown to be a useful method for predicting the most probable pull-out response of an individual fibre bridging the crack.

- The use of uniaxial single fibre pull-out test data may not be appropriate for predicting the pull-out response of a group of fibres subjected to a strain gradient, as exists across the cracked section of a beam in flexure. Furthermore, because the size of the fracture process zone in a flexural specimen can be extensive in the vicinity of the crack, some fibres may not actually pull-out as a result of the matrix fracturing around them.
- Current standard tests for the determination of compressive strength and static modulus of elasticity using standard cube or prism specimens appear to overestimate the compressive stresses developed in the compression zone of a beam in flexure. Therefore, care should be exercised when using data obtained from these tests to predict the flexural behaviour of a beam.
- The results of the modelling analysis showed that the accurate measurement of crack-widths immediately after the specimen first cracks (up to a crack width of 0.5mm) is essential for the accurate prediction of flexural load capacity in the corresponding region of the load-deflection response curve. This requirement should be reflected in the method adopted to measure the crack-width profiles for use in the model.

In terms of addressing the research needs identified in Section 4.2, the model may have the following implications on the design, specification and quality control of cast and sprayed steel fibre reinforced concrete.

- Firstly, the model gives an insight into the reinforcing mechanisms, fracture processes and failure modes associated with the flexural behaviour of fibre reinforced concrete. As such, it can be used to explain some of the characteristic features of the load-deflection response curve.
- Secondly, the model provides a mechanism for changing the constituents and properties of the fibre reinforced matrix in order to achieve a specified flexural response (or flexural toughness performance). Therefore, it could form the basis of a design tool for predicting flexural behaviour given only the matrix strength, fibre type, fibre volume content, beam size and loading geometry as design input parameters. Consequently, the model could offer a much needed link between flexural toughness performance (measured as a residual strength or load capacity) and structural design. This would benefit both designers and specifiers, by allowing

them to make informed - and more realistic - choices as regard to the hardened properties of the mix in order to meet the ultimate and serviceability requirements of a particular application.

8.3 RECOMMENDATIONS FOR FURTHER STUDY

8.3.1 Improving the experimental data for use in the model

- The single fibre pull-out test needs to be significantly re-engineered to ensure that a more appropriate fibre pull-out response is recorded. In particular, it is imperative that the tests are performed under closed-loop control using the specimen deformation as the controlling parameter. The test specimen should also be laterally restrained to more closely simulate the pulling out of the fibres from a flexural test beam, and to prevent sideways movements between the two halves of the specimen during the tests. The effect of strain gradients and the fracture process zone on the pull-out behaviour of single fibres should also be investigated.
- Improving the accuracy of the strain analysis test method should also be investigated. This should centre on improving the accuracy and sensitivity of the crack-width profile measurements particularly for crack-widths less than 0.5mm, and for improving the measurement of strain profile in the vicinity of a crack. Holographic Moiré techniques appear to be the only viable method currently available for achieving the required accuracy for use in the model. Therefore, this method should be investigated further provided that the necessary equipment is available and the cost is not restrictive.
- Further X-ray analysis tests need to be undertaken on both cast and sprayed specimens to improve the probabilities associated with the distribution of fibre embedment length and orientations of the fibres bridging a crack. In addition, the X-ray analysis test should be investigated to see if it is feasible to model the behaviour of each individual fibre bridging a cracked section. It is suggested that this will require, in addition to measurements of fibre embedment length and orientation, a measure of the lever arm between the neutral axis and each individual fibre in order to determine the flexural moment contribution of each fibre.
- Finally, a greater number of strain analysis tests needs to be undertaken using different beam sizes and fibre contents to provide further data relating to the shape

and magnitude of the strain/crack-width profiles for different fibre contents. It is further recommended that the tests are performed on notched specimens in order to ensure that the critical cracked section always occurs at mid-span, thereby avoiding the risk of wasted tests resulting from the specimen cracking outside the area of the middle-third region or not cracking through the strain gauge locations.

8.3.2 Development of a design method for steel fibre reinforced concrete

This study has shown that in principle the flexural behaviour of steel fibre reinforced concrete can be predicted from conventional principles of mechanics providing that the stress-block diagram can first be predicted for a given mid-span deflection. The basis of a design rationale has been proposed which is similar in concept to current reinforced concrete design methods, using a stress-block approach, and which uses design parameters which have readily understood meaning to the majority of structural engineers. Therefore, further research should concentrate on developing the model as part of a design rationale for sprayed or cast fibre reinforced concrete. In pursuit of this aim, the following is a summary of recommendations.

1) Development of analytical expressions and/or design curves to allow the designer to predict the principal model parameters from a specified set of design criteria. In particular, this should concentrate on developing the following relationships as a function of matrix compressive strength, fibre type, fibre volume, specimen size, applied loading geometry and method of placement (sprayed or cast):
   - CMOD versus mid-span deflection;
   - maximum compressive strain versus mid-span deflection;
   - CMOD versus maximum compressive strain;
   - compressive stress-strain behaviour;
   - fibre density as a function of fibre volume content; and
   - fibre density distribution over the depth of a beam.
2) Investigate the effect of different fibre types, mix designs, specimen sizes and methods of placement (i.e. different casting or spraying methods) on the resulting fibre distribution and, hence, the probabilistic fibre pull-out curve. The results of these investigations could be used to develop a generalised probabilistic curve as a function of measurable properties of the specimen. For example these could include:

fibre length, maximum aggregate size, the dimensions of the specimen, orientation factor, and whether the specimen was cast or sprayed.

3) Investigate the validity of the model for predicting the flexural behaviour of full-size specimens and/or other types of structural elements (e.g. slabs and walls). One particular area of investigation would be to develop the model for predicting the flexural behaviour of sprayed concrete tunnel lining under the influence of deforming ground. Such a model would have enormous benefit to the tunnelling and mining industries where current design methods are still largely based on empirical rules or past experience.
4) Development of computer software for the model which can automatically produce a prediction of the load-deflection response, and associated toughness characterisation data, from specified design parameters input by the user (i.e. characteristic matrix strength, fibre type, fibre content, beam size and loading geometry).
5) Evaluate and analyse the design procedure adopted in current reinforced concrete codes of practice (i.e. BS8110 or Eurocode 2), with a view to drafting a design guideline for fibre reinforced concrete which incorporates replacement clauses for use in conjunction with a standard code of practice.

REFERENCES

ACI 506R (1990) *Guide to Shotcrete*. American Concrete Institute, Detroit.

ACI 506.1R (1984) *State-of-the-Art Report on Fiber Reinforced Shotcrete*. American Concrete Institute, Detroit.

ACI 506.2 (1995) *Specification for Shotcrete*. American Concrete Institute, Detroit.

ACI 506.3R (1991) *Guide to Certification of Shotcrete Nozzleman.* American Concrete Institute, Detroit.

ACI 506.4R (1994) *Guide for the Evaluation of Shotcrete.* American Concrete Institute, Detroit.

ACI 544.4R (1988) *Design Considerations for Steel Fiber Reinforced Concrete.* American Concrete Institute, Detroit.

AFTES (1992) *Recommendations on Sprayed Concrete Shotcrete: Technology and Practice.* Report of AFTES Working Group No. 6, Paris.

Anderson, P.G. and Dalseg, A. (1993) High Capacity Shotcreting Equipment. *Procs. Int. Symp. On Sprayed Concrete*, Norwegian Concrete Association, Fagernes, Norway, 153-166.

Annett, M.F. and Varley, N.J. (1996) High Performance Wet-Shotcrete in London Clay. *Procs. of the 2nd International Symposium on Sprayed Concrete*, Norwegian Concrete Association, Gol, Norway, 1-14.

Armelin, H.S. and Helene, P. (1995) Physical and Mechanical Properties of Steel Fiber Reinforced Dry-Mix Shotcrete. *ACI Materials Journal*, Vol. 92, No. 3, 258-267.

Armelin, H.S. and Banthia, B. (1997) Predicting the Flexural Postcracking performance of Steel Fiber Reinforced Concrete from the Pullout of Single Fibers. *ACI Materials Journal*, Vol. 94, No. 1, 18-31.

Armelin, H.S., Banthia, N. and Morgan, D.R. (1996) Particle Kinematics in Dry-Mix Shotcrete - Research in Progress. *Sprayed Concrete Technology*, ed. Austin, S.A., E&FN Spon, London, 243-251.

ASTM C78 (1984) *Test for Flexural Strength of Concrete*, American Society of Testing and Materials, Philadelphia.

ASTM C469-94 (1994) *Test for Static Modulus of Elasticity and Poisson's Ratio of Concrete in Compression*, American Society of Testing and Materials, Philadelphia.

ASTM C1116-91 (1991) *Standard Specification for Fiber-Reinforced Concrete and Shotcrete*, American Society of Testing and Materials, Philadelphia.

ASTM C1018-94b (1994) *Standard Test Method for Flexural Toughness and First-Crack Strength of Fiber-Reinforced Concrete*, American Society of Testing and Materials, Philadelphia.

Austin, S.A. (1984) *Melt Extract Fibre Reinforced Composites*, Ph.D. Thesis, Loughborough University.

Austin, S.A. (1995) Introduction to Sprayed Concrete. *Sprayed Concrete - Properties, Design and Application*, eds. Austin, S.A. and Robins, P.J., Whittles Publishing, Caithness, 1-6.

Austin, S.A. (1995a) Production and Installation. *Sprayed Concrete - Properties, Design and Application*, eds. Austin, S.A. and Robins, P.J., Whittles Publishing, Caithness, 31-51.

Austin, S.A. (1995b) Materials Selection, Specification and Quality Control. *Sprayed Concrete - Properties, Design and Application*, eds. Austin, S.A. and Robins, P.J., Whittles Publishing, Caithness, 87-112.

Austin, S.A. and Robins, P.J. (1993) Test Methods for Strength and Toughness of Sprayed Fibre Concrete. *Procs. of International Symposium on Sprayed Concrete*, Norwegian Concrete Association, Fagernes, Norway, October, 7-19.

Babut, R. and Brandt, A.M. (1978) The Method of Testing and Analysing of Steel Fibre Reinforced Concrete Elements in Flexure. *Proceedings of the RILEM Symposium 1978*, edited by R.N. Swarmy, The Construction Press, Lancaster, England, 479-486.

Balaguru, P.N. and Shah, S.P. (1992) *Fiber-Reinforced Cement Composites*, McGraw-Hill, New York.

Balaguru, P., Narahari, R., and Patel, M. (1992) Flexural Toughness of Steel Fiber Reinforced Concrete. *ACI Materials Journal*, Vol. 89, No. 6, 541-546.

Banthia, N. (1990) A Study of some Factors Affecting the Fiber-Matrix Bond in Steel Fiber Reinforced Concrete. *Canadian journal of Civil Engineering*, Vol. 17, 610-620.

Banthia, N. and Trottier, J.F. (1994) Concrete Reinforced with deformed Steel Fibres Part I: Bond-Slip Mechanisms. *ACI Materials Journal*, Vol. 91, No. 5, 435-446.

Banthia, N. and Trottier, J.F. (1995) Test methods for Flexural Toughness Characterisation of Fiber Reinforced Concrete: Some Concerns and a Proposition. *ACI Materials Journal*, Vol. 92, No. 1, 48-57.

Banthia, N. and Trottier, J.F. (1995a) Concrete Reinforced with deformed Steel Fibres Part II: Toughness Characterisation. *ACI Materials Journal*, Vol. 92, No. 2, 146-154.

Banthia, N., Trottier, J.F., Beaupre, D. and Wood, D. (1994) Properties of Steel Fiber Reinforced Shotcrete. *Canadian Journal of Civil Engineering*, Vol. 21, 564-575.

Banthia, N., Trottier, J.F., Beaupre, D. and Wood, D. (1994a) Influence of Fiber Geometry in Steel Fiber Reinforced Wet-Mix Shotcrete. *Concrete International*, Vol. 16, No. 5, 27-32.

Banthia, N., Trottier, J.F., Beaupre, D. (1994b) Steel Fibre Reinforced Wet-Mix Shotcrete: Comparisons with Cast Concrete. *Journal of Materials in Civil Engineering*, Vol. 6, No. 3, 430-437.

Banthia, N., Trottier, J.F., Wood, D. and Beaupre, D. (1992) Influence of Fiber Geometry in Steel Fiber Reinforced Dry-Mix Shotcrete. *Concrete International*, Vol. 14, No. 5, 24-28.

Banthia, N., Trottier, J.F., Pigeon, M. and Krishnadev, M.R. (1992) Deformed Steel Fiber Pull-Out: Material Characteristics and Metallurgical Processes. *High Performance Reinforced Cement Composites*, Eds. Reinhardt, H.W. and Naaman, A.E., RILEM, E&FN Spon, London, 457-466.

Barr, B. and Newman, P.D. (1985) Toughness of Polypropylene Fibre-Reinforced Concrete. *Composites*, Vol. 16, No. 1, 48-53.

Barr, B., Gettu, R., Al-Oraimis, K. A. and Bryars, L.S. (1996) Toughness Measurement - The Need to Think Again. *Cement and Concrete Composites*, Vol. 18, 281-297.

Barton, N. and Chryssanthakis, P. (1996) Design of Tunnels for NMT Using Fibre Reinforced Shotcrete and Bolting as Permanent Support. *Procs. of the 2nd International Symposium on Sprayed Concrete*, Norwegian Concrete Association, Gol, Norway, 15-30.

Barton, N., Grimstad, E., and Palmstrom, A. (1995) Design of Tunnel Support. *Sprayed Concrete - Properties, Design and Application*, eds. Austin, S.A. and Robins, P.J., Whittles Publishing, Caithness, 150-170.

Bartos, P.J.M. (1981) Review Paper: Bond in Fibre Reinforced Cement and Concretes. *The International Journal of Cement Composites*, Vol. 3, No. 3, 159-177.

Bartos, P.J.M., and Duris, M. (1994) Inclined Tensile Strength of Steel Fibres in a Cement-Based Composite. *Composites*, Vol. 25, No. 10, 945-952.

Batson, G.B. (1994) Review of the State-of-the-Art of Steel Fiber Reinforced Concrete. *Proceedings of the Workshop on Fibre Reinforced Cement and Concrete*, National Science Foundation (USA), Sheffield, July, 88-106.

Bazant, Z.P. and Oh, B.H. (1983) Crack Band Theory for Fracture of Concrete. *Materials and Structures*, Vol. 16, 155-157.

Beaupre, D. and Mindess, S. (1993) Compaction of Wet Shotcrete and its Effect on Rheological Properties. *Procs. Int. Symp. On Sprayed Concrete*, Norwegian Concrete Association, Fagernes, Norway, 167-181.

Beaupre, D. and Mindess, S. (1996) Fundamentals of Wet-Mix Shotcrete. *Sprayed Concrete Technology*, ed. Austin, S.A., E&FN Spon, London, 252-261.

Beaupre, D. and Mindess, S. and Morgan, D.R. (1993) Development of High Performance Shotcrete. Proc. Engineering Foundation Conference *Shotcrete for Underground Support VI*, ASCE, Niagara, Canada, 1-8.

Beaupre, D., Talbot, C., Gendreau, M., Pigeon, M. and Morgan, D.R. (1994) Deicer Salt Scaling Resistance of Dry and Wet-Process Shotcrete. *ACI Materials Journal*, Vol. 91, No. 5, 487-494.

Bekaert S.A. (1997) *Design Guidelines for Dramix® Steel wire Fibre Reinforced Concrete*, N.V. Bekaert S.A., Zwevegem, Belgium.

Blanks, R.F. and McNamara, C.C. (1935) Mass Concrete Tests in Large Cylinders. *Journal of American Concrete Institute*, Vol. 31, 280-303.

BS 12 (1991) *Specification for Portland Cements*, British Standards Institution, Milton Keynes.

BS 812: Section 103.1 (1983) *Testing Aggregates: Sieve Tests*, British Standards Institution, Milton Keynes.

BS 812: Part 2 (1985) *Testing Aggregates: Methods for Determination of Physical Properties*, British Standards Institution, Milton Keynes.

BS 882 (1992) *Aggregates from Natural Sources for Concrete*, British Standards Institution, Milton Keynes.

BS 1881: Part 102 (1983) *Method for Determination of Slump*, British Standards Institution, Milton Keynes.

BS 1881: Part 111 (1983) *Method of Normal Curing of Test Specimens (20° C method)*, British Standards Institution, Milton Keynes.

BS 1881: Part 114 (1983) *Methods for Determination of Density of Hardened Concrete*, British Standards Institution, Milton Keynes.

BS 1881: Part 116 (1983) *Method for Determination of Compressive Strength of Concrete*, British Standards Institution, Milton Keynes.

BS 1881: Part 118 (1983) *Method for Determination of Flexural Strength*, British Standards Institution, Milton Keynes.

BS 1881: Part 121 (1983) *Method of Determination of Static Modulus of Elasticity in Compression*, British Standards Institution, Milton Keynes.

BS 8110: Part 1 (1985) *Structural Use of Concrete: Code of Practice for Design and Construction*, British Standards Institution, Milton Keynes.

Burakiewicz, A. (1978) Testing of Fibre Bond Strength in Cement Matrix. *Proceedings of the RILEM Symposium 1978*, edited by R.N. Swarmy, The Construction Press, Lancaster, England, 355-265.

Canadian Standards Association (1984) *Design of Concrete Structures for Buildings* (CAN3-A233-M84), Canadian Standards Association, Rexdale, Canada.

Casanova, P.A. and Rossi, P.C. (1995) Characterisation and Design of Steel Fibre Reinforced Shotcrete in Tunnelling. Procs. Engineering Foundation Conference *Shotcrete for Underground Support VII*, ASCE, Telfs, Austria, 217-226.

CEN Technical Committee TC 104 (1997) *Draft Specification for Sprayed Concrete*, CEN, Paris.

Chandler, J.H. and Padfield, C.J. (1996) Automated Digital Photogrammetry on a Shoestring. *Photogrammetry Record*, 15(88), 545-559.

Chang, C.T., Liu, H.S. and Chen, Y.M. (1993) Application of Steel Fiber Reinforced Shotcrete for Underground Structures in Taiwan. *Procs. Int. Symp. On Sprayed Concrete*, Norwegian Concrete Association, Fagernes, Norway, 120-132.

Chanvillard, G. (1992) Energy Dissipation During Steel Fibre Pull-Out. *Fibre Reinforced Cement and Concrete*, edited by R.N. Swarmy, RILEM, E & FN Spon, London, 380-389.

Chanvillard, G., and Aitcin, P.C. (1992) On the Modelling of the Pull-Out Behaviour of Steel Fibres. *High Performance Fiber Reinforced Cement Composites*, edited by H.W. Reinhardt and A.E. Naaman, RILEM, E & FN Spon, London, 467-478.

Chen, L., Mindess, S., and Morgan, D.R. (1994) Specimen Geometry and Toughness of Steel-Fiber Reinforced Concrete. *Journal of Materials in Civil Engineering*, Vol. 6, No. 4, 529-541.

Chen, L., Mindess, S., Morgan, D.R., Shah, S.P., Johnston, C.D. and Pigeon, M. (1995) Comparative Toughness of Fiber Reinforced Concrete. *Testing of Fiber Reinforced Concrete*, SP155-4, ACI, Detroit, 41-75.

Cotterell, B., Paramasivam, P., and Lam, K.Y. (1992) Modelling the Fracture of Cementitious Materials. *Materials and Structures*, Vol. 25, 14-20.

Coverdale, T., Champa, J. and Eckert, L. (1996) Total Consistency Control for Wet Shotcrete - A Slump Killing System for Improved Performance. *Procs. of the 2nd International Symposium on Sprayed Concrete*, Norwegian Concrete Association, Gol, Norway, 182-192.

Dally, J.W. and Riley, W.F. (1991) *Experimental Stress Analysis*, 3rd edition, McGraw-Hill Inc., Singapore.

DIN 18551 (1991) *Sprayed Concrete: Production and Quality Control.* Deutsches Institut fur Normung, Berlin.

Dwarakanath, H.V. and Nagaraj, T.S. (1991) Comparative Study of Predictions of Flexural Strength of Steel Fiber Concrete. *ACI Structural Journal*, Vol. 88, No. 6, 714-720.

Earnshaw, G. (1997) *Personal Communication following a site visit to the Heathrow Express Project - Heathrow Airport, UK.*

Edgington, J. and Hannant, D.J. (1972) Steel fibre Reinforced Concrete - The Effect on Fibre Orientation of Compaction by Vibration. *Materials and Structures*, Vol. 5, No. 25, 41-44.

EFNARC (1993) *Draft Specification for Sprayed Concrete.* European Federation of National Association of Specialist Repair Contractors and Material Suppliers for the Construction Industry, Aldershot, UK.

EFNARC (1996) *European Specification for Sprayed Concrete.* European Federation of National Association of Specialist Repair Contractors and Material Suppliers for the Construction Industry, Aldershot, UK.

El-Shakra, M. and Gopalaratnam, V.S. (1993) Deflection Measurement and Toughness Evaluations for Fiber Reinforced Concrete. *Cement and Concrete Research*, Vol. 23, 1455-1466.

Evans, R.H. and Marathe, M.S. (1968) Microcracking and Stress-Strain Curves for Concrete in Tension. *Materials and Structures*, Vol. 1, No.1, 61-64.

Fail, R.W. and Taylor, C.E. (1990) An Application of pattern Mapping to Plane Motion. *Experimental Mechanics*, December, 404-410.

Fanella, D.A. and Naaman, A.E. (1985) Stress-Strain Properties of Fiber Reinforced Mortar in Compression. *ACI Journal*, Vol. 82, July-August, 475-483.

Franzen, T. (1992) Shotcrete for Underground Support: A State of the Art Report with Focus on Steel Fibre Reinforcement. *Tunnelling and Underground Space Technology*, Vol. 7, No. 4, 383-391.

Franzen, T. and Malmberg, B. (1996) Standardisation of sprayed Concrete Within CEN - Status Report Related to Rock Support Applications. *Procs. of the 2nd International Symposium on Sprayed Concrete*, Norwegian Concrete Association, Gol, Norway, 60-69.

Garshol, K.F. (1995) Practical Experience of Steel Fibre Reinforced Wet Shotcrete in Large Underground Construction Projects. Proc. Engineering Foundation Conference *Shotcrete for Underground Support VII*, ASCE, Telfs, Austria, 189-196.

Garshol, K.F. and Melbye, T.A. (1996) Practical Experience with Alkali-Free, Non-Caustic Liquid Accelerators for Sprayed Concrete. *Procs. of the 2nd International Symposium on Sprayed Concrete*, Norwegian Concrete Association, Gol, Norway, 257-268.

Giaccio, G. and Zerbino, R. (1992) Discussion of paper 'Bond-Slip Mechanisms of Steel Fibre Concrete' by Naaman, A.E., and Najm, H. (1991). *ACI Materials Journal*, Vol. 89, No. 1, 108-109.

Glinicki, M.A. (1994) Toughness of Fiber Reinfoirced Mortar at High Tensile Rates. *ACI Materials Journal*, Vol. 91, No. 2, 161-166.

Gonnerman, H.F. (1925) Effect of Size and Shape of Test Specimen on Compressive Strength of Concrete. *Proc. of ASTM*, Vol. 25, Part II, 237-250.

Gonzalez, R.C. and Woods, R.E. (1992) *Digital Image Processing*, Addison-Wesley Publishing, London.

Gopalaratnam, V.S. and Shah, S.P. (1985) Strength, Deformation and Fracture Toughness of Fibre Cement Composites at Different Rates of Flexural Loading. *Steel Fibre Concrete*, eds. Shah, S.P. and Skarendahl, A., Swedish Cement and Concrete Research Institute, Stockholm, 229-331.

Gopalaratnam, V.S. and Shah, S.P. (1985a) Softening Response of Plain Concrete In Direct Tension. *ACI Journal*, Vol. 82, May-June, 310-323.

Gopalaratnam, V.S. and Shah, S.P. (1987) Tensile Failure of Steel Fiber-Reinforced Mortar. *Journal of Engineering Mechanics*, Vol. 113, No. 5, 635-652.

Gopalaratnam, V.S. and Abu-Mathkour, H.J. (1987) Investigation of the Pull-Out Characteristics of Steel fibers from Mortar Matrices. *Proceedings of the Int. Symp. on Fibre Reinforced Concrete*, December 16-19, Madras, India, 2.201-2.211.

Gopalaratnam, V.S. and Gettu, R. (1995) On the Characterisation of Flexural Toughness of Fiber Reinforced Concretes. *Cement and Concrete Research*, Vol. 17, 239-254.

Gopalaratnam, V.S., Shah, S.P., Batson, G.B., Criswell, M.E., Ramakrishnan, V., and Wecharatana, M. (1991) Fracture Toughness of Fiber Reinforced Concrete. *ACI Materials Journal*, Vol. 88, No. 4, 339-353.

Gray, R.J. and Johnston, C.D. (1978) The Measurement of Fibre-Matrix Interfacial Bond Strength in Steel Fibre-Reinforced Cementitious Composites. *Proceedings of the RILEM Symposium 1978*, R.N. Swarmy (ed.), The Construction Press, Lancaster, England, 317-327.

Gray, R.J. and Johnston, C.D. (1984) The Effect of Matrix Composition on Fibre/Matrix Interfacial Bond Strength in Fibre-Reinforced Mortar. *Cement and Concrete Research*, Vol. 14, 285-296.

Green, M.F., Oakley, D.R. and Proctor, B.A. (1978) Tensile Testing of Glass Reinforced Cement Sheet. *Proceedings of the RILEM Symposium 1978*, edited by R.N. Swarmy, The Construction Press, Lancaster, England, 439-449.

Green, P. (1993) FHWA Tries Performance Specs. *ENR*, September, 30-32.

Grimstad, E. and Barton, N. (1993) Updating the Q-System for NMT. *Procs. Int. Symp. On Sprayed Concrete*, Norwegian Concrete Association, Fagernes, Norway, 46-66.

Hannant, D.J. (1978) *Fibre Cements and Fibre Composites*, J. Wiley & Sons Ltd., Chichester, England.

Hasen, R., Dahl, H.I. and Bull, H. (1993) Use of Sprayed Concrete for Strengthening of Road Tunnels. *Procs. Int. Symp. On Sprayed Concrete*, Norwegian Concrete Association, Fagernes, Norway, 358-374.

Hearn, E.J. (1968) *Stress Analysis*, Design and Engineering Handbook, Product Journals Ltd., England.

Hillerborg, A. (1980) Analysis of Fracture by Means of the Fictitious Crack Model, Particularly for Fibre Reinforced Concrete. *The International Journal of Cement Composites*, Vol. 2, No. 4, 177-184.

Hillerborg, A. (1983) Analysis of a Single Crack. *Fracture Mechanics of Concrete*, edited by F.H. Wittmann, Elsevier Science, Amsterdam, 223-249.

Hillerborg, A. (1985) Determination and Significance of the Fracture Toughness of Steel Fibre Concrete. *Steel Fibre Concrete*, eds. Shah, S.P. and Skarendahl, A., Swedish Cement and Concrete Research Institute, Stockholm, 257-271.

Hillerborg, A., Modeer, M., and Peterson, P.E. (1976) Analysis of Crack Formation and Crack Growth in Concrete by Means of Fracture Mechanics and Finite Elements. *Cement and Concrete Research*, Vol. 6, 773-782.

Holtman, J.P. and Opsahl, O.A. (1996) State of the Art and Future Developments of Sprayed Concrete Technology in Norway. *Procs. of the 2nd International Symposium on Sprayed Concrete*, Norwegian Concrete Association, Gol, Norway, 395-400.

Hughes, B.P. and Fattuhi, N.I. (1975) Fibre Bond Strengths in Cement and Concrete. *Magazine of Concrete Research*, Vol. 27, No. 92, 161-167.

Hughes, B.P. and Fattuhi, N.I. (1978) Methods and Recommendations for Testing Fibre Reinforced Concrete. *Proceedings of the RILEM Symposium 1978*, edited by R.N. Swarmy, The Construction Press, Lancaster, England, 409-416.

Institution of Civil Engineers (1996) *Sprayed Concrete Linings (NATM) for Tunnels in Soft Ground*, Thomas Telford, London.

International Tunnelling Association (1991) *Status Report on Shotcrete in Tunnelling*. BeFo, Swedish Rock Engineering Foundation, Stockholm.

Jamet, D., Gettu, R., Gopalaratnam, V.S., and Aguado, A. (1995) Toughness of Fiber Reinforced High Strength Concrete from Notched Beams. *Testing of Fiber Reinforced Concrete*, SP155-4, ACI, Detroit, 23-39.

Japan Society of Civil Engineers (1984) Guideline for Construction of Steel Fibre Reinforced Shotcrete. *Concrete Library of JSCE*, Vol. 3, 31-39.

Japan Society of Civil Engineers (1984a) Method of Tests for Steel Fibre reinforced Concrete. *Concrete Library of JSCE*, Vol. 3, 25-74.

Japan Society of Civil Engineers (1984b) Method of Test for Flexural Strength and Flexural Toughness of Fibre Reinforced Concrete. Standard JSCE-SF4, *JSCE Standards for Test Methods of Fibre Reinforced Concrete*, June, 45-51.

Jenq, Y.S. and Shah, S.P. (1986) Crack Propagation in Fiber-Reinforced Concrete. *Journal of Structural Engineering*, Vol. 112, No. 1, 19-34.

Johnson, C.D. (1995) Deflection Measurement Considerations in Evaluating Fiber Reinforced Concrete Performance Using ASTM C1018. *Testing of Fiber Reinforced Concrete*, SP155-4, ACI, Detroit, 1-22.

Johnston, C.D. and Gray, R.J. (1978) Uniaxial Tensile Testing of Steel Fibre Reinforced Cementitious Composites. *Proceedings of the RILEM Symposium 1978*, Swarmy, R.N. (ed.), The Construction Press, Lancaster, England, 451-461.

Karihaloo, B.L. (1995) *Fracture Mechanics and Structural Concrete*, Longman Scientific & Technical, Harlow, UK.

Kasperkiewicz, J., Malmberg, B. and Skarendahl, A. (1978) Determination of Fibre Content, Distribution and Orientation in Steel Fibre Concrete by X-ray Technique. *Proceedings of the RILEM Symposium 1978*, Swarmy, R.N. (ed.), The Construction Press, Lancaster, England, 297-305.

Keer, J.G. and Hannant, D.J. (1986) The Prediction of the Load-Deflection Behaviour of a Fibre Reinforced Cement Composite. *Developments in Fibre Reinforced Cement and Concrete - Volume 1*, RILEM, eds. Swarmy, R.N. *et al.*, Paper 1.6.

Kirsten, H.A.D. (1992) Comparative Efficiency and Ultimate Strength of Mesh- and Fibre-Reinforced Shotcrete as Determined by Full Scale Bending Tests. *Journal of the South African Institute of Mining and Metallurgy*, Vol. 92, No. 11/12, 303-323.

Kirsten, H.A.D. (1993) Equivalence of Mesh- and Fibre- Reinforced Shotcrete at Large Deflections. *Canadian Geotechnical Journal*, Vol. 30, 418-440.

Kirsten, H.A.D. and Labrum, P.R. (1990) The Equivalence of Fibre and Mesh Reinforcement in the Shotcrete Used in Tunnel Support Systems. *Journal of the South African Institute of Mining and Metallurgy*, Vol. 90, No. 7, 153-171.

Kong, F.K. and Evans, R.H. (1987) *Reinforced and Prestressed Concrete*, 3rd edition, Van Nostrand Reinhold (UK), England.

Krenchel, H. (1975) Fibre Spacing and Specific Fibre Surface. *Fibre Reinforced Cement and Concrete*, RILEM Symposium, Construction Press Ltd., Lancaster, England, 69-79.

Krishnadev, M.R., Berrada, S., Banthia, N., and Trottier, J.F. (1992) Deformed Steel Fiber Pull-Out Mechanics: Influence of Steel Properties. *Fibre Reinforced Cement and Concrete*, edited by R.N. Swarmy, E & FN Spon, London, 390-399.

Lewis, A. (1997) The Jubilee Line Extension. *Concrete*, Vol. 31, No.1, 28-34.

Lewis, R. (1996) Microsilica. *Concrete*, Vol. 30, No. 1, 23-25.

Li. V.C., Stang, H. and Krenchel, H. (1993) Micromechanics of Crack-Bridging in Fibre-Reinforced Concrete. *Materials and Structures*, Vol. 26, 486-494.

Li, V.C. and Maalej, M. (1996) Toughening in Cement Based Composites. Part I: Cement, Mortar and Concrete. *Cement & Concrete Composites*, Vol. 18, 223-237.

Li, V.C. and Maalej, M. (1996a) Toughening in Cement Based Composites. Part II: Fiber Reinforced Cementitious Composites. *Cement & Concrete Composites*, Vol. 18, 239-249.

Lierse, J. and Ringkamp, M. (1983) Investigations into Cracked Reinforced Concrete Structural Elements with the Aid of Photoelastic Methods. *Fracture Mechanics*, edited by F.H. Wittmann, Elsevier Science, Amsterdam, 96-111.

Lim, T.Y., Paramasivam, P., and Lee, S.L. (1987) Bending Behaviour of Steel-Fiber Concrete Beams. *ACI Structural Journal*, Vol. 84, Nov-Dec, 524-536.

Maage, M. (1977) Interaction Between Steel fibers and Cement Based Matrices. *Materials and Structures*, Vol. 10, No. 59, 297-301.

Maage, M. (1978) Fibre Bond and Friction in Cement and Concrete. *Proceedings of the RILEM Symposium 1978*, Swarmy, R.N. (ed.), The Construction Press, Lancaster, England, 329-336.

Maalej, M. and Li, V.C. (1994) Flexural Strength of Fiber Cementitious Composites. *Journal of Materials in Civil Engineering*, Vol. 6, No. 3, 390-406.

Mai, D. and Burge, T.A. (1996) High Performance Concrete with High Durability. *Procs. of 2nd Int. Symp. On Sprayed Concrete*, Norwegian Concrete Association, Gol, Norway, 242-256.

Maidl, B.R. (1991) Shotcrete Robot for Improving Working Conditions, Quality and Economy in Civil Engineering Tunnelling. *Procs. 8th Int. Symp. on Automation and Robotics in Construction*, Stuttgart, Germany, 85-94.

Maidl, B.R. and Sommavilla, P. (1995) Equipment for the Production of Sprayed Concrete. *Sprayed Concrete - Properties, Design and Application*, eds. Austin, S.A. and Robins, P.J., Whittles Publishing, Caithness, 171-203.

Maidl, B.R. and Feyerabend, B. (1995) Technical and Economical Aspects Concerning Shotcreting in Tunnels. Proc. Engineering Foundation Conference *Shotcrete for Underground Support VII*, ASCE, Telfs, Austria, 1-18.

Malmberg, B. (1993) Shotcrete for Rock support: a Summary Report on the State of the Art in 15 Countries. *Tunnelling and Underground Space Technology*, Vol. 8, No. 4, 441-470.

Mandel, J.A. (1985) Micromechanical Modelling of Steel Fiber Reinforced Cementitious Materials. *Steel Fibre Concrete*, eds. Shah, S.P. and Skarendahl, A., Swedish Cement and Concrete Research Institute, Stockholm, 219-255.

Mandel, J.A., Wei, S., and Said, S. (1987) Studies of the Properties of the Fiber-Matrix Interface in Steel Fiber Reinforced Mortar. *ACI Materials Journal*, Vol. 84, March-April, 101-109.

Mangat, P.S. and Gurusamy, K. (1987) Flexural Strength of Steel fibre-Reinforced Cement Composites. *Journal of Material Science*, Vol. 22, 3103-3110.

Measurements Group (1992) *Student manual for Strain Gage Technology*, Bulletin 309D, Measurements Group Inc., Hampshire, UK.

Melbye, T.A. (1993) New Advanced Shotcrete Admixtures. *Procs. Int. Symp. On Sprayed Concrete*, Norwegian Concrete Association, Fagernes, Norway, 233-249.

Melbye, T.A. (1994) *Shotcrete for Rock Support*, 2nd Edition, MBT Europe (MAC spa).

Melbye, T.A. (1995) Internal Curing. Proc. Engineering Foundation Conference *Shotcrete for Underground Support VII*, ASCE, Telfs, Austria, 284-290.

Melbye, T.A., Opsahl, O. and Holtman, J. (1995) Shotcrete for Rock Support. *Sprayed Concrete - Properties, Design and Application*, eds. Austin, S.A. and Robins, P.J., Whittles Publishing, Caithness, 317-356.

Miller, D. (1995) Site Safety. *Sprayed Concrete - Properties, Design and Application*, eds. Austin, S.A. and Robins, P.J., Whittles Publishing, Caithness, 266-275.

Mobasher, B. and Shah, P.S. (1989) Test Parameters for Evaluating Toughness of Glass-Fiber Reinforced Concrete Panels. *ACI Materials Journal*, Vol. 86, No. 5, 448-458.

Moens, J. and Nemeeger, D. (1991) Designing Fiber reinforced Concrete Based on Toughness Characterisation. *Concrete International*, Vol. 13, No. 11, 38-43.

Morgan, D.R. (1988) Dry-Mix Silica Fume Concrete in Western Canada. *Concrete International*, Vol. 10, No. 1, 24-32.

Morgan, D.R. (1991) Steel Fiber Reinforced Shotcrete for Support of Underground Openings in Canada. *Concrete International*, Vol. 13, No. 11, 56-64.

Morgan, D.R. (1991a) High Early Strength Blended-Cement Wet-Mix Shotcrete, *Concrete International*, Vol. 13, No. 5, 35-39.

Morgan, D.R. (1992) New Developments in Shotcrete for Repairs and Rehabilitation. *Proc. of Int. Conf. on Advances in Concrete Technology*, Athens, 699-739.

Morgan, D.R. (1995) Special Sprayed Concretes. *Sprayed Concrete - Properties, Design and Application*, eds. Austin, S.A. and Robins, P.J., Whittles Publishing, Caithness, 229-265.

Morgan, D.R., Chen, L. and Beaupre, D. (1995) Toughness of Fiber Reinforced Shotcrete. Proc. Engineering Foundation Conference *Shotcrete for Underground Support VII*, ASCE, Telfs, Austria, 66-87.

Naaman, A.E. and Shah, S.P. (1975) Bond Studies on Orientated and Aligned Steel Fibres. *Fibre Reinforced Cement and Concrete*, RILEM Symposium, Construction Press Ltd., Lancaster, 171-178.

Naaman, A.E. and Shah, S.P. (1976) Pull-Out Mechanism in Steel Fiber-Reinforced Concrete. *Journal of the Structural Division*, ASCE, Vol. 102, August, 1537-1548.

Naaman, A.E. and Najm, H. (1991) Bond-Slip of Steel Fibers in Concrete. *ACI Materials Journal*, Vol. 88, No. 2, 135-145.

Naaman, A.E., Namur, G.G., Alwan, J.M., and Najm, H.S. (1991) Fiber Pullout and Bond Slip. Part I: Analytical Study. *Journal of Structural Engineering*, Vol. 117, No. 9, 2769-2790.

Naaman, A.E., Namur, G.G., Alwan, J.M., and Najm, H.S. (1991a) Fiber Pullout and Bond Slip. Part II: Experimental Validation. *Journal of Structural Engineering*, Vol. 117, No. 9, 2790-2800.

Nammur, G. and Naaman, A.E. (1989) Bond Stress Model for Fiber Reinforced Concrete Based on Bond Stress-Slip Relationship. *ACI Materials Journal*, Vol. 86, No. 1, 45-57.

Narayanan, R. and Kareen-Palanjian, A.S. (1986) Factors Influencing the Strength of Steel Fibre Reinforced Concrete. *Developments in Fibre Reinforced Cement and Concrete -Volume 1*, RILEM, Swarmy *et al.* (eds.), Paper 3.1.

Nemegeer, D.E. (1996) Design Guidelines for Dramix® Steel Wire Fibre Reinforced Concrete. *The Indian Concrete Journal*, October, 575-584.

Nemegeer, D.E. and Tatnall, P.C. (1995) Measuring Toughness Characteristics of SFRC - A Critical View of ASTM C1018. *Testing of Fiber Reinforced Concrete*, SP155-4, ACI, Detroit, 77-91.

Neville, A.M. (1995) *Properties of Concrete*, 4th Edition. Longman Scientific and Technical, Harlow, England.

Norwegian Concrete Association (1993) *Sprayed Concrete for Rock Support - Technical Specification and Guidelines*. Norsk Betongforening (NB), Publication No. 7.

Okada, T. (1995) Innovative Shotcreting in Japan. Proc. Engineering Foundation Conference *Shotcrete for Underground Support VII*, ASCE, Telfs, Austria, 117-126.

Ono, K. (1996) Health and Safety in Shotcreting. *Tunnelling and Underground Space Technology*, Vol. 11, No. 4, 391-409.

Oplinger, D.W. (1982) Application of Moire Methods to Evaluation of Structural Performance of Composite Materials. *Optical Engineering*, Vol. 21, No. 4, 626-632.

Opsahl, O.A. and Buhre, K.E. (1985) Why Wet Process Steel Fibre Reinforced Shotcrete? *Steel Fibre Concrete*, eds. Shah, S.P. and Skarendahl, A., Swedish Cement and Concrete Research Institute, Stockholm, 51-65.

Overlie, F.E. and Rippentropp, G. (1987) Steel Fiber Microsilica Shotcrete with Remote Controlled Equipment. *Rapid Excavation and Tunnelling Conference Proceedings - Volume 2*, eds. Jacobs, J.M. and Hendricks, R.S., Society of Mining Engineers, Colorado, 351-370.

Pacios, A. and Shah, S.P. (1995) Measurement of the Pull-Out Force at Different Rates of Loading. *Testing of Fiber Reinforced Concrete*, SP155-10, ACI, Detroit, 189-216.

Parker, D.G. (1985) Microsilica Concrete - Part 1 - The Material. *Concrete*, October, 21-22.

Parker, D.G. (1986) Microsilica Concrete - Part 2 - In Use, *Concrete*, March, 19-21.

Parks, V.J. (1982) Strain Measurement Using Grids. *Optical Engineering*, Vol. 21, No. 4, 633-639.

Payton, L. (1997) *Distribution and Orientation of Steel Fibres in a Sprayed Concrete Mix*, B.Eng. Final Year Report, Loughborough University.

Phillips, D.V. and Binsheng, Z. (1993) Direct Tension Tests on Notched and Un-Notched Plain Concrete Specimens. *Magazine of Concrete Research*, Vol. 45, No. 162, 25-35.

Pinchin, D.J. and Tabor, D. (1978) Interfacial Contact Pressure and Frictional Stress Transfer in Steel Fibre Cement. *Proceedings of the RILEM Symposium 1978*, Swarmy, R.N. (ed.), The Construction Press, Lancaster, England, 337-344.

Pompo, A., Stupak, P.R., Nicolais, L. and Marchese, B. (1996) Analysis of Steel Fibre Pull-Out from a Cement Matrix Using Video Photography. *Cement & Concrete Composites*, Vol. 18, 3-8.

Prat, E. and Frouin, L. (1996) New Liquid Alkali-Free Setting Agent: A Step Forward in Sprayed Concrete Technology. *Procs. of the 2nd International Symposium on Sprayed Concrete*, Norwegian Concrete Association, Gol, Norway, 269-276.

Purkiss, J.A. and Blagojevic, P.B. (1993) Comparison Between the Short and Long Term Behaviour of Fibre Reinforced and Un-reinforced Concrete Beams. *Composite Structures*, Vol. 25, 45-49.

Ramakrishnan, V. (1985) Steel Fibre Reinforced Shotcrete - A State of the Art Report. *Steel Fibre Concrete*, eds. Shah, S.P. and Skarendahl, A., Swedish Cement and Concrete Research Institute, Stockholm, 7-24.

Ramakrishnan, V., Coyle, W.V., Dahl, L.F. and Schrader, E.K. (1981) A Comparative Evaluation of Fiber Shotcretes. *Concrete International*, January, 59-69.

Ramakrishnan, V., Yalamanchi, S.S. and Kakodkar, S. (1994) Parameters Influencing the Flexural Toughness of Steel Fibre Reinforced Concrete. National Science Foundation (USA), *Proc. of Workshop on Fibre Reinforced Cement and Concrete*, Sheffield, July, 181-193.

Rastogi, P.K. and Denarie, E. (1994) Measurement of the Length of Fracture Process Zone in Fiber-Reinforced Concrete Using Holographic Moire. *Experimental Techniques*, July-August, 11-17.

RILEM Committee 50 - Fracture Mechanics of Concrete (1985) Determination of the Fracture Energy of Mortar and Concrete by Means of Three-Point Bend Tests on Notched Beams. *Materials and Structures*, Vol. 18, No. 106, 285-290.

Robins, P.J. (1995) Materials. *Sprayed Concrete - Properties, Design and Application*, eds. Austin, S.A. and Robins, P.J., Whittles Publishing, Caithness, 7-15.

Robins, P.J. (1995a Physical Properties. *Sprayed Concrete - Properties, Design and Application*, eds. Austin, S.A. and Robins, P.J., Whittles Publishing, Caithness, 52-86.

Robins, P.J. and Austin, S.A. (1985) Sprayed Steel Fibre Concrete: Part 2. *Concrete*, Vol. 19, No. 4, 18-20.

Robins, P.J., Austin, S.A. and Jones, P.A. (1996) Flexural Strength Modelling of Steel Fibre Reinforced Sprayed Concrete. *Sprayed Concrete Technology*, E & FN Spon, London, 107-114.

Romualdi, J.P. and Mandel, J.A. (1964) Tensile Strength of Concrete Affected by Uniformly Distributed and Closely Spaced Short Lengths of Wire Reinforcement. *Journal of the American Concrete Institute*, June, 657-670.

Sakai, M. and Nakamura, N. (1986) Analysis of Flexural Behaviour of Steel Fibre reinforced Concrete. *Developments in Fibre Reinforced Cement and Concrete -Volume 1*, RILEM, edited by R.N. Swarmy *et al.*, Paper 1.4.

Schmidt, M. (1995) Research and Latest Developments of Materials for Shotcreting. Proc. Engineering Foundation Conference *Shotcrete for Underground Support VII*, ASCE, Telfs, Austria, 45-52.

Sevenhuijsen, P.J. (1993) The Photonical, Pure Grid Method. *Optics and Lasers in Engineering*, Vol. 18, 173-194.

Sevenhuijsen, P.J., Sirkis, J.S. and Bremand, F. (1993) Current Trends in Obtaining Deformation Data from Grids. *Experimental Techniques*, May-June, 22-26.

Shah, S.P. (1990) Fracture Toughness of High-Strength Concrete. *ACI Materials Journal*, Vol. 87. May-June, 260-265.

Shah, S.P. and Ouyang, C. (1992) Mechanical Behaviour of Fiber-Reinforced Cement-Based Composites. *Journal of the American Ceramic Society*, Vol. 74, No. 11, 2727-38 & 2947-53.

Shah, S.P, Stroeven, P., Dalhuisen, D. and Stekelenburg, P. (1978) Complete Stress-Strain Curves for Steel Fibre Reinforced Concrete in Uniaxial Tension and Compression. *Proceedings of the RILEM Symposium 1978*, edited by R.N. Swarmy, The Construction Press, Lancaster, England, 399-408.

Sirkis, J.S. (1990) System Response to Automated Grid Methods. *Optical Engineering*, Vol. 29, No. 12, 1485-1493.

Sirkis, J.S. and Taylor, C.E. (1990) Displacement Pattern Matching and Boundary-Element Methods for Elastic-Plastic Stress Analysis. *Experimental Mechanics*, March, 26-33.

Sirkis, J.S. and Lim, T.J. (1991) Displacement and Strain Measurement with Automated Grid Methods. *Experimental Mechanics*, December, 382-388.

Soroushian, P. and Lee, C.D. (1989) Constitutive Modelling of Steel Fiber Reinforced Concrete Under direct Tension and Compression. *Fibre Reinforced Cement and Composites*, eds. R.N. Swarmy and B. Barr, Elsevier Applied Science, London, UK, 363-377.

Soroushian, P. and Lee, C.D. (1990) Distribution and Orientation of Fibers in Steel Fiber Reinforced Concrete. *ACI Materials Journal*, Vol. 87, No. 5, 433-439.

Soroushian, P. and Bayasi, Z. (1991) Fiber-Type Effects on the Performance of Steel Fiber Reinforced Concrete. *ACI Materials Journal*, Vol. 88, No. 2, 129-134.

Stang, H. (1992) Evaluation of Properties of Cementitious Fiber Composite Materials. *High Performance Fiber Reinforced Cement Composites*, edited by Reinhardt, H.W. and Naaman, A.E., RILEM, E & FN Spon, London, 388-406.

Stille, H., Holmgren, J., and Malmberg, B. (1995) Design Principles for Use When Shotcrete is the Method of Support for the Stockholm Ring Road System. Proc. Engineering Foundation Conference *Shotcrete for Underground Support VII*, ASCE, Telfs, Austria, 245-250.

Stroeven, P. (1986) Stereology of Concrete Reinforced With Short Steel Fibres. *Heron*, Vol. 31, No. 2, 15-28.

Stroeven, P. (1993) On Simulation, Image Analysis and Structural Modelling of Steel Fibre Concrete. *Advanced Technologies*, edited by Beheshti, M.R. and Zreik, K., Elsevier Science, Amsterdam, 399-404.

Stroeven, P. and Shah, S.P. (1978) Use of Radiography-image Analysis for Steel Fibre Reinforced Concrete. *Proceedings of the RILEM Symposium 1978*, edited by R.N. Swarmy, The Construction Press, Lancaster, England, 275-288.

Stroeven, P. and Stroeven, M. (1995) Stereological Characterisation of Fibre Dispersions in Concrete. *ACTA Stereol 1995*, 14/1, 5-16.

Stroeven, P., de Haan, Y.M. and Bouter, C. (1978) Pull-Out Tests of Steel Fibers. *Proceedings of the RILEM Symposium 1978*, edited by R.N. Swarmy, The Construction Press, Lancaster, England, 345-353.

Sturman, G.M., Shah, S.P. and Winter, G. (1965) Effects of Flexural Strain Gradients on Microcracking and Stress-Strain Behaviour of Concrete. *Journal of the American Concrete Institute*, July, 805-821.

Swarmy, R.N. and Mangat, P.S. (1974) A Theory for the Flexural Strength of Steel Fiber Reinforced Concrete. *Cement and Concrete Research*, Vol. 4, 313-325.

Swift, D.G. and Smith, R.B.L. (1978) The Physical Significance of the Flexural Test for Fibre Cement Composites. *Proceedings of the RILEM Symposium 1978*, edited by R.N. Swarmy, The Construction Press, Lancaster, England, 463-478.

Swoboda, G. and Moussa, A. (1994) Numerical Modelling of Shotcrete and Concrete Tunnel Linings. *Tunnels and Ground Conditions*, Salam, A. (ed.), Balkema, Rotterdam, 427-436.

Swoboda, G. and Hafez, N.M. (1995) Structural Analysis of Shotcrete in Tunnelling. Proc. Engineering Foundation Conference *Shotcrete for Underground Support VII*, ASCE, Telfs, Austria, 170-179.

Tattersall, G.H. and Urbanowicz, C.R. (1974) Bond Strength in Steel-Fibre-Reinforced Concrete. *Magazine of Concrete Research*, Vol. 26, No. 87, 105-113.

Taylor, M.R., Lyndon, F.D. and Barr, B.I.G. (1996) Toughness Characterisation of Fibre-Reinforced Concrete. *The Indian Concrete Journal*, October, 525-531.

Tazawa, Y. (1995) Admixtures and Fibres for Shotcrete in Japan. Proc. Engineering Foundation Conference *Shotcrete for Underground Support VII*, ASCE, Telfs, Austria, 127-136.

Toutanji, H.A. and El-Korchi, T. (1994) Uniaxial Tensile Strength of Cementitious Composites. *Journal of Testing and Evaluation*, ASTM, Vol. 22, No. 3, 226-232.

Vandewalle, M. (1990) *Tunnelling the World.* N.V. Bekaert S.A., Zwevegem, Belgium.

Vandewalle, M. (1993) Steel Fibre Reinforced Shotcrete Design. Proc. Engineering Foundation Conference *Shotcrete for Underground Support VI*, ASCE, Niagara, Canada, 99-109.

Vervaeke, K. and Moyson, D. (1996) Shotcrete Applications with Steel Fibers. *The Indian Concrete Journal*, October, 544-548.

Wang, Y., Li, V.C. and Backer, S. (1988) Modelling of Fibre Pull-Out From a Cement Matrix. *International Journal of Cement Composites and Lightweight Concrete*, Vol. 10, No. 3, 143-149.

Ward, R.J. and Li, V.C. (1990) Dependence of Flexural Behaviour of Fiber Reinforced Mortar on Material Fracture resistance and Beam Size. *ACI Materials Journal*, Vol.87, No. 6, 627-637.

Wecharatana, M., and Shah, S.P. (1983) A Model for Predicting Fracture Resistance of Fiber Reinforced Concrete. *Cement and Concrete Research*, Vol. 13, 819-829.

Wei, S., Mandel, J.A. and Said, S. (1986) Study of the Interface Strength in Steel Fibre-Reinforced Cement-Based Composites. *ACI Journal*, Vol. 83, July-August, 597-605.

References

Wolsiefer, J. and Morgan, D.R. (1993) Silica Fume in Concrete. *Concrete International*, Vol. 15, No. 4, 34-39.

Wood, D.F. (1990) Design and Uses of Reinforced Shotcrete in Underground Projects in Canada. Proc. Engineering Foundation Conference *Shotcrete for Underground Support V*, ASCE, Uppsala, Sweden, 10-26.

Zangerle, D. (1996) Modern and Advanced Equipment for Ecological Use of Wet Mix Sprayed Concrete. *Procs. of the 2nd International Symposium on Sprayed Concrete*, Norwegian Concrete Association, Gol, Norway, 316-330.

APPENDIX I

FLEXURAL TOUGHNESS TEST RESULTS

				EFNARC		Residual strength (MPa)				
Ref.	Fibre content (kg/m3)	Beam depth (mm)	specimen	Deflection at flexural strength (mm)	Flexural strength (Mpa)	0.5mm	1mm	2mm	4mm	failure mode
U/1	0	75	1	0.12	4.8	0.5	0.0	0.0	0.0	SINGLE CRACK
			2	0.10	4.6	0.3	0.0	0.0	0.0	SINGLE CRACK
			3	0.13	4.9	0.5	0.0	0.0	0.0	SINGLE CRACK
			average	**0.12**	**4.8**	**0.4**	**0.0**	**0.0**	**0.0**	
			stan. dev.	0.02	0.2	0.1	-	-	-	
			c.o.v (%)	13.02	3.2	26.6	-	-	-	
U/2	40	75	1	0.10	4.8	3.5	3.6	3.0	2.5	SINGLE CRACK
			2	0.14	5.2	4.0	4.3	4.0	3.2	SINGLE CRACK
			3	0.14	5.5	4.2	4.5	4.2	3.0	SINGLE CRACK
			average	**0.13**	**5.2**	**3.9**	**4.1**	**3.7**	**2.9**	
			stan. dev.	0.02	0.4	0.4	0.5	0.7	0.4	
			c.o.v (%)	16.10	6.9	9.6	11.4	17.5	12.4	
U/3	80	75	1	0.20	5.8	5.0	5.0	6.0	4.0	SINGLE CRACK
			2	0.20	6.2	6.9	7.1	6.0	4.2	TWO CRACKS
			3	0.17	6.5	7.1	7.4	7.4	5.9	MULTIPLE CRACKS
			average	**0.19**	**6.2**	**6.3**	**6.5**	**6.5**	**4.7**	
			stan. dev.	0.01	0.3	1.1	1.3	0.8	1.0	
			c.o.v (%)	7.69	5.5	18.1	20.2	13.0	22.2	
U/4	120	75	1	0.25	6.6	7.4	7.6	6.7	5.5	SINGLE CRACK
			2	0.25	7.0	8.1	9.2	8.4	5.0	MULTIPLE CRACKS
			3	0.22	6.6	7.5	8.4	7.0	4.0	MULTIPLE CRACKS
			average	**0.24**	**6.7**	**7.7**	**8.4**	**7.4**	**4.8**	
			stan. dev.	0.02	0.2	0.4	0.8	0.9	0.8	
			c.o.v (%)	6.28	3.3	4.9	9.9	12.7	15.8	

Table I.1 Cast 75mm deep unnotched beams (Matrix C)

				EFNARC		Residual strength (MPa)				
Ref.	Fibre content (kg/m3)	Beam depth (mm)	specimen	Deflection at flexural strength (mm)	Flexural strength (Mpa)	0.5mm	1mm	2mm	4mm	failure mode
U/5	0	75	1	0.14	5.2	0.5	0.0	0.0	0.0	SINGLE CRACK
			2	0.13	4.8	0.4	0.0	0.0	0.0	SINGLE CRACK
			3	0.10	4.5	0.5	0.0	0.0	0.0	SINGLE CRACK
			average	**0.12**	**4.8**	**0.5**	**0.0**	**0.0**	**0.0**	
			stan. dev.	0.02	0.4	0.1	-	-	-	
			c.o.v (%)	14.65	7.8	13.7	-	-	-	
U/6	40	75	1	0.14	5.0	4.2	4.3	3.6	2.4	SINGLE CRACK
			2	0.13	5.1	3.1	3.3	2.9	2.3	SINGLE CRACK
			3	0.15	5.4	4.4	4.7	4.3	3.2	SINGLE CRACK
			average	**0.14**	**5.2**	**3.9**	**4.1**	**3.6**	**2.7**	
			stan. dev.	0.01	0.2	0.7	0.7	0.7	0.5	
			c.o.v (%)	7.97	3.9	17.8	17.3	18.4	17.0	
U/7	80	75	1	0.16	5.9	6.7	6.5	5.8	4.1	SINGLE CRACK
			2	0.16	5.9	6.7	7.1	6.8	5.6	MULTIPLE CRACKS
			3	0.15	5.7	6.6	7.4	7.3	5.1	TWO CRACKS
			average	**0.16**	**5.9**	**6.7**	**7.0**	**6.6**	**4.9**	
			stan. dev.	0.01	0.1	0.1	0.4	0.8	0.8	
			c.o.v (%)	3.83	2.0	1.3	5.9	11.3	15.9	
U/8	120	75	1	0.23	7.0	7.6	8.1	6.9	5.6	MULTIPLE CRACKS
			2	0.20	6.6	7.6	7.1	6.4	4.2	TWO CRACKS
			3	0.17	6.5	7.6	8.6	8.5	6.3	MULTIPLE CRACKS
			average	**0.20**	**6.7**	**7.6**	**7.9**	**7.3**	**5.4**	
			stan. dev.	0.03	0.3	0.0	0.8	1.1	1.1	
			c.o.v (%)	14.30	3.8	0.5	9.8	14.8	19.8	

Table I.2 Cast 75mm deep unnotched beams (Matrix B)

				EFNARC		Residual strength (MPa)				
Ref.	Fibre content (kg/m3)	Beam depth (mm)	specimen	Deflection at flexural strength (mm)	Flexural strength (Mpa)	0.5mm	1mm	2mm	4mm	failure mode
U/9	0	75	1	0.08	3.6	0.2	0.0	0.0	0.0	SINGLE CRACK
			2	0.10	3.6	0.5	0.0	0.0	0.0	SINGLE CRACK
			3	0.10	3.9	0.2	0.0	0.0	0.0	SINGLE CRACK
			average	**0.10**	**3.7**	**0.3**	**0.0**	**0.0**	**0.0**	
			stan. dev.	0.01	0.2	0.2	-	-	-	
			c.o.v (%)	10.54	5.2	60.3	-	-	-	
U/10	40	75	1	0.15	4.9	4.7	4.7	4.5	4.0	MULTIPLE CRACKS
			2	0.12	4.6	4.3	4.4	4.0	3.3	SINGLE CRACK
			3	0.14	4.5	4.7	4.3	3.9	2.8	SINGLE CRACK
			average	**0.14**	**4.6**	**4.6**	**4.5**	**4.1**	**3.4**	
			stan. dev.	0.01	0.2	0.3	0.2	0.3	0.6	
			c.o.v (%)	10.37	4.9	5.7	4.4	7.9	17.4	
U/11	80	75	1	0.20	5.0	5.6	5.7	6.0	4.4	TWO CRACKS
			2	0.24	6.0	6.6	6.8	6.3	4.7	TWO CRACKS
			3	0.14	4.9	6.1	6.5	5.6	4.0	SINGLE CRACK
			average	**0.19**	**5.3**	**6.1**	**6.3**	**6.0**	**4.4**	
			stan. dev.	0.05	0.6	0.5	0.5	0.3	0.3	
			c.o.v (%)	26.53	11.5	8.3	8.7	5.3	7.7	
U/12	120	75	1	0.19	5.3	5.1	6.0	5.9	4.7	SINGLE CRACK
			2	0.21	5.5	6.5	7.4	6.2	4.7	MULTIPLE CRACKS
			3	0.22	6.0	7.1	7.3	7.7	6.8	MULTIPLE CRACKS
			average	**0.21**	**5.6**	**6.3**	**6.9**	**6.6**	**5.4**	
			stan. dev.	0.02	0.4	1.0	0.8	0.9	1.2	
			c.o.v (%)	7.31	6.4	16.2	11.4	14.4	22.8	

Table I.3 Cast 75mm deep unnotched beams (Matrix A)

				EFNARC		Residual strength (MPa)				
Ref.	Fibre content (kg/m3)	Beam depth (mm)	specimen	Deflection at flexural strength (mm)	Flexural strength (Mpa)	0.5mm	1mm	2mm	4mm	failure mode
U/15	40	50	1	0.16	4.1	4.2	4.1	2.8	2.2	SINGLE CRACK
			2	0.12	3.8	3.8	4.0	4.2	4.0	SINGLE CRACK
			3	-	-	-	-	-	-	TEST ABORTED
			average	**0.14**	**4.0**	**4.0**	**4.1**	**3.5**	**3.1**	
			stan. dev.	0.03	0.2	0.3	0.1	1.0	1.2	
			c.o.v (%)	18.19	6.0	7.8	2.5	29.8	39.6	
U/19	40	100	1	0.09	4.1	3.1	3.0	2.8	1.9	SINGLE CRACK
			2	0.08	4.4	4.5	4.6	4.0	2.9	TWO CRACKS
			3	0.07	4.0	3.4	3.3	3.0	2.2	SINGLE CRACK
			average	**0.08**	**4.2**	**3.7**	**3.6**	**3.3**	**2.3**	
			stan. dev.	0.01	0.2	0.8	0.9	0.6	0.5	
			c.o.v (%)	10.46	5.1	21.1	23.8	19.8	22.2	
U/16	80	50	1	0.27	5.5	5.4	5.8	6.2	5.7	SINGLE CRACK
			2	0.24	5.0	5.8	5.2	4.8	4.1	SINGLE CRACK
			3	-	-	-	-	-	-	TEST ABORTED
			average	**0.25**	**5.3**	**5.6**	**5.5**	**5.5**	**4.9**	
			stan. dev.	0.02	0.3	0.3	0.4	1.0	1.1	
			c.o.v (%)	8.80	6.0	5.5	8.1	18.0	22.9	
U/20	80	100	1	0.14	5.0	5.6	6.0	5.3	3.2	TWO CRACKS
			2	0.13	4.6	5.2	5.9	5.5	3.5	MULTIPLE CRACKS
			3	0.08	4.2	5.8	6.2	5.3	3.3	TWO CRACKS
			average	**0.12**	**4.6**	**5.5**	**6.0**	**5.4**	**3.3**	
			stan. dev.	0.03	0.4	0.3	0.2	0.1	0.2	
			c.o.v (%)	25.38	9.3	5.6	2.8	2.7	6.0	

Table I.4 Cast 50mm and 100mm deep unnotched beams (Matrix A)

				EFNARC		Residual strength (MPa)				
Ref.	Fibre content (kg/m3)	Beam depth (mm)	specimen	Deflection at flexural strength (mm)	Flexural strength (Mpa)	0.5mm	1mm	2mm	4mm	failure mode
U/13	40	50	1	0.27	4.4	3.2	3.0	2.9	2.9	SINGLE CRACK
			2	0.25	4.3	3.9	3.8	4.2	3.5	SINGLE CRACK
			3	0.26	4.6	4.1	3.9	4.1	3.0	SINGLE CRACK
			average	**0.26**	**4.4**	**3.7**	**3.6**	**3.7**	**3.1**	
			stan. dev.	0.01	0.1	0.5	0.5	0.7	0.3	
			c.o.v (%)	3.74	3.2	13.5	13.6	18.4	10.7	
U/14	80	50	1	-	-	-	-	-	-	TEST ABORTED
			2	0.32	5.8	6.4	6.8	7.7	6.8	MULTIPLE CRACKS
			3	0.30	5.3	5.6	6.3	6.6	5.4	SINGLE CRACK
			average	**0.31**	**5.5**	**6.0**	**6.6**	**7.1**	**6.1**	
			stan. dev.	0.01	0.3	0.6	0.3	0.8	0.9	
			c.o.v (%)	4.33	6.0	9.2	5.3	11.0	15.3	
U/17	40	100	1	0.11	5.3	5.3	4.0	3.3	2.3	TWO CRACKS
			2	0.09	4.6	4.7	5.1	4.3	3.1	ONE CRACK
			3	0.12	4.7	3.9	4.2	3.8	2.7	ONE CRACK
			average	**0.11**	**4.9**	**4.6**	**4.4**	**3.8**	**2.7**	
			stan. dev.	0.02	0.4	0.7	0.6	0.5	0.4	
			c.o.v (%)	14.35	7.9	14.5	13.1	13.7	14.5	
U/18	80	100	1	0.11	5.1	5.4	5.6	4.5	2.7	TWO CRACK
			2	0.13	5.3	6.0	6.7	6.5	3.8	ONE CRACK
			3	0.15	6.0	6.3	6.5	5.4	3.2	ONE CRACK
			average	**0.13**	**5.5**	**5.9**	**6.3**	**5.4**	**3.3**	
			stan. dev.	0.02	0.4	0.4	0.6	1.0	0.5	
			c.o.v (%)	17.61	7.9	7.5	9.8	18.1	16.4	

Table I.5 Cast 50mm and 100mm deep unnotched beams (Matrix C)

				EFNARC		Residual strength (MPa)				
Ref.	Fibre content (kg/m3)	Beam depth (mm)	specimen	Deflection at flexural strength (mm)	Flexural strength (Mpa)	0.5mm	1mm	2mm	4mm	failure mode
S/1	0	75	1	0.11	4.0	0.5	0.1	0.0	0.0	SINGLE CRACK
	0	75	2	0.14	4.2	0.2	0.0	0.0	0.0	SINGLE CRACK
	0	75	3	0.12	4.0	0.4	0.1	0.0	0.0	SINGLE CRACK
	0	**75**	**average**	**0.12**	**4.1**	**0.4**	**0.1**	**0.0**	**0.0**	
			stan. dev.	0.01	0.1	0.2	-	-	-	
			c.o.v (%)	9.70	2.3	46.0	-	-	-	
S/2	32	75	1	0.13	5.0	3.2	2.6	1.8	1.2	ONE CRACK
	21	75	2	-	-	-	-	-	-	ACKED OUTSIDE MIDDLE THIRD
	26	75	3	0.18	4.7	3.7	3.4	2.4	1.7	ONE CRACK
	29	**75**	**average**	**0.16**	**4.8**	**3.5**	**3.0**	**2.1**	**1.4**	
			stan. dev.	0.03	0.2	0.3	0.6	0.4	0.4	
			c.o.v (%)	19.29	4.3	9.3	19.8	20.4	25.7	
S/3	71	75	1	-	-	-	-	-	-	TEST ABORTED
	63	75	2	0.16	5.3	6.3	5.8	2.8	1.5	TWO CRACKS
	64	75	3	0.17	6.1	6.8	7.2	4.7	2.3	MULTIPLE CRACKS
	63.5	**75**	**average**	**0.16**	**5.7**	**6.6**	**6.5**	**3.7**	**1.9**	
			stan. dev.	0.00	0.6	0.3	1.0	1.3	0.6	
			c.o.v (%)	2.42	10.1	5.2	15.7	34.8	31.5	

Table I.6 Sprayed 75mm deep beams (Matrix C)

				EFNARC		Residual strength (MPa)				
Ref.	Fibre content (kg/m3)	Beam depth (mm)	specimen	Deflection at flexural strength (mm)	Flexural strength (Mpa)	0.5mm	1mm	2mm	4mm	failure mode
S/4	59	75	1	0.19	5.1	5.6	4.5	2.7	1.9	TWO CRACKS
	53	75	2	0.17	4.9	4.9	4.4	2.8	2.0	ONE CRACK
	47	75	3	0.15	5.3	4.8	5.2	3.6	2.1	TWO CRACKS
	53	**75**	**average**	**0.17**	**5.1**	**5.1**	**4.7**	**3.0**	**2.0**	
			stan. dev.	0.02	0.2	0.4	0.5	0.5	0.1	
			c.o.v (%)	11.06	4.4	8.0	10.0	15.3	4.6	
S/5	68	75	1	0.18	5.0	5.0	4.8	3.7	2.4	MULTIPLE CRACKS
	63	75	2	0.22	5.0	3.4	3.2	1.9	1.0	ONE CRACK
	63	75	3	0.21	5.1	5.3	5.0	3.8	2.4	ONE CRACK
	65	**75**	**average**	**0.20**	**5.0**	**4.5**	**4.3**	**3.1**	**1.9**	
			stan. dev.	0.02	0.1	1.0	0.9	1.1	0.8	
			c.o.v (%)	10.01	1.5	22.8	21.9	34.8	40.1	
S/6	62	75	1	0.19	4.4	4.7	5.0	5.1	3.8	TWO CRACKS
	56	75	2	-	-	-	-	-	-	TEST ABORTED
	49	75	3	0.19	3.9	4.4	4.1	3.9	3.0	ONE CRACK
	56	**75**	**average**	**0.19**	**4.1**	**4.6**	**4.5**	**4.5**	**3.4**	
			stan. dev.	0.00	0.3	0.2	0.6	0.8	0.5	
			c.o.v (%)	1.31	7.7	4.6	12.8	17.5	15.9	

Table I.7 Sprayed 75mm deep beams (Matrix B & A)

				EFNARC		Residual strength (MPa)				Crack mouth opening displacement (mm)					
Ref.	Fibre content (kg/m3)	Beam depth (mm)	specimen	Deflection at flexural strength (mm)	Flexural strength (Mpa)	0.5mm	1mm	2mm	4mm	CMOD at flexural strength (mm)	0.5mm	1mm	2mm	4mm	failure mode
N/1	0	85	1	0.10	4.5	0.4	0.0	0.0	0.0	0.03	0.40	1.00	-	-	SINGLE CRACK
			2	0.09	4.5	0.3	0.0	0.0	0.0	0.03	0.42	0.90	-	-	SINGLE CRACK
			3	0.10	4.8	0.5	0.0	0.0	0.0	0.03	0.47	0.96	-	-	SINGLE CRACK
			average	**0.10**	**4.6**	**0.4**	**0.0**	**0.0**	**0.0**	**0.03**	**0.43**	**0.95**	**-**	**-**	
			stan. dev.	0.00	0.2	0.1	-	-	-	0.00	0.04	0.05	-	-	
			c.o.v (%)	0.84	4.1	22.2	-	-	-	5.69	8.70	5.26	-	-	
N/2	40	85	1	0.12	5.4	5.7	6.0	5.7	-	0.04	0.43	0.93	1.80	-	SINGLE CRACK
			2	0.09	4.6	4.5	4.5	4.0	-	0.03	0.38	0.81	1.70	-	SINGLE CRACK
			3	0.10	4.9	5.3	5.7	5.5	-	0.03	0.36	0.78	1.68	-	SINGLE CRACK
			average	**0.10**	**5.0**	**5.2**	**5.4**	**5.1**	**-**	**0.04**	**0.39**	**0.84**	**1.73**	**-**	
			stan. dev.	0.02	0.4	0.7	0.8	0.9	-	0.01	0.04	0.08	0.07	-	
			c.o.v (%)	15.54	7.7	12.7	14.8	18.3	-	18.30	9.37	9.00	3.83	-	
N/3	80	85	1	-	-	-	-	-	-	-	-	-	-	-	DID NOT CRACK AT NOTCH
			2	0.22	7.2	7.4	7.6	6.5	-	0.09	0.35	0.85	1.67	-	SINGLE CRACK
			3	0.20	6.0	6.9	7.2	5.9	-	0.09	0.30	0.75	1.63	-	SINGLE CRACK
			average	**0.21**	**6.6**	**7.2**	**7.4**	**6.2**	**-**	**0.09**	**0.33**	**0.80**	**1.65**	**-**	
			stan. dev.	0.01	0.9	0.4	0.3	0.4	-	0.00	0.04	0.07	0.03	-	
			c.o.v (%)	7.23	13.1	4.9	4.2	7.1	-	1.52	10.88	8.84	1.78	-	
N/4	120	85	1	0.25	7.1	8.5	8.6	7.3	-	0.09	0.23	0.67	1.53	-	SINGLE CRACK
			2	-	-	-	-	-	-	-	-	-	-	-	TEST ABORTED
			3	0.23	7.9	9.2	9.6	8.5	-	0.09	0.21	0.60	1.50	-	SINGLE CRACK
			average	**0.24**	**7.5**	**8.8**	**9.1**	**7.9**	**-**	**0.09**	**0.22**	**0.63**	**1.51**	**-**	
			stan. dev.	0.01	0.5	0.5	0.7	0.9	-	0.00	0.01	0.05	0.02	-	
			c.o.v (%)	3.54	6.9	5.5	7.8	11.1	-	4.66	6.37	7.88	1.58	-	

Table I.8 Cast 85mm notched beams (Matrix C)

				EFNARC		Residual strength (MPa)				Crack mouth opening displacement (mm)					
Ref.	Fibre content (kg/m3)	Beam depth (mm)	specimen	Deflection at flexural strength (mm)	Flexural strength (Mpa)	0.5mm	1mm	2mm	4mm	CMOD at flexural strength (mm)	0.5mm	1mm	2mm	4mm	failure mode
N/5	0	85	1	0.08	4.7	0.5	0.0	0.0	0.0	0.02	0.40	-	-	-	SINGLE CRACK
			2	0.08	4.9	0.3	0.0	0.0	0.0	0.02	0.41	-	-	-	SINGLE CRACK
			3	0.08	4.6	0.4	0.0	0.0	0.0	0.03	0.42	-	-	-	SINGLE CRACK
			average	**0.08**	**4.7**	**0.4**	**0.0**	**0.0**	**0.0**	**0.02**	**0.41**	-	-	-	
			stan. dev.	0.00	0.2	0.1	-	-	-	0.00	0.01	-	-	-	
			c.o.v (%)	0.70	3.9	18.5	-	-	-	9.30	1.84	-	-	-	
N/6	40	85	1	0.09	4.9	5.4	5.8	5.3	4.5	0.03	0.37	0.81	1.72	3.55	SINGLE CRACK
			2	0.10	5.2	4.8	5.4	5.5	4.3	0.03	0.35	0.80	1.74	3.53	SINGLE CRACK
			3	0.09	5.2	5.5	5.2	4.8	3.6	0.02	0.34	0.86	1.98	3.87	SINGLE CRACK
			average	**0.09**	**5.1**	**5.2**	**5.4**	**5.2**	**4.1**	**0.03**	**0.36**	**0.82**	**1.81**	**3.65**	
			stan. dev.	0.01	0.2	0.4	0.3	0.4	0.5	0.00	0.01	0.03	0.15	0.19	
			c.o.v (%)	6.08	3.0	8.0	6.0	7.1	11.8	11.40	4.12	3.55	8.11	5.15	
N/7	80	85	1	0.12	5.7	7.8	6.8	6.1	3.7	0.04	0.38	0.81	1.68	3.56	SINGLE CRACK
			2	-	-	-	-	-	-	-	-	-	-	-	DID NOT CRACK AT NOTCH
			3	0.09	4.9	5.4	6.0	6.0	4.5	0.03	0.36	0.78	1.66	3.53	SINGLE CRACK
			average	**0.11**	**5.3**	**6.6**	**6.4**	**6.1**	**4.1**	**0.04**	**0.37**	**0.80**	**1.67**	**3.54**	
			stan. dev.	0.02	0.5	1.7	0.6	0.0	0.6	0.01	0.01	0.02	0.02	0.02	
			c.o.v (%)	17.64	10.1	26.3	9.0	0.5	13.9	21.02	3.43	2.34	0.97	0.64	
N/8	120	85	1	0.21	8.2	9.2	10.2	10.1	8.1	0.09	0.20	0.53	1.51	3.62	SINGLE CRACK
			2	-	-	-	-	-	-	-	-	-	-	-	DID NOT CRACK AT NOTCH
			3	0.19	6.4	7.1	7.1	6.3	4.9	0.10	0.35	0.80	1.73	3.58	SINGLE CRACK
			average	**0.20**	**7.3**	**8.2**	**8.6**	**8.2**	**6.5**	**0.09**	**0.28**	**0.67**	**1.62**	**3.60**	
			stan. dev.	0.01	1.3	1.4	2.2	2.7	2.2	0.00	0.11	0.19	0.16	0.03	
			c.o.v (%)	6.50	17.4	17.7	25.3	33.0	34.0	3.71	38.98	29.07	9.70	0.82	

Table I.9 Cast 85mm notched beams (Matrix B)

				EFNARC		Residual strength (MPa)				Crack mouth opening displacement (mm)					
Ref.	Fibre content (kg/m3)	Beam depth (mm)	specimen	Deflection at flexural strength (mm)	Flexural strength (Mpa)	0.5mm	1mm	2mm	4mm	CMOD at flexural strength (mm)	0.5mm	1mm	2mm	4mm	failure mode
N/9	0	85	1	0.07	3.0	0.5	0.0	0.0	0.0	0.03	0.38	-	-	-	SINGLE CRACK
			2	0.08	3.8	0.4	0.0	0.0	0.0	0.03	0.43	-	-	-	SINGLE CRACK
			3	0.07	3.7	0.6	0.2	0.0	0.0	0.02	0.44	0.89	-	-	SINGLE CRACK
			average	**0.07**	**3.5**	**0.5**	**0.1**	**0.0**	**0.0**	**0.03**	**0.42**	**0.89**	-	-	
			stan. dev.	0.01	0.5	0.1	0.1	-	-	0.00	0.03	-	-	-	
			c.o.v (%)	8.85	12.9	16.9	-	-	-	13.97	7.70	-	-	-	
N/10	40	85	1	0.12	4.6	5.2	5.7	5.0	3.5	0.05	0.35	0.76	1.61	3.47	SINGLE CRACK
			2	0.14	5.0	5.6	5.6	5.2	3.7	0.06	0.36	0.75	1.60	3.38	SINGLE CRACK
			3	0.14	4.7	5.0	5.1	5.2	4.1	0.06	0.34	0.75	1.62	3.34	SINGLE CRACK
			average	**0.13**	**4.7**	**5.3**	**5.4**	**5.1**	**3.8**	**0.06**	**0.35**	**0.75**	**1.61**	**3.40**	
			stan. dev.	0.01	0.2	0.3	0.3	0.1	0.3	0.01	0.01	0.00	0.01	0.07	
			c.o.v (%)	8.78	4.3	6.2	5.5	1.8	8.4	11.58	2.15	0.50	0.62	2.04	
N/11	80	85	1	0.17	5.1	5.9	6.5	6.4	5.4	0.08	0.32	0.72	1.58	3.32	SINGLE CRACK
			2	-	-	-	-	-	-	-	-	-	-	-	DID NOT CRACK AT NOTCH
			3	0.19	5.6	6.5	7.2	6.7	5.4	0.10	0.34	0.77	1.65	3.40	SINGLE CRACK
			average	**0.18**	**5.3**	**6.2**	**6.9**	**6.6**	**5.4**	**0.09**	**0.33**	**0.74**	**1.61**	**3.36**	
			stan. dev.	0.02	0.3	0.4	0.5	0.2	0.0	0.02	0.01	0.03	0.05	0.06	
			c.o.v (%)	10.40	6.5	7.0	7.3	3.6		21.54	4.11	4.25	2.91	1.72	
N/12	120	85	1	0.23	7.5	8.1	8.3	7.6	5.8	0.10	0.25	0.75	1.81	4.06	SINGLE CRACK
			2	0.21	6.3	7.8	8.4	7.5	5.8	0.101	0.30	0.57	1.57	3.55	SINGLE CRACK
			3	0.20	5.7	7.2	8.0	6.9	5.8	0.11	0.33	0.76	1.75	3.63	SINGLE CRACK
			average	**0.21**	**6.5**	**7.7**	**8.2**	**7.4**	**5.8**	**0.10**	**0.29**	**0.69**	**1.71**	**3.75**	
			stan. dev.	0.01	0.9	0.4	0.2	0.4	0.0	0.00	0.04	0.11	0.13	0.27	
			c.o.v (%)	5.36	13.9	5.8	2.6	4.8	0.6	3.92	13.78	15.23	7.40	7.25	

Table I.10 Cast 85mm notched beams (Matrix A)

				EFNARC		Residual strength (MPa)				Crack mouth opening displacement (mm)					
Ref.	Fibre content (kg/m3)	Beam depth (mm)	specimen	Deflection at flexural strength (mm)	Flexural strength (Mpa)	0.5mm	1mm	2mm	4mm	CMOD at flexural strength (mm)	0.5mm	1mm	2mm	4mm	failure mode
N/13	40	60	1	0.17	5.9	5.4	5.8	6.4	5.1	-	-	-	-	-	SINGLE CRACK
			2	0.19	5.6	5.8	6.6	6.4	6.0	-	-	-	-	-	SINGLE CRACK
			average	**0.18**	**5.8**	**5.6**	**6.2**	**6.4**	**5.6**	-	-	-	-	-	
			stan. dev.	0.01	0.2	0.3	0.6	0.0	0.6	-	-	-	-	-	
			c.o.v (%)	8.18	2.7	4.7	9.0	0.5	11.4	-	-	-	-	-	
N/14	80	60	1	0.21	6.6	7.4	8.3	9.0	7.1	-	-	-	-	-	SINGLE CRACK
			2	0.25	5.9	6.5	6.9	6.8	5.6	-	-	-	-	-	SINGLE CRACK
			average	**0.23**	**6.3**	**6.9**	**7.6**	**7.9**	**6.3**	-	-	-	-	-	
			stan. dev.	0.03	0.5	0.6	0.9	1.6	1.1	-	-	-	-	-	
			c.o.v (%)	10.97	7.2	9.1	12.4	19.9	17.4	-	-	-	-	-	

Table I.11 Cast 60mm notched beams (Matrix C)

APPENDIX II

STRAIN ANALYSIS: STRAIN GAUGE TEST RESULTS

(A) UNCRACKED BEAM DATA

(a) 0.05mm			strain gauge readings (microstrain)				
specimen reference	beam depth (mm)	fibre content (kgm-3)	sg5	sg4	sg3	sg2	sg1
sa7-1	60	40	50	-4	-30	-58	-76
sa7-2	60	40	49	-2	-32	-54	-78
sa9-1	60	80	54	4	-20	-41	-63
sa9-2	60	80	72	8	-20	-52	-76
average			**56**	**2**	**-26**	**-51**	**-73**
standard dev.			**10.7**	**5.4**	**6.3**	**7.4**	**6.7**

(b) 0.1mm			strain gauge readings (microstrain)				
specimen reference	beam depth (mm)	fibre content (kgm-3)	sg5	sg4	sg3	sg2	sg1
sa7-1	60	40	128	2	-55	-115	-151
sa7-2	60	40	106	0	-60	-100	-151
sa9-1	60	80	130	15	-37	-79	-128
sa9-2	60	80	118	9	-44	-97	-145
average			**120**	**7**	**-49**	**-98**	**-144**
standard dev.			**10.9**	**6.7**	**10.4**	**14.5**	**11.1**

Table II.1 60mm notched beams.

(a) 0.05mm			strain gauge readings (microstrain)							
specimen reference	beam depth (mm)	fibre content (kgm-3)	sg8	sg7	sg6	sg5	sg4	sg3	sg2	sg1
sa1-1	75	40	66	48	22	-1	-25	-52	-70	-86
sa1-2	75	40	77	49	19	-8	-35	-62	-87	-
sa3-1	75	80	53	34	16	-5	-24	-49	-66	-67
sa3-2	75	80	65	42	14	-10	-35	-60	-83	-87
sa4-1	75	120	74	49	23	3	-20	-41	-62	-76
sa4-2	75	120	77	50	26	3	-17	-40	-63	-82
average			**69**	**45**	**20**	**-3**	**-26**	**-51**	**-72**	**-79**
standard dev.			**9.3**	**6.1**	**4.8**	**5.3**	**7.7**	**9.4**	**10.4**	**8.2**

(b) 0.1mm			strain gauge readings (microstrain)							
specimen reference	beam depth (mm)	fibre content (kgm-3)	sg8	sg7	sg6	sg5	sg4	sg3	sg2	sg1
sa1-1	75	40	124	85	44	3	-43	-94	-129	-163
sa1-2	75	40	-	94	46	-5	-57	-106	-152	-
sa3-1	75	80	94	61	28	-9	-45	-92	-125	-
sa3-2	75	80	114	80	28	-18	-67	-117	-159	-
sa4-1	75	120	144	105	54	12	-33	-74	-118	-125
sa4-2	75	120	122	117	59	10	-30	-76	-123	-165
average			**120**	**90**	**43**	**-1**	**-46**	**-93**	**-134**	**-151**
standard dev.			**17.9**	**19.6**	**12.9**	**11.6**	**14.2**	**16.7**	**16.8**	**22.5**

Table II.2 75mm unnotched beams.

(a) 0.05mm

specimen reference	beam depth (mm)	fibre content (kgm-3)	strain gauge readings (microstrain) sg8	sg7	sg6	sg5	sg4	sg3	sg2	sg1
sa2-1	85	40	-	39	8	-16	-41	-62	-89	-
sa2-2	85	40	-	45	10	-17	-41	-67	-94	-
average			**-**	**42**	**9**	**-17**	**-41**	**-64**	**-92**	**-**
standard dev.			**-**	**4.6**	**1.5**	**0.4**	**0.1**	**3.6**	**3.3**	**-**

(b) 0.1mm

specimen reference	beam depth (mm)	fibre content (kgm-3)	strain gauge readings (microstrain) sg8	sg7	sg6	sg5	sg4	sg3	sg2	sg1
sa2-1	85	40			38	-28	-84	-132	-199	
sa2-2	85	40			59	-13	-69	-128	-190	
average			**-**	**-**	**48**	**-21**	**-77**	**-130**	**-195**	**-**
standard dev.			**-**	**-**	**14.7**	**11.0**	**10.9**	**2.8**	**6.6**	**-**

Table II.3 85mm notched beams.

(a) 0.05mm

specimen reference	beam depth (mm)	fibre content (kgm-3)	strain gauge readings (microstrain) sg8	sg7	sg6	sg5	sg4	sg3	sg2	sg1
sa8-1	100	40	126	61	30	-20	-41	-62	-79	-106
sa8-2	100	40	111	54	19	-40	-62	-80	-100	-109
sa10-1	100	80	105	59	30	-18	-37	-55	-67	-92
sa10-3	100	80	-	72	38	-13	-34	-56	-77	-98
average			**114**	**62**	**29**	**-23**	**-43**	**-63**	**-80**	**-101**
standard dev.			**10.8**	**7.3**	**8.0**	**11.7**	**12.5**	**11.3**	**13.9**	**7.9**

(b) 0.1mm

specimen reference	beam depth (mm)	fibre content (kgm-3)	strain gauge readings (microstrain) sg8	sg7	sg6	sg5	sg4	sg3	sg2	sg1
sa8-1	100	40	-	156	68	-35	-77	-119	-156	-206
sa8-2	100	40	-	136	86	-56	-108	-152	-197	-218
sa10-1	100	80	-	123	62	-37	-80	-120	-145	-195
sa10-3	100	80	-	134	78	-21	-64	-105	-144	-181
average			**-**	**137**	**74**	**-37**	**-82**	**-124**	**-161**	**-200**
standard dev.			**-**	**13.8**	**10.7**	**14.5**	**18.4**	**19.8**	**25.0**	**15.9**

Table II.4 100mm unnotched beams.

APPENDIX II

STRAIN ANALYSIS: STRAIN GAUGE TEST RESULTS

(B) CRACKED BEAM DATA

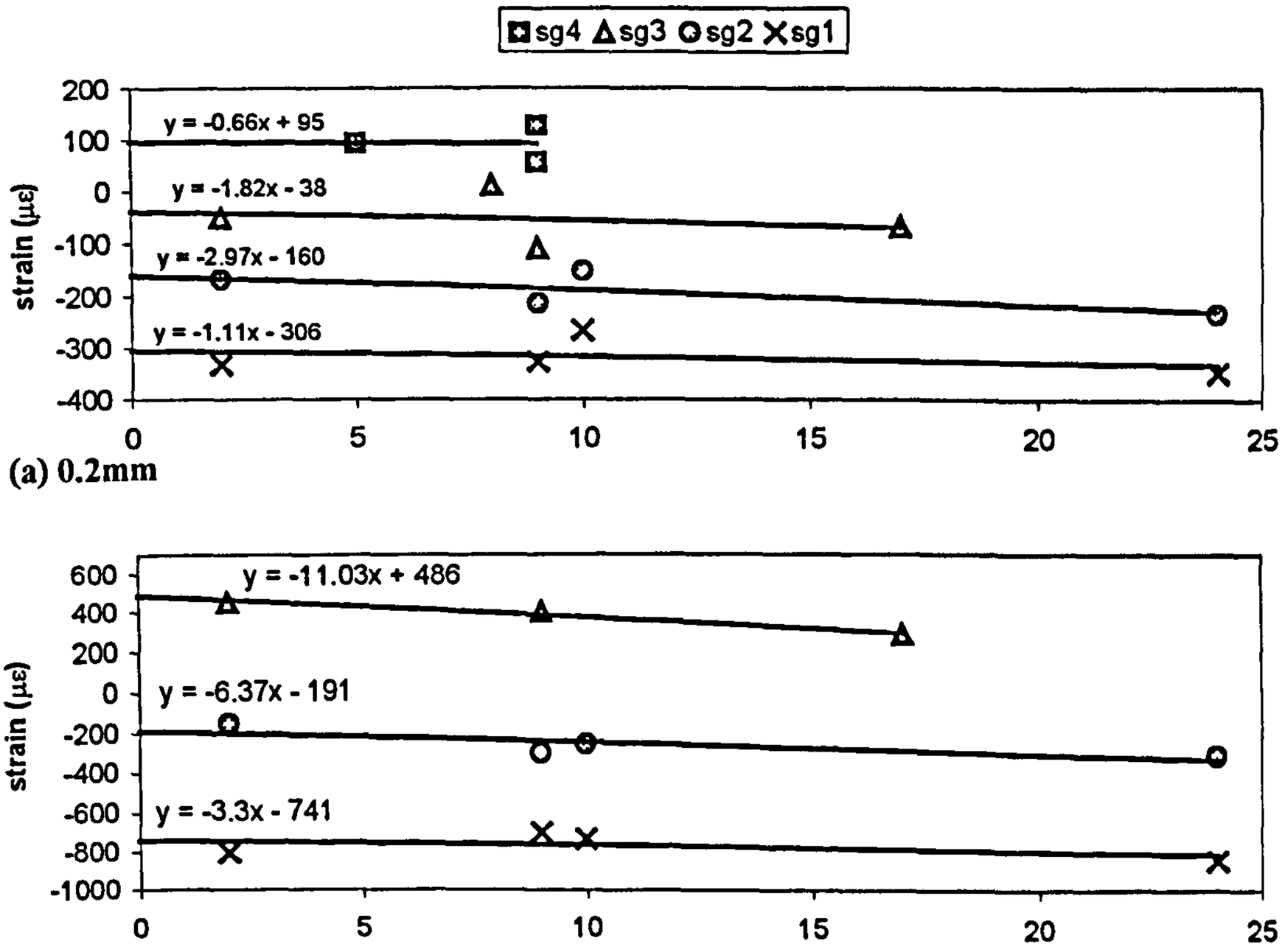

(a) 0.2mm

(b) 0.5mm

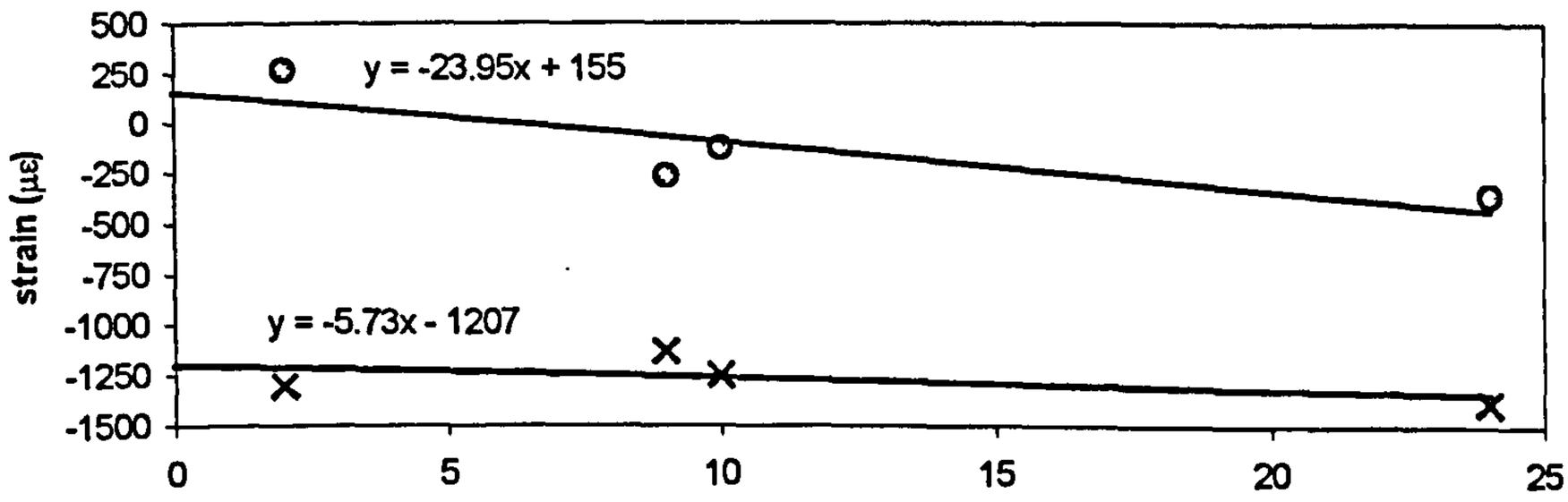

(c) 1.0mm

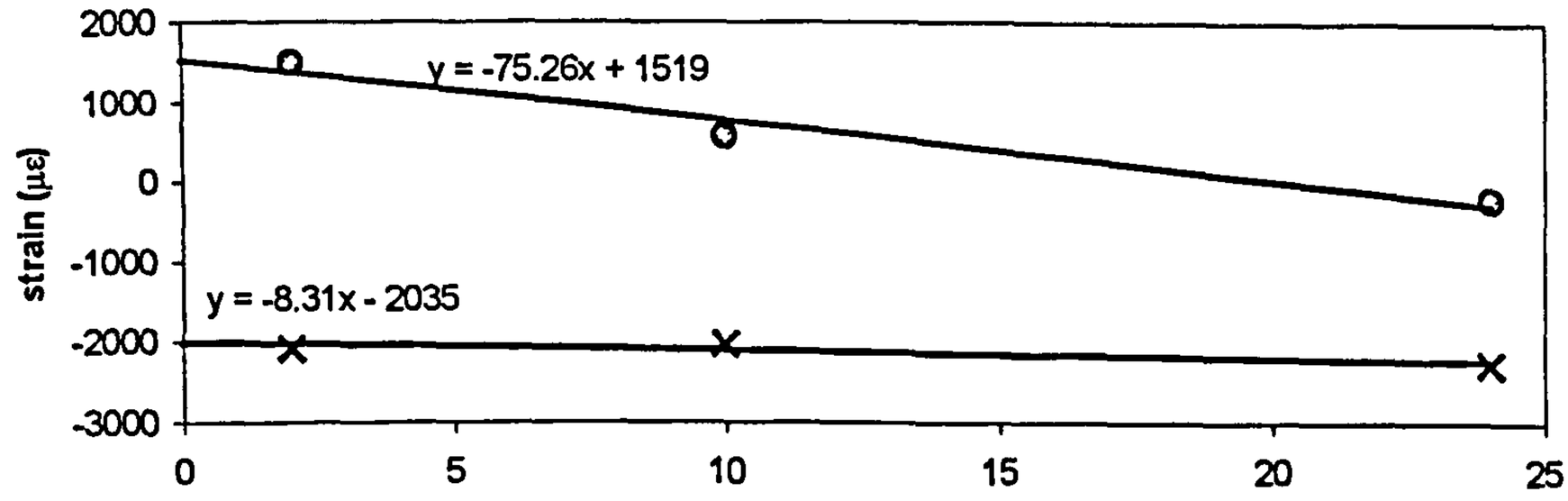

(d) 2.0mm

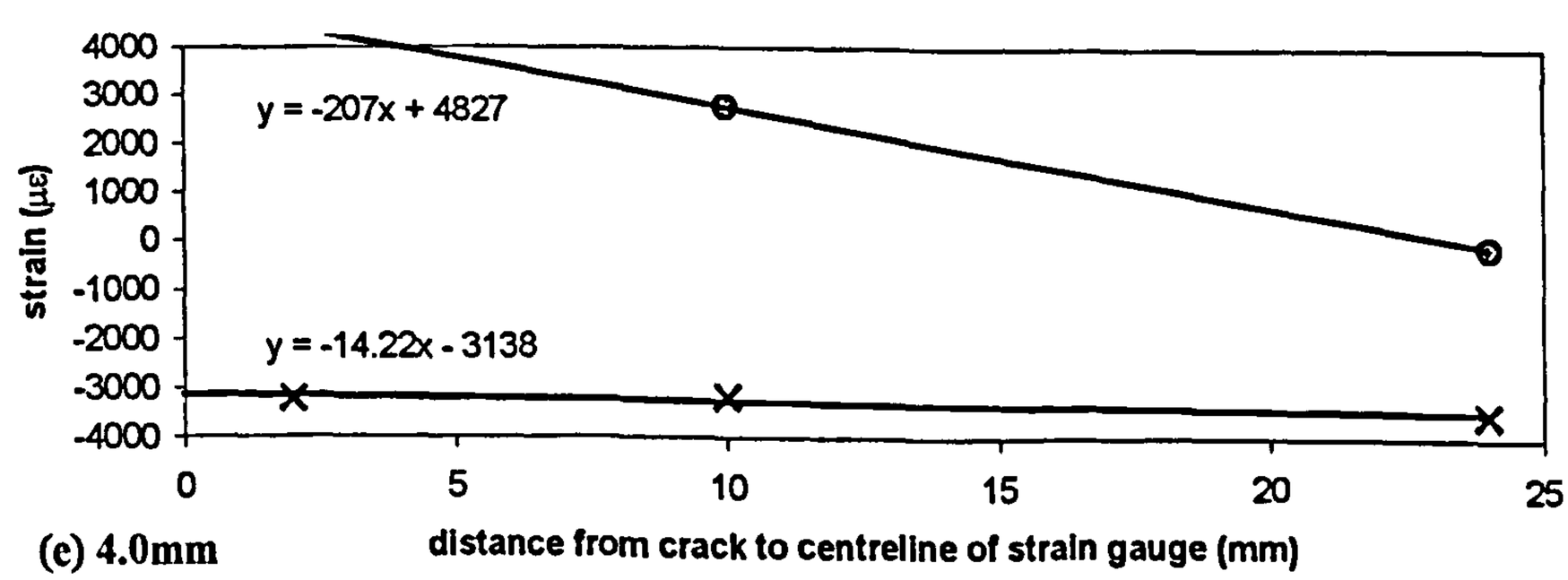

(e) 4.0mm

Figure II.1 60mm notched beams.

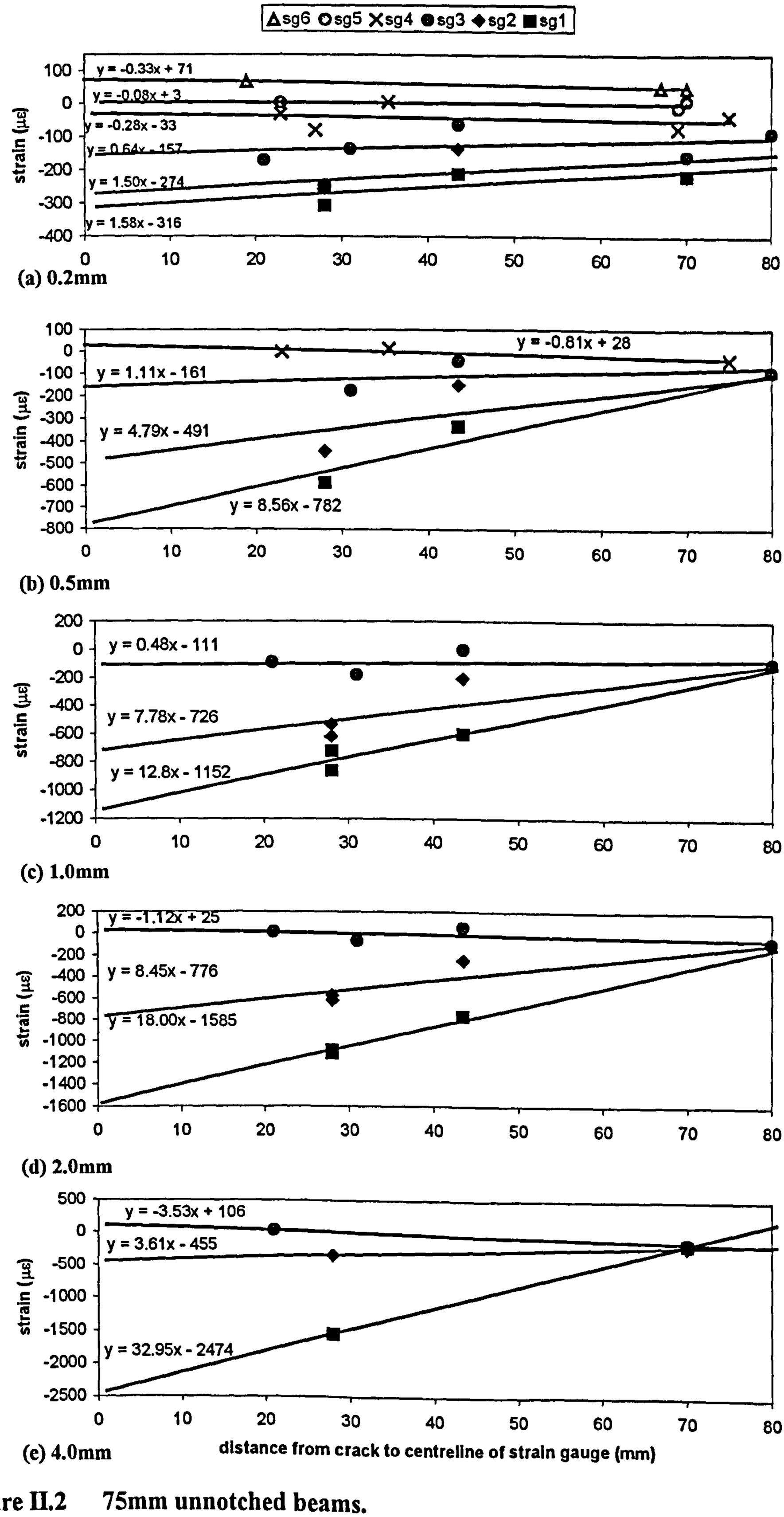

Figure II.2 75mm unnotched beams.

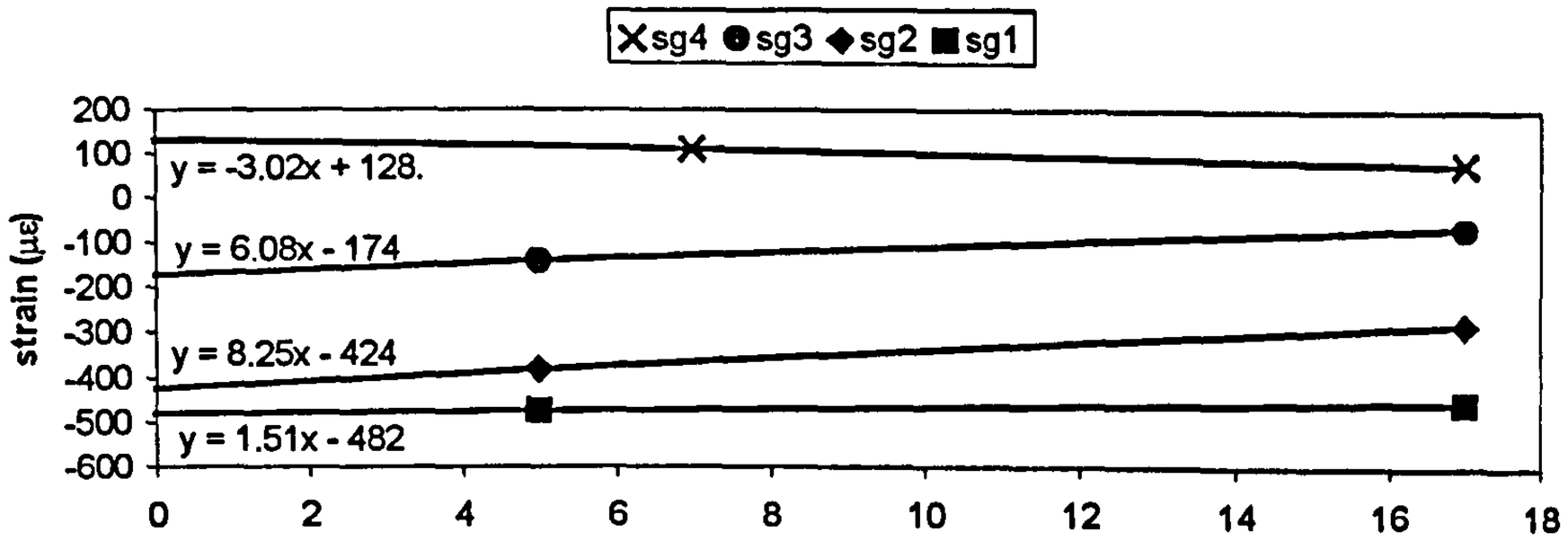

(a) 0.2mm

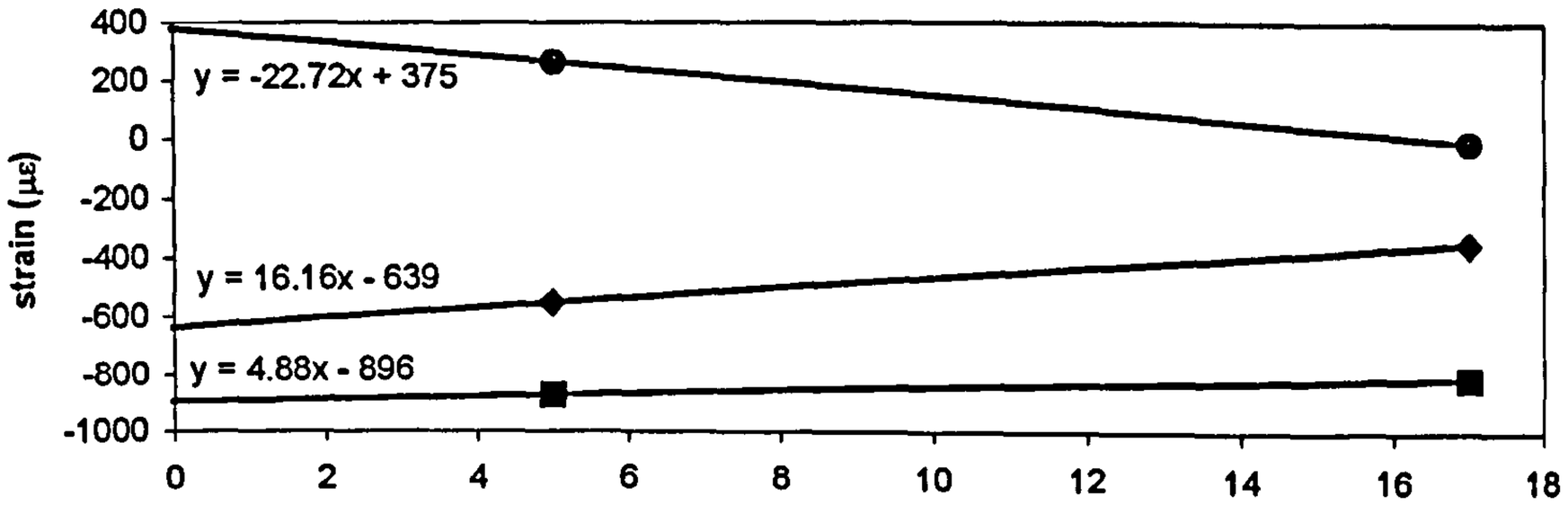

(b) 0.5mm

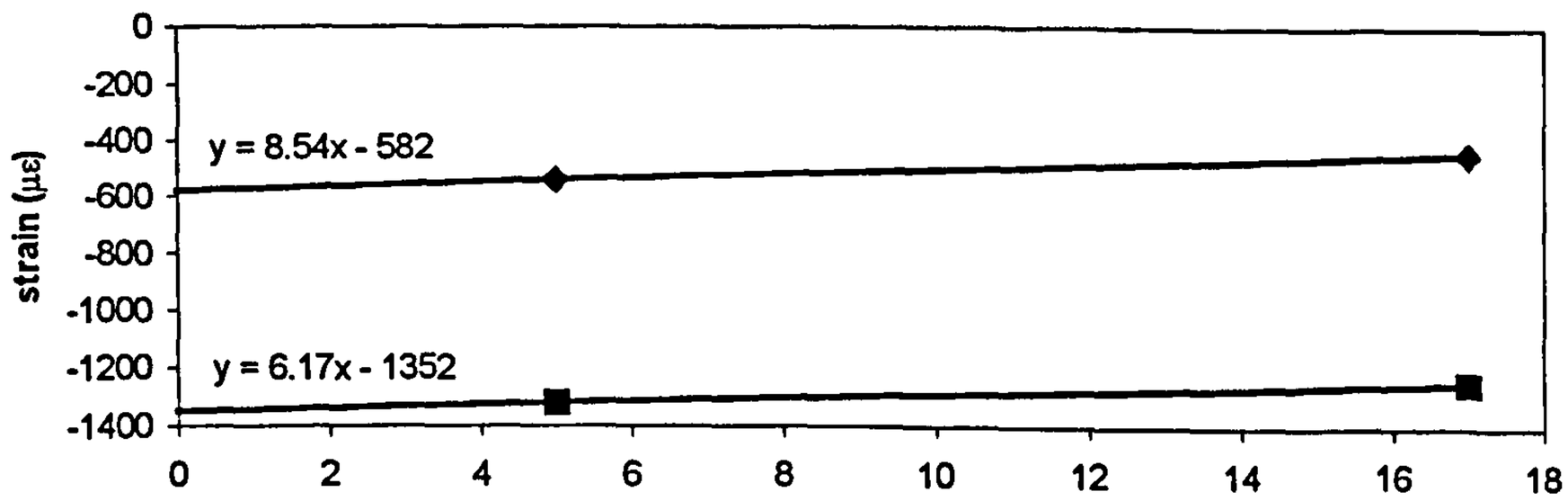

(c) 1.0mm

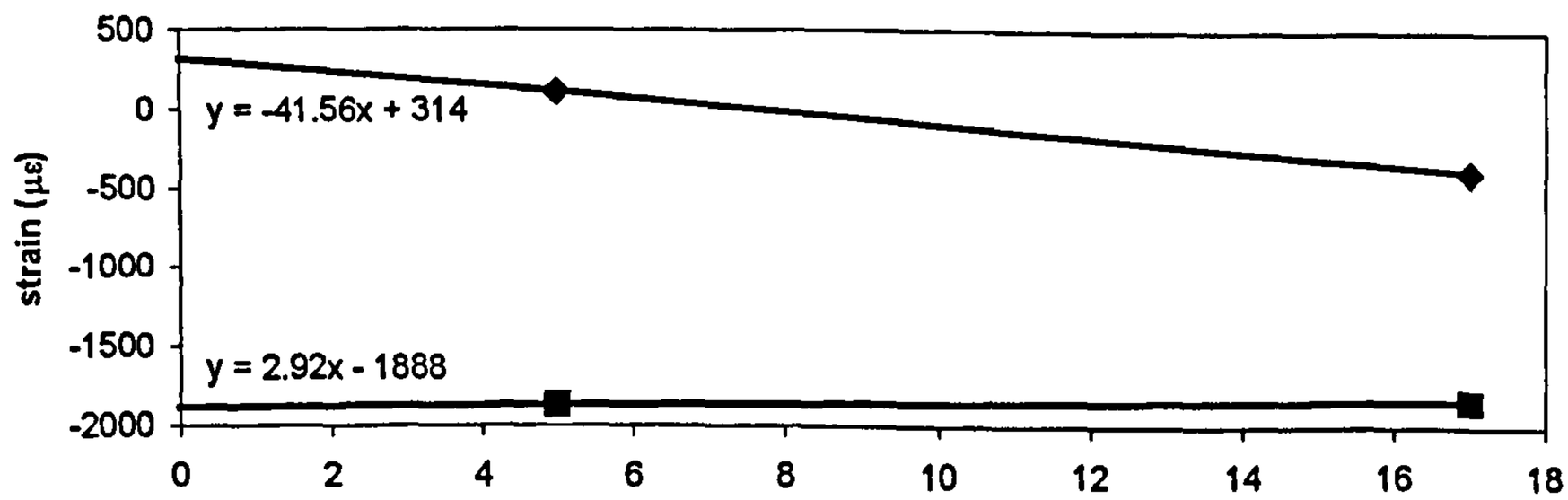

(d) 2.0mm

Figure II.3 85mm notched beams.

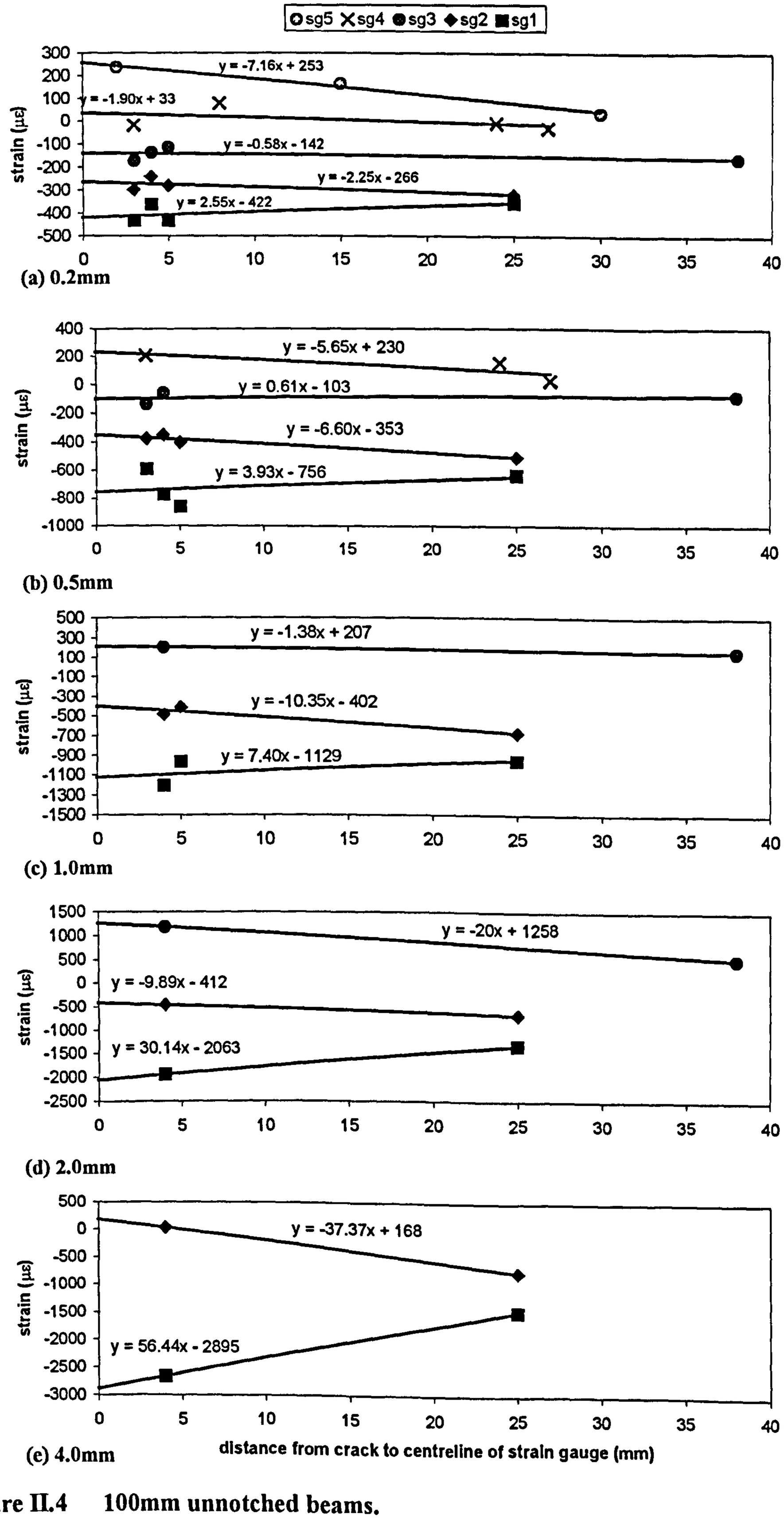

(a) 0.2mm

(b) 0.5mm

(c) 1.0mm

(d) 2.0mm

(e) 4.0mm

Figure II.4 100mm unnotched beams.

APPENDIX III

STRAIN ANALYSIS: STRAIN BLOCKS

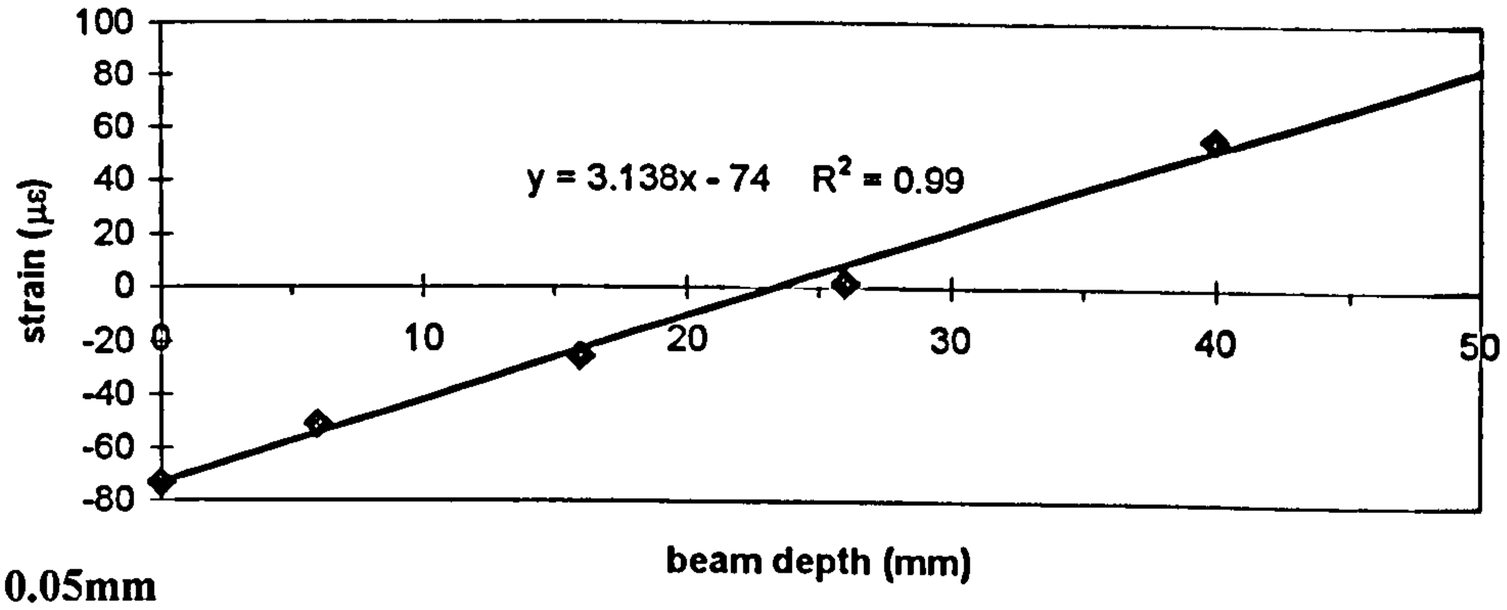

(a) 0.05mm

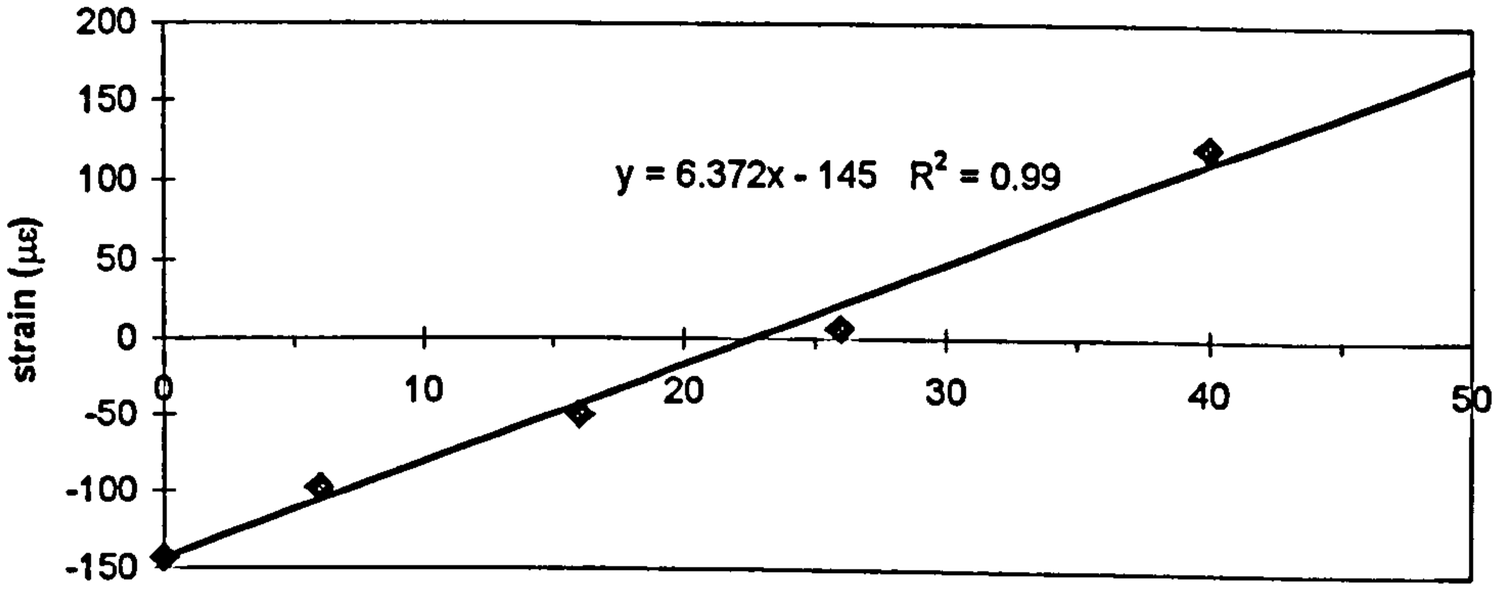

(b) 0.1mm

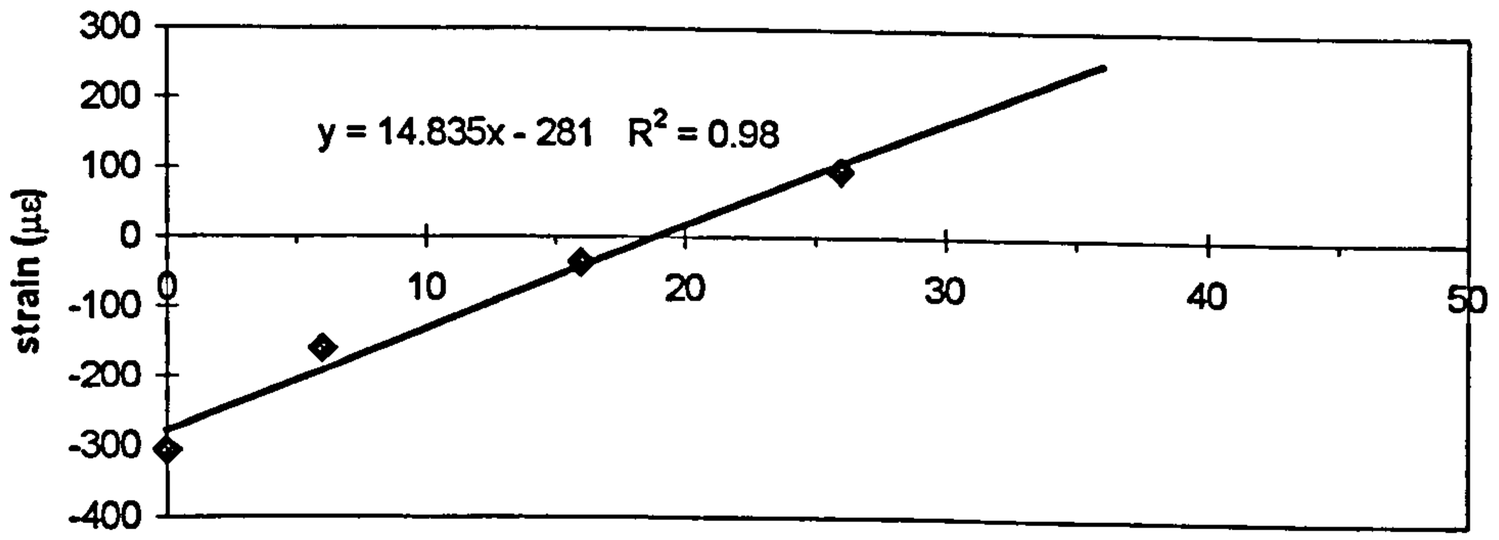

(c) 0.2mm

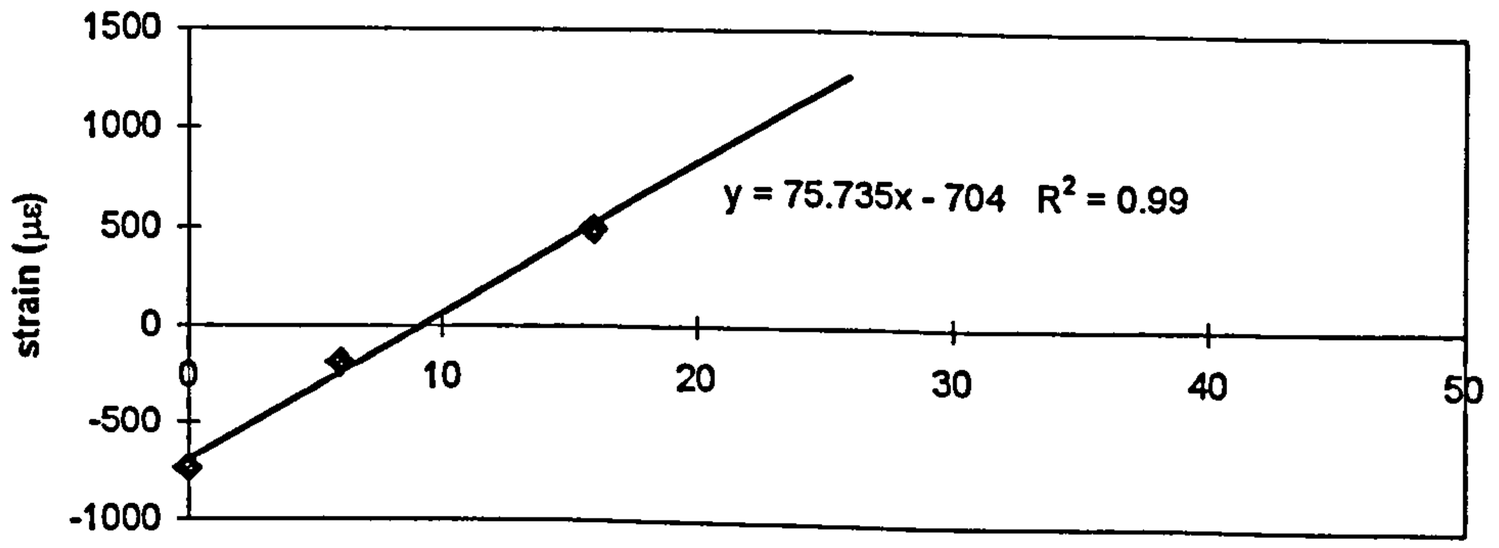

(d) 0.5mm

Figure III.1 60mm notched beams.

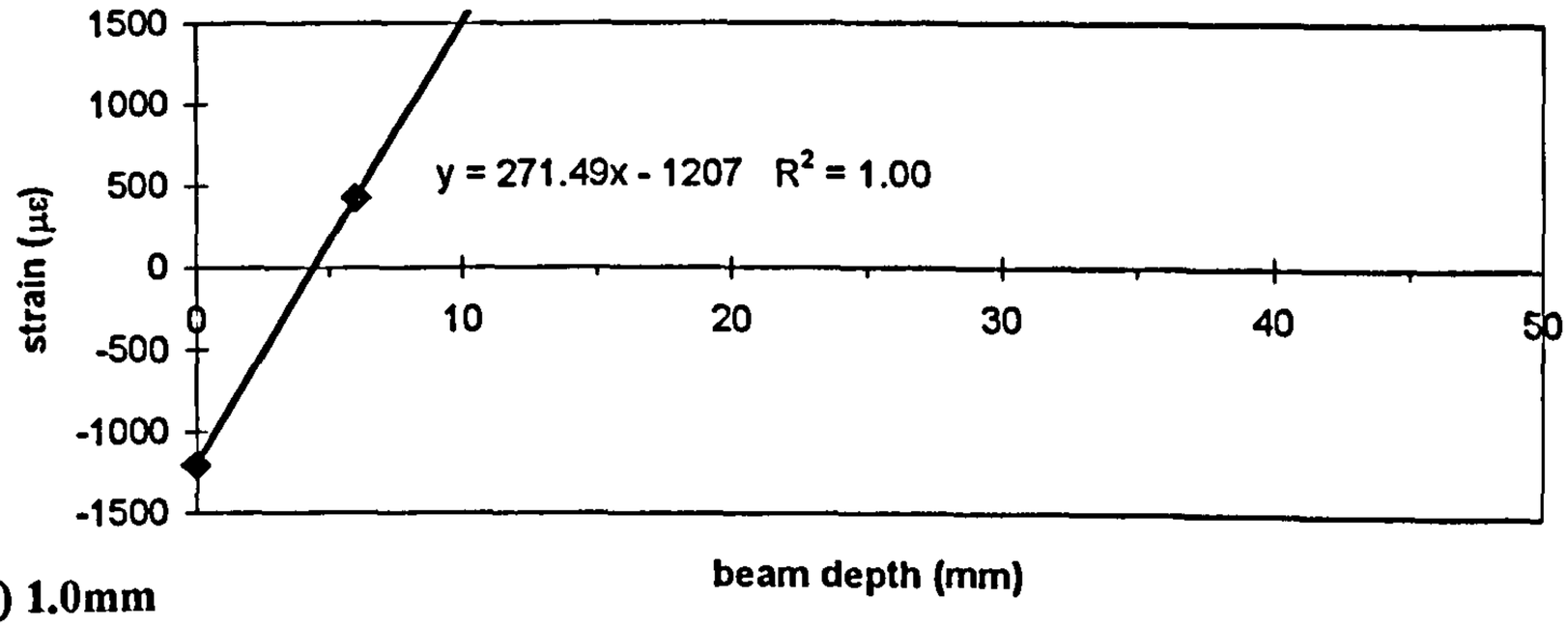

(e) 1.0mm

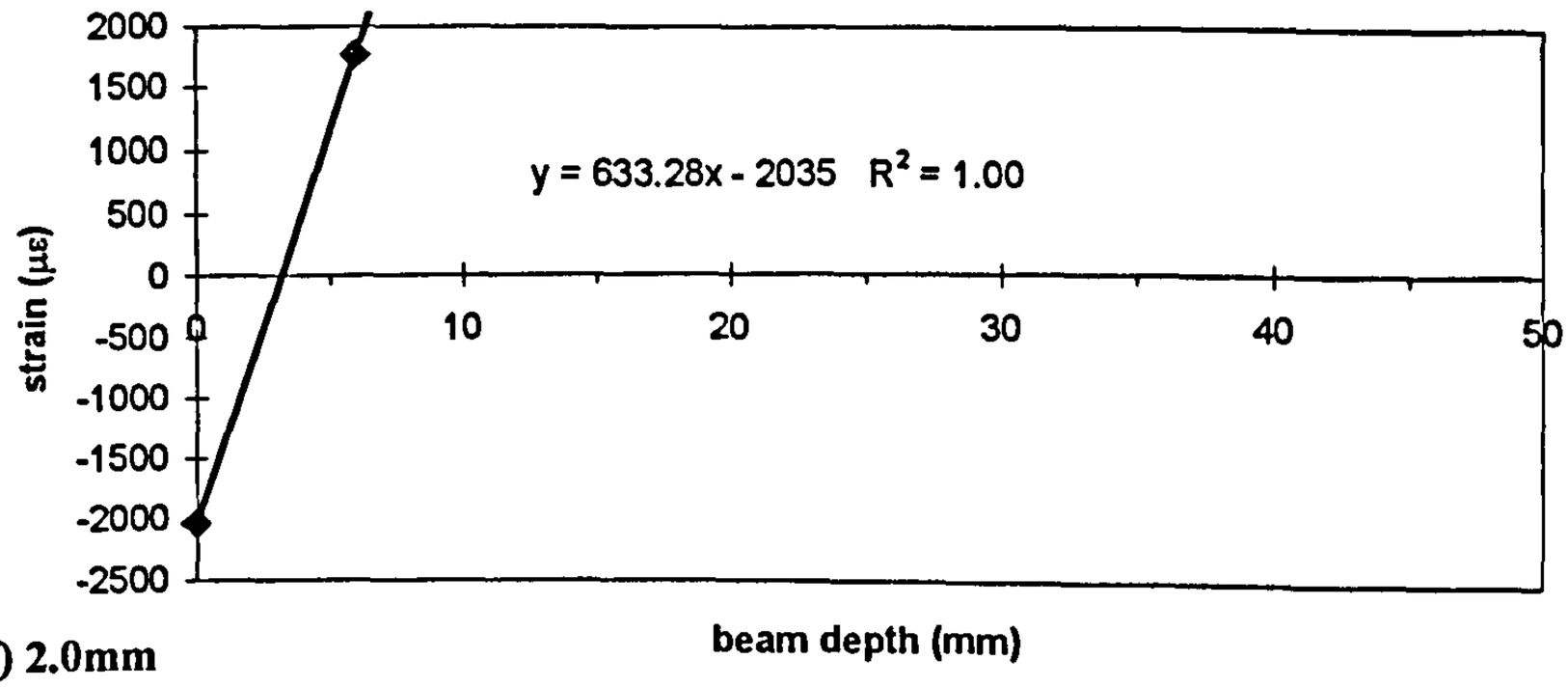

(f) 2.0mm

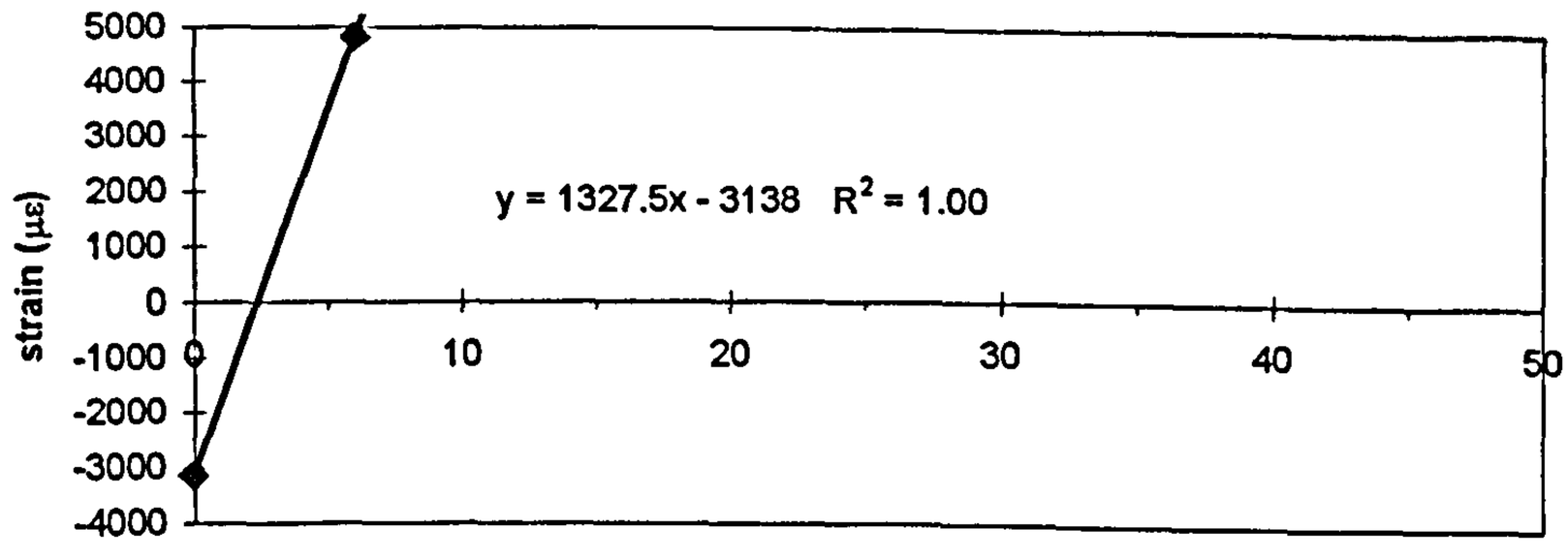

(g) 4.0mm

Figure III.1 60mm notched beams (continued).

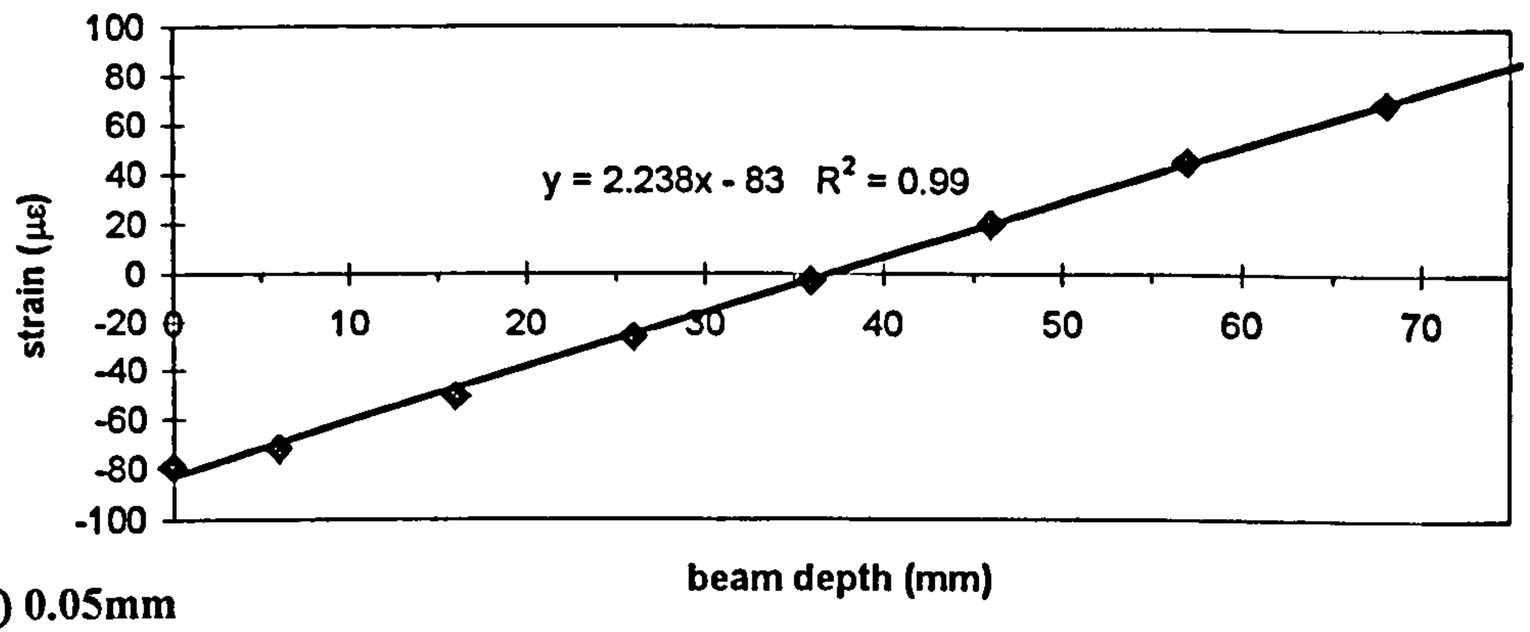

(a) 0.05mm

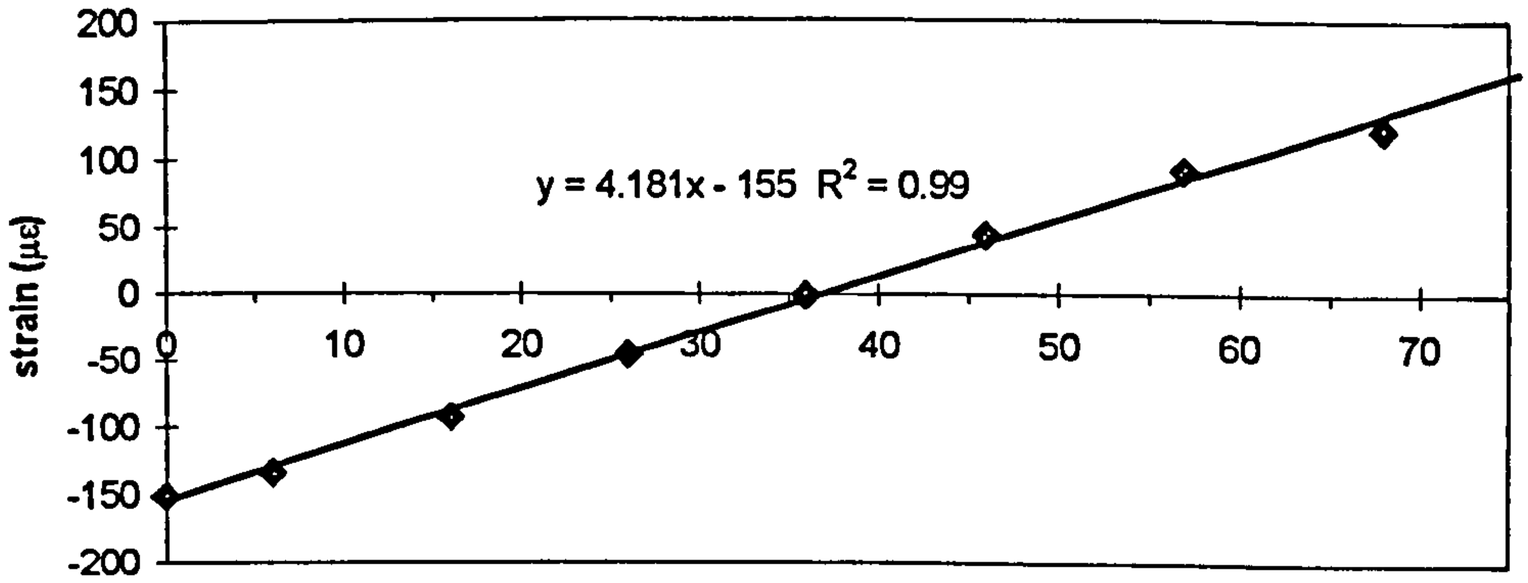

(b) 0.1mm

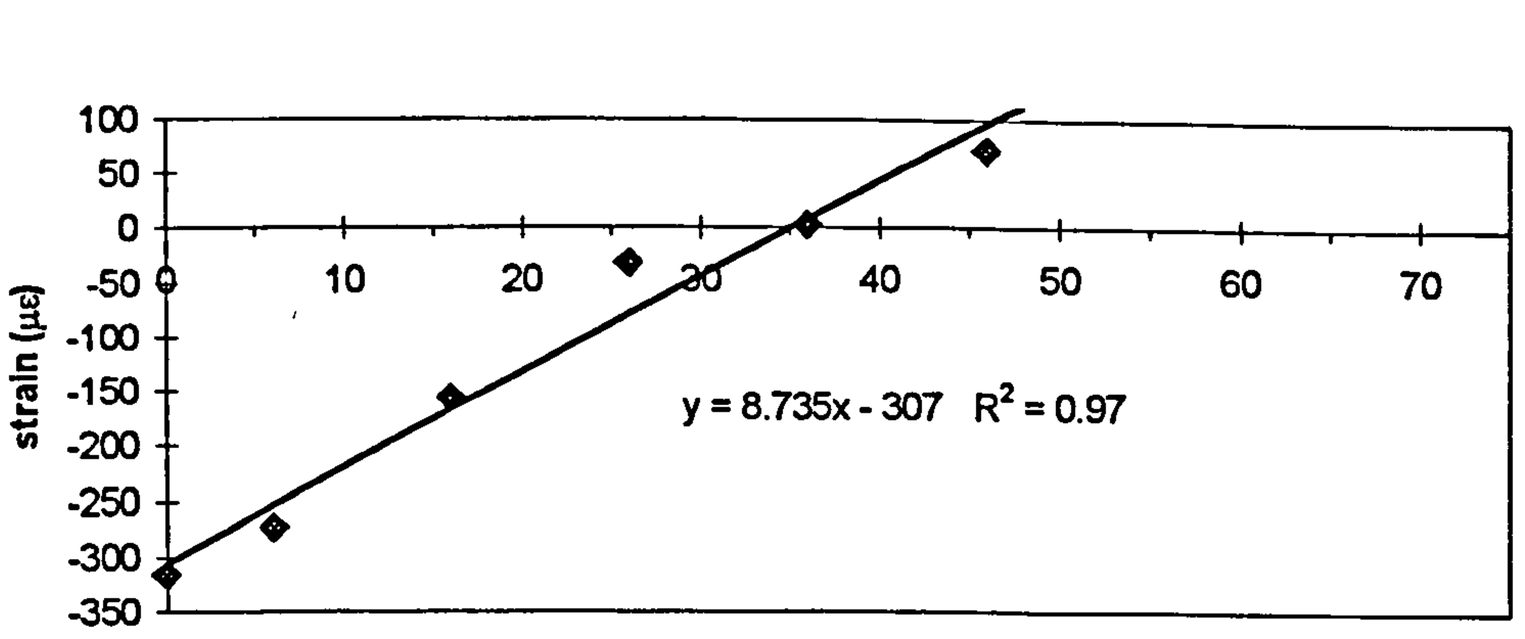

(c) 0.2mm

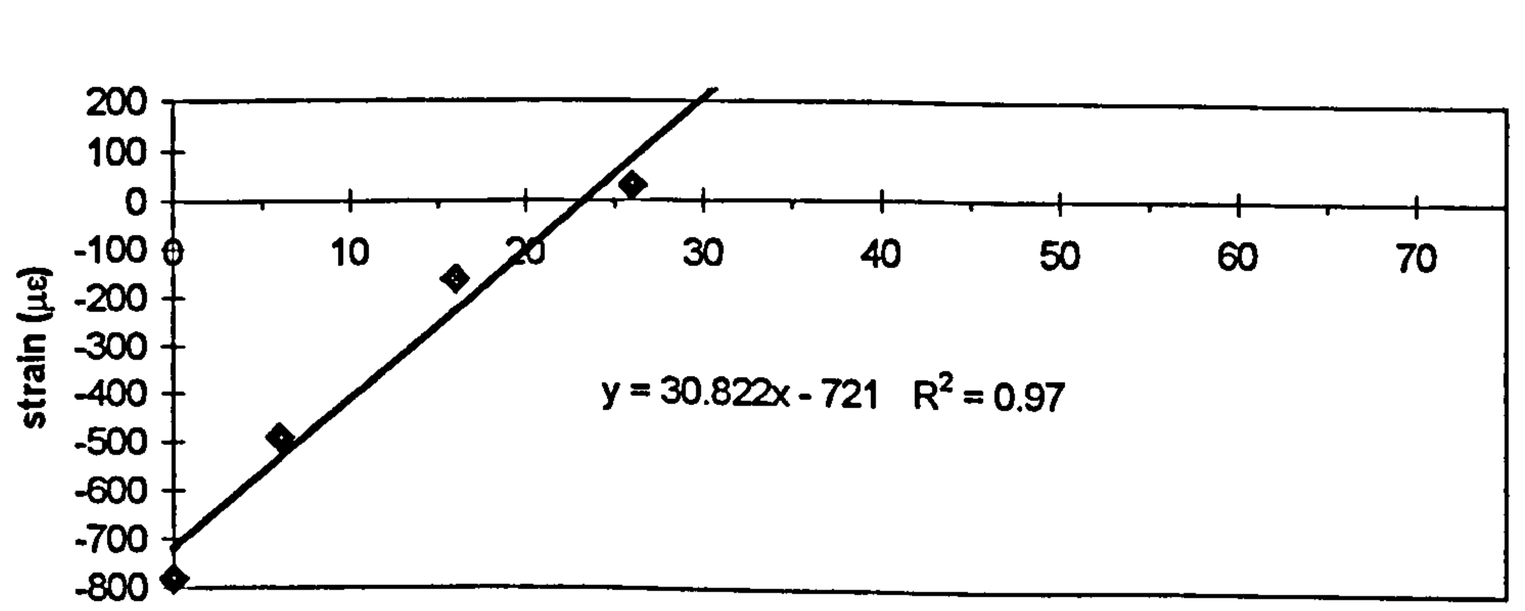

(d) 0.5mm

Figure III.2 75mm unnotched beams.

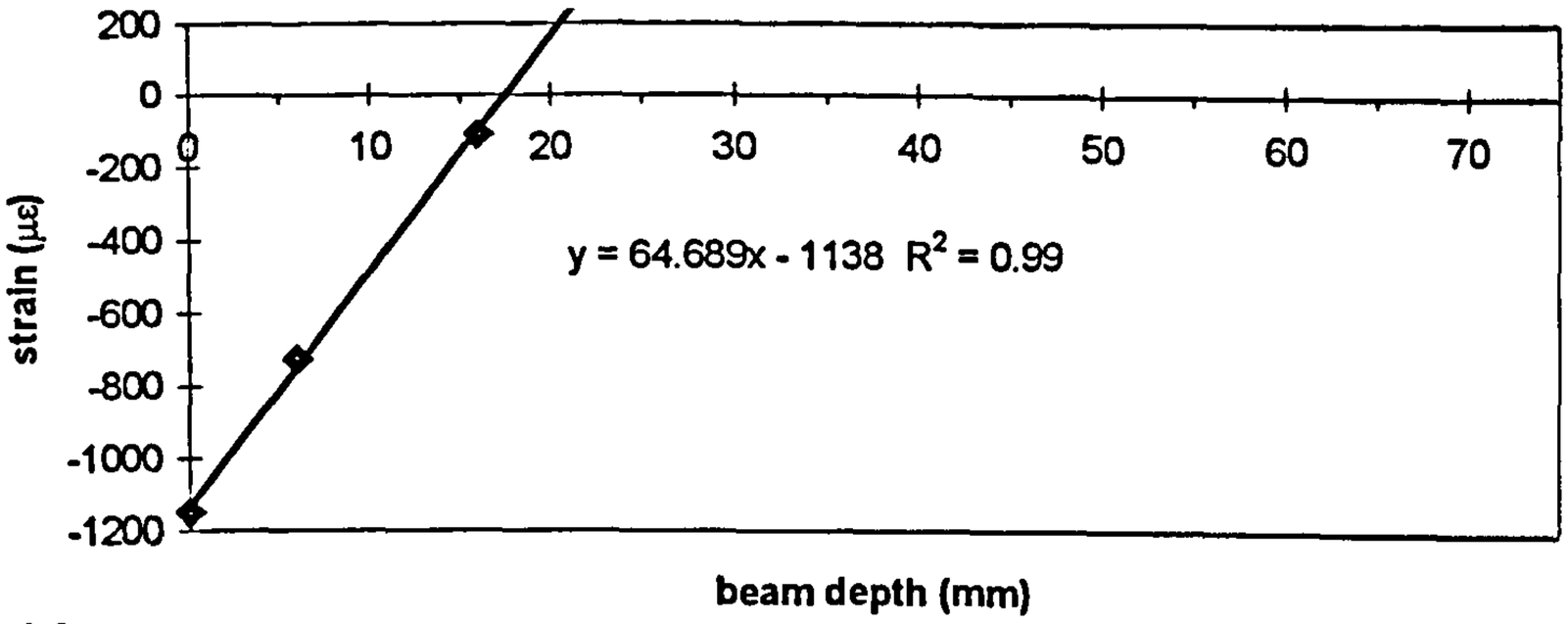

(e) 1.0mm

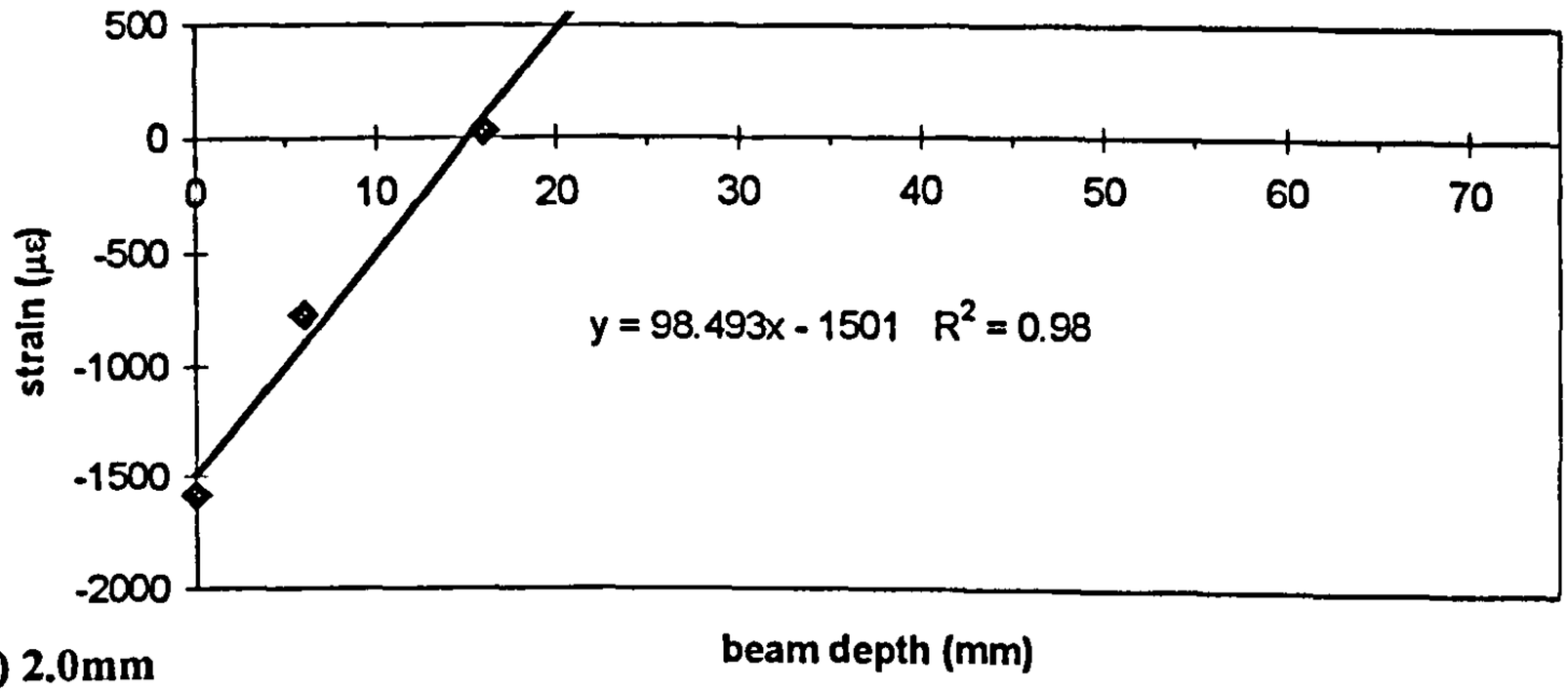

(f) 2.0mm

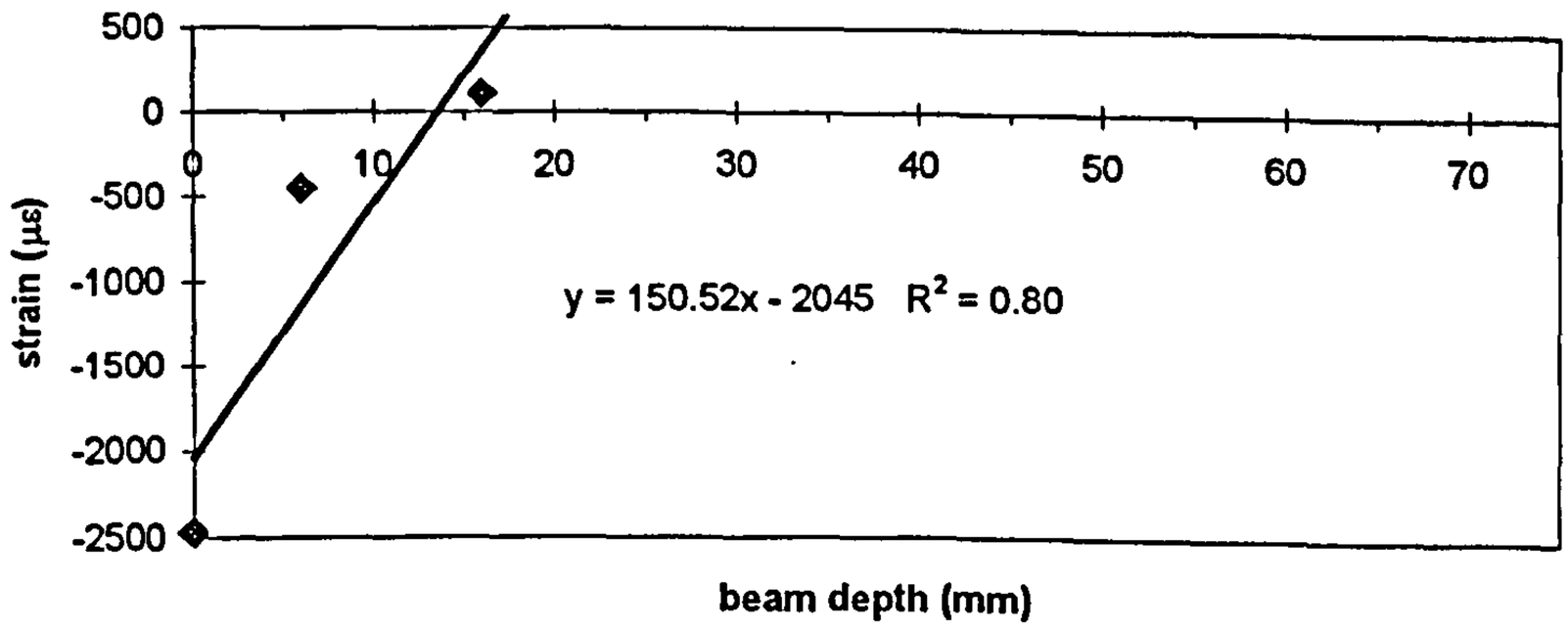

(g) 4.0mm

Figure III.2 75mm unnotched beams (continued).

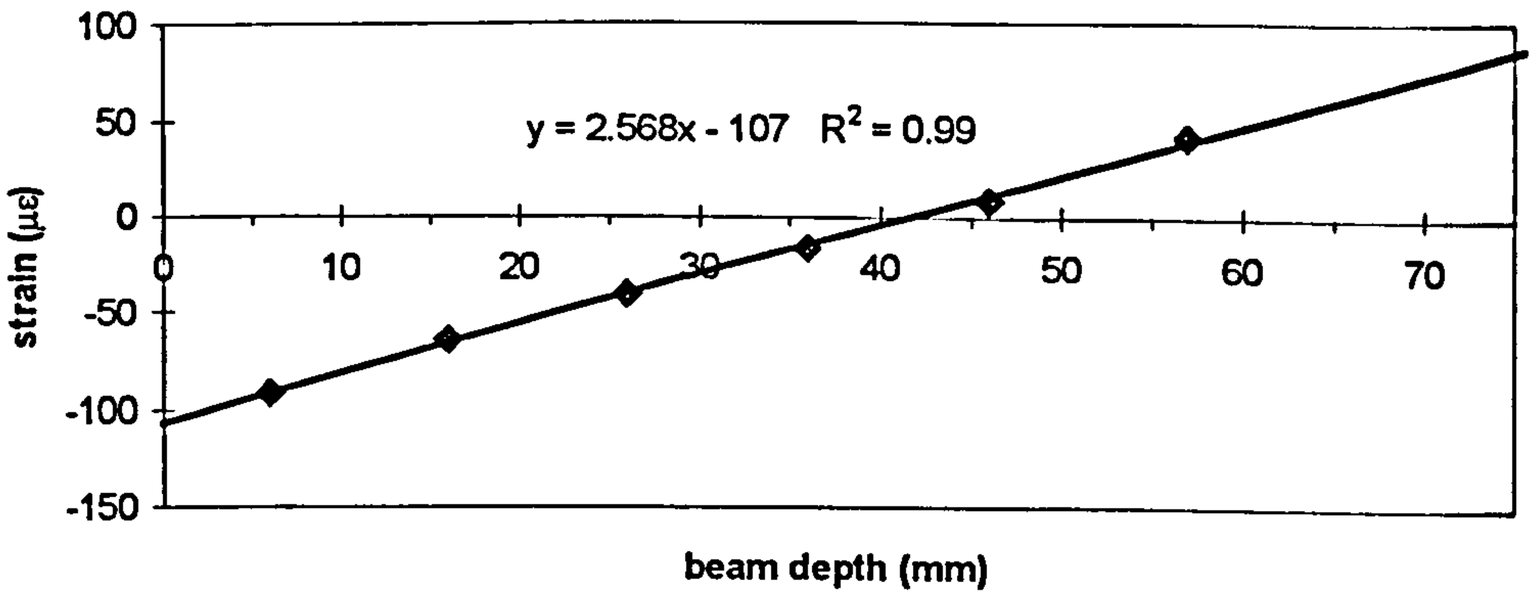

(a) 0.05mm

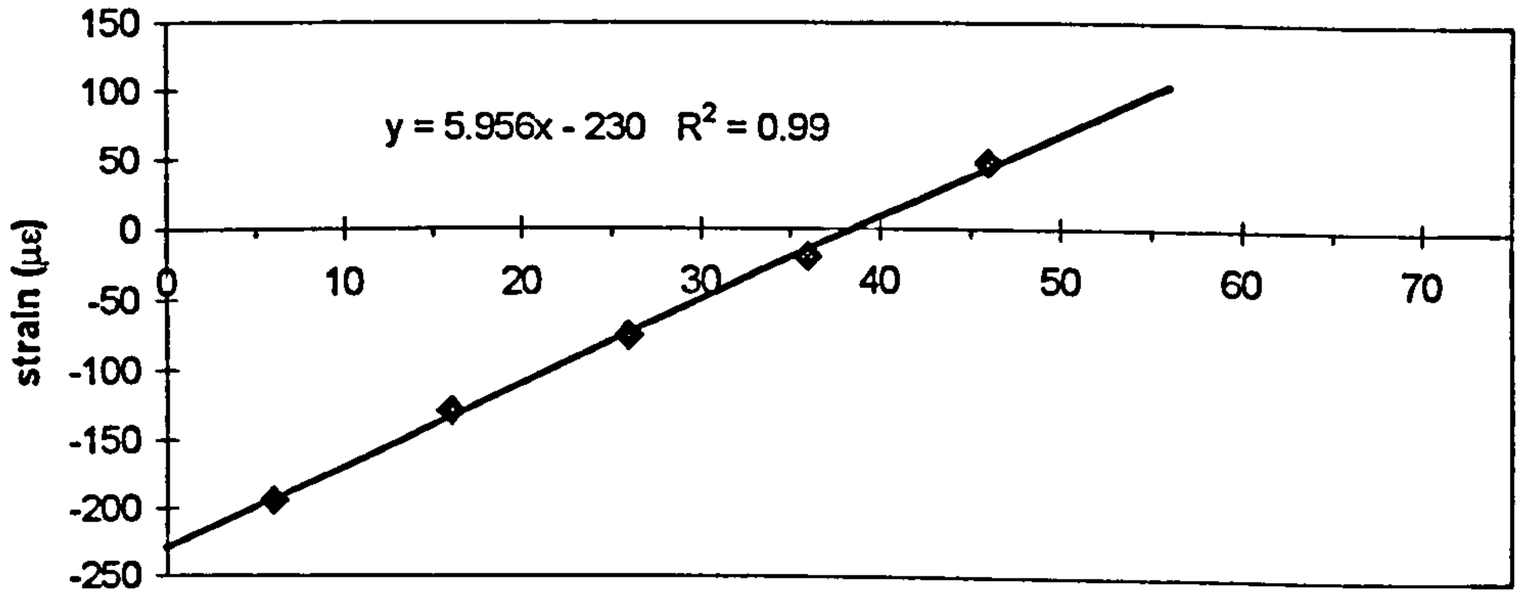

(b) 0.1mm

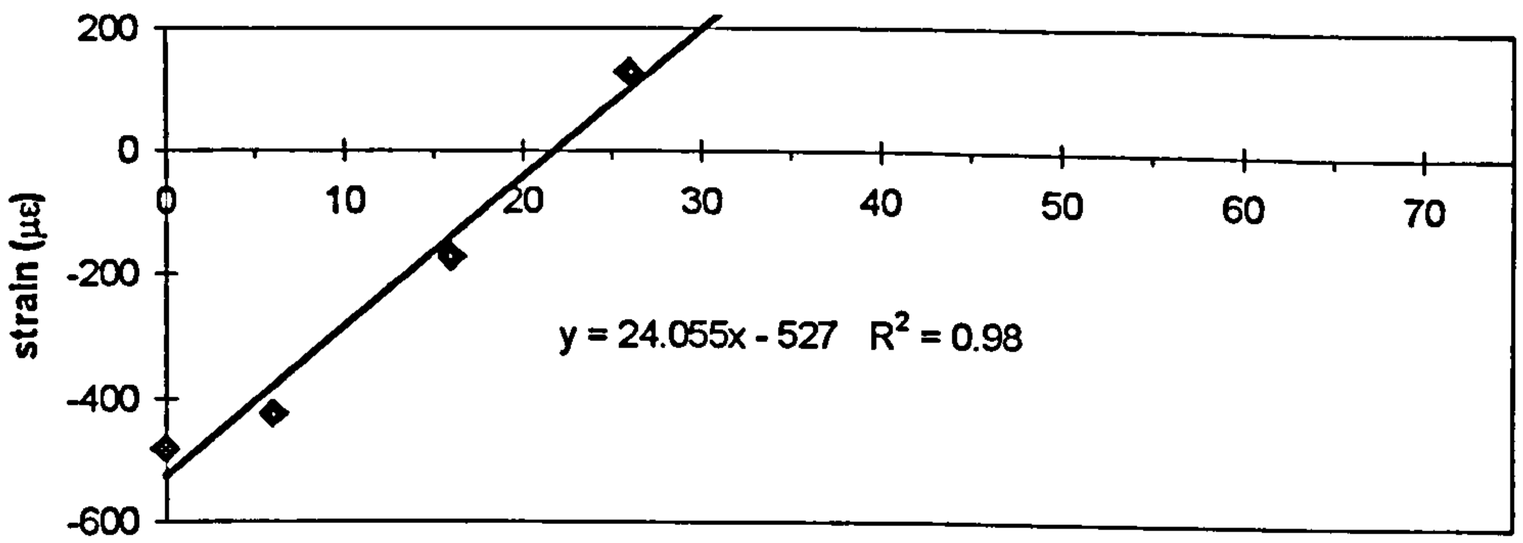

(c) 0.2mm

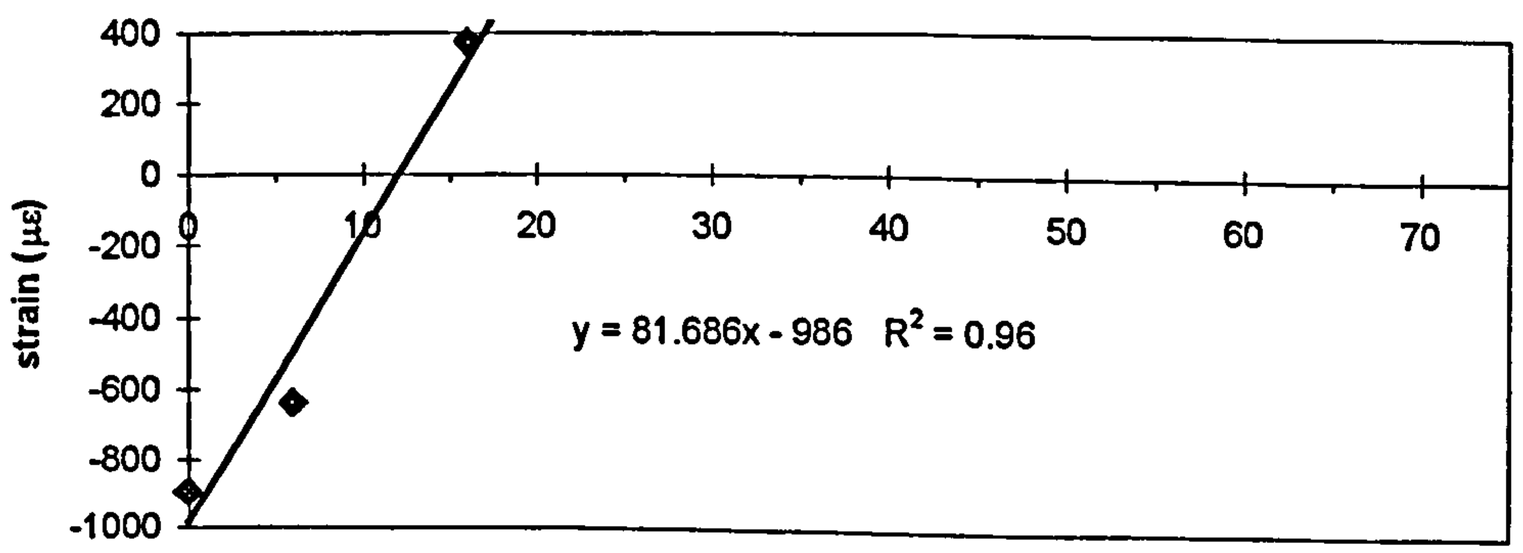

(d) 0.5mm

Figure III.3 85mm notched beams.

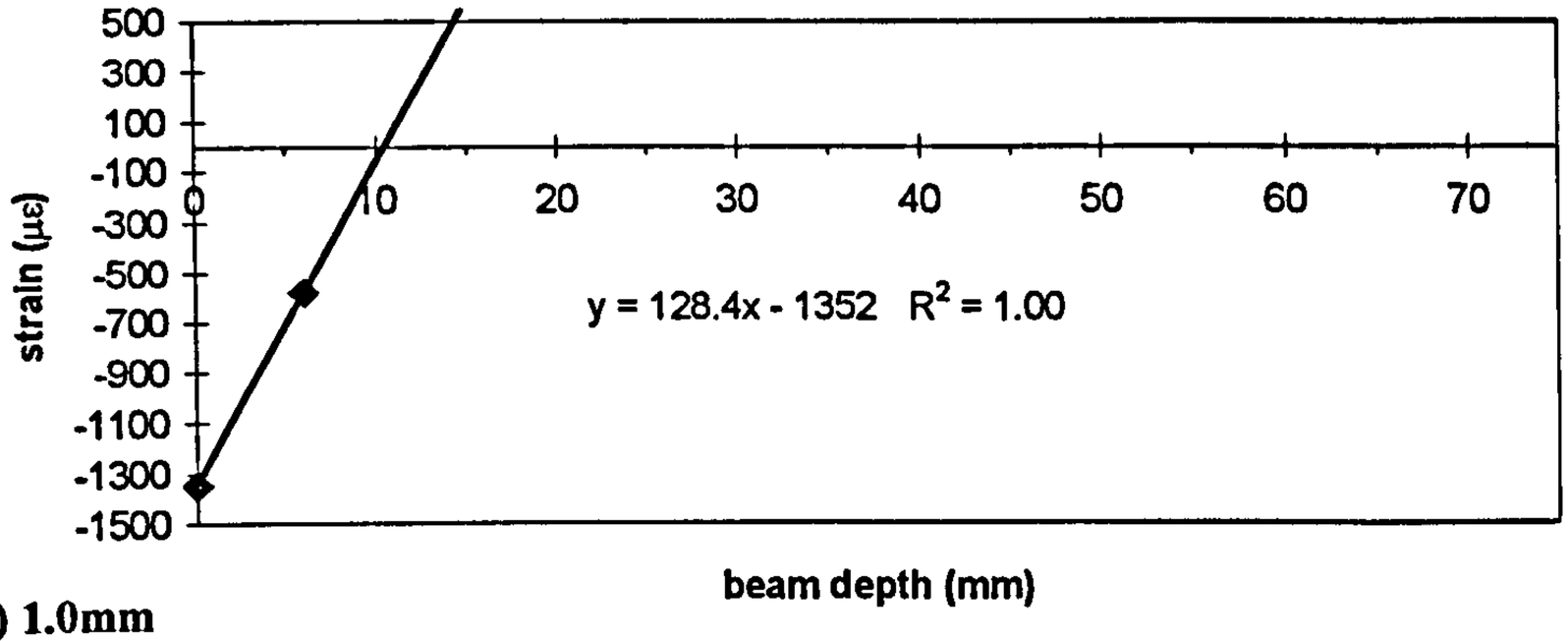

(e) 1.0mm

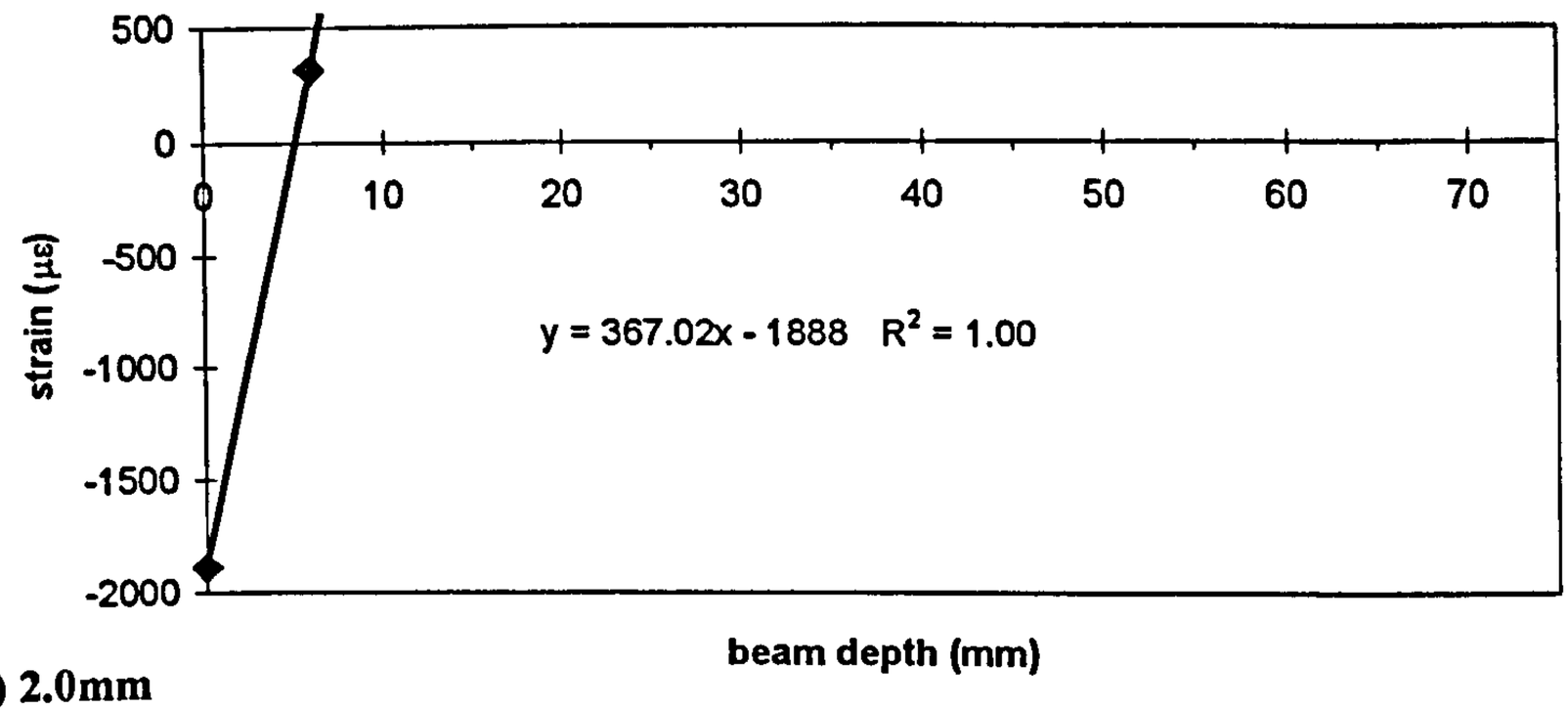

(f) 2.0mm

Figure III.3 85mm notched beams (continued).

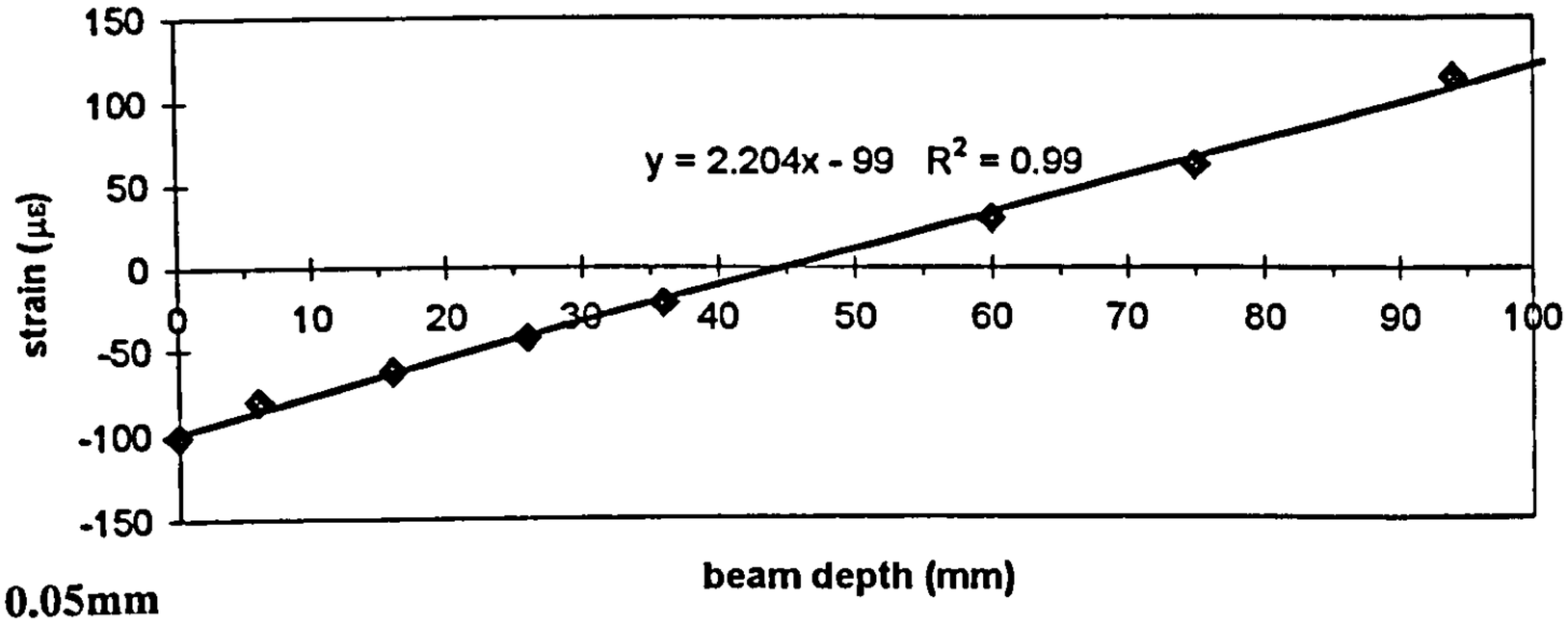

(a) 0.05mm

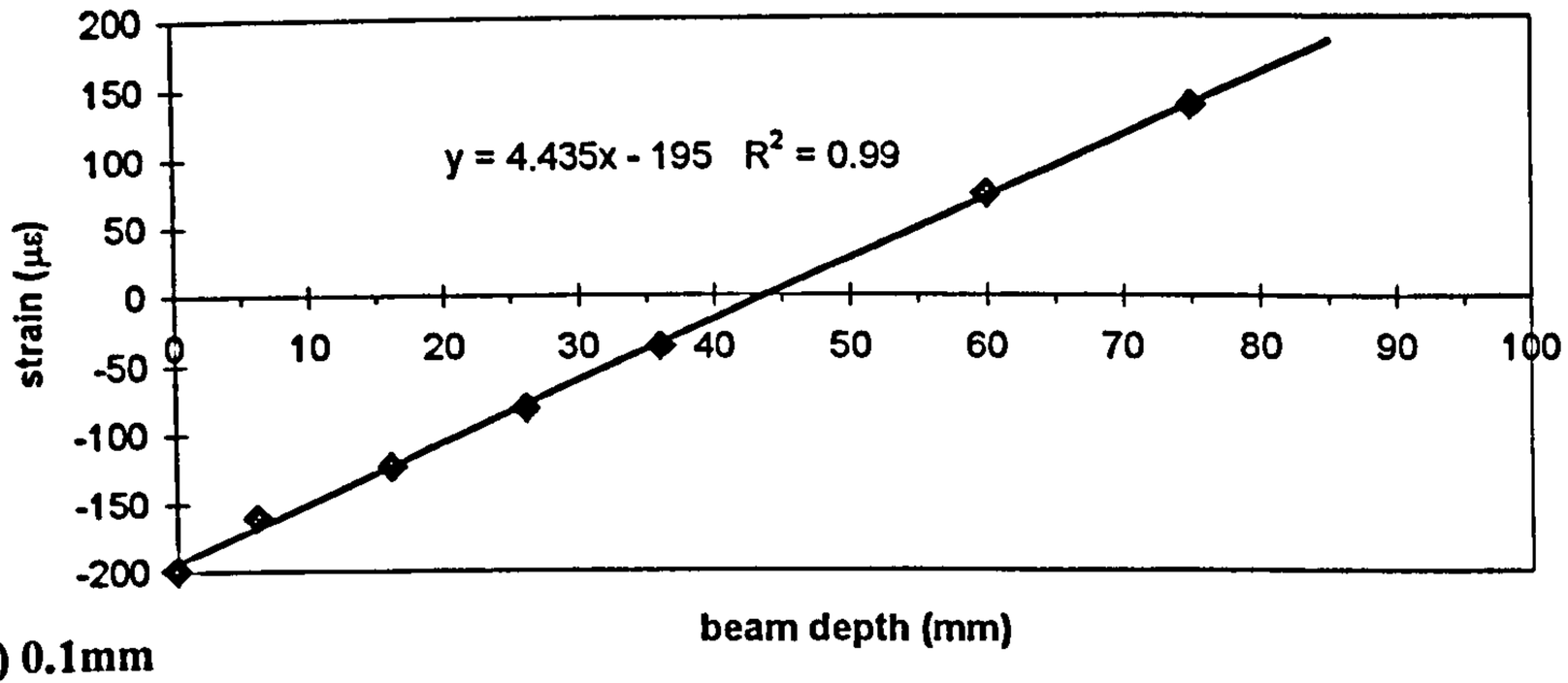

(b) 0.1mm

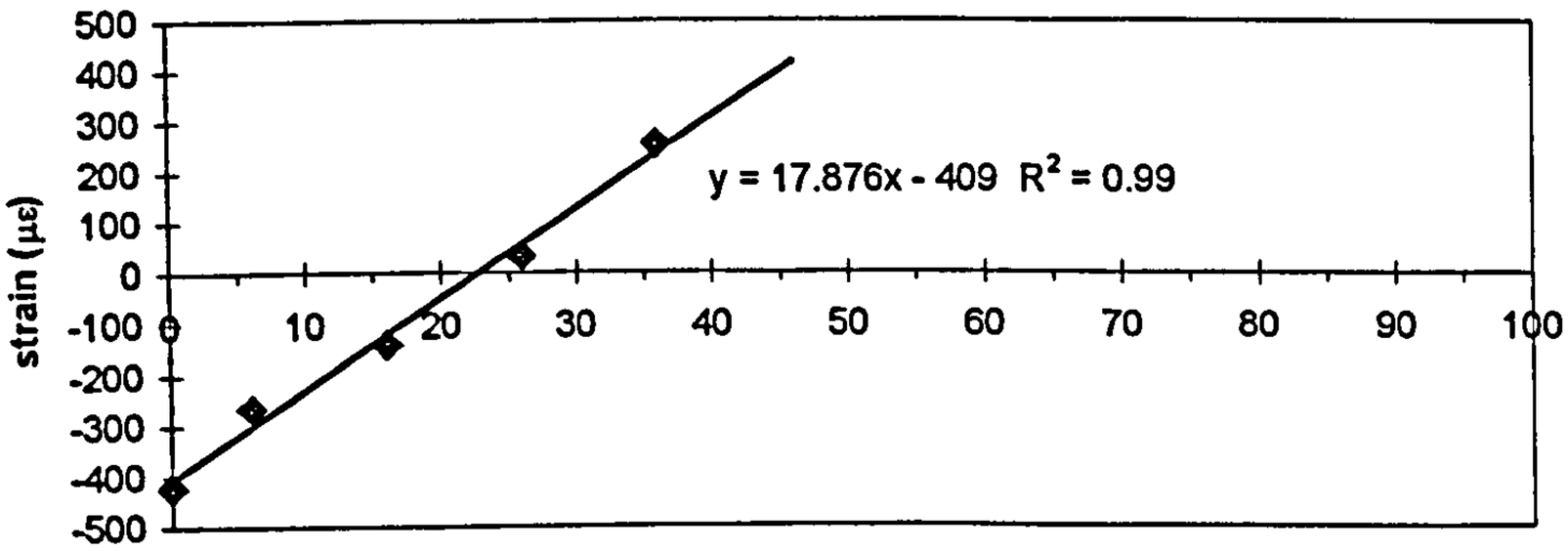

(c) 0.2mm

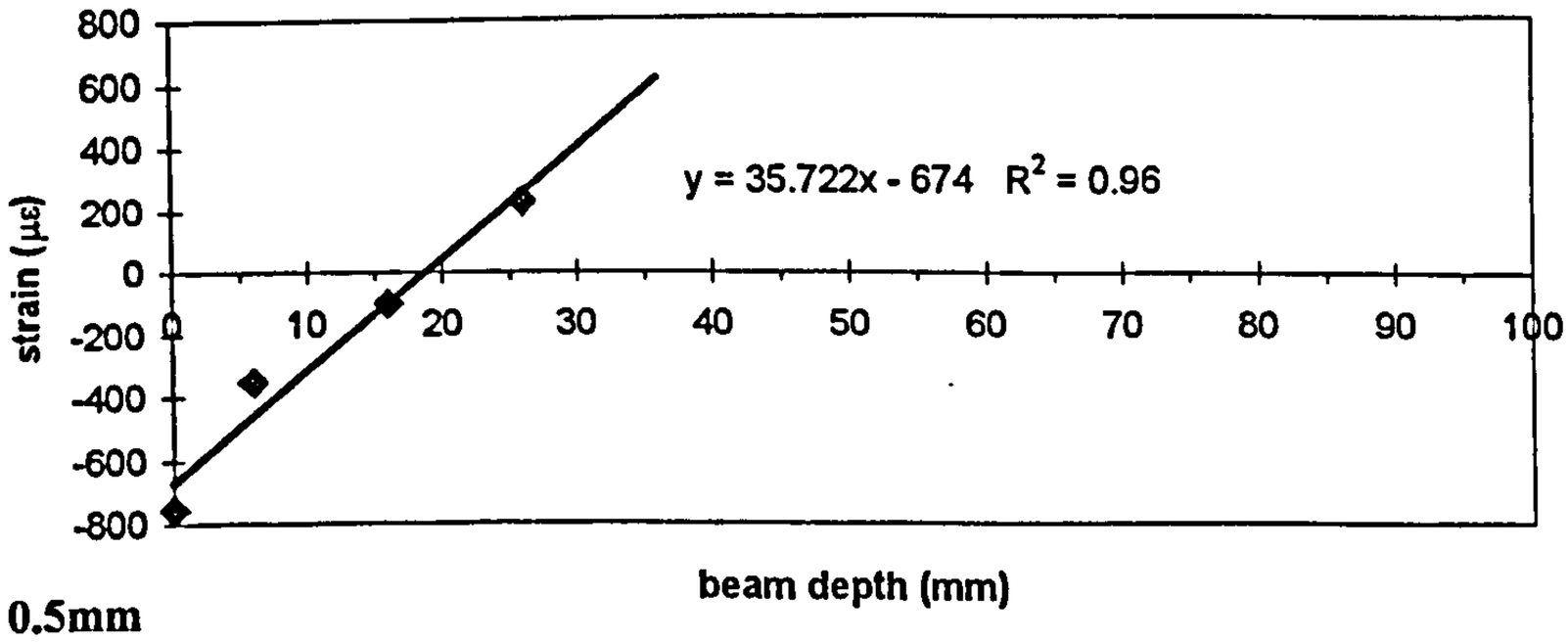

(d) 0.5mm

Figure III.4 100mm unnotched beams.

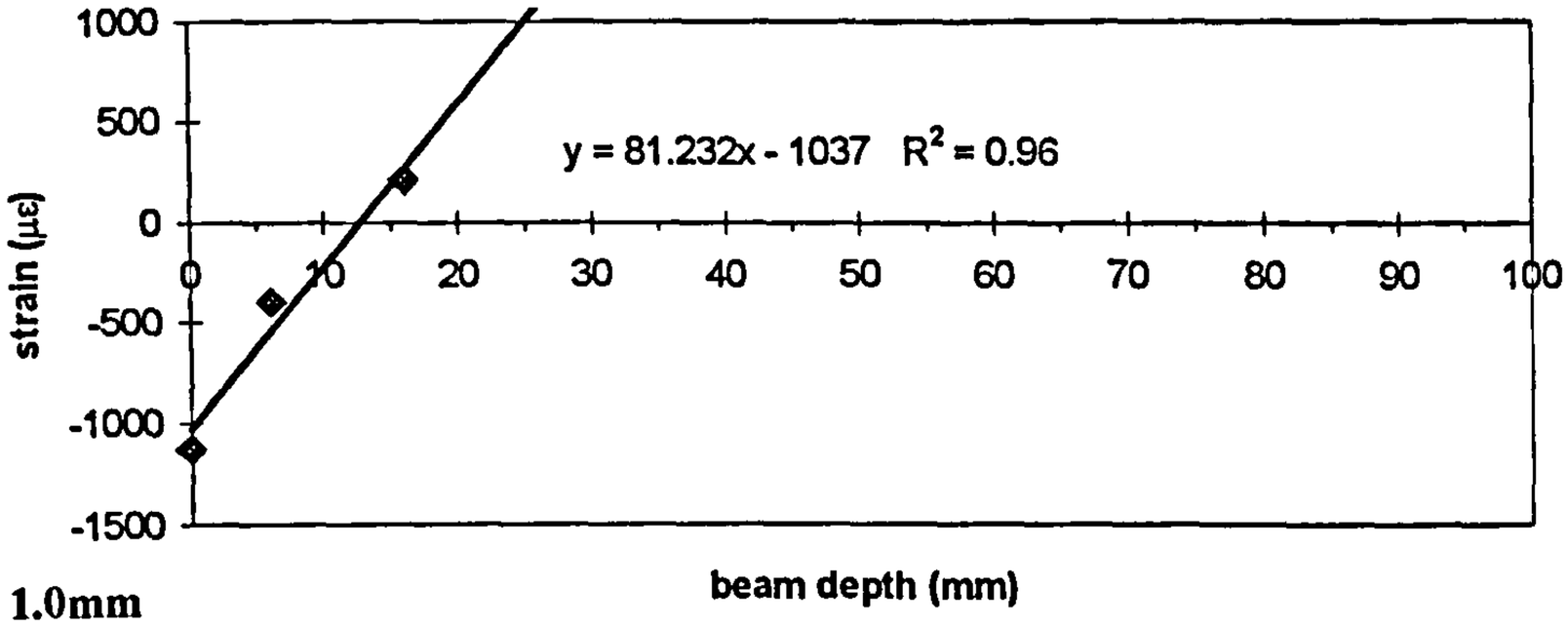

(e) 1.0mm

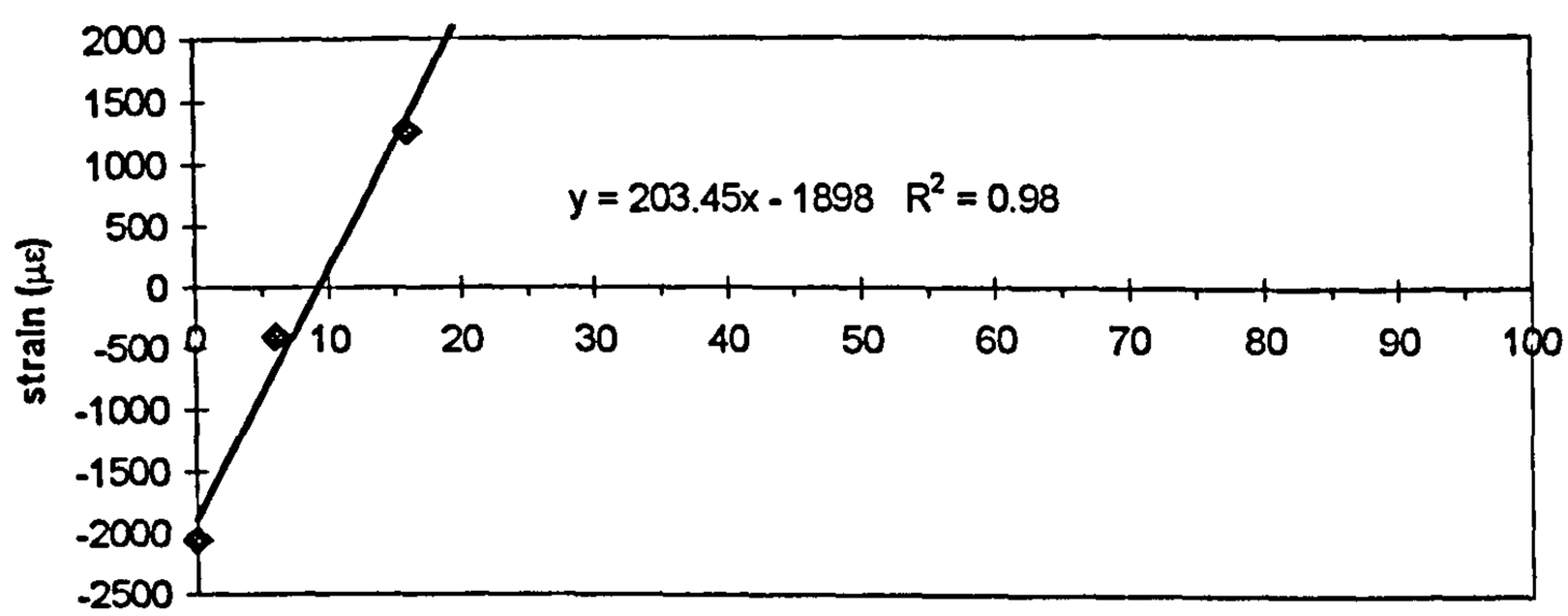

(f) 2.0mm

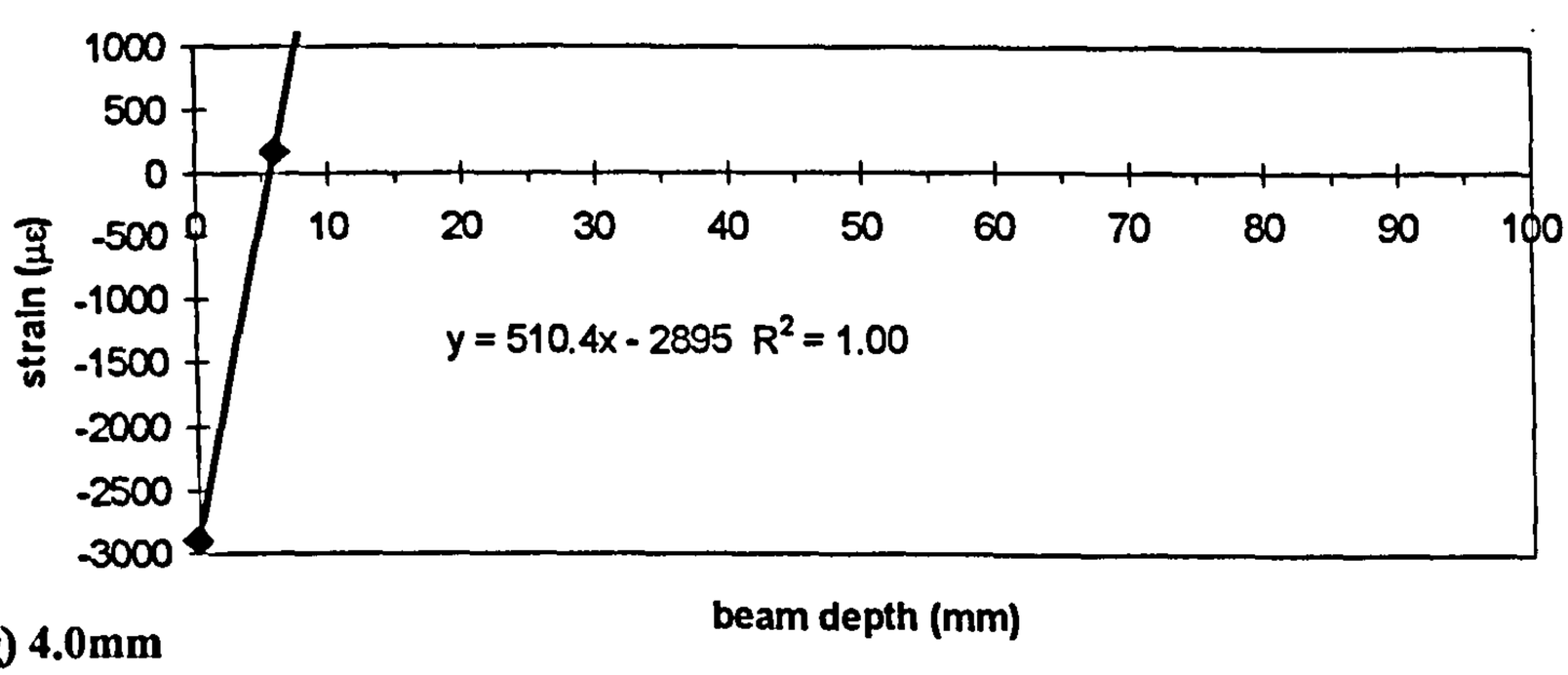

(g) 4.0mm

Figure III.4 100mm unnotched beams (continued).

APPENDIX IV

STRAIN ANALYSIS: MODIFIED CRACK-WIDTH PROFILES

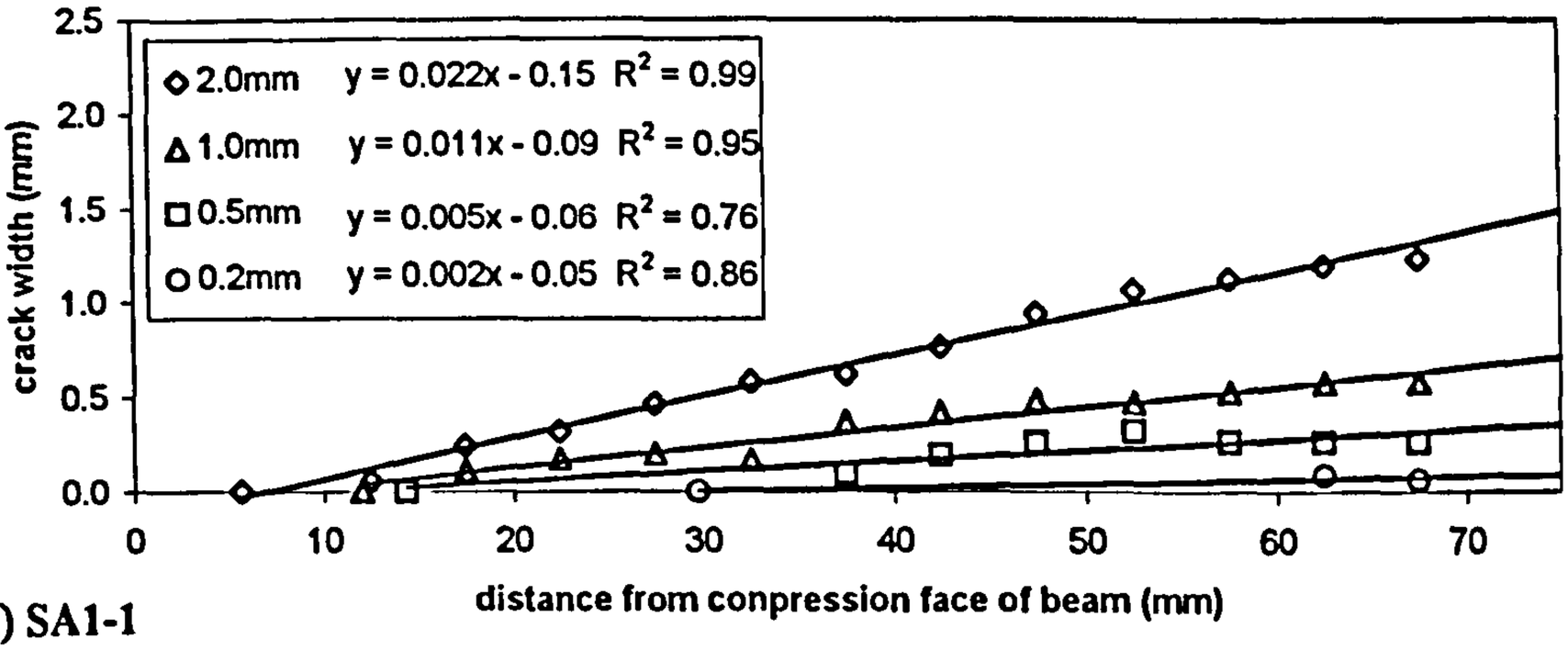

(a) SA1-1

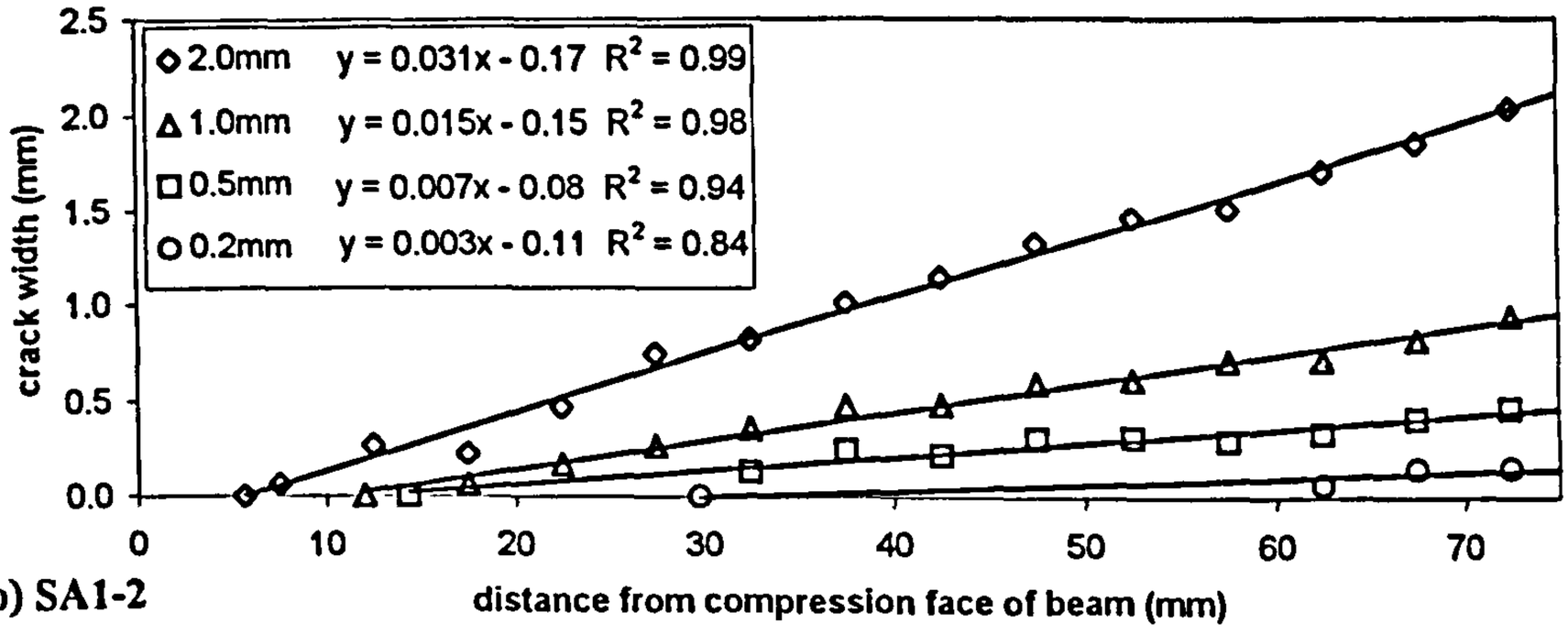

(b) SA1-2

Figure IV.1 75mm unnotched beams.

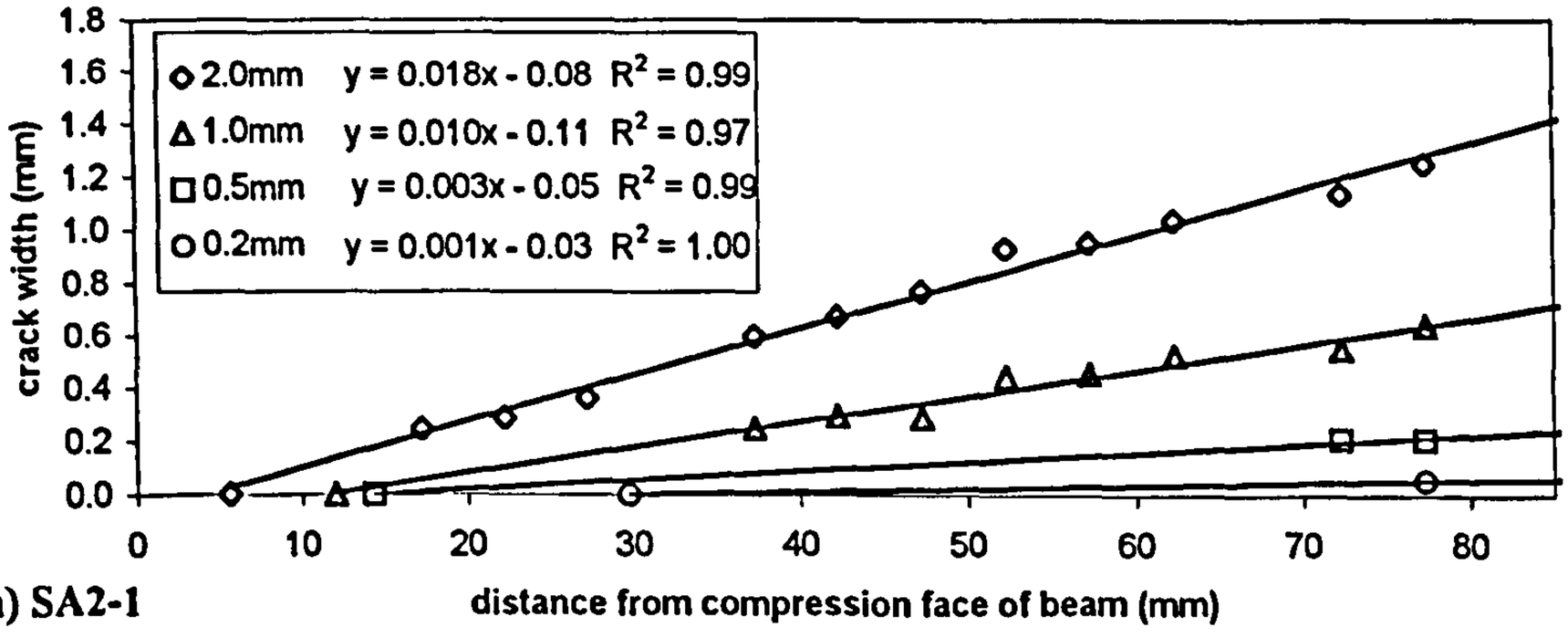

(a) SA2-1

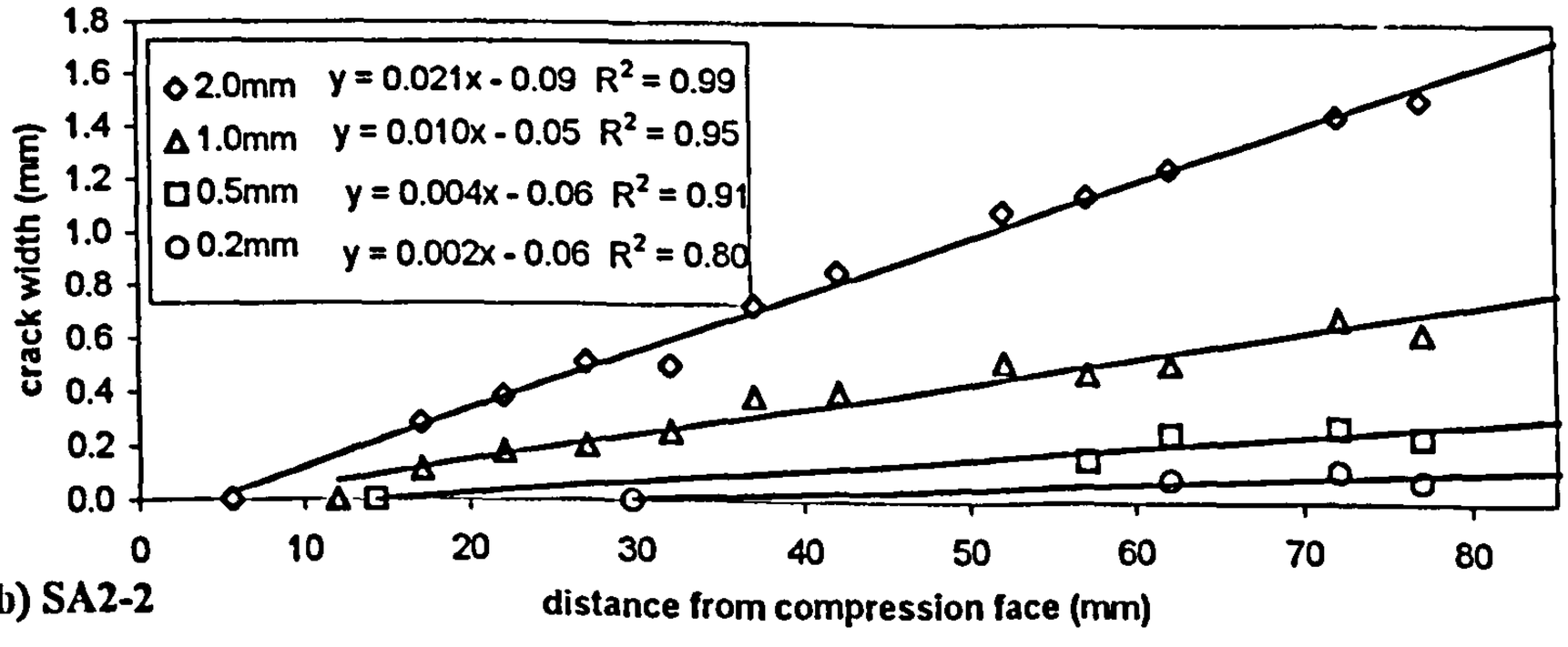

(b) SA2-2

Figure IV.2 85mm notched beams.

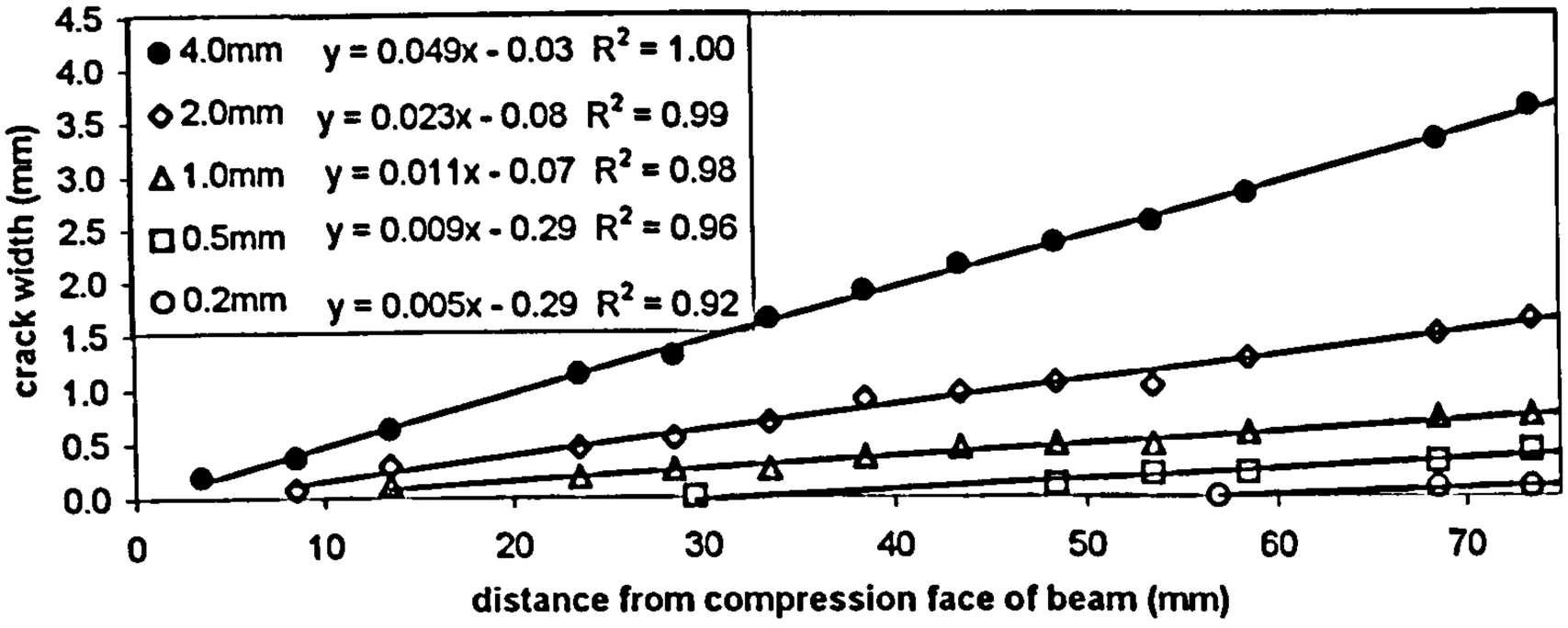

Figure IV.3 75mm unnotched beams (sprayed) - SA5-1.

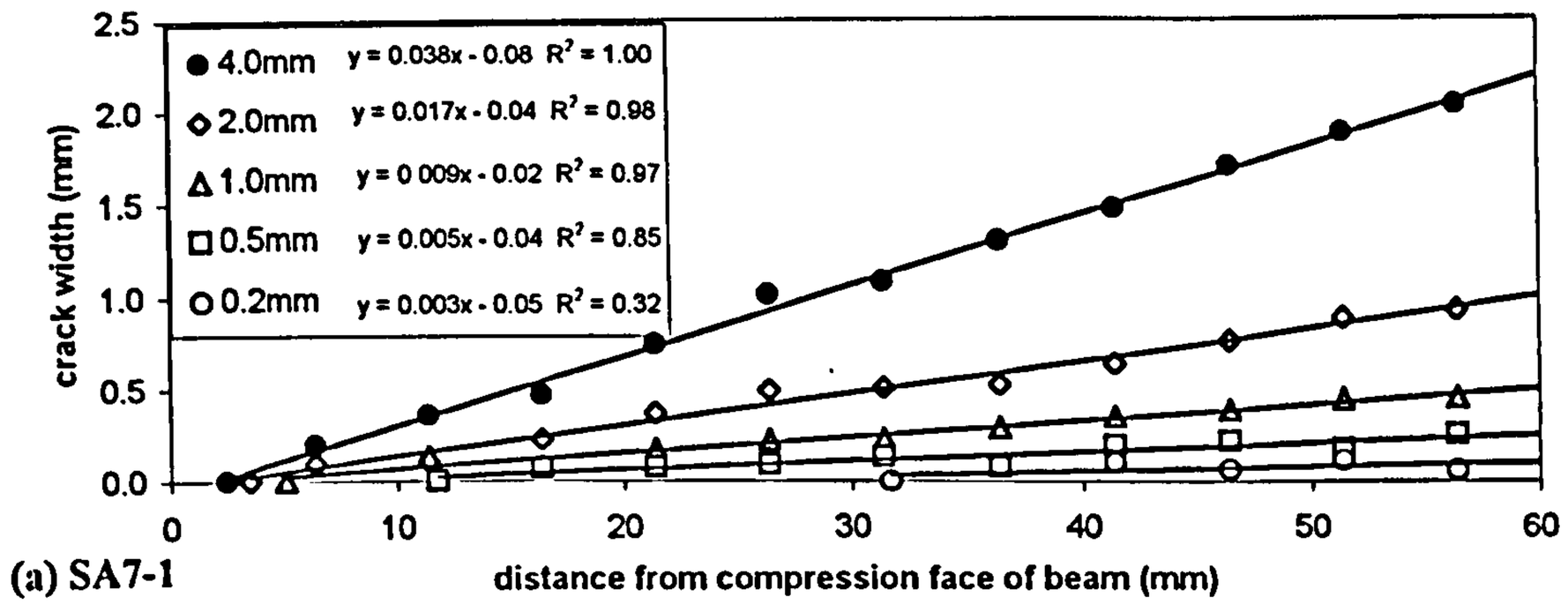

(a) SA7-1

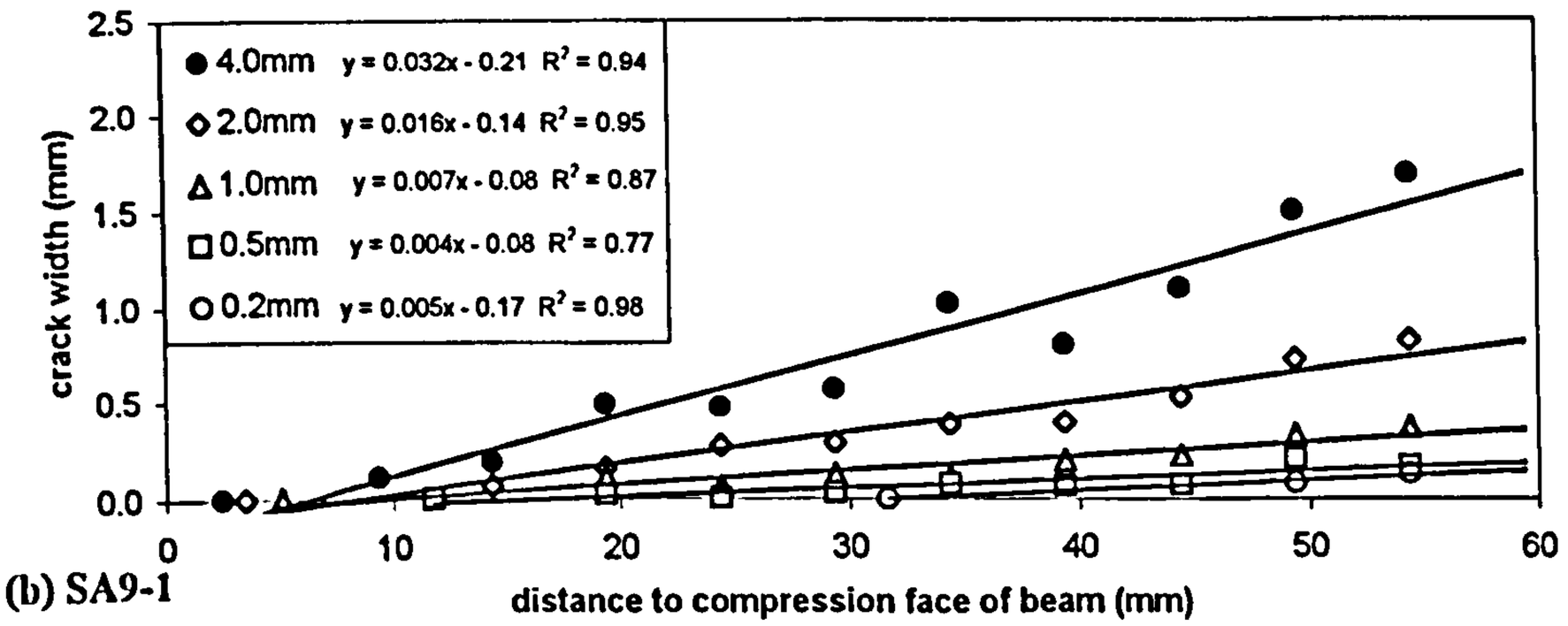

(b) SA9-1

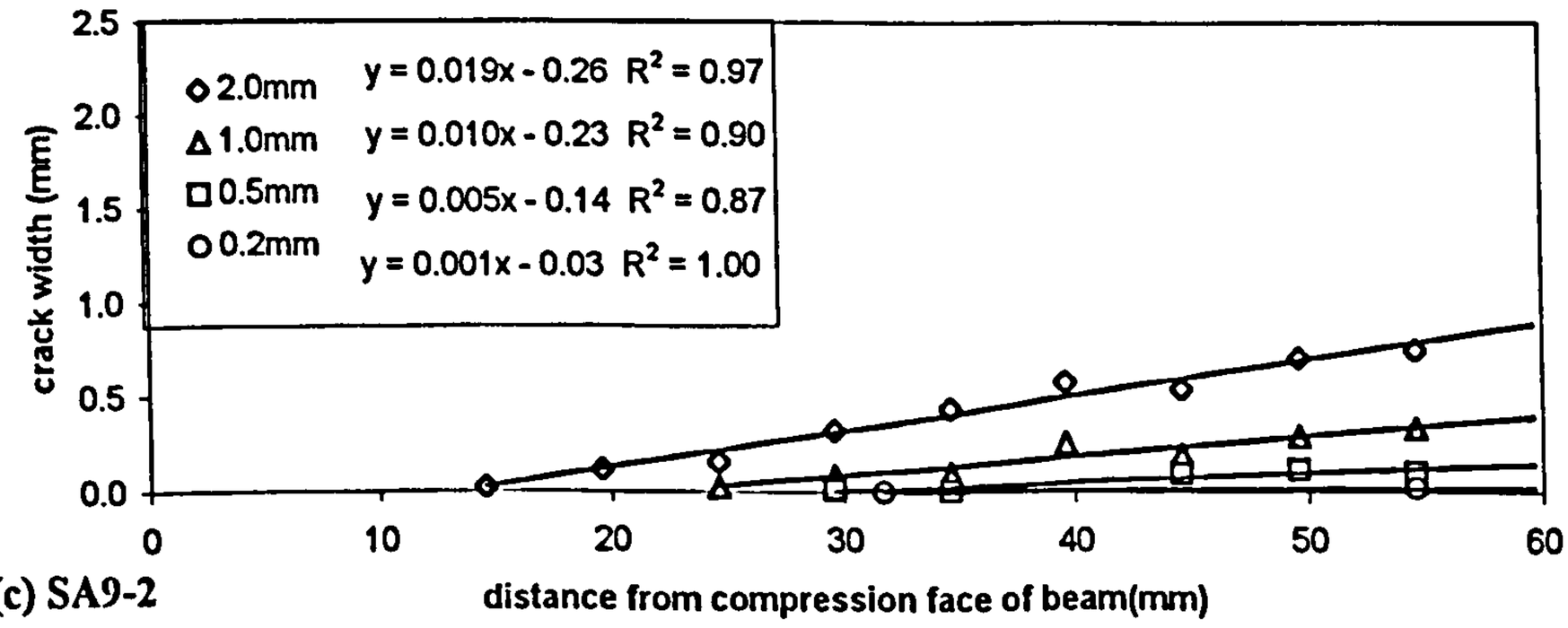

(c) SA9-2

Figure IV.4 60mm notched beams.

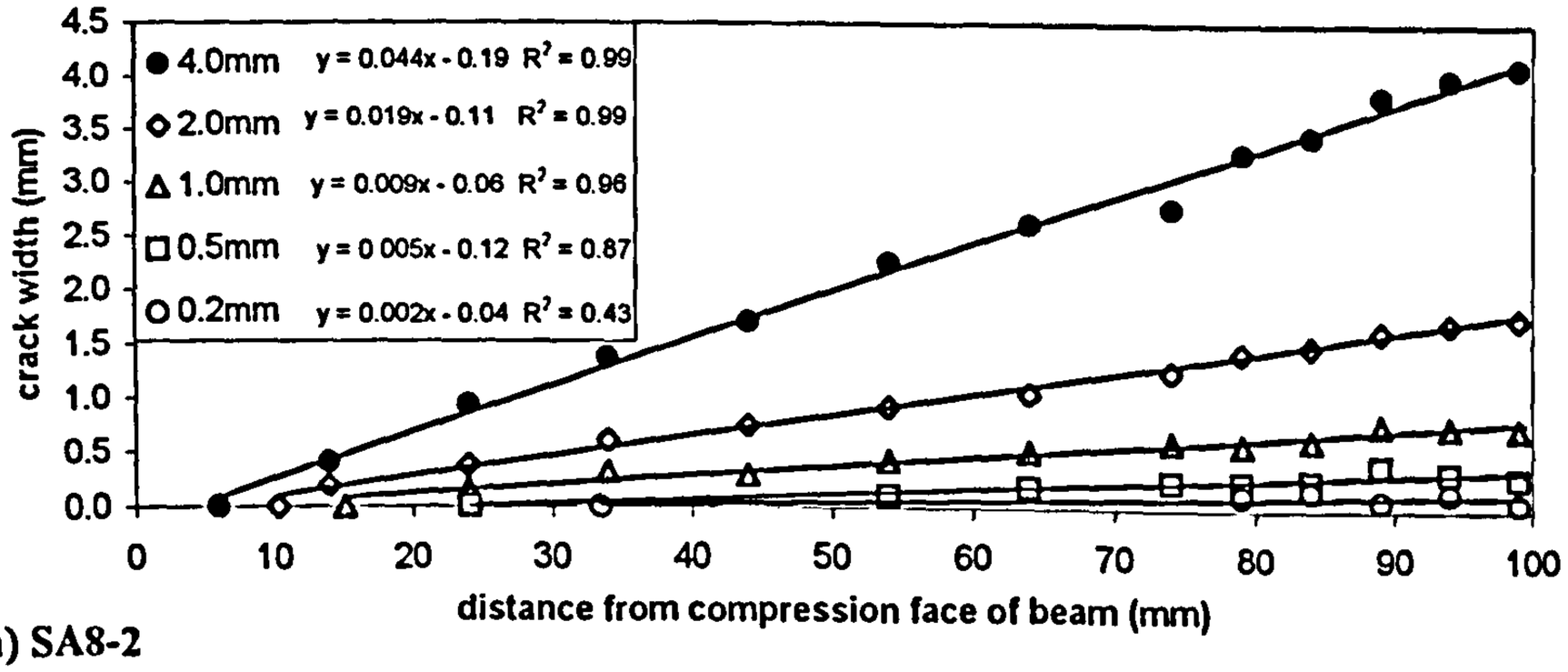

(a) SA8-2

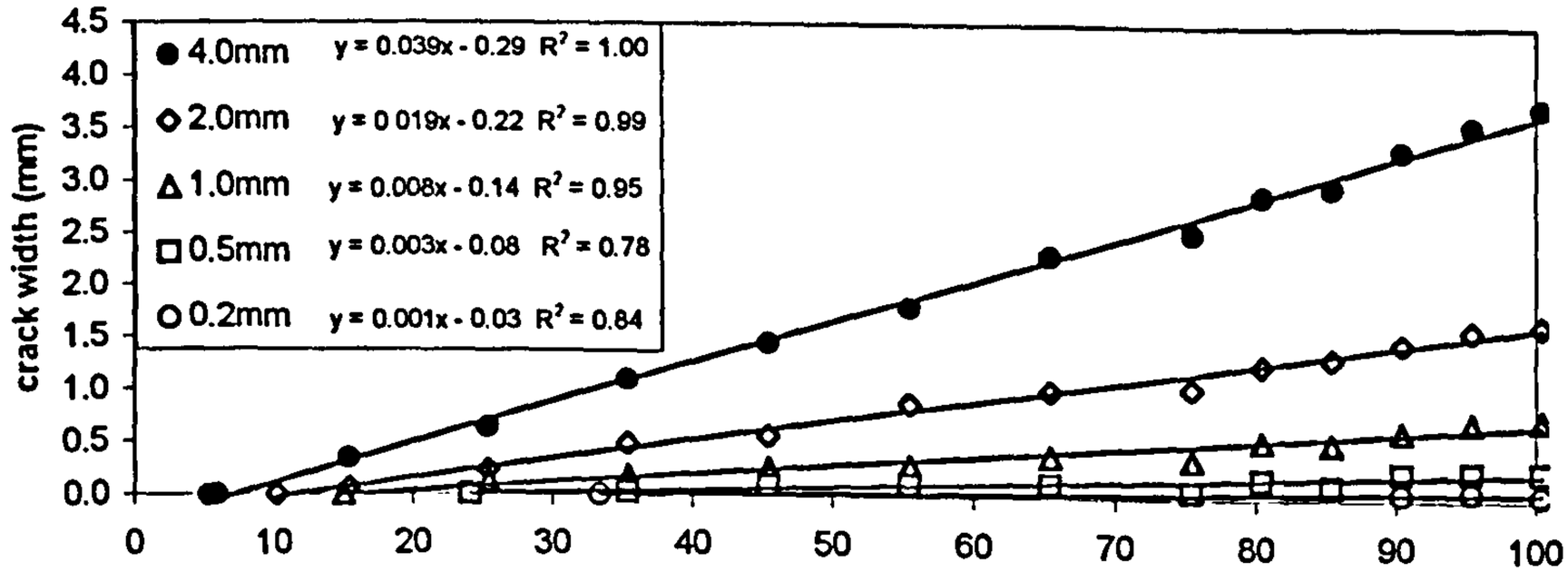

(b) SA10-3

Figure IV.5 100mm unnotched beams.

APPENDIX V

STRAIN ANALYSIS TEST BEAMS:

MEASURED VERSUS PREDICTED LOAD-DEFLECTION CURVES

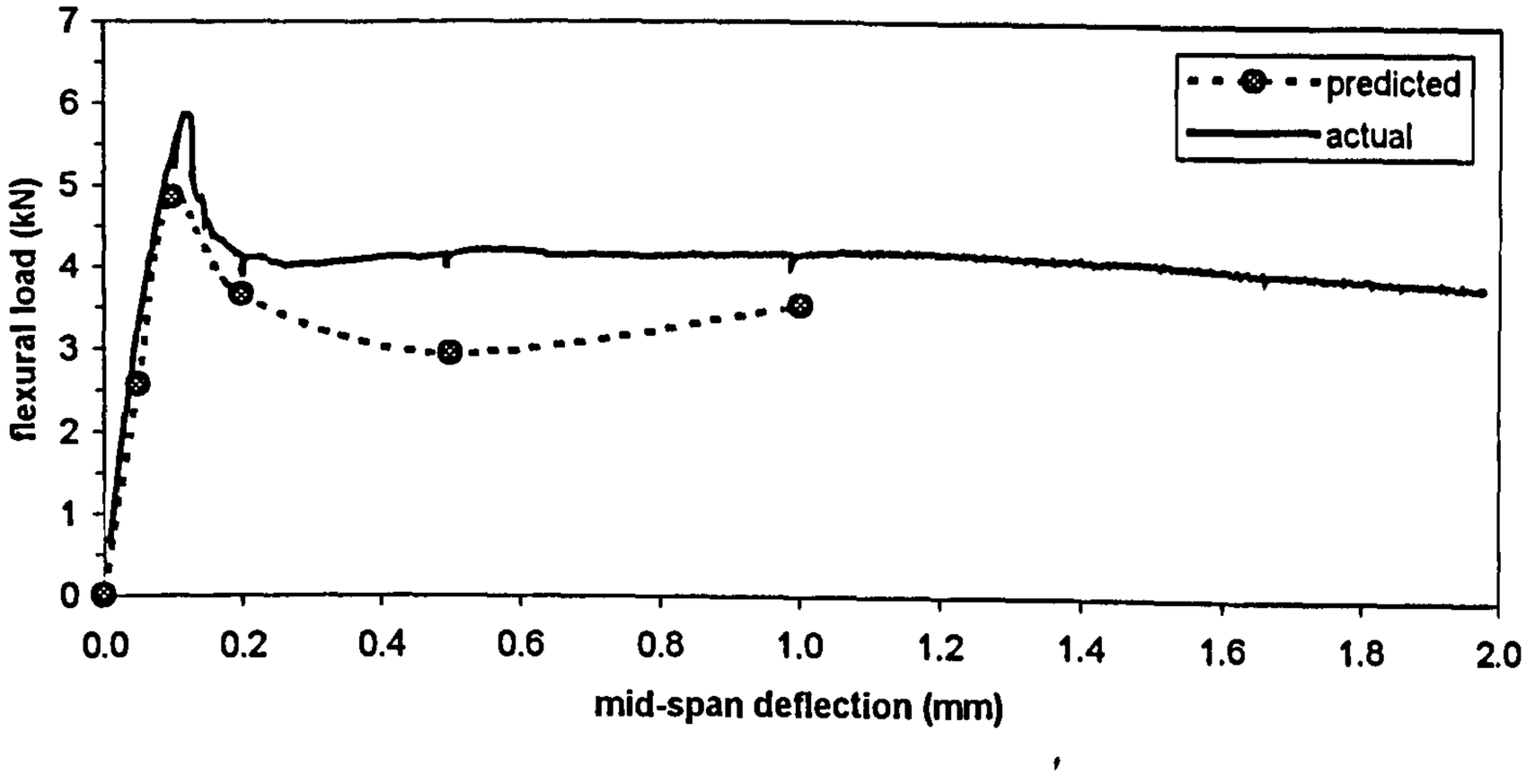

Figure V.1 Beam SA1-1.

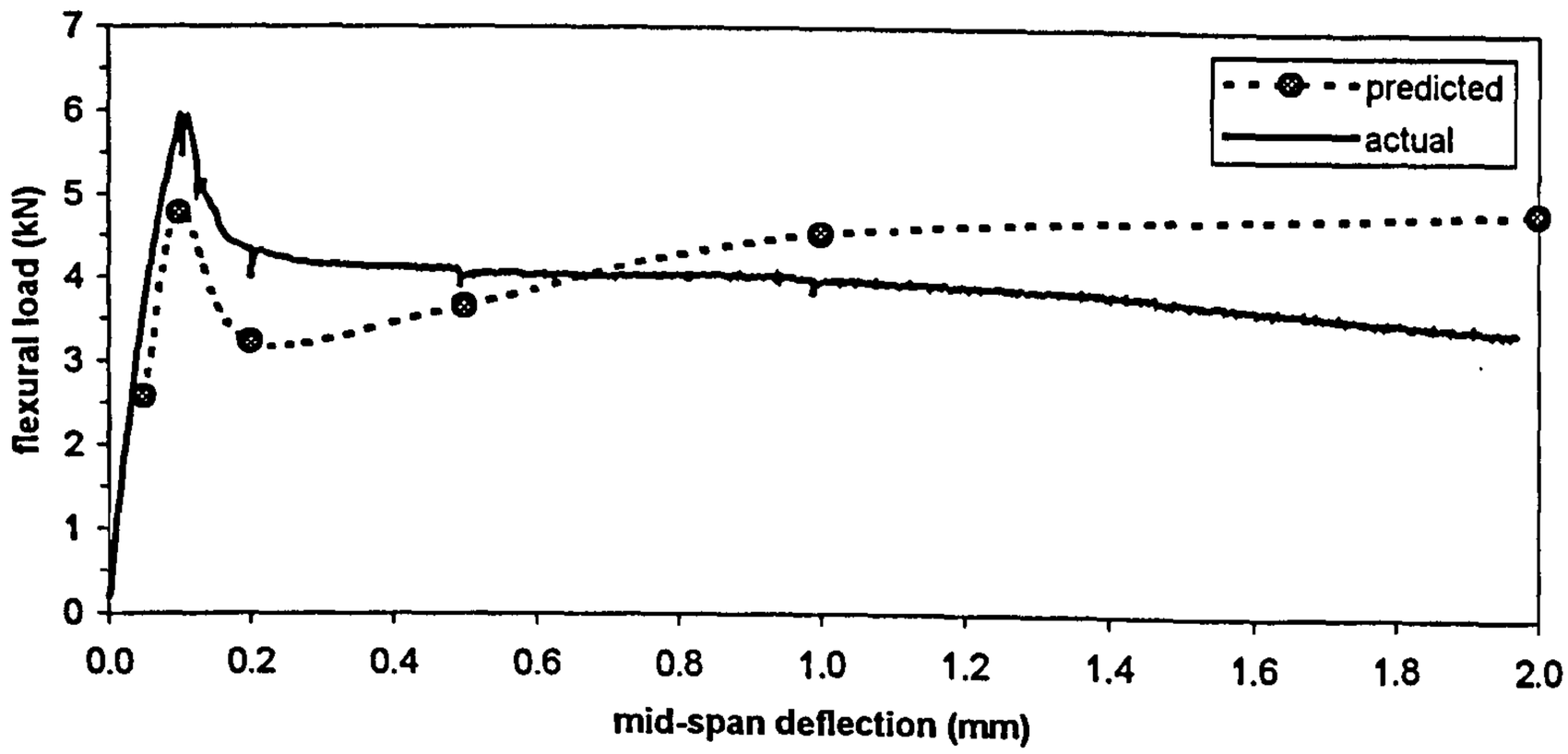

Figure V.2 Beam SA1-2.

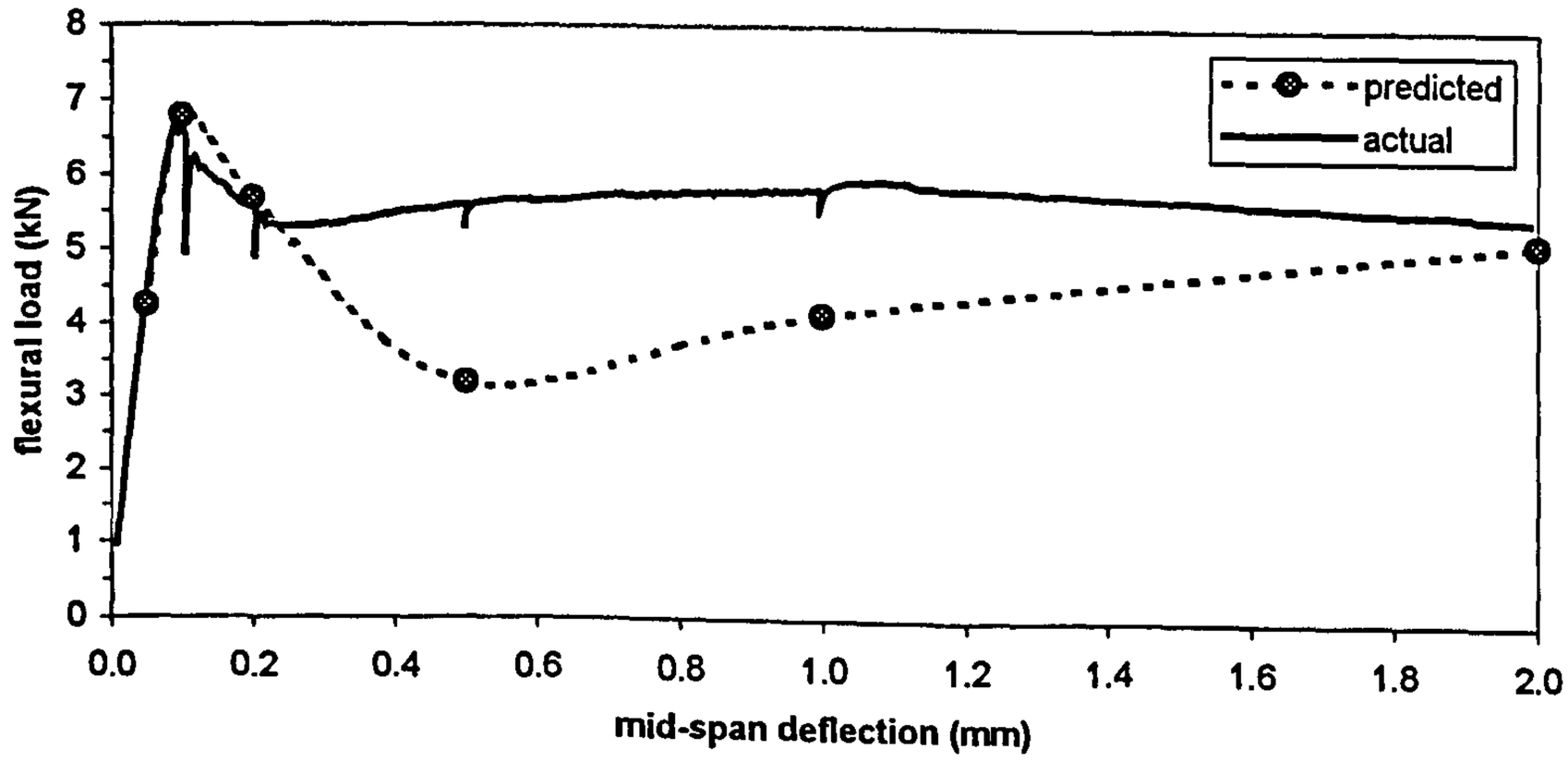

Figure V.3 Beam SA2-1.

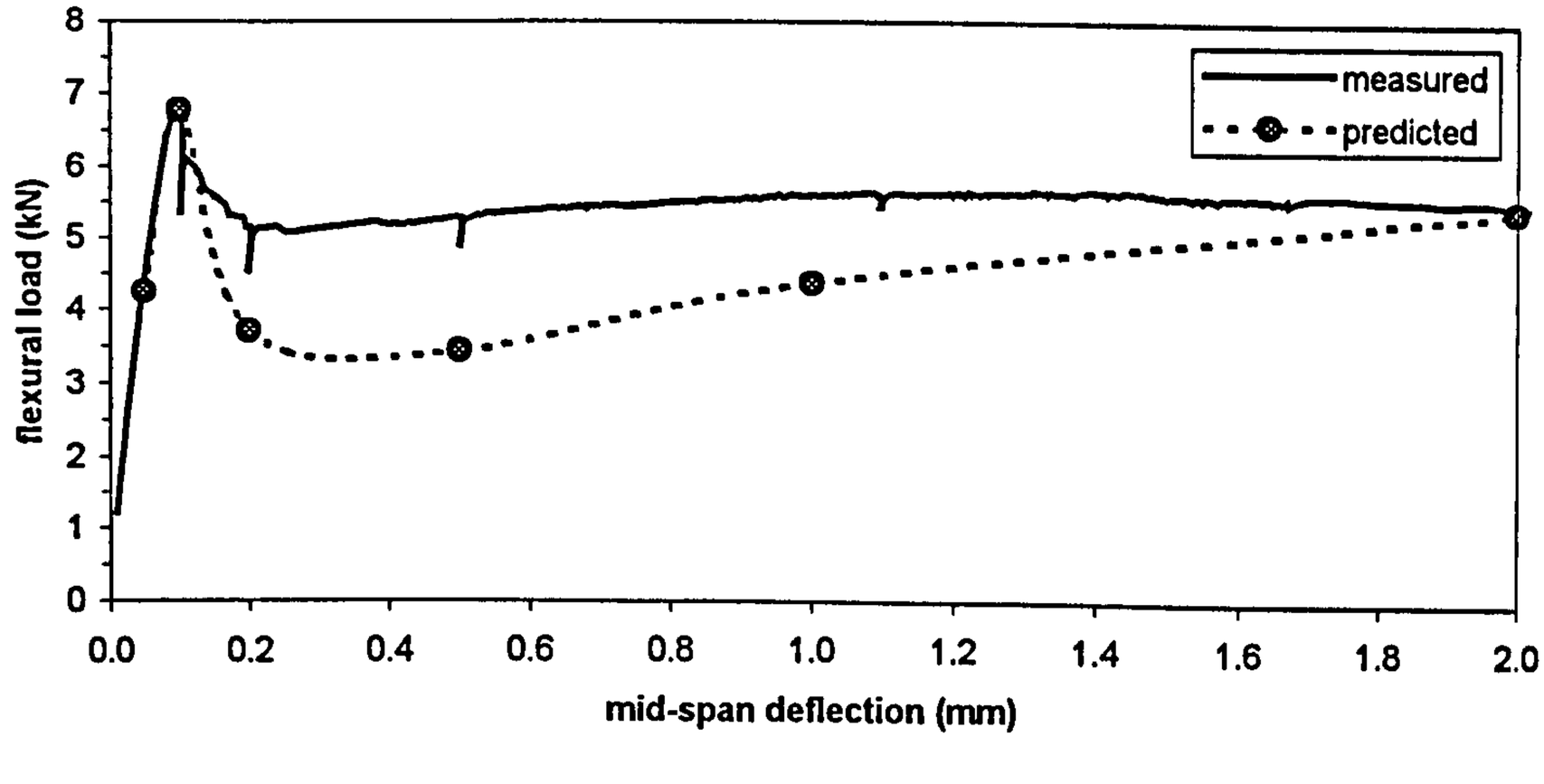

Figure V.4 Beam SA2-2.

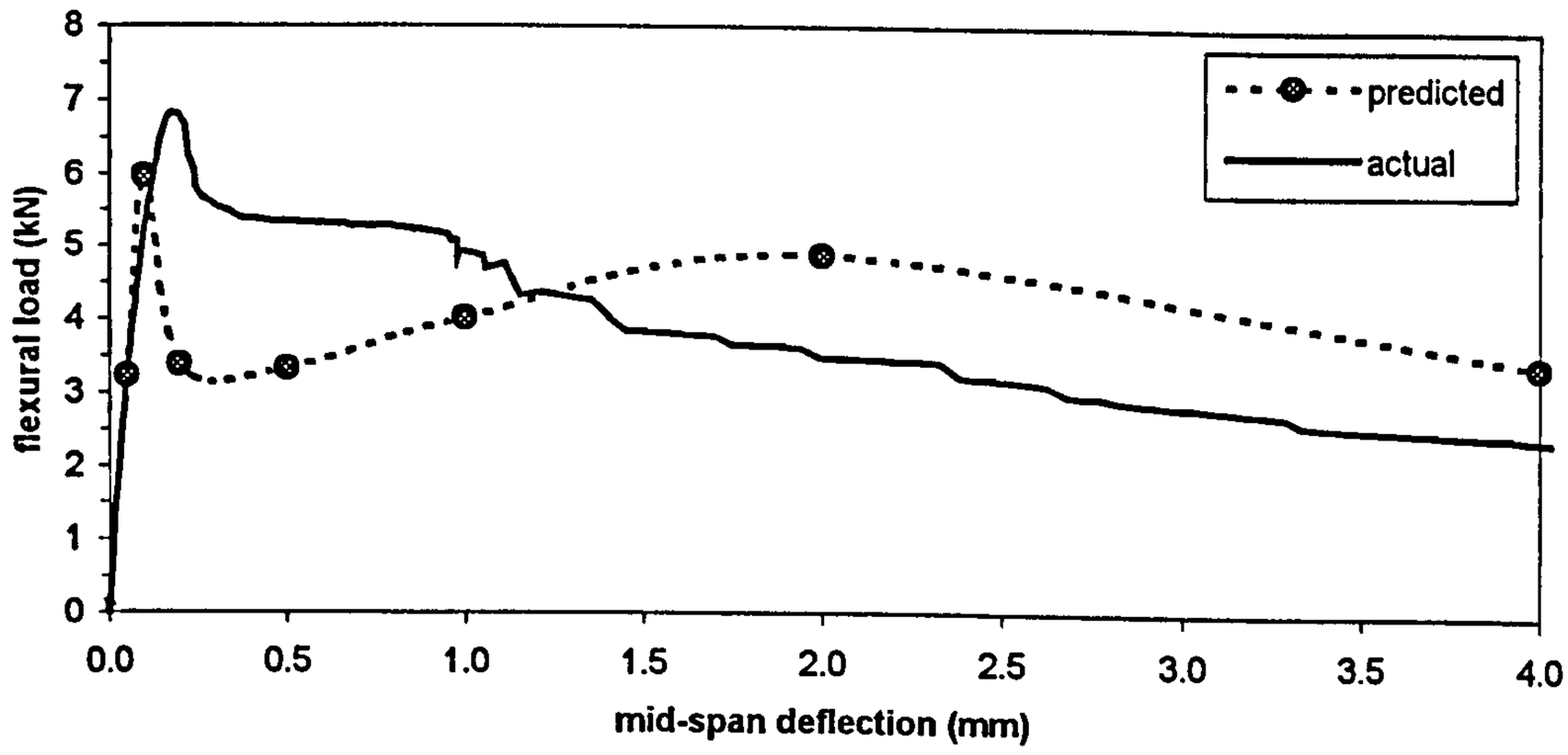

Figure V.5 Beam SA5-1.

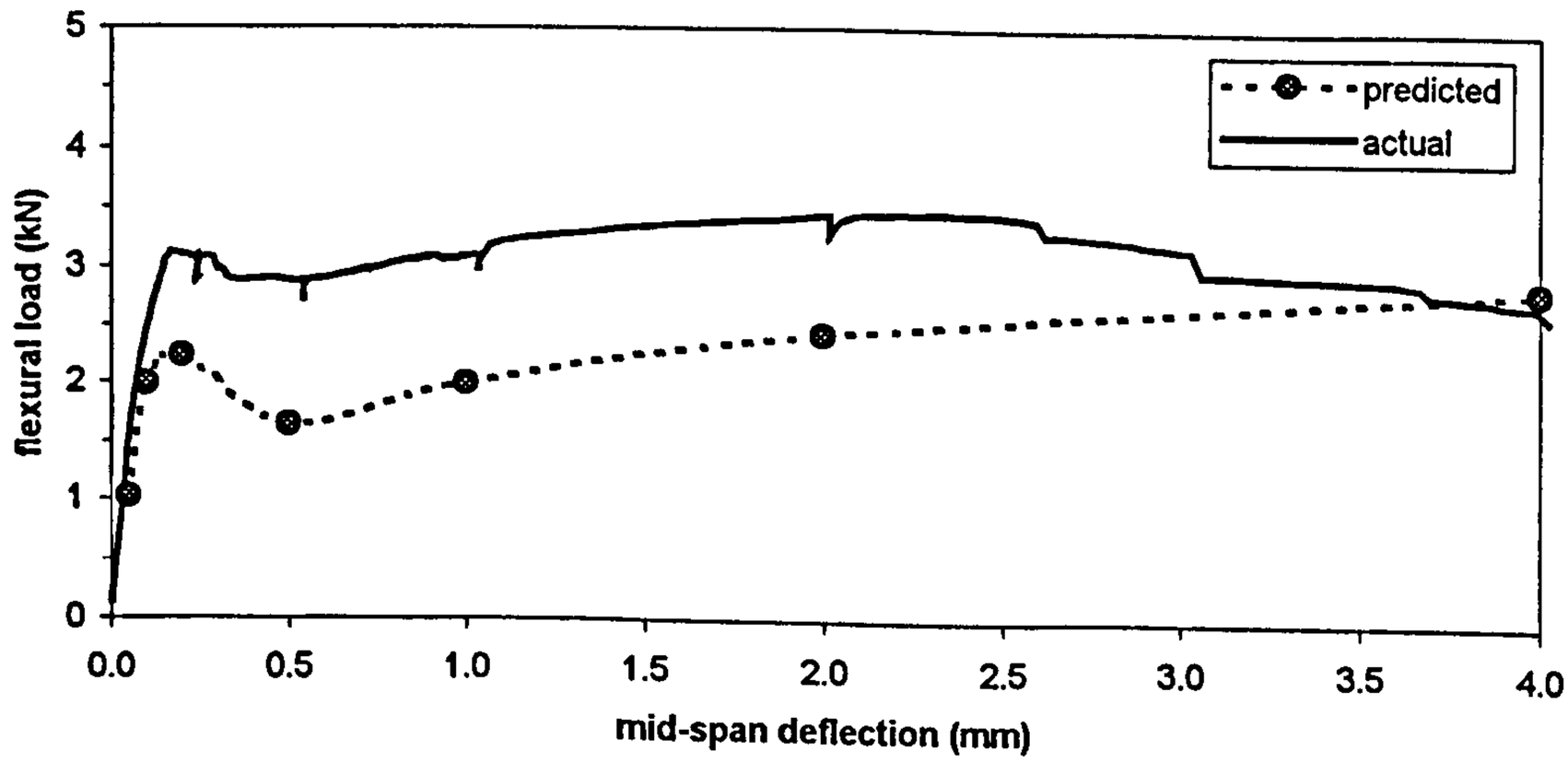

Figure V.6 Beam SA7-1.

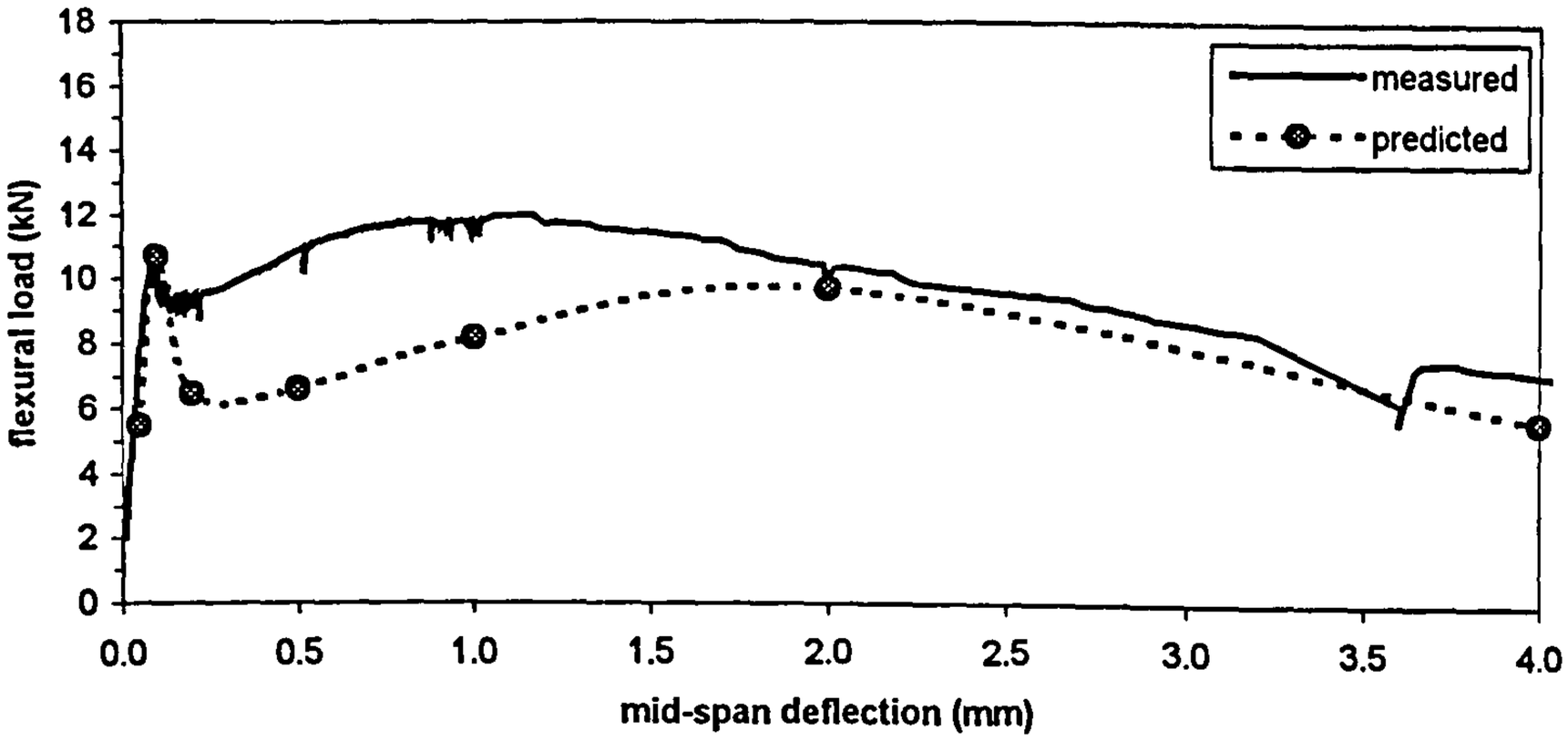

Figure V.7 Beam SA8-2.

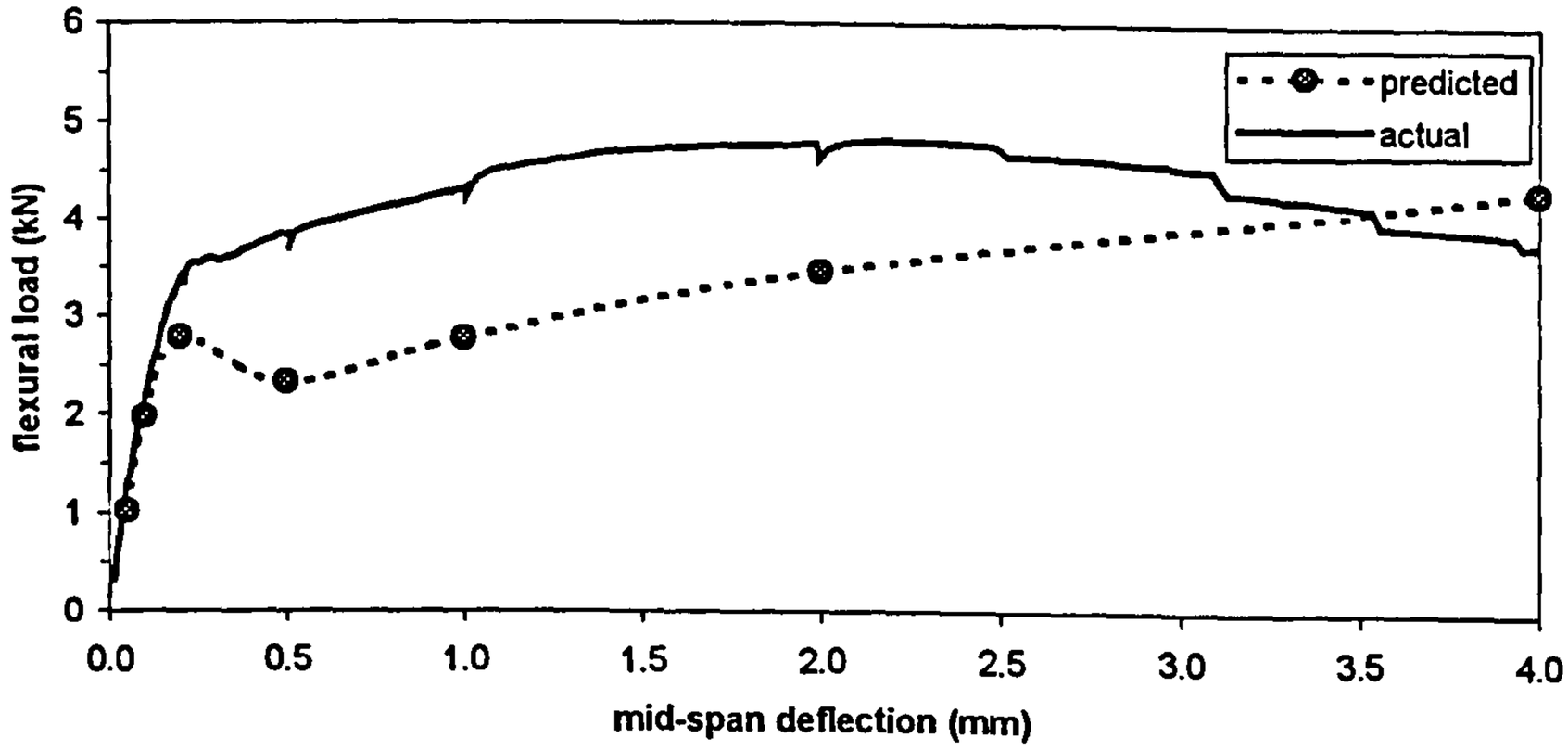

Figure V.8 Beam SA9-1.

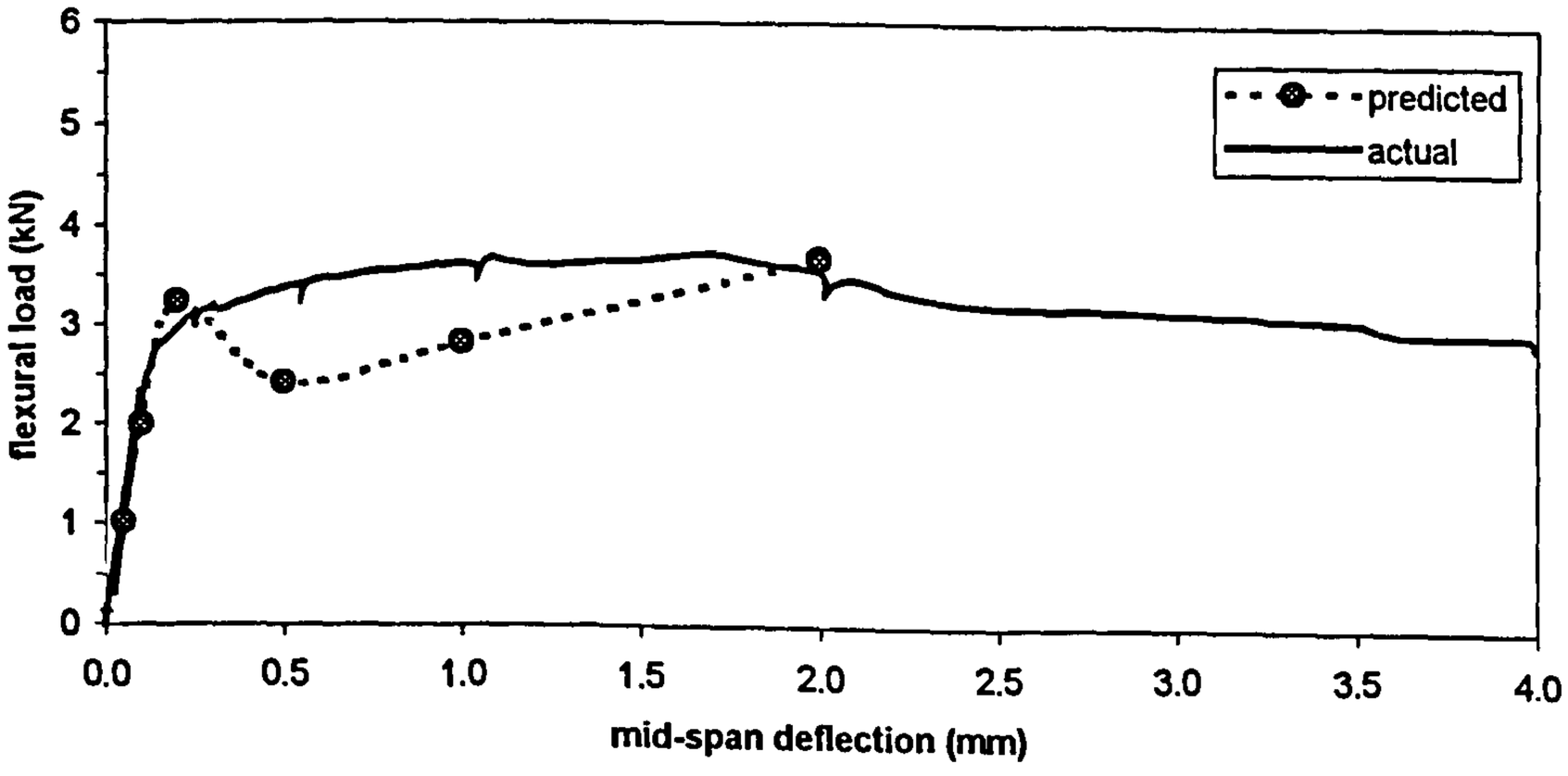

Figure V.9 Beam SA9-2.

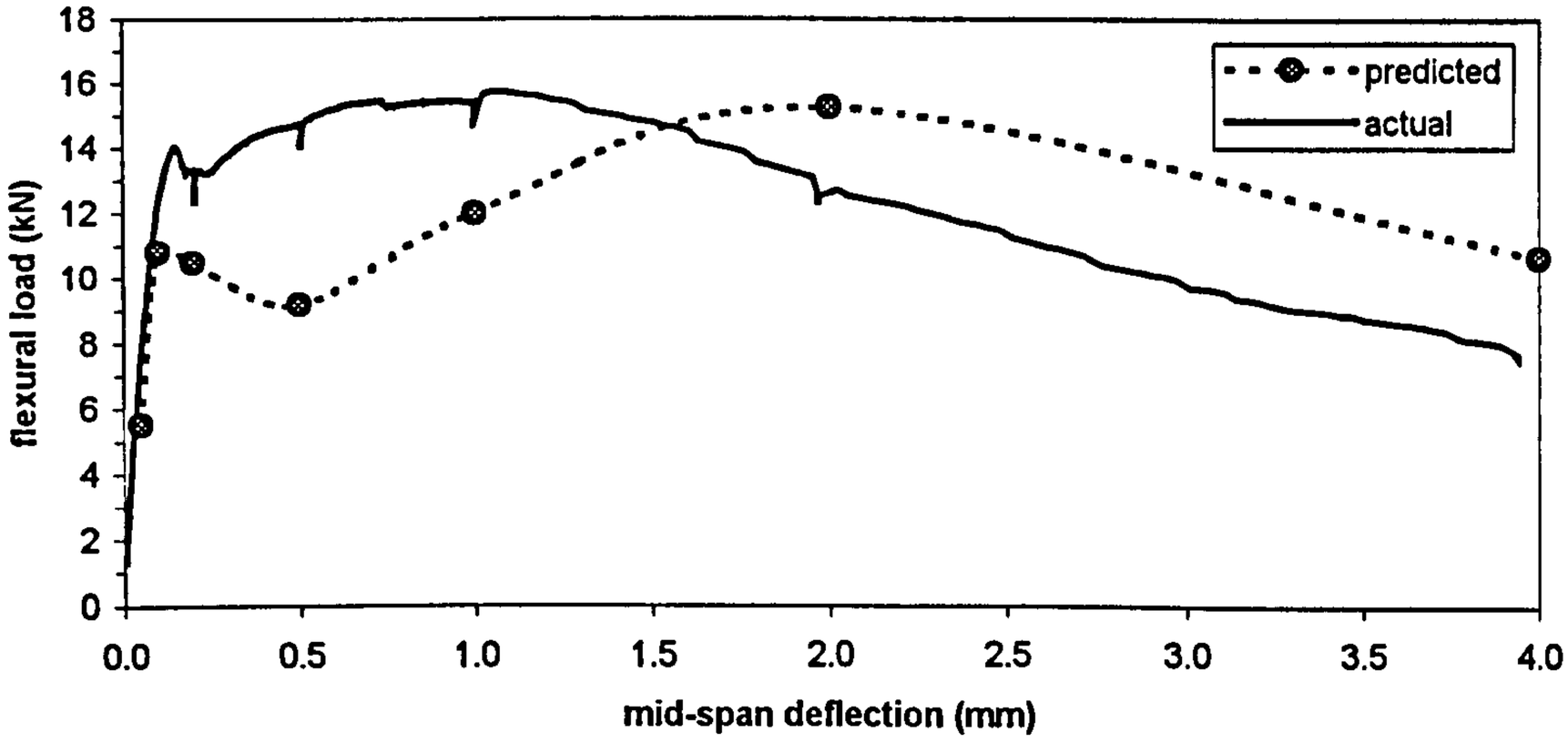

Figure V.10 Beam SA10-3.

APPENDIX VI

GENERALISED MODELLING ANALYSIS: MEASURED VERSUS PREDICTED LOAD-DEFLECTION CURVES

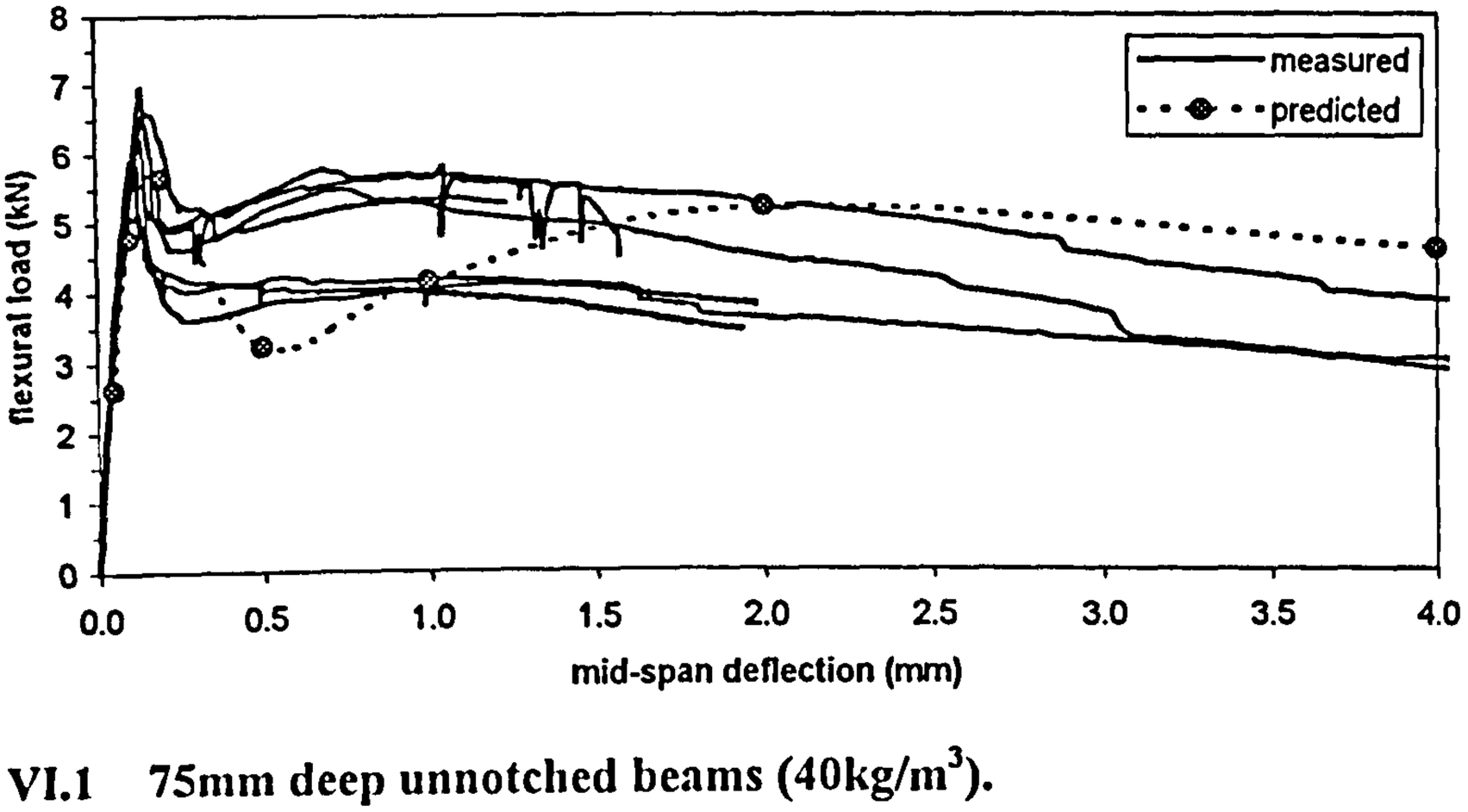

Figure VI.1 75mm deep unnotched beams (40kg/m^3).

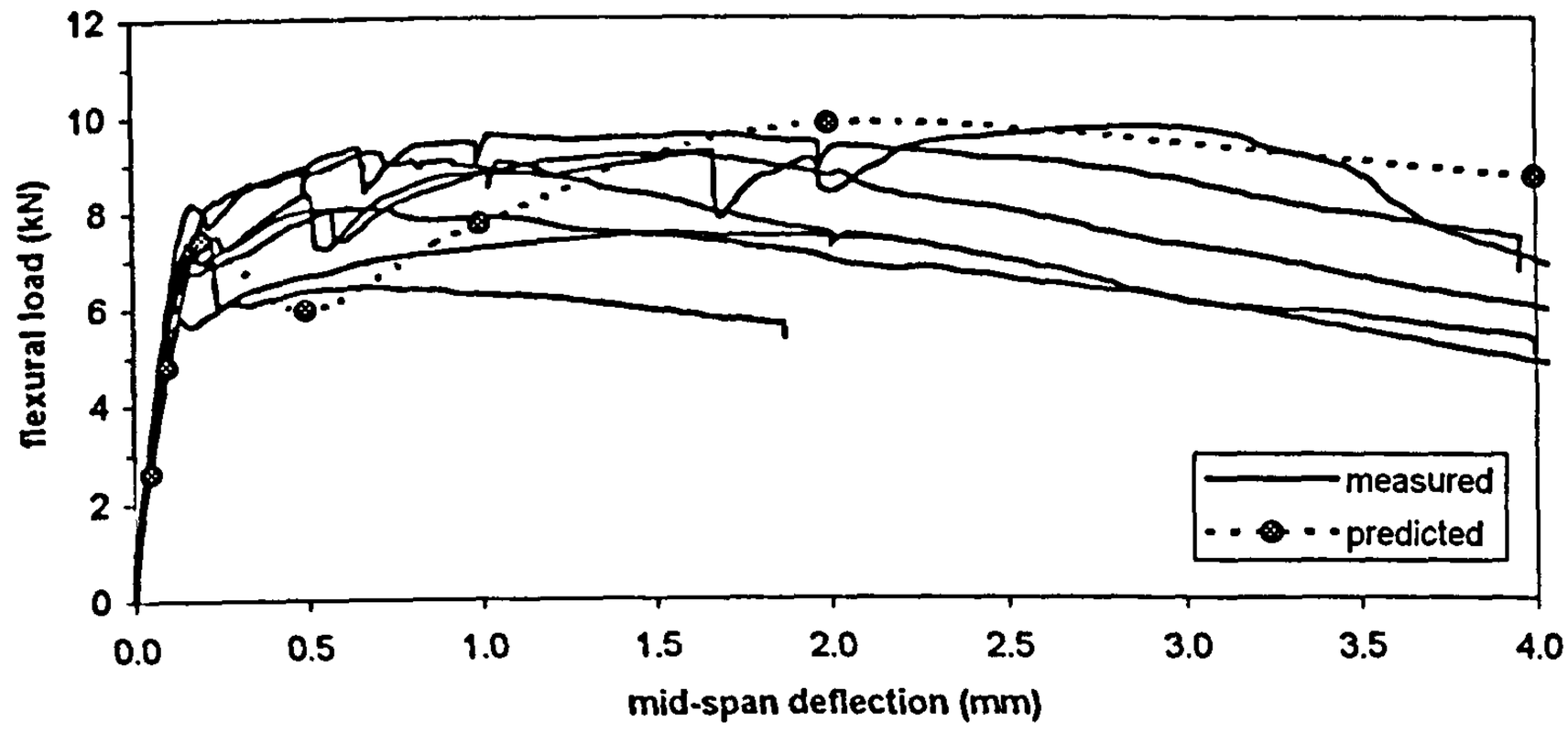

Figure VI.2 75mm unnotched beams (80kg/m^3).

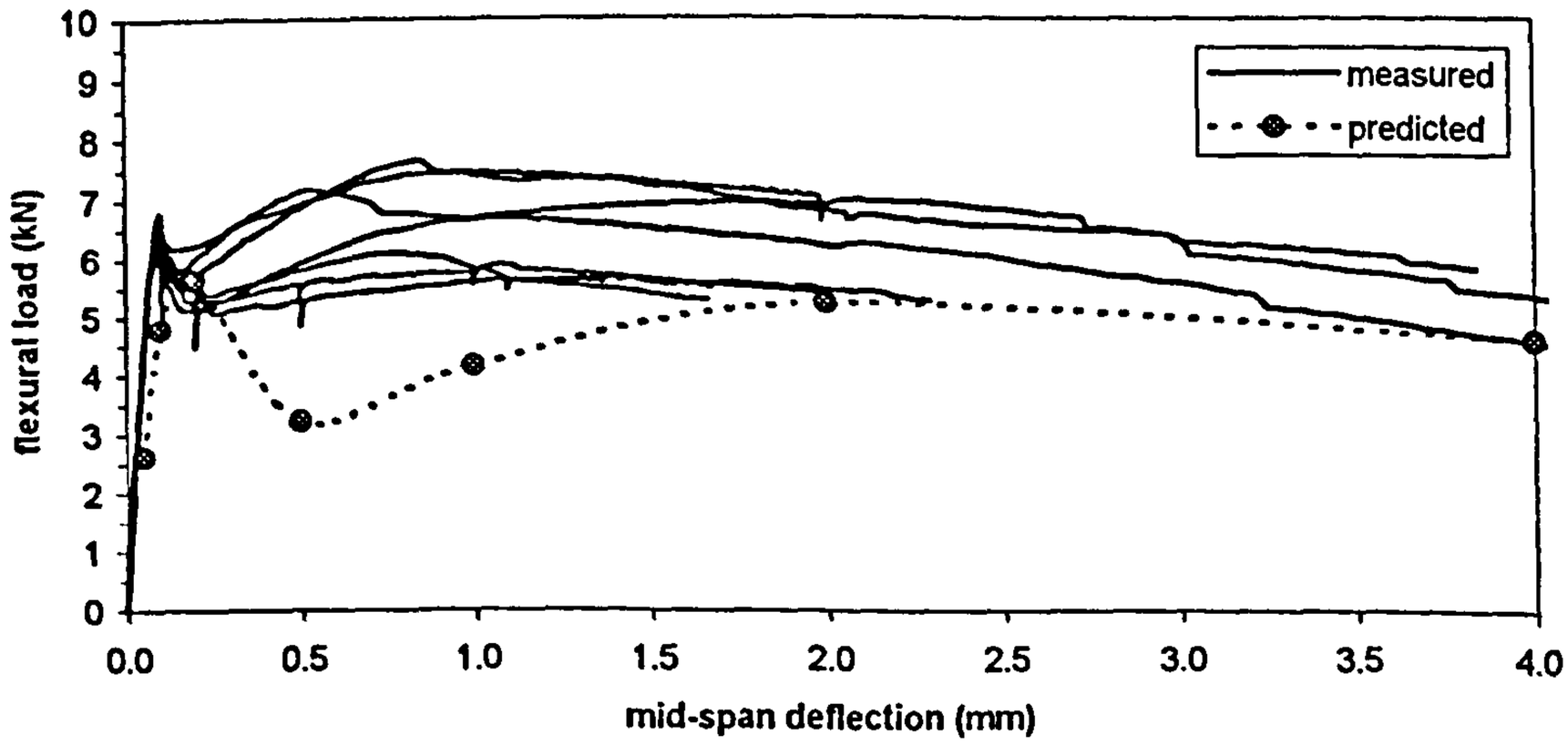

Figure VI.3 85mm notched beams (40kg/m^3).

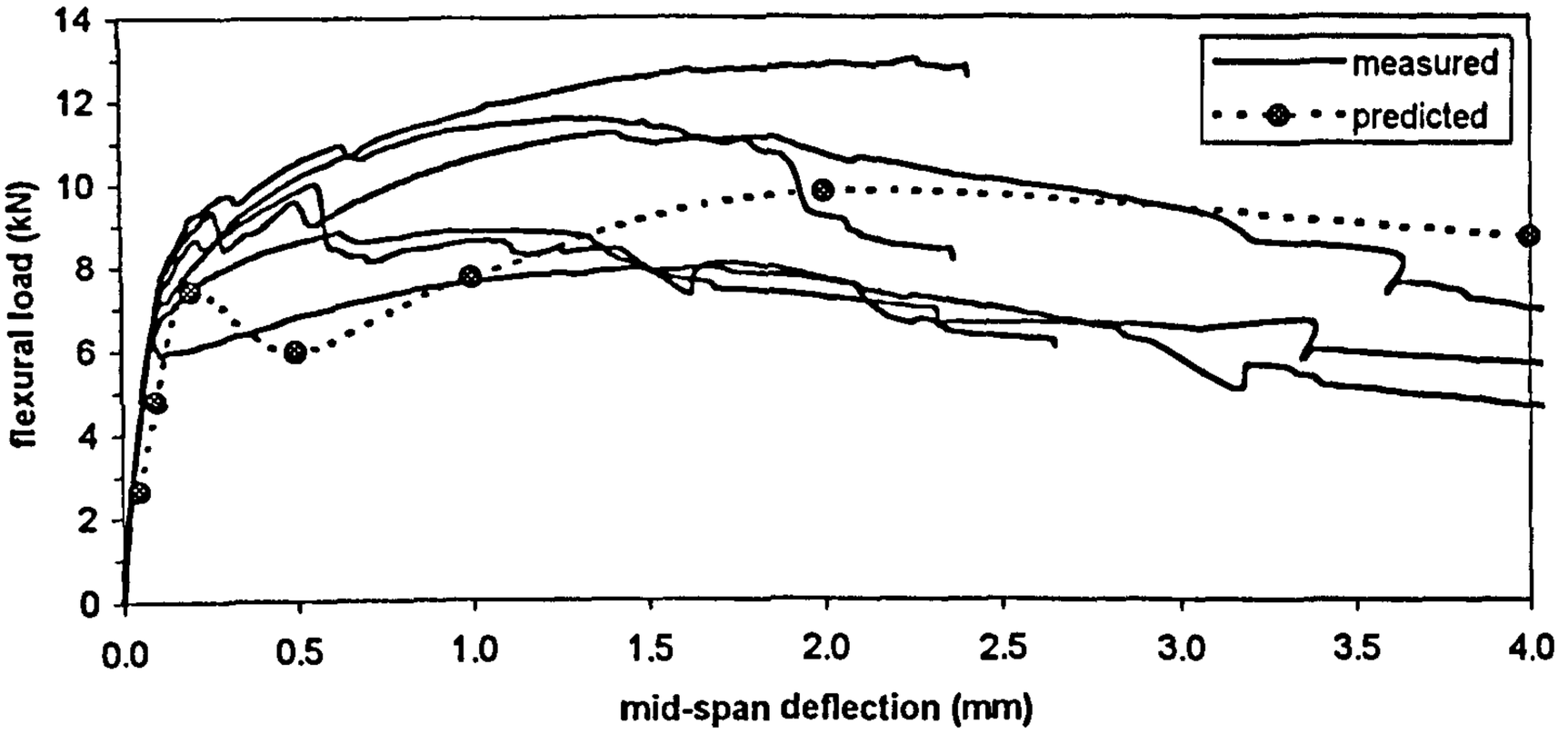

Figure VI.4 85mm notched beams (80kg/m^3).

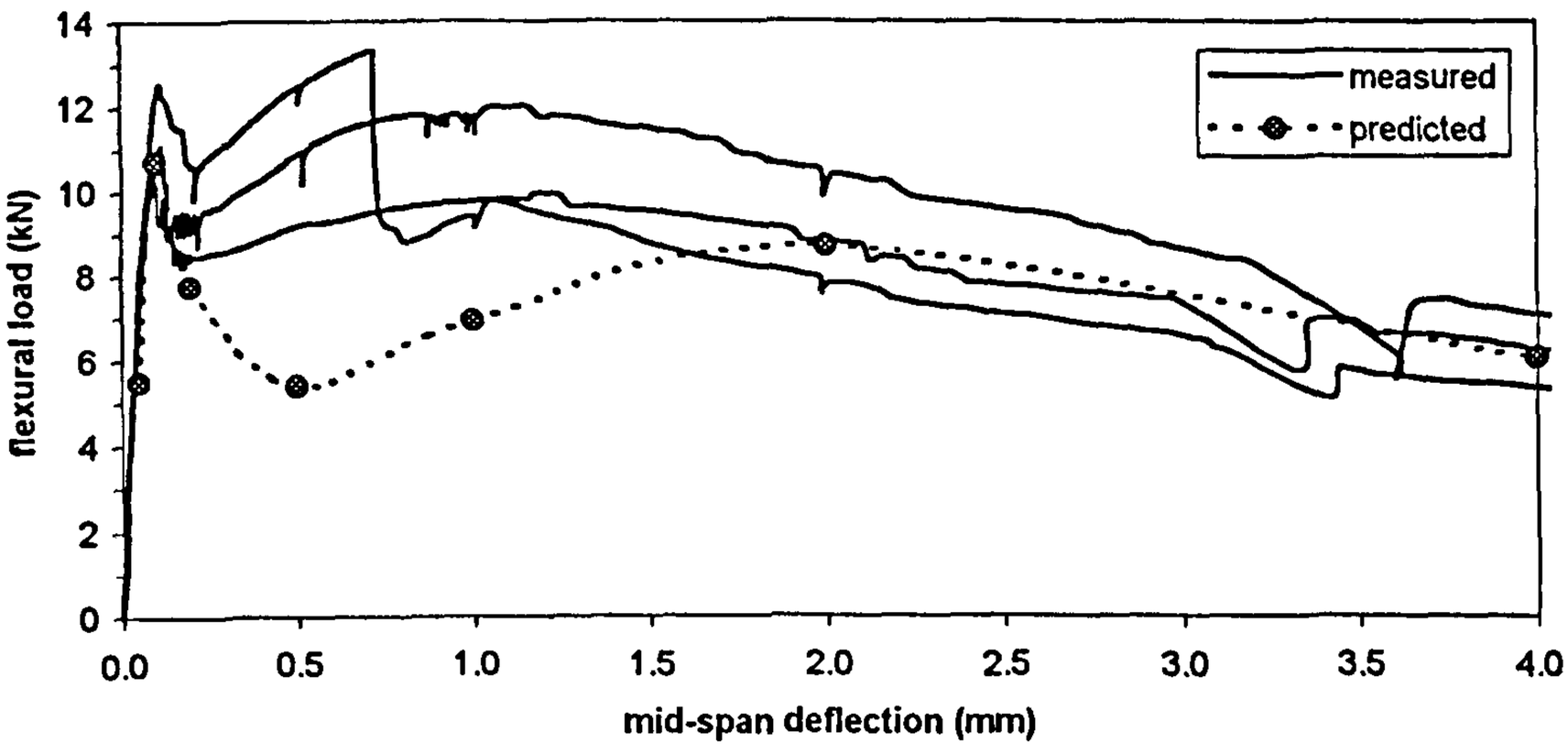

Figure VI.5 100mm unnotched beams (40kg/m^3).

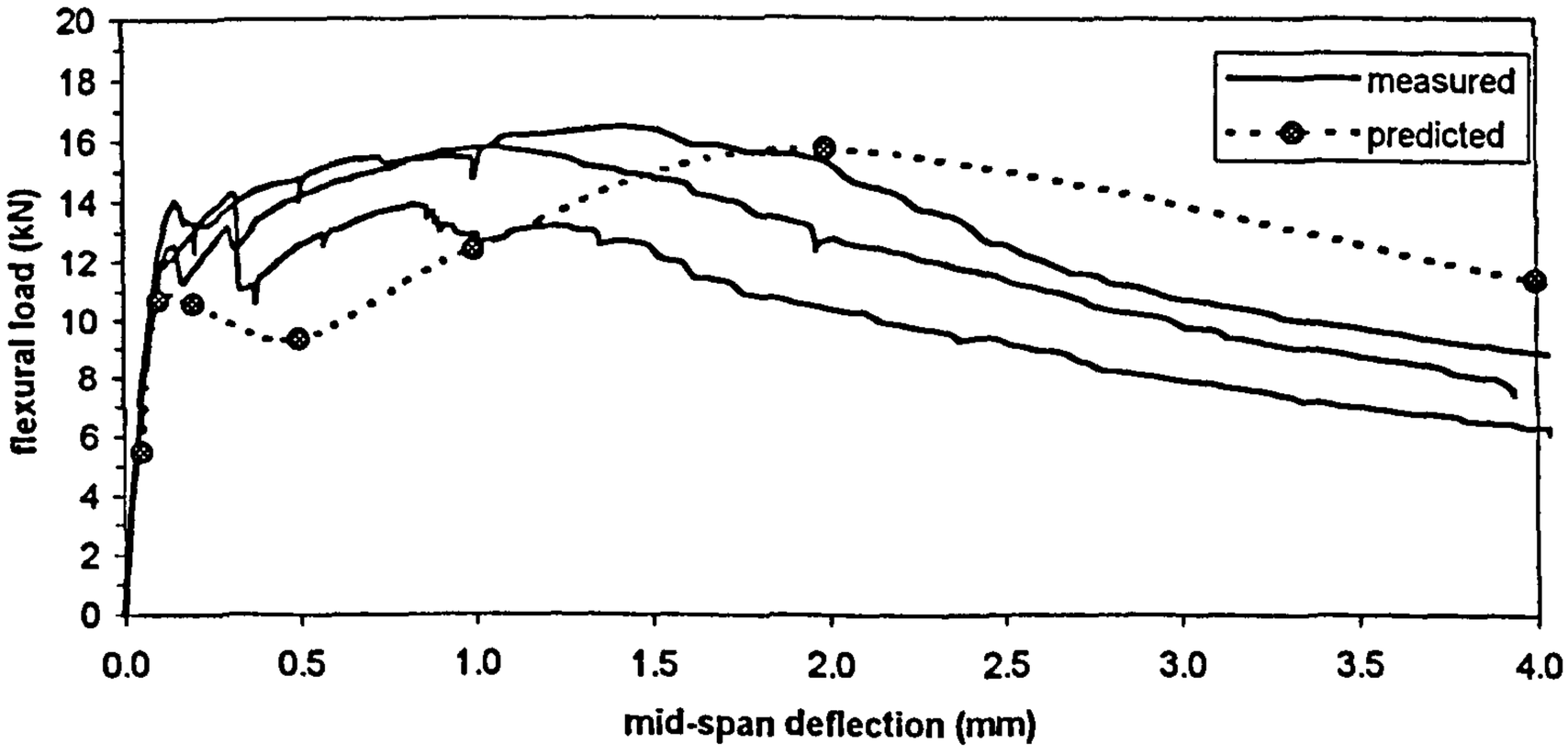

Figure VI.6 100mm unnotched beams (80kg/m^3).

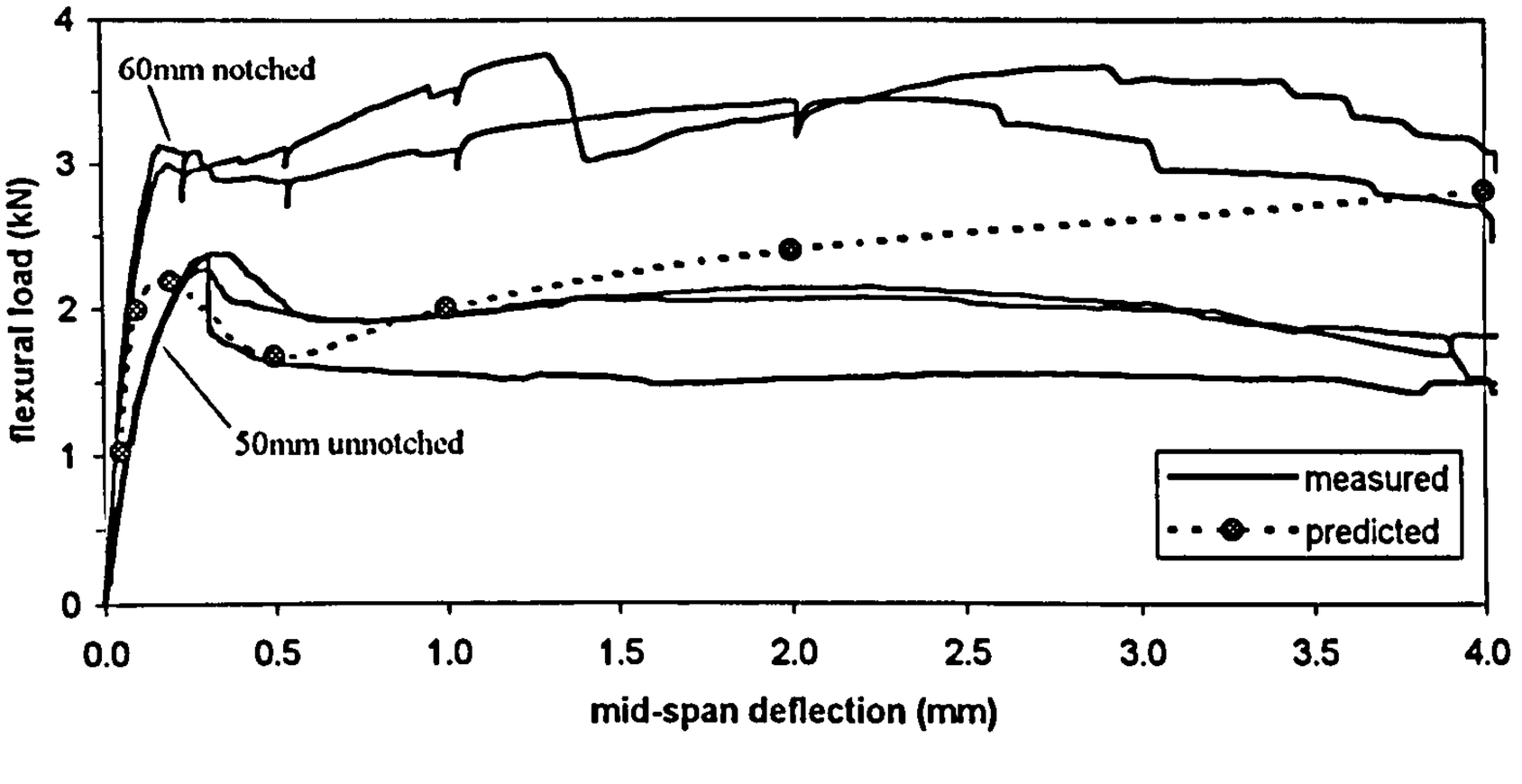

Figure VI.7 50mm unnotched/60mm notched beams (40kg/m^3).

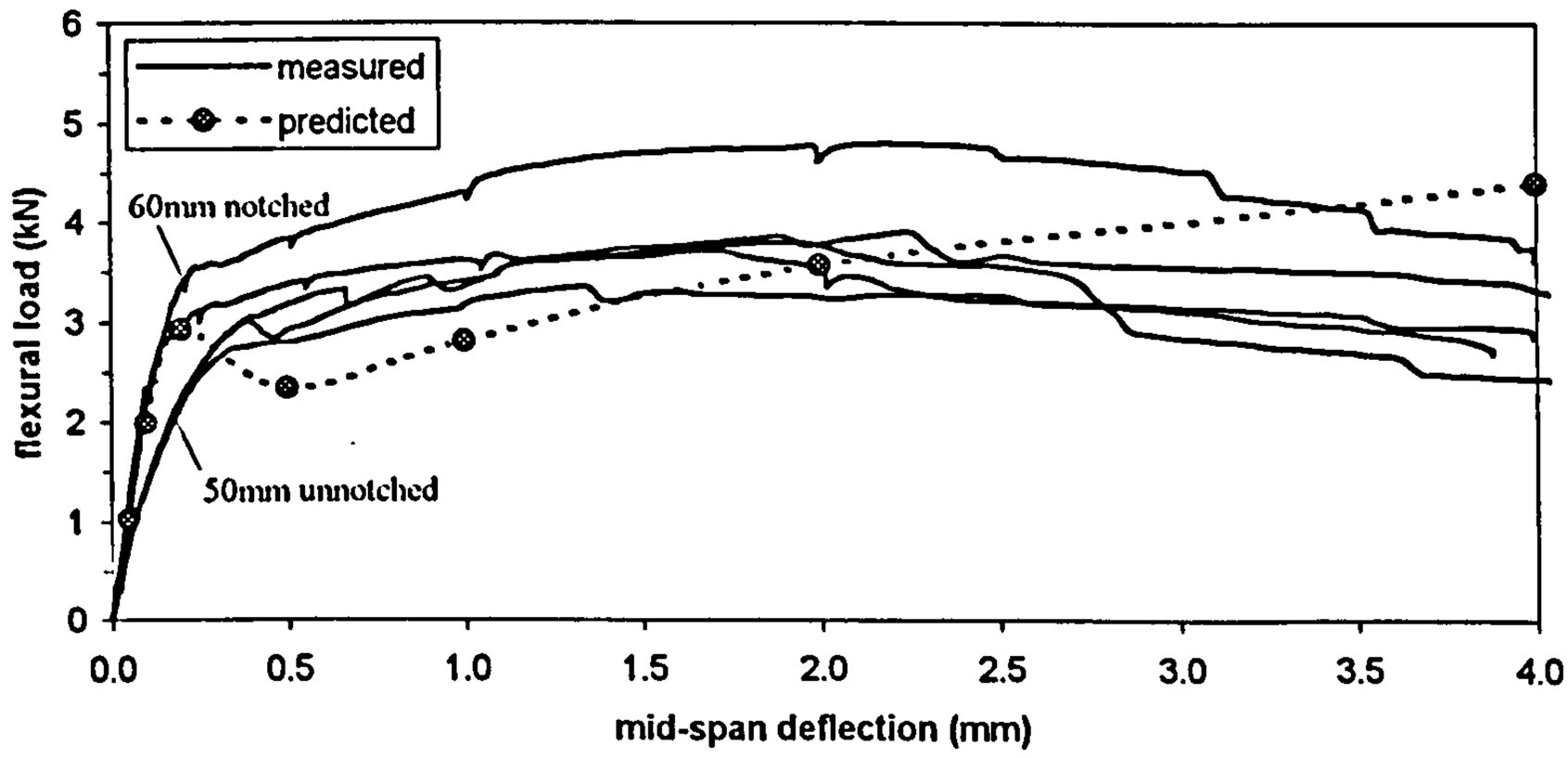

Figure VI.8 50mm unnotched/60mm notched beams (80kg/m^3).

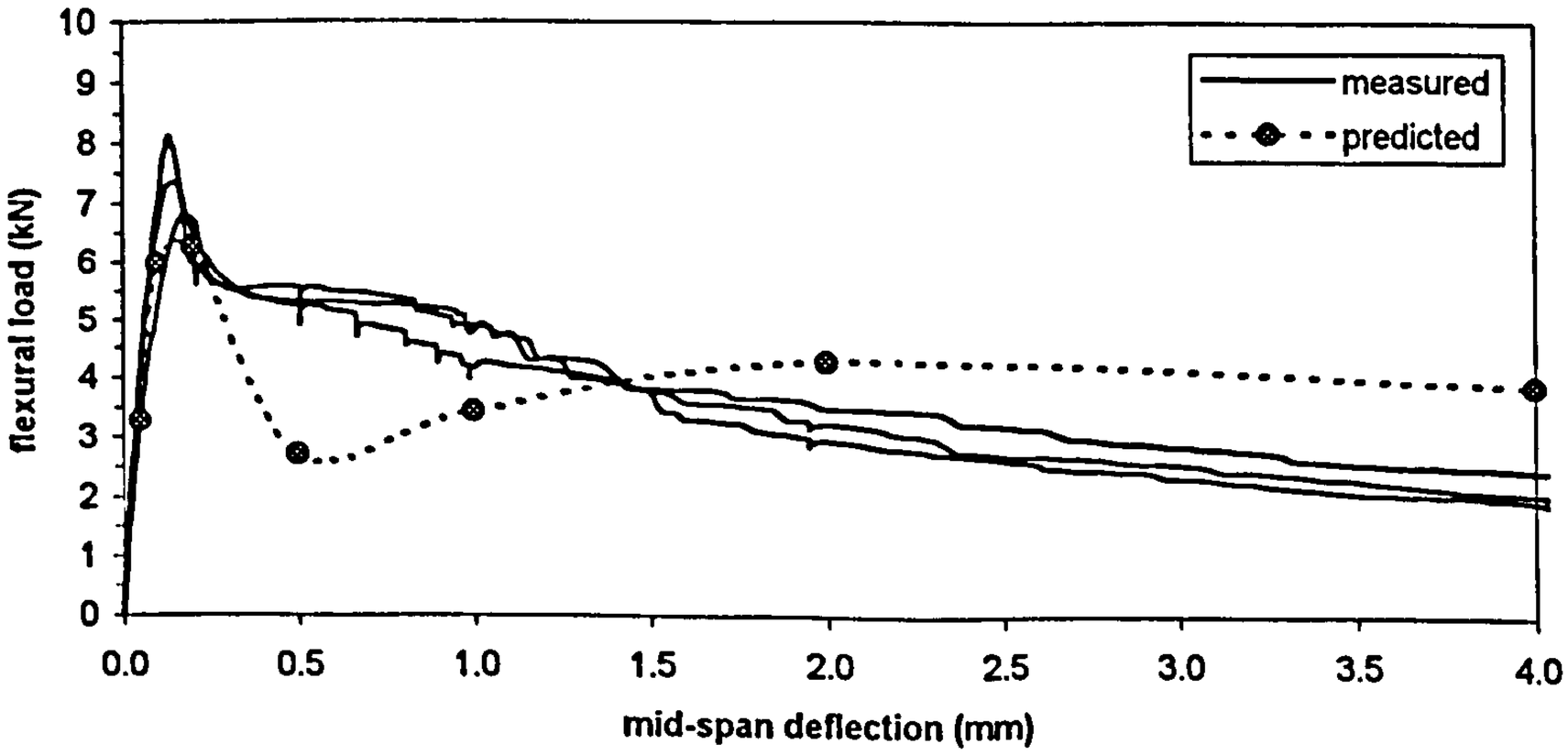

Figure VI.9 75mm sprayed beams (26kg/m^3).

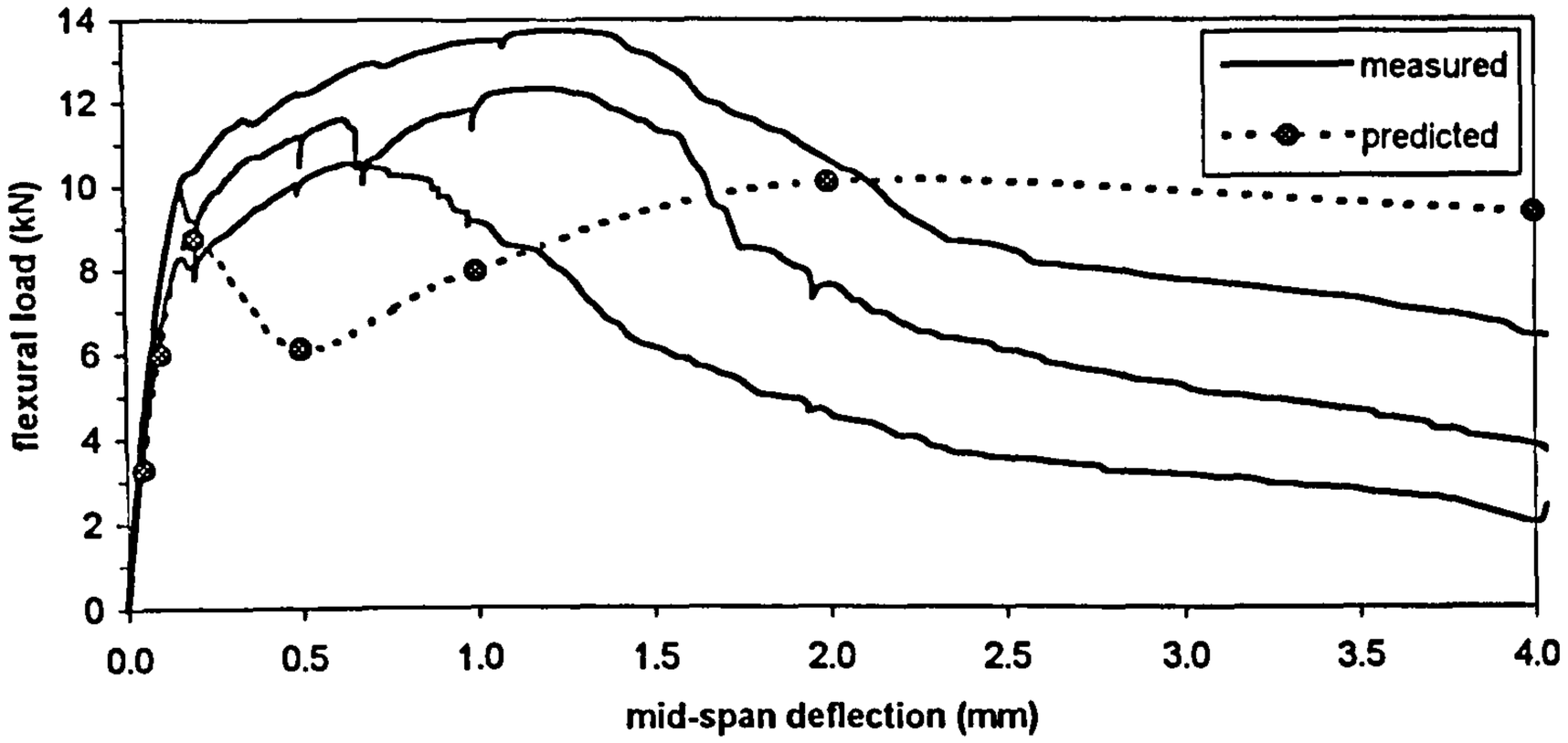

Figure VI.10 75mm sprayed beams (66kg/m^3).